EARTHQUAKE RESISTANT DESIGN

OF REINFORCED CONCRETE WALLS

A thesis submitted for the degree of Doctor of Philosophy
in the Faculty of Engineering of the University of London
and for the Diploma of membership of Imperial College

by

Kypros Pilakoutas BSc (Eng), ACGI

Engineering Seismology and Earthquake Engineering Section

Civil Engineering Department

Imperial College of Science Technology and Medicine

University of London

May 1990

To my father

for teaching me

Pursuit of Knowledge

Who as a young boy jumped off the bicycle of his rich uncle who was taking him to be registered at the secondary school.

Στον πατερα μου

που με διδαξε

Αγαπη για μαθηση

Που πηδηξε κατω απο το ποδηλατο του πλουσιου θειου του, καθ οδον στο γυμνασιο για εγγραφη.

To my grand father

for teaching me

Courage and Perseverance

Στον παππου μου

που με διδαξε

Θαρρος και επιμονη

and

To my mother

for teaching me

Patience

και

Στην μητερα μου

που με διδαξε

Υπομονη

ABSTRACT

This thesis deals with aspects of earthquake resistance of reinforced concrete (RC) walls, including experimental testing results, analytical studies and design considerations.

The experimental research programme was conducted on scaled RC models, which were tested under shaking table and cyclic loading conditions. A procedure suitable for small scale dynamic modelling of RC members was developed. A comprehensive presentation of the experimental set-up, instrumentation, control and manufacture of models is undertaken and a full description of the experiments and results is provided. A number of reinforcement patterns were employed and different failure modes were observed.

A computer program was developed for the analysis of the tested elements based on the method of section analysis. Cyclic material models were used for both steel and concrete. For steel, a modified massing model with stiffness degradation was developed and calibrated to experimental results. For concrete, the cyclic model implemented takes into account the beneficial effects of the confining reinforcement. The flexural deformations are established first and a shear model is proposed for calculating the shear deformations. The flexural model was used in conducting a parametric study which included the main quantities that affect the behaviour of RC members.

The results from both the experimental and analytical programmes are critically appraised. Good agreement between the analytical and experimental limit states was observed. Differences in the results arise mainly due to the expansion of the wall as a consequence of imperfect crack closure. Comparisons and discussion of all results is presented.

A method of assessing of the plastic hinge length is proposed. A procedure for designing for ductility is discussed. A new approach to design for shear was developed from first principles and demostrated to yield significant reduction in shear reinforcement without affecting ductility and energy absorption capacity. The different parameters affecting the shear capacity are discussed.

ACKNOWLEDGEMENTS

I would like to express my deepest gratitude to my supervisors, Dr. Amr S. Elnashai for his continuous support and inspiration, even when the project seemed to be starved of funding at birth, and Professor Nicholas N. Ambraseys for his encouragement and lateral thinking.

I would also like to acknowledge all the researchers of room 411, who provided a pleasant and intellectual working environment. Especially, I would like to thank Mario Lopes and Ahmed El-Ghazouli for the many useful discussions and their patience and assistance during the long hours of testing.

Having worked in the laboratories I have made many friends whom I am indebted for their expert technical support. I thank in particular :

- The supervisors of the Concrete Laboratory Peter Jellis and Tony Boxall for the technical support, Stefan Algar for doing an excellent job in setting up the test-rig with minimum resourses, Bill Bobinski and Andrew Hearnshaw for their help and patience during the experiments, Mike Hobbins for his steel fixing and assisting in casting and Roby Wilson for fabricating the formwork.

- Jack Neale, George Scopes and Bob Philpott, for their technical support in the structures laboratory.

- Clive Hargreaves for his help during the shake-table experiments.

Finally the Science and Engineering Research Council is acknowledged for the partial support of the experimental programme.

TABLE OF CONTENTS

		Page
ABSTRACT		3
ACKNOWLEDGEMENTS		4
TABLE OF CONTENTS		5
LIST OF TABLES		10
LIST OF FIGURES		11
ABBREVIATIONS		18
NOTATION		19
ERRATA		25
1	**INTRODUCTION**	26
1.1	Introductory remarks	26
1.2	Research objectives	27
1.3	Layout of the thesis	28
2	**LITERATURE REVIEW ON TESTING AND DESIGN OF RC WALLS**	31
2.1	Experimental Investigations on Flexural RC Walls	31
	2.1.1 US Portland Cement Association	31
	2.1.2 Earthquake Engineering Research Center at the University of California, Berkley	33
	2.1.3 Other American and Japanese programmes	36
	2.1.4 New Zealand	37
	2.1.5 Europe	39
2.2	Design philosophies	46
	2.2.1 Truss model	47
	2.2.2 Compressive force path approach	49
2.3	Design of RC Walls	51
	2.3.1 Section Flexural Capacity	52
	2.3.2 Detailing for ductility	53
	2.3.3 Shear design	57
2.4	Discussion	62
3	**EXPERIMENTAL METHODOLOGY**	64
3.1	Introduction	64
3.2	Small scale reinforced concrete modelling procedure in dynamics	64
	3.2.1 Geometry similitude	66
	3.2.2 Force similitude	66

	3.2.3 Dynamic similitude	67
3.3	Experimental set-up	69
	3.3.1 Shake-table test-rig	69
	3.3.2 Small scale cyclic test-rig	72
	3.3.3 Experimental set-up for cyclic experiments on 1:2.5 scale models	72
3.4	Model manufacture and materials	75
	3.4.1 Concrete	76
	3.4.2 Steel reinforcement and details	79
3.5	Instrumentation and control	82
	3.5.1 Shake-table test	82
	3.5.2 Cyclic tests at scale 1:5	83
	3.5.3 Cyclic tests at scale 1:2.5	83
3.6	Analysis of measurements	84
	3.6.1 Shear and flexure deformation evaluation	84
3.7	Choice of loading regime	86
4	EXPERIMENTAL RESULTS	88
4.1	Shake-table model SW1	89
	4.1.1 Shake-table results	90
4.2	Static cyclic loading - Scale 1:5 model SW2	95
	4.2.1 Cracking of SW2	96
	4.2.2 Load-displacement curves	97
	4.2.3 Strain gauge results	97
4.3	Static cyclic loading - Scale 1:5 model SW3	97
	4.3.1 Cracking of SW3	98
	4.3.2 Load-displacement curves	99
	4.3.3 Strain gauge results	100
4.4	Static cyclic loading - Scale 1:2.5 model SW4	100
	4.4.1 General observations	101
	4.4.2 Load-displacement curves	104
	4.4.3. Strain gauge results	104
4.5	Static cyclic loading - Scale 1:2.5 model SW5	104
	4.5.1 General observations	105
	4.5.2 Load-displacement curves	108
	4.5.3 Strain gauge results	108
4.6	Static cyclic loading - Scale 1:2.5 model SW6	109
	4.6.1 General observations	109
	4.6.2 Load-displacement curves	112
	4.6.3 Strain gauge results	112

4.7 Static cyclic loading - Scale 1:2.5 model SW7 113
4.7.1 General observations 113
4.7.2 Load-displacement curves 116
4.7.3 Strain gauge results 116
4.8 Static cyclic loading - Scale 1:2.5 model SW8 117
4.8.1 General observations 117
4.8.2 Load-displacement curves 120
4.8.3 Strain gauge results 120
4.9 Static cyclic loading - Scale 1:2.5 model SW9 120
4.9.1 General observations 120
4.9.2 Load-displacement curves 123
4.9.3 Shear and flexural deformation components 123
4.9.4 Strain gauge results 124

5 REINFORCED CONCRETE ANALYSIS MODEL 125
5.1 Introduction 125
5.2 Section analysis method 126
5.2.1 Plane sections assumption 127
5.2.2 Strain compatibility 129
5.2.3 Independence of flexural deformation 129
5.3 Flexural model implementation 131
5.3.1 Steel model 131
5.3.2 Concrete model 134
5.3.2.1 Concrete confinement 134
5.3.2.2 Monotonic concrete model 141
5.3.2.3 Concrete model for cyclic loading 142
5.3.2.3.1 Unloading regime 143
5.3.2.3.2 Reloading regime 144
5.3.3 Ultimate compression strain 147
5.3.4 Dynamic effects 148
5.4 Computer program CRECASIC 148
5.4.1 A test run for wall SW9 150
5.4.2 Discussion of program results 150
5.5 Shear model 153

6 ANALYTICAL PARAMETRIC STUDY 157
6.1 Introduction 157
6.2 Geometry 157
6.3 Volumetric ratio and distribution of steel within the cross section 158
6.4 Concrete characteristics 164

6.5 Steel characteristics 168
6.6 Axial load 173
6.7 Cyclic loading 177
6.7.1 Confinement 177
6.7.2 Axial load 181

7 COMPARISONS AND DISCUSSION OF RESULTS 186
7.1 Introduction 186
7.2 Stiffness characteristics of specimens 186
7.2.1 Experimentally obtained stiffness 186
7.2.2 Elastic uncracked stiffness 190
7.3 Limit states 192
7.3.1 Yield level 193
7.3.2 Ultimate limit states 195
7.4 Horizontal deformations 198
7.4.1 Flexural and shear components of deformation 199
7.4.2 Strains of lateral reinforcement 202
7.5 Base rotation 204
7.6 Vertical deformations 205
7.6.1 Vertical displacements 205
7.6.2 Vertical strains 207
7.6.2.1 Bottom extreme fibre strains 207
7.6.2.2 Bottom boundary strains 208
7.6.2.3 Bottom web strains 209
7.6.2.4 Mid-height strains 209
7.6.2.5 Top wall strains 210
7.7 Plastic hinge length 210
7.8 Out-of plane displacements 213
7.9 Ductility 213
7.10 Effect of cyclic loading 216
7.11 Energy dissipation capacity 217

8 DESIGN IMPLICATIONS AND RECOMMENDATIONS 221
8.1 Introduction 221
8.2 Dimensioning of RC wall sections 221
8.3 Flexural capacity 223
8.3.1 Moment capacity 223
8.3.2 Ductility 224
8.4 Design for shear 226
8.4.1 Shear resistance of concrete in compression 227

8.4.2 Shear resistance of concrete under tensile axial strain 230
8.4.3 Comparison with experimental results 233
8.4.4 Parameters influencing shear resistance 235

9 CLOSURE 240
9.1 General conclusions 240
9.2 Suggestions for future work 244

REFERENCES 246

APPENDIX 'A' : EXPERIMENTAL RESULTS 252
A.(2) Load-displacement curves - Scale 1:5 model SW2 252
A.(2) Strain gauge readings - Scale 1:5 model SW2 256
A.(3) Load-displacement curves - Scale 1:5 model SW3 259
A.(3) Strain gauge readings - Scale 1:5 model SW3 262
A.(4) Load-displacement curves - Scale 1:5 model SW4 265
A.(4) Strain gauge readings - Scale 1:5 model SW4 273
A.(5) Load-displacement curves - Scale 1:5 model SW5 279
A.(5) Strain gauge readings - Scale 1:5 model SW5 286
A.(6) Load-displacement curves - Scale 1:5 model SW6 293
A.(6) Strain gauge readings - Scale 1:5 model SW6 301
A.(7) Load-displacement curves - Scale 1:5 model SW7 307
A.(7) Strain gauge readings - Scale 1:5 model SW7 315
A.(8) Load-displacement curves - Scale 1:5 model SW8 322
A.(8) Strain gauge readings - Scale 1:5 model SW8 329
A.(9) Load-displacement curves - Scale 1:5 model SW9 336
A.(9) Strain gauge readings - Scale 1:5 model SW9 346

APPENDIX 'B' : ANALYTICAL RESULTS 353

LIST OF TABLES

		Page
2.1	Experimental results of monotonic tests (Lefas, 1988)	41
2.2	Experimental results of cyclic tests (Lefas, 1988)	42
2.3	Rothe and König (1988) experimental test programme of RC walls	43
2.4	Relation between q-values and curvature ductility (Tassios, 1989)	56
3.1	Summary of experimental programme	67
3.2	Small scale dynamic modelling ratios for reinforced concrete	68
3.3	Concrete design mix	78
3.4	Concrete compressive strength	78
3.5	Steel reinforcement properties	80
3.6	Strong motion characteristics	87
4.1	Shake-table tests on model SW1	89
6.1	Volumetric % of reinforcement for parametric study walls	158
6.2	Position and distribution of reinforcement in walls	160
6.3	Variation of steel amount and distribution	161
6.4	Variation of concrete strength and confinement	165
6.5	Variation of steel characteristics	170
6.6	Variation of axial load and effect of confinement	174
6.7	Variation of cyclic loading and effect of confinement	178
6.8	Variation of axial loads for cyclic and monotonic lateral loading	182
7.1	RC wall stiffness at top wall level	192
7.2	Yield limit quantities	193
7.3	Confinement data	195
7.4	Ultimate limit state	196
7.5	Foundation rotations	204
7.6	Vertical maximum deformations	206
7.7	Plastic hinge height	211
8.1	Dimensioning equation results	222
8.2	Shear strength capacity of tested walls according to SRS approach	234
8.3	Predicted and actual model wall capacities	235

LIST OF FIGURES

		Page
2.1	EERC/UBC Details of testing arrangement and walls	34
2.2	Test assembly and loading arrangement (Goodsir, 1985)	38
2.3	Test rig arrangement and wall geometry (Lefas, 1988)	40
2.4	Schematic representation of RC wall failure (Lefas, 1988)	43
2.5	Test set-up for dynamic and static-cyclic tests and arrangement of reinforcement and cross-sections of Rothe and König (1988)	45
2.6	Truss models for resisting shear	48
2.7	The compressive force path in a RC wall (Lefas, 1988)	50
2.8	The variation of curvature ductility at the base of cantilever shear walls with aspect ratio of the walls and the imposed ductility demand (Paulay and Uzumeri, 1975)	55
2.9	Failure modes of RC walls critical regions (EC8 1988)	61
3.1	Influence of the variations in material properties of a reinforced concrete shear wall model (Menu and Elnashai, 1988)	67
3.2	Shake-table test rig arrangement and wall reinforcement details	69
3.3	Model SW1 in the test-rig on the shake-table	70
3.4	Test-rig for models SW2 and SW3	71
3.5	Schematic representation of test rig arrangement and instrumentation used for 1:2.5 scale tests	73
3.6	A detailed diagram of the 1:2.5 scale test-rig assembly	74
3.7	Plate of the 1:2.5 scale test-rig	74
3.8	Wall SW4 - SW9 : dimensions and details of lateral reinforcement	77
3.9	Reinforcement properties	80
3.10	Reinforcement details for walls SW4 through SW9	81
3.11	Top wall deflections assuming fixed base	85
3.12	Cantilever wall rotations	86
4.(1).1	Equivalent shear force and top wall displacement for El Centro (50%) of SW1 and MDL-2 of SW2	92
4.(1).2	Equivalent shear force and top wall displacement for Montenegro 100% of SW1 and MDL-5 of SW2	92
4.(1).3	Translation and rotation of the inertia mass	93
4.(2).1	Loading history for SW2	95
4.(2).2	Cracking stages for wall SW2	96
4.(3).1	Loading history for SW3	98
4.(3).2	Cracking stages for wall SW3	99
4.(4).1	Loading history for SW4	101
4.(4).2	Crack pattern of wall SW4 at MDL-2 and MDL-4	102
4.(4).3	Crack pattern of wall SW4 at MDL-8 and MDL-16	103

4.(4).4	Crack pattern of wall SW4 at MDL-22 and failure	103
4.(5).1	Loading history for SW5	105
4.(5).2	Crack pattern of wall SW5 at MDL-2 and MDL-4	106
4.(5).3	Crack pattern of wall SW5 at MDL-8 and MDL-10	107
4.(5).4	Crack pattern of wall SW5 at MDL-14 and MDL-24	108
4.(6).1	Loading history for SW6	109
4.(6).2	Crack pattern of wall SW6 at MDL-2 and MDL-4	110
4.(6).3	Crack pattern of wall SW6 at MDL-8 and MDL-16	111
4.(6).4	Crack pattern of wall SW6 at MDL-18 and MDL-22	112
4.(7).1	Loading history for SW7	114
4.(7).2	Crack pattern of wall SW7 at MDL-2 and MDL-4	114
4.(7).3	Crack pattern of wall SW7 at MDL-8 and MDL-14	115
4.(7).4	Crack pattern of wall SW7 at MDL-22	116
4.(8).1	Loading history for SW8	117
4.(8).2	Crack pattern of wall SW8 at MDL-2 and MDL-4	118
4.(8).3	Crack pattern of wall SW8 at MDL-6 and MDL-12	119
4.(8).4	Crack pattern of wall SW8 at MDL-22 and failure	119
4.(9).1	Loading history for SW9	121
4.(9).2	Crack pattern of wall SW9 at MDL-2 and MDL-4	121
4.(9).3	Crack pattern of wall SW9 at MDL-6 and MDL-14	122
4.(9).4	Crack pattern of wall SW9 at MDL-18 and failure	123
5.1	Cantilever subjected to shear force	127
5.2	Stress-strain diagram for steel used in analysis	132
5.3	Santhanam's α–β model for the uniaxial inelastic behaviour of mild steel	133
5.4	Analytical model and experimental results for confined concrete by Vallenas, Bertero and Popov (1977)	135
5.5	Effectively confined concrete area (Sheikh and Uzumeri, 1982)	136
5.6	Strain and stress distribution along the RC wall boundary element	138
5.7	Confined strength determination from lateral confining stresses for rectangular sections (Mander et al, 1988a)	140
5.8	Stress strain model for monotonic loading unconfined and confined concrete	142
5.9	Determination of plastic strain ε_{pl} and the unloading branch of the cyclic stress-strain curve for concrete	143
5.10	Stress-strain curves for reloading cases	146
5.11	Flow chart of computer program CRELIC	149
5.12	Positions of data presented from program CRELIC	150
5.13	Cumulative energy dissipated versus MDL	151

5.14	Energy dissipated per cycle	152
5.15	Shear deformations of a wall element	154
5.16	Reduced shear modulus versus tensile normal strain (ASCE, 1982)	155
6.1	Normalised section capacity versus percentage of flexural reinforcement for different types of distributions	162
6.2	Normalised section yield to ultimate capacity versus percentage of flexural reinforcement for different types of distributions	162
6.3	Normalised neutral axis depth at ultimate capacity versus percentage of flexural reinforcement for different types of distributions	163
6.4	Curvature ductility versus percentage of flexural reinforcement for different types of distributions	163
6.5	Displacement ductility versus percentage of flexural reinforcement for different types of distributions	164
6.6	Normalised section capacity versus mechanical confinement ratio ω_{wd} for different concrete strengths	166
6.7	Normalised section yield to ultimate capacity versus mechanical confinement ratio ω_{wd} for different concrete strengths	166
6.8	Normalised neutral axis depth at ultimate capacity versus mechanical confinement ratio ω_{wd} for different concrete strengths	167
6.9	Curvature ductility versus mechanical confinement ratio ω_{wd} for different concrete strengths	167
6.10	Displacement ductility versus mechanical confinement ratio ω_{wd} for different concrete strengths	168
6.11	Normalised section capacity versus steel yield stress for different ultimate to yield stress ratios	171
6.12	Normalised section yield to ultimate capacity versus steel yield stress for different ultimate to yield stress ratios	171
6.13	Normalised neutral axis depth at ultimate capacity steel yield stress for different ultimate to yield stress ratios	172
6.14	Curvature ductility versus steel yield stress for different ultimate to yield stress ratios	172
6.15	Displacement ductility versus steel yield stress for different ultimate to yield stress ratios	173
6.16	Normalised section capacity versus normalised axial force for different confinement values	175
6.17	Normalised section yield to ultimate capacity versus normalised axial force for different confinement values	175

6.18 Normalised neutral axis depth versus normalised axial force for different confinement values 176
6.19 Curvature ductility versus normalised axial force for different confinement values 176
6.20 Displacement ductility versus normalised axial force for different confinement values 177
6.21 Normalised section capacity versus confinement level for different ΔMDL values 179
6.22 Normalised section yield to ultimate capacity versus confinement level for different ΔMDL values 179
6.23 Normalised neutral axis depth versus confinement level for different ΔMDL values 180
6.24 Curvature ductility versus confinement level for different ΔMDL values 180
6.25 Displacement ductility versus confinement level for different ΔMDL values 181
6.26 Normalised section capacity versus axial load for monotonic and cyclic loading 183
6.27 Normalised section yield to ultimate capacity versus axial load for monotonic and cyclic loading 183
6.28 Normalised neutral axis depth versus axial load for monotonic and cyclic loading 184
6.29 Curvature ductility versus axial load for monotonic and cyclic loading 184
6.30 Displacement ductility versus axial load for monotonic and cyclic loading 185
7.1 Secant stiffness of SW1, SW2 and SW3 versus maximum displacement level 187
7.2 Secant stiffness of SW3, SW4 and SW6 versus maximum displacement level 188
7.3 Secant stiffness of SW5 and SW7 versus maximum displacement level 189
7.4 Secant stiffness of SW8 and SW9 versus maximum displacement level 189
7.5 Elastic deformations of RC walls 190
7.6 SW5 deformations at different MDLs 199
7.7 Force versus deformations at peak displacement 201
7.8 Ratios of component to total deformation versus MDL 201
7.9 Deformations at zero force versus MDL 202

7.10 Curvature versus displacement ductility for all parametric studies of chapter 6 214
7.11 Curvature distribution for control specimen at ultimate load 215
7.12 - 7.17 Energy dissipation per MDL for SW4 through to SW9 219
7.18 - 7.23 Cumulative energy dissipation versus MDL for SW4 through to SW9 220
8.1 Stress and strain diagram at yield level 223
8.2 Stresses in the compressive zone 228
8.3 Mohr-Coulomb failure envelope for concrete 229
8.4 Direction of failure in the tensile zone 231
8.5 Possible minimum SRS 232
8.6 Shear strength of concrete according to BS8100 and SRS method for the different percentages of flexural reinforcement 236
8.7 Shear strength versus compressive strength 237
8.8 Shear strength versus normalised axial load 238

A.(2).1 Load versus top wall horizontal displacement 252
A.(2).2 Load versus top mass horizontal displacement 253
A.(2).3 Top mass versus top wall horizontal displacement 253
A.(2).4 Load versus top left wall vertical displacement 254
A.(2).5 Load versus top right wall vertical displacement 254
A.(2).6 Load versus top average wall vertical displacement 255
A.(2).7 Top horizontal versus top-average vertical displacement 255
A.(2).8 Top wall shear deformation 256
A.(2).9 - A.(2).15 Force versus strain gauge 1 through to 7 256
A.(3).1 Load versus top wall horizontal displacement 259
A.(3).2 Load versus mid-wall horizontal displacement 259
A.(3).3 Mid-wall versus top wall displacement 260
A.(3).4 Load versus top-left wall vertical displacement 260
A.(3).5 Load versus top-right wall vertical displacement 261
A.(3).6 Load versus top-average wall vertical displacement 261
A.(3).7 Top wall shear deformations versus load 262
A.(3).8 - A.(3).15 Force versus strain gauge 1 through to 8 262
A.(4).1 - A.(4).10 Load versus wall SW4 displacement 3 through to 12 265
A.(4).11 Load versus wall SW4 displacement 15 270
A.(4).12 Load versus wall SW4 displacement 16 271
A.(4).13 Force versus top wall average vertical displacement for wall SW4 271
A.(4).14 Force versus mid-height average vertical displacement for wall SW4 272

A.(4).15 Force versus quarter-height average vertical displacement for wall SW4 272
A.(4).16 - A.(4).38 Load versus strain 1 through to 23 273
A.(5).1 - A.(5).10 Load versus wall SW5 displacement 3 through to 12 279
A.(5).11 Load versus wall SW5 displacement 15 284
A.(5).12 Load versus wall SW5 displacement 16 284
A.(5).13 Force versus top wall average vertical displacement for wall SW5 285
A.(5).14 Force versus mid-height average vertical displacement for wall SW5 285
A.(5).15 Force versus quarter-height average vertical displacement for wall SW5 286
A.(5).16 - A.(5).39 Load versus strain 1 through to 24 286
A.(6).1 - A.(6).10 Load versus wall SW6 displacement 3 through to 12 293
A.(6).11 Load versus wall SW6 displacement 15 298
A.(6).12 Load versus wall SW6 displacement 16 299
A.(6).13 Force versus top wall average vertical displacement for wall SW6 299
A.(6).14 Force versus mid-height average vertical displacement for wall SW6 300
A.(6).15 Force versus quarter-height average vertical displacement for wall SW6 300
A.(6).16 - A.(6).38 Load versus strain 1 through to 23 301
A.(7).1 - A.(7).10 Load versus wall SW7 displacement 3 through to 12 307
A.(7).11 Load versus wall SW7 displacement 15 312
A.(7).12 Load versus wall SW7 displacement 16 313
A.(7).13 Force versus top wall average vertical displacement for wall SW7 313
A.(7).14 Force versus mid-height average vertical displacement for wall SW7 314
A.(7).15 Force versus quarter-height average vertical displacement for wall SW7 314
A.(7).16 - A.(7).41 Load versus strain 1 through to 26 315
A.(8).1 - A.(8).10 Load versus wall SW8 displacement 3 through to 12 322
A.(8).11 Load versus wall SW8 displacement 15 327
A.(8).12 Load versus wall SW8 displacement 16 327
A.(8).13 Force versus top wall average vertical displacement for wall SW8 328
A.(8).14 Force versus mid-height average vertical displacement for wall SW8 328

A.(8).15 Force versus quarter-height average vertical displacement for wall SW8 329
A.(8).16 - A.(8).39 Load versus strain 1 through to 24 329
A.(9).1 - A.(9).10 Load versus wall SW9 displacement 3 through to 12 336
A.(9).11 Load versus wall SW9 displacement 15 341
A.(9).12 Load versus wall SW9 displacement 16 341
A.(9).13 Force versus top wall average vertical displacement for wall SW9 342
A.(9).14 Force versus mid-height average vertical displacement for wall SW9 342
A.(9).15 Force versus quarter-height average vertical displacement for wall SW9 343
A.(9).16 Force versus flexural component of top horizontal displacement by using method of area $\alpha 1$ 343
A.(9).17 Force versus flexural component of top horizontal displacement by using method of area $\alpha 2$ 344
A.(9).18 Top displacement versus flexural component of top horizontal displacement δ_{fa2} by using method of area $\alpha 2$ 344
A.(9).19 Top displacement versus shear component of top horizontal displacement by using method of area $\alpha 2$ 345
A.(9).20 Flexural displacement δ_{fa2} versus shear component of top horizontal displacement by using method of area $\alpha 2$ 345
A.(9).21 Force versus shear component of top horizontal displacement by using method of area $\alpha 2$ 346
A.(9).22 - A.(9).44 Load versus strain 1 through to 23 346
B.1 Top wall horizontal flexural displacement versus force 353
B.2 Top wall vertical displacement versus force 354
B.3 Top wall average vertical displacement versus force 354
B.4 Quarter height horizontal flexural displacement versus force 355
B.5 Quarter height vertical displacement versus force 355
B.6 Quarter height average vertical displacement versus force 356
B.7 - B.10 Bottom strain 1 through to 4 versus force 356
B.11 Quarter height strain 1 versus force 358
B.12 Top strain 1 versus force 359
B.13 Force versus shear component of top horizontal displacement 359
B.14 Flexural displacement versus shear component of top horizontal displacement 360

ABBREVIATIONS

ACI	-	American Concrete Institude
CB	-	Reinforcement concentrated in the boundaries
CFP	-	Compressive Force Path
CRELIC		Cyclic REinforced Concrete Analysis Imperial College
DC	-	Ductility Class
ΔMDL	-	Increment in maximum displacement level.
ΔΣE	-	Rate of increase of the cumulative energy per cycle.
EC	-	Eurocode
EQ	-	Earthquake
LHS	-	Left hand side (Negative displacements)
MDL	-	Maximum displacement level in mm
OPYM	-	Out-of-plane yield moment
PCA	-	Portland Cement Association
RC	-	Reinforced concrete
RHS	-	Right hand side (positive displacements)
SW	-	Shear wall
UBC	-	Uniform Building Code
UB	-	Uniform distribution of reinforement in the boundaries
UD	-	Uniform distribution of reinforcement in the cross-section

NOTATION

A	=	Area of the cross-section.
A_c	=	Concrete gross area along confined length.
$A_{f:s}$	=	Ratio of flexural to shear capacity of a section.
A_g	=	Gross area of section.
A_{ch}	=	Cross-sectional area of a structural member measured out-of-plane of transverse reinforcement.
A_o	=	Core concrete area along confined length.
a_r	=	Ratio of heigth of application of shear force to height of wall.
a_s	=	Modelling ratios.
A_s	=	Cross-sectional area of a reinforcement bar.
A_{sh}	=	Total cross-sectional area of rectangular hoop reinforcement.
A_{ss}	=	Cross-sectional area of shear reinforcement per unit length.
A_v	=	Area of horizontal shear reinforcement per distance s.
A_{sx}	=	Flexural reinforcement area.
A_{sy}	=	Confinement reinforcement area in y direction.
A_{sz}	=	Confinement reinforcement area in z direction.
b	=	Fundamental quantities for modeling.
b	=	Confined thickness of the wall (figure 5.6).
B	=	Thickness of the wall.
c	=	Distance from extreme compressive fibre to neutral axis.
d	=	Confined width of the wall or column (figure 5.6).
D	=	Width of wall.
d_e	=	Wall effective witdh.
d_L	=	Hoop diameter.
d_H	=	Hoop diameter.
E	=	Elastic modulus.
E_c	=	Tangent elastic modulus for concrete.
E_{re}	=	Reloading modulus of elasticity for concrete (figure 5.10).
E_{s1}	=	Steel stiffness after yield level.
E_{sa}	=	Steel reloading stiffness.
E_{sec}	=	Secant modulus for concrete.
E_{so}	=	Steel initial stiffness.
E_{su}	=	Ultimate steel strain.
E_t	=	Composite elastic moduli.

E_u = Initial unloading modulus of elasticity for concrete (figure 5.9).

f_c = Concrete compressive stress.

f_{cc} = Confined concrete compressive cylinder strength.

f_{co} = Unconfined concrete compressive cylinder strength.

f_{cu} = Unconfined concrete compressive cube strength.

f_l = Effective lateral concrete confining stress.

f_o = Foundamental frequency of response.

f(q) = A function of q (representing a number of phenomena in a physical system).

F(r) = A function of r (non-dimensional variables, representing the phenomena in a physical system).

f_{re} = Return point on monotonic stress-strain curve for concrete cyclic model (figure 5.10).

f_{ro} = Concrete stress at reloading reversal (figure 5.10).

f_{su} = Ultimate yield stress of steel.

f_{sy} = Initial yield stress of steel (before plastic strain accumulation).

F_{sy} = Confinement force in y direction.

F_{sz} = Confinement force in z direction.

f_t = Concrete tensile strenght.

f_{un} = Value of stress at maximum compressive strain achieved in concrete (figure 5.9).

f_{yh} = Specified yield strenght of transverse reinforcement.

g = Accelaration due to gravity.

G = Elastic modulus for shear or Modulus of rigitity.

G_{NL} = Nonlinear modulus for shear.

H = Height of cantelever wall.

h_c = Cross-sectional dimension of core measured centre-to-centre of confining reinforcement.

H_p = Height of the plastic hinge area.

I = Second moment of area of a cross section.

I_G = Rotational inertia.

I_s = Second moment of area of steel in a RC section.

k = Curvature at a section.

K_e = Elastic stiffness.

k_h = Elastic top wall horizontal stiffness.

K_θ = Rotational stiffness.

$K_{\theta b}$ = Rotational stiffness at the foundation level.

l_a = Lever arm.

l_c	=	Confined length in EC8.
m	=	Value of moment.
m*	=	Value of vitrual moment.
M_c	=	Factored moment capacity at section.
$M_{control}$	=	Section ultimate moment capacity for control specimen.
M_{cx}	=	Bending shear capacity of the unreinforced section.
M_{do}	=	Decompression moment, at the extreme tension fibre.
M_o	=	Maximum probable moment capacity at section.
m_o	=	Virtual moment due to a unit point load at the point .
M_{sd}	=	Design moment.
M_{ult}	=	Section ultimate moment capacity.
M_y	=	Yield moment at first yield of reinforcement.
N	=	Axial load.
P	=	Axial load in member.
q_n	=	A physical quantity.
r_n	=	A non-dimensional term, representing physical quantities.
S	=	Structural type factor as given in NZS 4203:1984.
s	=	Spacing of transverse reinforcement measured along the longitudinal axis of the structural member.
s	=	Spacing of transverse reinforcement measured along the longitudinal axis of the structural member.
s_i	=	Distance of steel bar from the centre of inertia of a section.
T_t	=	Total shear resistance of a particular shear resistance surface in the tensile zone.
u	=	Deformation inthe x-direction.
U_{co}	=	Energy stored per unit volume of unconfined concrete core.
U_{cc}	=	Energy stored per unit volume of confined concrete core.
u_e	=	Expansion at the top beam.
u_f	=	Flexural component of horizontal displacement including base rotation.
u_{fH}	=	Lateral displacement at top of wall due to flexure.
u_H	=	Total lateral displacement at top of wall.
u_s	=	Shear component of horizontal displacement .
U_{sb}	=	Strain energy due to secondary bending in the longitudinal reinforcement in compression.
U_{sc}	=	Additional energy required to maintain yield in the longitudinal reinforcement in compression.

u_{sH} = Lateral displacement at top of wall due to shear.
U_{sh} = Energy stored in transverse reinforcement.
u_t = Top wall horizontal displacement.
v = Deformation inthe y-direction.
v_c = Concrete shear resistance.
V_c = Applied shear force.
v_d = Ratio of maximum axial force to concrete compressive capacity at the critical section.
v_f = Flexural deformation inthe y-direction.
v_i = Total shear stress.
V_i = Ideal shear force derived from total shear stress v_i.
V_{MRD}= Minimum design shear strength against shear failure modes.
v_o = Virtual shear due to a unit point load at the point where deflections are required.
V_{RD} = Minimum design shear strength against shear failure modes.
v_s = Reinforcement contribution to shear resistance.
v_s = Shear deformation inthe y-direction.
V_u = Design shear force.
V_{ul} = Ultimate shear force corresponding to M_u.
V_y = Shear force corresponding to M_y.

Greek Symbols

α = Confinement coefficient depending on spacing and configuration of stirrups.
α = Stiffness degradation parameter for steel reinforcement (figure 5.2).
α_s = Shear ratio (Moment to shear force ratio).
β = Yield growth factor (figure 5.3).
β_1 = Factor accounting for presense of axial force in Eurocode 8 p.118.
γ = Shear strain rate of change.
ΔE_{ay} = Rate of increase of energy dissipated per MDL after yield.
δ = Increment of a certain quantitie.
δ_{fa1} = Flexural component of top horizontal displacement calculated by method of area a1.

δ_{fa2} = Flexural component of top horizontal displacement calculated by method of area a2.

δ_{ste} = Elastically recoverable shear deformation.

δ_{stp} = Permanent (plastic) shear deformation.

ε = Elastic properties' scaling factor.

ε_i = Strain in the direction i.

ε_c = Concrete compressive strain in the longitudinal direction.

ε_{cc} = Concrete compressive strain in the longitudinal direction at peak confined stress.

ε_{co} = Concrete compressive strain in the longitudinal direction at peak unconfined stress.

ε_{cu} = Ultimate confined concrete compressive strain in the longitudinal direction.

ε_{cuo} = Ultimate unconfined concrete compressive strain in the longitudinal direction.

ε_{pl} = Plastic strain in concrete model.

ε_{re} = Return point strain on monotonic stress strain curve for concrete cyclic model.

ε_{ro} = Concrete strain at reloading reversal.

ε_{sp} = Concrete compressive spalling strain in the longitudinal direction for unconfined concrete.

ε_{un} = Maximum compressive strain achieved in concrete (figure 5.9).

ε_{su} = Fracture steel strain.

ε_{sy} = Initial yield steel strain.

ε_x = Strain in the longitudinal direction.

κ = Curvature at a section.

κ_e = Coefficient of confinement effectiveness.

λ = Geometric scale factor for modelling.

μ_Δ = Displacement ductility factor.

μ_{1/r_o} = Reference curvature ductility factor for the unconfined section.

$\mu_{1/r}$ = Curvature ductility factor.

ν = Poisson's ratio.

ν = Velocity scale factor in modelling.

ξ = Normalised value of neutral axis depth with respect to the section width D.

ρ = Density scale factor.

ρ_h = Ratio of horizontal shear reinforcement to gross concrete area of vertical section.

ρ_v = Vertical web reinforcement.

σ_{cy} = Confinement stress in y direction.

σ_{cz} = Confinement stress in z direction.

σ_{max} = Maximum expected hoop stress.

σ_n = Normal stress.

σ_s = Stress in steel.

σ_x = Stress in the x direction.

σ_z = Stress in the z direction.

σ_{xy} = Shear stress.

τ_c = Average concrete shear stress capacity.

τ_{ct} = Average concrete shear stress capacity in the tensile zone.

τ_{Rd} = Shear stress obtained from table 4.1 of EC2.

τ_{xy} = Shear stress.

ϕ = Angle of crack direction with respect to the horizontal.

ϕ_o = Flexural overstrength factor.

ω_{wd} = Volumetric mechanical ratio of hoops.

ω_{ws} = Volumetric mechanical ratio of shear reinforcement.

ERRATA

Page	Par.	Line	Error	Correction
4	3	1	whom	to whom
7		32	CRECASIC	CRELIC
27	3	4	loading.	loading for isolated flexural walls of similar confinement levels.
29	5	1	parametres	parameters
31	1	3	to the those	to those
31	2	12	is outlined are	are outlined in
41	1	2	SW5	SW25
48	1	2	ties	struds
50	1	4	l	l'
51	4	9	very no	very little
60	2	4	It is evident	It is possible
60	3	1	capacity	demand
63	2	4	neither	either
63	2	5	nor	or
75	2	4	authors	author
82	1	8	as consequence a	as a consequence
85	1	9	a-priory	a-priori
91	3	5	then	system, then
91	3	5	are	is
91	3	12	4.1 and 4.2	4.(1).1 and 4.(1).2
93	2	3	fiqure 4.3	figure 4.(1).3
93	equation 4.3		$I_G = -k_\theta \theta + (u - s\theta)\, s$	$I_G \ddot{\theta} = -k_\theta \theta + \kappa_h (u - s\theta)\, s$
94	4	1	this	these
103	Figure 4.(4).4		MLD-22	MDL-22
106	1	11	which goes	which
108	Figure 4.(5).4		MDL-26	MDL-24
117	Section title			4.8 Static cyclic loading - Scale 1:25 model SW8
118	3	11	figure 4.(8).5	figure 4.(8).4
124	5	2	in the	in
125	1	13	imput	input
128	3	2	axis	axis towards the
128	4	1	plain	plane
132	Figure 5.2		Degridated stiffness	Reloading stiffness
132	2	1	massing	Massing
133	2	3	[missing line]	permanent strains are required to establish the stress from the current strain.
134	1	4	it's	its
139	2	4	Winker	Winkler
139	3	6	and 5.20	and 5.21
143	1	1	ε_a	ε_α

143	equation 5.25		a	α
143	2	1	ε_a	ε_α
147	2	2	build	built
150	Figure 5.13		a	α
151	Figure 5.14		a	α
151	2	1	B2	B.2
152	5	8	results.	results in chapter 7.
154	4	2	depended	dependent
154	5	6	of	of a shear dominated
155	3	1	give	define
157	1	8	chapter 8	chapter 7 and 8
157	2	2	qualitatively	quantitavely
169	1	1	yield to ultimate stress	ultimate stress to yield
169	3	2	extend	extent
169	3	3	mm2	mm^2
169	3	7	is	are
187	1	9	depended	dependent
191	4	2	1:5	1:2.5
192	2	5	significant.	significance.
193	2	1	while yielding	whilst yielding had
197	1	6	most of the	most
197	5	4	principle	principal
203	5	3	figure 3.7	figure 3.8
204	1	2	have contribute	have contributed
205	4	4	The is	This is
206	footnote §		is a net	if a net
206	footnote •		displacement	displacements
207	1	8	mechanism.	mechanisms.
208	1	12	occur	occurs
216	1	3	strenght	strength
216	1	4	strenght	strength
224	a)	2	equals 9.3	equals 0.93
224	b)	2	of 1.25	of 0.125
224	Section title		8.3.3 Ductility	8.3.2 Ductility
224	9	8	Form	From
`225	5	4	used at	used as
230	4	7	principle	principal
244	2	2	principle	principal
249	14	1	Winker	Winkler

CHAPTER 1

1 INTRODUCTION

1.1 Introductory remarks

Seismic forces are induced in buildings due to the inertia of the structural mass, responding to displacements imposed at ground level. The level of the maximum forces depends not only on the earthquake (EQ) characteristics, but also on the stiffness characteristics of the structure. In the past, relatively flexible structures were thought to perform better under earthquake loading due to the fact that in general they attract less seismic forces. However, following destructive earthquakes, it was observed that such structures sustain high storey drifts and consequently severe non-structural damage. Moreover, failure can be induced as a result of excessive ductility demands and from second order forces generated at large deformations.

Adequately designed reinforced concrete (RC) walls have been shown to reduce storey drifts and consequently non-structural damage. Due to their high stiffness RC walls attract a large proportion of the seismic forces at the critical lower storeys and, as a result, reduce the demand on the other structural components. However, the occurrence of brittle shear failures of RC walls led to the conservatism that exists in most codes of practice at present, where base shear coefficients are increased for wall or wall-frame configurations.

Existing analysis tools, such as simple equivalent models, hysteretic models, section analysis and finite element procedures, show different degrees of accuracy in predicting the flexural capacity, but fail to predict satisfactorily the shear behaviour of RC walls. Recent research in the subject has contributed to the better understanding of the behaviour of RC walls, but most of the available design procedures are still based on out dated methods and philosophies.

Under-estimates of the actual flexural capacity in design was shown to arise due to the simplification of the material models employed. In the design for shear, more precise determination for the ultimate capacity is required. It is generally accepted that the flexural capacity, ductility and energy dissipation capability of RC walls is considerably enhanced by the provision of confinement reinforcement in the critical zones. Modern codes, such as Eurocode 8 (EC8, 1988), proposed for the first time, design procedures that would allow specific ductility levels, determined from the overall structural behaviour, to be achieved by suitable detailing.

As far as shear resistance of walls is concerned, codes of practice still use empirical methods developed originally for beams and modified to account for the special features of RC walls. Different views exist amidst researchers as to the suitability of the existing methods and which direction research should be taking. A number of new approaches have been proposed in recent years but have not yet been widely accepted.

1.2 Research objectives

The work presented in this thesis was preceded, in the same department, by the work of Lefas (1988). Consequently, the research objectives were initially directed towards the clarification of some of the conclusions arrived at in the above-mentioned thesis, under severe cyclic loading. These are summarised below:

- The flexural overstrength observed in RC wall is primarily due to high concrete compressive stresses in the confined area.
- The ultimate capacity of RC members is independent of the concrete strength and loading history.
- The shear resistance of RC walls is provided by the confined area in compression and shear reinforcement, according to the 'compressive force path' method, is only necessary where the 'path' changes direction.

On the other hand, the independent objectives of the current project, notwithstanding previous work at IC, were identified to be the following:

- Development of a dynamic small scale modelling procedure for reinforced concrete.

- Development of an analytical program capable of estimating section capacity and flexural deformations for cyclic and monotonic loading.

- Development of a methodology suitable for estimating shear deformations based on normal strains obtained from the flexural model.

- Appraisal of the current design procedures and provision of improved design guidance.

- Assessment of the effectiveness of the different flexural distributions of steel and the role of web reinforcement in contributing towards shear resistance and energy dissipation capacity.

- Investigation of the parameters that affect the ductility and energy dissipation capability of RC walls.

- Assessment of the effect of different parameters on the shear resistance of concrete.

- Calibration of the analytical model by comparison to the experimental data and use of the model for parametric studies covering a range and variation of parameters that would be difficult to conduct experimentally.

The above objectives are addressed in the subsequent chapters, following the layout given below.

1.3 Layout of the thesis

In chapter 2, a literature survey is presented. The chapter begins with a brief historical note on research in RC walls and, subsequently, emphasis is

given to the research of selected establishments. Various design philosophies are also presented. The design procedures in some of the most important codes of practice are discussed, thus highlighting the differences in design approaches.

The development of a small scale dynamic modelling procedure for reinforced concrete walls is given in chapter 3. The same chapter contains all the information concerning the experimental work including description of the different test-rigs designed and built for this programme, instrumentation of the specimens, control of the tests, details of model manufacture, properties of materials used, and the choice of loading. The procedures for processing the results are also outlined.

The description of each experiment is presented in chapter 4, together with details of the loading procedure, the crack development and of the immediate observations, as well as special difficulties encountered during testing. All figures from the experimental results are given in Appendix A.

Chapter 5 provides details on the analytical part of this work. The choice of the analysis method and assumptions made are firstly considered. A cyclic steel model is developed for use with the implemented concrete model. The latter was chosen from literature due to its direct applicability to the section analysis method used. Some modifications were included in the implementation of the model, especially with respect to the effects of confinement. The main features of the developed computer program are outlined and comparisons are made for a chosen test case. A shear model suitable for the method of section analysis is finally developed and results are presented and discussed for a test case. For the sake of compactness, figures from analytical data are given in Appendix B.

In chapter 6, an analytical parametric study is undertaken.The choice of parametres and the range of variation is followed by presentation of all the results in tabular and graphical forms.

Comparison between analysis and experiments as well as general discussion of the results is made in chapter 7. The stiffness characteristics are compared with results obtained from analytical predictions and the different limit states are given. Deformational characteristics are investigated by making reference to the experimental results and observations are discussed.

The separation of shear and flexural deformations is given for one of the walls. A method for estimating the plastic hinge length is developed. The results from the parametric study on the ductility are compared with the Eurocode 8 (EC8, 1988) recommendations. The effects of cyclic loading are also discussed as well as the energy dissipation capacity of the tested walls.

Chapter 8 is concerned mainly with design recommendations. RC wall dimensioning and design procedures for flexure are proposed. After examining the method of design for ductility given in EC8 (1988) a modification is proposed. A model for shear design is developed from first principles, based on the estimation of the surface of lowest shear resistance. The different parameters affecting shear strength are examined and compared with the results given by the model. Comparisons are also made with the experimental data.

In the final chapter, the general conclusions from the present study are drawn together with recommendations for further research and developments in the subject.

CHAPTER 2

2 LITERATURE REVIEW ON TESTING AND DESIGN OF RC WALLS

In this chapter, the most relevant literature available on design and testing of RC walls is presented. Emphasis is given to experiments on flexural isolated rectangular walls of similar nature to the those undertaken for the purposes of this research. A brief description of design philosophies is then followed by a discussion of the design procedures of the most important codes of practice.

2.1 Experimental Investigations on Flexural RC Walls

Experiments investigating the behaviour of RC walls under EQ loading have been conducted mainly in the USA, Japan, New Zealand, and Europe. Prior to the 1970s, research in this field has been very limited and was mainly part of the investigations for shear in RC members. The pioneers in research on RC walls were Benjamin and Williams (1957) who tested squat walls. Publication SP-42 (ACI,1974) of the American Concrete Institute and two reports by Regan (1971 a & b) to CIRIA include a significant amount of the state-of-the-art on shear in USA and the UK until then. After 1970 much more attention was given to the behaviour of RC walls, either isolated or coupled with the structural frame. A few of the main research programmes on flexural type isolated walls published since 1970 in the USA and other more recent work elsewhere is outlined are this section.

2.1.1 US Portland Cement Association

Researchers at the US Portland Cement Association (PCA) were amongst the pioneers in the field in the 1970s. Cardenas et al (1973) tested thirteen RC walls at a scale of 1:2. Four of the specimens had a shear ratio of 2 and were subjected to monotonic loading. The wall shear reinforcement was kept constant while the flexural reinforcement amount and

distribution was varied. The effect of axial load has been found to increase moment capacity but reduce ultimate curvature. It was noted that higher ductility can be achieved if vertical reinforcement is concentrated near the edge boundaries of RC walls. Minimum shear reinforcement (0.27% of the cross section area) was demonstrated to be adequate in walls for the development of flexural capacity. Specimens with lower shear ratios resisted in general higher shear stresses which were attributed to a higher contribution to the shear resistance by concrete.

Oesterle, Fiorato, and Corley, (1983), and Oesterle, Aristizabal-Ochoa, Shiu, and Corley (1984) reported an extensive test programme on flexural isolated walls of scale 1:3, having as the primary aim investigation of the strength, ductility and energy dissipation of walls under cyclic loading. The walls had a length of 190 cm (75") a width of 10 cm (4") and a shear ratio of 2.4. In this series the total number of tests was twenty one as reported by Oesterle and Fiorato (1984). Variables included axial load, quantity of reinforcement, concrete strength and loading history. Flanged, barbell, and rectangular sections were investigated.

The first two types of section were found to be susceptible to web crushing while one of the rectangular sections suffered out-of-plane instability. Walls with 'low nominal shear stress' (less than 0.25 $\sqrt{f_{co}}$ MPa) were reported to develop near horizontal cracks and flexural failure modes were observed. Walls with 'high nominal shear stress' (more than 0.58 $\sqrt{f_{co}}$ MPa) developed inclined cracks forming compression strut systems for transferring shear in a truss mechanism. Failure occurred either by web crushing or diagonal tension failure. Sliding shear was also observed in one of the cyclic experiments.

Flexural capacities of walls subjected to inelastic load reversals were 15% less than monotonic capacities. Monotonic tests also yielded larger deformation capacities. In cyclic tests, the behaviour of walls was observed to be more dependent on the level of prior maximum deformation sustained than on the sequence of load application.

The moment capacity of a wall section and the corresponding maximum applied shear was found to be dependent on the amount and distribution of the vertical flexural reinforcement . The design flexural capacity was shown to underestimate the actual capacity since the actual material properties were higher than the specified properties. It was concluded that this could lead to an underestimate of the actual shear force. The concentration of flexural reinforcement into the wall boundaries was

again proved to lead to higher moment capacities and ultimate curvatures than uniformly distributed reinforcement.

It was also concluded that shear reinforcement supplied according to correct estimates of the maximum possible flexural capacity is sufficient to avoid shear failure. Any extra amount of shear reinforcement would have little effect on other possible modes of failure such as diagonal tension, web crushing and sliding shear. It was also reported that hoop reinforcement improved the inelastic behaviour of RC walls. The functions of hoop reinforcement as demonstrated by the experiments, according to Oesterle et al (1983), in addition to increasing concrete strain capacity are :

a) Support vertical reinforcement against buckling.

b) Together with vertical bars, it contains fractured concrete within a confined core.

c) Improves shear capacity and stiffness of boundary elements.

Axial loads of less than 10% of the axial capacity also proved to have a beneficial effect on the flexural capacity. Shear deformations were reduced and larger base rotations were sustained prior to web crushing.

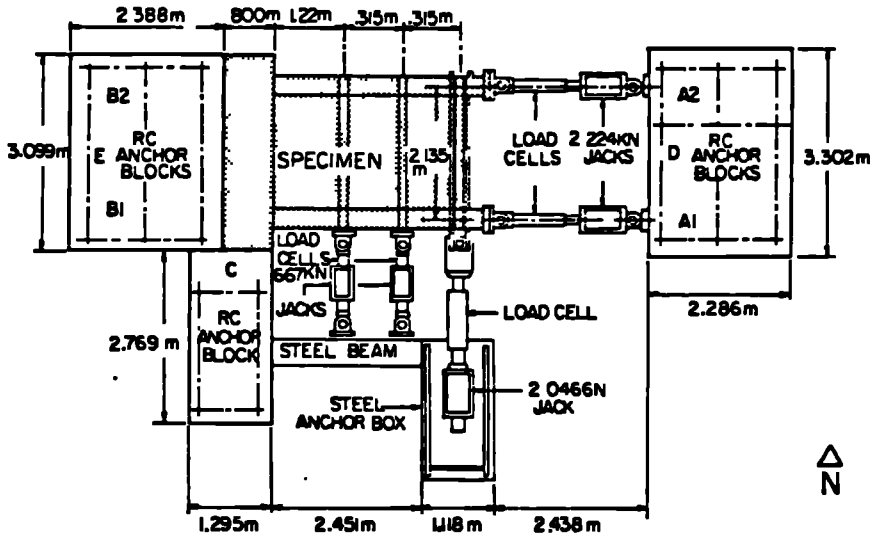
Concrete strength was reported to affect the web crushing capacity and the abrasion resistance along crack interfaces.

More recently (Daniel, Shiu and Corley, 1985), experiments were conducted to investigate the effect of openings on the behaviour of RC walls. Two comparable isolated wall specimens, one with openings and one without, were tested at a scale of 1:3 under cyclic loading. Failure occurred due to shear deterioration after achieving the flexural capacity and undergoing several cycles in the post-elastic range.

2.1.2 Earthquake Engineering Research Center at the University of California, Berkeley

Significant experimental research in the 1970s has also taken place at the Earthquake Engineering Research Centre, University of California Berkeley (EERC/UCB). A total of eight walls were tested. Research started by Wang, Bertero and Popov (1975) with two scale 1:3 framed barbell walls with spirally reinforced boundary elements. The walls represented the first three floors of a 10-storey building designed according to the 1973 Uniform

Building Code. The walls were tested horizontally as shown in figure 2.1. After testing all walls were repaired and re-tested.



(a) Plan

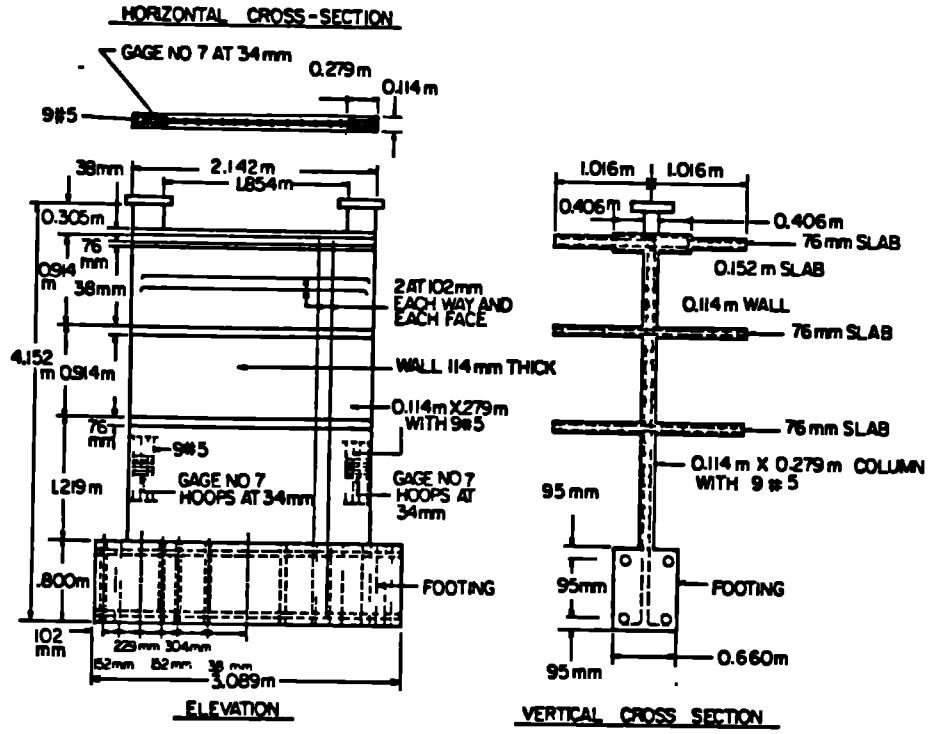


Figure 2.1 EERC/UBC Details of testing arrangement and walls

Vallenas, Bertero and Popov (1979) tested two models similar to the above-discussed, in addition to two rectangular walls (figure 2.1). The parameters under investigation included, the shape, boundary element

confinement, shear stress and loading history. Higher flexural capacity than predicted by code formulae was reported. However, it was proposed that analysis based on realistic material mechanical properties and the assumption that plane sections remain plane, can give good predictions of strength at various limit states.

It was observed that when the walls were subjected to very high moment and shear, wide flexural and diagonal cracks opened on the tension side of the neutral axis. The interface shear transfer along these cracks was thought to be very low and hence, it was suggested that shear should be resisted in the confined compressed area with higher stresses than prescribed by codes. It was also noted that code recommendations, which are based on monotonic tests, do not account for aggregate interlock deterioration which occurs under cyclic loading. In the rectangular walls, the maximum nominal shear stresses resisted without shear failure were $0.783 \sqrt{f_{co}}$ MPa.

Fixed end rotations were reported to be responsible for between 7 and 11% of the total deflections. For the rectangular sections, the ratio of shear to flexural deformations was 0.43 for the monotonic tests and increased with load reversals to 0.87.

As far as local buckling of the reinforcement is concerned it was proposed that it is determined mainly by the diameter of the longitudinal reinforcement, the spacing of the lateral confinement and the strain levels to be reached. Overall wall buckling was observed to be governed by the ratio of the unsupported wall height to width and the compressive strain that can be achieved.

Iliya and Bertero (1980) continued by investigating the effects of the amount and arrangement of the web reinforcement on the hysteretic behaviour of two flanged walls. Good agreement between observed and estimated flexural capacity was reported. Estimates of the flexural capacity by code were however, lower due to the fact that strain hardening of the reinforcement and true concrete strength was not included. It was also concluded that boundary confinement was more important to the ductility of RC walls than the web reinforcement and that diagonal reinforcement can improve the displacement ductility significantly.

2.1.3 Other American and Japanese programmes

In the more recent joint U.S.-Japan Research programme, tests on RC walls were undertaken under static, cyclic, pseudo-dynamic and shake-table loading on both full scale and scaled models. The experiments on isolated and framed walls were directly related to the full-scale seven story building tested during the programme. Hiraishi, Nakata, Kitagawa and Kaminosono (1985) reported tests on 1:2 scale models representing the wall-beam assemblies of the prototype. Six tests were carried out ; two static-cyclic, two on the shake-table and two pseudo-dynamic tests. Morgan, Hiraishi and Corley (1985) tested 1:3.5 scale models of isolated walls and wall-beam assemblies. Wallace and Krawinkler (1984) tested at 1:12.5 scale. The first reports from this research programme indicate that the model tests simulated the prototype structural behaviour satisfactorily in terms of capacity as well as in qualitative terms. However, less success in predicting the stiffness and the initial dynamic characteristics was reported.

Yamaguchi, Sugano, Higashibata and Nagashima (1980) tested sixteen scale 1:5 models of isolated barbell walls with main variables the shear span ratio, the axial stress and the amount of longitudinal reinforcement. Ten cycles were applied at each displacement which was progressively increased. Different modes of failure were observed, depending on the values of the main variables. Empirical equations were proposed to estimate the flexural and shear capacity. The ratio of the two capacities '$A_{f:s}$', was found to determine the type of failure. It was proposed that for values of $A_{f:s}$ less than 0.86 shear failure is expected while for values of $A_{f:s}$ more than 1.10 a flexural mode is likely to prevail.

Aoyama and Yoshimura (1980) tested eight reinforced concrete walls under bi-axial loading. The degree of out-of plane loading varied from zero to a load corresponding to the out-of plane yield moment (OPYM) in different experiments. It was reported that moments less than half the OPYM had no effect on the in-plane behaviour of walls. On the contrary, for out-of plane moments more than half the OPYM, ultimate in-plane strength and displacement was reduced and failure occurred by out-of plane bending.

In Mexico, Hernandez and Zermeno (1980) tested 22 scale 1:8 models of isolated RC walls under cyclic loading failing in shear. Eight of the specimens were rectangular in cross section and the rest were barbell shaped. Other variables of the investigation included the shear span ratio,

concrete strength, amount and distribution of the reinforcement, axial load and the presence of intermediate slabs on wall height. It was concluded that RC walls failing in shear have inadequate hysteretic behaviour by their progressive deterioration in strength under cyclic loading. Intermediate slabs acted as stiffeners, increasing initial stiffness but not strength. Based on the experiments equations for concrete shear resistance were developed which take into account only the shear ratio and axial load. For walls of shear ratio 1.9 or more and no axial load, concrete shear resistance was observed to be equal to $0.5 \sqrt{f_{co}}$.

2.1.4 New Zealand

Over the years, a number of researchers at the University of Canterbury, New Zealand, have contributed to the understanding of the behaviour of reinforced concrete. Recently, Goodsir (1985) tested 1:3 scale cantilever walls under eccentric axial and lateral loading. Three rectangular sections (100 x 1500 mm) and a tee section, were tested under a cyclic lateral load history simulating seismic actions. The test assembly and loading arrangement is shown in figure 2.2.

The research aims were to examine the premature inelastic wall instability and the effect of hoop reinforcement for confining the highly compressed zones.

Out-of-plane displacements were observed in all walls and lateral instability was the cause of failure of at least one of the specimens. It was proposed that the conditions leading to lateral instability due to buckling are complex and include :

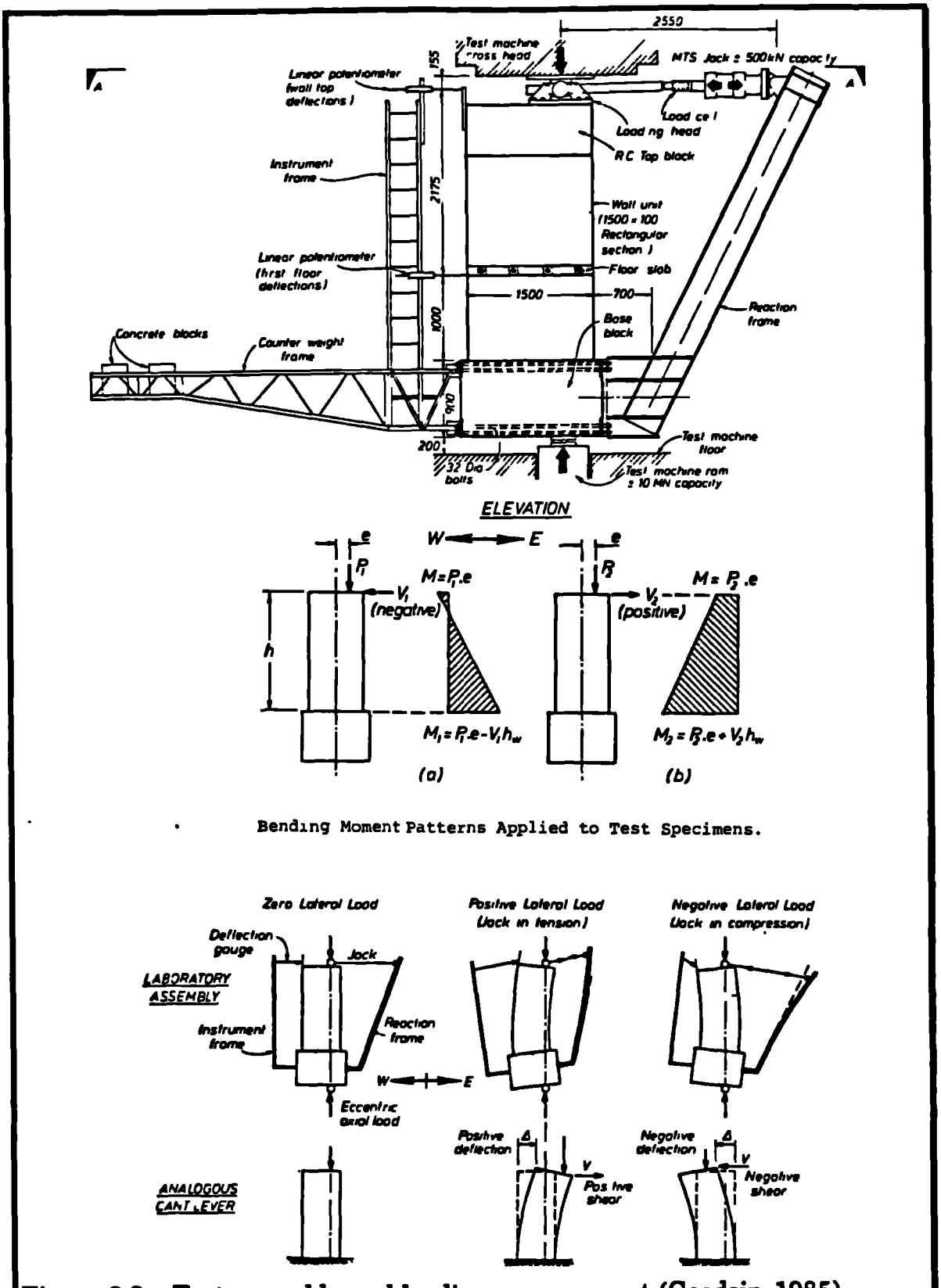
a) The reinforcement stress-strain condition after considerable inelasticity.

b) The imperfect closing of cracks in concrete especially in the presence of shear.

c) The effect of cyclic loading and level of axial load.

d) The uneven spalling of the concrete cover.

e) The spacing of the hoop reinforcement (Local buckling).



Bending Moment Patterns Applied to Test Specimens.

Figure 2.2 Test assembly and loading arrangement (Goodsir, 1985)

One of the main conclusions was that the 1:10 breadth to width ratio recommended by codes offers a reasonable degree of protection against section instability.

It was proposed that the hoop reinforcement be extended further into the cross-section than the outer half of the compressive block (strain of 0.0015), as is currently recommended in the New Zealand standards (NZS 3101:1982). This was considered necessary as an increase in the ideal neutral axis depth (as calculated by the ACI methodology) is expected, due to:

a) Reduction of the cross-section due to loss of concrete cover after spalling translates the compressive area further in the section.

b) Out-of-plane displacements.

c) The increase in concrete compressive area required to maintain flexural capacity under the effect of strength degradation.

The shear reinforcement provided proved to be adequate even though, the required demand exceeded the code allowable concrete shear resistance of $0.6\sqrt{(P/A_g)}$ MPa by 35%.

2.1.5 Europe

Lefas (1988) at Imperial College tested fifteen scale 1:2.5 isolated walls of aspect ratios of one and two. Twelve of the tests were monotonic and three cyclic (with a small number of reversals) with load control, as shown in figure 2.3. The first six monotonic tests (SW1-SW6) were conducted on squat walls of shear ratio of about 1 and the remaining walls (SW21-SW26 and SW31-SW33) with shear ratio of about 2. Of direct interest are the latter ones, since the current study is considered to be an extension of the above mentioned work, to deal with earthquake loading conditions.

All nine specimens had dimensions as shown in figure 2.3. The parameters under investigation were the variation of vertical loading, the concrete strength and the amount of shear reinforcement. Specimens SW21-SW25 had identical flexural and shear reinforcement and were designed according to ACI-318 1983. Specimen SW26 contained half the amount of shear reinforcement provided in the other walls.

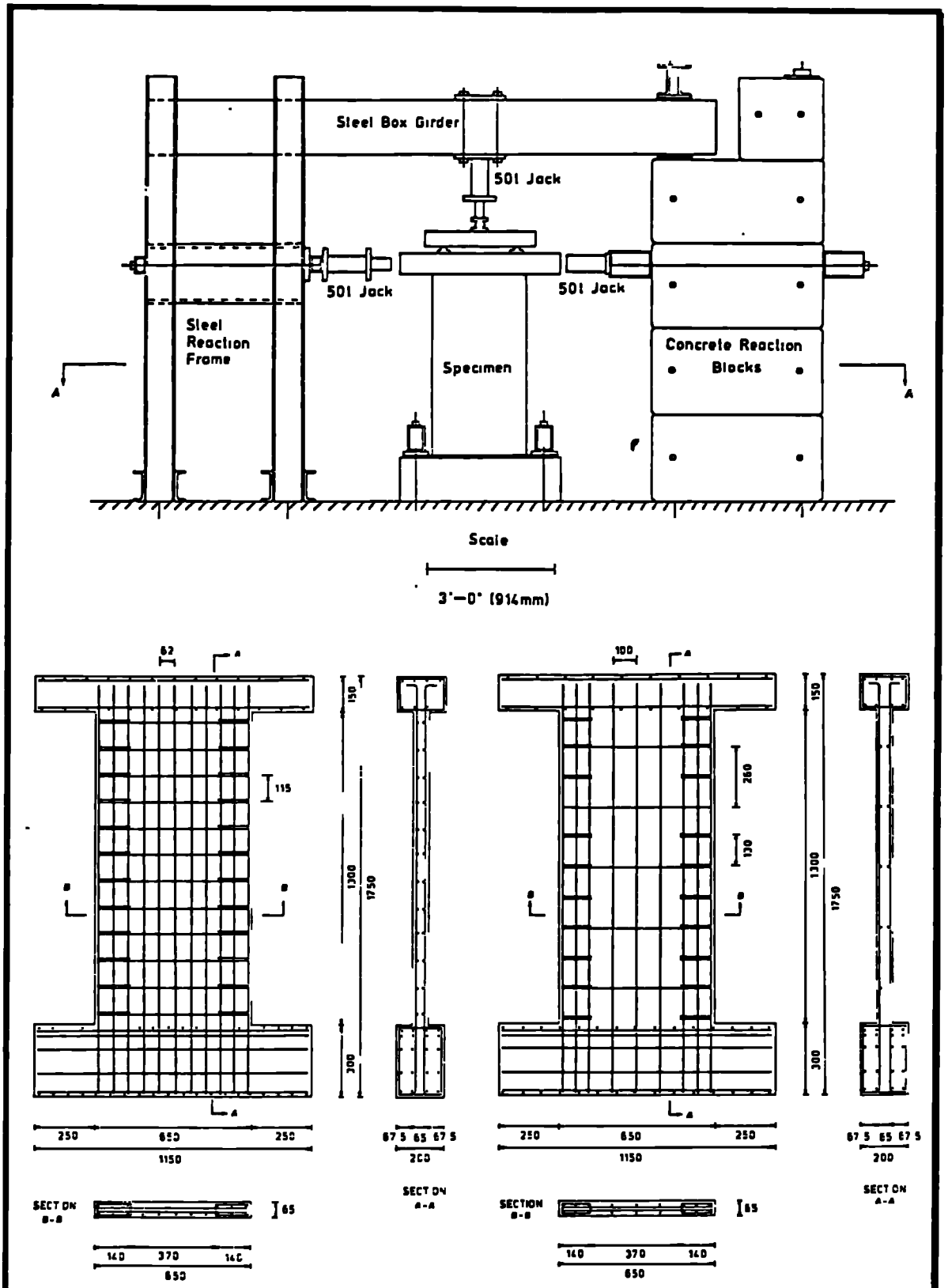


Figure 2.3 Test rig arrangement and wall geometry (Lefas, 1988)

A summary of the experimental results is given in table 2.1 below.

Table 2.1 Experimental results of monotonic tests (Lefas, 1988)

Specimen Code	Axial Load (KN)	Axial Load Normalised	Yield Displ (mm)	Yield Load (KN)	Ultimate Displ (mm)	Ultimate Load (KN)
SW21	0	0	5.81	80	20.61	127
SW22	182.0	0.1	4.91	110	15.30	150
SW23	343.1	0.2	5.20	120	13.19	180
SW24	0	0	6.23	80	18.13	120
SW25	324.8	0.2	5.87	130	9.47	150
SW26	0	0	5.51	68	20.94	123

In all walls failure was due to crushing of concrete in the compressive area. Wall SW5 failed prematurely, due to eccentricity of the axial load.The effect of the axial load, apart from increasing the ultimate moment capacity, was to reduce the yield and ultimate displacements. The analytical predictions based on the finite element method, for both lateral and axial stiffness were higher than the experimental results.

Specimens SW31-SW33 had similar dimensions and boundary flexural reinforcement as the previous walls of the same aspect ratio. However, shear reinforcement supplied was 0.35% of the cross-section and web reinforcement was 60% of that used before. The cube strength of concrete was a variable in these experiments being 35.2 N/mm^2, 53.6 N/mm^2 and 49.2 N/mm^2, in SW31, SW32 and SW33, respectively.The walls were subjected to a small number of load controlled reversals. Specimens SW31 and SW32 were subjected to 4 cycles to a ductility level of 1 and 2 respectively before being tested to failure. Specimen SW33 was subjected to 2 cycles at ductility level of 2, 2 cycles at ductility level 4 and then half cycle to a ductility of about 3 before taken to failure. A summary of the cyclic experimental results is given in table 2.2 below.

Table 2.2 Experimental results of cyclic tests (Lefas, 1988)

Specimen Code	No of cycles μ_Δ=1	No of cycles μ_Δ=2	Yield Displ (mm)	Yield Load (KN)	Ultimate Displ (mm)	Ultimate Load (KN)
SW31	4	-	4.19	64.9	22.22	115.8
SW32	-	4	4.40	64.9	24.51	111.0
SW33	2	2	5.73	71.5	24.97	111.5

Failure of the specimens tested under cyclic loading was also due to crushing of concrete in compression. Unexpectedly, a higher ultimate load was achieved in the specimens with lower concrete cube strength.

In all cases, significant flexural overstrength was reported which lead to the conclusion that the triaxial compressive stresses in the confined boundary element can be several times the uniaxial compressive strength. For example according to results presented based on triangular distribution of stresses within the concrete compressed area, the maximum concrete compressive stress in specimen SW26 was calculated as three times the uniaxial strength.

It should be noted here, that the unconventional use of the triangular stress distribution is not customary in ultimate capacity analysis of RC members. Furthermore, back analysis of this type should not be based on the unconfined concrete ultimate strain, but the confined strain should be estimated through an iterative procedure.

By using a three dimensional concrete model by Kotsovos and Newman (1981), confining stresses necessary to develop the calculated concrete stresses were evaluated. The three normal stresses were then transformed to the octahedral stress space. A failure criterion (Kotsovos, 1980) in terms of the octahedral stress shown in equation 2.1 was then used to obtain the ultimate octahedral shear stress '$\tau_{o,ult}$'. By comparing actual to ultimate octahedral shear stresses it was observed that the latter was always greater than the former.

$$\frac{\tau_{o,ult}}{f_{cu}} = 0.944\left(\frac{\sigma_o}{f_{cu}} + 0.05\right)^{0.724} \qquad (2.1)$$

Failure was reported to occur when tensile cracks propagate into the triaxially confined area. A proposed failure mechanism for the development of tensile stresses in the compressive area is shown in figure 2.4. As a result of bond failure between concrete and tensile reinforcement, the equilibrium conditions are perturbed. Extension of the lower crack is necessary to increase the lever arm length and hence higher compressive stresses are induced in this area. When the critical stress is reached, volume dilation in concrete will induce tensile stresses. When these stresses exceed the tensile strength of concrete vertical cracking will occur and failure will follow.

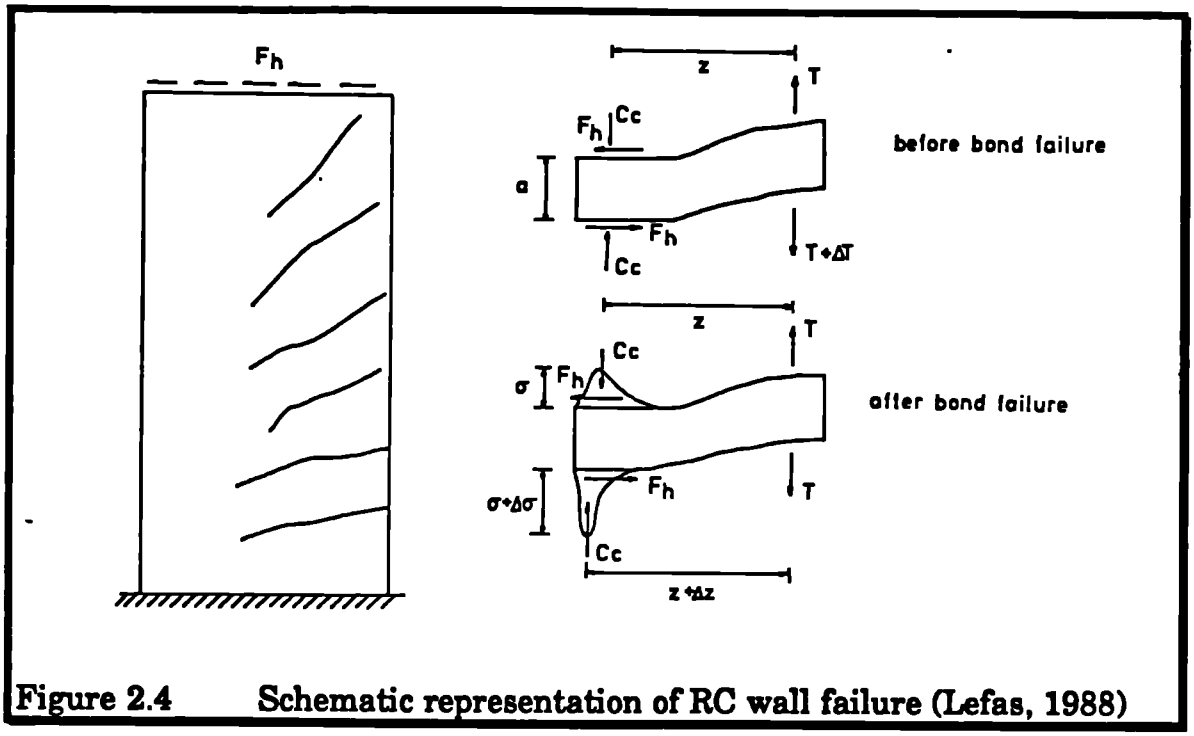


Figure 2.4 Schematic representation of RC wall failure (Lefas, 1988)

From the cyclic experiments, it was concluded that the strength and response of the walls is independent of the cyclic loading regime as well as of the concrete strength. The verification of this radical conclusion is one of the objectives of this thesis.

Extension of the results through a finite element parametric study also showed that code provisions overestimate the shear capacity of walls with high percentages of reinforcement. It was suggested that the omission of axial force in the calculation of wall shear strength can lead to uneconomical design. The results were consistent with the 'compressive force path' (CFP) approach for shear design discussed in subsequent sections.

An on-going research programme into the behaviour and modelling of RC walls at Darmstadt in FRG, included work by Rothe and König (1988) who tested 11 specimens of shear ratio 1.5 as shown in table 2.3 and in figure 2.5.

Table 2.3 Rothe and König (1988) experimental test programme of RC walls

No.	Code	Type	Reinforcement		Axial	Loading
			Vertical	Horizontal	Force	Regime
1	T01	R	6Φ6 mm	2Φ6 mm, e=15	No	Dynamic
2	T02	T	6Φ6 mm	1Φ6 mm, e=15	No	Dynamic
3	T03	T	6Φ8 mm	1Φ6 mm, e=15	No	Dynamic
4	T04	R	6Φ6 mm	-	No	Dynamic
5	T05	R	6Φ8 mm	6Φ6 mm, e=15	No	Dynamic
6	T06	T	6Φ8 mm	1Φ6 mm, e=15	No	Static
7	T07	T	6Φ6 mm	1Φ6 mm, e=15	Yes	Static
8	T08	T	6Φ8 mm	1Φ6 mm, e=15	Yes	Static
9	T09	T	6Φ6 mm	1Φ6 mm, e=15	No	Static
10	T10	R	6Φ6 mm	2Φ6 mm, e=15	No	Static
11	T11	R	6Φ6 mm	2Φ6 mm, e=15	Yes	Static

R = RECTANGLE, T = BARBELL SHAPE

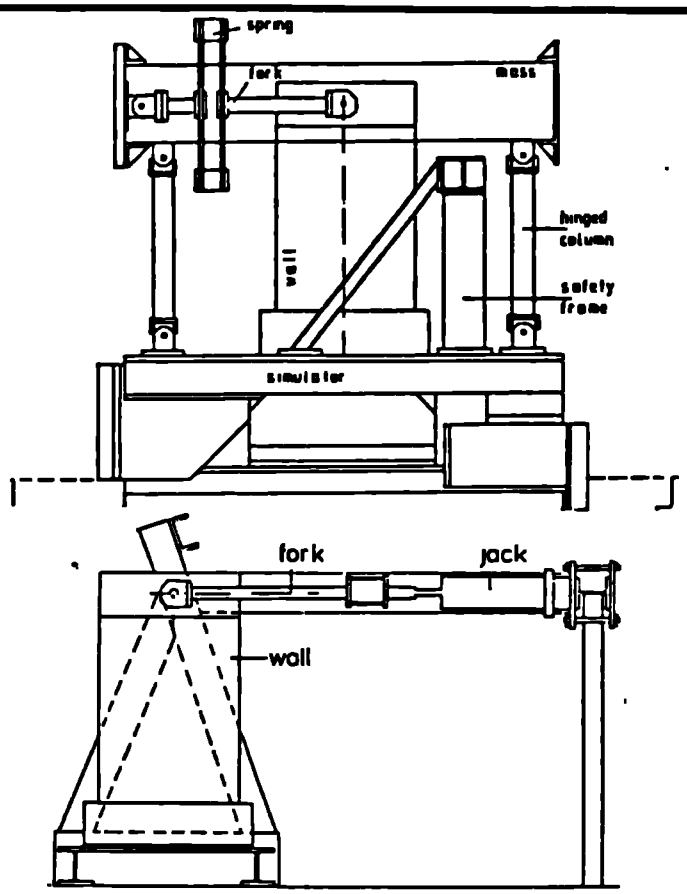


Figure 2.5 Test set-up for dynamic and static-cyclic tests and arrangement of reinforcement and cross-sections of Rothe and König (1988)

For the five walls that were tested on the shake-table a single degree-of-freedom system was assumed as shown in figure 2.5. The mass of 7.2 tons was supported by external columns so that no axial force was taken by the walls. The inertia of the mass was transferred to the wall through springs which were intended to reduce the response frequency and represent upper stories in a building. The El Centro 1940 acceleration time history was imposed on the specimens once until cracking and once until yield. In the final run a harmonic sinusoidal waveform was used. Equivalent damping up to 5% for virgin cycles and 2-3% for subsequent cycles was calculated.

For the cyclic static tests the load was applied through a displacement controlled hydraulic jack. For comparison purposes the top displacements obtained from the shake table tests were used as input in some of the dynamic tests. Axial load was applied through external prestressing rods in three of the walls.

Failure modes varied depending on the cross section, axial force and reinforcement ratio. Bar fracture was observed in under-reinforced walls.

Sudden web failure was observed in the barbell sections while the rectangular sections failed in a more ductile manner. For well designed walls stable hysteretic behaviour was observed up to a stiffness deterioration of 10.

2.2 Design philosophies

Several RC design philosophies which exist on the global structural level as well as on the methods of analysis are discussed in this section.

The 'Capacity design philosophy' advocated by Park and Paulay (1975), is now fully incorporated in the New Zealand Standards. The critical sections of the structure at which plastic hinging would develop and where most of the energy dissipation is expected to take place, are pre-selected and suitably designed. Sufficient reserve strength is provided to the rest of the structure so as to avoid any significant inelastic deformation demand and preclude the formation of an alternative mechanism.

In order to achieve the above, the strength of the section is categorised in a number of different ways. 'Ideal' strength, is the strength obtained by using the code theory for analysis and the actual dimensions and specified material strengths. A 'dependable' strength would be a lower bound of strength and is lower than the 'ideal' strength. 'Probable' strength uses probable strength of materials and is the expected strength to be used for dynamic considerations. 'Overstrength' is an upper limit to the strength that can be achieved and is used to calculate the shear forces acting on the critical section.

The capacity design is incorporated in the draft EC8 (1988), and a significant amount of the section of code referring to reinforced concrete is based on research from New Zealand.

Similar to the above design methodology is the 'Conceptual design procedure' proposed by Aktan and Bertero (1985). The sources of overstrength from the structural and element level should be estimated so as to establish the shear 'demand' on the member. The 'supply' should take into account all the different limit states.

In general, flexural design of RC members is based on section analysis. Several simplifications are allowed by codes to facilitate design, such as the use of an elastic perfectly plastic model for steel, and triangular or equivalent rectangular stress blocks for concrete. The controlling strain is usually the concrete crushing strain at the extreme fibre. In confined members enhancement of the crushing strain and stress can be achieved, which leads to higher moment capacity and ductility.

Both the 'Capacity' and 'Conceptual' design methodologies assume that the plastic hinge zone will be adequately designed and detailed to sustain the rotational ductility demand. However,only recently, in the proposed EC8 (1988) the provisions for member ductility has been related to the overall structural behaviour and design for a specific ductility is possible.

The design for shear is still the subject of research and debate, and several different philosophies exist. The most widely accepted and used methodology is based on the truss model, and is discussed in the following section. The compressive path method advocated in the research programme at Imperial College prior to the current one, is also presented.

2.2.1 Truss model

The conventional truss model shown in figure 2.6 (a) and (b) is still used by most codes for calculating the amount of shear reinforcement. The model considers that the RC wall will behave along its length as if it consisted of tensile horizontal ties and diagonal compression struts. Web crushing due to failure of diagonal compression struts and yielding of the horizontal ties provide the limits for shear capacity of such a member.

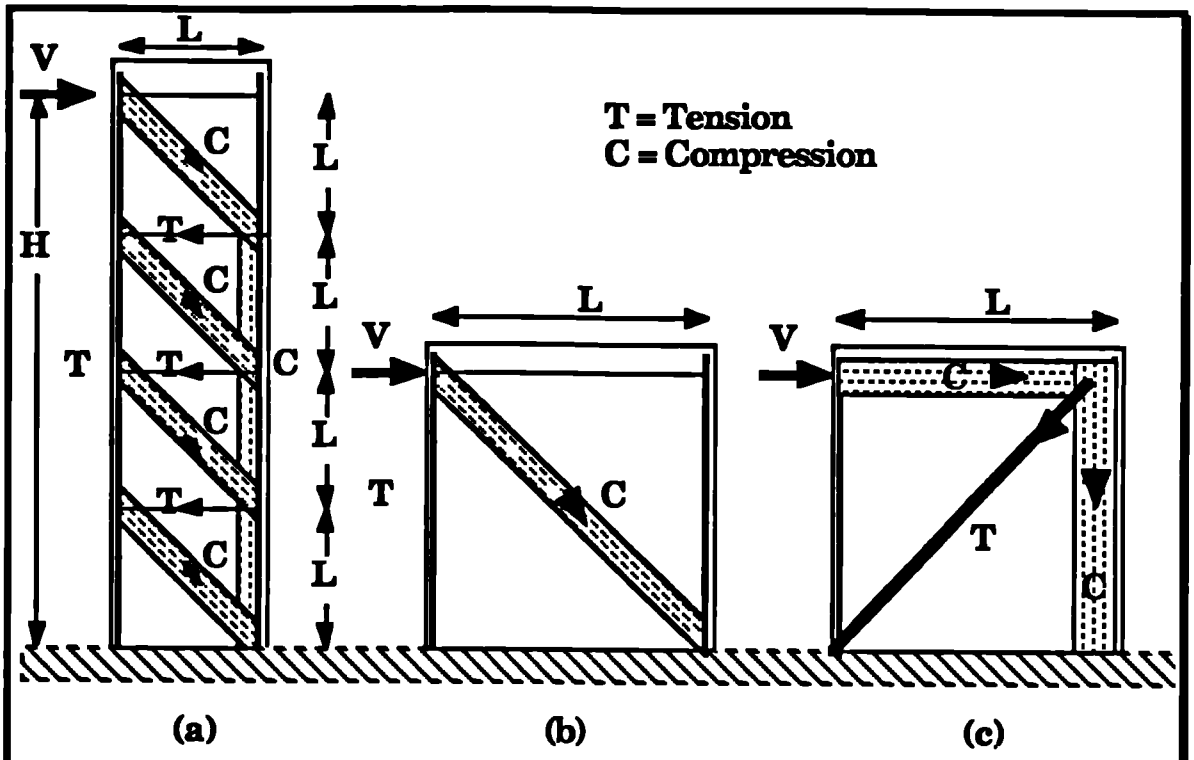


Figure 2.6 Truss models for resisting shear

However, for low aspect ratios the top beams or slabs of walls could act as ties and the arching effect is more effective in transferring forces. An alternative truss model could be employed for low aspect ratios as shown in figure 2.6 (c). As a result the effectiveness of the conventional truss model is very much reduced. Many of the codes recognise this, and hence emphasize the contribution of the vertical web reinforcement in such cases of low aspect ratios.

In all codes, the contribution to shear resistance by concrete alone is calculated by considering average shear stress 'τ_c' over the entire width of the member section. For RC walls where the reinforcement could be uniformly distributed, a slightly reduced width is used so as to account for the reduced lever arm.

The values of τ_c used by codes are empirically derived from experimental work on beams and walls. In deriving these values the contribution of any existent lateral reinforcement is subtracted and the rest is assumed to be resisted uniformly by concrete. However, it is widely accepted that the distribution of shear stresses within the section is neither linear nor parabolic, as given by elasticity. Furthermore, dowel action of the longitudinal reinforcement cannot be easily decoupled from concrete shear

resistance. Despite the over-simplicity and empirical nature of the method it still has very few credible adversaries.

2.2.2 Compressive force path approach

The 'compressive force path' concept (Kotsovos, 1983) considers that shear resistance is available only in areas of concrete compression. The region of compressive stresses is called the 'compressive force path' (CFP). A figure depicting the CFP in a wall is shown in figure 2.7. Failure will occur when tensile stresses develop within the CFP. Lefas (1988) gives the main reasons for the development of such stresses as :

(a) Change in the CFP direction.

For equilibrium purposes a change in the CFP direction would lead to the development of tensile stresses. The location of such change in direction is a central aspect of the method, and depends on the aspect and shear ratio.

(b) Varying intensity of the compressive stress field along the CFP.

The level of compressive stress is highest when the cross-section of the CFP is minimum. When the compressive stress reaches a critical level, concrete dilation will induce tensile stresses to the surrounding concrete. This would be considered by other researchers as compressive failure.

(c) Tip of inclined cracks.

From fracture mechanics principles, tensile stress concentrations will develop at crack tips in the direction of the crack adjacent to the compressive zones.

(d) Bond failure.

Bond failure of the vertical reinforcement will reduce the cross section of the CFP and hence lead to the same results as (b) above.

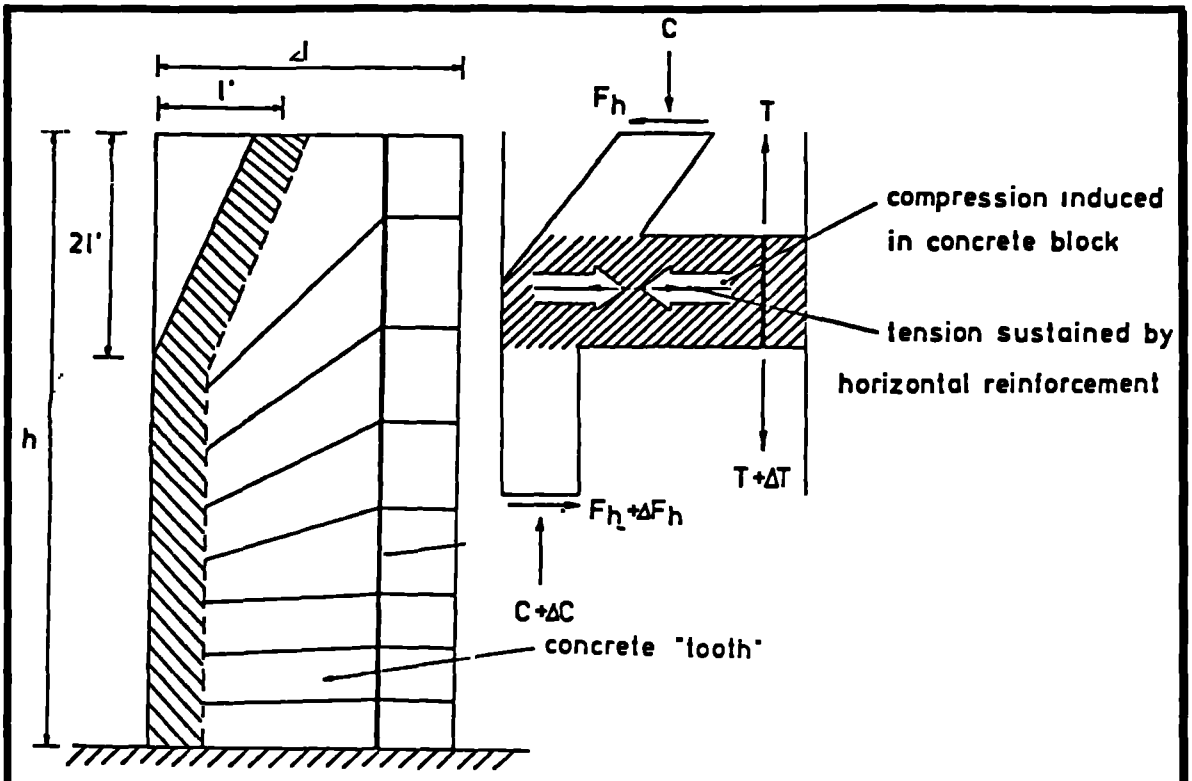


Figure 2.7 The compressive force path in a RC wall (Lefas, 1988)

The mechanism of load transfer, shown in figure 2.7, comprises an inclined branch and a vertical branch. The concrete between the cracks in the web are considered to be 'comb teeth' tied by the reinforcement and capable of bending resistance. The length of 2 l' (where l' is as defined in figure 2.7) for the inclined branch is considered to be equal to 2 D/3 and 3 D/4 plus the depth of the neutral axis for aspect ratios of 1 and 2 respectively.Wall strength is predominantly provided by the tied frame with the concrete 'teeth' between cracks making only a small contribution to wall load-carrying capacity through the bond forces which develop between concrete and tensile reinforcement.

A flexural mode is expected for aspect ratios higher than 2. Furthermore, the stress and strain enhancement due to the presence of confinement should also be taken into account when calculating the flexural capacity 'M_c'.

The shear capacity of the unreinforced section in terms of bending, 'M_{cx}', is to be obtained by an empirical equation derived for beams by Bobrowski and used by Lefas (1988) for RC walls. If M_{cx} is higher than M_c, then only nominal reinforcement is required.

In order to avoid the development of tensile forces at the point of change of direction of the CFP, horizontal reinforcement should be provided to neutralise the horizontal component of the inclined compression strut. According to the method (figure 2.7), this reinforcement also subjects the shaded web area to compression. The area of reinforcement required may be calculated from the difference between the applied shear force and the shear force resisted by concrete. It is recommended that this area is distributed over a length equal to the width of the wall.

In the vertical part of the CFP, no horizontal reinforcement is required, but in order to prevent tensile stresses developing, confinement reinforcement should be provided.

None of the RC walls tested by Lefas (1988) have been designed according to the CFP method. None of the walls failed in shear despite having less reinforcement than required by ACI-318 (1983) which means that the concrete possessed higher shear strength than assumed by this code. The fact that the Bobrowski equation gave a lower prediction for the concrete shear strength was considered as vindication of the CFP method for walls.

There seems to be a gap between the CFP theory and strain compatibility in the area of the inclined branch of the CFP. By using basic principles of mechanics it can be shown that it is not possible to develop an inclined compressive strut at the top of a wall, without inducing compressive stresses in the extreme fibres. Moreover, in order to change the direction of the applied horizontal shear force at the top of the wall as shown in figure 2.7, a tensile force is also required which is not being accounted for. Additionally, the design equation seems to have no association with the CFP theory, and very no information is provided on its origins. Finally, tests conducted by Lopes (1990), on a wall designed and detailed according to the CFP gave a capacity 10% lower than the code-designed counterpart; the wall failing in shear.

2.3 Design of RC Walls

The state-of-practice as represented by existing codes is outlined here, in view of the fact that one of the purposes of this research is to

contribute towards the enhancement of code provisions. Different aspects of design are presented with reference to the American Concrete Institute code (ACI 318-83), the Uniform Building Code (UBC 1988), the New Zealand Standard (NZS 3101:1982) and the Eurocodes (EC). The number of codes in the current World List of Earthquake resistant regulations (IAEE, 1988) is 36, and in order to avoid excessive repetition, the number to be discussed has been narrowed down to the most relevant to the current work.

In all the chosen codes the aim of earthquake resistant design is to avoid brittle failures in RC walls by ensuring that steel yielding occurs prior to the attainment of the shear capacity. If this is achieved, considerable energy dissipation and reduction of the maximum expected forces can therefore be expected. The first stage in design, however, is to obtain a section that can resist the required ultimate bending moment, whilst the second stage is to detail the member for the required ductility. The final step is to ensure that the shear capacity is higher than the shear demand.

Material safety factors and capacity reduction factors are not included in the following section so that the methodologies and design philosophies used by the various codes in order to realise the ultimate capacity may be compared.

2.3.1 Section Flexural Capacity

The design assumptions as given by the ACI 318-83 and UBC (1988) are as follows:

a) For flexural members of aspect ratio more than 0.4, linear strain distribution to be used for both steel and concrete.

b) For ultimate flexure calculations the maximum strain in concrete compression 'ε_{co}' to be 0.003.

c) The tensile strength of concrete is neglected.

d) Any shape of stress-strain distribution for concrete may be used as long as it agrees with comprehensive tests. Codes in general suggest simplified distributions for use such as the equivalent rectangular block.

e) Steel behaviour is linear elastic perfectly plastic.

In EC2 (1984) the value of ε_{co} is 0.0035. EC8 (1988) recognises an increase in ε_{co} depending on the available confinement. The same code gives different limiting values of minimum strain in reinforcement depending on the ductility class (DC). For DC high, "H", a minimum elongation of 0.012 is specified. Additionally, for the same ductility class the code requires the ratio of tensile failure to yield ratio to be between 1.3 and 1.45 with actual to nominal yield ratio not to exceed 1.15.

Based on the above assumptions, some of the codes, as well as most of the handbooks of concrete design, provide simplified equations for assessing the strength of a section, and guidance for dimensioning and supplying reinforcement for achieving the required strength. However, such equations usually apply to a specific types of section within a limited range of steel distributions and hence should be used with care. An alternative to using design charts is to conduct section analysis, accounting for the exact area and location of reinforcement and concrete stress-strain relationship, as described in chapter 5.

2.3.2 Detailing for ductility

In order to achieve ductile behaviour through the development of a plastic hinge, codes impose dimensional limitations and include provisions for hoop reinforcement. As part of the special provisions for seismic design of RC walls, both ACI 318-83 and UBC (1988) require the provision of boundary elements where the compressive stress is more than 0.2 f_{co}.These boundary elements should be designed to resist all the axial loads imposed on the member and are to be designed as columns. The minimum area of rectangular hoop reinforcement 'A_{sh}' shall not be less than that given by either of the following equations.

$$A_{sh} = 0.3 \left(\frac{s\, h_c\, f_{co}}{f_{yh}} \right) \left[\left(\frac{A_g}{A_{ch}} \right) - 1 \right] \qquad (2.2)$$

$$A_{sh} = 0.12\, s\, h_c\, f_{co} / f_{yh} \qquad (2.3)$$

The spacing of transverse reinforcement should not exceed B/4 or 100 mm (where B is the thickness of the wall), and should be over a length not less than the width of the wall 'D' or H/6 or 450 mm (where H is the height of the wall).

The NZS 3101 (1982) code requires confinement for the outer half of the compression zone where strains exceed 0.0015, provided the neutral axis depth exceeds a given limit. The area of hoop reinforcement, 'A_{sh}', to be provided is obtained by multiplying equations 2.2 and 2.3 by {0.5+0.9 c /D} (to account for an increase in neutral axis depth 'c' due to the presence of an axial load 'P'). The spacing of the hoop reinforcement should not exceed B/3 or 150 mm or six times the diameter of vertical bars confined. Hoop reinforcement should be provided over a length equal to D. By complying with the above requirements, the designer avoids further detailed calculation for curvature ductility capacity '$\mu_{1/r}$'.

From experiments conducted on columns in New Zealand, Zahn, Park, Priestley and Chapman (1986) reported that code prescribed confinement would yield a value of $\mu_{1/r}$ of about 20. The relation between curvature ductility and displacement ductility is shown to be dependent not only on the aspect ratio of the wall but also on the length of the plastic hinge. Paulay and Uzumeri (1975) considered two different equations for the length of the plastic hinge, which form the limits of the shaded bands depicted in figure 2.8. The above work has been used in the design for ductility of EC8 (1988).

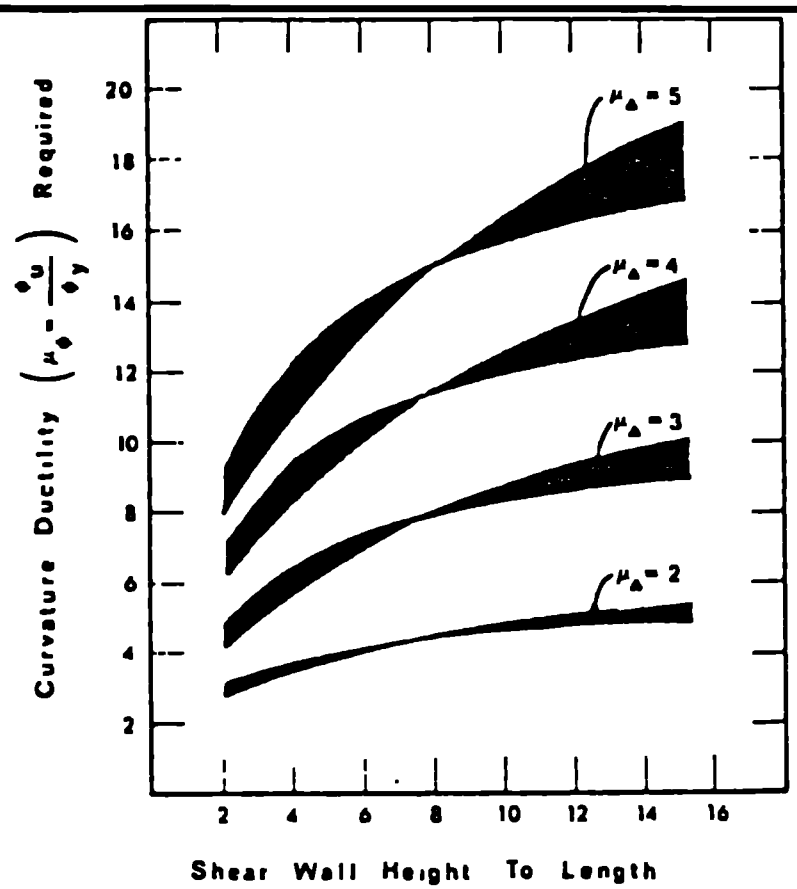


Figure 2.8 The variation of curvature ductility at the base of cantilever shear walls with aspect ratio of the walls and the imposed ductility demand (Paulay and Uzumeri, 1975)

The proposed EC8 (1988) assigns behaviour values 'q' values for different structural systems and different ductility classes. Having assigned the q-value the required displacement ductility 'μ_Δ' can be obtained directly. Based on the assumption that for a cantilever wall plastic yielding would occur in the bottom 10% of the height, the curvature ductility is given by:

$$\mu_{1/r} = 1 + 3.5\,(\mu_\Delta - 1) \qquad (2.4)$$

Table 2.4 shows the relationship between the q-values and $\mu_{1/r}$ for the different ductility classes as given by Tassios (1989) in a background document on the EC8 for both coupled and isolated walls. Two methods are used yielding two different values for displacement ductility, $\mu_{\Delta 1}$ and $\mu_{\Delta 2}$. The first value is based on the equal energy principle (Tassios and Chronopoulos, 1988), but the average is used to calculate the curvature ductilities.

Table 2.4 Relation between q-values and curvature ductility (Tassios, 1989)

DC	q	$\mu_{\Delta 1}$ $0.5(q^2+1)$	$\mu_{\Delta 2}$ q	μ_{Δ} $0.5(\mu_{\Delta 1}+\mu_{\Delta 2})$	$\mu_{1/r}$ $1+2.5(\mu_{\Delta}-1)$ (coupled walls)	$\mu_{1/r}$ $1+3.5(\mu_{\Delta}-1)$ (isolated walls)
"L"	1.5	1.63	1.5	1.56	2.40	2.97
	2.0	2.5	2.0	2.35	4.13	---
"M"	2.5	3.63	2.5	3.06	6.16	8.22
	3.0	5.0	3.0	4.00	8.50	---
"H"	3.5	6.63	3.5	5.06	11.16	15.21
	4.0	8.5	4.0	6.25	14.13	---
	4.5	10.63	4.5	7.56	17.41	---
				Approximation	$\mu_{1/r} \cong q^2$	$\mu_{1/r} \cong 1.2\ q^2$

The curvature ductility is used to obtain the required confinement volumetric mechanical ratio, 'ω_{wd}', by using equation 2.5.

$$\omega_{wd} = 0.9\sqrt[3]{\mu_{1/r}}\left[\ 0.01\ \mu_{1/r} + 0.15\ \frac{A_c}{A_o}\ v_d - 0.4\ \right] \qquad \geq 0.2 \qquad (2.5)$$

where A_c is the concrete gross area and A_0 is the core concrete area along the confined length 'l_c'. The confined area should be extended horizontally so as to cover concrete with expected maximum strains equal to 1.5%. Vertically, l_c should be greater than D, a sixth of the wall height, or storeys height. Detailing of hoops over this height is specified as for columns. The minimum diameter, 'd_H', allowed for hoops is 6 mm, at spacing of B/4, 6 d_L (where d_L is the diameter of the longitudinal reinforcement) or 100 mm whichever is less. The diameter of d_H should be about 0.4 d_L. Strict provisions for hoop arrangements are to be used. Single hoop is not allowed for DC "H".

EC8 recognises an increase of the concrete strain at failure due to hoop reinforcement as shown in the equation 2.6.

$$\varepsilon_{cu} = 0.0035 + 0.10\,\omega_{wd}\,\alpha \qquad (2.6)$$

The value of 'α' depends on the hoop configuration. Confinement is also considered to enhance the ultimate concrete strength as well as the strain at which this is achieved.

2.3.3 Shear design

The design against brittle shear failure is the aim of all codes. It is therefore important, that the design shear force 'V_u' is not just the force required to induce the maximum applied design moment 'M_c', but the force corresponding to the maximum probable section strength 'M_o'. For this effect, the NZS 3101 (1982) code considers the flexural overstrength (M_o/M_c) when determining V_u. The ideal section shear force 'V_i', is calculated from the equation below:

$$V_i = v_i\,B\,d_e \qquad (2.7)$$

where the effective depth, 'd_e', is to be taken as 0.8 D unless determined by strain compatibility analysis. To calculate the section shear stress capacity 'v_i' the separate contributions from concrete 'v_c' and steel 'v_s' are summed-up as shown below:

$$v_i = v_c + v_s \qquad (2.8)$$

The American codes use section shear forces instead of stresses for the same effect. However, the potential flexural overstrength of the member is not taken into account directly by the above codes.

Upper limits for the maximum permitted shear capacity are specified in all codes. The value of v_i according to the more conservative NZS 3101 (1982) should not exceed 0.2 f_{co}, 6 MPa or the value from equations 2.9 and 2.10.

$$v_i = 0.9\sqrt{f_{co}} \qquad (2.9)$$

$$v_i = (\,0.3\,\phi_o\,S + 0.16\,)\sqrt{f_{co}} \qquad (2.10)$$

The American codes use a value of 0.83 $\sqrt{f_{co}}$ in equation 2.9. The above limiting equations are introduced so as to prevent web failure due to diagonal compression.

The structural type factor (equation 2.10), S, as given in NZS 4203 (1984) accounts implicitly for the ductility demand on the section. For single cantilever walls, the value of S ranges between 1.2 and 2. The higher the value, the lower the ductility demand and hence, higher shear can be resisted. Similarly, the value of ϕ_0 (flexural overstrength factor) being about 1.4 for high strength reinforcement, is expected to reduce the ductility demand and hence, increase the shear capacity.

For walls of ductility class "H", the proposed EC8 (1988) requires checks for three limiting equations corresponding to three different types of failure as discussed below:

(a) For web diagonal compression failure, the code differentiates between critical and non-critical sections. The average shear stress shall not exceed :

  (i) $0.2\ f_{co}$ in critical sections and

  (ii) $0.3\ f_{co}$ in non-critical sections.

(b) For web diagonal tension failure, the code considers different mechanisms of shear resistance from the steel reinforcement for shear ratios 'α_s' on either side of a value of 1.3. The concrete contribution to shear resistance, is independent of the value of α_s, and the section capacity is limited according to the following criteria :

  (i) average axial stress less than $0.1\ f_{co}$

    - zero in the critical sections of the wall and

    - $2.5\ \tau_{Rd}$ (τ_{Rd}, stress obtained from table 4.1 of EC2) for sections outside the potential hinge areas.

  (ii) average axial stress more than $0.1\ f_{co}$

    - $2.5\ \tau_{Rd}$ (τ_{Rd}, stress obtained from table 4.1 of EC2) for critical sections and

    - $2.5\ \tau_{Rd}\ \beta_1$ ($\beta_1 = 1 + M_{do}/M_{sd} \leq 2$ as defined in notation) for sections outside the potential hinge areas.

  (1) For α_s more than 1.3, only the contribution of horizontal shear reinforcement, according to the truss analogy, is taken into account. Vertically distributed reinforcement of an amount

equal to the horizontal should be provided when the axial load is zero. The amount of this reinforcement can be reduced by the equivalent minimum axial force on the section.

(2) For α_s less than 1.3, the contribution of horizontal shear reinforcement is linearly reduced to zero for α_s of 1.3 - 0.3, whilst the contribution of vertical reinforcement is linearly increased to the sectional yield strength for the same range of α_s.

The minimum amount of ρ_h and ρ_v is 2.5%, of diameter less than B/10 but not less than 8 mm, at a spacing not more than 20 bar diameters or 200 mm.

(c) For shear sliding failure at the bottom horizontal section, the code considers resistance from the dowel action of vertical and diagonal web bars, as well as the effect of the axial load. Dowel action for each vertical bar is defined as $1.5\ A_s \sqrt{(f_{co}\ f_{sy})}$ and for inclined bars $2\ A_s\ f_{sy} \cos\theta$ (θ angle to the horizontal). One third of the average minimum axial stress is considered to be a safe lower value of concrete-to-concrete friction under cyclic loading.

The New Zealand code, in a section for special provisions for earthquake resisting walls, requires that within the potential plastic hinge zone a more stringent equation for concrete shear resistance is to be used. The height over which the special provisions should be applied is given as the largest of D or one sixth of the height of the wall, up to a maximum height of 2D. The concrete contribution to shear 'v_c' over this height is considered to be dependent only on the level of axial stress, as given in equation 2.11.

$$v_c = 0.6 \sqrt{\frac{P}{A_g}} \qquad (2.11)$$

The ACI 318-83 and UBC (1988) link the nominal shear strength to the wall aspect or shear ratio (the larger of the two) rather than axial load. For a value higher than 2, the concrete shear resistance is given as $0.166 \sqrt{f_{co}}$, whilst an increase of 50% of this resistance is allowed for a decrease in the shear or aspect ratio from 2 to 1.5, linearly interpolated for intermediate values.

In the NZS 3101 (1982), for the area outside the plastic hinge zone, the ordinary provisions for shear apply. The value of v_c should be the lesser of equations 2.12 and 2.13, given below

$$v_c = 0.27\sqrt{f_c} + \frac{P}{4A_g} \tag{2.12}$$

$$v_c = 0.05\sqrt{f_{co}} + \frac{D\left(0.1\sqrt{f_{co}} + 0.2\frac{P}{A_g}\right)}{\left(\frac{M}{V} - \frac{D}{2}\right)} \tag{2.13}$$

where P is negative in tension. Equation 2.13 does not apply when the denominator is negative. These equations are the same as given in the ACI 318-83 code which, however, does not differentiate between the plastic hinge zone and the rest of the wall. It is evident, therefore, that even though the NZS 3101 (1982) is more conservative in the plastic hinge area, it may overall be a more economic code than the American codes.

In all codes when the shear capacity 'v_i' is greater than the shear demand 'v_e', then horizontal shear reinforcement is required. The amount of reinforcement is calculated according to the principles of the truss analogy and is similar in all codes of practice (except for walls of shear ratio α_s less than 1.3 in EC8, as mentioned already) as shown below.

$$A_v = \frac{(v_i - v_c)\,B\,s_2}{f_{yh}} \tag{2.14}$$

where 'A_v' is the area of horizontal shear reinforcement within a vertical spacing 's_2'. The spacing, 's', should not exceed D/5, 3B, nor 450 mm.

In the plastic hinge zone, the NZS 3101 (1982) requires this amount not to be less than given by the equation 2.15 below, which corrects for the centre of forces in the hypothetical truss which is supposed to be formed in the section.

$$\rho_h = \frac{4}{3}\left[\left(\frac{l_a\,V\,f_{yn}\,\rho_n}{M\,f_{yh}}\right) - \frac{v_c}{f_{yh}}\right] \tag{2.15}$$

The American codes require the horizontal reinforcement ratio, 'ρ_h', not to be less than the vertical web reinforcement ratio, 'ρ_v', (for walls with shear or aspect ratio less than 2 but not less than 0.0025. Codes recognize the contribution of vertical web reinforcement in controlling the shear

crack width. The value of ρ_v is given by equation 2.16, but should not be less than 0.0025 and not more than 0.06.

$$\rho_v = 0.0025 + 0.5\,(\,2.5 - H/D)\,(\,\rho_h - 0.0025\,) \qquad (2.16)$$

The NZS 3101 (1982) code requires that the ratio of ρ_v to gross concrete area of horizontal section not to be less than $0.7/f_{yh}$ and not more than $16/f_{yh}$. The spacing of this reinforcement shall not exceed D/3, 3B, nor 450 mm.

An interesting distinction between slender and squat walls is based on the expected type of failure mode by EC8 (1988) as shown in figure 2.9.

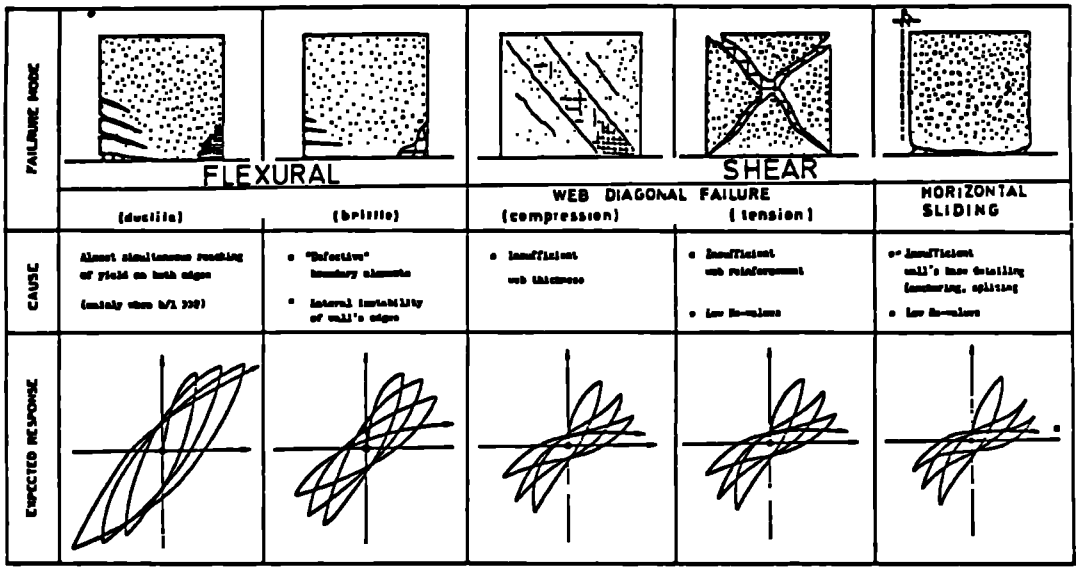


Figure 2.9 Failure modes of RC walls critical regions (EC8, 1988)

The probability of a particular type of failure is associated with the level of shear resistance available in the section. Failure is related to a value 'υ', which is the ratio of minimum design shear strength, 'V_{RD}', to the single shear force, 'V_{MRD}',that would cause the design moment, as shown in equation 2.16.

$$\upsilon = V_{RD} / (\,\gamma_{RD}.\, V_{MRD}\,) \qquad 2.16$$

The value of 'γ_{RD}' represents the uncertainties in estimating the level of the exact forces. For walls of DC "M" and "H" the value of γ_{RD}. is 1.3 and 1.4

respectively. For these two ductility classes the different probable failures are as follows:

$1.00 < \upsilon$	Flexure type of failure is highly probable
$0.75 < \upsilon \leq 1.00$	Mixed type of failure of a prevailing flexural character is probable
$0.50 < \upsilon \leq 0.75$	Shear type of failure is probable
≤ 0.50	Shear type of failure is certain

Based on the above, walls of aspect ratio higher than 1.5 are considered 'slender' and of aspect ratio less than 0.5 are considered 'squat'. The more conservative New Zealand standards consider walls of aspect ratio higher than 2 as 'slender' and impose a higher penalty through the structural factor for 'squat' walls of aspect ratio less than 2.

Dimensional limitations in the codes are provided in order to eliminate lateral instability. For rectangular walls an effective height to width ratio of 10 is considered adequate for stability considerations.

2.4 Discussion

The actual flexural capacity of RC wall sections is higher than the design flexural capacity due to the simplifications used in the design process and material variability. During EQ loading the ultimate flexural capacity may be reached and hence an accurate estimate of the shear forces is necessary for the shear design of the member. Several factors contribute towards the overstrength, and in this thesis their effect are investigated, in view of the conclusions drawn by Lefas (1988).

It is recognised, by previous researchers as well as by the present author, that concentrating the reinforcement at the boundaries is a cost effective means of utilising flexural reinforcement; such arrangements do not seem to be widely researched. A reason for this may be the assumption that web reinforcement is necessary for enhancing the shear resistance of walls. This aspect of wall behaviour is further investigated in the current thesis.

Estimation of the stiffness of RC walls is an issue that few researchers addressed. In several dynamic investigations of small scale RC members, more flexible behaviour than expected was encountered. Since the determination of the dynamic characteristics depends on the stiffness of the structural components, the relation between the predicted and initial stiffness, as well as the stiffness deterioration, is worthy of investigation.

The shear resistance of RC members continues to be a subject of research. Considerable controversy surrounds the applicability and indeed the validity of the truss analogy. The CFP method, advocated by Lefas (1988) for the design of RC walls, has not been linked adequately neither to the experiments nor to the design equation. A more detailed study of the problem is necessary and is presented in this thesis.

A number of new design ideas have been put forwards in the proposed in EC8 (1988). Design for ductility and prediction of the mode of failure are two of the ideas that are investigated, through the analysis and experiments conducted in the course of the current research programme.

Finally, a significant part of the research on which code recommendations are based was based on monotonic test observations. More severe loading conditions are expected during earthquakes, and hence, a severe cyclic regime is more appropriate when the research is directed towards EQ resistant design.

In conclusion, whereas significant advancement in understanding the behaviour of RC walls under EQ loading was achieved, there is still a pressing need for work directed towards the resolution of a number of key issues. This is particularly important due to the significance of the role played by RC walls in the overall response of buildings to strong ground motion.

CHAPTER 3

3 EXPERIMENTAL METHODOLOGY

3.1 Introduction

The experimental programme comprised nine tests as shown in Table 3.1 below. In this chapter, the modelling procedures and choice of the experimental parameters, the test-rig set-up and the design and material strength of the specimens are presented.

Table 3.1 Summary of experimental programme

WALL NUMBER	MODEL RATIO	DIMENSIONS (cm)	ASPECT RATIO	M/VL a_r	LOADING REGIME
SW1	1:5	60 x 30 x 3.2	2	2.92	SHAKE-TABLE
SW2	1:5	60 x 30 x 3.0	2	2.92	CYCLIC
SW3	1:5	60 x 30 x 3	2	2.10	CYCLIC
SW4-SW9	1:2.5	120 x 60 x 6	2	2.10	CYCLIC

3.2 Small scale reinforced concrete modelling procedure in dynamics

Experiments SW1-SW3 were performed on 1:5 scale models. SW1 was tested on the shake-table while SW2 and SW3 were tested under cyclic displacement control loading. In this section, the development of a small scale dynamic modelling procedure for RC walls, necessary for shake-table testing, is presented.

Small scale model analysis is based on dimensional analysis (Elnashai, Pilakoutas and Ambraseys, 1988 a). Given the basic model ratios, the similitude relationships can be determined by using Buckingham 'Π' theorem. The theorem considers that any number of 'n' different quantities 'q' that represent the phenomena in a given physical system are represented by a certain function 'f(q)', as shown below.

$$f(q_1,q_2,.....q_n) = 0 \tag{3.1}$$

This function can be transformed into a new function 'F(r)', having 's' non-dimensional independent terms 'r', by using powers of the quantities 'q' in terms of chosen fundamental quantities 'b', i.e.,

$$F(r_1,r_2,.....r_s) = 0 \tag{3.2}$$

The difference 's' between the number of variable quantities 'n' and the number of fundamental quantities is given by:

$$s = n-b \tag{3.3}$$

The theory of models is developed herein by using the principles described above. Equation 3.2 becomes the relationship for both the prototype (subscript $_p$) (equation 3.4) and model (subscript $_m$) (equation 3.5), where the independent non-dimensional terms have to include the 'b' fundamental quantities to be modelled.

$$F_p\,(r_{1p},r_{2p},.....r_{sp}) = 0 \tag{3.4}$$

$$F_m\,(r_{1m},r_{2m},.....r_{sm}) = 0 \tag{3.5}$$

The above two equations can be rearranged to give equations 3.6 and 3.7.

$$F'_p\,(r_{2p},r_{3p},.....r_{sp}) = r_{1p} \tag{3.6}$$

$$F'_m\,(r_{2m},r_{3m},.....r_{sm}) = r_{1m} \tag{3.7}$$

The general design or prediction equation, therefore, becomes :

$$a_s = \frac{r_{sp}}{r_{sm}} = \frac{F_p'\,(r_p)}{F_m'\,(r_m)} \tag{3.8}$$

Since there are three fundamental dimensions, length, time and force, for true modelling, only three independent scale factors can be

chosen arbitrarily. The ratios between the three fundamental quantities can be selected freely but all secondary equations should be satisfied, subject to technological and financial constraints. Provided that this is achieved, the model is called 'complete' and the prediction equations and model ratios 'a_s' can be used to calculate the required prototype quantities from the model measurements, and vice versa. It is not necessary to know the function F'(r) and it is only required to record the necessary variable quantities 'r_{sm}' for the interpretation of results.

For dynamic and shake-table testing, the three arbitrarily chosen model ratios should relate to the geometric, force and dynamic similitude relationships. The technological limitations of small shake-tables usually govern the first two model ratios.

3.2.1 Geometry similitude

The size of the model is limited by the maximum shake-table force and hence, the geometric scale factor 'λ' is determined by consideration of the force similitude. A lower bound value for the scale factor is imposed by the material properties.

3.2.2 Force similitude

Force scaling is necessary to reproduce stresses of interest and as a result, it is influenced by material properties such as the stress-strain relationship, shear transfer, creep, bond, cracking and crushing. In order to avoid material scaling effects, the same concrete mix was used throughout the experimental programme. For the same reason, specially manufactured model reinforcement (Noor, Raveendran and Evans, 1985) was utilized. As a result, the elastic properties' scaling factor 'ε' was chosen as unity. However, it has been demonstrated analytically by Menu and Elnashai (1988), that a 30% variation in the concrete elastic modulus of RC walls will influence the overall stiffness and result in fundamental frequency variations of up to 15% as shown in figure 3.1. The effect of Poisson ratio variation has no effect on the dynamic characteristics. This suggested that final "tuning" of the experimental programme and choice of

the modelling ratio that affects the dynamic behaviour is better performed after material properties have been measured.

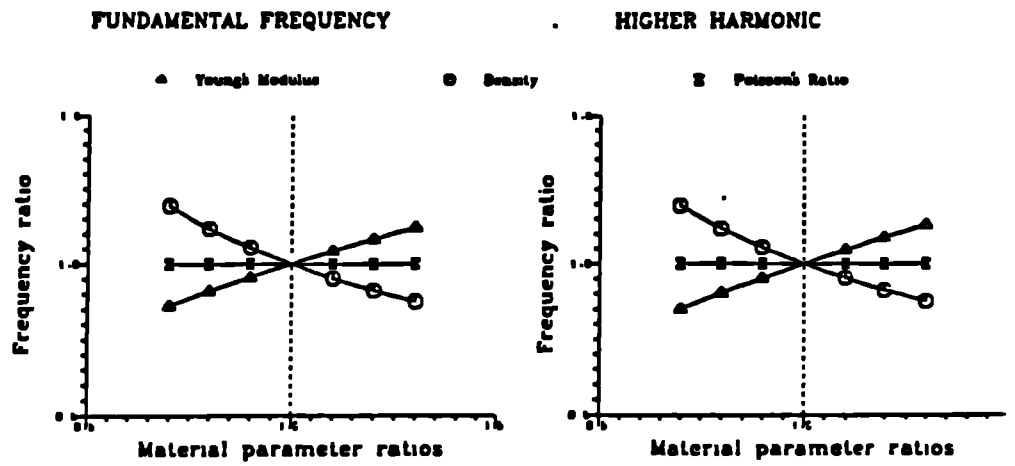


Figure 3.1 Influence of the variations in material properties of a reinforced concrete shear wall model (Menu and Elnashai, 1988)

3.2.3 Dynamic similitude

In small scale modelling on shake-tables, the exact and simultaneous reproduction of stiffness and inertia forces is not possible. In RC walls, however, self-weight gravity (or inertia) forces in shear walls are generally negligible compared to the overall building gravity forces to be resisted and hence, the scaling factor 'ρ' which determines these forces can be neglected. As a result, a similitude relationship which uses 'ρ' as the third variable model scale factor is usually used. This factor, when used together with 'λ' and 'ε', influences only time-dependent quantities including the velocity. Since for a material such as concrete the velocity of loading and propagation of cracks is an important dynamic parameter, it is proposed that the velocity scale factor 'ν' should be chosen as the third modelling parameter. The resulting model parameters are given in table 3.2.

Table 3.2 Small scale dynamic modelling ratios for reinforced concrete

QUANTITY	DIMENSION	MODEL	SCALE	FACTOR
Length	L	λ		
Elastic E	$F L^{-2}$		ε	
Density	$F L^{-4} T^2$		ε	ν^{-2}
Area	L^2	λ^2		
Volume	L^3	λ^3		
Mass	$F L^{-1} T^2$	λ^3	ε	ν^{-2}
Force	F	λ^2	ε	
Moment	F L	λ^3	ε	
Stress	$F L^{-2}$		ε	
Time	T	λ		ν^{-1}
Frequency	T^{-1}	λ^{-1}		ν
Velocity	$L T^{-1}$			ν
Acceleration	$L T^{-2}$	λ^{-1}		ν^2

3.2.4 Choice of model parameters

The geometric and dynamic model parameters must yield model quantities within the shake-table capabilities. For horizontal excitation the maximum dynamic force of the Imperial College shake-table is 48 KN and the maximum payload is 4895 Kg at a height of 1 metre. The frequency range is 1-40 Hz and the minimum time interval 'Δt' that would allow an adequate number of data acquisition channels to be used is 0.005 seconds. Preliminary analysis of a full size isolated RC wall of aspect ratio 2 yielded a strength of about 1000 KN, hence, a model scale force factor of 25 was chosen. Since the elastic properties scale factor was chosen as unity, it follows that 'λ' is 5. For 'ν' of 1 the time 'τ' and acceleration scale factor 'α' would be 5 and 1/5 respectively. In order to avoid very high accelerations, for the pilot experiment, the inertia mass was chosen to be 2000 Kg and 'α' set to unity. Additionally, earthquakes of original $\Delta t = 0.02$ s were scaled to 0.005 s rather than 0.004 s in order to maintain the required data acquisition capability. This deviation from the proposed modelling procedure would result in a different prototype real scale. However, since the only objective of this pilot experiment is the comparison with models

tested statically, full satisfaction of the dynamic similitude conditions is not of utmost significance.

3.3 Experimental set-up

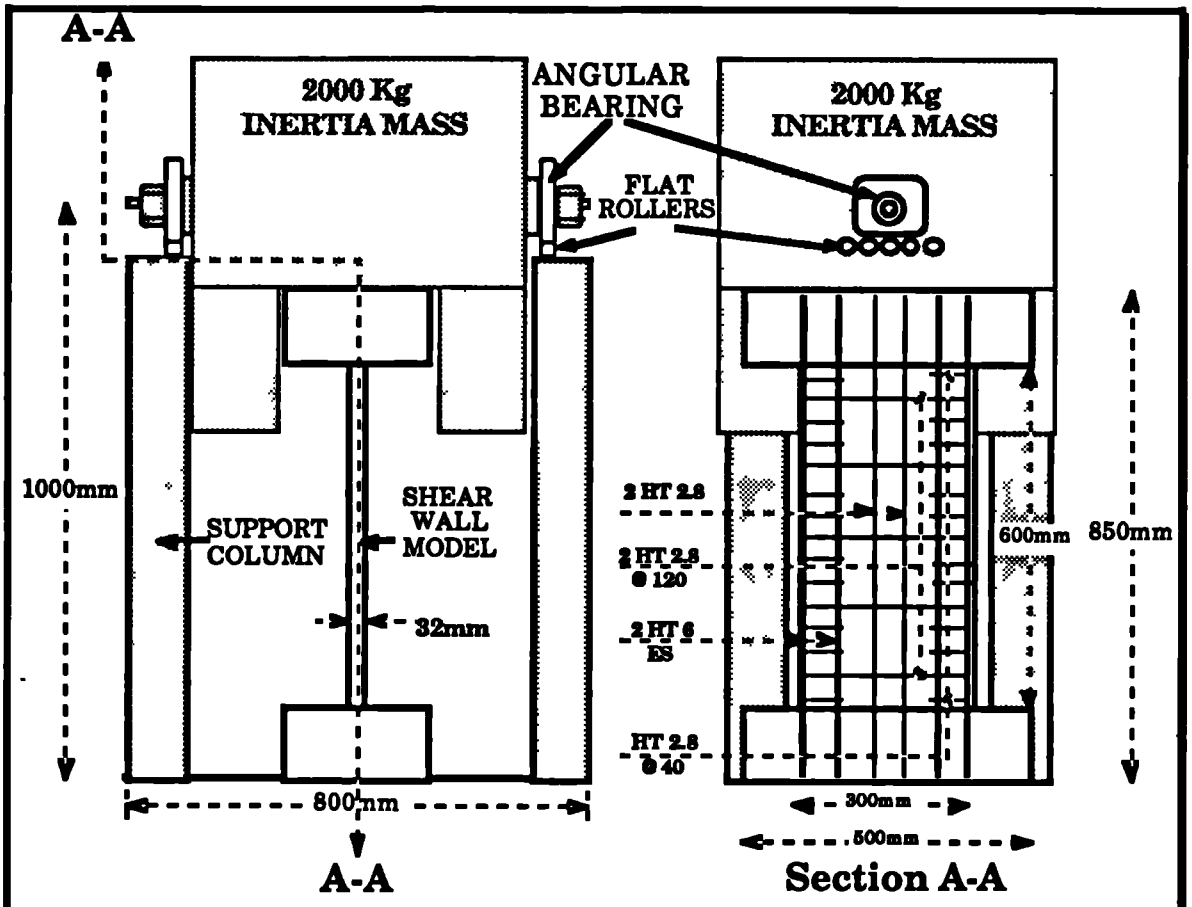


Figure 3.2 Shake-table test rig arrangement and wall reinforcement details

3.3.1 Shake-table test-rig

The design of the shake-table test-rig shown in figure 3.2 was intended to satisfy the following:

(a) Support the 2000 Kg mass at a centre of gravity of 1 metre or less above the table platform.

(b) Allow free translation and rotation in the direction of shaking to satisfy the isolated wall boundary conditions.

(c) Prevent all out-of-plane degrees of freedom.

(d) Be stable during all stages of assembly and testing including impact loading due to brittle wall failure.

Additionally, the test-rig lateral stiffness (in the absence of the wall and with the mass locked) was designed to coincide with the expected initial wall stiffness. With this approach, time-history matching was performed on the test-rig without damaging the reinforced concrete specimen.

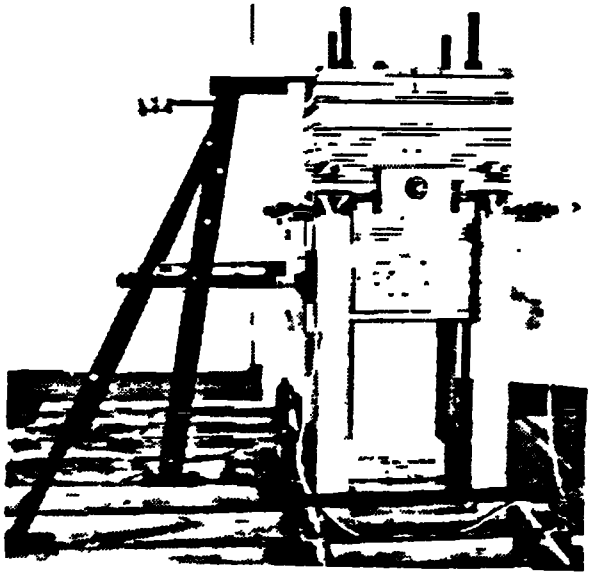


Figure 3.3 Model SW1 in the test-rig on the shake-table

Fifty per cent of the volume of steel required as mass should be below the centre of gravity. Consequently, the top part of the wall model is concealed as seen from figures 3.2 and 3.3. The test plates which comprise the mass were prestressed together on a central extended plate through which both support and degrees of freedom are provided. This was achieved by welding a rod in the line of the axis of gravity on the central plate. The rotational degree of freedom was offered by a circular roller encased in a rectangular steel plate. The horizontal degree of freedom was ensured by flat rollers at the base of the rectangular steel plate. The axial load was

transferred to the test rig columns by the beam which was in contact with the rollers as shown in figure 3.2. There were several reasons for not allowing the wall to support the axial load of the inertia mass. A matter of primary importance was safety, since the unexpected consequences of a catastrophic wall failure should be avoided. Moreover an axial load was not intended to be applied on the models tested subsequently under cyclic loading conditions.

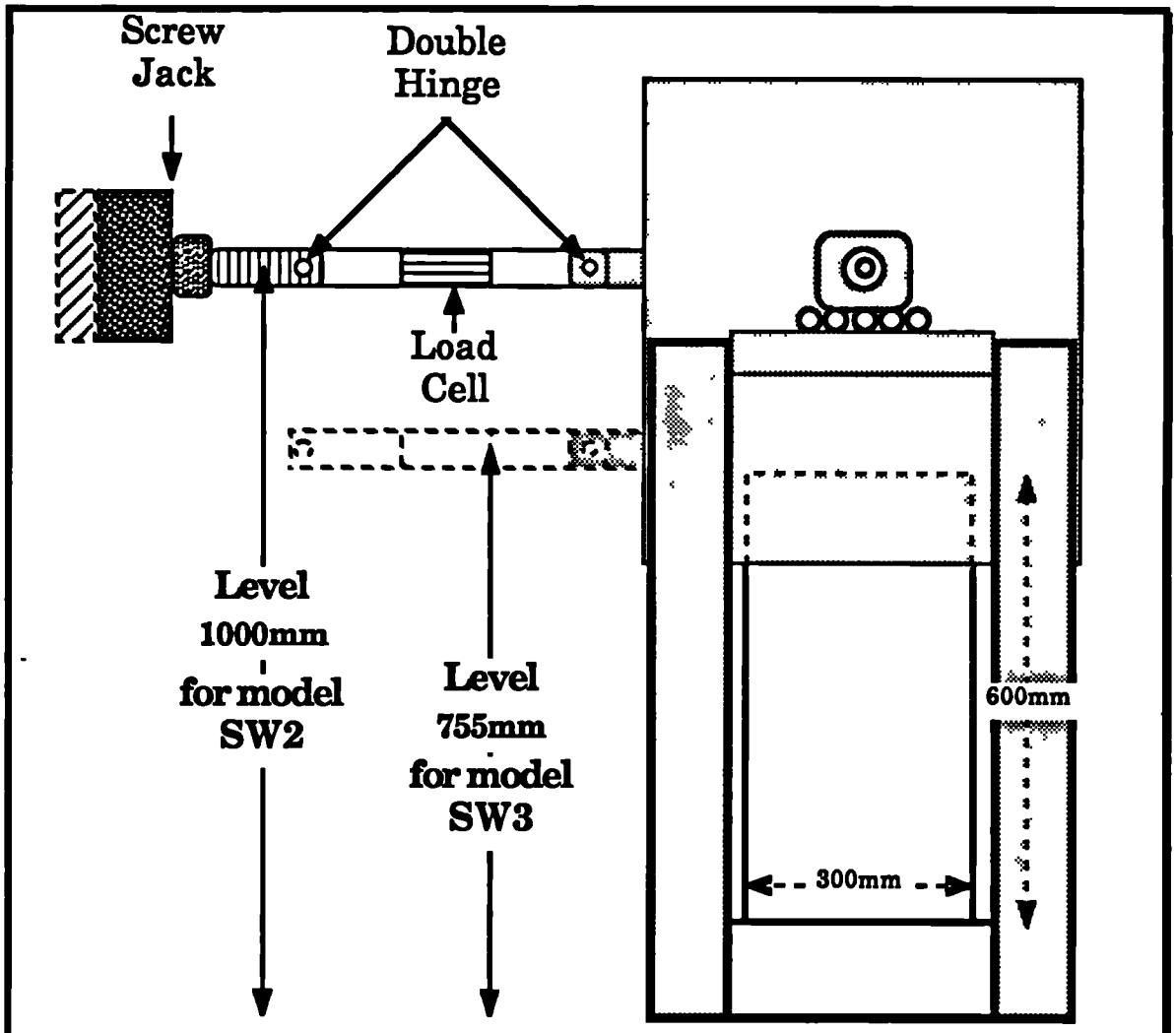


Figure 3.4 Test-rig for models SW2 and SW3

Several levels of safety were implemented for the shake-table experiment. Cushioned end beams were introduced connecting the columns in the front and back elevations. The beams were designed to withstand the impact of the mass at an acceleration of 3 g in the unlikely event of a sudden loss of strength and stiffness of the wall. Before hitting the end beams, the mass would trigger the emergency stops on two displacement limits; first a digital and then a mechanical one.

Additionally, the prestressing rods connecting the inertia mass were extended downwards, to just a few centimetres from the base, making the remote possibility of overturning of the mass impossible.

3.3.2 Small scale cyclic test-rig

The shake-table test-rig was adjusted for the 1:5 scale cyclic tests by clamping it onto the laboratory strong floor. A double hinge with a load cell in the centre was then fitted at the required level, as shown in figure 3.4. The screw jack assembly described in section 3.3.3 was lowered to the appropriate height and attached to the test-rig through the hinge. For specimen SW2 the load was applied at the height of 1 m, similar to the centre of gravity of the shake-table test. For specimen SW3 the load was applied at a height of 756 mm which was equivalent to the height at which the load was applied in all scale 1:2.5 experiments.

3.3.3 Experimental set-up for cyclic experiments on 1:2.5 scale models

The six walls SW4-SW9 were tested as isolated cantilever walls in a specially designed and constructed test-rig. The schematic representation of the testing arrangement and transducer location is shown in figure 3.5. A detailed drawing is presented in figure 3.6, and the actual set-up in figure 3.7.

A reaction wall was assembled from standard concrete blocks available in the laboratory. Two columns of three blocks were bedded on a thin layer of cement grout and were prestressed onto the concrete strong floor on the 90 x 90 cm (3' x 3') grid. Forty tonnes prestressing force was applied presenting thus the capacity of resisting rigidly a moment of 720 KN m. A yoke of two 30 cm x 20 cm RHS's were stressed at the right height on the reaction blocks so as to provide the push and pull capability for the jack.

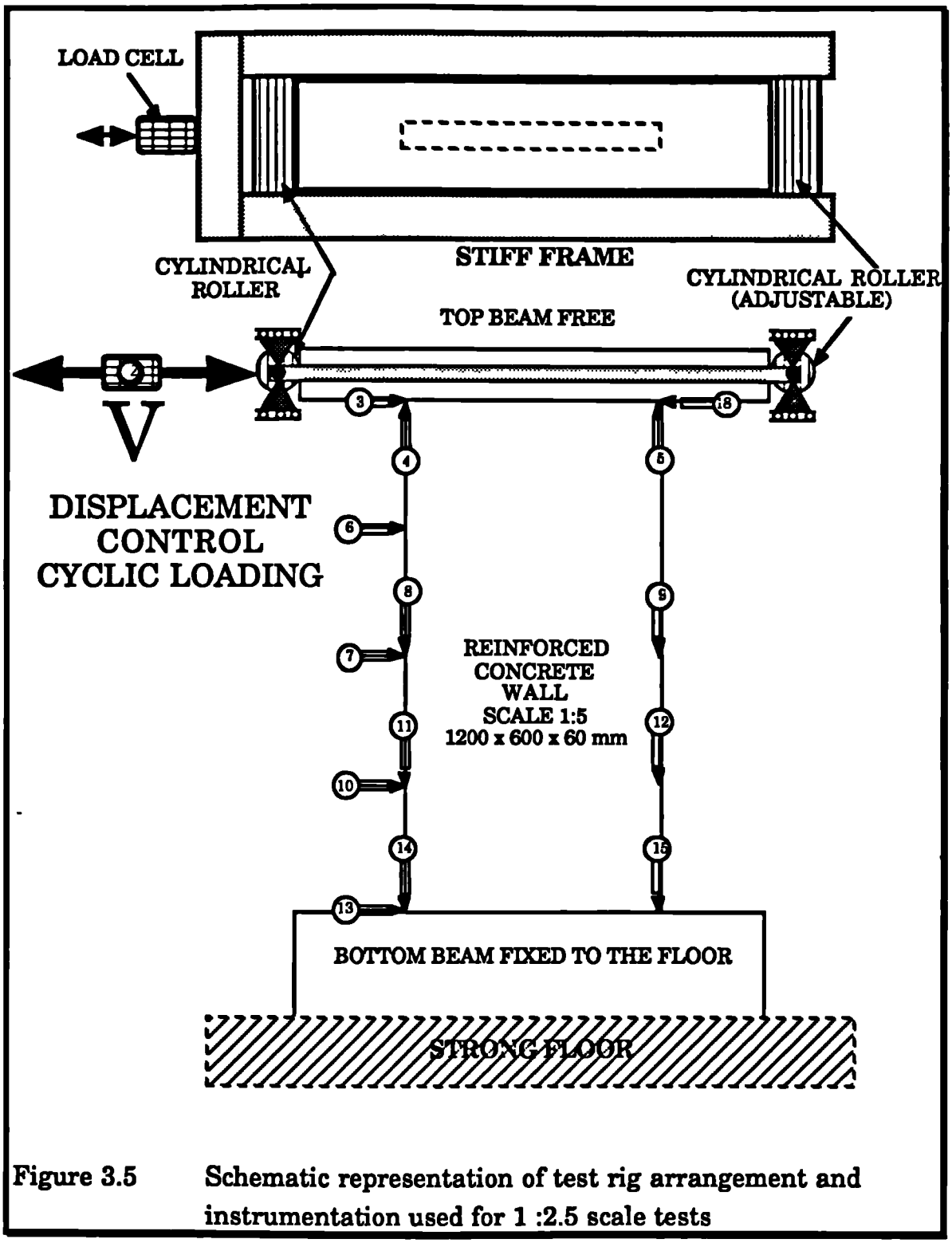


Figure 3.5 Schematic representation of test rig arrangement and instrumentation used for 1 :2.5 scale tests

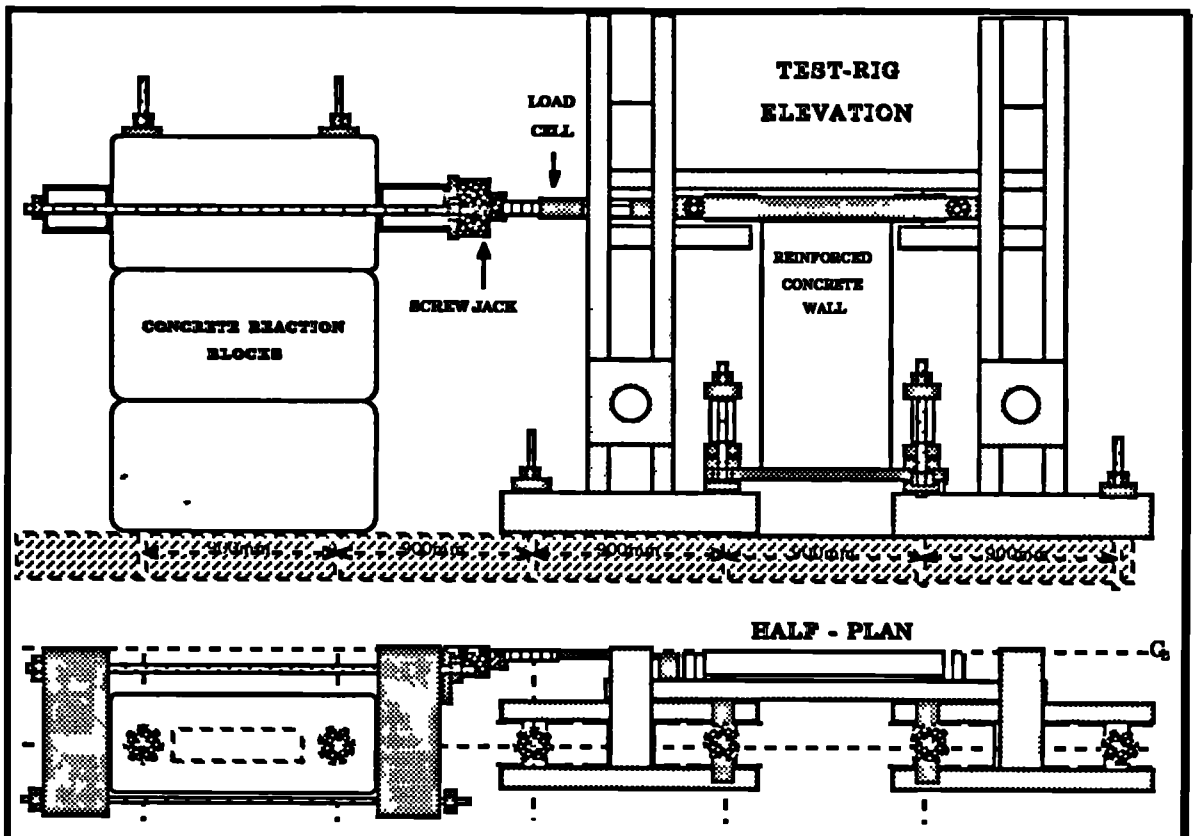


Figure 3.6 A detailed diagram of the 1 :2.5 scale test-rig assembly

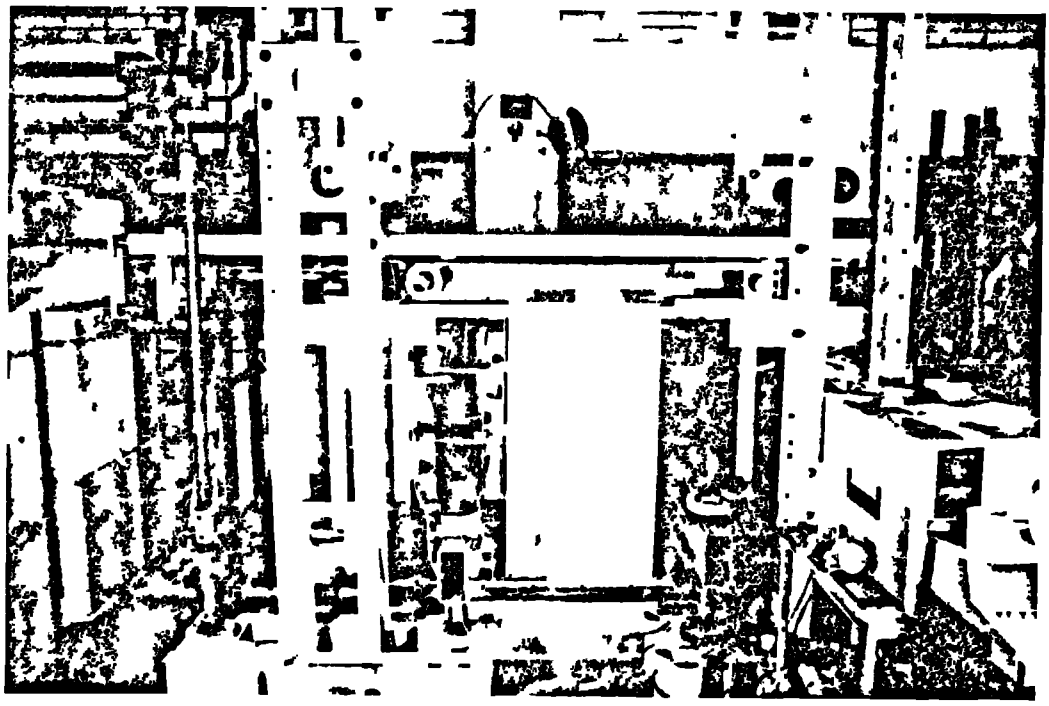


Figure 3.7 Plate of the 1:2.5 scale test-rig

The load was applied by a seven inch (17.5 cm) stroke, 20 tonne capacity screw jack reacting against the concrete blocks. The jack was driven by an electrical motor at a constant speed of about 0.1 mm per second. A 10 volt (strain gauged cylinder type) load cell was connected between the jack and the stiff collar RHS frame containing the rollers.

The boundary conditions at the top, as shown in Figure 3.6, assume a horizontal load at a constant height. The load had to be applied through a pin so as to eliminate tangential frictional forces due to the extension of the wall, a problem that was recognised by the authors in previous tests (Lefas, 1988). This was accomplished by cylindrical rollers made of solid steel and fitted with two circular bearings at either end. A roller was used at each end of the loading beam. In order to avoid local crushing, a steel spreader plate was fixed at each end of the beam. The front roller was embedded in the collar frame while the end roller had an adjustable horizontal position through a screw arrangement. The loading collar frame was free with respect to in-plane horizontal movement, but was restrained from displacing vertically and out-of-plane by a system of flat rollers reacting against two standard laboratory assembly portal frames. With this arrangement the specimen and the load transferring members were totally encased in a safe way.

The full fixity condition required at the base was achieved by prestressing two hollow section beams on top of the central frame bolts. A total of 100 tonne prestressing force was distributed by a pair of spreader beams on the bottom concrete beam which was designed accordingly.

The horizontal load was applied through the top beam which was intended to spread the load in the wall panel. It is inevitable that the beam stiffness will influence the local stress conditions. However, this would not affect the behaviour of the critical zones of the wall.

3.4 Model manufacture and materials

The specimen beams were designed to provide fixity at the bottom, transfer the load uniformly to the wall, provide anchorage for the

longitudinal wall reinforcement and, for the shake-table test, prevent uplifting of the inertia mass.

The scale 1:5 (SW1 - SW3) wall dimensions were as shown in figure 3.2. The thickness of wall SW3 was chosen to be 30 mm and 4 mm undeformed reinforcement was used instead of 2.8 mm model reinforcement. The scale 1:2.5 (SW4-SW9) wall dimensions are shown in figure 3.8.

3.4.1 Concrete

The moulds were manufactured from 3/4" (19 mm) plywood. Before each cast, the inside of the mould was coated with a releasing agent. Concrete was mixed in the laboratory by using suitable size concrete mixers. All models were cast horizontally in a single cast. The 1:5 scale models were vibrated on the vibrating table, whilst for the 1:2.5 scale models, pocket and hammer vibrators were used. The wet concrete was placed and vibrated in three layers. First the bottom third of the beams, followed by the wall area and the middle of the beams, and finally the top third of the beams. Control specimens were taken from the same batch prior to casting the wall. Strict compacting and levelling was imposed on the wall surface, so as to eliminate voids and minimize geometric irregularities.

The specimens were trowel finished two hours after completion of casting and covered with wet hessian and nylon after about 4 hours. This type of curing was maintained for a week until a control cube was crushed. Control specimens were demolded the day after casting and placed on top of the horizontal wall for identical curing conditions. Curing was stopped on the seventh day unless a weaker strength than expected was recorded. Subsequently, the wall and control specimens were stored under standard laboratory conditions next to the test-rig.

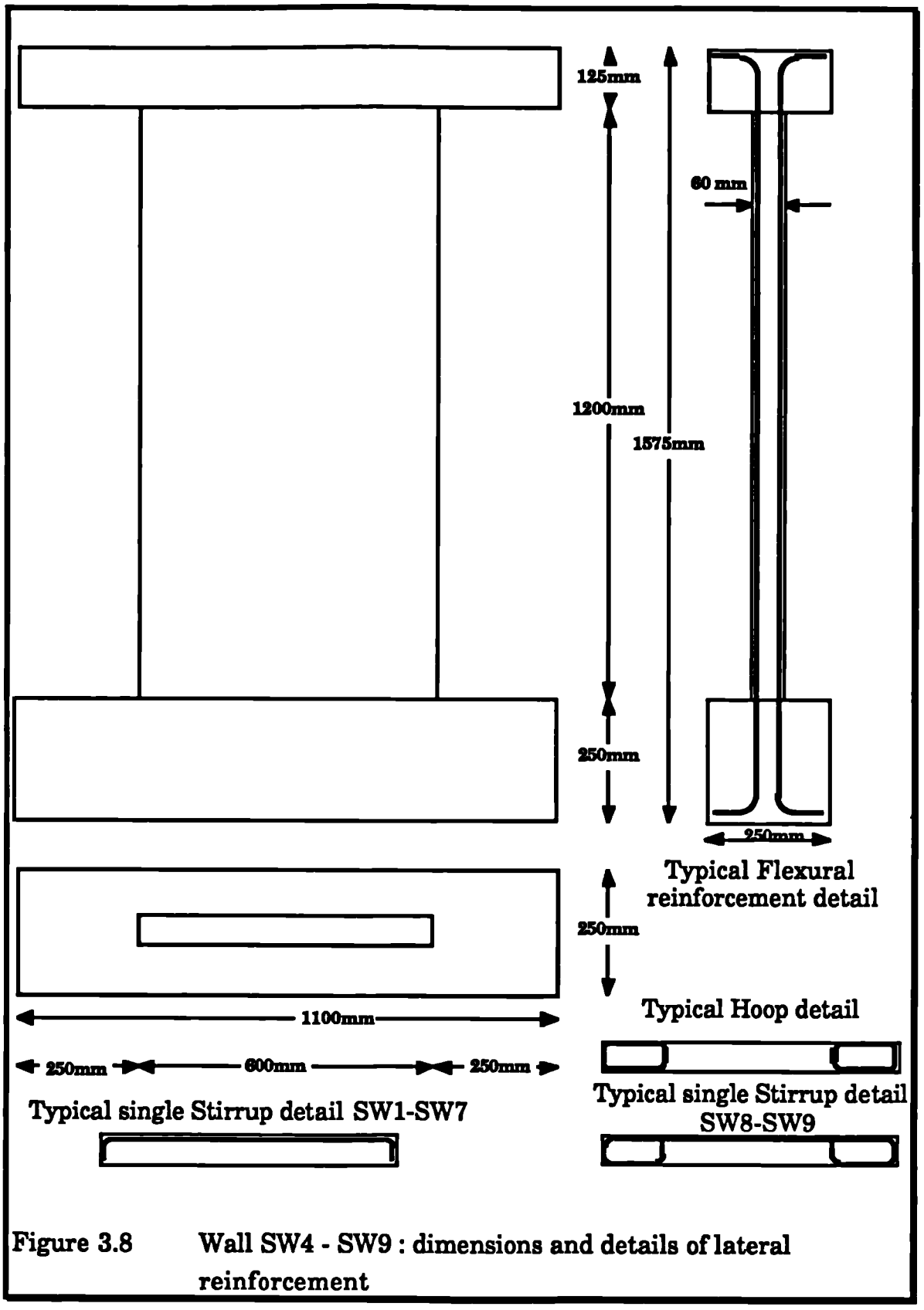


Figure 3.8 Wall SW4 - SW9 : dimensions and details of lateral reinforcement

The concrete mix shown in table 3.3 was used in all walls. It should be noted that the material supply sources differed for the last two walls. The 28 day design cube strength was 46 N/mm^2.

Table 3.3 Concrete design mix

MIX PROPORTIONS BY WEIGHT	DESIGN MIX RATIO
O.P.Cement	1.00
10 mm aggregate	3.15
Coarse sand	2.00
Fine sand	0.89
Free water	0.68

Table 3.4 Concrete compressive strength

SPECIMEN CODE	DAY OF TESTING	CUBE STRENGTH f_{cu} -N/mm2	CYLINDER STRENGTH f_{cu} -N/mm2	PEAK STRAIN ε_{cuo} x 1E06
SW1	80	47.2	38.9	_
SW2	146	47.2	_	_
SW3	232	47.2	_	_
SW4	62	49.5	36.9	2093
SW5	48	47.5	31.8	2286
SW6	47	49.6	38.6	2141
SW7	74	45.2	32 0	1950
SW8	76	53.7	45.8	1960
SW9	33	53.7	38.9	2400
MEAN VALUE	_	49.0	37.6	2138
STANDARD DEVIATION	_	2.98	4.78	178
MEAN VALUE SW1-SW7	_	47.6	35.64	2117
STANDARD DEVIATION	_	1.52	3.5	138

Two 4"x 10" cylinders and six 4" cubes were cast and used as control specimens. At least three of the cubes were tested at the end of each experiment. The cylinders for the 1:2.5 scale walls were all tested at the end of the experimental programme. For strain measurement, a single transducer was mounted at the centre third of the cylinders between a pair of collars 10 centimetres apart. The strengths and peak strains obtained are shown in table 3.4.

3.4.2 Steel reinforcement and details

Model reinforcement was used for shear reinforcement in scale 1:5 models. Commonly available British reinforcement was used in all other cases with a characteristic strength of 460 N/mm^2. The actual properties of reinforcement used is shown in table 3.5 and figure 3.9. The yield strength is not very well defined in bars less than 12 mm in diameter, with a gradual change to the yield plateau. In order to account for any significant reduction in the cross section due to the grinding necessary for placing strain-gauges, six bars were tested for each diameter. Two were left unground and four were ground in two positions within the stressed area. The loss in strength was only significant in the six millimetre diameter bars which subsequently failed at less than half the ultimate strain of the unground specimens. Strains were measured both by strain gauges and by a device utilising a transducer to measure extension within a sample length of 250 mm. The extension device proved much more successful in monitoring strains during the entire strain-controlled test. Most of the strain gauges were unstuck after about 20,000 microstrains whilst others were unreliable after yield. The analytical model used in subsequent chapters utilises a tri-linear representation for steel stress-strain properties. For this reason a value for E_{s1} was determined as shown in figure 3.2. As with the value of yield strength, difficulties in obtaining the tangent of a slowly changing curve mean that the tri-linear representation of the stress-strain characteristics may differ from the actual characteristics near the yield point.

Table 3.5 Steel reinforcement properties

STEEL TYPE	E_{so} N/mm^2	f_{sy} N/mm^2	E_{s1} N/mm^2	f_{su} N/mm^2	ε_{ul} Strain x10E6
2.8 Deformed	200,000	480	1100	590	85000
4 Round	200,000	400	2600	460	60,000
6 Deformed	200,000	545	2200	590	20,000
10 Deformed	200,000	430-530	3000	660	42000
12 Deformed	200,000	470-500	1300	600	85000
16 Deformed	205,000	535	1075	590	75000

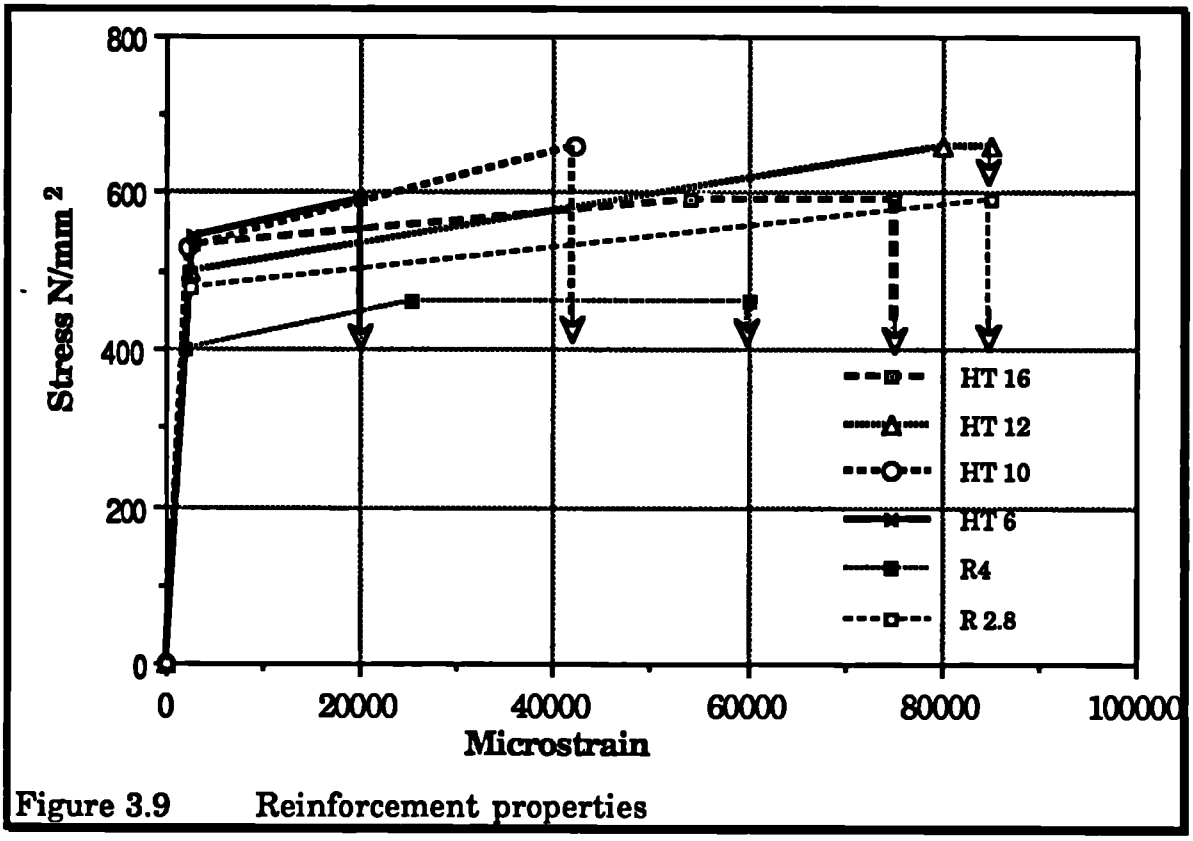


Figure 3.9 Reinforcement properties

The reinforcement details and strain gauge locations are shown in figure 3.2 for the 1:2.5 scale and in figure 3.10 for the 1:5 scale models.

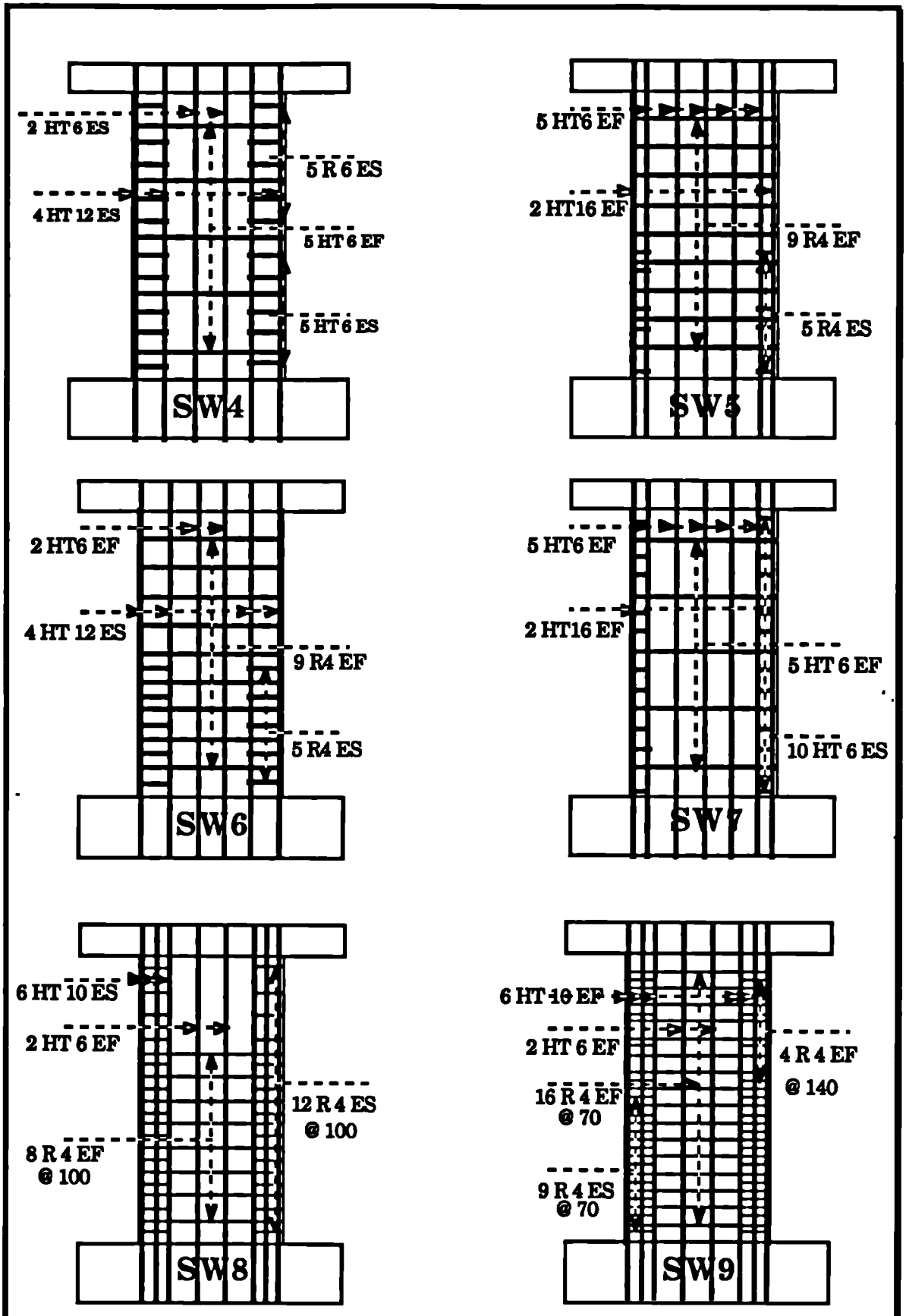


Figure 3.10 Reinforcement details for walls SW4 through SW9

Walls were designed in three pairs; each pair having identical flexural reinforcement but different shear reinforcement. In all cases an attempt was made to concentrate the reinforcement in the boundary elements so as to maximise the flexural capacity for the particular type of reinforcement. The web reinforcement was always nominal. Shear reinforcement was varied in each pair of walls so as to investigate the effect of various degrees of safety margins in shear. The confinement of the boundary elements varied as consequence a of the variation of shear reinforcement.

3.5 Instrumentation and control

3.5.1 Shake-table test

As already pointed out, the choice of modelling parameters has taken into consideration the data acquisition system characteristics and control time interval. A total of 10 channels can be sampled at an interval (Δt) of 5 milliseconds. Four of these channels were dedicated to the control of the shake-table; two accelerometers and two displacement transducers. The other six channels were used for data acquisition. Vertical and horizontal accelerations and displacements were measured at the top beam level and accelerations only at the bottom beam level. Ten channels were recorded independently as an analogue signal; eight strain gauges were fixed at the bottom main reinforcement bars and two out-of-plane accelerometers. A frequency analyser was used to determine the dominant response frequency of the wall during testing. For damping measurements, an oscilloscope was used to record the acceleration signal from the free vibration response due to a pendulum impact. High speed video as well as ordinary video recorders were used to film the tests.

3.5.2 Cyclic tests at scale 1:5

The instrumentation and control were similar to the one described for the 1:2.5 scale models in section 3.5.3. However, only eight strain gauges were used, as in the shake-table experiment.

3.5.3 Cyclic tests at scale 1:2.5

The load applied to the wall through the stiff collar frame was measured by a tension/compression electrical load cell. A single voltage output was obtained in the same way as with the linear voltage differential transducers (LVDT's). Sixteen 10 Volt LVDT's of stroke lengths ± 25 mm and ±37 mm were used. The positions of the transducers are shown in Figure 3.6. The transducers were fixed on a firm scaffold pole frame which is independent of the loading arrangement. In this way absolute displacements are measured. A separate ±5 mm transducer was used to measure strains between Demac points at 80 mm spacing.

Strain on the steel reinforcement was measured at 30 locations as shown in the force versus strain diagrams in chapter 4. The strain gauge length was chosen so as to avoid averaging the varying strains of a flexural member. However, it is anticipated that due to the large number of cycles, following yield, the local strains may be affected by permanent plastic straining. Different types of electrical strain gauges were used for the different types and diameters of steel reinforcement. All gauges were located facing the centre of the wall so as to avoid damaging them during casting and levelling of the concrete. The deformed bars were ground at the strain gauge locations. The gauges and wiring were subsequently waterproofed. The gauges were connected to a quarter bridge circuit available with the data logger.

Data acquisition was performed through a Hewlett Packard data logging system. Fifty channels were monitored in each reading. Due to the large amount of data obtained in each cycle, it was necessary to store the data on tape every cycle and hence, the loading had to be stopped whilst performing data acquisition. Calculation of measured quantities from voltages was performed at the same time for control purposes. An X-Y plotter was also used for load vs top displacement plots. The stored data

were subsequently transferred through the College network (PAD) to the main frame computers for further processing and presentation. The cracks were marked on the specimens after every cycle

The Loan Pool, Science and Engineering Research Council AGA Thermovision infra-red heat-sensing camera was used to investigate the energy dissipated in the plastic hinge zones.

3.6 Analysis of measurements

3.6.1 Shear and flexure deformation evaluation

The LVDT measurements are total displacements at a point with reference to an external fixed frame of reference. For analytical purposes it is desirable that these measurements can be decomposed into the different components of deformation as shown in equation 3.9.

$$u_t = u_f + u_s + u_e \qquad (3.9)$$

Where 'u_t' is the top displacement, 'u_f' is the flexural component including base rotation, 'u_s' is the shear component and 'u_e' is the possible expansion at the top beam. Figure 3.11 (subscripts $_l$ & $_r$ stand for left and right) shows top wall deflections.

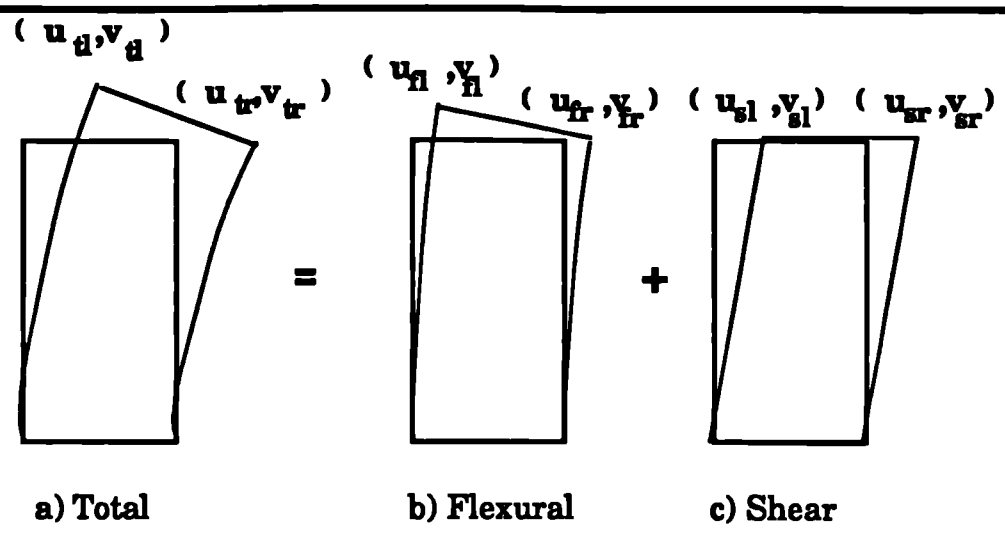


Figure 3.11 Top wall deflections assuming fixed base

The existence of the top beam will prevent any significant expansion occurring at the top level. Expansion in the middle of the wall should be restrained by the shear reinforcement, thus establishing the procedure for separating shear from flexure remains the only objective in this section. Shear deformation does not cause section rotations and hence, in the absence of expansion it is best demonstrated by its effect on the diagonals. Many researchers make use of diagonal measurements to determine shear. In fact, these measurements are not sufficient to determine shear deformations, unless the flexural deformations are known a-priory, or the effect of flexural deformations on the diagonals is known. It is, therefore, more objective to determine the flexural deformations first and utilise them to obtain shear deformations. As shown in equation 3.6, flexural deformations can be obtained from section rotations, hence from the vertical displacements. In a cantilever wall element, the distribution of rotations along the height can be assumed as shown in figure 3.12.

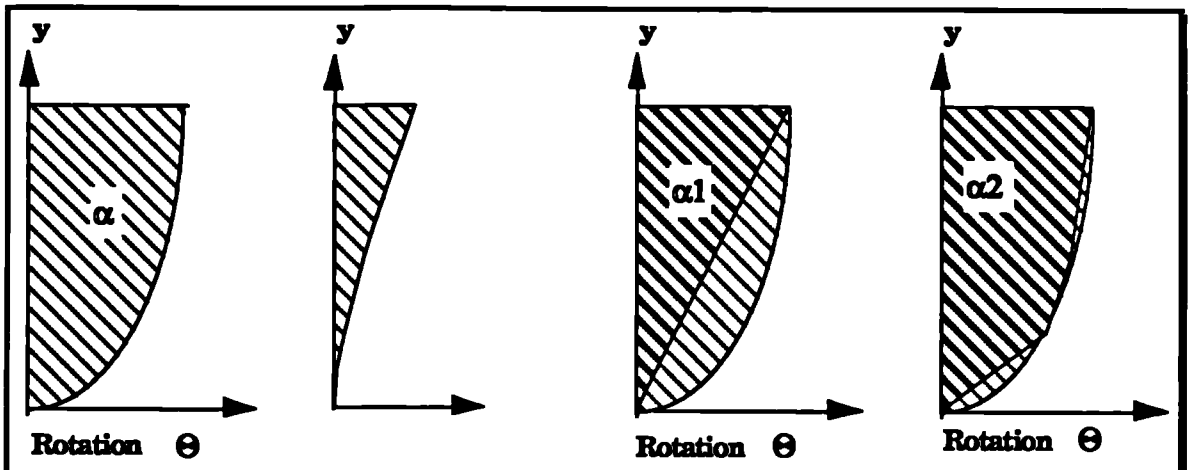


Figure 3.12 Cantilever wall rotations

The accuracy of calculating flexural deformations depends on the information available on the shape of the rotation diagram. If the area under the curve 'α' (figure 3.12) is known then the flexural deformation is determined exactly. If only the rotation at the top is available or only the difference of the two diagonals is used (Hiraishi, 1984), then, by using area 'α1', flexural deformation would be underestimated. Consequently, shear deformation would be overestimated. In the scale 1:2.5 experiments, rotations were measured at three heights; at the top, at mid-height and at quarter-height. The area under this curve 'α2' is very close to the actual area 'α' and hence, an accurate estimate of flexural deformation can be obtained.

3.7 Choice of loading regime

For the shake-table test, careful consideration was given to a number of parameters relating to the characteristics of the input signal which can be chosen from a large number of EQ records available from the Imperial College strong-motion data bank. The length of the record could not exceed 1024 points due to computer storage limitations. The response of the wall in prototype quantities was expected to be in the range of 2-2.5 Hz and accounting for an inevitable decrease in frequency due to stiffness deterioration, the predominant frequencies required in the 5% damping acceleration elastic response spectra should be between 1-2.5 Hz. Response

accelerations in the expected range of frequencies should not exceed 1.0 g at ultimate load testing. Table 3.6 shows the strong-motion characteristics after time history matching. The records used were scaled in time from 0.02 to 0.005 seconds and were matched at an acceleration gain of 25-100%.

Table 3.6 Strong motion characteristics

SM RECORD	DATE	CODE	MAX. BASE ACCEL. (g)	MAX. RESPONSE ACCEL. (g)
El Centro	19 May 40	(EC)	0.335	1.1
Parkfield	28 Jun 66	(PA)	0.499	1.6
Montenegro	15 Apr 79	(MO)	0.440	1.9
San Fernando	09 Feb 71	(SA)	1.121	3.0

For the cyclic tests, a loading regime that would represent the extreme conditions experienced during a severe EQ was desired. During strong shaking, a large number of load reversals is expected at the lower displacement levels, decreasing with increased displacement. For the first cyclic experiment (SW2) ten cycles were imposed at MDL-1 mm. Ten cycles were imposed for every 1 mm increment (ΔMDL) in MDL until yield. The immediate observation was that insignificant deterioration occurred after the second cycle up to the yield level. It was, therefore, decided that a loading regime of two cycles at each displacement level is to be followed, up to failure. The ΔMDL was 1 mm and 2 mm, for scale 1:5 and 1:2.5 models, respectively.

CHAPTER 4

4 EXPERIMENTAL RESULTS

The experiments on the 1:5 scale models were designed to be the link between the 1:2.5 scale models and shake-table experiments. The description of the models and the experimental procedure is given in Chapter 3. Due to funding restrictions, only one model was tested on the shake-table. It is expected that more shake-table experiments will be undertaken at a later stage so that the experience from the pilot experiment is further utilised.

For each of the cyclic tests, a brief description of the experiment carried out is given. This is followed by a general description of the experiment including details of the cracking pattern and mode of failure. The graphs for displacements and strains versus load are included in Appendix A. In order to assist in the identification of experimental results, figure numbers include the experiment number in parenthesis (e.g. 4.(3).2 refers to figure 2 of SW3 in chapter 4). In all the figures, the solid line represents the virgin cycle at the particular maximum displacement while the dotted line represents subsequent cycles. Maximum displacement levels (MDL - millimeters) are levels imposed in both directions. Displacement increments to a new MDL were 1 mm and 2 mm each at scale 1:5 and 1:2.5, respectively.

The degree of success of instrumentation in different experiments was variable. A large number of the strain gauges failed after significant inelastic excursions, while some of them failed just after the yield strain was achieved. There are several reasons for strain gauge failure ranging such as workmanship, ageing of adhesive, loss of waterproofing during steel fixing, breaking of the bridge wires at high strains and loss of bond, gauge physical limits in strain, cyclic loading and local plasticity. In this chapter, only readings from strain gauges that were registering the correct resistance at the beginning of the tests are presented. When failure occurred due to interruption of the electric current passing through the resistance, the readings are not shown. However, for other types of failure it is not easy to determine the exact point of gauge breakdown and hence, the full results are presented.

Difficulties with the transducer readings, though less, were associated with the reference points on the walls. Spalling of the concrete or opening of stirrups near a reference point affected some of the transducers. Additionally, a very small number of parasitic readings arising from noise or errors in the data acquisition equipment were not totally eliminated from the presented results.

4.1 Shake-table model SW1

The model was subjected originally to a very low excitation signal, for which the response acceleration did not exceed 0.05 g. This was necessary for checking the instrumentation and control of the shake-table. Even at this stage, some degree of stiffness deterioration was indicated by a drop in response frequency from about 8.8 Hz to 8.0 Hz. Table 4.1 shows the main parameters for the earthquake time histories imposed on the wall until failure. The record codes given in the first column of this table are described in table 3.6. Due to the fact that the stiffness was much lower than initially thought, the chosen earthquakes for the shake-table experiment were not as effective as expected. However, significant stiffness deterioration occurred before reaching steel yield limits. This is demonstrated by the drop in the response frequency as obtained by the frequency analyser.

Table 4.1 Shake-table tests on model SW1

RECORD CODE (Table 3.6)	GAIN	Max. Wall Displ.mm	Max. Wall Accel.(g)	Response Freq.(Hz) Before - After	Damping %
EC	25%	0.62	0.09	8.0 - 6.0	3.2
EC	50%	1.38	0.190	6.0 - 5.6	3.9
EC	100%	3.44	0.4	5.6 - 5.2	5.2
PA	50%	2.11	0.266	5.2 - ---	
MO	50%	2.65	0.333	4.8 - 4.8	5.4
MO	100%	4.50	0.476	4.8 -4.8	5.4
SA	100%	6.91	-----	4.8 - 4.0	5.9
SA	100%	7.62	-----	4.0 - 3.6	-
Harmonics	3.4 Hz	12.2	1.2	3.6 - 3.4	-

Due to high frequency noise originating from metal to metal contact, the acceleration records have been contaminated with parasitic peaks. Unfortunately, such peaks triggered the shake-table emergency shut down mechanism during the San Fernando EQ experiment, hence the peak acceleration could not be obtained even after filtering. High energy harmonic excitations were used to break the wall at very high displacements.

An attempt to calculate damping was made by swinging a pendulum from a constant angle, imposing an impact load onto the wall. The decay of the ensuing free vibration was used to estimate the damping coefficient shown in table 4.1. One of the disadvantages of this method, however, is that the energy input by the pendulum is very low. As a result, the motion is at very low excitation levels and cannot represent accurately the real damping of the component in the nonlinear range. This highlights a common dilemma in estimating dynamic characteristics from forced vibration measurements. On the one hand, if the amplitude is too small, linear elastic values are obtained. On the other hand, damage of the model will increase if large amplitude vibrations are used to assess damping in the nonlinear range.

The obtained experimental results have been plotted versus time. Due to the large amount of data obtained and the limited information relevant to this thesis, these results are not presented here. As noted earlier, it was also clear from these results that the acceleration readings were contaminated with high frequency noise, arising most probably from metal to metal contact. Consequently, the results were transferred to the mainframe computers for digital filtering. An elliptic filtering program (Menu, 1987) was applied to all acceleration records. The filtered acceleration results were plotted against top wall displacement. These results are discussed in the following section.

4.1.1 Shake-table results

Before focusing on the experimental results, the elastic dynamic behaviour of the system is reviewed in order to assess the completeness of the obtained data.

By assuming a simple single degree-of-freedom system and ignoring viscous damping, the first mode of vibration is expected at a frequency 'f_o' of:

$$f_o = \sqrt{\left(\frac{k_h}{m}\right)} \frac{1}{2\pi} \qquad (4.1)$$

The uncracked top wall elastic stiffness 'k_h' based on code design elastic properties is of the order of 10 KN/mm, hence the corresponding f_o is 11.25 Hz (mass 'm' is 2 tonnes). If the tensile strength of concrete is ignored, as can be assumed for cracked sections then the stiffness obtained is about 3.2 KN/mm and the corresponding f_o is 6.4 Hz. The initial response frequency indicates that the stiffness of the specimen lies between these two values.

By using the experimental results of SW2, the relation between the displacements at the point of application of the load and the top of the wall is known. From figure A.(2).3 the ratio of the two displacements is about 1.5. Assuming that, at least initially, the wall-mass assembly responds as a single degree-of-freedom then the acceleration at the centre of gravity are directly proportional to the acceleration at the top wall level where the recordings were made. This assumption is supported also by using the results of table 4.1 with equation 4.1 to predict the response frequency. Therefore, the equivalent shear force can be calculated by multiplying the wall inertia with the top wall acceleration. Forces obtained from such calculations using the filtered accelerations are shown for two of the tests prior to yielding of the main reinforcement, in figures 4.1 and 4.2.

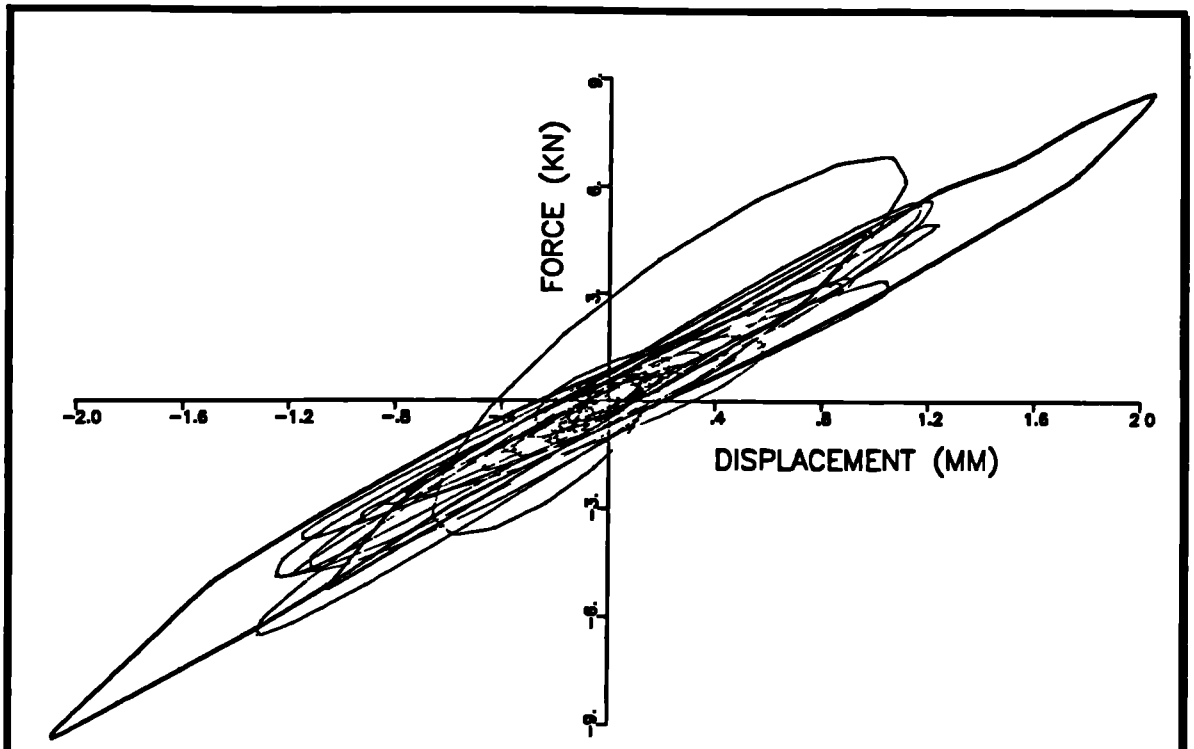


Figure 4.(1).1 Equivalent shear force and top wall displacement for El Centro 50% of SW1 and MDL-2 of SW2

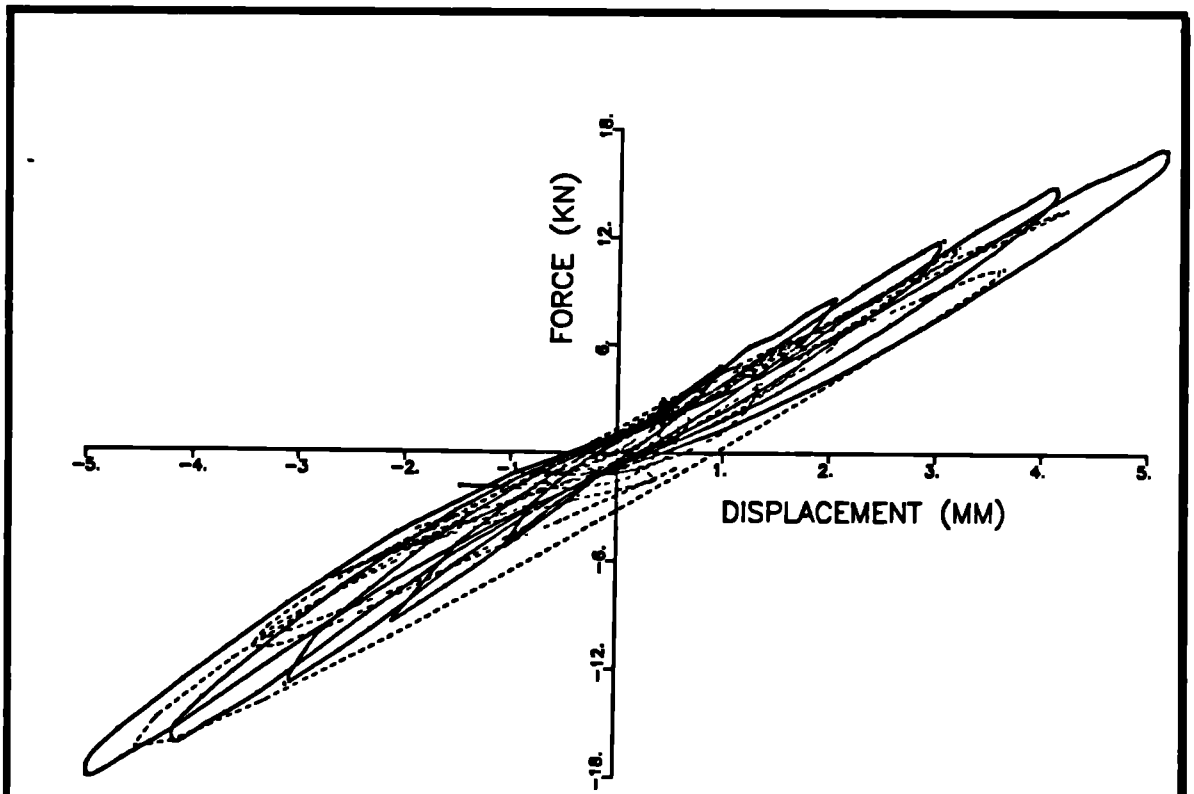


Figure 4.(1).2 Equivalent shear force and top wall displacement for Montenegro 100% of SW1 and MDL-5 of SW2

The accuracy of the results is surprising, bearing in mind the fact that actual mass accelerations were not recorded. However, the real inertia mass is not concentrated at a point as the single degree-of-freedom system model assumes and the rotational inertia may induce rocking modes when the rotations of the top mass become significant. As a result, the assumptions used would be invalidated.

The cantilever nature of the wall provides both translational stiffness k_h and rotational stiffness k_θ, corresponding to the degrees of freedom of the inertia mass as shown in a simplified diagram in figure 4.3.

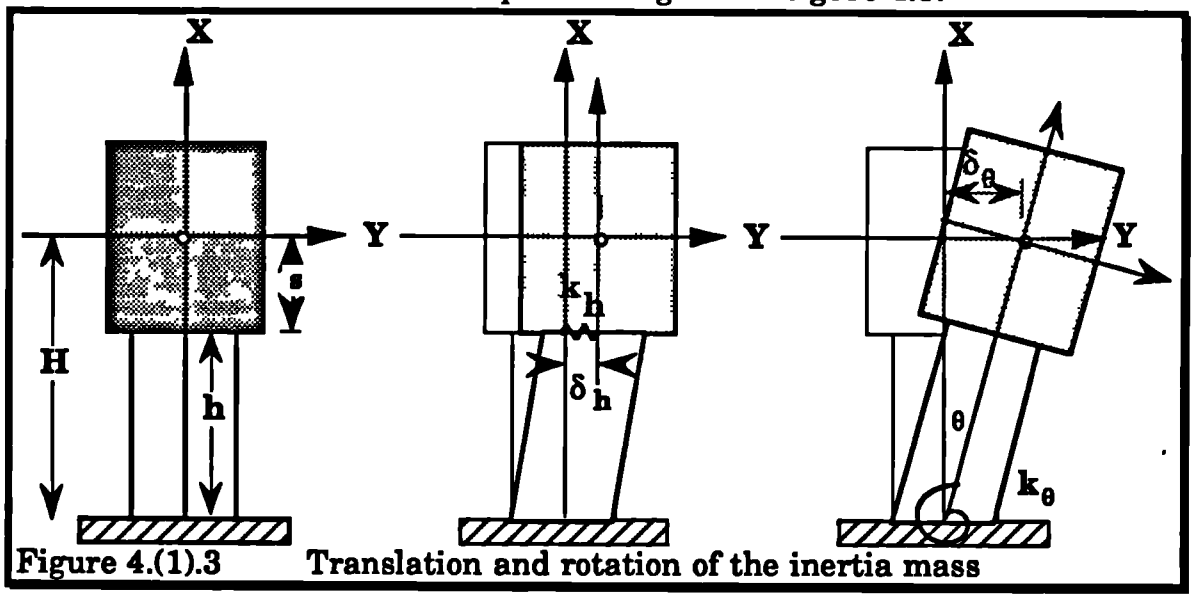


Figure 4.(1).3 Translation and rotation of the inertia mass

The modes and frequencies of rocking vibration can be found by using a two degree-of-freedom system. Beginning by considering equilibrium of forces in y-direction and moments about the inertia mass centroid, respectively, equations 4.2 and 4.3 are derived.

$$m\ddot{u} = -k_h (u - s\theta) \tag{4.2}$$

$$I_G \ddot{\theta} = -k_\theta \theta + (u - s\theta)\, s \tag{4.3}$$

Wakabayashi (1986) solved the problem as shown below by assuming that u and θ are $\bar{u}\, e^{(i\omega t)}$ and $\bar{\theta}\, e^{(i\omega t)}$, respectively. By substituting in equations 4.2 and 4.3 and rearranging the following is obtained:

$$(-\omega^2 m + k_h)\,\bar{u} - k_h\, s\,\bar{\theta} = 0 \tag{4.4}$$

$$-k_h\, s\,\bar{u} + (-\omega^2 I_G + k_\theta + k_h\, s^2)\,\bar{\theta} = 0 \tag{4.5}$$

In order to solve the simultaneous equations for the non-trivial solution the determinant of the coefficient matrix should be zero and hence,

$$\omega^4 - \left(1 + \frac{e_o^2}{i_o^2} + \frac{s^2}{i_o^2}\right)\omega_h^2\,\omega^2 + \frac{e_o^2}{i_o^2}\,\omega_h^4 = 0 \tag{4.6}$$

where $\omega_h^2 = k_h/m$, $i_o^2 = I_G/m$, and $e_o^2 = k_\theta/k_h$. From this equation, the natural frequencies ω_1 and ω_2 are obtained as :

$$\frac{\omega_1^2}{\omega_h^2} = \frac{1}{2}\left\{1 + \frac{e_o^2}{i_0^2} + \frac{s^2}{i_o^2} - \left[\left(1 + \frac{e_o^2}{i_o^2} + \frac{s^2}{i_o^2}\right) - 4\,\frac{e_o^2}{i_o^2}\right]^{\frac{1}{2}}\right\} \tag{4.7}$$

$$\frac{\omega_2^2}{\omega_h^2} = \frac{1}{2}\left\{1 + \frac{e_o^2}{i_0^2} + \frac{s^2}{i_o^2} + \left[\left(1 + \frac{e_o^2}{i_o^2} + \frac{s^2}{i_o^2}\right) - 4\,\frac{e_o^2}{i_o^2}\right]^{\frac{1}{2}}\right\} \tag{4.8}$$

From these frequencies the rocking mode shapes are obtained for the rigid body by substituting in equations 4.4 and 4.5. The rotation centres for the first and second rocking modes are given by:

$$h_1 = \frac{s}{1 - \left(\frac{\omega_1}{\omega_h}\right)^2} \tag{4.9}$$

$$h_2 = \frac{s}{1 - \left(\frac{\omega_2}{\omega_h}\right)^2} \tag{4.10}$$

According to this equations it has been demonstrated that the centre of rotation of the first mode lies below the centroid of the inertia mass and the second above. A significant contribution from the second mode of vibration will render the problem much more complicated to instrument in practice. The second mode of vibration could be seen from the high speed video recordings to be present in the response of SW1 at high input accelerations. Since experimental results obtained for SW1 were limited by the data acquisition capabilities, further correlation of the shake-table results with the static-cyclic results is difficult to achieve.

4.2 Static cyclic loading - Scale 1:5 model SW2

The loading regime imposed on this model was initially intended to investigate the importance of a large number of load reversals prior to yielding of the main reinforcement. This was an attempt to simulate the effect of the low amplitude earthquake signals imposed on SW1 and deduce whether they had an impact on the stiffness characteristics.

The first load reversal was at MDL-1. The initial stiffness at MDL-1 was about 5 KN/mm. A typical loop had a thickness at the zero load axis of 0.25 mm. The 'virgin' loop had a larger area than all subsequent loops which differed very little from each other. Frequent interruptions of loading were made so as to perform data acquisition. During all these halts, displacement was maintained by the nature of the loading arrangement. However, there was a slight load drop in the carried load, attributable to relaxation of the specimen and possibly of the test-rig. On increasing the displacement, the drop in load was recovered instantaneously. At the maximum displacement level, initial unloading was almost vertical before the normal stiffness was recovered.

The number of load reversals at each displacement level was reduced to five for displacements 3 mm to 5 mm, then to three for displacements 6 mm to 9 mm and to two until failure, as shown in figure 4.(2).1. Failure occurred after achieving MDL-12 by fracture of the end main bars.

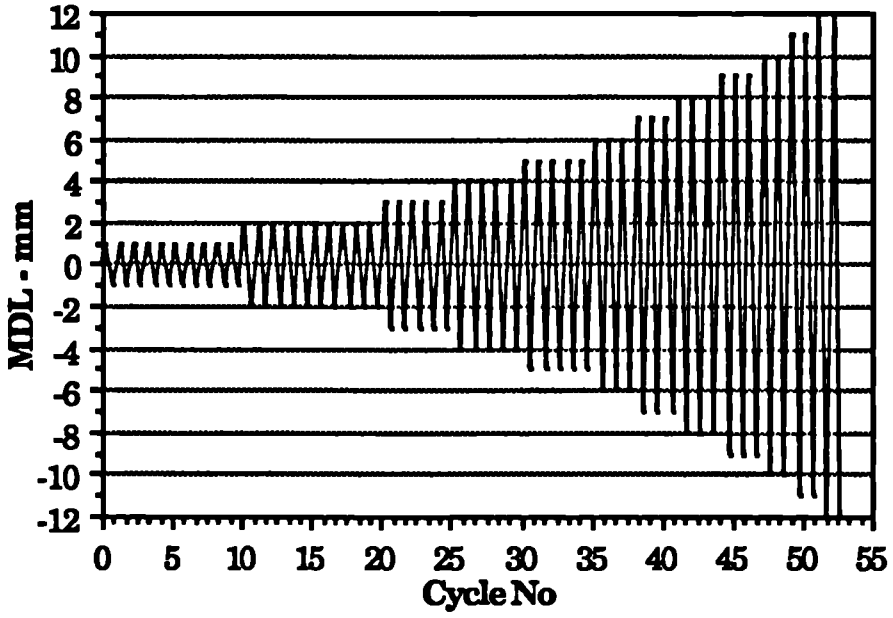


Figure 4.(2).1 Loading history for SW2

4.2.1 Cracking of SW2

At MDL-2 extensive cracking was observed spreading from the bottom of the wall upwards. First cracking was nearly horizontal and was located at the bottom half of the wall in the tensile zone. On reversal, cracks developed in the other half of the wall in a symmetric manner as shown in figure 4.(2).2. More surface cracking became apparent even after the virgin cycle, up to the third cycle at this MDL.

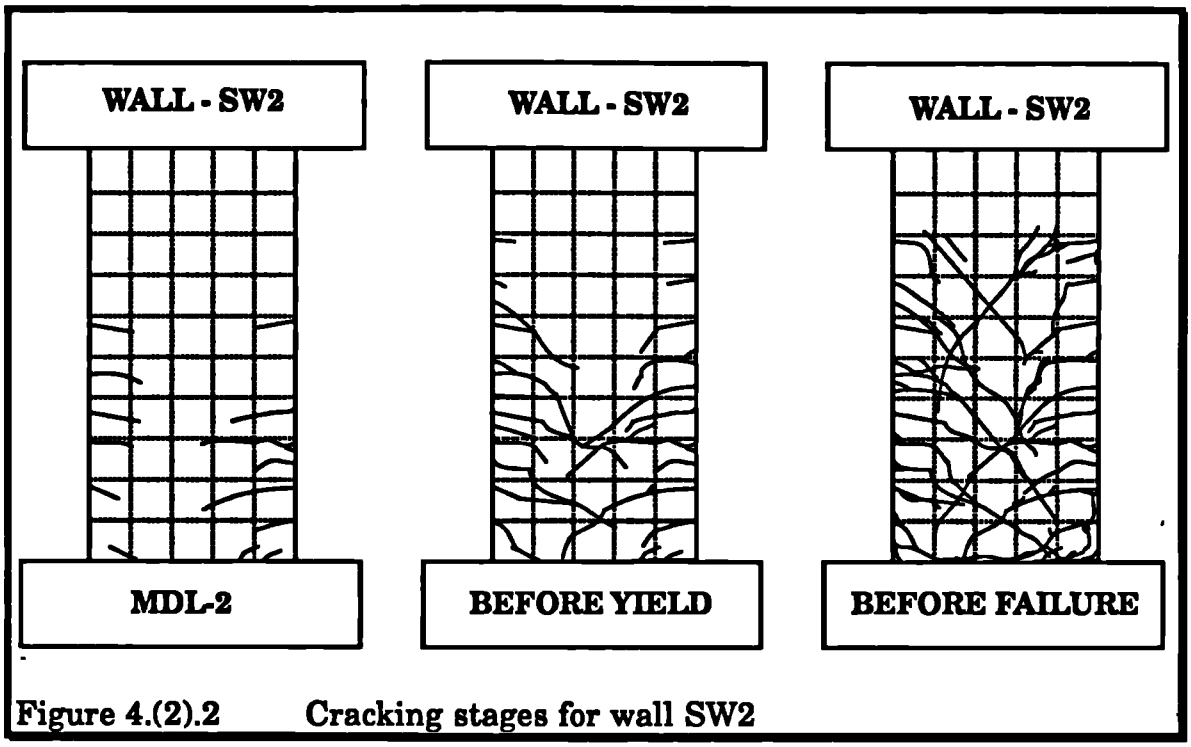


Figure 4.(2).2 Cracking stages for wall SW2

An increase in cracking continued in a similar manner until yielding of the main reinforcement. Cracks at the boundaries of the wall were less inclined and more dense than cracks in the web of the wall. Cracking seemed to initiate from the location of the lateral reinforcement. In the web, the cracks took a rather sharp change in direction and traversed the web at about 45 degrees to the horizontal, this value being lower at the lower sections of the wall and higher further up. After yield, the density and distribution of cracking increased. Cracks spread throughout the height of the wall, even though it was only possible to mark them up to the accessible level. Flexural cracks originating from the higher regions of the wall progressed through the web up to the opposing compressive area and being unable to penetrate, they progressed at much sharper angles. Some vertical cracking appeared in the bottom end zones of the wall, which were seen later to be a result of concrete spalling.

4.2.2 Load-displacement curves

The load versus top wall displacement graph is given in figure A.(2).1. The graph of load versus displacement at the height of load application is shown in figure A.(2).2. For comparison purposes, the above mentioned two displacements are plotted in figure A.(2).3. Vertical displacements are shown in figures A.(2).4 and A.(2).5. The average of the two vertical displacements is also shown versus the load and horizontal top wall displacement in figures A.(2).6 and A.(2).7, respectively.

Yielding was not marked by a distinct change in the load displacement curve but seems to have started in some bars just before achieving MDL-5. Section rotations can only be determined at the top and hence, flexural deformations can only be obtained at this stage by using the method of area 'α1' from figure 3.12. Shear deformations obtained by using this method are given in figure A.(2).8.

4.2.3 Strain gauge readings

The strain gauge readings in microstrains are given in figures A.(2).9 to A.(2).15. The gauge numbers refer to the location shown in each figure. All gauges were located on the flexural reinforcement at the bottom level.

4.3 Static cyclic loading - Scale 1:5 model SW3

The geometry and loading boundary conditions of model SW3 represent a scaled down version of wall SW4. The loading regime imposed on this model was intended to confirm that until yield, only two cycles are necessary at each displacement level. Five cycles were imposed at MDL-1 and three cycles for subsequent displacement levels until yield. After first yield, two cycles were imposed at each displacement level until failure, as shown in figure 4.(3).1. As in SW2 failure occurred after MDL-12 by fracture of the end main bars.

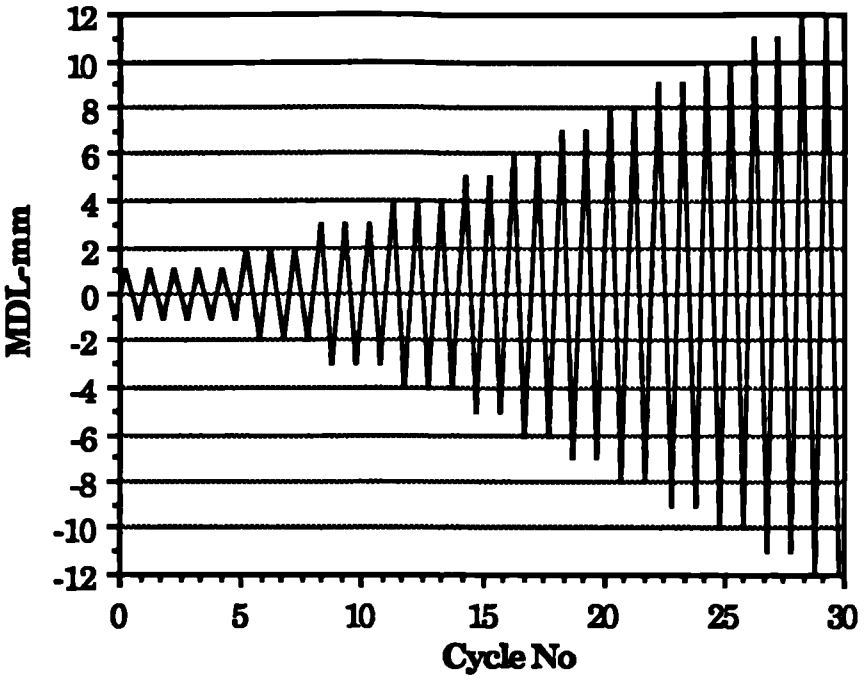


Figure 4.(3).1 Loading history of SW3

The first load reversal was at MDL-1. The initial stiffness at this maximum displacement was about 7.5 KN/mm. The 'virgin' loop had a larger area than all subsequent loops which differed very little from each other as observed in SW2.

4.3.1 Cracking of SW3

At MDL-2, extensive cracking occurred, spreading from the bottom of the wall upwards. First cracking was almost nearly horizontal and was located in the tensile zones. On reversal, cracks developed in the other half of the wall in an almost symmetric manner as shown in figure 4.(3).2. More surface cracking became apparent even after the virgin cycle, including the third cycle at the early MDL's.

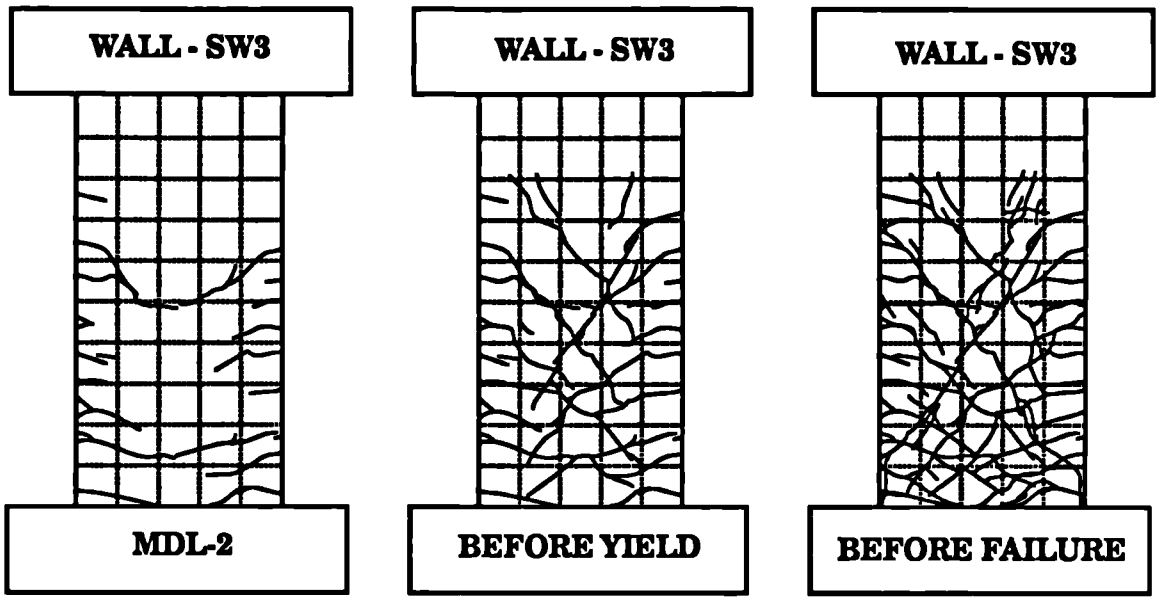


Figure 4.(3).2 Cracking stages for wall SW3

Until yielding of the main reinforcement, crack spreading continued in a similar way as for SW2. Cracks at the boundaries of the wall were less inclined and more dense than cracks in the web of the wall. In the web, the cracks took a rather sharp change in direction and crossed the web at about 45 degrees to the horizontal, this value being lower at the lower sections of the wall and higher further up. The extent of cracking just before yield was higher than for SW2, the main difference being due to cracks that originated in the upper half of the wall progressing at steeper angles. The same pattern of cracking prevailed until failure. The density of cracking was higher than for SW2 at failure. In each direction, one main crack originating in the top half seemed to penetrate the compression area. Vertical cracking was also observed near the boundaries at the bottom due to spalling of the cover concrete.

4.3.2 Load-displacement curves

The load versus top wall displacement graph is given in figure A.(3).1. The load versus displacement at mid-wall height is shown in figure A.(3).2. Mid-height and top wall displacement are shown in figure A.(3).3. The vertical displacements at both ends of the wall are shown in figures A.(3).4 and A.(3).5. The average of the two vertical displacements is also shown against load in figure A.(3).6.

Yielding was not marked by a distinct change in the load-displacement curve, but was initiated in the extreme tensile bars when displacement was increased from 5 mm to 6 mm. After reaching the ultimate load, it became apparent that the mid-height transducer was being affected by the stirrup, which was opening at the anchored end. Shear deformations by using the method of area '$\alpha 1$' are given in figure A.(3).7.

4.3.3 Strain gauge readings

The strain gauge readings are given in figures A.(3).8 to A.(3).15. Four strain gauges were located on the flexural reinforcement at the bottom and four at the top of the wall.

4.4 Static cyclic loading - Scale 1:2.5 model SW4

Wall SW4 was the first to be tested at this scale and the number of channels for data acquisition was tripled. With more space available along the height of the wall, the number of LVDT's increased to the maximum allowed by the data acquisition system used. Contact of the transducer shaft with the wall was established by glueing metal strips perpendicular to the LVDT shaft and bearing on circular rods glued on the wall. Vertical transducers had to be positioned out of the wall plane so as to avoid contact with the moving wall, and hence, the circular rods were protruding outward from the wall plane. The adhesive used did not prove to be satisfactory and as a result a number of vertical transducers lost contact with the wall at different stages of the experiment. This made processing of the results more difficult and less complete than for the rest of the experiments.

As in all subsequent experiments, two full cycles were imposed at each MDL until failure. The loading regime for SW4 is shown in figure 4.(4).1.

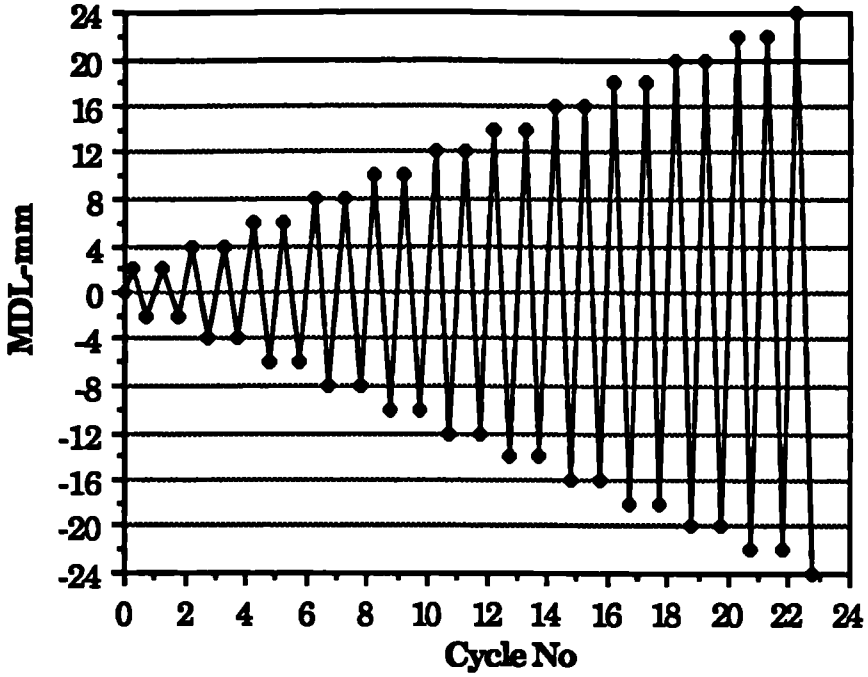


Figure 4.(4).1 Loading history for SW4

4.4.1 General observations

Unlike the scale 1:5 experiments, cracking was observed before reaching the first MDL, after 1 mm of displacement. The initial wall stiffness as calculated at 0.5 mm was 31 KN/mm. The stiffness at MDL-2 was 19.3 KN/mm.

Cracking at MDL-2 is shown in figure 4.(4).2. Cracks propagated from the wall boundaries towards the centres and from the bottom upwards. Near the boundaries, cracks were nearly horizontal while further away they were inclined to the horizontal. The inclination increased along with the height. Cracking was apparent up to just above the middle of the wall. By MDL-4, cracks propagated to the entire wall height. At the boundaries, the density of the cracks increased while in the web, the number of main cracks was limited to about three to four on each side. The propagation of these main web cracks towards the opposite side was more in the lower part of the wall. Consequently, traversing of cracks was more frequent in this area. The same pattern of cracking continued until yield.

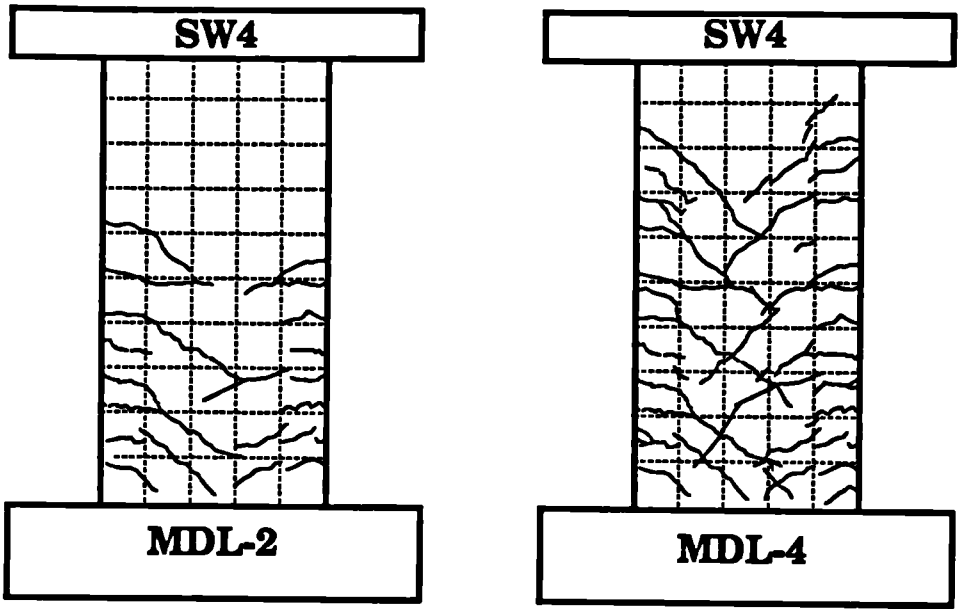


Figure 4.(4).2 Crack pattern of wall SW4 at MDL-2 and MDL-4

First yield occurred just before MDL-6, but MDL-8 will be presented as the first post-yield displacement in figure 4.(4).3. Following yield, cracking became denser and several boundary cracks joined to meet the end of the web cracks. The number of web cracks increased and so did the apparent inclination of the wall. The latter was due to the joining of web cracks with cracks originating higher up in the boundaries. By MDL-16 (figure 4.(4).3) the lower web cracks had opened up considerably more than all the others. Vertical cracking also appeared near the bottom of the wall at the boundaries, approximately at the position of the main reinforcement. This may indicate that there was spalling of the concrete cover at these locations.

With increasing MDL, the concrete in the lower part of the wall began to show signs of deterioration. At MDL-22 (figure 4.(4).4), just before failure, the concrete confined by the lowest two hoops in both boundary elements was spalling considerably. Failure occurred in this area, during cycles at MDL-24, by crushing of core concrete (figure 4.(4).4). By MDL-22 the stroke of the control LVDT's was also exhausted in one direction and hence, results are only presented up to the latter level.

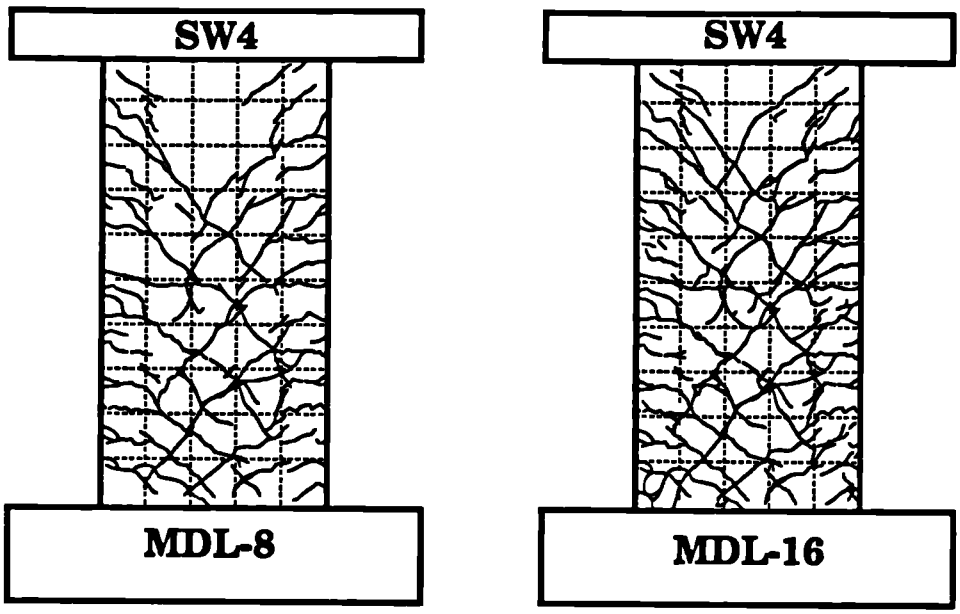


Figure 4.(4).3 Crack pattern of wall SW4 at MDL-8 and MDL-16

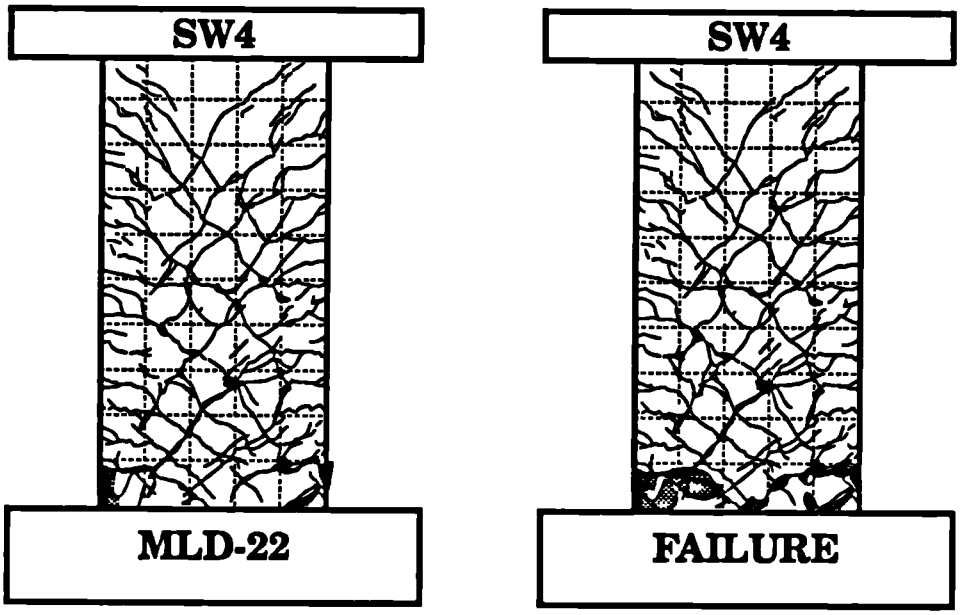


Figure 4.(4).4 Crack pattern of wall SW4 at MDL-22 and failure

4.4.2 Load-displacement curves

The load-displacement curves are given in figures A.(4).1 - A.(4).10 for displacements 3 to 12. Base vertical and out-of-plane displacements are shown in figures A.(4).11 and A.(4).12, respectively. The wall extensions at top, half and quarter height locations is shown in figures A.(4).13 - A.(4).15, respectively.

4.4.3. Strain gauge results

Strain gauge readings are plotted against force in figures A.(4).16 to A.(4).38. The value of strain is always given in microstrain. Very few of the strain gauges lasted long after yield level, which means that all strain gauges located on the flexural reinforcement at the bottom level stopped functioning before achieving the ultimate load. Six of the strain gauges were located on the stirrups but only number 19 seemed to be operational throughout the test.

4.5 Static cyclic loading - Scale 1:2.5 model SW5

Wall SW5 has more of the main reinforcement concentrated at the boundaries, hence was expected to sustain a higher flexural load if shear failure did not predominate. In order to avoid problems with the fixing of the reference rods, as encountered in SW4, a different type of adhesive was used, whilst the perpendicular plates were soldered at the end of the transducer shaft .

Two full cycles were imposed at each MDL until failure. Thereafter a different loading regime was imposed so as to avoid excessive deterioration at early stages as explained later. The loading regime for SW5 is shown in figure 4.(5).1.

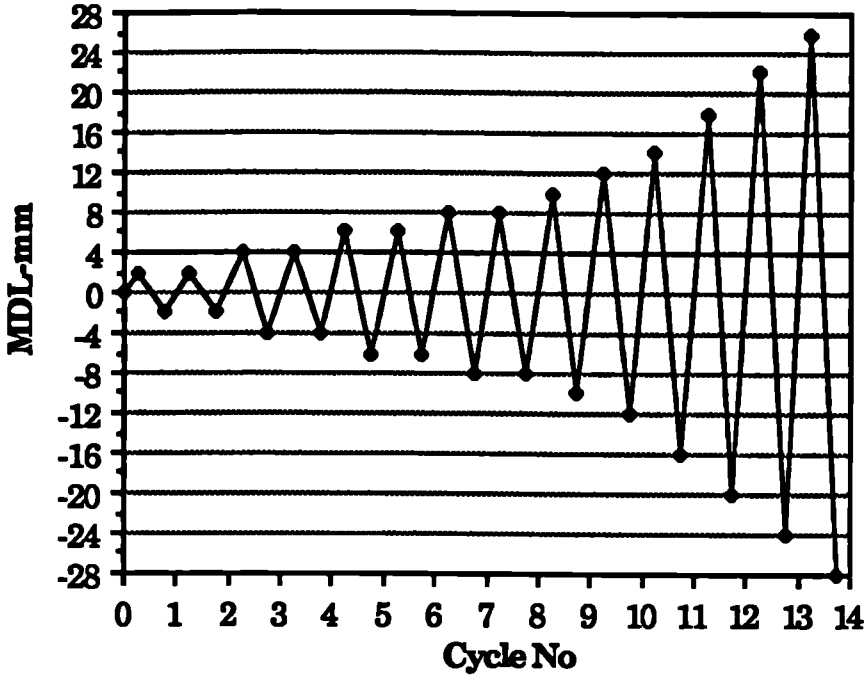


Figure 4.(5).1 Loading history for SW5

4.5.1 General observations

Cracking was observed before reaching the first MDL at 1 mm of displacement. The initial wall stiffness as calculated at 0.5 mm was about 34 KN/mm. The stiffness at MDL-2 was 21.7 KN/mm.

Cracking at MDL-2 is shown in figure 4.(5).2. Cracks propagated from the wall boundaries towards the centre and from the bottom upwards. Cracking was apparent up to three quarters of the height of the wall. In the lower half, the frequency of cracks near the boundary was higher than in the web. However, the inclination of these cracks was steeper than that for wall SW4. The inclination of the main web cracks was about 30° to the horizontal. By MDL-4 cracks propagated to the whole wall length as shown in figure 4.(5).2. In the lower half of the wall, at the boundaries, the density of the cracks increased while in the web the number of main cracks was limited to about four to five in each direction. The inclination of these main web cracks was about 45° in the lower part of the wall. Higher up, the inclination was much steeper up to 60°, indicating the shear nature of these cracks.

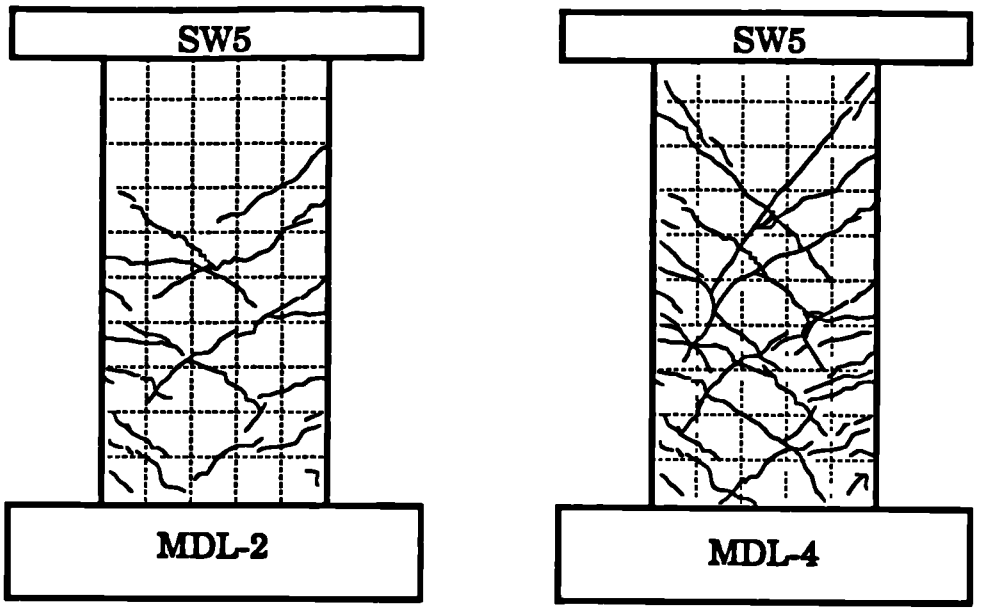


Figure 4.(5).2 Crack pattern of wall SW5 at MDL-2 and MDL-4

By MDL-8 the frequency of cracking in the boundaries increased considerably as shown in figure 4.(5).3. The main web cracks started joining with cracks originating higher in the boundary than before and hence, increased their apparent inclination.The most precarious crack seemed to be that originating at the top right hand side of the wall. MDL-10 was achieved in one direction at a load of 117.3 KN. Yield level was just achieved in the shear reinforcement, but the flexural reinforcement was just below yield. On attempting to achieve MDL-10 in the reverse direction, abrupt failure occurred at a load of about 110 KN. At this stage two of the main web cracks opened up significantly as shown in figure 4.(5).3. However, the crack that caused failure was the lower one which goes penetrated the compressive area.

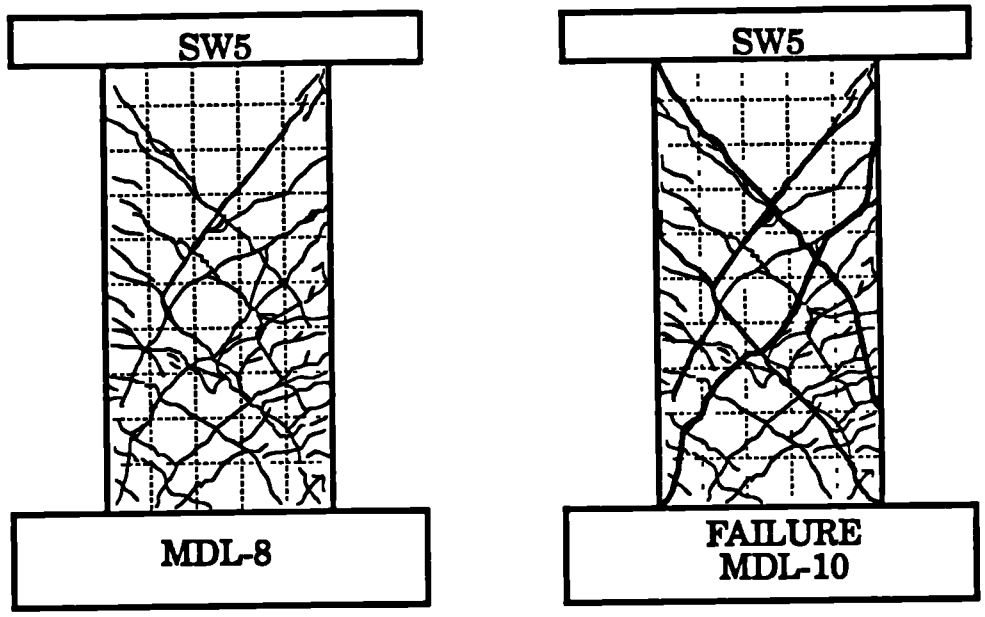


Figure 4.(5).3 Crack pattern of wall SW5 at MDL-8 and MDL-10

Following failure in one direction, it was decided to avoid cycling the wall twice at the same MDL and failure in the other direction was immediate after exceeding MDL-10 at a load of about 108 KN. The last MDL imposed in both directions was MDL-12. For the sake of demonstrating the effect of cycling on a wall that failed in shear, displacements were increased by 2 mm in each direction as shown in figure 4.(5).1, until the limits of the control transducers were reached. The state of the wall at MDL-14 is shown in figure 4.(5).4, demonstrating failure in the forward direction which was caused by the crack originating at the top left corner. Again two main cracks have opened considerably. After failure, several hoops and stirrups opened up and considerable opening was noticed in the middle sections of the wall. Additionally, it could be seen that the wall was displacing in a rigid body mode above the main cracks. The considerable degradation of the wall at MDL-26 is shown in figure 4.(5).4.

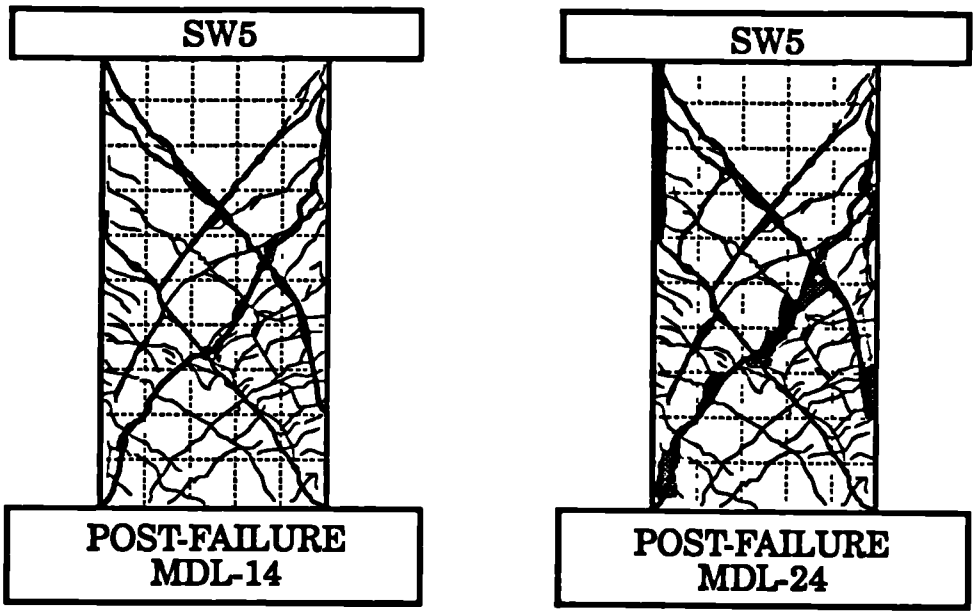


Figure 4.(5).4 Crack pattern of wall SW5 at MDL-14 and MDL-26

4.5.2 Load-displacement curves

The load-displacement curves are given in figures A.(5).1 - A.(5).10 for displacements 3 to 12. Base vertical and out-of-plane displacements are shown in figures A.(5).11 and A.(5).12 respectively. The wall extensions at top, mid and quarter height locations is shown in figures A.(5).13 - A.(5).15, respectively.

4.5.3 Strain gauge results

Strain gauge readings are plotted against force in figures A.(5).16 to A.(5).40. The value of strain is given in microstrain. Two of the strain gauges were located on the hoop reinforcement, very close to the bottom of the beam. Four gauges were located on the stirrups Interestingly, the strain gauge located very near the top beam indicated that no significant strains excist at that level.

4.6 Static cyclic loading - Scale 1:2.5 model SW6

Wall SW6 had identical flexural reinforcement to wall SW4 but considerably less lateral reinforcement, identical to the one used in wall SW5. The loading regime for SW6 is shown in figure 4.(6).1.

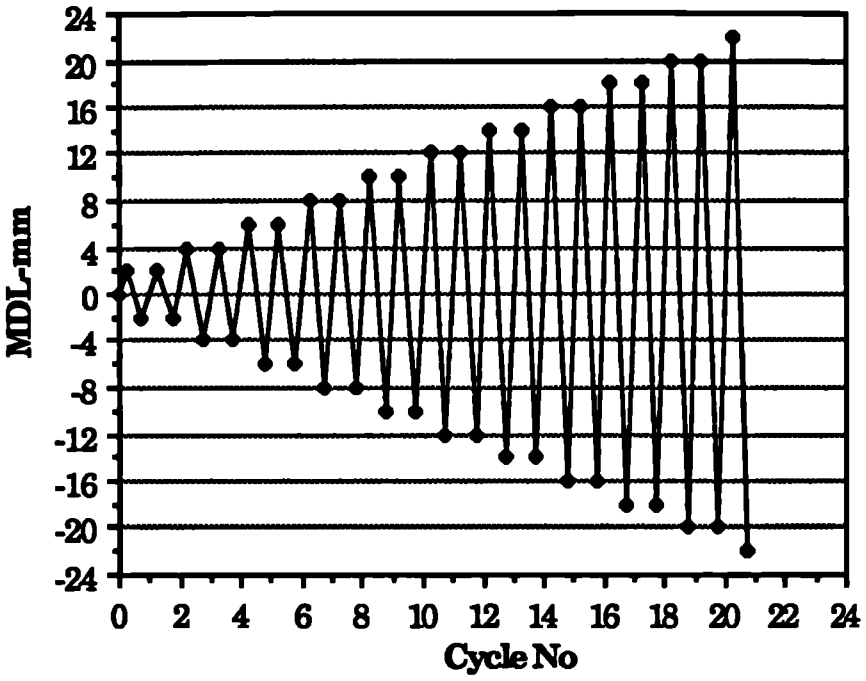


Figure 4.(6).1 Loading history for SW6

4.6.1 General observations

Cracking was again observed before reaching the first MDL, at 1 mm of displacement. The initial wall stiffness as calculated at 0.5 mm was about 33.5 KN/mm and at MDL-2 was 20 KN/mm. These two stiffnesses are both slightly higher than the corresponding values of SW4.

The pattern of cracking at MDL-2 is shown in figure 4.(6).2. Despite the apparent slightly higher stiffness, cracking was as extensive as in SW4 at this stage. The pattern and extent was also almost identical. It is worth noting that web cracks in both walls propagated deeper into the section in the RHS by MDL-2. At MDL-4 cracking increased its density, progressed deeper into the section and propagated to the whole length exactly as in SW4. The pattern of cracking was maintained until yielding of the main flexural reinforcement just before MDL-6.

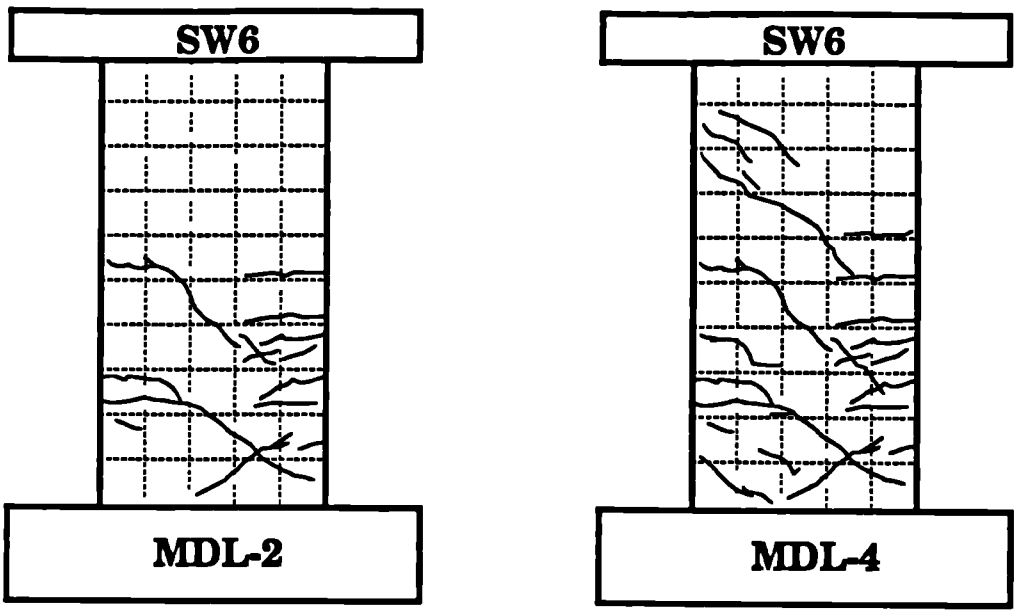


Figure 4.(6).2 Crack pattern of wall SW6 at MDL-2 and MDL-4

After yield, the extent of cracking in the web increased considerably as shown in figure 4.(6).3. The main web cracks started joining with cracks originating higher in the boundary, hence increased more their apparent inclination than in SW4. Following MDL-8, the width of cracking started to open considerably more than in SW4. However, by MDL-16 (figure 4.(6).3) the maximum load achieved was 107 KN which was higher than the ultimate for SW4. Diagonal cracking propagated from the web into the opposite boundaries and seemed to have pushed the neutral axis, at least in the surface, very close to the edge. Concrete spalling was also noted in the bottom end of the wall.

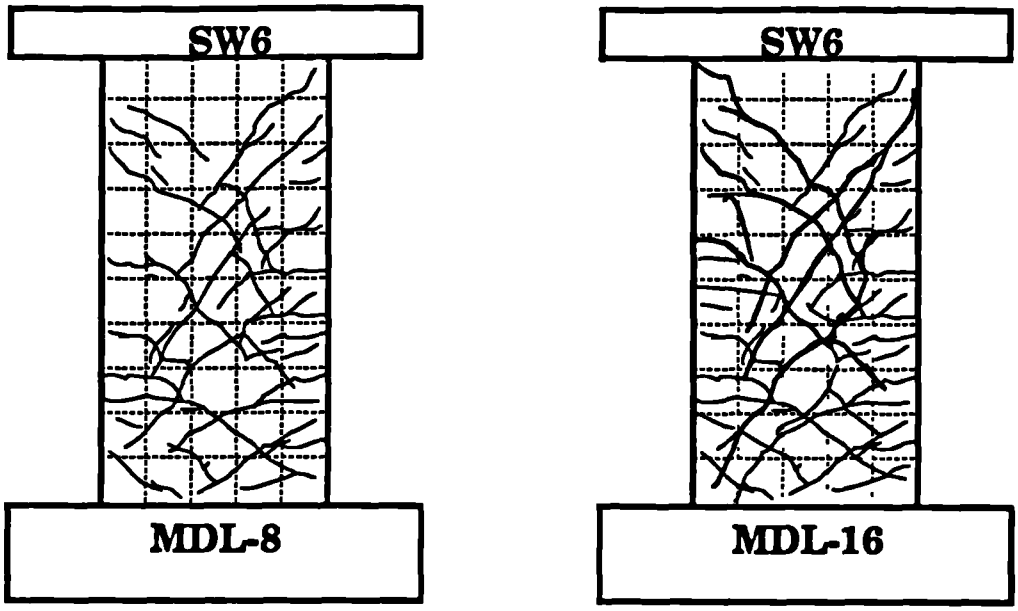


Figure 4.(6).3 Crack pattern of wall SW6 at MDL-8 and MDL-16

By MDL-18 (figure 4.(6).4), the concrete deterioration started affecting the strength and even though the maximum load was achieved during the RHS MDL, less load was resisted when the displacement was reversed. An opening of the stirrup in the lower level was observed at this MDL as well as progression of the cracks through the compressed area. Crushing of concrete was initiated just before achieving MDL-20 in the LHS. The loss of strength continued in the subsequent cycles and by MDL-22 the load was below 75% of ultimate in the RHS direction as well. In this direction, a wide crack crossing through the bottom boundary area was observed. MDL-22 (figure 4.(6).4) was the last displacement to be imposed since the wall was considered to have failed.

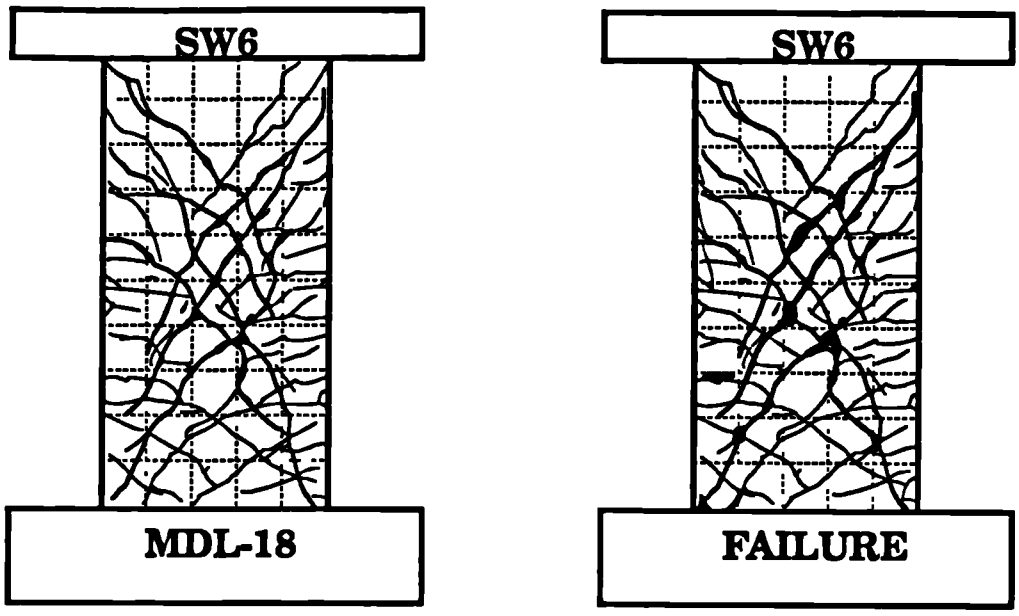


Figure 4.(6).4 Crack pattern of wall SW6 at MDL-18 and MDL-22

4.6.2 Load-displacement curves

The load-displacement curves are given in figures A.(6).1 - A.(6).10 for displacements 3 to 12. Base vertical and out-of-plane displacements are shown in figures A.(6).11 and A.(6).12, respectively. The wall extensions at top, mid and quarter height locations is shown in figures A.(6).13 - A.(6).15, respectively.

4.6.3 Strain gauge results

Strain gauge readings are plotted against force in figures 4.(6).16 to 4.(6).38. The value of strain is given in microstrain. Most of the strain gauges were distributed along the height of the wall on the flexural reinforcement. Three strain gauges were located on the stirrups and two on the hoop reinforcement near the bottom.

4.7 Static cyclic loading - Scale 1:2.5 model SW7

Wall SW7 had most of the main reinforcement concentrated at the boundaries, similar to SW5, but had a higher shear reinforcement percentage, similar to that of wall SW4. The expected flexural strength was higher than all other specimens. During the process of this experiment several technical problems were encountered. The voltmeter of the data acquisition system developed some problems at the early stages of the experiment and had to be repaired. As a result, an insignificant number of data was lost at the end of MDL-4. The other problems were associated with the transmission box between the electrical motor and the screw jack. Due to ageing and the high repeated loading imposed on the gear box, the motor could not drive the jack on reverse high loads. Manufacturing new parts meant additional delay in the completion of this particular experiment.

4.7.1 General observations

Cracking was observed before reaching the first MDL at 1 mm of displacement. The initial wall stiffness as calculated at 0.5 mm was about 33 KN/mm, dropping to 21.3 KN/mm at MDL-2. The loading regime for SW7 is shown in figure 4.(7).1.

Cracking for MDL-2 is shown in figure 4.(7).2. Cracks initially propagated in a similar manner to wall SW5. Cracking was observed up to three quarters of the height of the wall. In the lower half, the intensity of cracking near the boundary was higher than in the web. By MDL-4, cracks propagated to the whole wall length as shown in figure 4.(7).2. In the lower half of the wall, at the boundaries, the density of the cracks increased while in the web the number of main cracks was limited to about four to five in each direction. The inclination of these main web cracks was less than or equal to 45°, and in general less steep than for SW5.

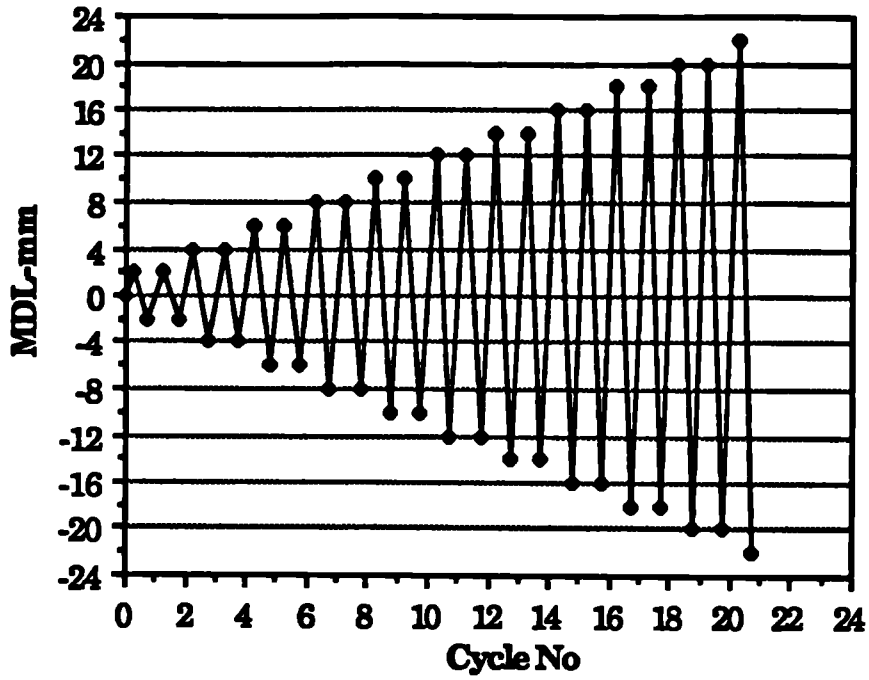


Figure 4.(7).1 Loading history for SW7

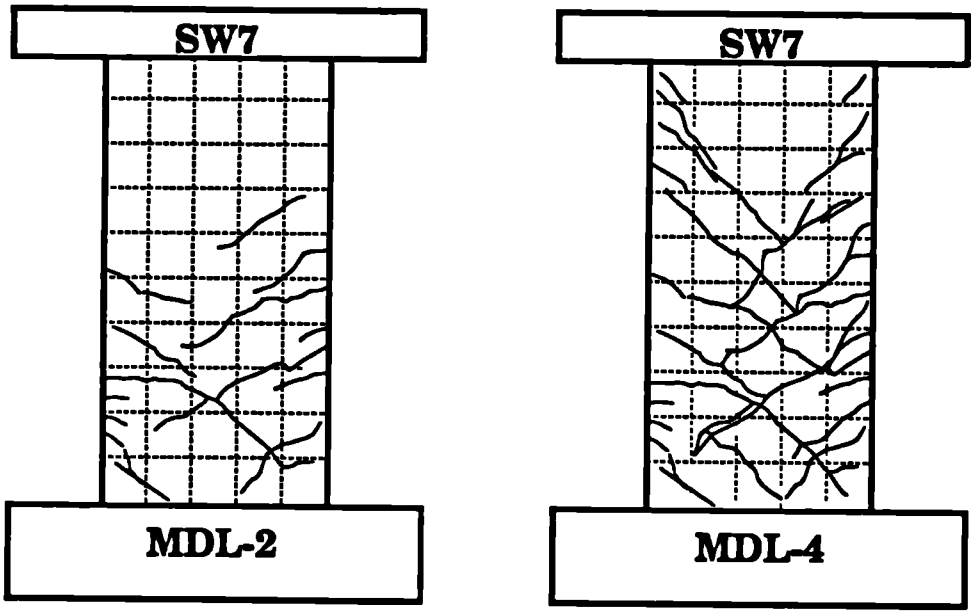


Figure 4.(7).2 Crack pattern of wall SW7 at MDL-2 and MDL-4

At MDL-8, the extent of cracking at the boundaries increased considerably as shown in figure 4.(7).3. The main web cracks started joining with cracks originating higher in the boundary, hence increased

their apparent inclination but not to the extent seen for SW5. Following MDL-8, cracking continued to become denser at the boundaries with an average inclination of more than 45°, unlike for walls SW4 and SW6 where the boundaries were wider. By MDL-14 (figure 4.(7).3), the main web cracks were wider than before and seemed to have penetrated the compressive area, at least on the surface.

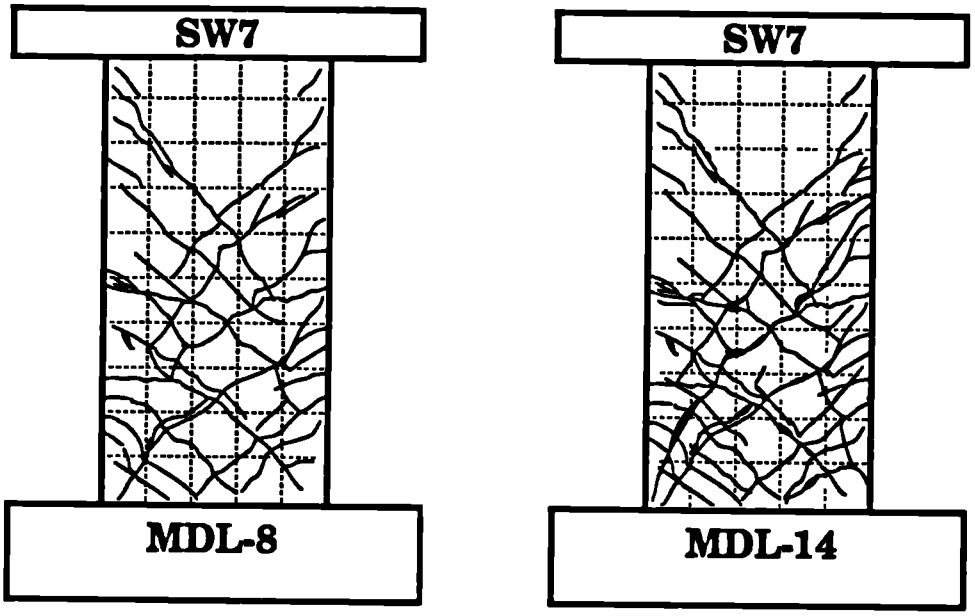


Figure 4.(7).3 Crack pattern of wall SW7 at MDL-8 and MDL-14

The load capacity peaked at MDL-18 corresponding to a load of 127.3 KN. Following that,the widening of the web cracks increased and there was some loss of strength at MDL-22 in the RHS direction. However, failure occurred at MDL-22 by fracturing of a 6 mm reinforcement bar on the LHS virgin cycle. A second bar snapped during the completion of this MDL and the strength was reduced to less than half .The considerable degradation of the wall at MDL-22 is shown in figure 4.(7).4.

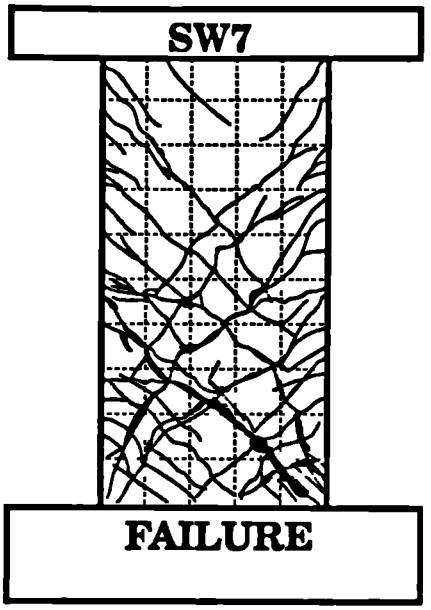


Figure 4.(7).4 Crack pattern of wall SW7 at MDL-22

4.7.2 Load-displacement curves

The load-displacement curves are given in figures A.(7).1 - A.(7).10 for displacements 3 to 12. Base vertical and out-of-plane displacements are shown in figures A.(7).11 and A.(7).12, respectively. The wall extensions at top, mid and quarter height locations is shown in figures A.(7).13 - A.(7).15, respectively.

4.7.3 Strain gauge results

Strain gauge readings are plotted against force in figures A.(7).16 to A.(7).41. The value of strain is given in microstrain. Almost all the strain gauges in this wall lasted until considerable plastic strains were achieved. Seven strain gauges were located on stirrups and one on the bottom LHS hoop.

Wall SW8 was designed so that the flexural reinforcement was concentrated in the edge members. Shear reinforcement was distributed according to the SRS method described in chapter 8. The amount of shear reinforcement was half of that required by EC2 and was distributed only over two thirds of the wall height. The loading regime for SW8 is shown in figure 4.(8).1.

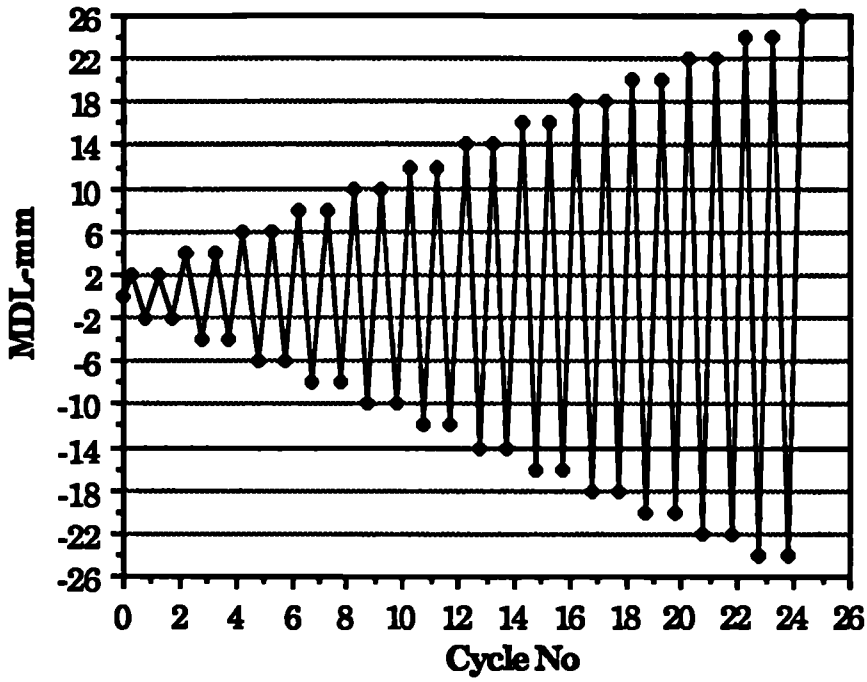


Figure 4.(8).1 Loading history for SW8

4.8.1 General observations

Cracking was observed before reaching the first MDL after 1 mm of displacement. The initial wall stiffness as calculated at 0.5 mm was about 27.8 KN/mm dropping to 18.6 KN/mm at MDL-2.

Cracking at MDL-2 is shown in figure 4.(8).2. Cracks initially propagated in a similar manner to wall SW4. Cracking was apparent up to just over half the height of the wall. In the lower half, the density of cracks near the boundary was higher than in the web and were most probably located above the hoop reinforcement. By MDL-4, cracks propagated to the whole wall length as shown in figure 4.(8).2. In the lower half of the wall, more cracks propagated from the boundaries towards the web, compared to all other walls. The inclination of the main web cracks was about 45°.

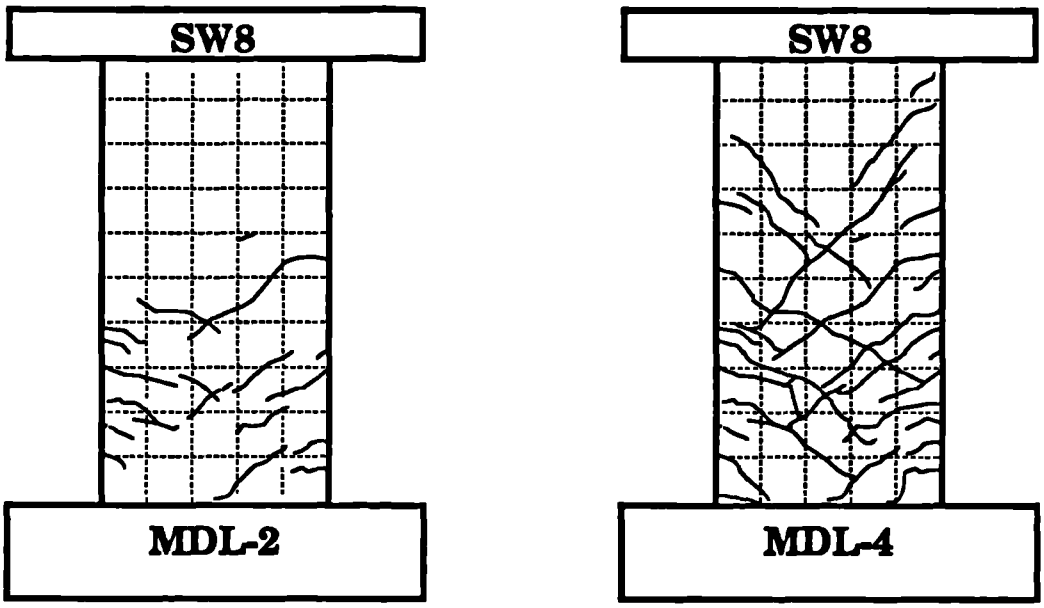


Figure 4.(8).2 Crack pattern of wall SW8 at MDL-2 and MDL-4

At MDL-6, a crack originating from the top corner propagated through the web at an angle slightly higher then 45° to meet the web crack below, as shown in figure 4.(8).3. After MDL-6, cracking continued to become denser at the boundaries but the number of opening main cracks in the web stabilised to about four to five. By MDL-12 (figure 4.(8).3), the same pattern of cracking continued, but the main web cracks were wider than before.

By MDL-18, the lower web cracks were opening more than the ones higher up. Spalling of the concrete on the inside of the boundary element indicated the degradation of the concrete at that location. At this stage, vertical cracks which appeared by MDL-14 at the bottom end main reinforcement level were also visible (figure 4.(8).4). Following MDL-18, the widening of the web cracks increased and more spalling of concrete within the web took place at the intersection of the main cracks. Loss of the concrete cover at the extreme bottom parts of the wall exposed the flexural reinforcement by MDL-24. Due to the considerable degradation, the wall lost some strength by the second cycle LHS MDL-24 and RHS MDL-26, as shown in figure 4.(8).5 The test was stopped at MDL-26 as soon as the load dropped below 75% of the ultimate, so as to avoid excessive damage to the specimen.

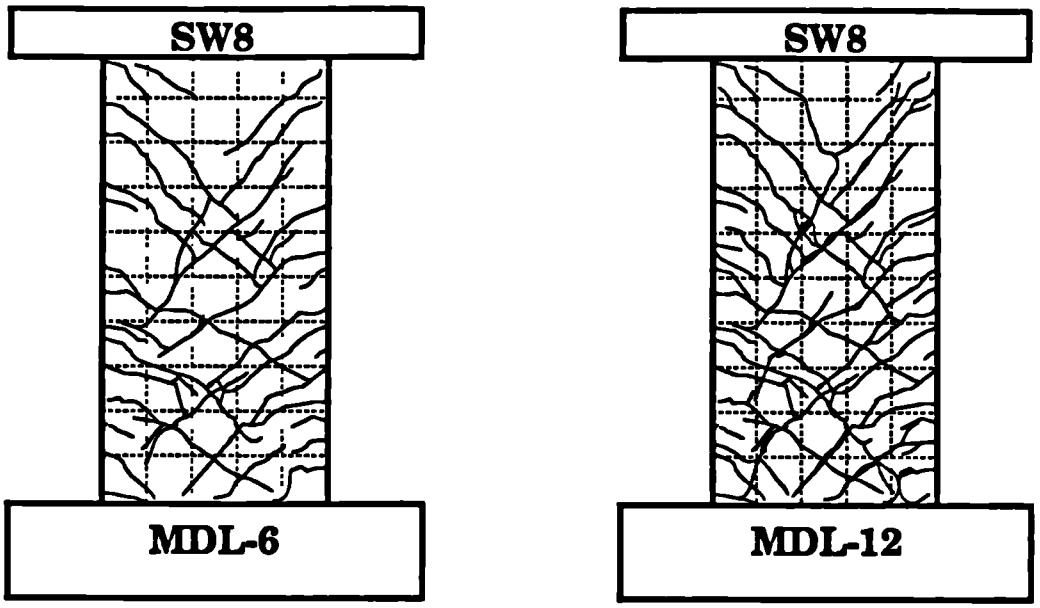


Figure 4.(8).3 Crack pattern of wall SW8 at MDL-6 and MDL-12

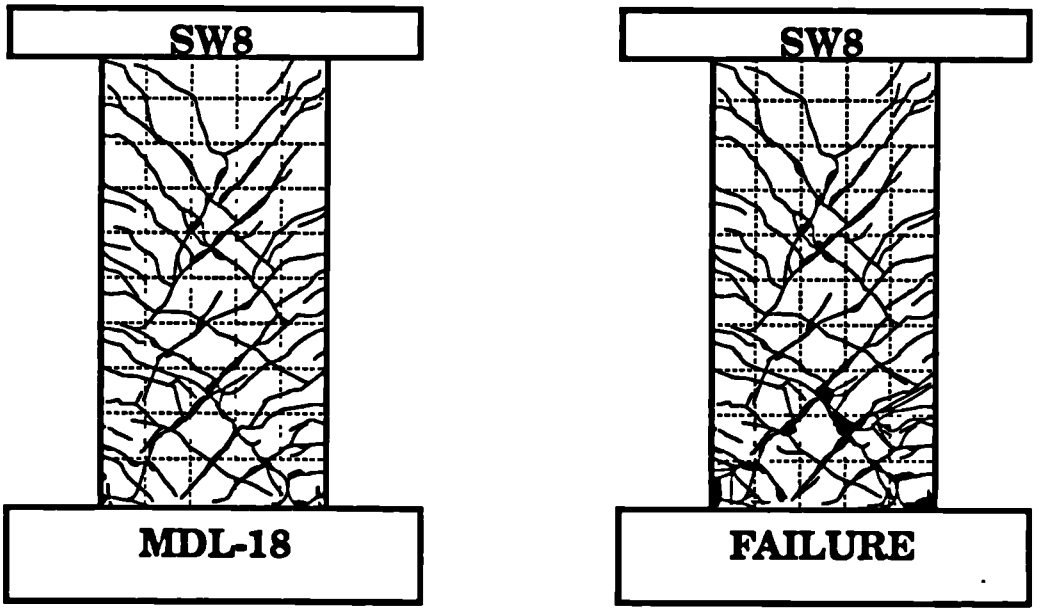


Figure 4.(8).4 Crack pattern of wall SW8 at MDL-18 and failure

4.8.2 Load-displacement curves

The load-displacement curves are given in figures A.(8).1 - A.(8).10 for displacements 3 to 12. Base vertical and out-of-plane displacements are shown in figures A.(8).11 and A.(8).12 respectively. The wall extensions at top, mid and quarter height locations is shown in figures A.(8).13 - A.(8).15, respectively.

4.8.3 Strain gauge results

Strain gauge readings, in microstrain, are plotted against force in figures A.(8).16 to A.(8).39. The stirrup reinforcement extended only up to two thirds of the height and seven out of eight strain gauges located on them were operational at the beginning of the test, five of which survived until the final stages of the test, even after yield strains were recorded.

4.9 Static cyclic loading - Scale 1:2.5 model SW9

Wall SW9 had identical main reinforcement to wall SW8, but the lateral reinforcement was designed according to the requirements of EC2. The loading regime for SW9 is shown in figure 4.(9).1.

4.9.1 General observations

Cracking was observed before reaching the first MDL after 1 mm of displacement. The initial wall stiffness, as calculated at 0.5 mm, was about 38 KN/mm. The stiffness by MDL-2 was a little higher than for SW8, at 29.8 KN/mm. Cracking at MDL-2 and MDL-4 is shown in figure 4.(9).2. Cracks propagated in a similar manner to wall SW8.

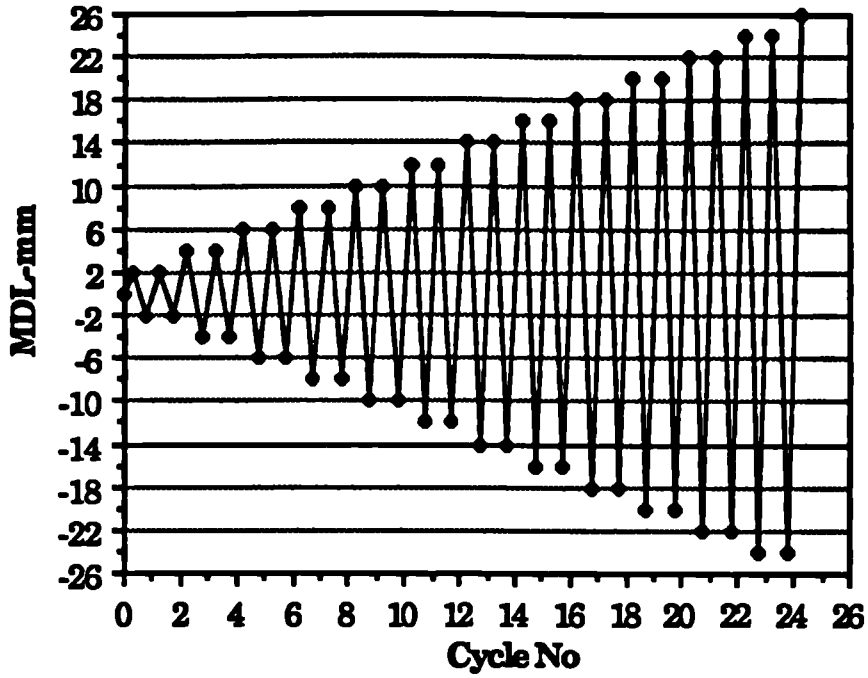


Figure 4.(9).1 Loading history for SW9

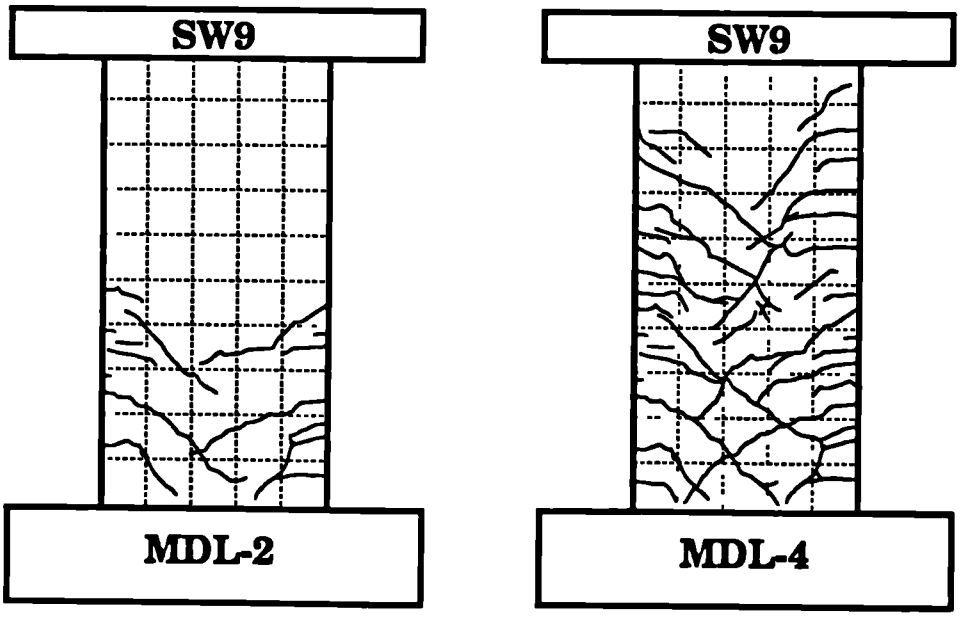


Figure 4.(9).2 Crack pattern of wall SW9 at MDL-2 and MDL-4

By MDL-6, the frequency of cracking in the boundaries increased considerably as shown in figure 4.(9).3. However, the top crack, which also appeared in SW8 at this stage, had a shallower angle. After MDL-6,

cracking continued to increase in density as observed for all previous walls. By MDL-14, (figure 4.(9).3) the main lower web cracks were wider than before and seemed to be opening faster than the top ones.

The cracking pattern until MDL-18 was similar to SW8 as shown in figure 4.(9).4. Subsequently, the upper cracks of SW9 were not opening as much as the corresponding ones for SW8. Spalling of concrete in the web at the intersections of main cracks was only confined to the lower quarter of the wall. The wall survived both cycles at MDL-24 and lost strength during the virgin cycle reverse and at the second cycle RHS MDL-26. MDL-26 is considered to be failure as shown in figure 4.(9).4.

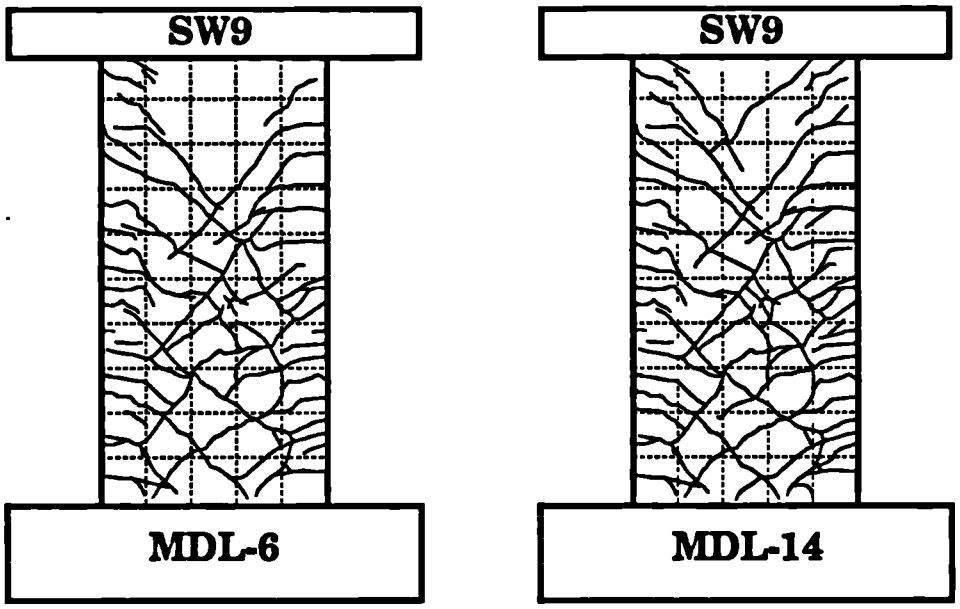


Figure 4.(9).3 Crack pattern of wall SW9 at MDL-6 and MDL-14

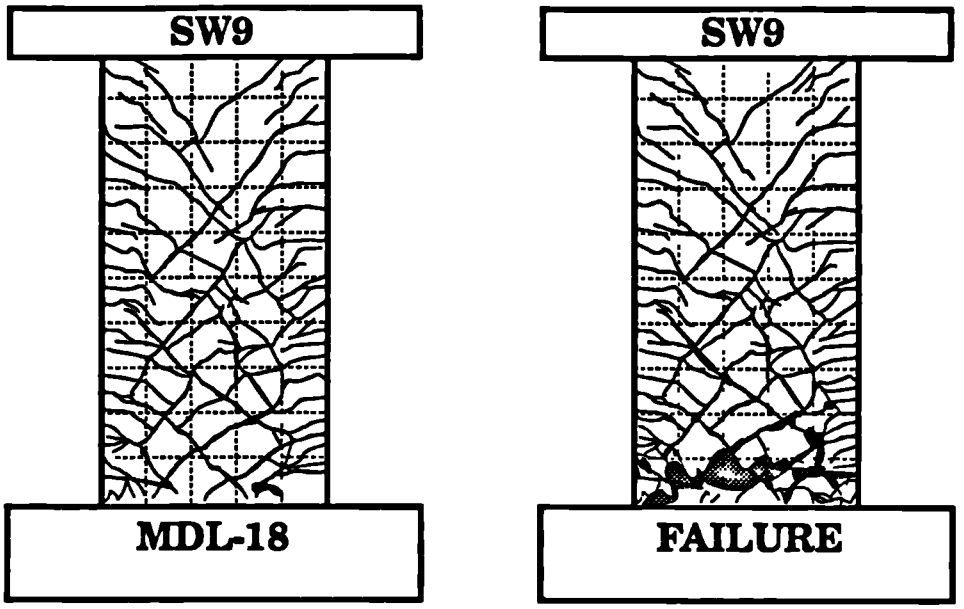


Figure 4.(9).4 Crack pattern of wall SW9 at MDL-18 and failure

4.9.2 Load-displacement curves

The load-displacement curves are given in figures A.(9).1 - A.(9).10 for displacements 3 to 12. Base vertical and out-of-plane displacements are shown in figures A.(9).11 and A.(9).12 respectively. The wall extensions at top, half and quarter height locations is shown in figures A.(9).13 - A.(9).15, respectively.

4.9.3 Shear and flexural deformation components

As discussed in section 3.6, shear deformations can be separated from the total horizontal deformations after calculating the flexural contribution. The flexural contribution in scale 1:5 walls was calculated by using area '$\alpha 1$' of figure 3.12 since only top displacements were available. The shear deformation diagrams as calculated by this method are given in sections 4.2 and 4.3. For scale 1:2.5 walls, the flexural contribution could be obtained by using the improved approximation of area '$\alpha 2$'. The results of wall SW9 can be used as an example to demonstrate the differences between

the two methods. Figures A.(9).16 and A.(9).17 show the force versus the flexural component of the top horizontal displacement, by using areas 'α1' and 'α2', respectively.

As expected, the results from method of area 'α1' yield much lower values for the flexural component. The ratio of displacements $\delta_{f\alpha 2} : \delta_{f\alpha 1}$ varies within the same cycle and with increasing MDL. At peak displacements the value of this ratio varies from about 1.4 before yield to about 1.7 at ultimate displacements. The effect on this on the calculations for shear deformation is not, however, straightforward, since the relationship between the different components of the horizontal displacement is not linear, as demonstrated by figures A.(9).18 to A.(9).20.

The ratio of $\delta_{f\alpha 2}$ to δ_3 is nearly constant up to yield. Subsequently, the ratio becomes smaller as the shear deformations become more dominant. In order to relate the discussion to an independent variable, the component of shear is plotted against force in figure A.(9).21.

4.9.4 Strain gauge results

Strain gauge readings, in microstrain, are plotted against force in figures A.(9).22 to A.(9).44. Five strain gauges were located on the stirrups, but none of the hoop strain gauges gave any meaningfull results.

The discussion of all the experimental results and comparisons with the analytical studies described in chapters 5 and 6 is presented in the chapter 7.

CHAPTER 5

5 REINFORCED CONCRETE ANALYSIS MODEL

5.1 Introduction

The analysis of RC structures under transient loading requires the use of a mathematical model representing the structure and a suitable analytical tool for providing the solution of the ensuing equations. In design, a common practice is to simplify the structure into 2-dimensional frames and to reduce the dynamic loading into equivalent static loading. By assuming elastic material properties, structural analysis results can be obtained either through the solution of closed form equations or by finite element analysis. More elaborate elastic methods solve the dynamic problem by either using a suitable time history as input loading, or by employing spectral analysis. In elastic methods, output member forces may be reduced by a factor depending on the ductility of the particular member and structural form. Alternatively, a 'design spectrum', accounting for excursions into the nonlinear range is used as imput to modal analysis.

The main disadvantage of elastic methods in reinforced concrete analysis is the fact that the elastic properties of reinforced concrete represent an over-simplification of the nonlinear behaviour of the material. Furthermore, a structure in not in the assumed elastic state even before the earthquake forces are imposed. It is also certain that as soon as the structure is subjected to even moderate lateral loading, the change in stiffness will affect the dynamic characteristics, hence elastic dynamic analysis depart significantly from the anticipated behaviour. Consequently, inelastic analysis is essential for predicting the behaviour of reinforced concrete under both static and dynamic analysis. The structural representation of the building will not vary from that used in the elastic case, but the analytical tool will have to take into account the material inelasticity.

In the past two decades, with the advancement of computers and computational methods, the finite element method has been used extensively in both linear and nonlinear structural analysis. Sophisticated material models have been implemented and various approaches have been developed to transform the essentially discontinuous problem of cracked concrete into a continuum mechanics model. However, a number of problems still remain to be solved before a particular model is deemed accurate in predicting the inelastic behaviour of RC members. In particular for members such as walls, with high shear stresses and significant shear deterioration, following severe cyclic loading poses a formidable problem. Moreover, extensive parametric studies aimed at complimenting existing experimental data require more efficient and economical solutions than finite element analysis can offer. The same requirement exists in design practices, where simplified solutions are more suitable than detailed modelling techniques.

Based on section analysis, a simple computational tool for reinforced concrete analysis has been developed for the purpose of this research programme. In subsequent sections, the description and assumptions of this method alongside material models used, are presented. Verification and error analysis of the model as well as recommendations for future work form the concluding section of this chapter.

5.2 Section analysis method

The assumptions on which the section analysis method is based are as follows:

a) Plane sections remain plane.

b) Full strain compatibility exists between concrete and steel reinforcement.

c) Flexural deformations are independent of shear deformations.

d) The total deformation is the sum of shear and flexural deformation.

In the following, the assumptions listed above are appraised and the material models used are described.

5.2.1 Plane sections assumption

The assumption that plane sections remain plane is reasonable in elastic analysis of slender elements. However, for elements having low aspect ratios, secondary deflections should be considered. In such cases the boundary deformations will tend to deform as shown in figure 5.1 below, which violates the plane section assumption.

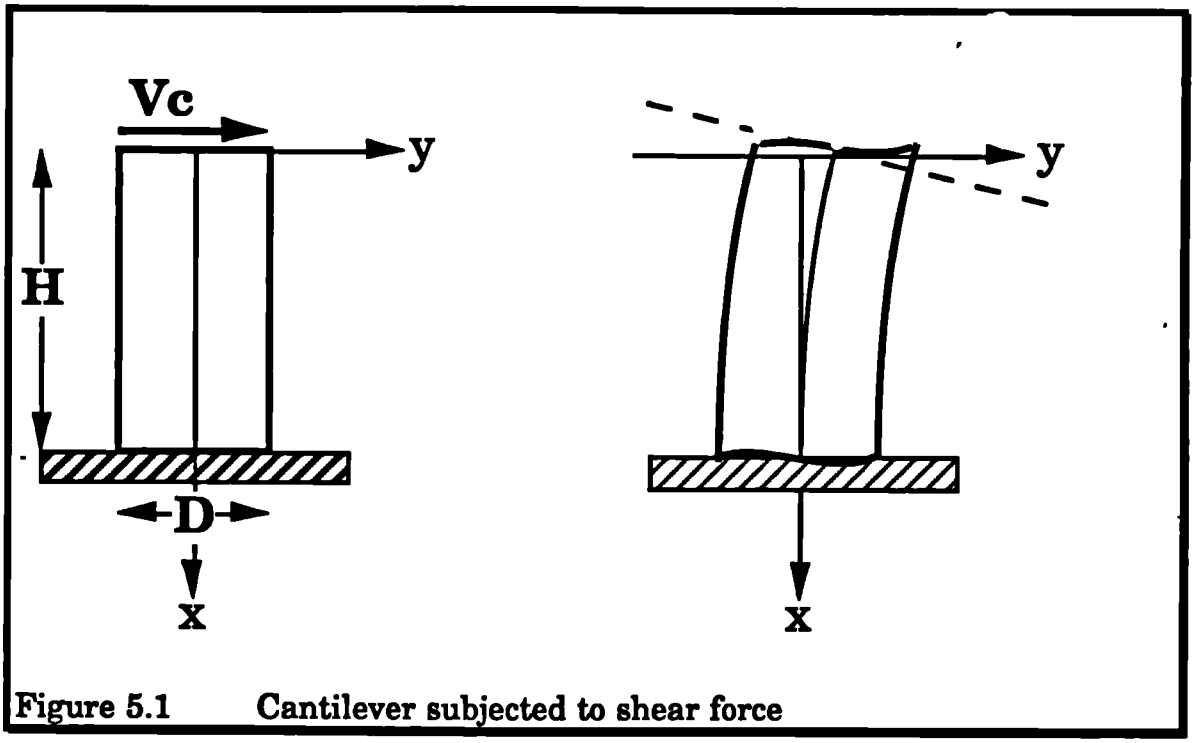


Figure 5.1 Cantilever subjected to shear force

The elasticity solution obtained by solving the Airy stress function after satisfying the boundary conditions (for loads) gives the following stress distributions:

$$\sigma_y = 0 \tag{5.1}$$

$$\sigma_x = \frac{-V_c \, x \, y}{I} \tag{5.2}$$

$$\tau_{xy} = \frac{V_c (D^2 - y^2)}{2I} \tag{5.3}$$

This solution is the equivalent of the classical beam theory approach and is valid for the parabolic shear distribution of equation 5.3 (Timoshenko and Goodier, 1982). By integrating the plane-stress equations the displacements u and v in the x and y directions, respectively, may be obtained, as detailed in the following equations. The centre of the beam at y = H is taken as fixed and having no rotation with respect to the vertical axis as shown in figure 5.1.

$$u = \frac{V_c x^2 y}{2EI} - \frac{\nu V_c y^3}{6EI} + \frac{V_c y^3}{6GI} + \left(\frac{V_c H^2}{2EI} - \frac{V_c D^2}{2GI} \right) y \qquad (5.4)$$

$$v = \frac{\nu V_c x y^2}{2EI} + \frac{V_c x^3}{6EI} + \frac{V_c H^3}{3EI} - \frac{V_c x D^2}{2EI} \qquad (5.5)$$

As expected at the centre of the free end (x=0, y=0) the horizontal deflection v is $V_c H^3 / 3EI$. However, the gradient of du/dy is not independent of y, as assumed by plane sections remain plane. Furthermore, in order to impose compatibility at the boundaries, the top and bottom beams will exert a certain amount of moment and hence, deform. The exact deformed shape is a function of the relative stiffness between the beams and the panel. The local effect of the beam stiffness is a redistribution of both the shear and normal stresses. A brief investigation by using a fine finite element mesh and imposing plane sections at the top and bottom of the cantilever showed that the shear stress is not any more parabolic (as obtained from equation 5.3) but peaks very near the ends, where the normal stresses are also much higher than predicted by the beam theory.

In the case of reinforced concrete, the loss of the tensile strength due to cracking causes a shift of the neutral axis compression side. Therefore, as far as the compressive area is concerned, the depth of the section is considerably reduced and hence, the secondary strains are minimised. In the tensile side, the plane section condition is imposed at the fixed and top ends by the presence of the stiff beams. However, at mid-height of the cantilever, higher normal strains may be obtained at the extreme fibres due to the plane section assumption. Following yield of the reinforcement, this effect is negligible for equilibrium purposes.

It can, therefore, be expected that the plain sections assumption would yield accurate results for flexure, even in deep reinforced concrete members. However, the shear stress distribution is not expected any more

to comply with the parabolic distribution obtained by elasticity and hence, should be dealt separately.

5.2.2 Strain compatibility

The strain compatibility of reinforced concrete under temperature changes is due to a coincidence in the thermal expansion properties of steel and concrete, but when external loads are imposed the compatibility between strains has to be maintained by bond forces at the interface. Modern high tensile steels for reinforcement are always deformed, and hence, provide bond through the effective process of mechanical interlocking rather than chemical adhesion and friction. Additionally, in section analysis, strain compatibility is more important when the materials are sharing the resistance to normal stresses, i.e. only in compression. It is expected that until a considerable compressive strain is induced, bond would be sufficient to transmit the forces between the materials.

It should be noted that during load reversals, if bond is lost in the main bars of a RC wall, the stress distribution will not obey the beam theory but will be in accordance with a combination of the beam and 'arch and tie' mechanisms. The arch and tie situation arises in the case of total debonding so that the force in the tensile bars is uniform throughout. The implications of the 'arch and tie' mechanism are further discussed in chapter 7.

5.2.3 Independence of flexural deformation

By using the principle of virtual work, flexural deformations are calculated by integrating the product of virtual moment m_o and curvature k over the length under consideration i.e:

$$v_f = \int_0^H m_o \, k \, dx \qquad (5.6)$$

Assuming that the maximum moment is known, curvature at different levels can be established by satisfying equilibrium. Numerical integration can then be used to obtain flexural deflections. In order to establish equilibrium from an assumed curvature value, only normal

strains and stresses can be used rendering the method uniaxial. The stresses in steel bars can be determined accurately in this manner, but stresses in concrete are a function of the triaxial state of stress. Two-dimensional elasticity yields no stresses laterally as shown in equation 5.1. Nevertheless, the confinement and shear reinforcement, when provided, induce lateral stresses and should be accounted for. In the compressive area, both types of reinforcement contribute towards higher confinement of the concrete which improves normal and shear stress resistance, as discussed hereafter.

The existence of shear stresses in the compressive area is usually assumed not to influence the stiffness characteristics of concrete. In elasticity, the addition of a shear stress component leads to a rotation of the principal stress axis system and an increase in the major axis stress as well as a decrease in the minor axis stress. This may influence the accuracy of obtaining ultimate stresses and hence, indirectly affect the calculations for flexure. Direct stress section analysis is incapable of predicting shear deformations, and need arises for an independent shear deformation model.

The assumed boundary condition at the bottom is fixity, and no rotations are allowed. In reality fixity is achieved for equilibrium purposes. In practice, however, in order to develop the boundary stresses, especially tensile stresses in the reinforcement, a certain degree of extension as well as compression deformation will occur within the foundation. The resultant rotation at this level could have a significant effect on the overall deflection. Paulay and Williams (1980) suggested that anchorage deformations could be as high as 20% of the flexural deformations. Base rotation can also be a result of uplifting of the bottom beam in the case of experimental work. For the purposes of this test programme the bottom beams were prestressed to the floor with forces higher than the expected uplift forces due to moment, and, hence the axial stiffness of the beam is assumed to be infinite. The effectiveness of the used method is examined in chapter 7.

If the assumption that flexural deformations are independent of shear deformations is accepted, then the total deflection can be obtained by superposition of the flexural and shear components.

5.3 Flexural model implementation

The method of section analysis assumes a certain strain distribution within a particular section, which is varied until force equilibrium is established. In order to achieve this, material models are used to calculate stresses for given strains. The cyclic models used for steel and concrete are discussed below.

5.3.1 Steel model

The most commonly used steel model in design is the linear elastic perfectly plastic model. There are two significant draw-backs in simplifying the steel behaviour to an elastoplastic model:

a) Ignoring strain hardening.

b) Ignoring stiffness degradation after inelastic load reversals.

The extent of strain hardening varies considerably in different steels and modern codes have identified this discrepancy and recommend limits for the ratio of ultimate to yield stress of steels. The effect of ignoring strain hardening is to lead to an under-estimate of the section strength. Consequently, the accuracy in estimating the flexural strength, required for the shear design may be forfeited.

The degradation of stiffness under cyclic loading exceeding yield stresses is a material property that cannot be estimated from standard monotonic testing. The degree of degradation has significant impact on the energy dissipated by the steel and hence, by the structural member. Additionally, the stiffness of steel on reloading will determine the load level at which concrete will be re-mobilised following the load reversal and, consequently, influences indirectly the behaviour of the reinforced concrete member in shear.

In order to represent simply the behaviour of the variety of steels used, a tri-linear cyclic model has been formulated as shown in figure 5.2. Monotonic experiments, as described in chapter 3, are used to obtain the model envelope. A yield level is determined by using the monotonic yield

load and the strain hardening stiffness 'E_{s1}'. A maximum stress 'fsu' is not to be exceeded at any value of strain. Exceeding an ultimate strain 'ε_{su}' will result in the bar fracture and total loss of strength. Loading and unloading up to the yield level and down to zero follows the initial stiffness 'E_{so}'. On reloading, a stiffness 'E_{sa}' is used. Once the yield level is achieved, stress increases according to stiffness 'E_{s1}'.

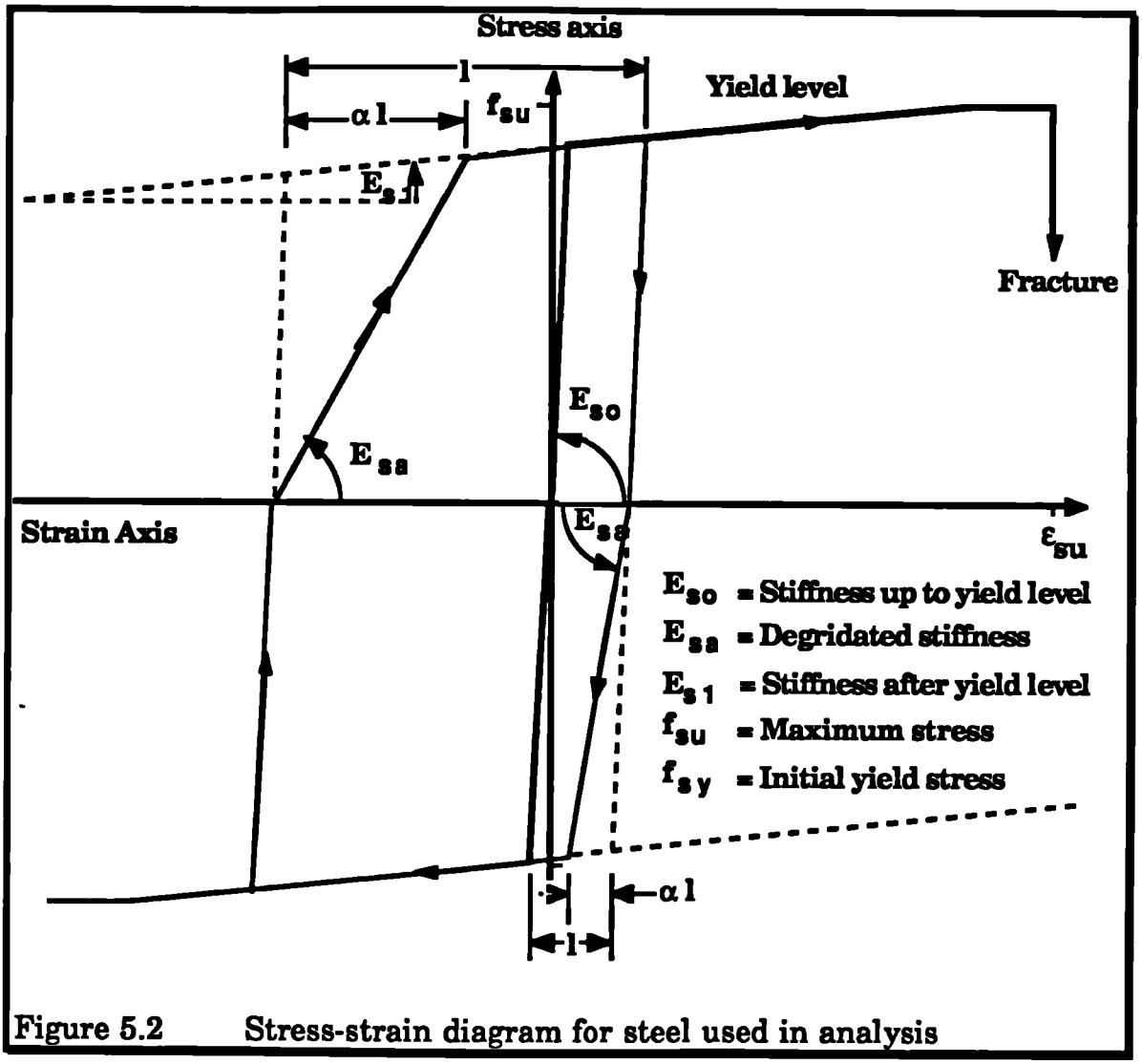


Figure 5.2 Stress-strain diagram for steel used in analysis

The above simple model was developed by using the massing model (Hays, 1981) in a slightly modified form and the stiffness degradation factor 'α' from the work of Santhanam (1979). However, the latter reference used mild steel and as a result the monotonic model includes a yield plateau prior to the onset of strain hardening. This plateau was observed in some of the tests on steel described in chapter 3, but not in all. Consequently, this plateau was removed from the present model for all bar diameters for the sake of simplicity. This implies that the need of the yield growth factor 'β' used by Santhanam to increase the yield stress on reloading above the yield

reloading above the yield plateau level, as shown in figure 5.3, is eliminated. Based on the experimental work of Popov and Peterson (1978) on steel tubes subjected to torsional loading, the range of 0.15 - 0.3 for the value of 'α' has been proposed. The stiffness degradation model proposed by Clough (1966), made use of a degraded stiffness equivalent to a value of 'α' of unity. In the absence of cyclic data for the steels used in the experiments, the value of 'α' is obtained herein by making use of the actual experimental data.

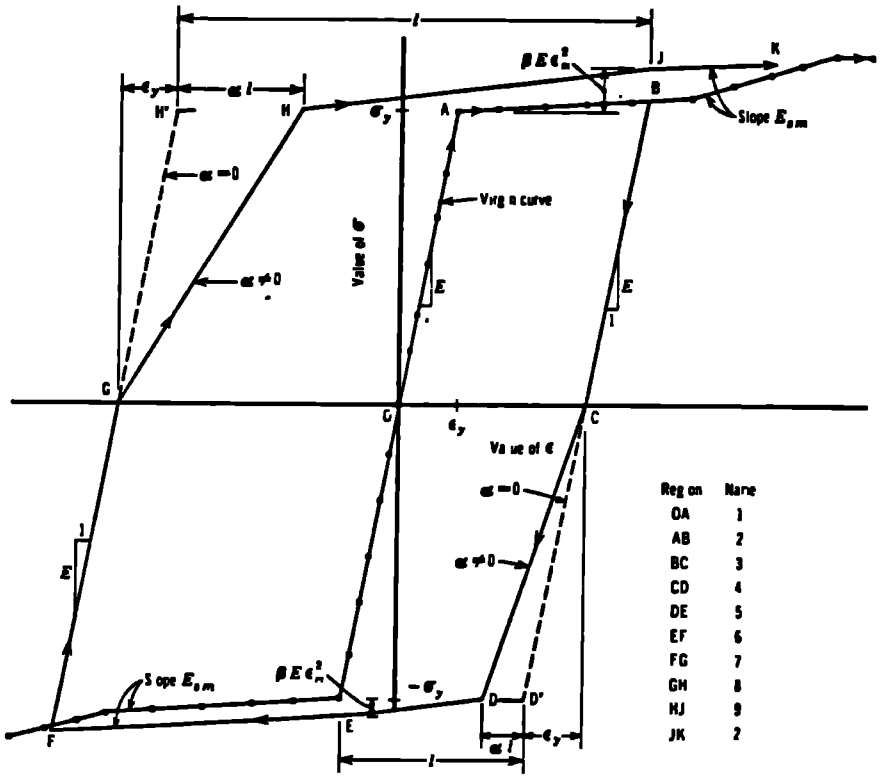


Figure 5.3 Santhanam's α–β model for the uniaxial inelastic behaviour of mild steel

The implementation of the steel model in a computer program is simple and only the current and previous maximum and minimum

5.3.2 Concrete model

The concrete model used is based on the work of Mander et al (Mander J.B, Priestley J.N. & Park R. 1988 a & b). It was chosen for its direct applicability to the method of sections and was implemented with some modifications. The model though uniaxial in it's formulation, takes into account the confining stresses.

5.3.2.1 Concrete confinement

Experimental work on confinement of concrete has been carried out by many researchers and there is a large number of biaxial and triaxial concrete models. However, in most of these experiments active confining stress was applied as a uniform hydraulic pressure. The effect of steel reinforcement in providing passive confinement has long been recognised and several models have been presented based on RC column experiments. A description of early work is given by Vallenas, Bertero and Popov (1977). Their own experiments were conducted on rectangular RC columns despite the fact that the objective was to obtain a model that would be used in the research work on RC walls. Their model is shown in figure 5.4 below and contains the basic features of models to follow, such as an increased strain for the increased maximum stress and extended unloading branch to an ultimate strain.

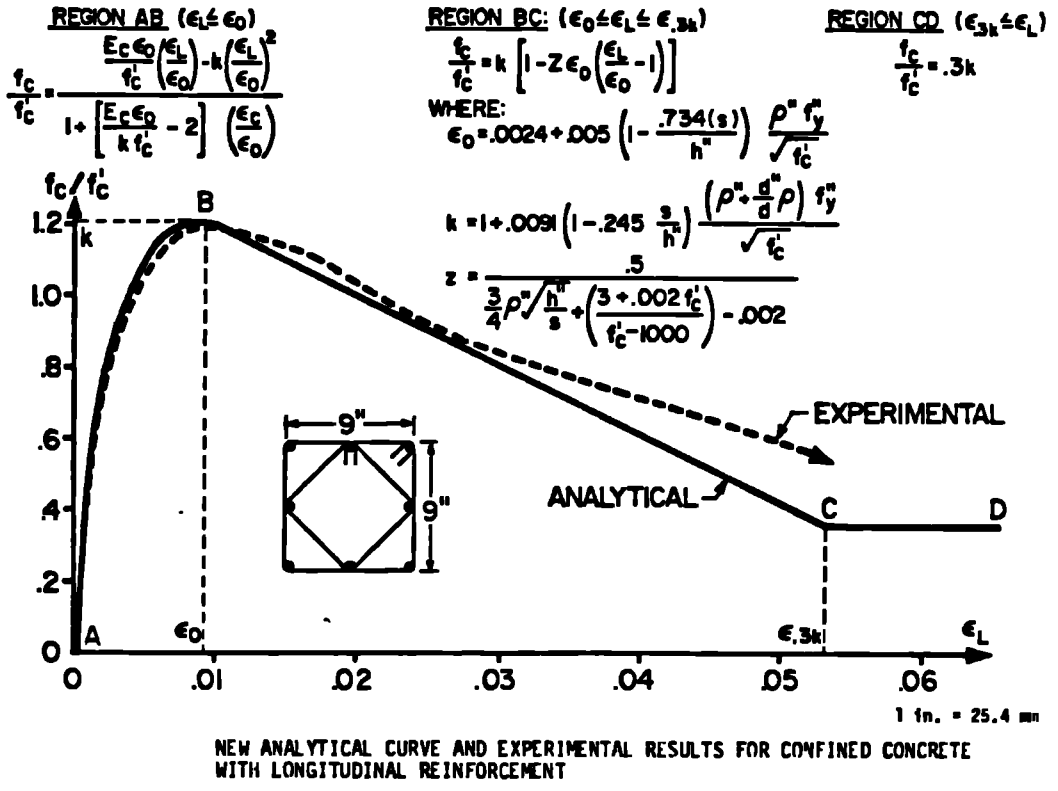


Figure 5.4 Analytical model and experimental results for confined concrete by Vallenas, Bertero and Popov (1977)

Sheikh and Uzumeri (1980) conducted experiments at the University of Toronto and developed a model (Sheikh and Uzumeri, 1982) which placed particular emphasis on the effect of the rectilinear reinforcement, as shown in figure 5.5 below.

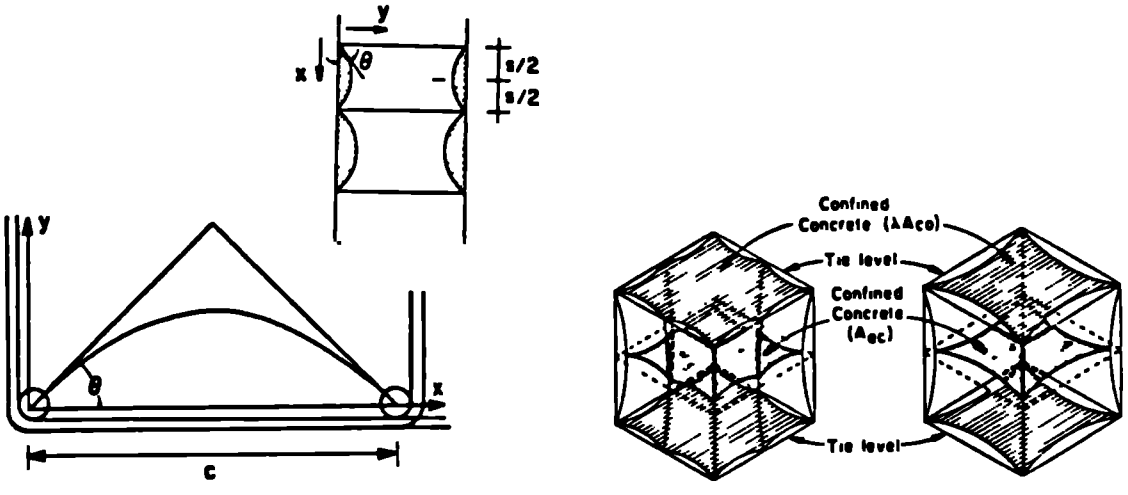


Figure 5.5 Effectively confined concrete area (Sheikh and Uzumeri, 1982)

Mander et al placed equal emphasis on the effect of confinement and proposed a confinement model similar to Sheikh and Uzumeri. The objective of a confinement model is to estimate an equivalent effective stress due to the maximum confining steel force at the least confined section of the column. The area of the least confined section can be calculated provided an assumed confinement profile is used. At ultimate conditions the unconfined area is expected to spall off, and hence the increased capacity is counter-balanced by the reduction in cross section. Consequently, two discrete areas are considered, namely confined and unconfined areas.

Despite the elaborate calculations and assumptions of the existing confinement models, several points of concern remain for RC walls under cyclic loading, as discussed below :

a) The compressed area of walls under bending is loaded by a varying strain through the section and not constant as in columns.

b) The variation of the confining stress along the height is not taken into account.

c) The confinement force of the steel is not related to the normal stress and material properties of the concrete.

d) The initial prestress of the reinforcement due to shrinkage is not accounted for.

e) The effect on the stiffness of the confined elements is not easy to evaluate.

f) The models and the experiments on which they are based are monotonic with either active or passive uniform confining pressure.

As shown in figure 5.6, the development of the lateral force in the steel depends on the elastic properties of concrete as well as the axial strain. It would be expected that initial shrinkage of concrete would leave some initial prestress in the steel reinforcement. The exact initial value of this compressive strain is difficult to estimate but it is not expected to be large and as a result it will only reduce the effect of confinement only at the early stages of loading.

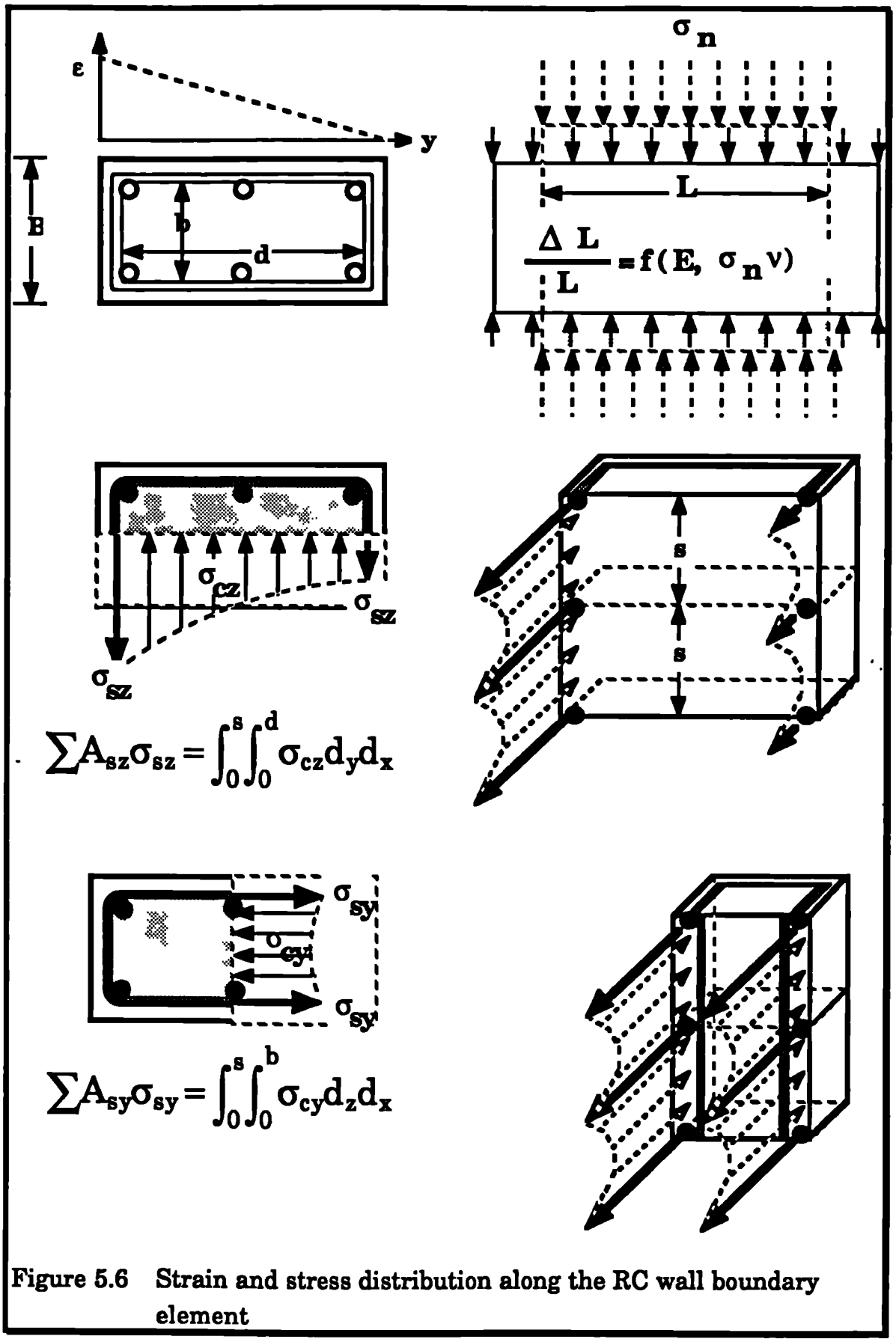


Figure 5.6 Strain and stress distribution along the RC wall boundary element

As a first estimate, the lateral strains 'ε_y' and 'ε_z' and stress 'σ_s' can be calculated from elasticity as the product of normal strain 'ε_x' and Poisson's ratio 'ν'.

$$\varepsilon_y = \varepsilon_z = \nu \varepsilon_x \qquad (5.7 \& 5.8)$$

$$\sigma_s = \nu \varepsilon_x E_{so} \qquad (5.9)$$

The resulting forces 'F_{sy}' and 'F_{sz}' due to the confinement are given by:

$$F_{sy} = A_{sy} \sigma_{sy} = A_{sy} \nu \varepsilon_x E_{so} \qquad (5.10 \& 5.11)$$

$$F_{sz} = A_{sz} \sigma_{sz} = A_{sz} \nu \varepsilon_x E_{so} \qquad (5.12 \& 5.13)$$

This force spreads into the concrete and consequently, the confining stress will decrease. This effect was not considered by many of the previous researchers even though it is likely to have a similar or larger impact than the reduction of the confined area at the critical sections.

For the purposes of section analysis the average values of concrete confinement stresses (σ_{cy}, σ_{cz}) are required between sections so that the stiffness and deformations are estimated correctly.

$$\sigma_{cy} = \kappa_e A_{sy} \nu \varepsilon_x E_{so} / (b\ s) \qquad (5.14)$$

$$\sigma_{cz} = \kappa_e A_{sz} \nu \varepsilon_x E_{so} / (d\ s) \qquad (5.15)$$

For elastic sections where the confinement steel is distributed evenly and linear distribution of strain prevails, the value of confinement effectiveness 'κ_e' is equal to 0.5. For the critical section, 'κ_e' should take into account not only the variation of the effectively confined area but also the variation of the confining stress along the section.

In order to avoid the elaborate calculations proposed by many researchers for evaluating the confinement factors, the effectiveness of the confinement is provided to the section analysis program as an input. Simple calculations to account for the hoop pattern and spacing in square columns are given by Tassios (1989) in a background document to EC8 (1988).

Experimental work on triaxial compressive properties of concrete is conducted with equal confining lateral pressures and hence, it is convenient to use a single value for the confining stress 'fl'. The value of 'fl' is calculated by using the confining stresses σ_{cy} and σ_{cz} as shown in figure 5.7 below. An alternative simple equation is used in the program proportional to $(\sqrt{\sigma_{cy}} + \sqrt{\sigma_{cx}})^2$.

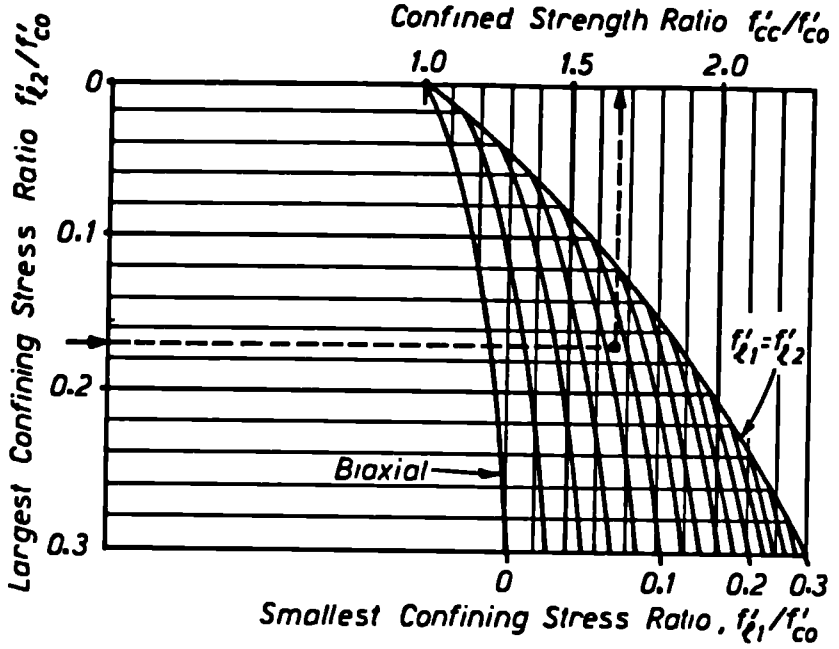


Figure 5.7 Confined strength determination from lateral confining stresses for rectangular sections (Mander et al, 1988a)

Mander et al (1988 a) used equation 5.16 for the confined compressive concrete strength 'f_{cc}' (f_{co} is the unconfined concrete compressive cylinder strength). This is based on the failure surface model of Willam and Warnke (1975), the experimental results of Schickert and Winker (1979) and was implemented by Elwi and Murray (1979).

$$f_{cc} = f_{co}\left(-1.254 + 2.254\sqrt{1 + \frac{7.94\, f_l}{f_{co}}} - 2\frac{f_l}{f_{co}}\right) \qquad (5.16)$$

From the formulation of the solution providing variable confinement it can be seen that the level of confinement is dependent on the axial strain 'ε_x' and the Poison's ratio 'v' (equations 5.14 and 5.15). Furthermore, all confinement models assume that the maximum axial strain is a function of the maximum confinement stress as defined by the yield of the hoop reinforcement (equation 5.16 and 5.20 or equation 5.17). This is best

illustrated by considering the simplified equation 2.6 for confinement given in Appendix A of EC8 (1988), where 'ω_{wd}' is the volumetric mechanical ratio of hoops and 'α' is a coefficient depending on the hoop steel configuration.

$$\varepsilon_{cu} = 0.0035 + 0.10\ \omega_{wd}\ \alpha = \varepsilon_x \qquad (5.17)$$

Substituting in 5.14 (assuming equal lateral reinforcement in y and z directions) gives the maximum expected hoop stress σ_{max}.

$$\sigma_{max} = (0.0035 + 0.10\ \omega_{wd}\ \alpha)\ \kappa_e\ A_{sy}\ \nu\ E_{so} / (b\ s) \qquad (5.18)$$

If it is accepted that the value of ν will be about 0.5 at failure, equation 5.18 shows that for a given amount and distribution of confinement reinforcement, a certain level of stress will be induced at ultimate conditions. If the stress in the hoop is not to exceed the yield level, then for a given type of reinforcement, a certain critical volumetric mechanical hoop ratio ω_{wcrit} exists, over which further enhancement of the axial strain and stress is not possible. In fact, it appears that the level of confinement is dependent on the hoop yield strain as well as on the volumetric ratio. This has not been reported in the literature. Hence, the lateral strain is assumed to vary with the axial strain in such a way that they will both reach the maximum values simultaneously, whilst initially they are related to the initial value of the Poisson's ratio. This assumption will give accurate results at low levels of axial loads as well as at the ultimate conditions, but further research is required to determine the accuracy intermediately.

5.3.2.2 Monotonic concrete model

For a uniform confining stress, the monotonic confined compressive stress-strain curve is as shown in figure 5.8 and is given by:

$$f_c = \frac{f_{cc}\ x\ r}{r - 1 + x^r} \qquad (5.19)$$

where

$$x = \frac{\varepsilon_c}{\varepsilon_{cc}} \qquad (5.20)$$

$$\varepsilon_{cc} = \varepsilon_{co}\left[1 + 5\left(\frac{f_{cc}}{f_{co}} - 1\right)\right] \tag{5.21}$$

$$r = \frac{E_c}{E_c - E_{sec}} \tag{5.22}$$

$$E_c = 5{,}000\sqrt{f_{co}} \text{ (MPa)} \tag{5.23}$$

$$E_{sec} = \frac{f_{cc}}{\varepsilon_{cc}} \tag{5.24}$$

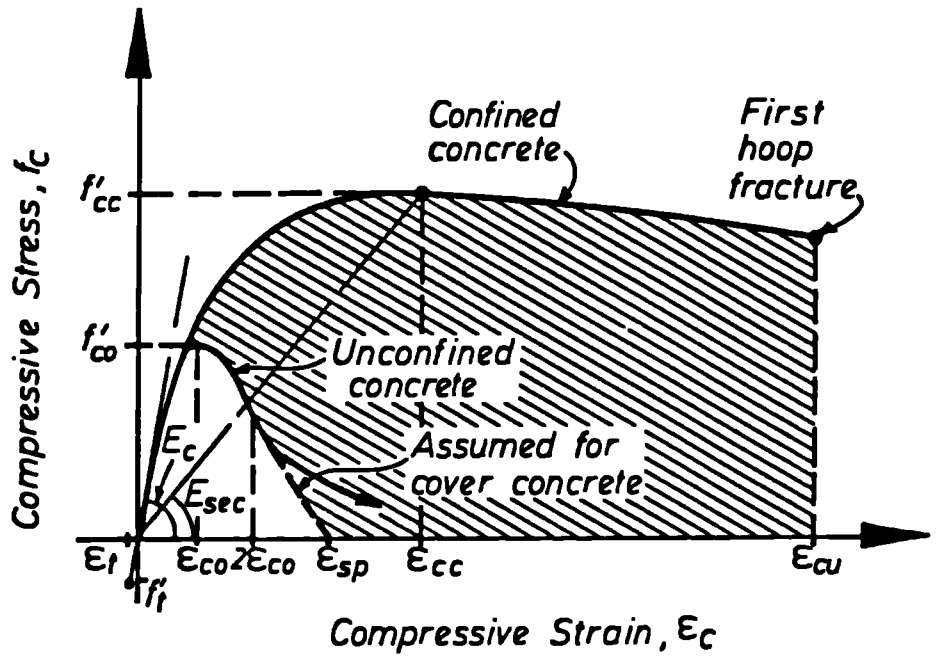


Figure 5.8 Stress strain model for monotonic loading; unconfined and confined concrete

For the unconfined areas, such as the cover and the web area of RC walls, the falling branch after twice 'ε_{co}' (concrete compressive strain in the longitudinal direction at peak unconfined stress) is defined as a straight line which reaches zero stress at the strain of 'ε_{sp}'. In the computer program, concrete was considered to crush instantaneously, and hence, there is no unloading branch.

For monotonic tensile loading, concrete can carry tensile stresses up to a limit of 'f_t' with stiffness equivalent to the tangent modulus of elasticity 'E_c'. The tensile strength may be affected by micro-cracking initially, and

will be lost at the initial stages of cyclic loading. Therefore, in the implementation of the above model the tensile strength has been ignored.

5.3.2.3 Concrete model for cyclic loading

It is generally accepted that the monotonic stress-strain curve can be considered to be the envelope to the cyclic loading response. To describe a cyclic model, the unloading and reloading branches should be defined as follows.

5.3.2.3.1 Unloading regime

On complete unloading, the stress drops to zero at a plastic strain 'ε_{pl}'. The value of the plastic strain depends on the previous maximum reversal point (ε_{un}, f_{un}) and strain 'ε_a' as shown in figure 5.9. For strains less than 'ε_{pl}', the stress is considered to be zero.

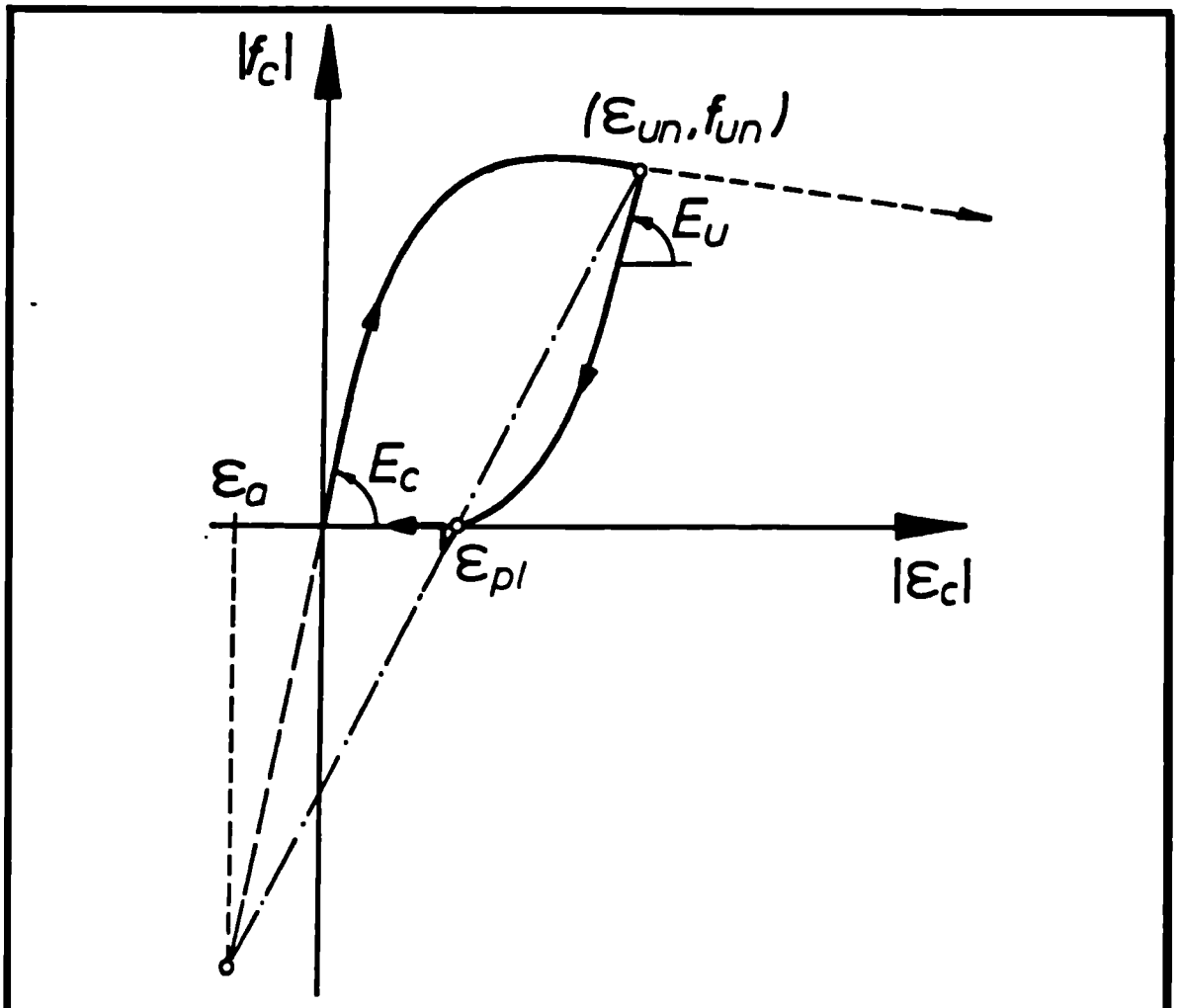


Figure 5.9 Determination of plastic strain ε_{pl} and the unloading branch of the cyclic stress-strain curve for concrete

The strain 'ε_a' is given as :

$$\varepsilon_\alpha = a\sqrt{\varepsilon_{un}\,\varepsilon_{cc}} \tag{5.25}$$

Where, in order to suit the confinement model, the value of 'α' is the greatest of the two values given in equation 5.26.

$$\alpha \geq \left\{ \frac{\varepsilon_{cc}}{\varepsilon_{cc}+\varepsilon_{un}} \text{ or } \frac{0.09\,\varepsilon_{un}}{\varepsilon_{cc}} \right\} \tag{5.26}$$

Strain 'ε_a' is used to define a pivot point in the stress-strain space by using the initial tangent modulus which in turn is used to obtain the plastic unloading secant slope. The plastic strain lies at the intersection of the line through the return point (ε_{un}, f_{un}) and pivot point, with the zero stress line and is given by:

$$\varepsilon_{pl} = \varepsilon_{un} - \frac{(\varepsilon_{un}+\varepsilon_\alpha)\,f_{un}}{(f_{un}+E_c\,\varepsilon_\alpha)} \tag{5.27}$$

The unloading path is of similar form to the monotonic loading of equation 5.19 as shown in figure 5.8, but is modified to pass through the point (0, ε_{pl}), as shown in figure 5.9 and below:

$$f_c = f_{un} - \frac{f_{un}\ x\ r}{r-1+x^r} \tag{5.28}$$

where

$$r = \frac{E_u}{E_u - E_{sec}} \tag{5.29}$$

$$E_{sec} = \frac{f_{un}}{\varepsilon_{un}-\varepsilon_{pl}} \tag{5.30}$$

$$x = \frac{\varepsilon_c - \varepsilon_{un}}{\varepsilon_{pl}-\varepsilon_{un}} \tag{5.31}$$

$$E_u = bcE_c \tag{5.32}$$

The value of the initial unloading modulus of elasticity 'E_u' has been calibrated by Mander, Priestly and Park (1984) on experimental results with the following parameters:

$$b = \frac{f_{un}}{f_{co}} \geq 1 \tag{5.33}$$

$$c = \left(\frac{\varepsilon_{cc}}{\varepsilon_{un}}\right)^{0.5} \leq 1 \tag{5.34}$$

5.3.2.3.2 Reloading regime

Reloading can occur from different previous unloading history cases and hence the different possibilities ought to be examined.

a) Reloading from a strain less than ε_{pl}.

b) Reloading from a strain 'ε_{ro}' and stress 'f_{ro}' where 'ε_{ro}' is less than 'ε_{un}' and greater than 'ε_{pl}'.

c) Reloading to a strain higher than 'ε_{un}'.

d) Reloading to a strain higher than 'ε_{re}'.

For case (a) the stress remains zero until ε_{pl} is exceeded and then the case (b) is used to obtain the stresses. A linear stress strain relation is assumed between the return point (ε_{ro},f_{ro}) and a new target point (ε_{un},f_{new}) which accounts for the cyclic degradation in strength as shown in figure 5.10 and the following equations:

$$f_c = f_{ro} + E_r\,(\varepsilon_c - \varepsilon_{ro}) \tag{5.35}$$

$$f_{new} = 0.92\, f_{un} + 0.08\, f_{ro} \tag{5.36}$$

where

$$E_r = \frac{f_{ro} - f_{new}}{\varepsilon_{ro} - \varepsilon_{un}} \tag{5.37}$$

For a strain exceeding 'ε_{un}' and up to 'ε_{re}', Mander et al (1988a) suggested a parabolic transition curve between the target point (ε_{un},f_{new}) and a common return point (ε_{re},f_{re}) as shown in equation 5.38.

$$\varepsilon_{re} = \varepsilon_{un} + \frac{f_{un} - f_{new}}{E_r\left(2 + \frac{f_{cc}}{f_{co}}\right)} \qquad (5.38)$$

The value of 'ε_{re}' as obtained from this equation is found by using a stiffness higher than the reloading linear branch E_r,since the value of $(2+f_{cc}/f_{co})$ in the denominator is at least three. This does not conform with observations from a number of cyclic experiments conducted on the control cylinders and probably that was not the intention of the authors of the paper. For the purposes of this work the value of 'ε_{re}' was obtained by dividing 'E_r' by the parenthesis value (instead of multiplying it) and a modified parabolic transition curve has been derived on the same principles. To derive this second order equation, the three boundary conditions used were the two end points (ε_{un},f_{new}) & (ε_{re},f_{re}) and the gradient at the first point being E_r. The modified transition curve is given by:

$$f_c = f_{re} + E_{re}\, x + A\, x^2 \qquad (5.39)$$

where

$$x = (\varepsilon_c - \varepsilon_{re}) \qquad (5.40)$$

$$A = \frac{(f_{new} - f_{re}) - E_{re}\,(\varepsilon_{un} - \varepsilon_{re})}{(\varepsilon_{un} - \varepsilon_{re})^2} \qquad (5.41)$$

For strains higher than 'ε_{re}' reloading continues on the monotonic curve as shown is figure 5.10.

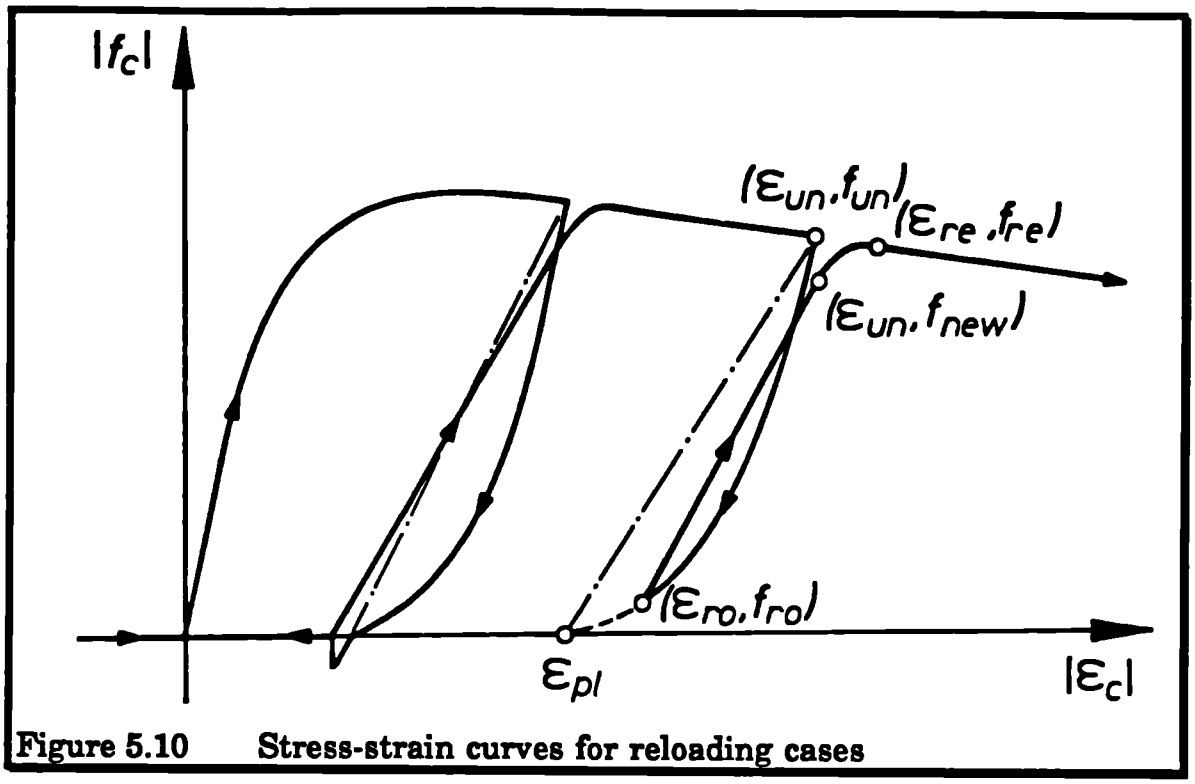


Figure 5.10 Stress-strain curves for reloading cases

5.3.3 Ultimate compression strain

The ultimate compression strain for confined concrete is necessary as to define the failure of a certain section provided some other type of failure has not taken place. A number of empirical equations are available in literature for this, the most comprehensive of which link concrete failure to the hoop reinforcement fracture. Mander et al (1984) progressed further and proposed an energy balance approach. According to this method, the extra energy per unit volume of concrete core available under the confined stress-strain curve for concrete (Ucc - Uco) *'plus additional energy required to maintain yield in the longitudinal reinforcement in compression'* 'U_{sc}', is equivalent to the energy stored in the transverse reinforcement 'U_{sh}' as shown below:

$$U_{sh} = U_{cc} - U_{co} + U_{sc} \qquad (5.41)$$

The contribution of the transverse reinforcement to the increase in energy capacity of confined concrete is well-established. Additionally, the strain energy due to secondary bending 'U_{sb}' of the longitudinal

reinforcement can have a similar effect as the transverse reinforcement, but has been ignored. Moreover, the strain energy due to longitudinal reinforcement should not be included in the energy balance of confined concrete, since for a given strain this energy is present irrespective of the state of confinement , and is also not included when deriving the stress-strain curves for confined concrete. Hence, a proposed modified energy balance equation becomes :

$$U_{sh} + U_{sb} = U_{cc} - U_{co} \qquad (5.42)$$

The above equation is equivalent to considering that all additional energy in confined concrete is equivalent to the steel strain energy build up in confining the concrete laterally. The solution of the above equation is beyond the scope of the current thesis. However, it is considered that the critical importance in solving the above equation is the exact determination of the lateral strains in the longitudinal reinforcement.

5.3.4 Dynamic effects

Both the strength and stiffness of confined and unconfined concrete have been observed to increase with the increase in strain-rate. Mander et al (1984) proposed that the quasi-static stress-strain relationships can be used to describe the behaviour of the problem under high strain rates by modifying only the main material control parameters. This approach provides the necessary simplicity and versatility that is necessary for the method of section analysis. A number of equations have been calibrated to experimental results by Mander et al (1984) representing:

a) Dynamic strength f_{co}

b) Dynamic stiffness E_c

c) Dynamic strain at peak stress ε_{co}

5.4 Computer program CRELIC

The computer program CRELIC (Cyclic REinforced concrete anaLysis Imperial College) developed on the basis of section analysis and material models described in earlier sections was implemented on the Microvax computer of the ESEE section in Fortran 77. The solution procedure is outlined by the flow chart in figure 5.11.

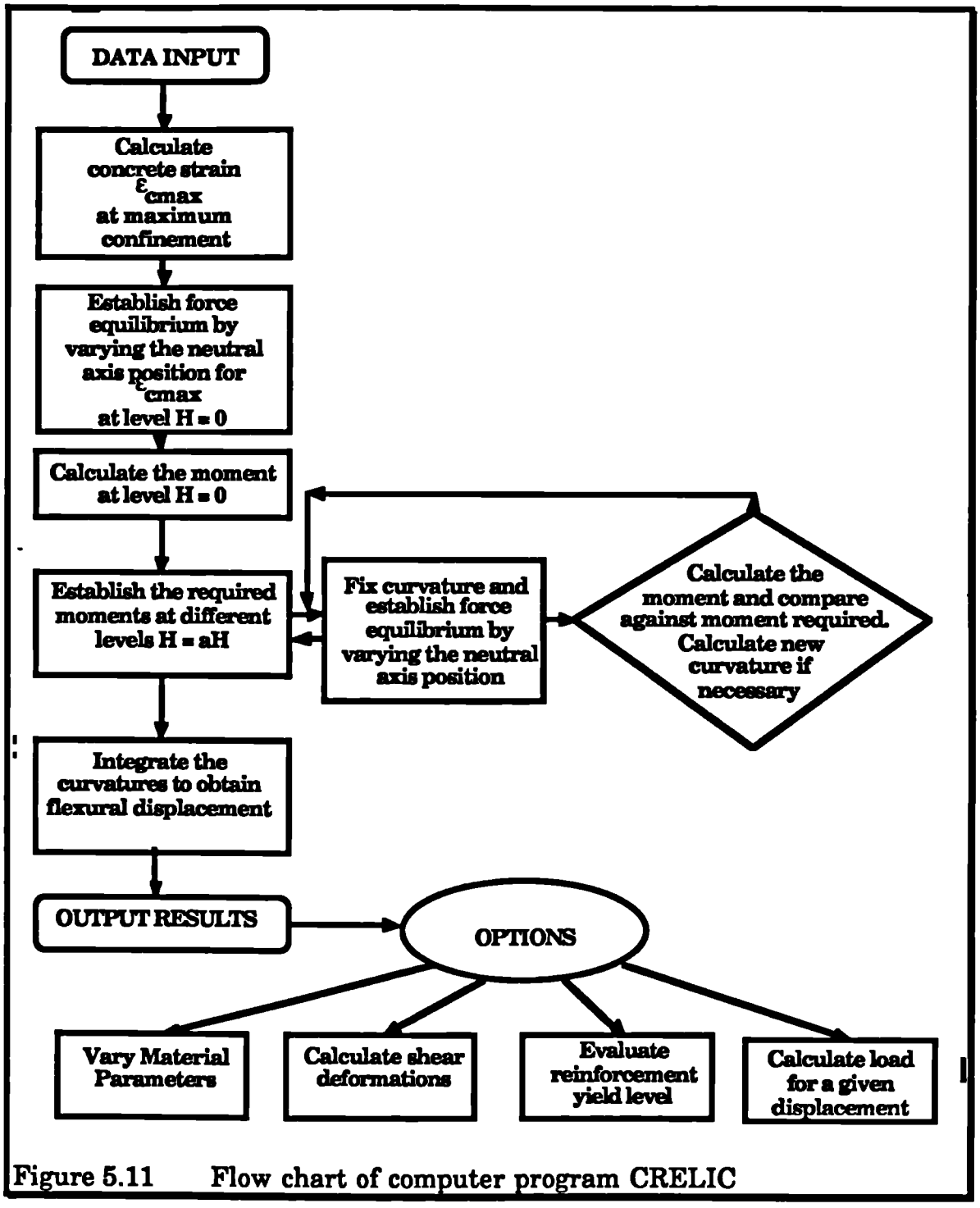


Figure 5.11 Flow chart of computer program CRELIC

Data input include information on the geometry, loading, material characteristics, and confinement. Control data are also required, to indicate desired accuracy for the different iterations. The analysis can be performed as a remote operation or interactively.

After reading the data input, the program calculates automatically the displacement corresponding to the maximum confined strain in concrete. Following that, control is returned to the user through various options. For cyclic loading, the displacement control option allows for following the hysteretic behaviour of the member at prescribed displacements or automatic cycling.

5.4.1 A test run for wall SW9

The program was checked by using SW9 as a test case. The experimental flexural deformations, obtained by the improved method suggested in Chapter 3, were imposed at the top of the wall. Only a small portion of the output information is possible to be presented here in graphical form, and is included in Appendix B. Results for key locations selected for output are shown in figure 5.12 below.

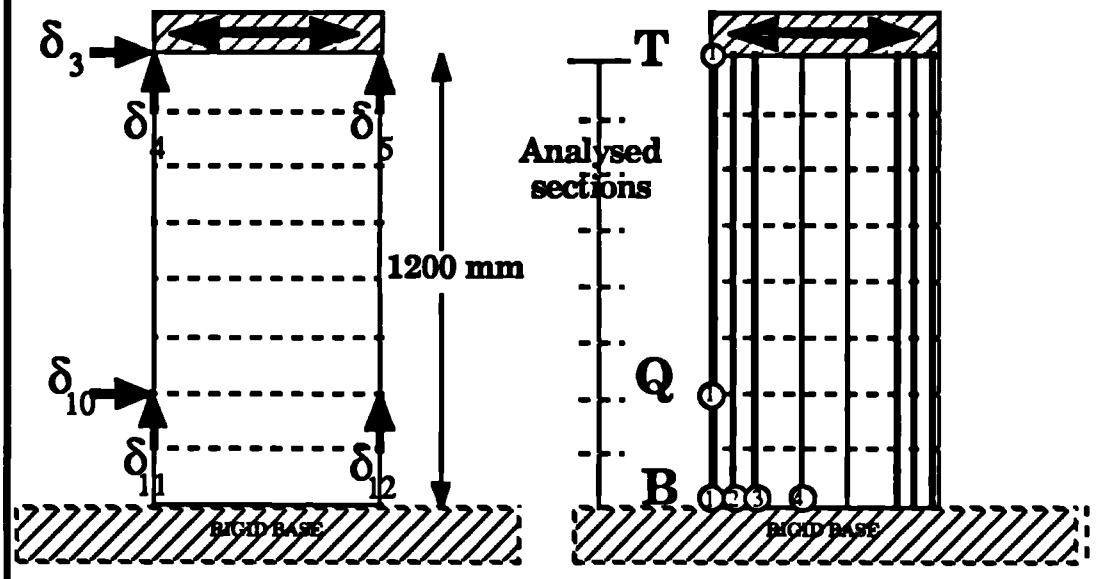


Figure 5.12 Positions of data presented from program CRELIC

The top horizontal flexural displacement δ3, the vertical displacement δ4 and the top average displacement are shown in figures B1 -

B3, while the corresponding displacements at quarter height are shown in figures B4 - B6. Strains at the locations shown are presented in figures B7 - B12.

5.4.2 Discussion of program results

The load versus flexural displacements δ3 compare well with the experimental data. A slightly higher load is achieved in the analytical results. This may be attributed to the simplification of the post-yield steel behaviour in the analytical model. The relaxation at peak displacement, observed in the experimental results is not seen in the analytical results since this effect has not been modelled. The reloading stiffness is reproduced accurately, and this indicates that the used value of 0.5 for the steel stiffness degradation factor 'α' is reasonable. Lower values of 'α' gave higher initial reloading stiffness and more energy dissipation as shown in figures 5.13 and 5.14. The energy dissipation from the analytical results at 'α' equal 0.5, is still higher than the one from the flexure experimental curves. This is mostly due to the higher strength and no relaxation effects in the analytical model. It is however, less than the overall energy dissipated by the experimental model.

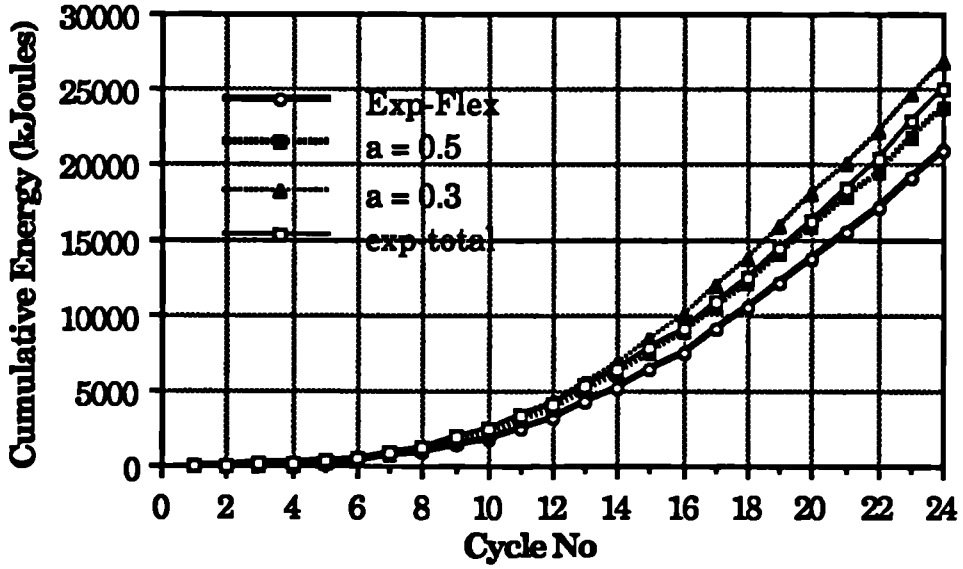


Figure 5.13 Cumulative energy dissipated versus MDL

Of particular interest is the difference exhibited by the hysteretic energy per cycle in the early loops as shown in figure 5.14. The analytical

results indicate much less hysteretic energy being absorbed, probably due to the absence of tensile strength in the concrete model used.

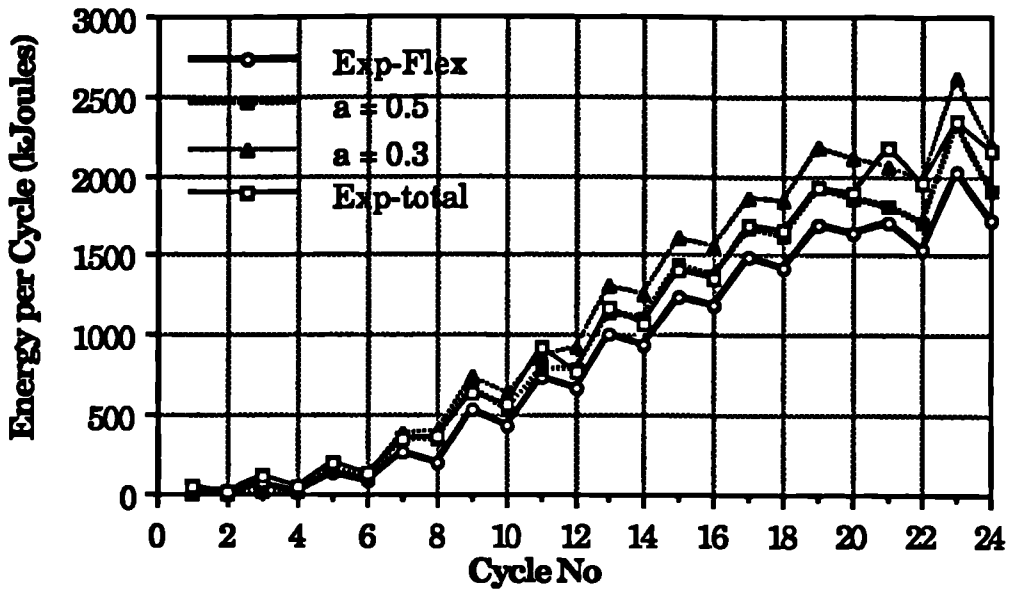


Figure 5.14 Energy dissipated per cycle

The load versus top vertical displacement δ4 (figure B2) plot demonstrates that a significant difference exists between the analysis and experiments in the compression displacements. Whilst, experimentally the compressive loads do not completely reverse the tensile plastic displacements, in analysis compressive displacements are always recovered even after yield. The same effect is observed in strains of the extreme fibre reinforcement (B.7), whilst for bars located further inside the wall section (B.8 to B.10), the reversal of tensile strains is still much less than in the experiments. The net wall extension, however, seems to be less affected by this effect. A difference worth noting in the wall extensions (B.3) is that in the analytical results, the minimum extension for a particular cycle after significant inelasticity occurs on reloading at a much higher load than in the experiments.

All the above observations may be a result of concrete dilation at crack interfaces. Due to shear deformations, the opposing crack surfaces do not match on closure and due to their roughness, contact is established even when tensile strains in the reinforcement are still observed. This mechanism, termed 'aggregate interlock', is considered to be responsible for shear transfer through cracks as a consequence of the co-existent normal stresses. Tassios and Vintzeleou (1987) demonstrated

experimentally the shear transfer mechanism and concrete dilatancy of cracked surfaces during cycling for low constant normal stresses. Dilatancy degradation was also noted to occur during cycling and *'formalistic'* models were proposed for different crack roughness surfaces.

An attempt to evaluate the dilatancy effects on the concrete stress-strain cyclic relationship has been made by Zhu, Wu and Zhang (1980) who proposed an empirical model based on a limited number of experimental results. Unfortunately, as with many other shear stiffness formulations, explicit use is made of a crack width, something which can not be calculated directly by the method of sections.

The strains at the extreme fibre at quarter height (B.11) were predicted accurately by the analytical model. A tensile shift of the strains in the experiment is attributed to the initiation of cracking and the resulting dilatancy.

The strains at the extreme fibre at the top of the wall (B.12) are predicted to be slightly higher than the average of the experimental data. This may indicate that total loss of the tensile strength does not occur so close to the point of zero moment. In fact, the initiation of cracking is clearly identifiable in the experimental results. This occurs during the increase of the load over the yield value with a distinct deviation from the nearly elastic uncracked behaviour to the cracked behaviour.

The results from the flexural analytical model seem to reproduce accurately the strength state of the cyclic model, and reasonably accurately the general behaviour of reinforced concrete walls subjected to cyclic loading. The flexural model is utilised further in chapter 6, to investigate a wide range of parameters which is beyond the scope of the experimental investigation undertaken in the course of this project. The model is also utilised for further comparisons with the experimental results in the general discussion of the results.

5.5 Shear model

Elastic shear stresses can be calculated by making use of the virtual work method. For a unit element shown in figure 5.15 these can be

calculated as the integral of the product of shear strains and a virtual shear force at the level of desired shear deformations given by:

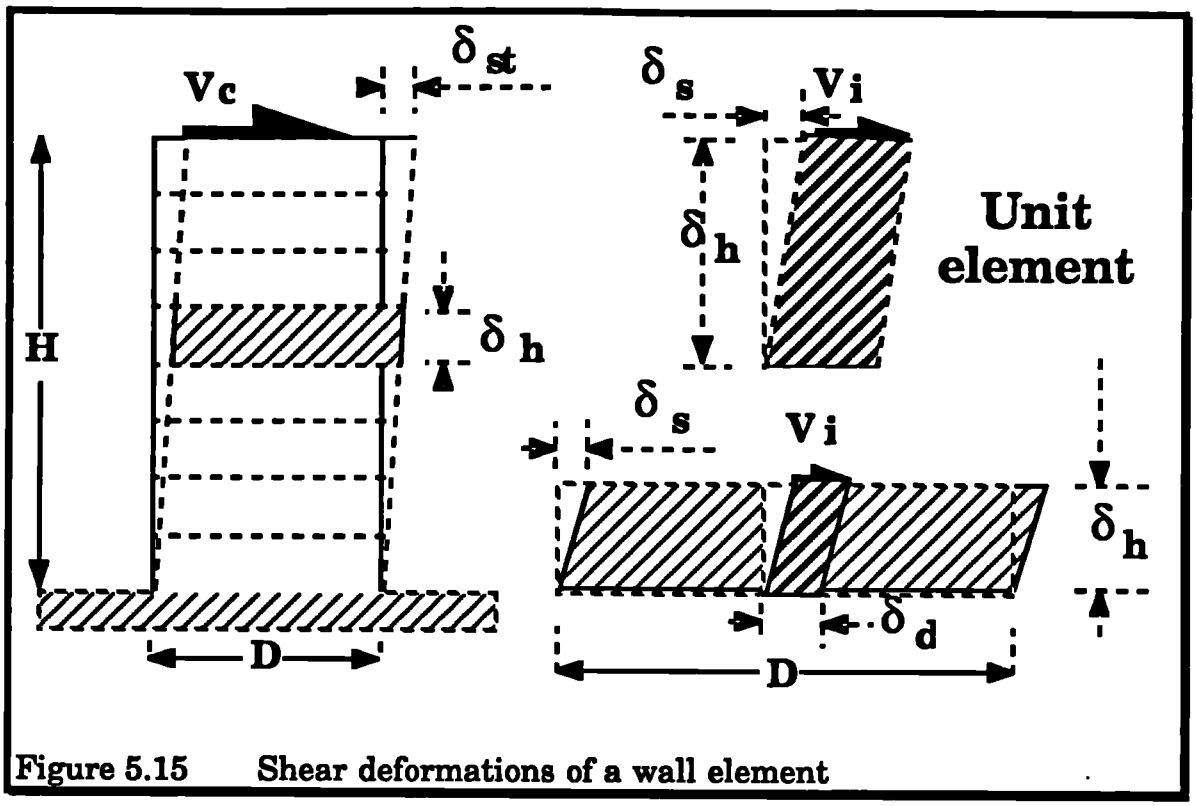


Figure 5.15 Shear deformations of a wall element

$$\delta_s = \int_0^{\delta_h} V_o \gamma \, dx \tag{5.43}$$

where

$$\gamma = \frac{V_i}{\beta G A} \tag{5.44}$$

For a rectangular section, 'β' is about 5/6. Equations 5.43 and 5.44 show that the elastic shear strain rate of change 'γ' is independent of the normal stresses since 'G', the modulus of rigidity (or modulus of elasticity in shear), is as shown below:

$$G = \frac{E}{2(1+\nu)} \tag{5.45}$$

Nevertheless, the stiffness of concrete is neither linear nor elastic and a nonlinear value of shear modulus 'G_{NL}' is assumed. The total shear deformation can be integrated from the deformations of the slice elements 'δ_s' as shown in the equation below.

$$\delta_s = \frac{V_i \, \delta_h}{\frac{5}{6} G_{NL} \, B \, \delta_d} \tag{5.46}$$

Within a section of height 'δ_h', 'δ_s' is constant, and the sum of 'V_i' should be equal to 'V_c' as shown below.

$$V_c = \sum_{d=0}^{D} V_i = \frac{5}{6} \frac{B \, \delta_s}{\delta_h} \sum_{d=0}^{D} G_{NL}(d) \, \delta_d \tag{5.47}$$

This implies that 'δ_s' can be calculated as a function of '$G_{NL}(d)$' as below:

$$\delta_s = \frac{V_c \, \delta_h \frac{6}{5B}}{\sum_{i=0}^{D} G_{NL}(d) \, \delta_d} \tag{5.48}$$

The total deformation can be calculated by summing the sectional deformations over the height. By assuming constant 'δ_D' and 'δ_H', 'δ_{st}' becomes:

$$\delta_{st} = \frac{6 \, V_c \, H}{5 \, A} \sum_{h=0}^{H} \frac{1}{\sum_{d=0}^{D} G_{NL}(h,d)} \tag{5.49}$$

The above formulation requires the determination of 'G_{NL}'. Since the modulus of rigidity is depended on the normal stiffness, it follows that nonlinear shear stiffness is a function of the flexural stiffness. A reasonable assumption is to consider the secant stiffness of concrete as 'E' in equation (5.45).

There are, however, a number of difficulties arising from the above assumption. The first one is associated with the shear stiffness of the reinforcing bars. In the absence of concrete, due to its slenderness, the steel cage is capable of resisting a very low level of shear force because of bending deformations. In reinforced concrete, the amount of shear resistance by the steel is expected to increase as a result of the different deformed shape. In

order to simplify the problem, in the current study, the steel shear stiffness is considered to be identical to the concrete stiffness.

The second difficulty arises from the formulation of the flexural model. As expected from the flexural cyclic results, the concrete section will have a tangent stiffness of zero below the value of 'ε_{pl}'. As a result, the shear displacements will be infinite. However, in practice, due to contact effects, reinforcement and aggregate interlock, there is always a degree of shear stiffness even for an open crack.

A possible solution to the above problem is to give 'G_{NL}' as a distinct function of normal strain. Such approach is used extensively in finite element analysis. Figure 5.16. below (ASCE, 1982) shows diagrammatically a number of such models.

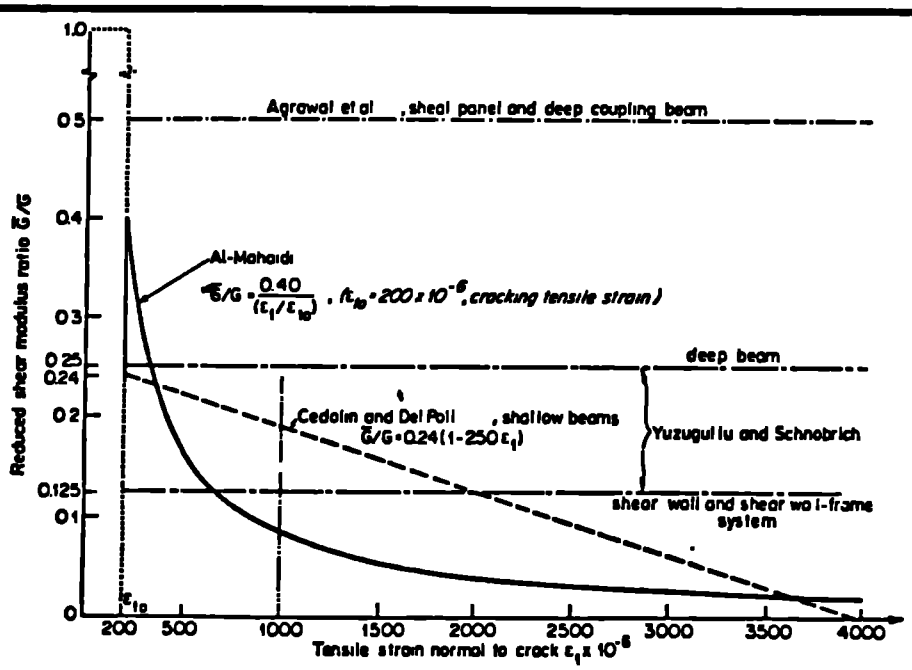


Figure 5.16 Reduced shear modulus versus tensile normal strain (ASCE, 1982)

The equation given by Al-Mahaidi (ASCE, 1982), was used for the range of strains shown in figure 5.16. In the range of strains not covered by the above-mentioned model, the secant stiffness as obtained from the flexural model was used, with a value of G not less than 0.4 times the elastic value.

The third difficulty associated with equation 5.48 is that the shear deformation is zero at zero values of shear force. This cannot be the case, especially if there are permanent or plastic shear deformations. Such

deformations are expected to develop when the concrete stresses are zero or very low, mostly during reloading. The above difficulty can be overcome within a model utilising an incremental approach, as shown in equation 5.49.

$$\Delta(\delta_{st}) = \frac{6\,\Delta(V_c)\,H}{5\,A}\,\Delta\left(\sum_{h=0}^{H}\frac{1}{\sum_{d=0}^{D} G_{NL}(h,d)}\right) \qquad (5.49)$$

The described model was implemented in a subroutine of CRELIC, and was tested by using SW9 as a test case. The results are shown in figures B.13 and B.14. The level of shear deformations obtained are slightly less than the experimental results shown in figures A.(9).19 and A.(9).20. Moreover, the reloading part of the force displacement curve is in general stiffer than for the experimental curve and continues up to higher levels of load. Similarly, the curve of shear versus flexural deformations does not indicate a shear dominated branch as observed in figure A.(9).20.

The above inaccuracies of the shear model reflect the problems encountered in the flexural model. The concrete dilation and contact effects influence the shear stiffness in a similar way to the flexural stiffness.

The Al-Mahaidi (ASCE, 1982) equation, used when no normal stress is given by the flexural model, gives satisfactory results as to the magnitude of the shear deformation obtained, but does not represent correctly the reloading branch of the curve. Though conceptually the use of the above empirical equation is legitimate in finite element analysis, a more realistic approach in the light of the above results would be the development of model which takes into account the contact effects in a more direct manner. Such a model would require the availability of experimental data on the element level or the integration of results from cracked surface experiments.

CHAPTER 6

6 ANALYTICAL PARAMETRIC STUDY

6.1 Introduction

The parametric study of this chapter was undertaken making use of the cyclic reinforced concrete section analysis computer program (CRELIC) discussed in chapter 5. The choice and range of parameters are discussed and the results, normalised whenever possible, are subsequently presented in graphical form. In normalising the moment capacity, the control model section capacity is used. The control model was chosen to represent walls similar to the ones tested previously. Discussion of the results and their implications is given in chapter 8.

6.2 Geometry

For analytical purposes the actual scale of the model will not influence the results qualitatively but only qualitatively. As a result, the model dimensions used in the experiments were retained to facilitate future comparisons. For stability purposes, the ratio of D/B is the important parameter, and a value of 1:10 is the limit of some codes. This value was found by Goodsir (1985) to provide a reasonable degree of protection against lateral instability. Therefore, the experimental cross-sectional dimensions of 60 mm x 600 mm were used for the parametric study.

For simplicity, the aspect and shear ratios were kept equal. This implies that there is no top beam as required in the experiments. The shear ratio value is irrelevant in moment capacity calculations since the only affected quantities are displacements. Shear displacements are dependent on the product of shear force and the height, hence would be constant for a certain cross section irrespective of the shear ratio. However, the flexural displacements are proportional to the square of the shear ratio. The

deterministic nature of the component displacements does not require an additional parametric study but is discussed further in chapter 7.

The lower limit to which section analysis applies is for shear ratios of about 1. For lower aspect ratios, the basic assumption of plane sections remain plane is not valid. Additionally, the boundary effects will influence the stresses in a larger portion of the wall.

6.3 Volumetric ratio and distribution of steel within the cross section

The volumetric ratio of steel within the cross section should not be a universal parameter in design since the yield strength of steel varies. Nonetheless, it is widely accepted since it is easy to use in practice. Values vary with a minimum of 0.25% and up to a maximum of 4% (sometimes related to yield strength $16/f_y$). The walls in the experimental part of the current research were tested at about 3%. A lower value of 1% has been chosen, with a mid-value of 2%.

Realistically, it is not always possible to arrange reinforcement in exact integer percentage values. For the purposes of this study, a minimum bar diameter of 4 mm (10 mm for a full scale wall) is assumed as the unit bar. The numbers of unit bars and exact percentages used in the section are given in the table below:

Table 6.1 Volumetric percentage of reinforcement for parametric study walls

CODE	Design %	Design area (mm^2)	Number of ϕ4 bars & area	Actual %
W1	1	360	30 - 377	1.05
W2	2	720	60 - 754	2.1
W3	3	1080	90 - 1131	3.15
W4	4	1440	120 - 1508	4.2

One of the most important parameters which influence the overall behaviour of the section is the distribution of the flexural reinforcement within the section. The uniform distribution (UD), though not a very efficient way of utilising reinforcement, is a common lower bound reference point. A good second distribution is based in supplying minimum reinforcement to the web and distributing evenly the rest in the confined area (UB) as was done in walls SW4, 6, 8, 9. Finally, the upper extreme distribution, not recommended in design, is based in supplying minimum reinforcement to the web and concentrating the remainder in the wall extreme fibres (CB). Such an arrangement was used in walls SW5, 7.

The reinforcement was distributed according to table 6.2. The concrete cover thickness at the boundaries was assumed to be 10mm. The minimum spacing was 60 mm. The amount of reinforcement is given in units of 4 mm diameter bars only for comparison purposes. As an example, the 8 mm and 16 mm diameter bars are equivalent to 4 and 16 unit bars respectively.

Table 6.2 Position and distribution of reinforcement in walls

CODE	10	60	120	180	240	300	360	420	480	540	590	R/ment Position / Distribution
W1UD	3	3	2	3	3	2	3	3	2	3	3	Uniform
W1UB	4	4	4	1	1	2	1	1	4	4	4	Boundaries
W1CB	10	1	1	1	1	2	1	1	1	1	10	Concentrated
W2UD	6	5	6	5	5	6	5	5	6	5	6	Uniform
W2UB	9	9	9	1	1	2	1	1	9	9	9	Boundaries
W2CB	25	1	1	1	1	2	1	1	1	1	25	Concentrated
W3UD	8	8	8	9	8	8	8	9	8	8	8	Uniform
W3UB	14	14	14	1	1	2	1	1	14	14	14	Boundaries
W3CB	40	1	1	1	1	2	1	1	1	1	40	Concentrated
W4UD	11	11	11	11	11	10	11	11	11	11	11	Uniform
W4UB	19	19	19	1	1	2	1	1	19	19	19	Boundaries
W4CB	55	1	1	1	1	2	1	1	1	1	55	Concentrated

The first parametric study involved the above 12 cases, as shown in table 6.3. The results of the parametric study concerned with the variation of the steel volumetric ratio and distribution are presented in figures 6.1 to 6.5.

Table 6.3 Variation of steel amount and distribution

Variable	a Steel %	b Distri-bution	c f_c N/mm²	d Confin. ω_w	e f_y N/mm²	f f_y / f_{ul} N/mm²	g ε_{ul}	h Degrad α.	i Shear ratio	j Axial force KN	k ΔMDL	Figure No
Control	3	UB	40	0.1	460	1.15	0.012	0.175	2	0	Mono	
Varying steel amount and distribition	1	UD										6.1-6.5
		UB										
		CB										
	2	UD										
		UB										
		CB										
	3	UD										
		CB										
	4	UD										
		UB										
		CB										

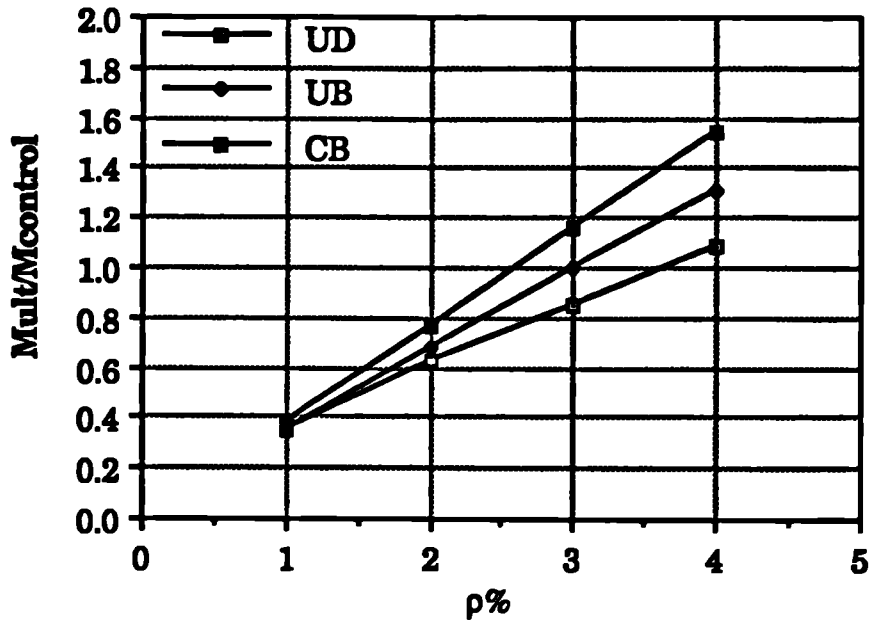


Figure 6.1 Normalised section capacity versus percentage of flexural reinforcement for different types of distributions

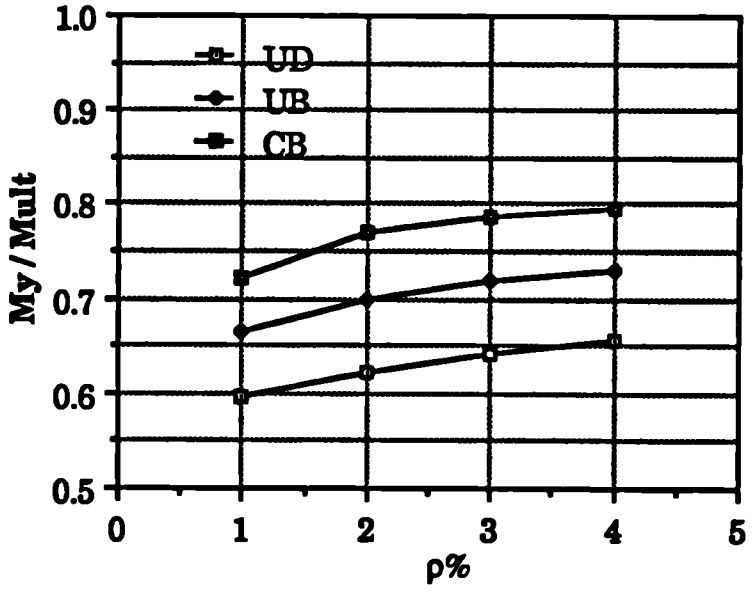


Figure 6.2 Normalised section yield to ultimate capacity versus percentage of flexural reinforcement for different types of distributions

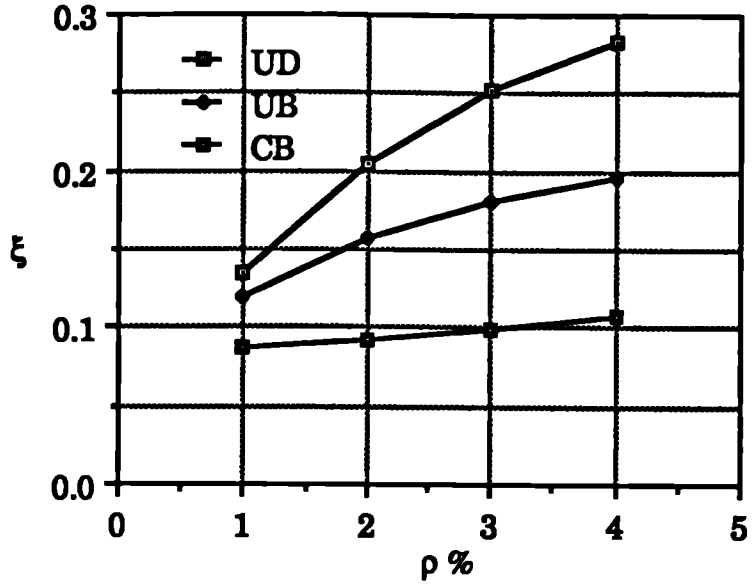


Figure 6.3 Normalised neutral axis depth at ultimate capacity versus percentage of flexural reinforcement for different types of distributions

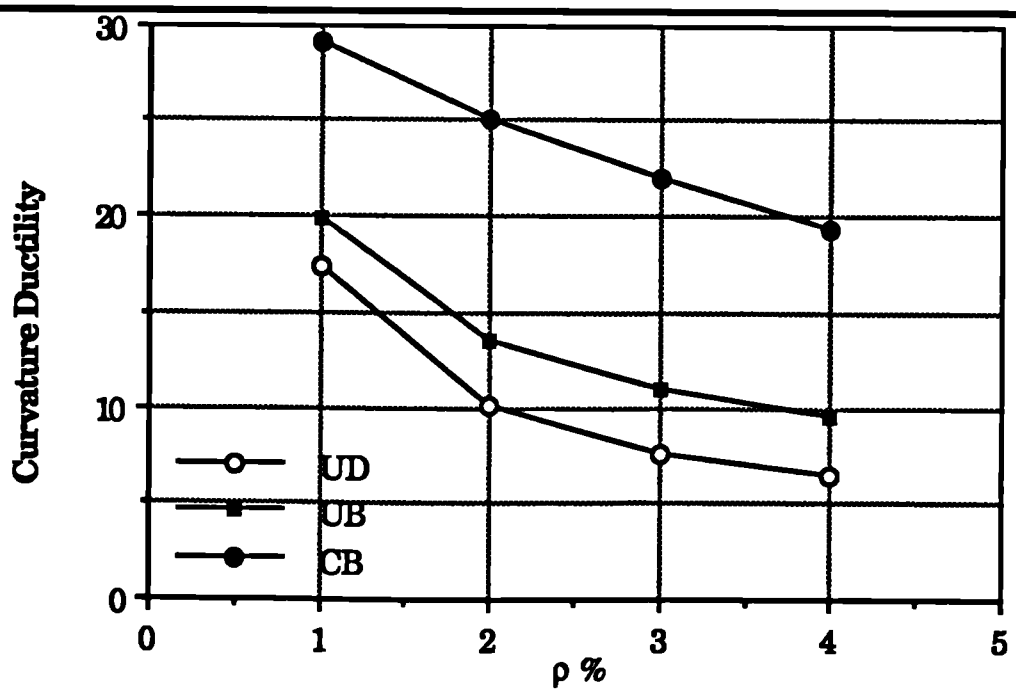


Figure 6.4 Curvature ductility versus percentage of flexural reinforcement for different types of distributions

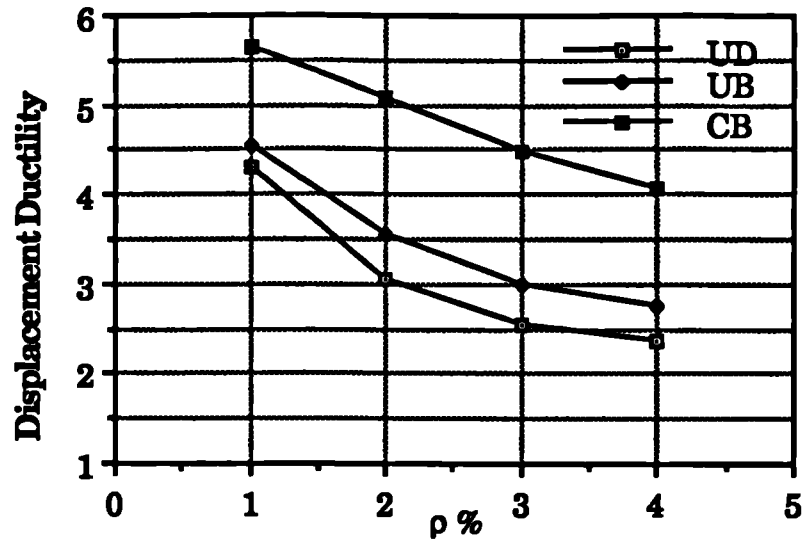


Figure 6.5 Displacement ductility versus percentage of flexural reinforcement for different types of distributions

6.4 Concrete characteristics

Most codes of practice consider the strain of 0.0035 to be the ultimate strain of concrete, ε_{cu}, in bending. The value of ε_{cu} varies slightly with the unconfined concrete compressive strength f_{co} but a far more important variation occurs with different amounts of lateral confinement reinforcement available in the element under compression.

The current parametric study investigated the variation of concrete strength and ultimate unconfined concrete compressive strain 'ε_{cuo}'. For the concrete strength 'f_{co}', values between 20 and 50 N/mm^2 are used. As far as 'ε_{cuo}' is concerned, there are a number of models that can be used to convert the supplied confinement into enhanced concrete strength 'f_{cc}', and ultimate concrete compressive strain 'ε_{cu}'. However, in order to facilitate comparisons with the modern trends in Europe, the EC8 Appendix A equations discussed in Chapters 2 and 5 are used in this section. The range of values is chosen so as to cover both branches of the bilinear confinement model given. An upper limit on strength enhancement factor of 2.5 is used. The confinement effectiveness factor 'α' is taken as 0.25. One would probably expect a slightly higher value for higher confinement ratios, but a single value is used for simplicity. Table 6.4 shows the parameters used. The results of this parametric study are presented in figures 6.6 to 6.10.

Table 6.4 Variation of concrete strength and confinement

Variable	a	b	c	d	e	f	g	h	i	j	k	Figure
Control	3	UB	40	0.1	460	1.15	0.012	0.175	2	0	Mono	
Concrete strength and confinement	3	UB	20	0.0								6.6-6.10
			30									
			40									
			50									
			20	0.1								
			30									
			50									
			20	0.2								
			30									
			40									
			50									
			20	0.5								
			30									
			40									
			50									
			20	1.0								
			30									
			40									
			50									

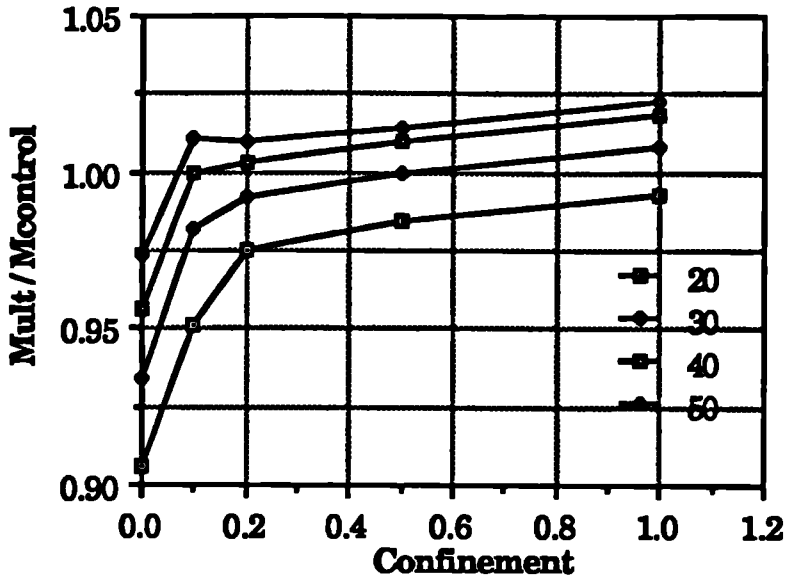


Figure 6.6 Normalised section capacity versus mechanical confinement ratio ω_{wd} for different concrete strengths

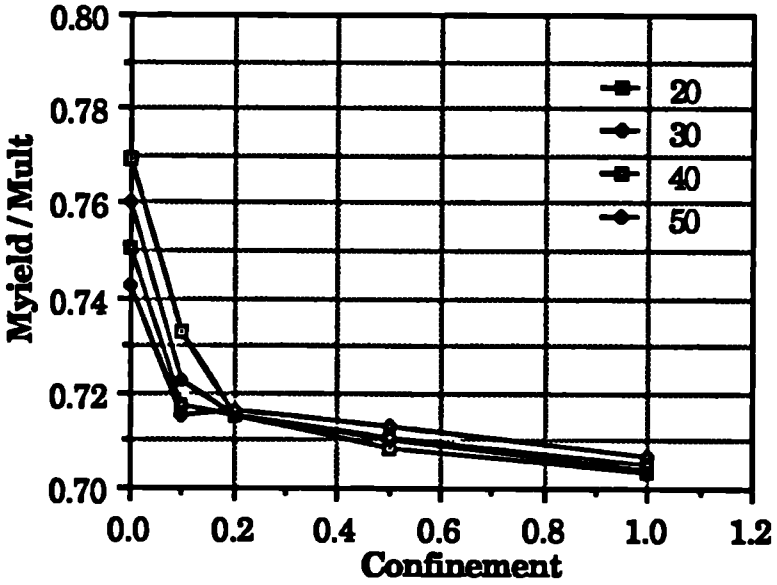


Figure 6.7 Normalised section yield to ultimate capacity versus mechanical confinement ratio ω_{wd} for different concrete strengths

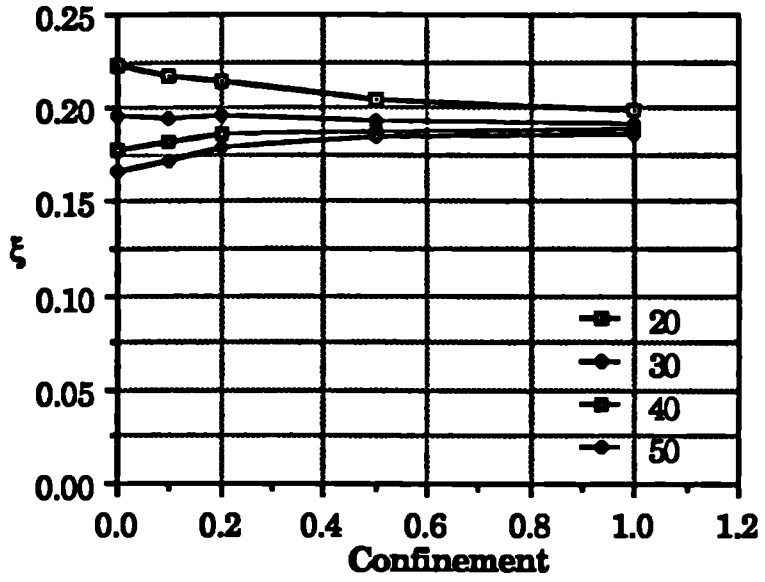


Figure 6.8 Normalised neutral axis depth at ultimate capacity versus mechanical confinement ratio ω_{wd} for different concrete strengths

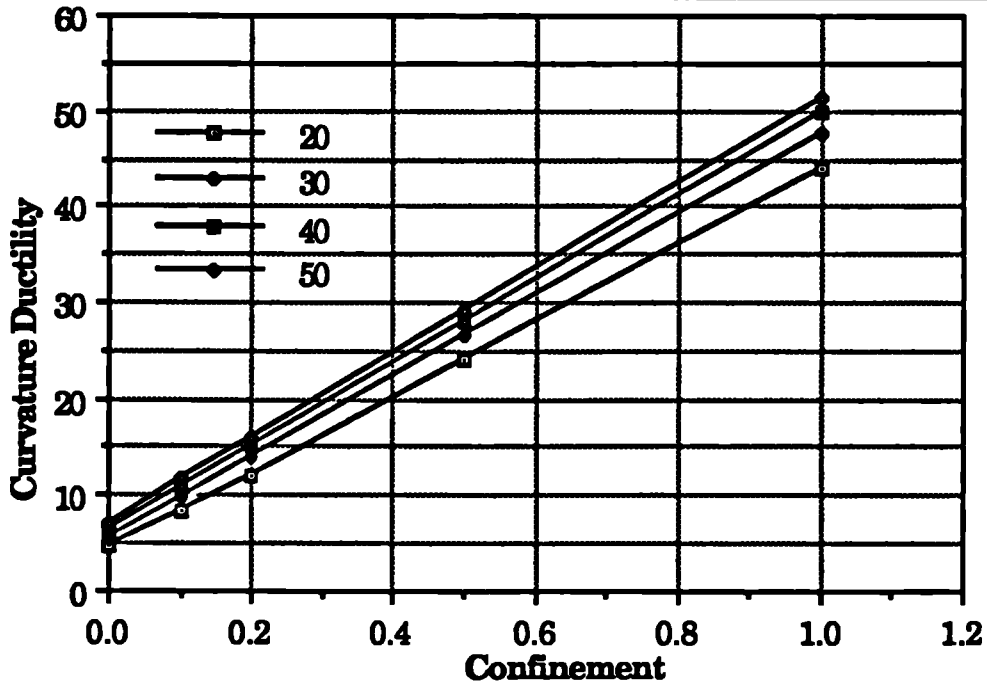


Figure 6.9 Curvature ductility versus mechanical confinement ratio ω_{wd} for different concrete strengths

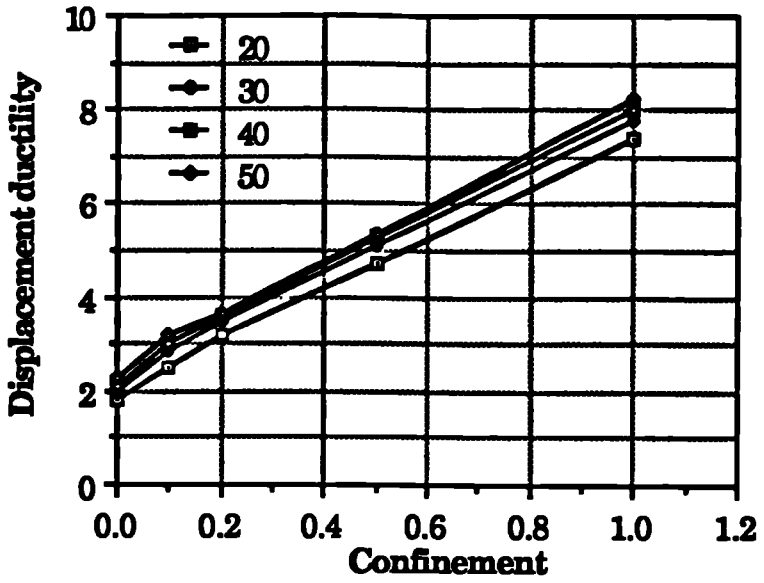


Figure 6.10 Displacement ductility versus mechanical confinement ratio ω_{wd} for different concrete strengths

6.5 Steel characteristics

Variation in nominal yield strength as well as unintentional variations can be investigated by varying the yield strength of flexural reinforcement. The value of actual to nominal yield strength is required by EC8 to be less than 1.25. The maximum yield strength used in this section is 575 N/mm^2 (1.25 x 460 N/mm^2) and the minimum 355 N/mm^2.

Of great significance to the section characteristics are also the steel yield to ultimate ratio, strain hardening stiffness, degradation parameter 'α' and ultimate strain of reinforcement. However, these parameters are interrelated in affecting strength, ductility, and energy dissipation. In defining the steel characteristics from the experiments described in chapter 3, a simple trilinear envelope model was used. However, only the reinforcement used in the tests was tested, and hence, the possible variability of these parameters could not be assessed for the more general purpose of this parametric study.

The EC8 limitation on the ratio of the yield to ultimate stress of 1.45 is used as an upper bound for this parameter.

The value of ultimate strain of 0.012, which is recommended by EC8 for the high ductility class walls, is used for the parametric studies. However, this variable is only a check on the mode of failure and does not affect otherwise the behaviour.

The strain hardening stiffness for the experiments was in the range of 1000 - 3000 N/mm^2. In order to limit the extend of the parametric study the higher value of 3000 N/mm2 was used, in an attempt to achieve the ultimate capacity without exceeding the ultimate strain limit. In fact, this is just possible for steels with the higher values of yield stress and high values of ultimate to yield stress ratio. In the limit, the results of this parametric study is expected to highlight the limitations of the used model, as well as the lack of comprehensive experimental data on steel reinforcement. Table 6.5 shows the parameters used and the results are presented in figures 6.11 to 6.15.

Table 6.5 Variation of steel characteristics

Variable	a	b	c	d	e	f	g	h	i	j	k	Figure
Control	3	UB	40	0.1	460	1.15	0.012	0.175	2	0	Mono	6.11-6.15
Varying steel characteristics					355	1.00 1.15 1.30 1.45						
					390	1.00 1.15 1.30 1.45						
					425	1.00 1.15 1.30 1.45						
					460	1.00 1.30 1.45						
					510	1.00 1.15 1.30 1.45						
					575	1.00 1.15 1.30 1.45						

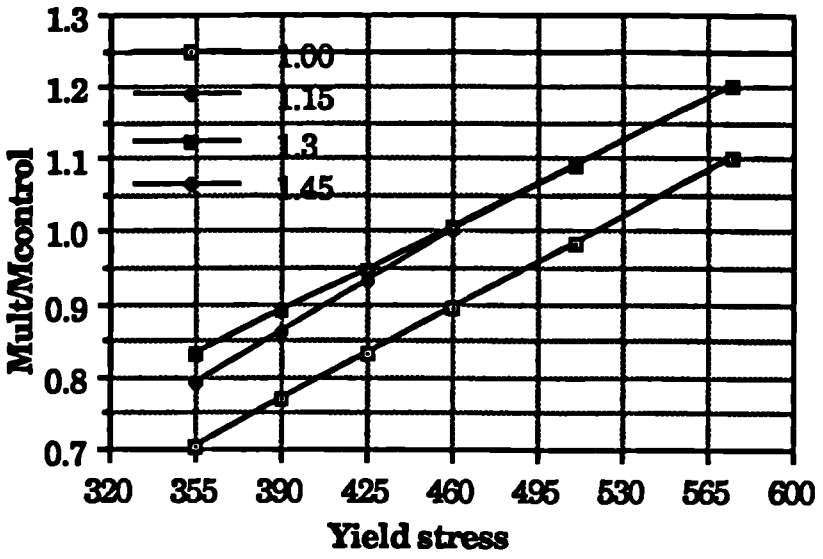


Figure 6.11 Normalised section capacity versus steel yield stress for different ultimate to yield stress ratios

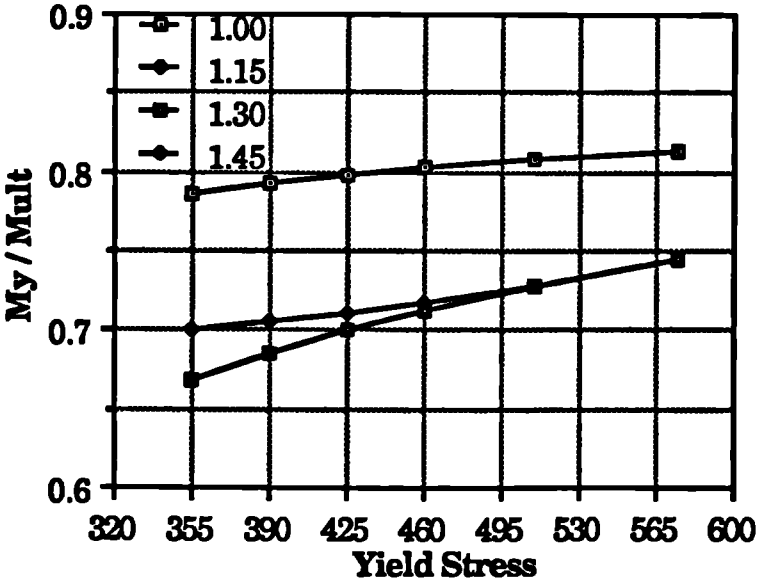


Figure 6.12 Normalised section yield to ultimate capacity versus steel yield stress for different ultimate to yield stress ratios

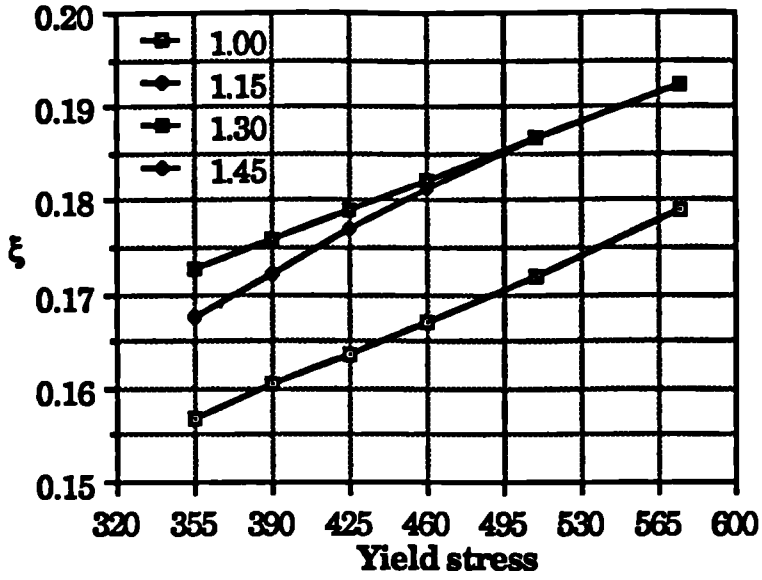


Figure 6.13 Normalised neutral axis depth at ultimate capacity steel yield stress for different ultimate to yield stress ratios

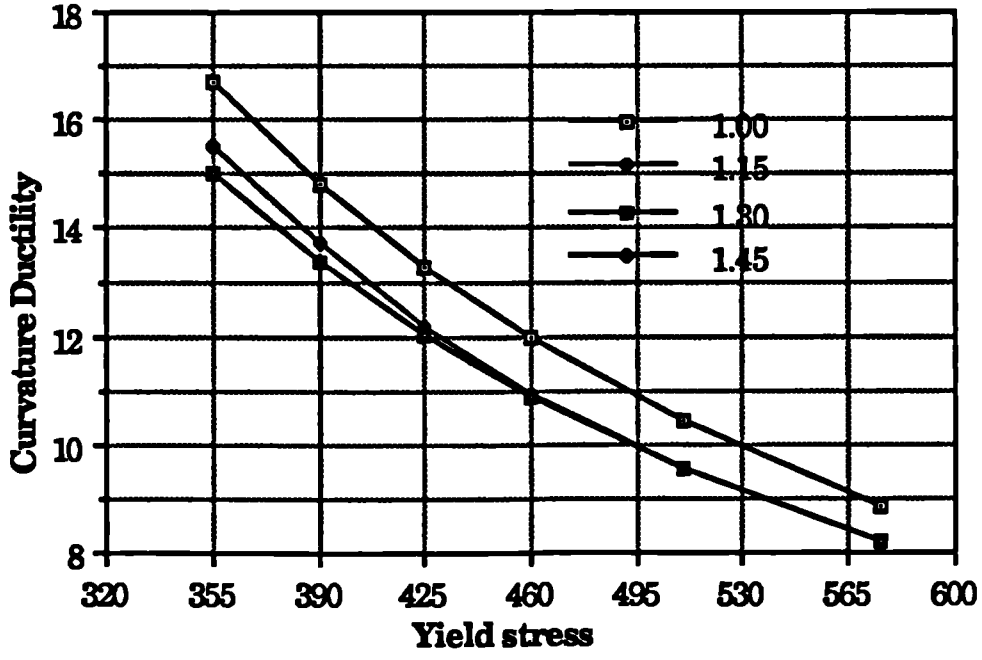


Figure 6.14 Curvature ductility versus steel yield stress for different ultimate to yield stress ratios

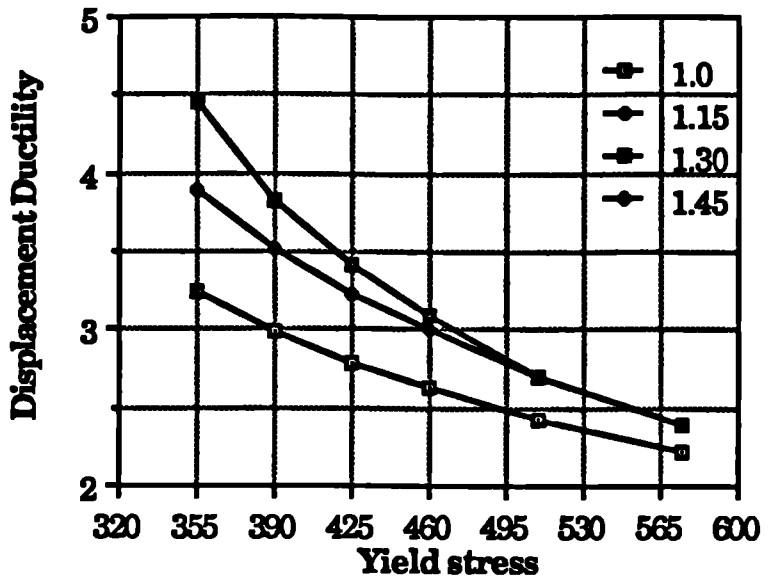


Figure 6.15 Displacement ductility versus steel yield stress for different ultimate to yield stress ratios

6.6 Axial load

Most codes limit the value of the axial load normalised with respect to axial crushing capacity to 0.35. As a result, the full interaction curve traditionally used for load bearing members is not required. The effects of tension are investigated through the lower range value of this parametric study. Since, the variation in the depth of the neutral axis is expected to be much higher than for the other cases, the confined area is extended to cover the whole section so as to avoid the possibility of web crushing. The amount of confinement is the second variable as shown in table 6.6. Results of this parametric study are presented in figures 6.16 to 6.20.

Table 6.6 Variation of axial load and effect of confinement

Variable	a	b	c	d	e	f	g	h	i	j	k	Figure
Control	3	UB	40	0.1	460	1.15	0.012	0.175	2	0	Mono	6.16-6.20
Variation of axial load and effect of confinement				0.0 0.1 0.2 0.5 1.0						-0.10		
				0.0 0.2 0.5 1.0						0.00		
				0.0 0.1 0.2 0.5 1.0						0.10		
				0.0 0.1 0.2 0.5 1.0						0.20		
				0.0 0.1 0.2 0.5 1.0						0.35		
				0.0 0.1 0.2 0.5 1.0						0.50		

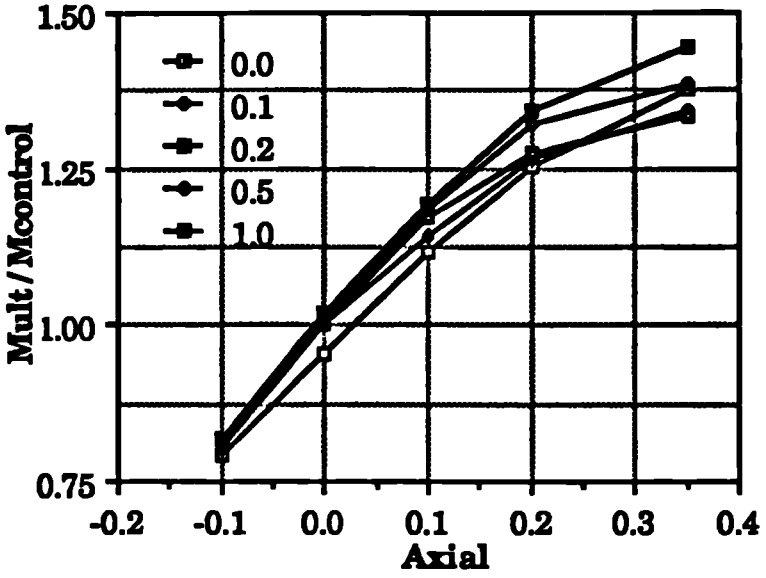


Figure 6.16 Normalised section capacity versus normalised axial force for different confinement values

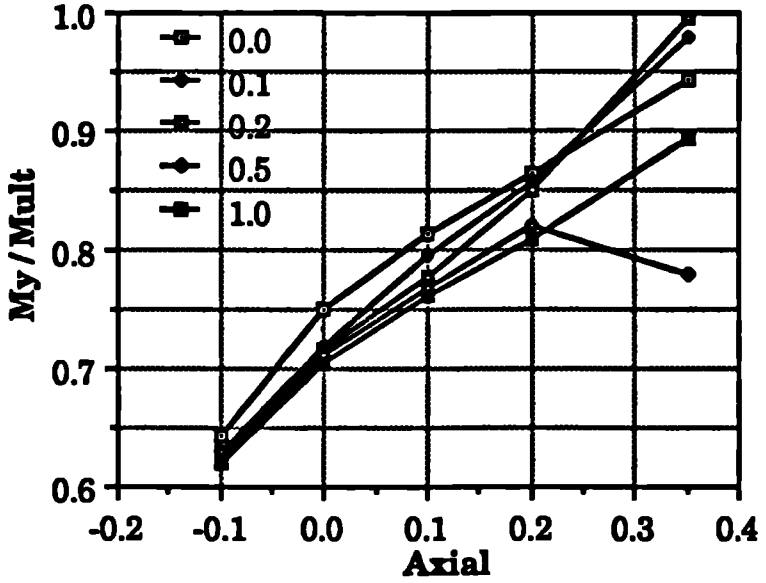


Figure 6.17 Normalised section yield to ultimate capacity versus normalised axial force for different confinement values

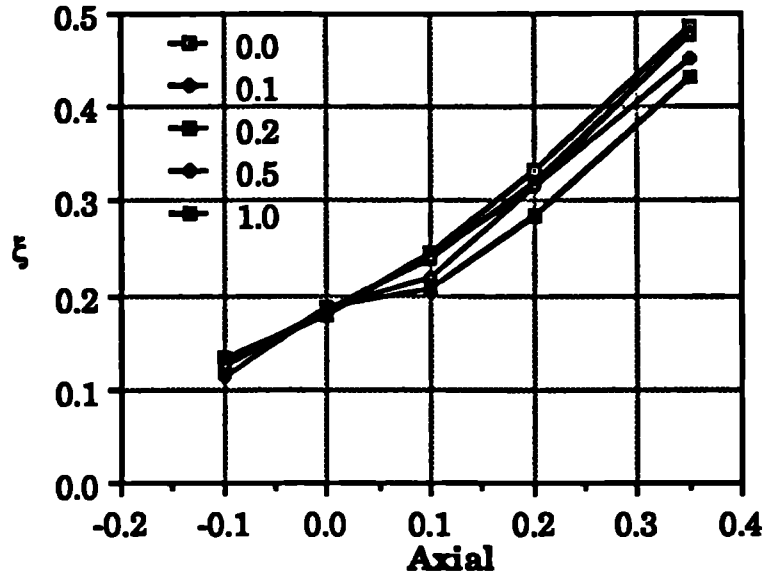


Figure 6.18 Normalised neutral axis depth versus normalised axial force for different confinement values

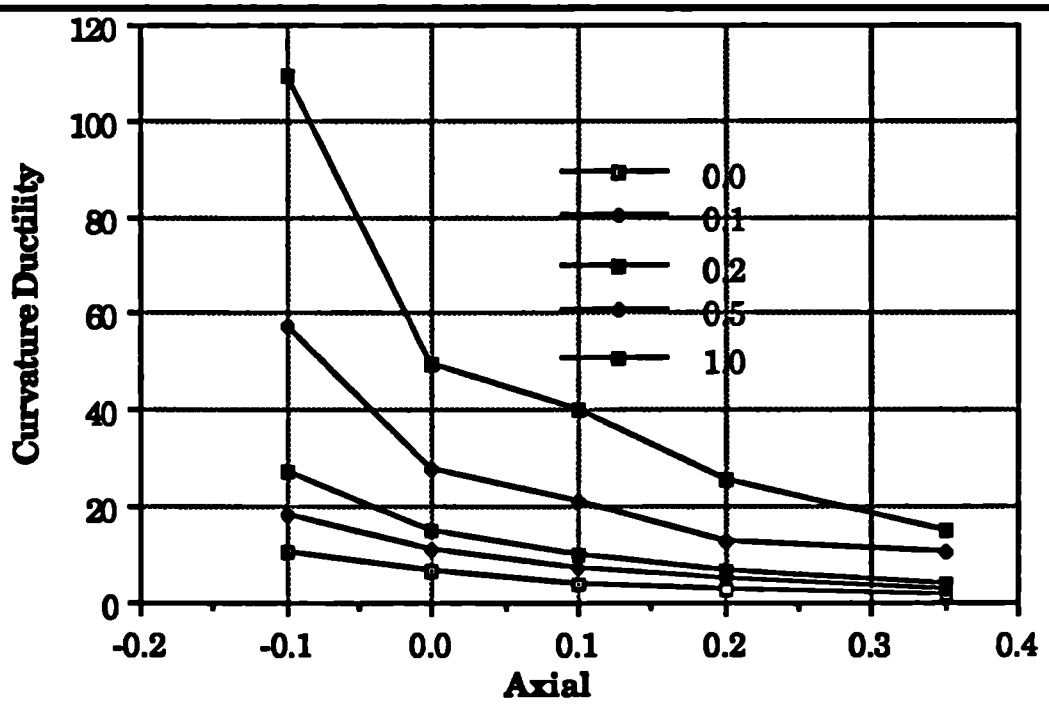


Figure 6.19 Curvature ductility versus normalised axial force for different confinement values

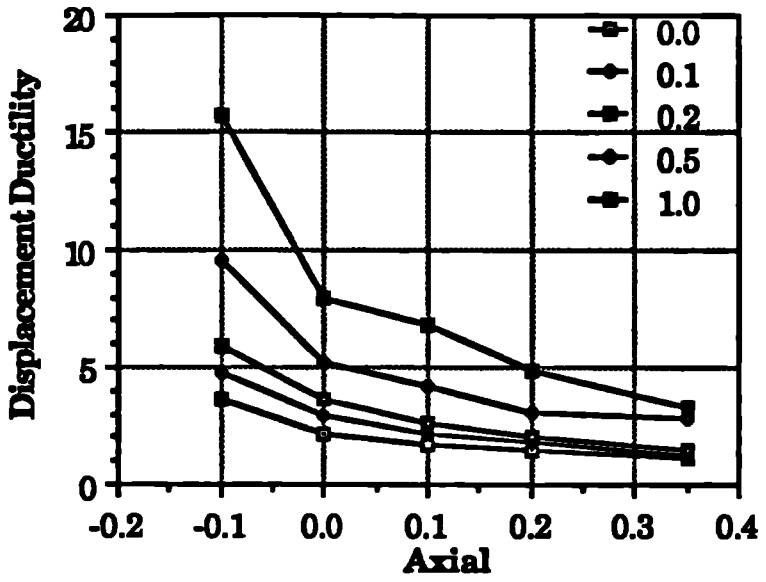


Figure 6.20 Displacement ductility versus normalised axial force for different confinement values

6.7 Cyclic loading

6.7.1 Confinement

The effect of cyclic loading on the wall behaviour was investigated for different increments in MDL. As with the experiments two cycles are imposed at each displacement level. The effects of the amount of confinement is again the second variable as shown in table 6.7. The results are shown in figures 6.21 to 6.25.

Table 6.7 Variation of cyclic loading and effect of confinement

Variable	a	b	c	d	e	f	g	h	i	j	k	Figure
Control	3	UB	40	0.1	460	1.15	0.012	0.175	2	0	Mono	
Variation of cyclic loading				0.0 0.1 0.2							Cyclic 0.5 mm	6.21-6.25
and effect of confinement		UB		0.0 0.1 0.2							Cyclic 1 mm	
		UB		0.0 0.1 0.2							Cyclic 2 mm	

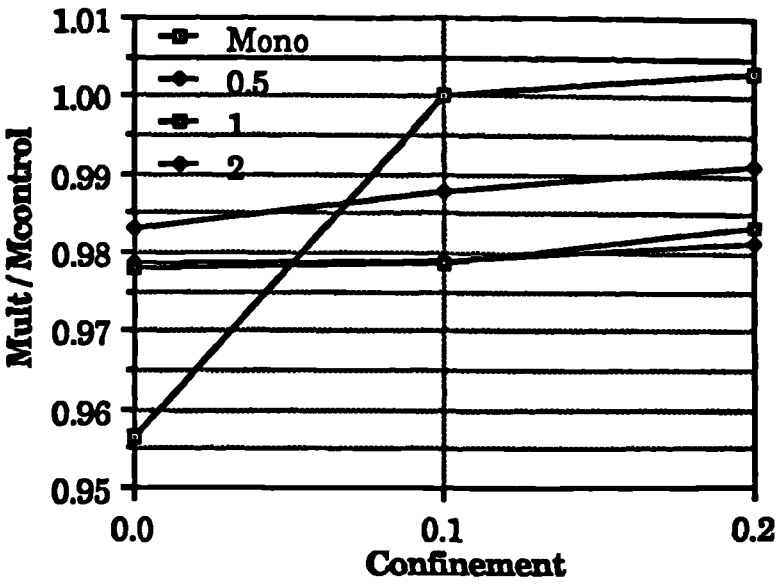


Figure 6.21 Normalised section capacity versus confinement level for different ΔMDL values

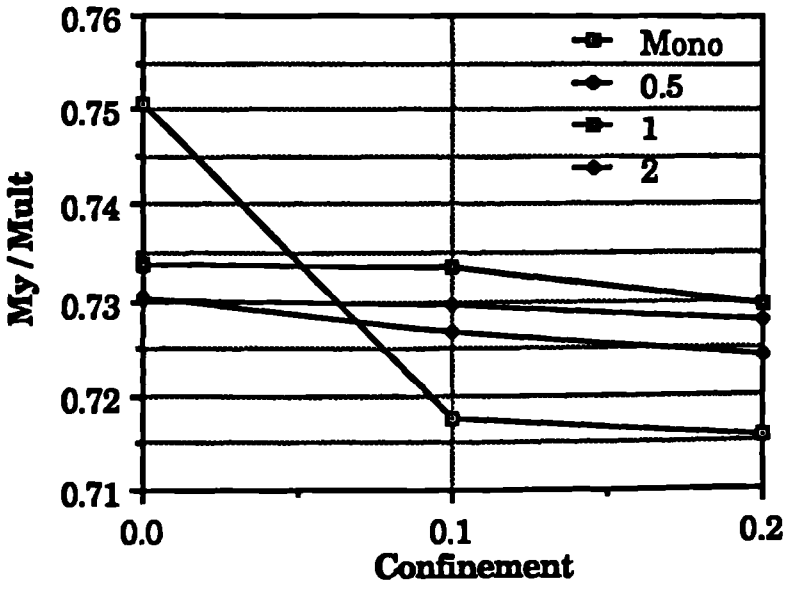


Figure 6.22 Normalised section yield to ultimate capacity versus confinement level for different ΔMDL values

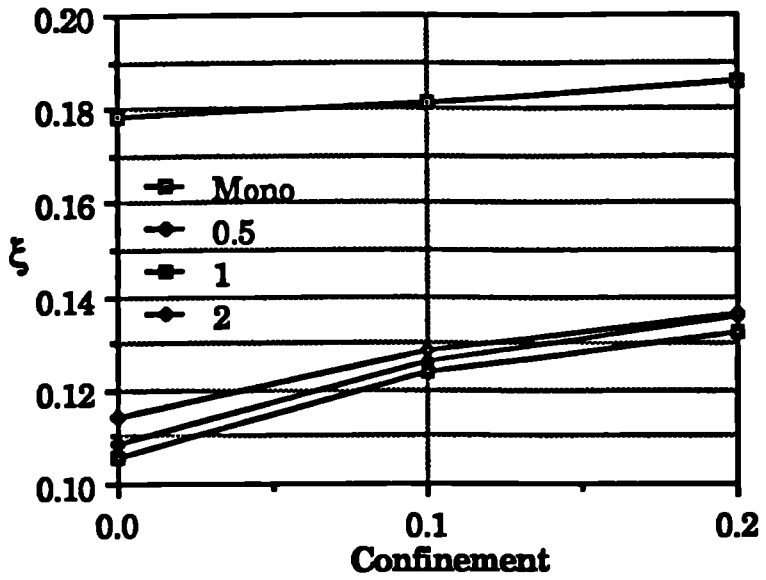


Figure 6.23 Normalised neutral axis depth versus confinement level for different ΔMDL values

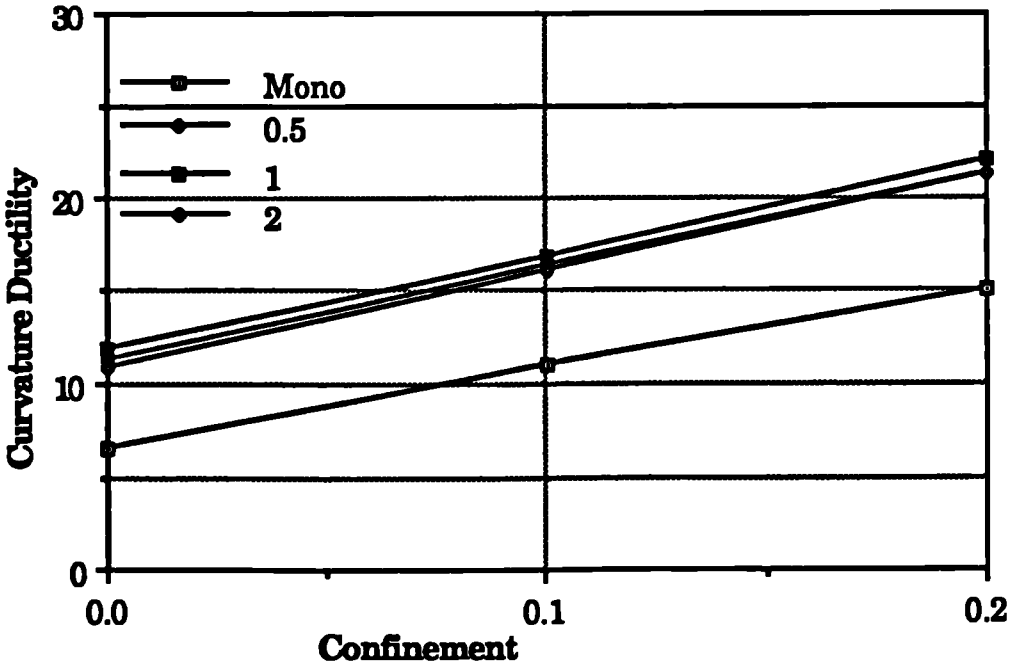


Figure 6.24 Curvature ductility versus confinement level for different ΔMDL values

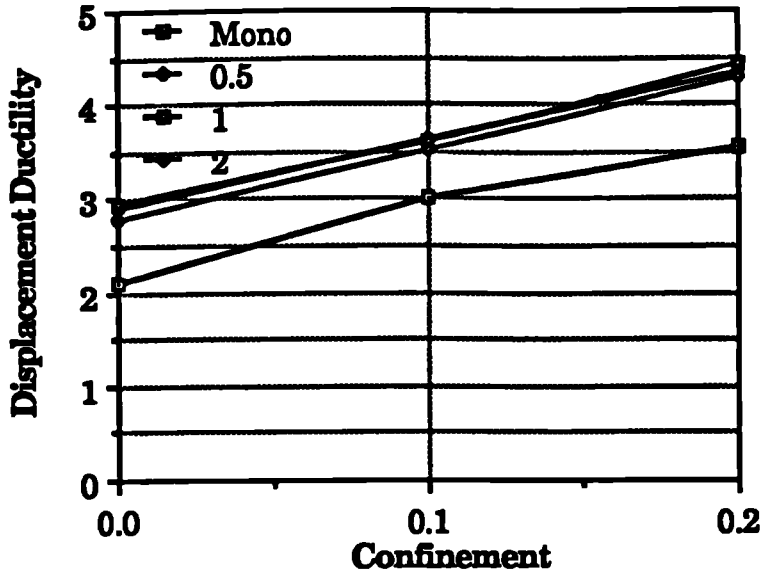


Figure 6.25 Displacement ductility versus confinement level for different ΔMDL values

6.7.2 Axial load

The effect of cyclic loading on the wall behaviour is investigated for an increment of 2 mm in MDL on walls with different axial load levels as shown in table 6.8. As with the experiments two cycles are imposed at each displacement level. The confinement of the wall is considered to cover the entire section, so as to avoid web crushing. The results together with the monotonic curves, are shown in figures 6.26 to 6.30.

Table 6.8 Variation of axial loads for cyclic and monotonic lateral loading

Variable	a	b	c	d	e	f	g	h	i	j	k	Figure
Control	3	UB	40	0.1	460	1.15	0.012	0.175	2	0	Mono	
Variation of axial loads for cyclic										-0.10 0.00 0.10 0.20 0.35		6.26-6.30
and monotonic lateral loading										-0.10 0.00 0.10 0.20 0.35	Cyclic 2 mm	

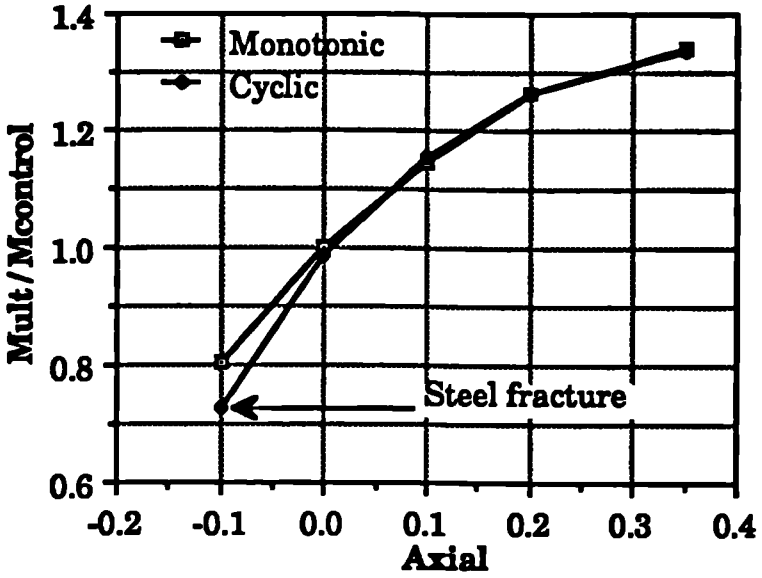


Figure 6.26 Normalised section capacity versus axial load for monotonic and cyclic loading

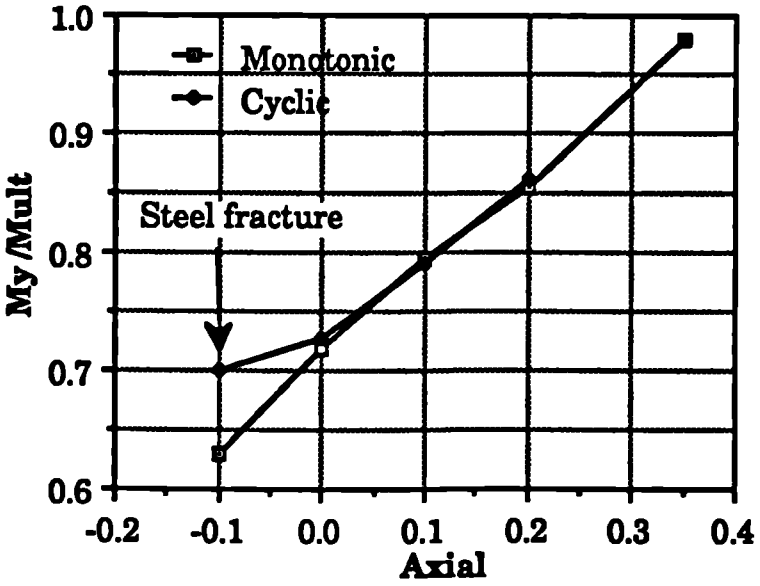


Figure 6.27 Normalised section yield to ultimate capacity versus axial load for monotonic and cyclic loading

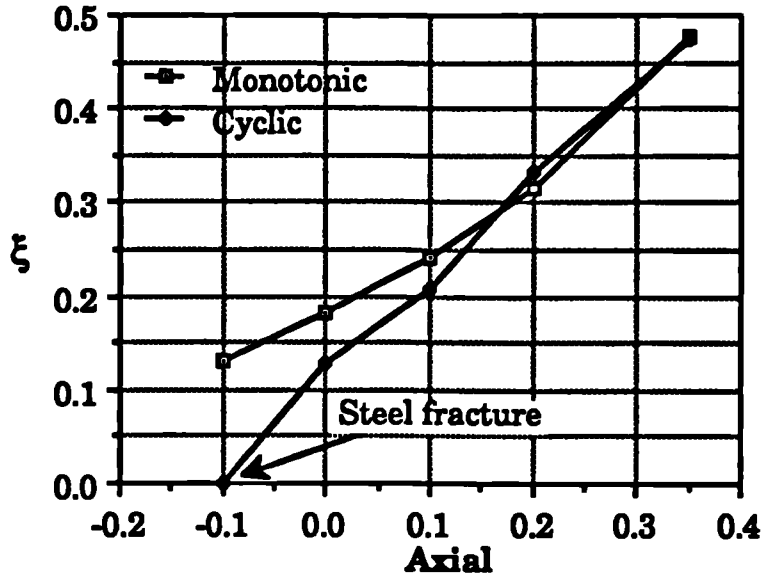


Figure 6.28 Normalised neutral axis depth versus axial load for monotonic and cyclic loading

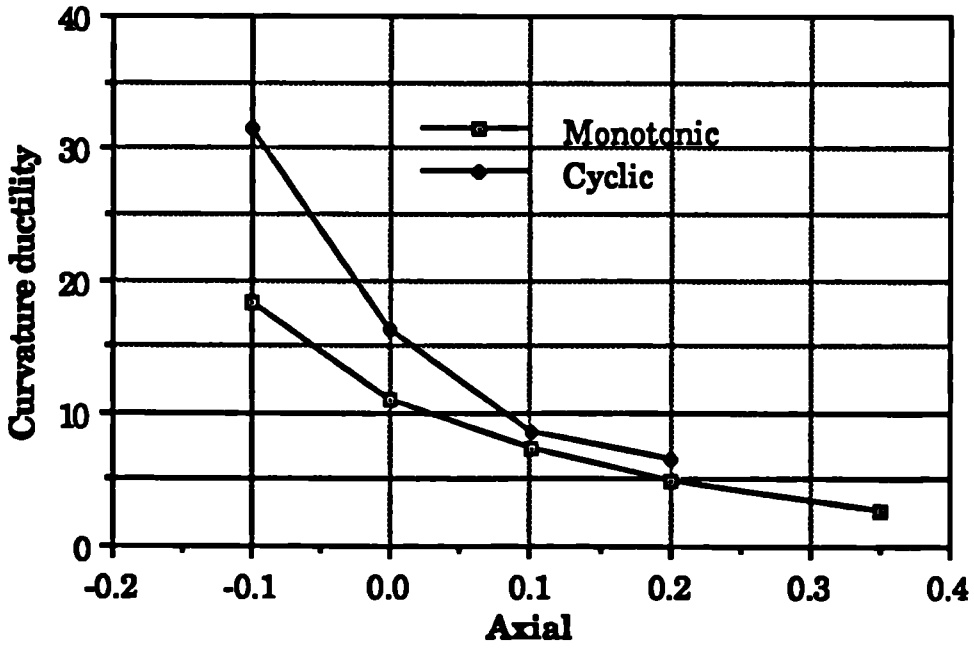


Figure 6.29 Curvature ductility versus axial load for monotonic and cyclic loading

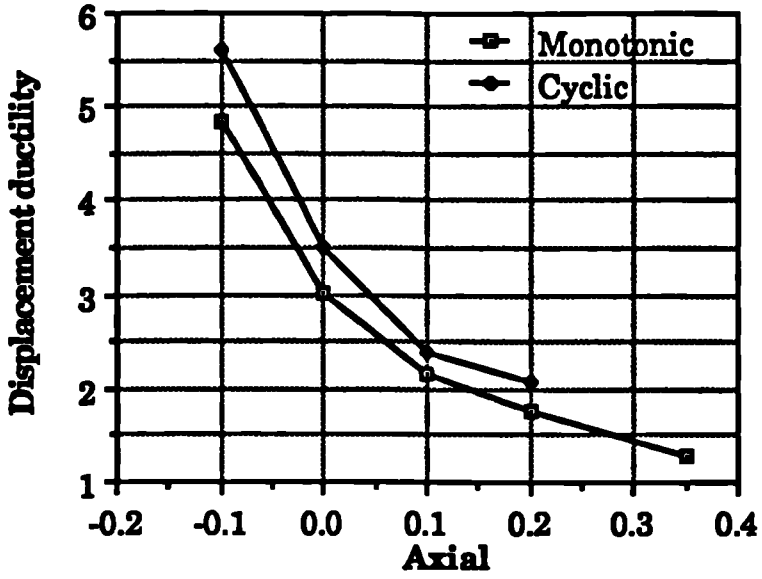


Figure 6.30 Displacement ductility versus axial load for monotonic and cyclic loading

The results of chapter 6 will be discussed together with the experimental results in chapter 7.

CHAPTER 7

7 COMPARISONS AND DISCUSSION OF RESULTS

7.1 Introduction

In this chapter a general discussion of the experimental and analytical results is presented. Design implications are also mentioned where relevant, however, a more design oriented discussion will be provided in chapter 8.

7.2 Stiffness characteristics of specimens

7.2.1 Experimental stiffness

The specimen secant stiffness during the cyclic loading is variable, depending on the loading history. However, due to the consistency in displacement of the loading regime employed, the secant stiffness at the MDL can be used to monitor the overall stiffness deterioration. The cracked section stiffness, shown in some of the figures, is calculated by using the flexural model presented in chapter 5 (by using computer program CRELIC).

For the shake-table test, the equivalent stiffness at the centre of mass has been calculated from the response frequency by assuming that the system is behaving elastically. The results have been plotted on the same graph as for SW2 and SW3, as shown in figure 7.1.

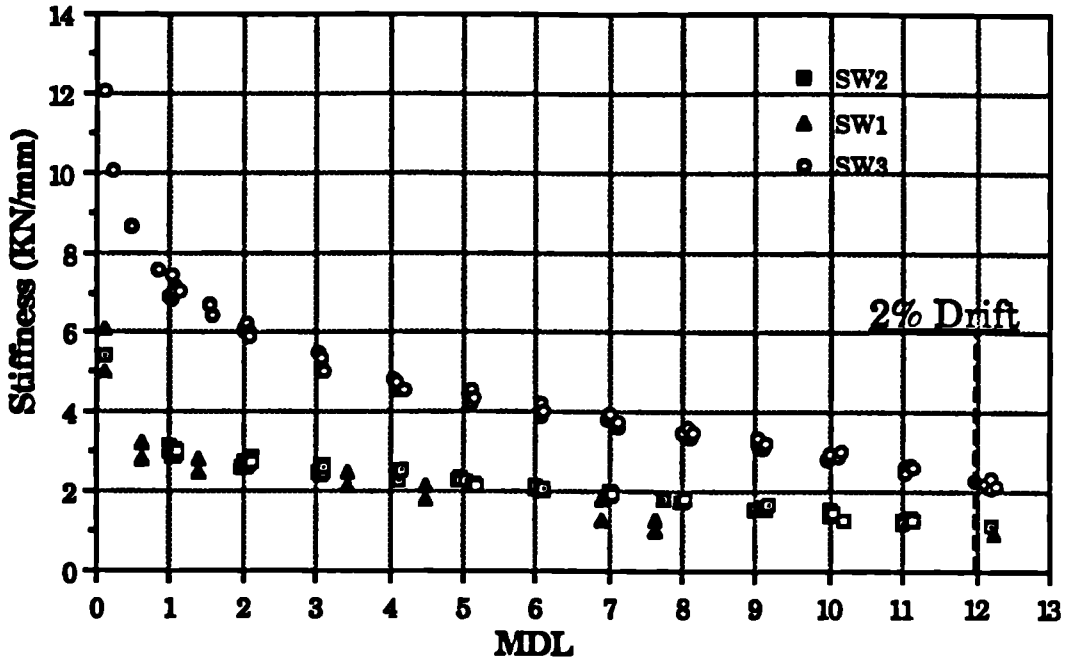


Figure 7.1 Secant stiffness of SW1, SW2 and SW3 versus maximum displacement level

As depicted in figure 7.1, the calculated stiffness of SW1 is in general less than the corresponding static-cyclic test. One of the reasons contributing to the decrease in pre-yield stiffness may be the large number of cycles imposed by the earthquake time histories prior to yield. In order to explore this further, during the first cyclic test SW2 a large number of load reversals was applied at low displacement levels. As can be seen from figure 7.1, the stiffness deterioration is insignificant, despite the large number of load reversals at the same MDL. It can be concluded, therefore, that prior to yield the stiffness degradation is more depended on the MDL rather than the number of cycles at a particular MDL. This conclusion is not expected to be valid after yielding due to the accumulation of plastic strains in the reinforcement.

The secant stiffness of SW3 at top wall level is higher, since the test was conducted at a different shear ratio from the other scale 1:5 walls (figure 7.1). This test was necessary as a link between the two scales used and comparisons can only be made with the walls SW4 and SW6 for which this wall can be considered to be a half scale model.

The secant stiffness of SW3 (scaled by 2:1), SW4 and SW6 is shown in figure 7.2. The initial stiffness of SW6, as obtained from information prior to MDL-2, is much closer to the uncracked section than all other walls.

However, after MDL-16 the same wall is showing faster stiffness deterioration. A comparison with SW3 indicates that at the smaller scale, the initial stiffness is reduced much more than at a larger scale. A possible explanation for this is the effect of micro-cracking due to shrinkage. The subsequent stiffness deterioration is similar at both scales, which indicates that the scaling was performed successfully.

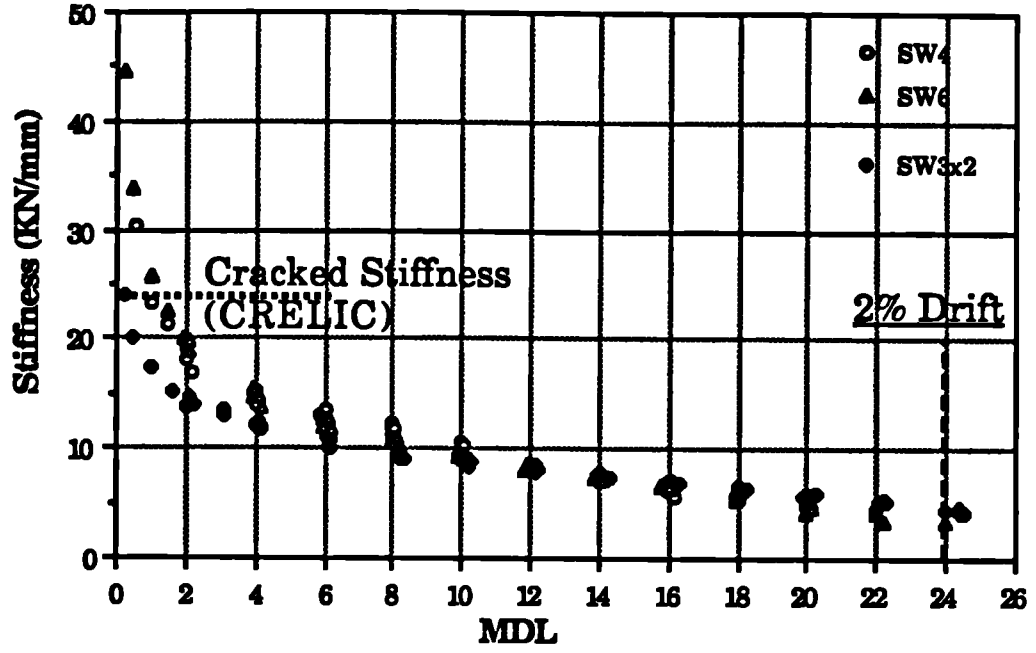


Figure 7.2 Secant stiffness of SW3, SW4 and SW6 versus maximum displacement level

Walls SW5 and SW7 (figure 7.3) have a higher elastic stiffness than all the other walls because of the concentration of the reinforcement near the boundaries. The stiffness of wall SW7, after initial cracking remains higher than all other walls. As expected the stiffness of SW5 drops sharply when shear failure occurs at MDL-10.

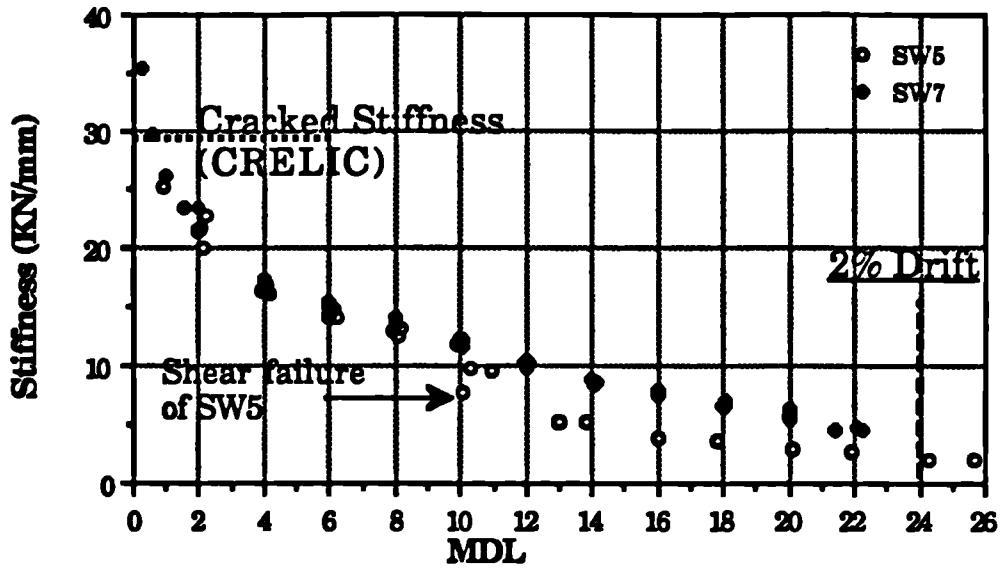


Figure 7.3 Secant stiffness of SW5 and SW7 versus maximum displacement level

No significant difference between the stiffness of walls SW8 and SW9 is noticeable in figure 7.4 at all load stages. This is despite the fact that wall SW8 had much less shear reinforcement than SW9. This is contrary to the idea that walls with low reserve in shear capacity will deteriorate in shear as proposed in EC8 (1988) and presented in chapter 2.

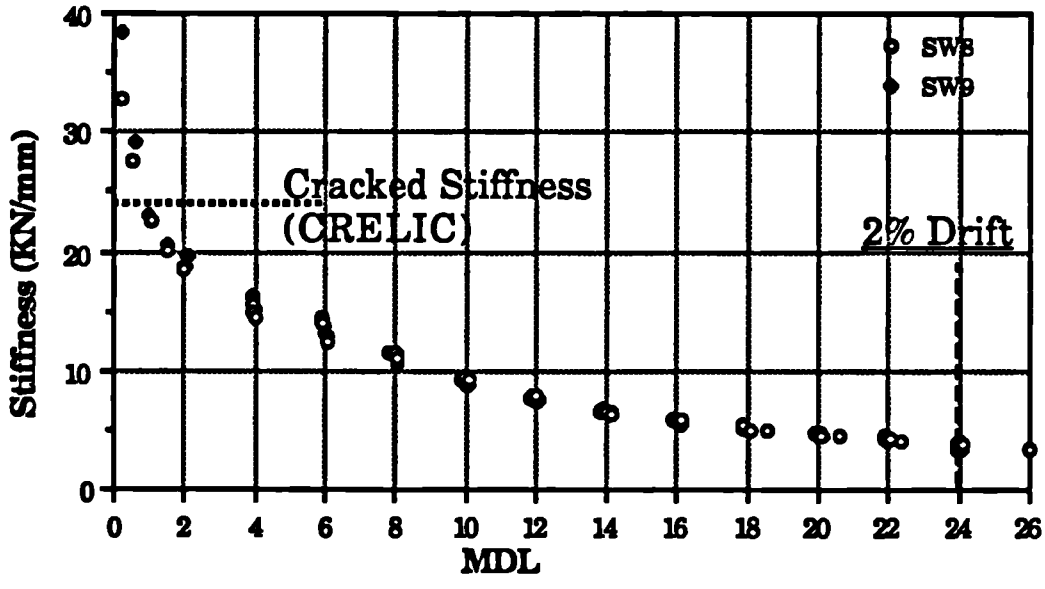


Figure 7.4 Secant stiffness of SW8 and SW9 versus maximum displacement level

7.2.2 Elastic uncracked stiffness

The elastic uncracked stiffness 'K_e' of an RC wall can be readily obtained in a closed form solution. By using the principles of virtual work and figure 7.5, shear deformations are given by equation 7.1.

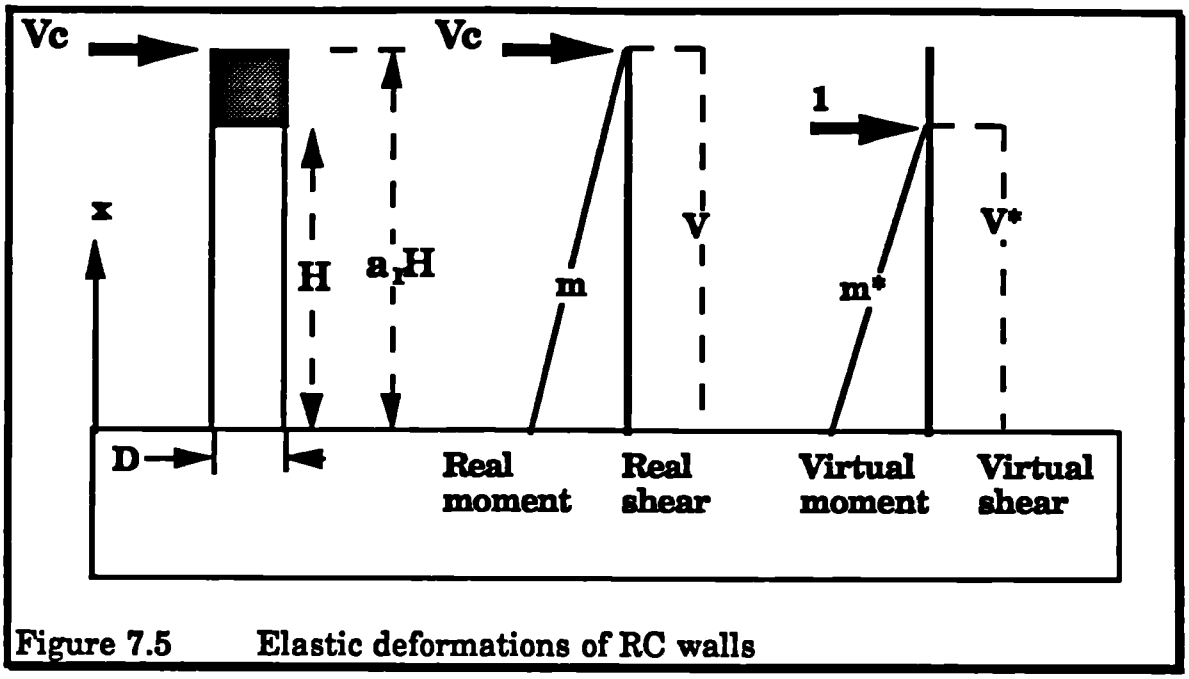


Figure 7.5 Elastic deformations of RC walls

$$u_{sH} = \int_0^H V^* \frac{V_c}{\beta G A} dx = \frac{V_c}{\beta G B}\left(\frac{H}{D}\right) = \frac{2.76\, V_c}{E_t B}\left(\frac{H}{D}\right) \tag{7.1}$$

which is obtained by assuming $\nu = 0.15$ in equation 7.2.

$$G = \frac{E}{2(1+\nu)} \tag{7.2}$$

Flexural deformations are given by equation 7.3.

$$u_{fH} = \int_0^H m^* \frac{m}{E_t I} dx = \frac{V_c H}{6 E_t I}(3 a_r H^2 - H^2)$$

$$= \left(\frac{2 V_c}{E_t B}\right)\left(\frac{H}{D}\right)^3 (3 a_r - 1) \tag{7.3}$$

The total deformations are the sum of equation 7.1 and 7.3, as given by equation 7.4.

$$u_H = u_{sH} + u_{fH} = \left(\frac{V_c}{E_t B}\right)\left(\frac{H}{D}\right)\left[(6 a_r - 2)\left(\frac{H}{D}\right)^2 + 2.76\right] \tag{7.4}$$

The composite value of elastic Modulus E_t is given by equation 7.5,

$$E_t = \frac{[E_c I_c + E_s I_s]}{I} \tag{7.5}$$

where

$$I_s = \sum_{i=1}^{n} (A_i \; s_i^2) \tag{7.6}$$

and s_i is the distance of the ith bar from the centre.

From equation 7.4, the elastic lateral stiffness K_e can be determined from,

$$K_e = \frac{V_c}{u_H} \tag{7.7}$$

By using equation 3.21 to evaluate the concrete elastic modulus and assuming E_s to be 200,000 KN/mm^2, the elastic stiffness is calculated as shown in table 7.1. The cracked section stiffness K_{cr} is calculated by using the flexural model presented in chapter 5 (by using computer program CRELIC). The value of stiffness given is in KN/mm.

The ratio between the experimental stiffness obtained at first maximum displacement level 'K_1' (MDL-1 at scale 1:5 & MDL-2 at scale 1:5) and the elastic analytical stiffness 'K_e', is about 1:4 and 1:3, for models at scale 1:5 and 1:2.5 respectively. It is obvious that from a very early stage of loading, the elastic stiffness does not represent the true stiffness. The deviation from linearity is likely to be dependent not only on the loading history but also on the material characteristics, dimensions and curing conditions.

The cracked stiffness, as obtained by the section analysis method , is much closer to the initial specimen stiffness than the elastic stiffness. The estimates of the cracked section stiffness would be further reduced by adding a reliable shear displacement estimate and allowing for the rotation at foundation level. For design purposes, it is therefore advisable to use the cracked stiffness rather than the elastic stiffness in the calculations not only for the static analysis but for the dynamic analysis.

Table 7.1 RC wall stiffness at top wall level

WALL CODE	I_s mm^4	E_t N/mm^2	K_e KN/mm	K_{cr} KN/mm	K_1 KN/mm	K_L KN/mm	K_e/K_1	K_e/K_L
SW1	3.15E06	39568	19.94	---	---	1.25		16.0
SW2	3.15E06	39568	19.94	4.5	3.0	1.25	6.6	16.0
SW3	3.15E06	39568	29.66	11.7	7.4	2.51	4.0	11.8
SW4	50.53E06	39576	59.33	23.2	19.3	4.6	3.1	12.9
SW5	75.78E06	43551	65.29	29.0	21.7	2.9	3.0	22.5
SW6	50.53E06	39576	59.33	23.1	20.0	3.4	3.0	17.5
SW7	75.78E06	43551	65.29	29.0	21.3	4.6	3.1	14.2
SW8	51.84E06	39782	59.64	23.7	18.6	4.0	3.2	14.9
SW9	51.84E06	39782	59.64	23.7	18.7	4.0	3.2	14.9

The stiffness at MDL-11 and MDL-22 are considered as an indication of stiffness at ultimate conditions for scale 1:5 and 1:2.5, respectively. For the aspect ratio 2 walls, the ratio of the elastic to ultimate stiffness was between 10 and 15, for specimens that failed in bending. A higher value was shown for SW6 which deteriorated due to shear, and was even higher for SW5 which failed in shear. For well designed walls, stiffness deterioration is a function of displacement ductility. In EQ resistant design, the expected shift in the response frequency, due to stiffness deterioration, should be taken into consideration since it may result into higher design forces.

7.3 Limit states

The different limit states achieved by the walls are presented in this section. The crack level is usually given by many researchers as the first limit state. As seen from section 7.2, some degree of micro-cracking was present in all specimens prior to testing and, consequently, defining the stage at which initial cracking is observed bears little significant.

7.3.1 Yield level

Yield level is defined here as the level at which the first main reinforcement bar yields. Table 7.2 shows the quantities at the yield limit for both experimental and analytical results. Top displacement δ4 (figure 3.5) is given for comparison purposes.

Table 7.2 Yield limit quantities

WALL CODE	Bar ϕ (mm)	Yield strain	Exp. δ4 (mm)	Anal. δ4 (mm)	Exp. Load (KN)	Anal. Load (KN)	Comments
SW1	6	2750		---	SA100		EQ
SW2	6	2750	1.8	1.12	17.5	16.2	
SW3	6	2750	1.8	0.85	22.5	22.4	
SW4	12	2500	2.2	1.55	76	75.0	Estimate §
SW5	16	2600	2.5	1.74	110	105.9	Failure•
SW6	12	2500	2.4	1.54	74	75	
SW7	16	2600	3.0	1.75	107	105.9	Bending ¶
SW8	10	2150	2.4	1.42	71	70.6	Estimate §
SW9	10	2150	2.4	1.42	70	70.6	Bending ¶

§ Both critical strain gauges were unreliable for walls SW4 and SW8. The experimental values given for these walls in the above table are estimates based on the remaining data and information from similar walls.

¶ In walls SW7 and SW9, one of the main extreme end bars yielded at a lower displacement than the other, hence out-of-plane bending is suspected to be one of the main reasons for non-uniform distribution of strains at the same section location.

• Shear failure prior to achieving the ultimate load.

SW5 failed just before achieving yield for LHS sway while yielding already started for RHS sway. For this wall strain gauge number 4 yielded at about 110 KN, which may indicate that the strain gauge readings of the bottom extreme locations are not very reliable and that a better correlation between experimental and analytical results may exist.

As shown in table 7.2, despite the difficulties in defining precisely the experimental yield load, there is a close agreement between the experimental and analytical values. Nevertheless, the top vertical displacements $\delta 4$ vary significantly. The experimental displacements are much higher than predicted analytically. Since at this load the bottom level strains are similar in analysis and experiments, the implication is that much higher levels of strain are present throughout the height of the wall in the experiments. This indicates that some type of concrete dilation is occurring even before yield during cyclic loading. As discussed in chapter 5, this dilation occurs due to the imperfect closing of the crack surfaces mostly as a consequence of shear deformation.

The level of yield load is an important design parameter, since it can be easily calculated. It can be used to predict the ultimate capacity, the plastic hinge zone and the ductility of a section. A number of parameters determine the absolute value of the yield moment M_y, as well as the ratio of yield to ultimate moment M_y/M_{ult}.

Both M_y and M_y/M_{ult} increase with increased percentage of flexural reinforcement $\rho\%$. The same effect is brought about by increasing the concentration of reinforcement near the wall extremities since the reduction of the lever arm after yield is minimised.

Increased concrete confinement does not increase M_y significantly, since the development of the confining stress does not occur at the early curvatures for walls with no axial loads. On the contrary, M_y varies almost proportionally with the steel yield stress.

In the useful range of variation, increased axial loads cause an increase in the section capacity. However, the increase in M_y is much more dramatic. At high axial loads, compressive yielding precedes tensile yielding, which, in some instances, does not occur at all.

Both experimental and analytical results indicate that the effect of cycling does not alter the level of M_y significantly. Experimentally, it has been shown, that prior to yield, cycling does not lead to significant deterioration of strength and stiffness. Nonetheless, some net extension does occur as will be discussed in section 7.5.

7.3.2 Ultimate limit states

The analytical calculations were based on ultimate strains given by equation 5.17, as shown in table 7.3 below. The confinement factor 'α' as given by the draft EC8 is considered to yield conservative results, and hence, for analytical flexural deformations these values were chosen so as to achieve a better · correlation with the experimental values.

Table 7.3 Confinement data

WALL CODE	Hoop ϕ (mm)	ω_{wd}	α	ε_{cc} x 10E06	ε_{cu} x 10E06	f_{cc} N/mm^2
SW1 - 3	2.8	0.185	0.5	3032	12750	49.25
SW4	6	0.24	0.5	3251	15500	51.00
SW5	4	0.12	0.25	2311	6500	43.00
SW6	4	0.085	0.5	2447	7750	44.25
SW7	6	0.31	0.25	2850	11250	47.75
SW8	4	0.125	0.5	2674	9750	46.25
SW9	4	0.18	0.5	3001	12500	49.00

The ultimate load and corresponding displacement is shown in table 7.4 for the experimental and analytical results. Displacement δ_3 refers to the top wall horizontal displacement as shown in figure 3.5.

The analytical ultimate forces are higher than the experimental ones for all scale 1:2.5 walls (except SW6). This is expected since the effects of cyclic load as well as shear are not considered in the analytical results. The ultimate capacity of SW6 is higher than the corresponding wall SW4 which has higher confinement and shear reinforcement. The only plausible explanation of this may be a higher than average steel strength. In fact, the definition of the experimental yield strength in the 12 mm diameter bars was not distinct. In the analysis the lower value of yield strength shown in table 3.6 has been used. The ultimate strength of the wall becomes 108.5 KN when the higher value of yield strength is used in the analysis, a value which is in better agreement with the experimental result.

The analytical predictions are very close to the experimental results for all the walls that failed by steel fracture. This is to be expected, since the reinforcement strength is known exactly at failure strain.

Table 7.4 Ultimate limit state

WALL CODE	Exp. δ_3 at V_{cmax} (mm) §	Exp. δ_3 at failure (mm) §	Anal. δ_3 at V_{cmax} (mm)	Exp. V_{cmax} (KN)	Anal. V_{cmax} (KN)	Comments on exp. failure
SW1	---	13.4	8.1 (10.4)	~24•	21.2 (20.6)	Steel fracture ¶
SW2	9	12	8.0 (10.15)	22.5	22.22 (21.6)	Steel fracture ¶
SW3	10	13	4.54 (6.18)	30.4	30.95 (30.3)	Steel fracture ¶
SW4	10	24	16.03	104.0	112.8	Crushing
SW5	10	9.6	9.37 (4.00)	117.3	131.4 (116.0)	Shear failure #
SW6	18	22	9.10	107.8	103.7	Crushing / Shear
SW7	18	22	10.44 (13.82)	127.3	128.3 (134.3)	Steel fracture ¶
SW8	22	26	12.16	95.3	107.0	Crushing
SW9	22	26	16.5	-97.4	112.1	Crushing

§ Two values are given for experimental displacements, one corresponding the to ultimate load and one to the displacement at failure. For the analytical results these two displacements are the same.

¶ Failure in all scale 1:5 models was due to fracture of the extreme 6 mm bars at the level of the bottom strain gauges. The failure of specimen SW7 was also due to failure of the 6 mm bars even though they were not positioned at the extremes. The values in parenthesis represent the analytical results with the steel ultimate strain as control.

• The shake-table wall failed at an equivalent force of about 24 KN, as estimated from filtered accelerations.

The values in parenthesis represent the analytical results close to the experimental failure load.

The ultimate moment capacity M_{ult} is required not only for flexural but also for shear design purposes. In calculating M_{ult}, a certain control parameter has to be satisfied. Limits are usually imposed on steel ultimate strain by codes, so as to avoid fracture of steel. Concrete ultimate strain becomes, therefore, the control parameter for the determination of M_{ult}. Moreover, other parameters also influence the value of M_{ult}, the most of the important of which are discussed below.

In the parametric study of chapter 6 the flexural moment capacity was normalised with respect to a control specimen. Hence, the results become independent of the wall scale, or even the shear ratio.

An almost linear increase in M_{ult} is shown in figure 6.1 with increase in the percentage of reinforcement. Charts derived in a similar manner can prove useful guides in design, enabling the rapid estimate of percentage of reinforcement for given wall dimensions. It is interesting to note that the uniform distribution 'UD' of reinforcement is effectively a lower bound, while the extreme boundary concentration 'BC" is an upper bound to the moment capacity. In design, it can be easily determined which type of distribution applies by comparing with the three given cases.

The effect of concrete strength f_{co} is more important in unconfined concrete walls than for moderately confined walls. Nonetheless, the overall effect of f_{co} is not very important. A 100% increase in the concrete strength increases M_{ult} by less than 5%, as shown in figure 6.6. The same effect can be achieved by increasing the ultimate concrete strain through confinement reinforcement.

The above highlights a common error by researchers who back-calculate the concrete strength from the section capacity. A 5% error in the value of M_{ult}, which can easily arise in experimental work, can lead to 100% overestimate of the concrete strength. Hence, one of the principle conclusions from the work of Lefas (1988), that the capacity of RC walls is independent of the uniaxial concrete strength, can only be a result of such errors. In fact, frictional forces due to the direct application of forces to the specimens in the above-mentioned research programme, are estimated to have increased the section capacity by up to 10%. Such errors cast considerable doubts regarding the shear strength calculations which were based on the large concrete overstrength reported.

The increase in M_{ult} is much less for high confinement levels, since the peak steel strength will control. Hence, the significance of the steel ultimate strain limits is demonstrated.

Increase in steel yield strength 'f_y' and ratio f_{ult}/f_y also increases the moment capacity. However, for the value of strain hardening stiffness used in the analytical model (3000 N/mm^2), the ultimate steel stress was not achieved for the f_{ult}/f_y ratios higher than 1.3. This highlights the following issue that should be considered in design. The post-yield capacity of steel will not necessarily be developed if it only occurs at very high strains.

A very significant variation in moment capacity may occur due to the presence of axial loads as shown in figure 6.16. Where a variable axial load is applied, such as in earthquake loading, the bending capacity should be designed with consideration of both lateral and axial forces. Alternatively, dimensioning should be undertaken based on the moment corresponding to the least compressive force.

7.4 Horizontal deformations

Horizontal measurement analysis has been discussed in section 3.6. It has been suggested that expansion at the top beam is negligible. This has been verified in the experiments by comparing top horizontal displacements 3 and 18 (figure 3.5). However, displacements within the wall height were not checked for expansion. It became obvious during the experiments that spalling of concrete and opening of the 4 mm diameter stirrups was affecting measurement reference points at post-yield displacement levels. This makes the obtained data difficult to utilise for shear calculations.

The deformed shape of the wall can be obtained by using the values of the displacements at the different heights. An interesting case is demonstrated for SW5 in figure 7.6. The effect of spalling, after failure in this case, is seen at the base level. Failure occurred on the reverse MDL-10 and the change in the deformed shape is clear. Deformation components attributed to each deformation mechanism (flexure and shear) are discussed hereafter.

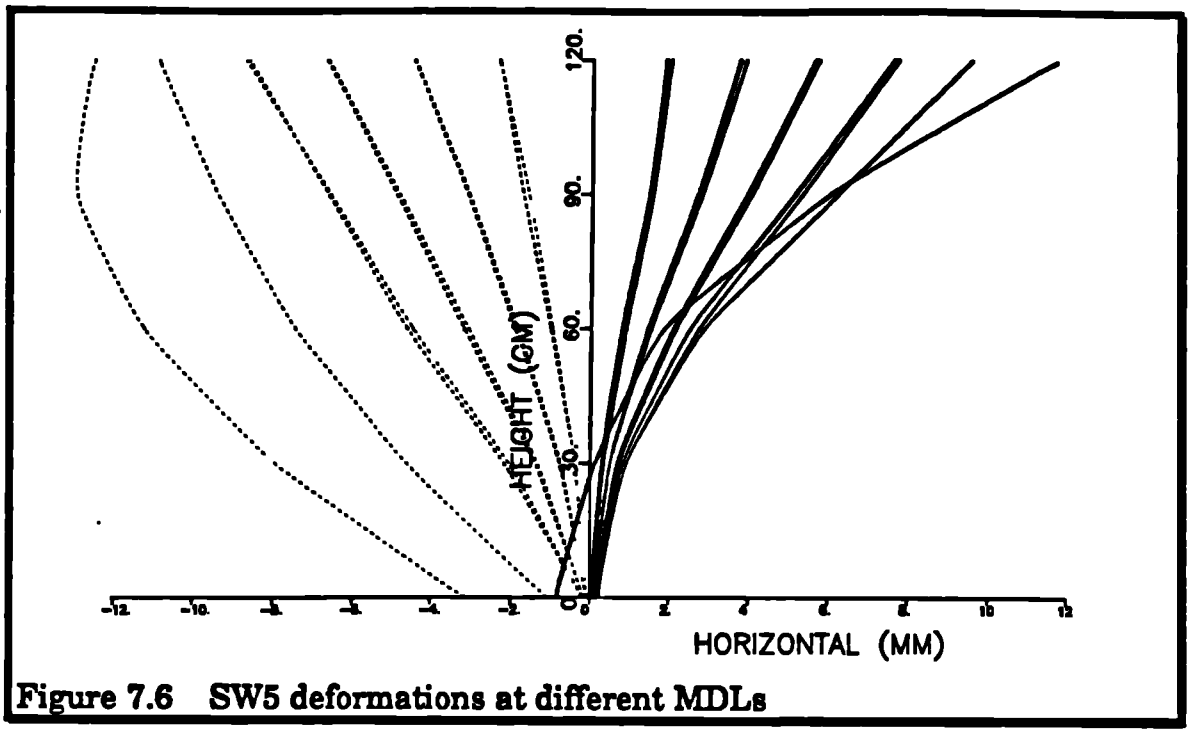


Figure 7.6 SW5 deformations at different MDLs

7.4.1 Flexural and shear components of deformation

The decomposition of flexural and shear displacements was performed for wall SW9. The general observations from the five graphs presented in Appendix A (Figures A.(9).16 - A.(9).21) are as follows:

(a) The flexural stiffness decreases at a very slow rate prior to yield. Thereafter, the unloading stiffness progressively decreases at a slow rate.

(b) The reloading flexural stiffness decreases much faster after yield. Near failure it is only about one third the level of the unloading stiffness.

(c) Shear stiffness decreases progressively until yield. As with the flexural unloading stiffness, following yield it progressively decreases at a slow rate.

(d) After yield, the shear deformations in reloading exhibit two distinctly different portions. In SW9, up to about one third of the reloading force, the shear stiffness is very low and a considerable reversal of displacement takes place. Up to this load level, the strains in all flexural bars are positive. The stress in the extreme bars should be at a state just before yielding in compression and hence, the average

strain of the bottom sections is positive. Under these conditions the compressive stresses in concrete should ideally be zero, in which case the moment is resisted purely by the steel cage. However, imperfect closing of cracks may induce some compression in concrete.

(e) The second portion of the reloading shear stiffness is much stiffer than the first , but is still lower that the unloading shear stiffness. The increase in stiffness may be attributed to the increased contribution of concrete in resisting shear. At this level the cracks in the compressive area from the previous loading direction would have closed.

(f) The area within the hysteresis loops which represents the energy dissipation is considerably higher in flexure than in shear.

(g) The flexural deformations given by using the method of area $\alpha 1$, are lower than predicted by method of area $\alpha 2$. This implies that calculations made by using information from just the top level can lead to inaccurate results.

The results were further processed at peak displacements. Figure 7.7 below shows the component displacements versus applied force.

It is clear that both the flexural and shear components of deformation increase much more rapidly after yield, despite the fact that the force increases only slightly. The above graph shows the results for both cycles at the same MDL, the load being higher on the virgin cycle rather than the second cycle. As it can be seen, especially in the post-yield stages, the shear deformations increase in the second cycle, and hence, the drop in the force is partly due to the drop in flexural deformations.

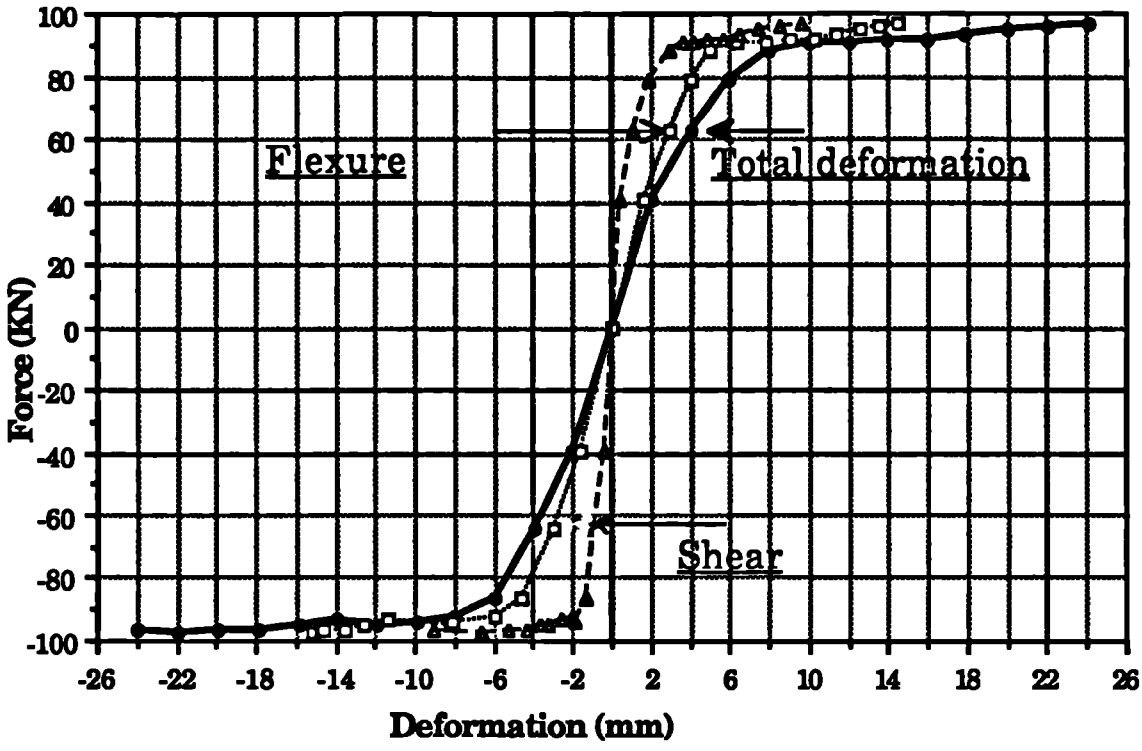


Figure 7.7 Force versus deformations at peak displacement

Of particular interest in understanding the components of each deformation, is the plot of the ratios with respect to the total deformation shown in figure 7.8.

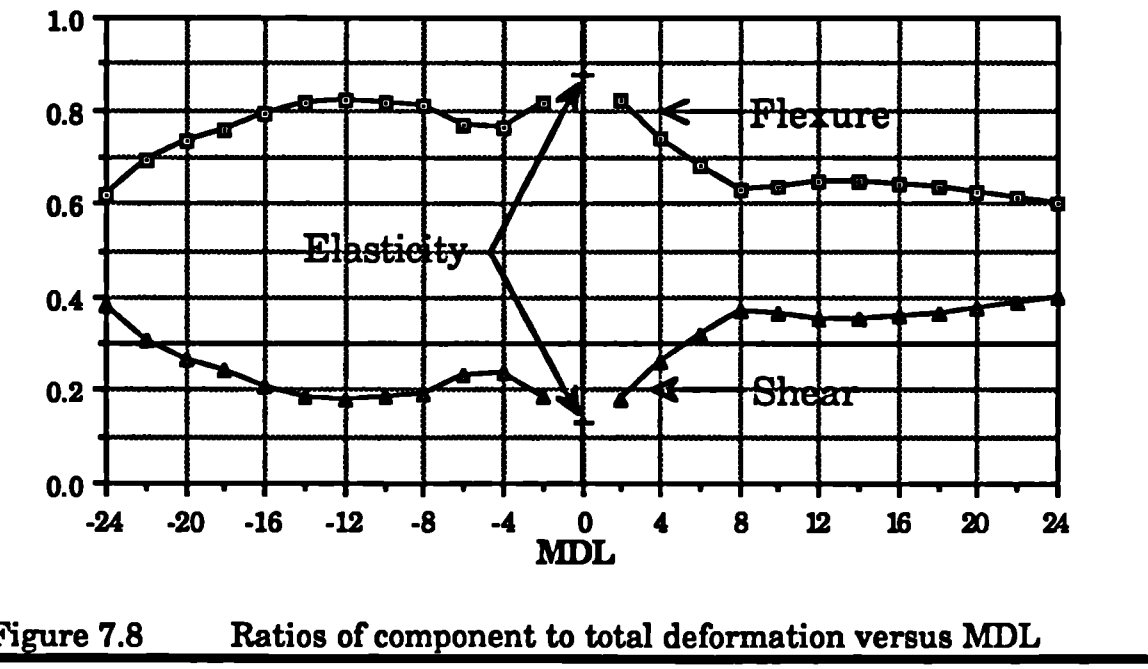


Figure 7.8 Ratios of component to total deformation versus MDL

The shear ratio is increasing from about 0.15 as obtained from elasticity calculations (section 7.2.2), to about 0.4 at ultimate conditions.

However, the deformations are not symmetric in both directions of loading. This implies a shift of the permanent shear deformations locked in after unloading. This is best illustrated in figure 7.9 showing the permanent deformations at zero load with respect to MDL.

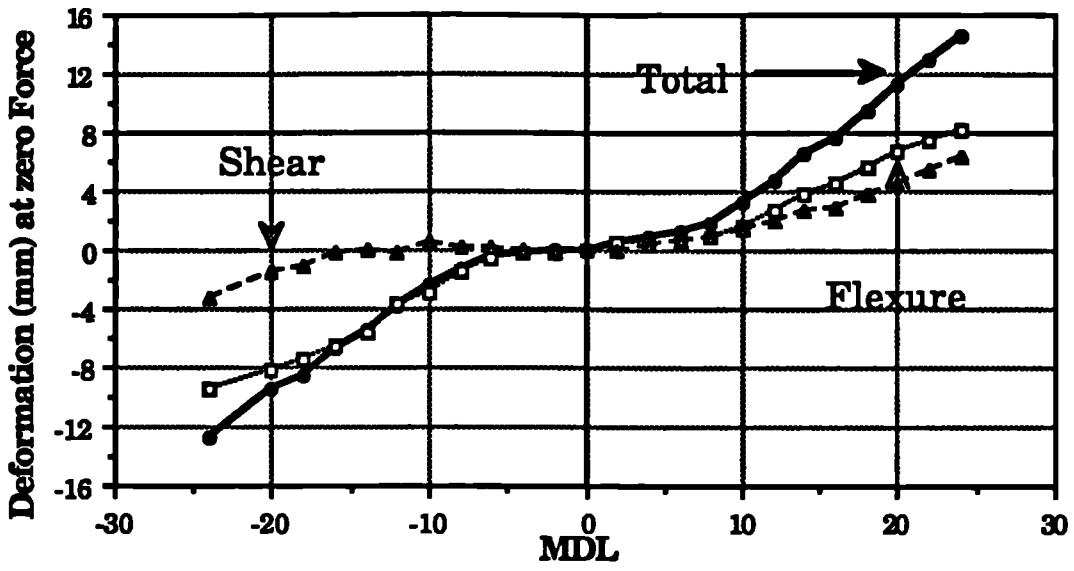


Figure 7.9 Deformations at zero force versus MDL

As seen from figure 7.9, the permanent shear deformations are higher for RHS than LHS MDL. Up to MDL-16 the RHS permanent shear deformations do not seem to be reversed. Reversal of permanent shear deformations is, nonetheless, observed after MDL-16. However, spalling of the concrete cover may be contributing towards the indicated reversal, since the horizontal transducer readings will be biased. It is therefore very difficult to conclude that shear deformations would be reversed at all during such type of loading. The above is a strong indication of the elastoplastic nature of shear deformations. Moreover, it seem that the stiffness during the low levels of load at which the permanent deformations are developed, is equal in both directions.

7.4.2 Strains in lateral reinforcement

The gauges on lateral reinforcement were used only in the 1:2.5 experiments. In general the readings are very low prior to web cracking. The opening of the web cracks causes a noticeable increase of the tensile strains when increasing the MDL at load levels prior to yield. At both RHS and LHS values of maximum force the strain is maximum and decreases with decreasing shear force. After cracking the tensile strain at zero load

progressively increases with increasing MDL. The lateral dilation of the wall is another indication of incomplete closing of the flexural cracks. The lateral extension of the wall induces additional tensile stresses in the shear reinforcement. This effect is equivalent to prestressing the wall laterally and may increase the shear stiffness prior to yielding of the shear reinforcement. Nonetheless, following yield of the lateral reinforcement, its effectiveness may be reduced in resisting shear in the opposite direction.

For the walls which eventually failed in flexure, following yield, the lateral strains varied almost linearly with the absolute value of the shear force. The maximum strain achieved was in general dependent on the amount of reinforcement available and the location of the stirrup. The stirrup closest to the top beam was not stressed at high strains. This is most probably due to the confining effect of the stiff top beam, as well as the presence of lower axial strains and fewer cracks.

In wall SW5 the lateral reinforcement yielded at mid-height of the wall just after yielding of the flexural reinforcement during RHS direction of loading. The consequence was an abrupt shear failure in the reverse direction. The stirrup closest to the bottom beam did not yield at failure but only afterwards. It is clear that stirrups not spanning the portion of the critical shear crack in the web do not contribute towards the ultimate shear resistance of the member. This is further discussed in chapter 8.

In SW6, gauge 21 (figure A.(6).36) indicated that the stirrup at three quarter height of the wall yielded after the wall exceeded the yield load. The other strain gauges on stirrups of this wall did not continue to operate after yield load. The yielding of the stirrups, was also followed by opening of stirrups at the boundary at very high MDLs. The consequence of the anchorage inadequacy of stirrups was the progressive deterioration of the shear stiffness of this wall.

In SW8, yielding of the top stirrup took place following MDL-10. Until then the behaviour of the wall was similar to SW9. Both these walls were constructed with the improved stirrup detail shown in figure 3.7. Yielding of stirrups progressed eventually downwards. The increase in post-yield strain was not high enough to allow damaging shear cracks to develop. Since following MDL-10 the ultimate load did not increase significantly, it is concluded that the spread of yield during cycling was not due to increased applied shear stresses. It is, therefore, a consequence of the deterioration of concrete shear strength with cycling. However, the extra strains due to the

imperfect closing of the cracks crossing the shear reinforcement is likely to have contribute to the same observation.

7.5. Base rotation

In experimental work some degree of rotation is unavoidable at the foundation level since, both the bending and axial stiffness of the bottom beam is not infinite. The base vertical transducers (δ14 - δ15 location shown in figure 3.5 & figures A.(4-9).11) were used to estimate the rotation and the equivalent vertical 'δ_{vtop}' and horizontal 'δ_{htop}' displacements at the top of the wall as well as the rotational stiffness.

Table 7.5 Foundation rotations

WALL CODE	Ultimate rotational stiffness KN/rad	δ_{vtop} at V_{cmax} (mm)	δ_{htop} at V_{cmax} (mm)	δ_{htop}/δ_h at yield %	δ_{htop}/δ_h at failure %
SW4	343900	0.175	0.35	4.8	1.5
SW5	900000	0.08	0.16	2.0	1.6
SW6	540000	0.12	0.24	2.9	1.3
SW7	331000	0.23	0.46	4.8	2.0
SW8	712500	0.08	0.16	2.2	0.6
SW9	650000	0.09	0.18	2.5	0.7

The rotational stiffness '$K_{\theta b}$' of the base varies with the level of maximum load applied to the specimen. Even though initially there seems to be softening of the stiffness prior to achieving the ultimate loads, $K_{\theta b}$ can be considered to be constant. The contribution of the base rotations to the lateral deformations at yield and ultimate loads does not exceed 5% and 2%, respectively. This was achieved by holding the foundation beam down close to the areas of transmission of the forces through the clamping system described in chapter 3. The effect of the base rotation can, therefore, be

considered to be negligible for the purposes of comparisons of experimental with analytical results.

7.6 Vertical deformations

7.6.1 Vertical displacements

As expected, top wall displacements in tension are much higher than displacements in compression. Whilst the experimental tensile deformations δ_4 progressively increased with increasing MDL, the compressive deformations δ_5 tend to stabilise to a maximum value. Table 7.6 gives the maximum tensile values of δ_4, δ_8, δ_{11} and maximum compressive values of δ_5, δ_9, δ_{12} for cyclic experiments at scale 1:2.5 and the corresponding top values for the remaining models, including the monotonic analytical results.

The cyclic loading is expected to affect the vertical extension to some extent. However, it is obvious from the above table that expected compressive displacements are also much smaller than the experimental. This suggests that the dilation of concrete causes extension in the entire wall and not just the tensile area. However, most of the net extension is a result of inelastic strains building up in the steel as will be seen in the next section 7.6.2.

The net wall extension as given by the average vertical displacements are included with the experimental results in Appendix A. It is clear from those figures that the net extension of the wall is concentrated in the bottom quarter where yielding of the flexural reinforcement takes place. The is true, to a lesser extent, for wall SW6 which has yielding occurring higher than the remaining models.

Table 7.6 Vertical maximum deformations

WALL CODE	Exp. δ_4 (mm) δ_8 (mm) δ_{11} (mm)	Anal. δ_4 (mm)	Exp. δ_5 (mm) δ_9 (mm) δ_{12} (mm)	Anal. δ_5 (mm)	Comments on exp. results
SW1	3.5	2.9	-.93	-0.82	BCs §
SW2	5.3	2.8	-1.65	-0.87	BCs §
SW3	5.3	2.4	-0.9	-0.75	
SW4	11.1 3.9 4.25	8.3	-0.7 -0.7 -0.9	-2.3	Accuracy ¶
SW5	3.2 2.2 1.6	2.0	-0.75 -1.0 -.75	-0.80	Shear failure
SW6	7.8 5.8 5.0	4.77	-0.75 -2.0 -2.0	-1.44	Not symmetric •
SW7	8.75 7.3 6.7	5.72	-1.1 -1.0 -1.0	-1.4	
SW8	11.0 10.5 10.2	6.14	-0.75 -0.9 -1.2	-1.7	
SW9	10.8 10.4 10.5	8.15	-0.75 -0.65 -0.7	-2.1	

§ The boundary conditions of the test-rig used necessitate that the inertia mass will be taken by the specimen is a net positive vertical displacement occurs

¶ The transducer readings were affected by loss of contact with the reference plates, and hence the accuracy is not good.

• The vertical displacement were not symmetric for the two directions of displacement.

Up to the yield load, net extension is very small at the quarter-height level and it seem that it is almost linear with height. At this stage, any net extension can only be attributed to concrete dilation. Near failure, the net extension deviates from its consistent increase. In the case of SW5, which failed in shear, the average of the vertical deformations sharply reverses to net shortening. This has a serious implication on adjacent structural components which will have to take not only the extra lateral load but also any axial load that the wall may have been carrying.

7.6.2 Vertical strains

7.6.2.1 Bottom extreme fibre strains

At the extreme fibres the load versus strain loops bear similarities with the load versus vertical displacement loops. The compressive strains increase until yield and then they seem to stabilise to a certain maximum value before they reduce, sometimes becoming tensile strains. In tension, the strains increase progressively and most of the times exceed the limits of the strain gauges used. The area inside each inelastic loop is considerable. This points towards the fact that the main steel reinforcement at the extremities constitutes one of the major energy dissipation mechanism.

At the lower quarter of the wall, the bars at the extremities were subjected to the highest reversals of strain. As a result, a large number of these gauges were not functioning properly; many of them failing just before yield. Since the strain gauges are located at a slightly weaker section due to grinding of the reinforcement, it is expected that slightly higher strains would be recorded than at adjacent sections. The effect of permanent plastic strains (both locally under the strain gauge and overall in the material) makes the determination of actual stresses from strains impossible.

From the limited number of gauges working after a very high number of excursions in the inelastic range (SW2 gauge 1,2,7; SW3 gauge 1,3,4; SW6 gauge 2; SW9 gauge 1,8,9), it is interesting to note the following :

(a) Initial unloading in tension and compression is at a constant sharp gradient; the latter being sharper.

(b) The gradient decreases when crossing the zero load from unloading.

(c) On reloading in compression a low gradient is followed up to about 50% of the ultimate load.

(d) On reloading in compression an increase in the gradient occurs after 50% of the ultimate load in reloading.

(e) On reloading in tension there is a gradual softening of the gradient. Increase in the maximum plastic strain occurs in general when a new MDL is applied.

The above observations are also valid for the analytical results given in Appendix B. Initial unloading takes place at the maximum stiffness both for steel and concrete and it is therefore expected to be almost identical to the initial loading stiffness. On complete unloading, the strains in the tensile reinforcement will start to reverse beginning first with the extreme fibre. Initial reloading occurs at a lower stiffness which depends on the previous values of maximum plastic strains. When the yield strength is exceeded, an even lower stiffness is present. In the analytical model, the concrete does not carry any stresses until the previous unloading plastic strain is reached. When the concrete on either side of the crack establishes contact during reloading, the stiffness increases. This occurs at about 50% in the experiments due to concrete dilation at the crack interfaces but occur at about 80% in analysis.

7.6.2.2 Bottom boundary strains

The gauges on the main longitudinal bars further away from the ends were subjected to less severe strain reversals (SW2 gauges 3,4,5,6; SW3 gauge 2; SW6 gauges 3,4,7; SW7 gauges 3, 7; SW8 gauges 3,5; SW9 gauges 7) and hence, lasted longer than the ones at the extremities. The most important features of the force versus strain curves of these bars is summarised below:

(a) After the yield load, the plastic tensile strain is not recovered and hence, a progressive increase in the value of strain is observed. This implies a continuous extension of these bars.

(b) Reloading in tension is at an almost linear gradient until yield. Increase in tensile plastic strains occurs when there is an increase in MDL.

(c) Unloading in tension is of similar gradient to reloading. Moreover, after yield at the end of the tensile half non-virgin cycle, the gain in maximum plastic strain is in general nearly zero.

(d) On reloading in compression the tensile unloading gradient is maintained until about 50% of the load. Following that, the strain remains almost constant, while in some cases a loop is observed in the force versus strain curve near the maximum load.

(e) During most of the unloading regime in compression, the strains remain almost unchanged.

(f) The energy in non-virgin cycles is very close to zero.

The above observations are less applicable to the longitudinal web reinforcement in walls SW8 and SW9. Additionally, the boundary bars in SW7 being closer to the ends of the wall, dissipate more energy and reverse part of the accumulated tensile plastic strains.

The analytical results comply in principle with most of the above observations. The main difference is in the accumulation of tensile plastic strains which is much less than in the experiments. Additional information that can be obtained from the analytical results is that at very high strain levels (not possible to monitor with the strain gauges used), the reloading stiffness in tension deteriorates in a similar manner to the extreme fibre bars.

The very sharp gradients and loops observed in the force versus strain curves at high compressive loads, are due to a shift of the neutral axis from one side of bar through to the other. In fact, this can be used as a guide for the location of the neutral axis depth.

7.6.2.3 Bottom web strains

The number of strain gauges in the web reinforcement is much less than in the boundaries. Gauges were placed only in the scale 1:5 walls. Gauges nearer to the boundaries behaved similar to the gauges described in the previous section. Only gauge 5 of SW7 was located exactly at the centre and in the limited number of inelastic excursions it was yielding in tension in both directions of loading. This implies a continuous extension of bars in the centre. Much higher levels of net plastic tensile stresses are also observed in the analytical results.

7.6.2.4 Mid-height strains

Gauge readings at mid-height levels are available only for the scale 1:2.5 walls. All strain gauges at this level were placed on the main reinforcement, most of them at the ends. The strain readings indicate that in general the flexural reinforcement remained elastic above the quarter height with the exception of wall SW6. The typical shape of force versus strain at this level consists of two nearly linear portions with two different gradients. Change of gradient occurs on reversal of load. The gradient in the sense of loading causing tension is four to five times less than the

opposite sense; this value being less for bars further in the section. All the above points are also observed in the analytical results for wall SW9.

In the experimental results a small shift of strains at zero load occurs progressively. Most of this shift occurs during the initial increments in MDL. It is attributed to the opening of cracks and the subsequent imperfect closing, leaving small residual tensile strains in the reinforcement.

7.6.2.5 Top wall strains

The top of the wall is subject to low levels of moment and as a result the flexural stresses should be small. However, for compatibility with the relatively stiff beam, a local state of distribution of stresses may prevail.

At the very early stages of loading the strains of the longitudinal reinforcement indicate a near elastic uncracked stiffness. The loss of tensile strength in concrete is indicated by a large increase of the tensile strain during the increase of MDL prior to yield. Following cracking of concrete, the shape of the curves are similar to the ones at mid-height at lower levels of strain and compare well with the analytical results. Surprisingly, the values of tensile strain reach many times more than half the value of yield strain. The implication of this is that the main flexural bars have achieved more than 50% of the ultimate force at the beam level.

7.7 Plastic hinge length

The most significant part of the overall vertical extension δ_{vt} is developed in the lowest quarter of the wall. In this portion of the wall considerable yielding of the flexural reinforcement occurs. The extent of spreading of yield in the main reinforcement 'H_p' (height of the plastic hinge zone) can be calculated from the experimental results by assuming that:

(a) The section will yield at a given level, if the applied moment exceeds the yield moment M_y as obtained at the base (or maximum moment location in the case of beams).

(b) The deterioration of the section and plastic strains in the part of the wall which has not yielded, or failed in shear, is insignificant.

(c) The ultimate moment capacity M_u of the section is known or can be calculated.Then,

$$H_p = \frac{(M_u - M_y)}{V_u} = \left(1 - \frac{V_y}{V_u}\right) a_r H \qquad (7.8)$$

By using tables 7.2 and 7.3 and equation 7.8, the length of the plastic hinge is calculated as shown in table 7.7. The difference between ultimate to yield stress as a ratio is also given since it is one of the variables that influences the plastic hinge length.

Table 7.7 Plastic hinge height

WALL CODE	$\frac{(f_{su} - f_{sy})}{f_{su}}$	. Exp. $H_p / a_r H$	Ana. $H_p / a_r H$	Exp. H_p (mm)	Ana. H_p (mm)
SW1	0.08	---	0.26	---	228
SW2	0.08	0.22	0.27	193	235
SW3	0.08	0.26	0.27	164	170
SW4	0.16 - 0.21	0.27	0.34	340	429
SW5	0.09	0	0.1	0	126
SW6	0.16 - 0.21	0.31	0.28	391	354
SW7	0.09	0.16	0.17	202	215
SW8	0.21 - 0.28	0.25	0.34	278	430
SW9	0.21 - 0.28	0.28	0.37	303	468

Despite the difference in the reinforcement properties and the predictions of analysis, specimens SW3 and SW4 have a similar spread of the plastic hinge. The concentration of main reinforcement near the extreme fibres in SW7 also seems to have reduced the height of the plastic hinge. In SW9 both gauges indicate yielding at quarter height. In SW8 one gauge showed considerable accumulation of plasticity which may be the result of out-of-plane bending. In SW6 the plastic hinge spreading above the one quarter height of the wall is seen from the strain gauge 10 - 13 readings.

The analytical results for all walls, with the exception of SW6, predict a longer plastic hinge length than determined experimentally. This is due to the higher ultimate moments calculated. For design purposes, the proposed method would therefore be on the conservative side, and can be used for determining and detailing the plastic hinge zone.

The heat sensing camera detected some temperature increase in the plastic hinge zones, but the increase was very close to the lower limits of the camera, and hence the measurements cannot be used for determination of the plastic hinge length. However, no heat was detected in the web area and hence, the energy dissipation in this area must be considerably lower than in the boundaries.

As shown above, the yield to ultimate moment capacity M_y/M_{ult} ratio is also the ratio of the unyielding part of the wall; the remainder of the wall being considered as the plastic hinge zone. In the parametric study of chapter 6, M_y/M_{ult} was plotted against all the variables.

The extent of the plastic hinge zone is observed to decrease with increasing percentage of flexural reinforcement $\rho\%$, as well as with increasing the concentration of the same reinforcement in the extreme fibres. An increase in the plastic hinge zone would occur with increasing amounts of confining reinforcement with a tendency to stabilise at high values of confinement since the steel full plastic capacity will be reached.

Predictions from an elastoplastic steel model with no strain hardening will underestimate the extent of the plastic hinge zone. High values of f_{ult}/f_y will result in larger plastic hinge zone.

If calculations for the M_y and M_{ult} are not available, 50% of the height from the base of the wall to the point of contraflexure can be considered as a safe upper bound for the extent of the plastic hinge zone for design purposes.

At high axial loads the plastic stresses will be present only in compression zone and the extent of the plastic hinge zone may be low. However, the detailing requirements for walls to resist high axial forces should be similar to the detailing of columns, unless the level of normalised axial load is limited to about 0.2.

7.8 Out-of-plane displacements

The out-of-plane displacements recorded were a consequence of the test-rig layout. The slightest misalignment between the loading frame and the ends of the beams, would tend to cause twisting of the top beam during loading. This can be seen in figures A.(4-9).14 as a change of slope when reversing the loading direction. However, during reversal of the loading, when the load is transferred from one end of the frame to the other, the wall is totally free from any forces. Consequently, if any of the out-of-plane deformations were due to the stiffness of the wall in that direction, a recovery of the elastic deformations could have occurred. This reversal did not take place after yielding since some of these deformations were locked in. In the last experiment it was possible to reverse the direction of movement in these deformations by adapting the adjustable end of the frame.

The initial stiffness of the wall out-of-plane is about 100 times less than for loading in-plane. The extra strains at the extreme fibres associated with 10 mm out-of-plane displacement are equivalent to 0.1 mm in-plane, and hence, cannot be considered to play any significant role in the overall behaviour. As discussed in section 2.2.3 Aoyama and Yoshimura (1982) demonstrated experimentally that the effect of out-of-plane loading was only important if it exceeded 50% of the out-of-plane yield moment OPYM. In this case even if the full out-of-plane deformation is considered to be due to a moment, this moment would not have exceeded 20% of the OPYM.

7.9 Ductility

The ductility of a section is dependent on the controlling strain at failure. Steel fracture can limit the ductility levels, as observed in walls SW1, SW2, SW3 and SW7. However, the culpable reinforcing bars had ultimate strains far lower than specified by earthquake resistant codes. By assuming that neither steel fracture nor shear failure will occur, the ductility of a section is limited only by the ultimate concrete strain.

By examining the results of the parametric study in Chapter 6, reference is made both to the curvature ($\mu_{1/r}$) and displacement ductility (μ_Δ). The basic difference between the two ductilities lie in the fact that $\mu_{1/r}$ can be calculated easily from the section properties, while μ_Δ is related to the member properties, and includes implicitly the length of the plastic hinge zone. Additionally, the correct determination of μ_Δ requires an accurate estimate of the shear deformation. The latter has not been included in the parametric study, and hence the value of μ_Δ represents only the flexural component of deformation.

The relation between the two ductilities is shown in figure 7.10 for all the parametric studies of chapter 6.

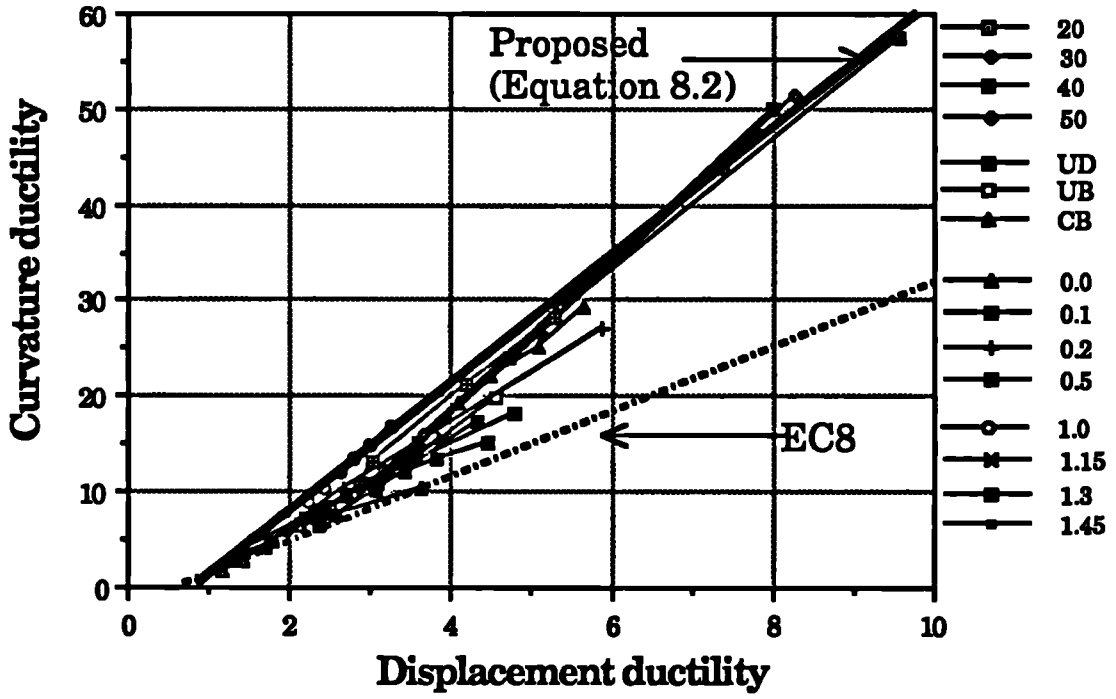


Figure 7.10 Curvature versus displacement ductility for all parametric studies of chapter 6

The EC8 equation (2.4) is based on the approximation that the curvature in the plastic hinge zone is constant as shown in figure 7.11. In CRELIC the curvature is calculated at 8 locations over the height of the wall and the curvature distribution at ultimate load for the control specimen of chapter 6 is also shown in figure 7.11. The analytical results indicate a lower value of displacement ductility than expected by the EC8 equation for the same curvature ductility. Nonetheless, accounting for the fact that the ratio of shear to the overall top displacement increases from yield to

ultimate levels, the displacement ductility will increase as well, and hence, the EC8 equation is on the right side of the expected shift of the results.

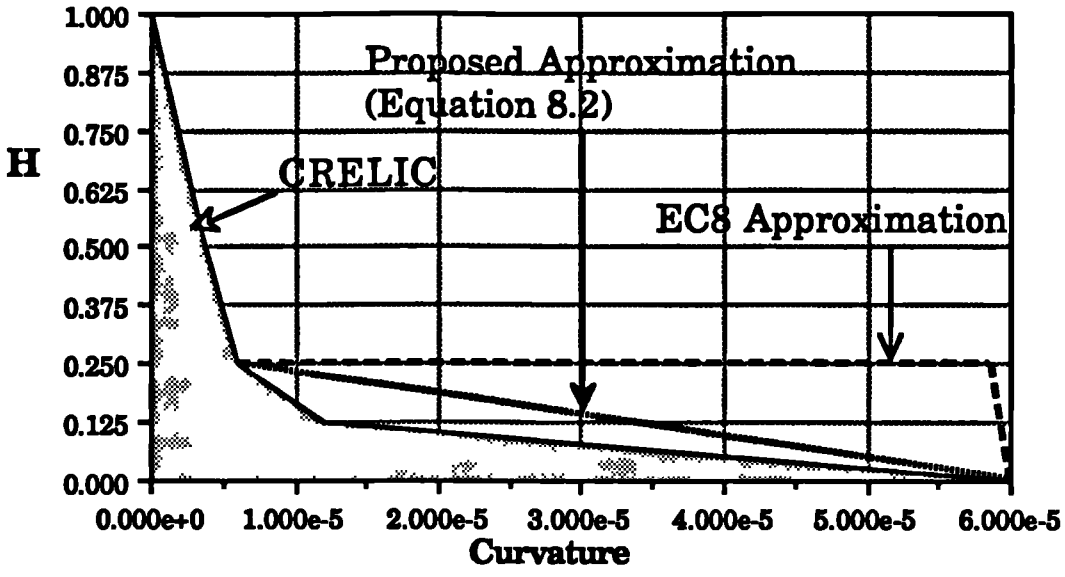


Figure 7.11 Curvature distribution for control specimen at ultimate load

The EC8 equation (2.5) for estimating the amount of confinement required to achieve a certain ductility seems to consider curvature ductility as a constant for a particular section. The other parameter in the equation v_d (ratio of maximum axial force to concrete compressive capacity at the critical section), takes into account implicitly the effects of axial load and shear ratio. From the parametric study it can be seen (figures 6.4 and 6.5) that ductility in general decreases with increasing percentage of reinforcement, despite the increase in ultimate moment. The distribution of reinforcement with higher amounts of steel closer to the boundaries is shown to exhibit much higher ductility than the uniform distribution. This is an indication of an improved utilisation of the material demonstrated by such distributions.

As expected, additional confinement of concrete is the most important parameter in enhancing ductility (figures 6.9 and 6.10). The increase in ductility is almost linear with increasing confinement. Moreover, the unconfined concrete strength seems to influence very little the ductility levels.

The steel characteristics also affect the ductility levels as seen from figures 6.14 and 6.15. A decrease in ductility is observed with increasing yield stress of the flexural reinforcement. This is despite the fact that the ultimate strain in steel was not the control strain. This highlights the fact

that high tensile steels even though they might be highly ductile on the material level, produce less ductile reinforced concrete members than the equivalent members with lower tensile yield strenght . Thus, a different design approach should be used in order to utilise the strenght advantages offered by this type of reinforcement.

An interesting point to note in figures 6.14 and 6.15 is the fact that the elastic perfectly plastic reinforcement gives a higher $\mu_{1/r}$ than steel with strain hardening, while it yields a lower μ_{Δ}. This is due to the fact that such reinforcement gives a shorter length of plastic hinge, and hence concentrates the rotation at the lower level.

An increasing axial load has a knock-down effect on the ductility of a section, as shown in figures 6.19 and 6.20. Higher confinement is clearly beneficial, but yielding of the tensile reinforcement is reduced at high confinements and high axial loads. Tensile loads enhance the ductility significantly, but the duration of their occurrence is not normally prolonged.

7.10 Effect of cyclic loading

The envelope of the cyclic load displacement curves is considered by many researchers to be within the of monotonic curve. For certain critical MDL increments (ΔMDL), depending on the material plastic properties, the virgin cyclic curves may recover the plastic strains and hence, the load achieved will be identical to the monotonic load. In a non-linear case where the stiffness is decreasing it is more likely that the ΔMDL required to shift the cyclic curve back to the monotonic increases with MDL. By close examination of the actual load displacement curves for SW4 (obtained by the plotter), for MDLs up to yield, the critical value of ΔMDL was about 0.5. Hence, up to the yield load the difference between the cyclic and monotonic load-displacement envelope is not expected to be significant.

The results of the parametric study of chapter 6 (figures 6.24, 6.25, 6.29 and 6.30) show that the ductility of the section is higher for the cyclic loading than for the monotonic. This can be attributed to the softening of the materials under cyclic loading. However, the program used did not take into account shear deformation deterioration which may lead to failure prior to achieving flexural ultimate limits. The noted increase in ductility

can not be utilised for design purposes and monotonic calculations can be considered adequate.

7.11 Energy dissipation capacity

Of particular significance to the dynamic behaviour of RC buildings is the energy dissipation capacity, or 'reserve energy' according to Blume, Newmark, and Corning (1961). The energy dissipated by a member is usually calculated by the area under the moment-rotation or force-displacement graph. This is summed up by the definition (Probst and Comrie 1951) which states that the increase in the kinetic energy of a moving rigid body is equal to the work done by the forces and moments acting on it. The external work done should also be equal to the internal work done or strain energy.

In the case of RC walls, the most convenient means of calculating the energy is by using the area under the force displacement curves. It should be noted that in the energy calculations for the experimental results, top wall displacement will be used instead of the actual screw-jack displacement. The area of a loop is calculated from the force top wall displacement data by using the trapezoidal rule. Since the number of points obtained per loop is variable, the values obtained are a lower bound for the exact integral. Two types of graphs are presented. Firstly, the energy dissipation per MDL, since at each MDL, two cycles are imposed, the virgin cycles (marked with a dot) are plotted separately from the second cycle (marked with a triangle) as shown in figures 7.12 to 7.17. Secondly, cumulative energy dissipated per cycle is shown in figures 7.18 to 7.23.

From the first set of figures, the immediate observations indicate that:

(a) a very small amount of energy is dissipated before yield,

(b) the virgin cycles dissipate much more energy than subsequent cycles before yield,

(c) in flexure dominated walls, there is a sharper rate of increase of energy dissipated per MDL after yield (ΔE_{ay}) which is almost constant up to failure,

(d) a drop in ΔE_{ay} is a manifestation of shear deterioration,

(e) as demonstrated by SW5, ΔE_{ay} is zero or negative after shear failure,

(f) the virgin cycles dissipate more energy than second cycles after yield,

(g) the rate of increase of the cumulative energy per cycle $\Delta\Sigma E$ is progressively increasing with MDL,

(h) shear deterioration or failure reduces the total cumulative energy significantly, but this can only be observed in comparison with flexure dominated walls.

As it can seen the energy dissipated per cycle, prior to failure, increases in two almost linear branches. The first branch reaches up to yield load and has a much lower gradient than the branch after yield. When failure occurs or shear deterioration takes place, the gradient of the branch after yield drops significantly, as seen for walls SW5, SW6 and SW7. Consequently, the capability to dissipate energy is dependent primarily on the ability of the member to resist the shear forces successfully during load reversals. Provided shear deterioration does not occur, energy dissipation becomes a function of the maximum displacement achieved. Figure 5.13 indicates that the energy dissipated by flexural deformations for SW9 are up to 85% of the total energy, even though shear deformations accounted for up to 40% of the total.

Comparatively low levels of energy is dissipated until yield, hence high displacement ductility would imply necessarily high energy dissipation. However, it is not advisable to consider the effect of shear deformations in the calculations for displacement ductility, since, as mentioned in the previous paragraph, very little energy is dissipated by the shear mechanism of deformation.

The total cumulative energy dissipation is dependent on the loading regime imposed, and cannot on its own be used as a comparative measure for assessing performance. For earthquake resistant design based on energy considerations, the rate of energy input is the important parameter. Failure will occur when the rate of energy input is higher than the rate of energy the structure can dissipate at the instant the demand is made. Thus the problem is related both to the previous MDL achieved as well as to maximum MDL that can be obtained prior to failure.

Figure 7.12 Energy dissipation per MDL for SW4

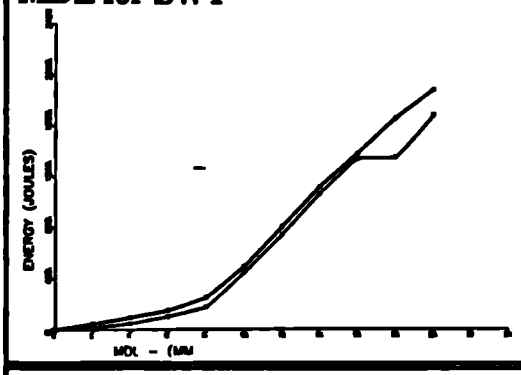


Figure 7.13 Energy dissipation per MDL for SW5

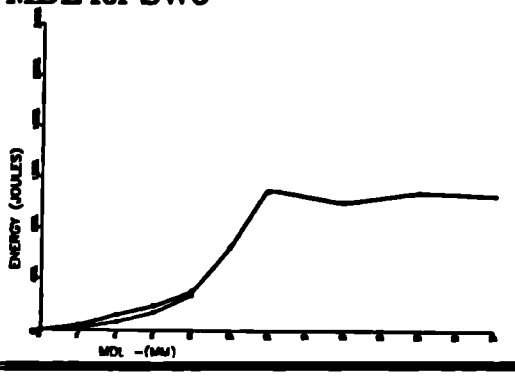


Figure 7.14 Energy dissipation per MDL for SW6

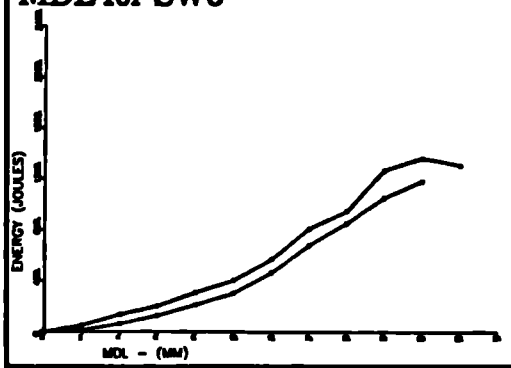


Figure 7.15 Energy dissipation per MDL for SW7

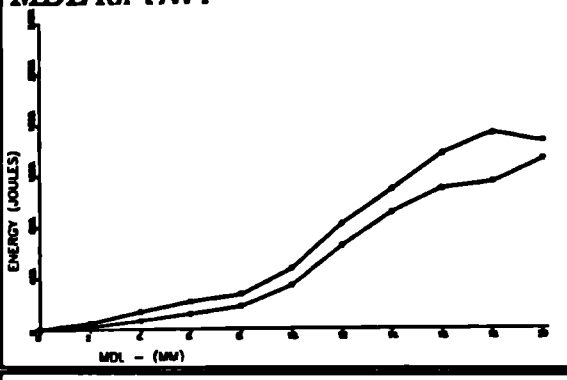


Figure 7.16 Energy dissipation per MDL for SW8

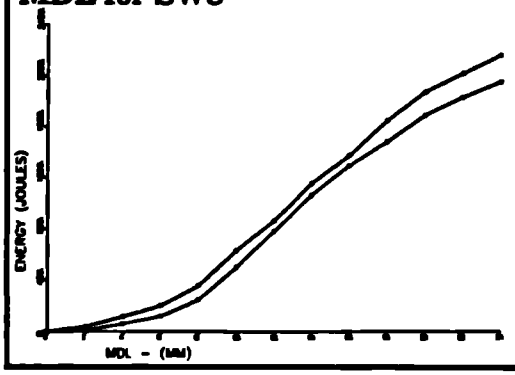


Figure 7.17 Energy dissipation per MDL for SW9

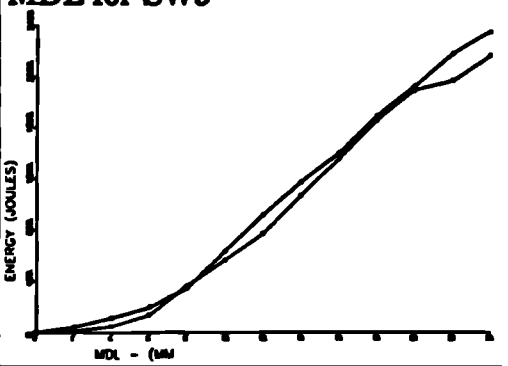


Figure 7.18 Cumulative energy dissipation versus MDL for SW4

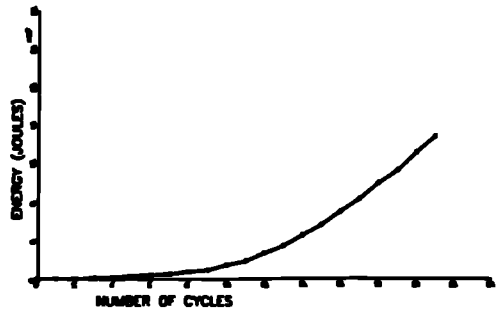


Figure 7.19 Cumulative energy dissipation versus MDL for SW5

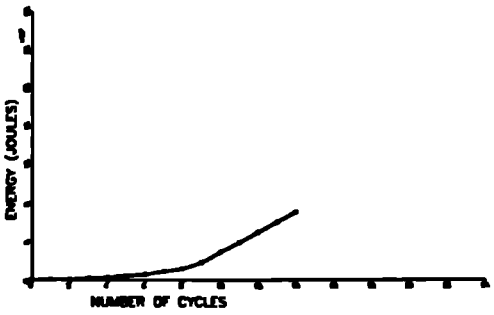


Figure 7.20 Cumulative energy dissipation versus MDL for SW6

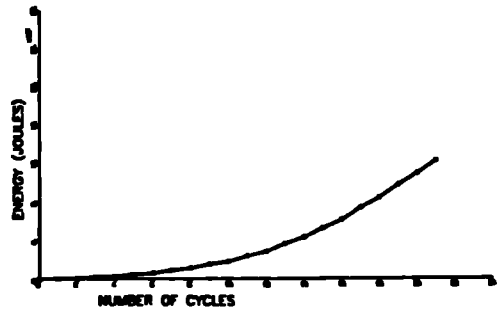


Figure 7.21 Cumulative energy dissipation versus MDL for SW7

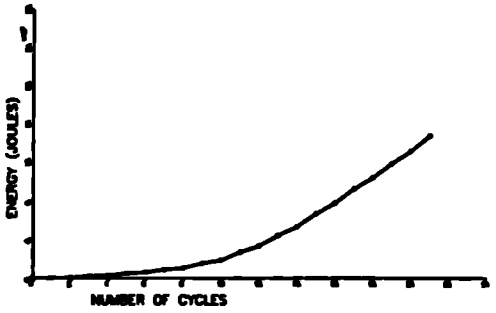
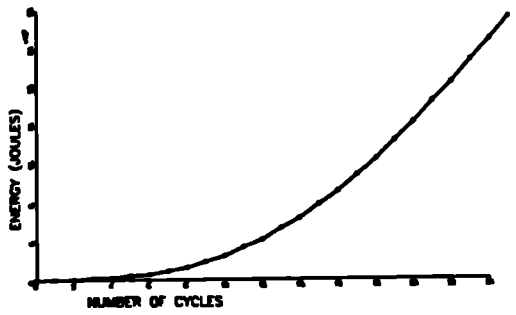


Figure 7.22 Cumulative energy dissipation versus MDL for SW8



Figure 7.23 Cumulative energy dissipation versus MDL for SW9



CHAPTER 8

8 DESIGN IMPLICATIONS AND RECOMMENDATIONS

8.1 Introduction

In this chapter it is assumed that the design forces to be resisted by an RC wall have been determined by using a suitable method of analysis. A method for dimensioning the cross section and quantifying the amount of reinforcement to be used is proposed. Designing for ductility based on the draft EC8 (1988) is discussed and modifications are proposed. Finally, a shear design procedure is developed and design recommendations are given.

8.2 Dimensioning of RC wall sections

Dimensioning of the cross-section is often unnecessary since the architectural considerations often dictate the layout and dimensions of structural members. In such a case, only checking the adequacy of the member to sustain the design loads is necessary. As with most design guidance, the equations given here can be used for the specified section, bearing in mind the following assumptions used in the derivation.

a) The main flexural reinforcement is symmetric and concentrated within boundary columns which are to be detailed separately for ductility.

b) Minimum web reinforcement of strength equivalent to 2% of the section compressive strength is to be provided, at maximum spacing specified by codes.

It has been found, through the parametric study of chapter 6, that for walls with uniform distribution in the boundary and minimum web reinforcement (UB), minimum confinement ω_{wd} of 0.1, the area of flexural

steel reinforcement 'A_{sx}' required to resist a certain moment 'M_{sd}' in the absence of axial load, can be estimated from the following equation:

$$A_{sx} = 2\,M_{sd} / (0.9\,f_{sy}\,D) - BD / 1000 \qquad (8.1)$$

The above equation was used to calculate the reinforcement required by the walls employed in the parametric study and the experimental work. Table 8.1 below shows the amounts required compared to the amounts used (B = 60 and D = 600).

Table 8.1 Dimensioning equation results

WALL CODE	f_{sy} N/mm^2	Analytical Moment (KNm)	A_{sx} Used	A_{sx} Calculated (Equation 8.1)	Ratio of calculated to used Asx
W1UB	460	52.4	377	386	1.02
W2UB	460	101.4	754	780	1.03
W3UB	460	147.8	1131	1154	1.02
W4UB	460	193.1	1508	1519	1.01
SW4	470	142.7	1018	1088	1.07
SW5	535	166.2	1086	1115	1.03
SW8	430	128.4	1056	1070	1.01

The results of table 8.1 indicate equation 8.1 gives a very accurate estimate of the reinforcement required to achieve a certain design moment. The maximum error is 3% for all walls except SW4 which has higher confinement than assumed by the method.

Alternatively, the above equation can be used to calculate the dimensions of the wall, by assuming a percentage of flexural reinforcement, in an iterative procedure. If stiffness considerations are also necessary, then the freedom in dimensioning is further reduced. Evaluation of shear capacity can only be undertaken after the dimensions and flexural reinforcement are established as will be discussed in section 8.4.

8.3 Flexural capacity

8.3.1 Moment capacity

For design purposes, the yield load can be estimated accurately, by section analysis, by using the unconfined properties of concrete and the steel yield strain as the control strain for calculations as shown in figure 8.1 below.

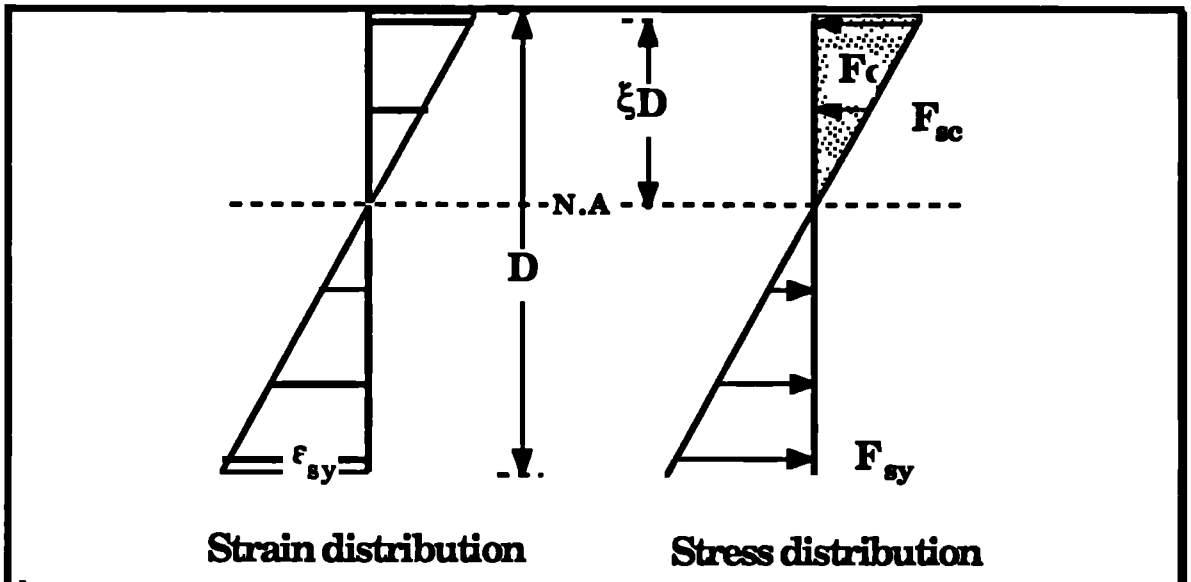


Figure 8.1 Stress and strain diagram at yield level

An initial value of neutral axis depth is assumed in order to obtain the initial strain distribution and the stresses are then determined. Forces are then calculated from stresses, and the horizontal equilibrium is checked. The neutral axis depth is varied until horizontal equilibrium is achieved and then the moment is calculated. For linear distributions of stress with strain as shown in the figure above, the neutral axis depth can found in a deterministic manner, by setting up the appropriate equations.

The exact wall ultimate flexural capacity can also be calculated by the method of section analysis taking into account the effects of confinement, especially in increasing the ultimate strains in concrete, and the true characteristics of steel. Nonetheless, this is not an easy design option, and the results are also very much dependent on the assumptions used. However, this has to be incorporated in design either by using computer programs like CRELIC, or design charts obtained from extensive parametric studies covering a wide spectrum of possible wall dimensions

and reinforcement arrangements.

For example the ultimate capacity of wall SW8 was to be estimated based on the results of the parametric study which are to be used as design charts then the following steps are to be followed:

a) Obtain a factor F1 from the percentage and type of distribution from figure 6.1. For 2.8% and UB distribution F1 equals 9.3.

b) Obtain a factor F2 from the confinement level and concrete strength from figure 6.6. For ω_{wd} of 1.25 and f_{co} of 45 N/mm^2, F2 equals 1.0.

c) Obtain a factor F3 based on the steel characteristics from figure 6.11. For f_{sy} of 430 and fsu/fsy of 1.45, F3 equal to 0.95.

d) Obtain a factor F4 depending on the axial load present. In this case since there is no axial load this factor equals to 1.

e) The moment capacity is then calculated by multiplying all factors by the control moment. The value of Msd is then equal to 0.93 x 0.95 x 147.8 = 130.5 KN/mm^2.

The above value is very close to the one calculated by using CRELIC and demonstrates the simplicity and accuracy of the method.

8.3.3 Ductility

A significant step towards designing for ductility is made in the draft EC8 (1988). There are four stages necessary in the design. The first stage is the determination of a behaviour 'q' factor, which is to be estimated on the overall structural level. The second stage is the estimation of the expected displacement ductility from the assigned 'q' factor. The third stage converts the displacement ductility to curvature ductility. The final stage involves the calculation of the required confinement to achieve the calculated curvature ductility. Form the results of the current study, stages three and four can be assessed.

The equation for converting displacement to curvature ductility given for isolated walls has been discussed in chapter 7 (figure 7.10). Since the analytical results do not account for shear, and the effect of shear is to increase the value of displacement ductility for the same value of curvature ductility, then the code equation is on the side of expected shift of the

analytical results. Typically for wall SW9 (of shear ratio 2) for which shear increased from 0.25 to 0.4 of the total deformation from yield to ultimate conditions, the increase in the actual value of displacement ductility will be about 25%.

However, the relative increase of shear to total deformations is a function of a number of parameters including the shear ratio, the level of axial force, the amount and detailing of the shear reinforcement as well as the cyclic regime to be imposed on a member. In order to be on the conservative side for all shear ratios, the increase in displacement ductility due to shear deformations should be ignored. This is not only due to the uncertainty in assessing the total displacement ductility but also due to the fact that shear deformations do not dissipate much energy. Consequently, it is recommended that the code should allow for a steeper gradient as shown in the proposed curve (figure 7.10) and equation 8.2 below.

$$\mu_{1/r} = 7 (\mu_{\Delta} - 1) + 1 \qquad (8.2)$$

The above equation is based on the assumption that the curvature within the plastic hinge zone varies linearly from the yield level to the ultimate moment curvature as shown in figure 7.11.

The final stage of converting curvature ductility to confinement is a more difficult task, since many parameters influence the ductility of an unconfined section, as discussed in chapter 7. It is proposed that a reference curvature ductility $\mu_{1/ro}$ is calculated first for the unconfined section, in which all the important section parameters are included, as shown in the equation below:

$$\mu_{1/ro} = F (f_{co}, f_{sy}, f_{su}, \alpha_s, \rho_v, N) \qquad (8.3)$$

The parametric study of chapter 6 could be used to determine the above function, in the same manner demonstrated for the ultimate moment capacity, provided that all the different ranges are investigated extensively. Alternatively, section analysis should be used at to determine the curvatures at yield and ultimate moments.

The final equation for calculating the confinement should include the ratio of ductility demand to $\mu_{1/ro}$, as well as the confinement pattern as shown below:

$$\omega_{wd} = F (\mu_{1/r} , \mu_{1/ro}) / \alpha \qquad (8.4)$$

The above equation implies that the confinement reinforcement enhances the ductility of the unconfined section. By using figure 6.9 an equation of the above format can be determined as shown in equation 8.5, where the value of α can be obtained as given in EC8 (1988).

$$\omega_{wd} = \frac{1}{32\,\alpha}\left(\frac{\mu_{1/r}}{\mu_{1/ro}} - 1\right) \qquad (8.5)$$

8.4 Design for shear

As mentioned in chapter 2, the classical approaches to design against shear failure separate the total shear resistance into components arising from concrete and shear reinforcement. The resistance of concrete to shear is determined as a function of a number of parameters including concrete strength, amount of flexural reinforcement and the level of axial force. Once this is determined, shear reinforcement has to be provided to resist the excess forces. The amount of shear reinforcement is determined by using the truss analogy principles and some factor is usually included to account for the internal lever arm of the theoretical truss.

In all RC codes, the shear resistance of concrete is always given in the plane of resisted shear force. This is probably a result of historical developments in design. However, in analytical terms, this approach can only lead to an upper bound solution. For design purposes, empirical relationships were developed based on the most conservative experimental results from series of tests mostly on beams for which failure must have occurred in different planes. In order to exemplify that the method is an upper bound, a comparison can be made with the yield line theory in RC slabs. By assuming a yield line it is possible to determine the strength of a particular yield pattern. It does not exclude the possibility of another yield line giving a weaker solution. Similarly, designing against shear on a horizontal plane in RC walls cannot always be a guarantee against failure on an inclined plane. In fact in flexural RC walls, shear failure will always occur in a diagonal line. Consequently, the design method developed hereafter has as one of the principle objectives the determination of the minimum "shear resistance surface" (SRS), as detailed below.

8.4.1 Shear resistance of concrete in compression

In considering a horizontal section, contrary to implicit code philosophy, most of the shear resistance is provided in the compressive zone. This is not just because of the compatibility of shear deformations within that level, but also due to the fact that tensile forces developed in the flexural bars are higher than expected from elasticity. This is equivalent to the development within the concrete member of the arch and tie mechanism, which transfers all the shear through the compressive area. Evidence of the high tensile forces at the top levels of walls was given in the preceding experimental and analytical results, as well as in the discussion of chapter 7. However, it should be emphasised that this phenomenon does not necessarily apply in the same way to walls with lower aspect ratios, and thus deserves further research efforts.

It is important for the determination of shear resistance to know accurately the amount of shear forces transmitted to the compressive element. As a first estimate it can be conservatively considered that the unreinforced horizontally tensile zone does not resist any shear. Hence, by considering the equilibrium of forces as shown in the figure 8.2 below, the angle Θ, at which the maximum shear stress 'v_{max}' is given by equilibrium, can be determined as a function of the geometry. In deriving this angle it has been assumed that the stress is uniform within the compressive zone.

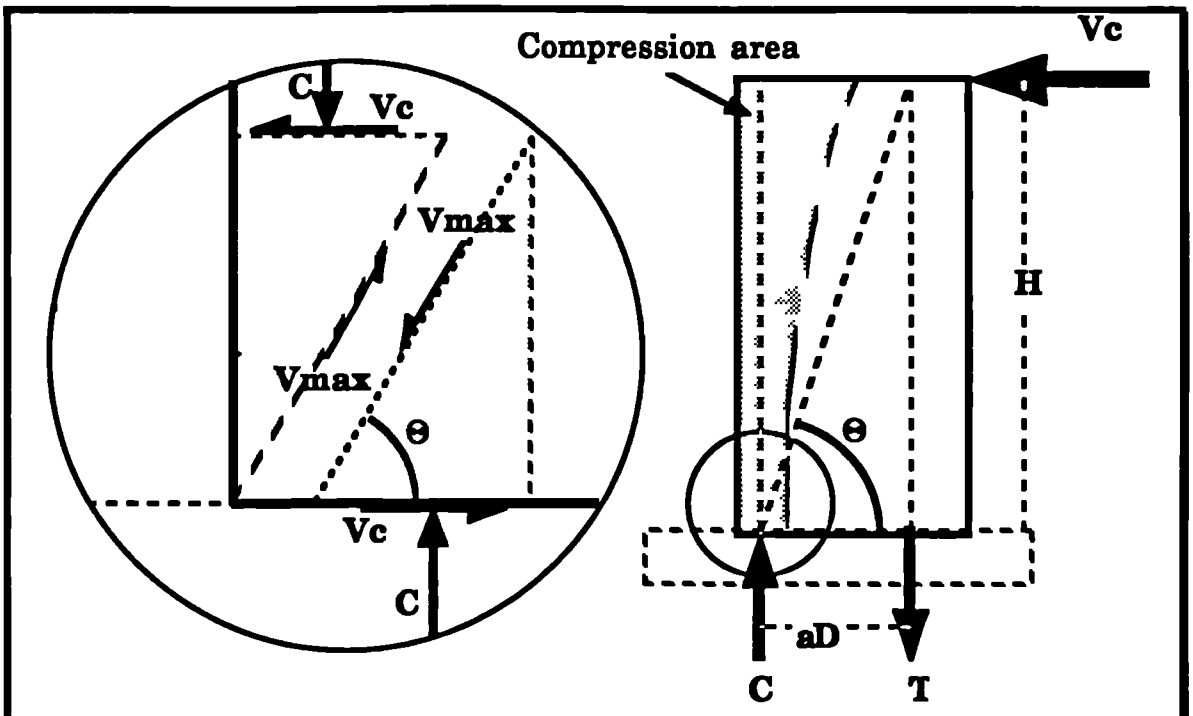


Figure 8.2 Stresses in the compressive zone

The resistance of concrete in shear can be obtained in terms of the principal normal stress through a Mohr-Coulomb type failure envelope as shown in the figure below. The value of shear resistance at zero axial load, τ_o, is a unique value characteristic of the concrete used. For concrete in compression, τ_o is the minimum value that can be resisted, and it occurs when the second principal stress is in tension. In flexural walls this value can be considered as a lower value for the shear resistance of concrete. Confining reinforcement will almost certainly impose compressive stresses in the lateral direction and hence, will enhance the shear resistance.

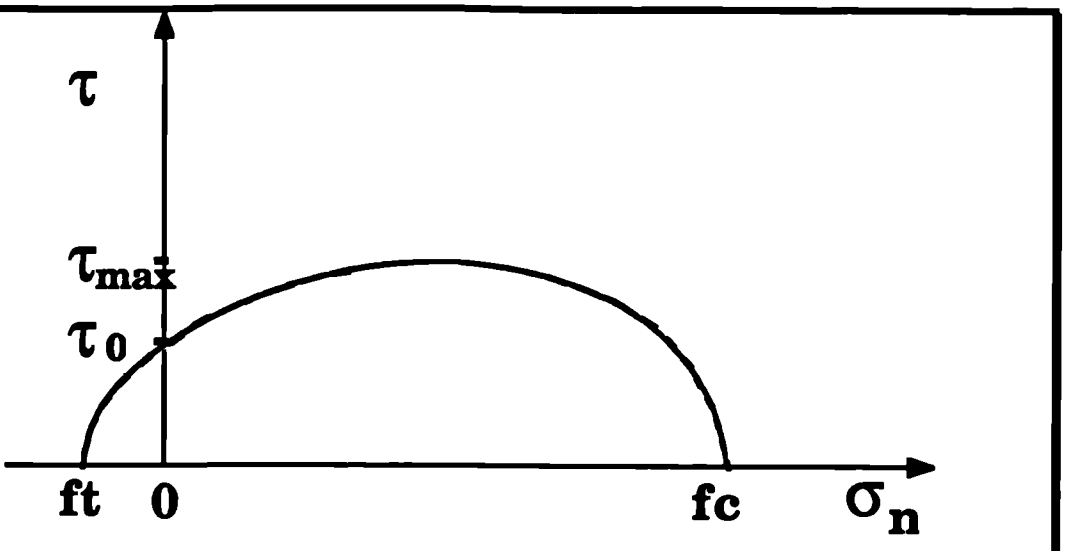


Figure 8.3 Mohr-Coulomb failure envelope for concrete

By considering a certain value for the neutral axis depth ξD, (where ξ, is the normalised neutral axis depth with respect to the section width) then the shear resistance T_θ as well as the applied shear force V_θ along this particular failure line can be determined as follows:

$$T_\theta = \tau_o \, \xi D / \cos \Theta \qquad (8.6)$$

$$V_\theta = V_c / \cos \Theta \qquad (8.7)$$

Shear failure in sections without shear reinforcement occurs when V_θ is greater than T_θ. It can be seen that the determination of the exact direction of the principal stress within the compression zone does not affect the value of minimum shear resistance since the term cos Θ exists in both equations. This implies that this method applies not only to a uniform stress distribution but to the general case of stress distribution within the compressive zone, since what matters is the projection of the minimum SRS to the horizontal.

Consequently, the neutral axis depth is the only quantity required from the properties of the section. It is expected that the depth of the neutral axis increases with the distance from the base of the wall. However, for design purposes, it is safe to use the value of ξ determined at the critical section.

The value of τ_o is a material property and is dependent on the concrete strength. The actual concrete compressive strength is a function of the confinement, and hence, an increase in strength due to confinement

should have a corresponding increase in τ_o. For design purposes, if the enhanced strength is unknown, it is conservative to use the value of τ_o calculated for unconfined concrete. The normalised value of τ_o with respect to f_{co} as given in the literature varies between 0.15 and 0.2 (Wagner and Bertero, 1982, Elnashai, 1984, Divakar, Fafitis and Shah, 1987) and the values of 0.15 and 0.20 will be used here for design and analysis purposes, respectively.

Additional conservatism of the method presented arises from the effect of the reinforcement present in the compressive area. By assuming that prior to failure, compatibility of strains exists within the compressive zone it can be demonstrated by using elasticity that the steel reinforcement stiffness is higher than that of concrete. This is expected to remain higher even after yield, but at a lower level due to plasticity and loss of bond. For very high percentages of flexural reinforcement in the compressive area (e.g. for composite walls), the actual shear resistance will be much higher than assumed by the above method and allowance should be made for that in analysis calculations by including the steel shear resistance.

8.4.2 Shear resistance of concrete under tensile axial strain

As depicted in figure 8.3, concrete when subjected to tensile stresses higher than the tensile strength f_t, cannot resist any stress, including shear. Notwithstanding, it does not crack totally but only in blocks. The distance between cracks depends on many parameters including material, strain state and geometric characteristics. The direction of these cracks is normal to the direction of principal tensile stress at the time of fracture. Ideally, no shear transfer can occur through tensile cracks. In practice, this is true only in cases when the crack widths are such that any deformations due to shear strains do not cause contact between the surfaces on either side of a crack. This 'aggregate interlock' is discarded in the proposed design method which aims to give conservative results.

The direction of principal tensile stress in the tensile zone is not known in a deterministic way, since it depends not only on the lateral stress 'σ_c' but also, on the shear stress 'σ_s' imposed in the direction shown in figure 8.4. Lateral compressive forces arise from lateral or 'shear' reinforcement. As was seen from the experimental results, this type of reinforcement is mobilised after the occurrence of web cracking. The determination of the direction of the principle tensile stresses is, therefore,

central in evaluating the shear resistance of a member. For flexural walls with uniform shear reinforcement the above will determine the minimum SRS.

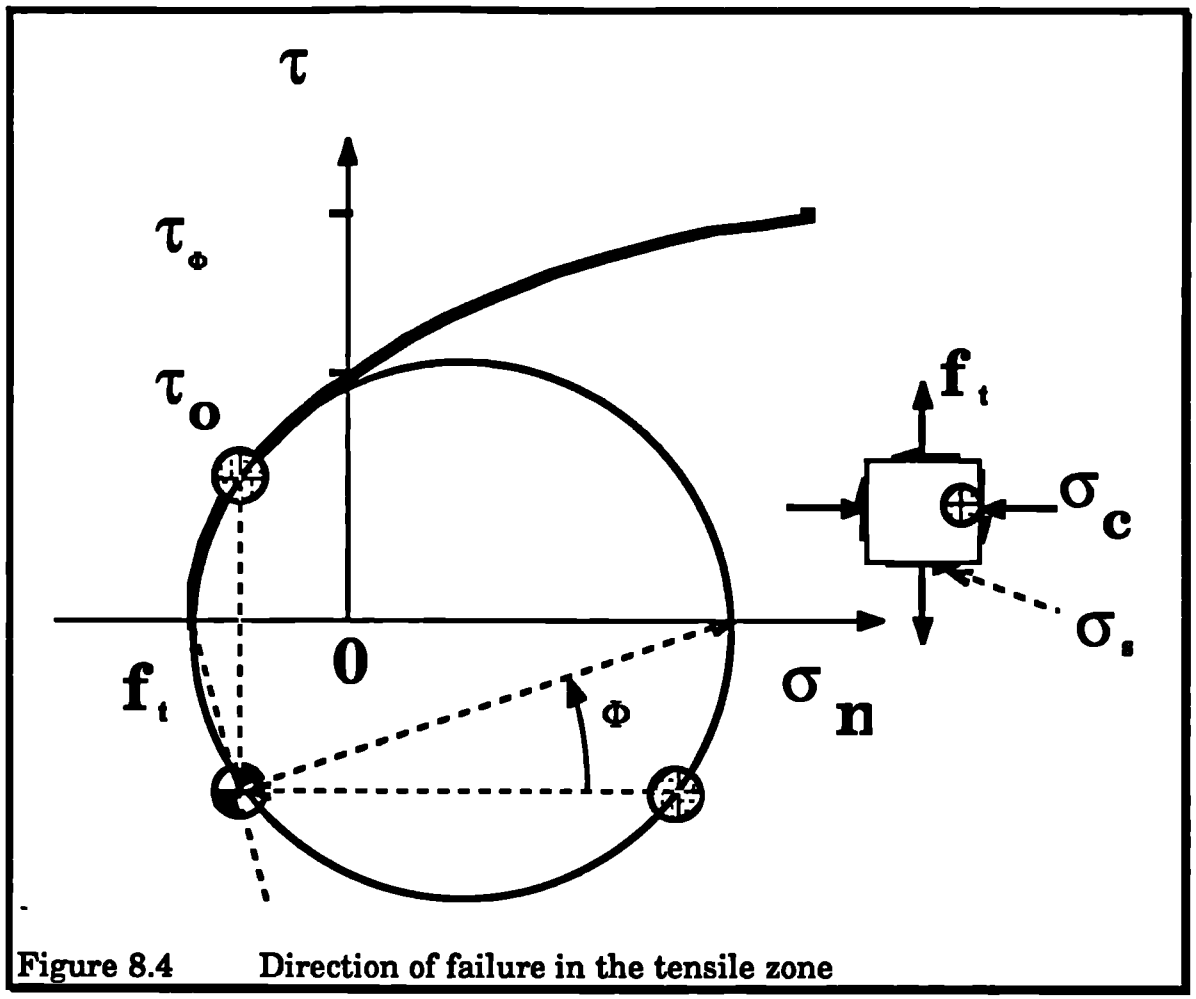


Figure 8.4 Direction of failure in the tensile zone

Under axial tensile stress conditions, if no shear stress is applied then the angle of tensile cracking 'ϕ' will be zero. This is the case initially at the wall extremities. As the imposed shear stress increases, ϕ increases until a maximum angle of 45° is reached. A function relating shear resistance in the tension zone 'τ_{ct}' to an angle 'θ' and 'ϕ' (both angles are with respect to the horizontal) can be determined in terms of the lateral compressive stress σ_c as shown below.

$$\tau_{ct} = 0.5 (\sigma_c - f_t) \sin(2\theta - 2\phi) \qquad (8.7)$$

However, the value of σ_c cannot increase more than the value given in equation 8.8 below (the tensile stress is assumed to be 0.1 f_{co}) since the failure envelope will be exceeded as shown in figure 8.4 above.

$$\sigma_{cmax} = 2.2 \tau_c - f_t = 0.22 f_{co} \qquad (8.8)$$

The above criterion is in agreement with code restrictions on the

maximum level of shear strength that a section can resist without web failure. The difference is that this restriction should be imposed as a maximum on the volumetric mechanical ratio 'ω_{ws}' of shear reinforcement.

Assuming that the angle of zero concrete shear resistance is at 45° then, for a uniform reinforcement pattern, the minimum SRS can be defined as shown in figure 8.5 below.

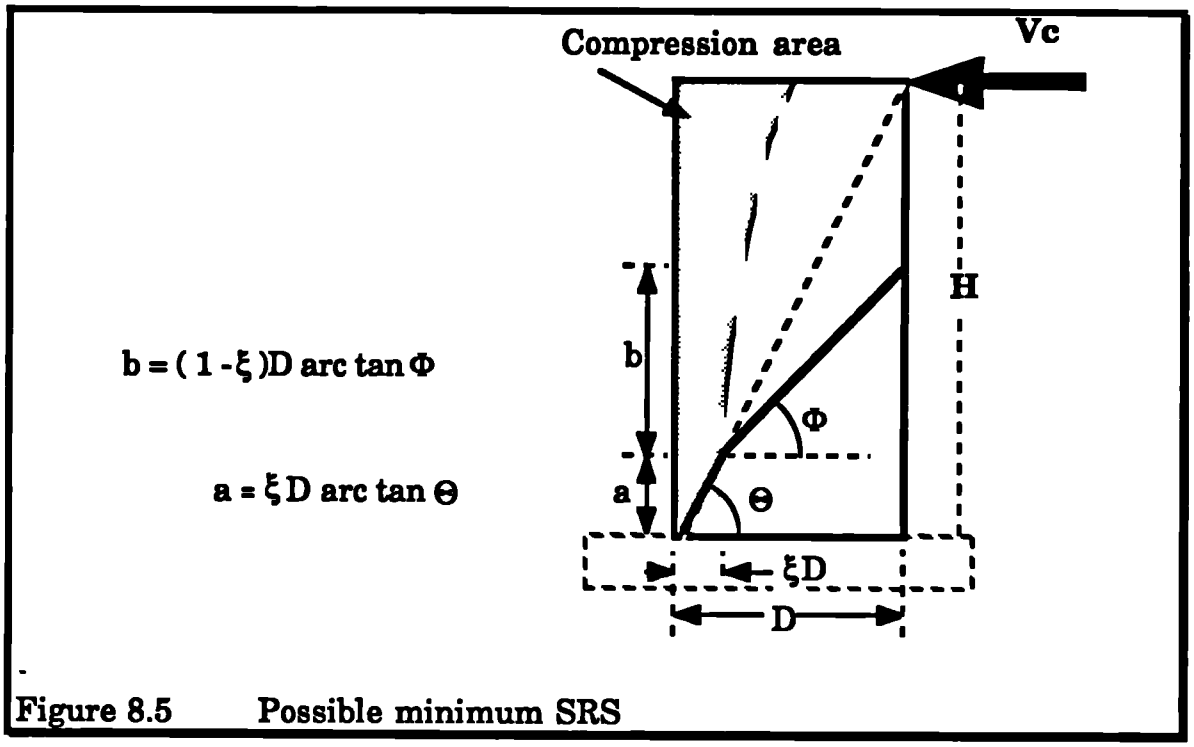


Figure 8.5 Possible minimum SRS

The total shear resistance in the tensile zone 'T_t' will be the resistance of concrete in tension plus the resistance offered by the shear reinforcement spanning the crack in tension. Any additional shear reinforcement above the crack is irrelevant for the shear resistance along this surface as shown in the equation 8.9 below.

$$T_t = b\, A_{ss}\, f_y / s + \tau_{ct} (1 - \xi)\, D\, B \qquad (8.9)$$

The above represents a force in the direction of applied shear force,where A_{ss} is the shear reinforcement per unit length at a spacing 's', B is the section width and 'a' and 'b' are as defined in figure 8.5.

The value of the angle θ in the tensile zone should be varied until the minimum value of T_t is obtained. For uniform distribution of shear reinforcement, and by assuming a value of θ and ϕ equal to 45° in equation 8.8, the minimum value of T_t reduces to:

$$T_t = (1- \xi) D A_{ss} f_y / s \qquad (8.10)$$

The above equation is equivalent to the results from the truss analogy. However, in order to determine the minimum SRS for non-uniform distributions of reinforcement, several possible SRS should be considered, since failure will occur on the one offering least resistance.

It is now apparent that for walls with an aspect ratio of less than (a + b) / D (see figure 8.5), the SRS will have to follow a path avoiding the top beam, and hence, the shear contribution of the concrete in tension becomes significant. Lopes and Elnashai (1990) recognised that and have undertaken testing of walls of aspect ratio close to 1 without a confining beam at the level of the point of contraflexure.

The value of (a + b) /D is expected to be around 1.3. It is worth noting that for shear ratios less than 1.3 the draft EC8 (1988) considers the contribution of lateral reinforcement to be reduced to zero for α_s of 1.3 - 0.3, whilst the contribution of vertical reinforcement is linearly increased up to the sectional yield strength for the same range of α_s. It is clear from figure 8.5 that the effect of lateral reinforcement over the decreasing length b is less significant in resisting shear, hence alternative reinforcement that would enhance the shear resistance in a different manner is required.

Frictional forces that may develop at the cracked surface due to 'aggregate interlock' as well as the dowel effect of the flexural reinforcement bars, have been ignored in the above derivations. It has been demonstrated experimentally that under cyclic loading, dilation of concrete takes place at crack interfaces, and as a result of the net wall extension, the reinforcement will impose higher compressive forces on the concrete. However, since it is not certain to what extent the frictional forces will be available to provide the extra resistance through cracks, for design purposes it is safe not take them into consideration. Analysts, however, who may wish to determine the actual resistance of a member, should allow for all the extra contributions that are available.

8.4.3 Comparison with experimental results

An evaluation of the shear strength available in the walls tested in the process of this research based on the SRS approach is given in the table 8.2.

Table 8.2 Shear strength capacity of tested walls according to SRS approach

WALL CODE	ξ	Concrete shear Force (KN)	Steel Force § (KN)	SRS V_{cmax} (KN)	Exp. V_{cmax} (KN)	Comments on failure mode
SW1	0.195	11.23	17.73 (6 ϕ 2.8)	29.0	~24	Steel fracture
SW2	0.20	11.52	17.73 (6 ϕ 2.8)	29.25	22.5	Steel fracture
SW3	0.21	11.34	30.16 (6 ϕ 4)	41.50	30.4	Steel fracture
SW4	0.20	43.20	92.46 (6 ϕ 6)	135.66	104.0	Crushing
SW5	0.15 [0.23]	32.40 [66.90]	50.27 (10 ϕ 4) [57.8]	82.67 [124.70]	117.3	Shear failure ¶ •
SW6	0.20	43.20 [57.60]	50.27 (10 ϕ 4) [57.80]	93.47 [115.40]	107.8	Crushing / Shear ¶
SW7	0.15	32.40 [43.20]	92.46 (6 ϕ 6) [100.01]	124.86 [143.21]	127.3	Steel fracture ¶
SW8	0.20	43.20	60.32 (12 ϕ 4)	103.52	95.3	Crushing
SW9	0.20	43.20	70.37 (14 ϕ 4)	113.57	97.4	Crushing

§ The estimated number of bars crossed by the SRS is shown in parenthesis.

¶ The values shown in square brackets are the expected values by assuming the compression shear resistance to be up to 0.2 f_{co}, and the ultimate stress for the shear reinforcement.

• For SW5 the expected strength is based on the neutral axis depth calculated at the load achieved in the experiments.

It should be pointed out that in the analysis the effect of cyclic loading was not taken into account. The strength enhancement due to confinement, the increase of the neutral axis over the depth, dowel action and friction forces due to aggregate interlock were also ignored which are conservative assumptions.

As can be seen in table 8.2, the SRS design method yields conservative results in cases of shear failure (SW5) and shear deterioration (SW6). Despite the simplicity of the method, the expected values predict accurately

all the modes of failure. The predicted and actual capacities for the tested walls are also shown in table 8.3 including to the unfactored capacities of EC2 (1984) and ACI 318-83.

Table 8.3 Predicted and actual model wall capacities

WALL CODE	ACTUAL CAPACITY [EXPERIMENTAL] [KN]	FLEXURAL CAPACITY [CALCULATED] [KN]	SRS DESIGN (¶) [KN] (§)	SHEAR CAPACITY [EC2] [KN] (§)	SHEAR CAPACITY [ACI-83] [KN] (§)
SW4	104.0	112.8	135.7 (1.30)	111 (1.07)	94 (0.90)
SW5	117.3	131.4	82.7 (0.70) {124.7} (1.07)	78 (0.66)	61 (0.52)
SW6	107.8	103.7	93.5 (0.9) {115.4} (1.07)	78 (0.7)	61 (0.57)
SW7	127.3	128.3	124.9 (0.98) {143.2} (1.12)	111 (0.87)	95 (0.75)
SW8	95.3	107.0	103.5 (1.09)	74 (0.78)	56 (0.59)
SW9	97.4	112.1	113.6 (1.17)	115 (1.18)	98 (1.01)

§ The normalised force with respect to the actual capacity is given in parenthesis.
¶ The expected value by assuming the compression shear resistance to be 0.2 f_{co}, and the ultimate stress for the shear reinforcement, is given in brackets{}.

Compared with the other codes of practice, the predictions are closer to the experimental results, yet are always on the conservative side.

8.4.4 Parameters influencing shear resistance

Here, the way in which the different parameters used in the parametric study of chapter 6 influence the shear resistance are discussed and design recommendations are given.

According to BS 8110 code of practice, one of the most important parameters influencing the shear resistance of concrete, apart from the axial force, is the amount of flexural reinforcement. The shear stresses given in the code in a tabulated form were based on experimental results on beams.

The results of BS 8100 for the control specimen of the parametric study are shown in figure 8.6.

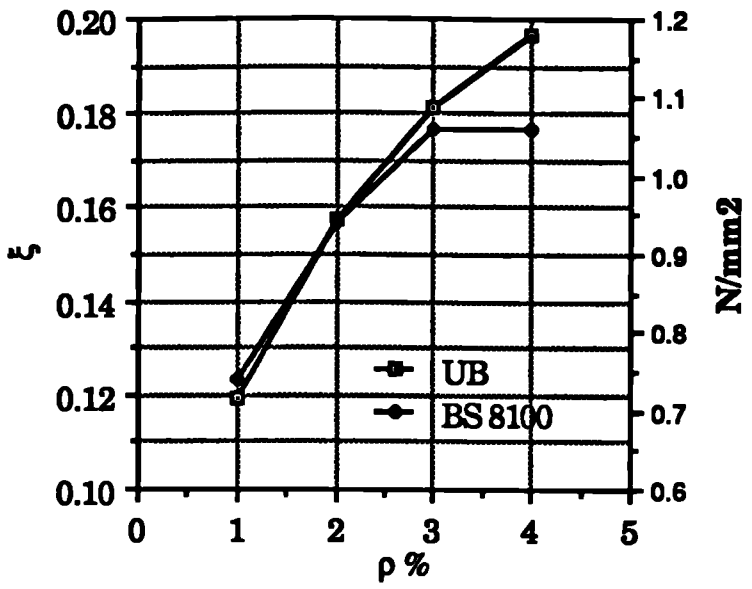


Figure 8.6 Shear strength of concrete according to BS8100 and SRS method for the different percentages of flexural reinforcement

The closeness of the results up to ρ of 3% is of significance. The difference at ρ of 4% is due to the fact that BS8100 does not consider values of ρ greater that 3%. Moreover, by making reference to figure 6.3 it can be seen that the SRS method would take into consideration not only the amount of flexural reinforcement but also the distribution of the reinforcement within the section. For this particular case the SRS method would give more conservative results for walls with concentrated reinforcement at the extremities, and allow for higher capacity in walls with distributed reinforcement. In fact the view held by some researchers that web reinforcement assists in resisting shear may arise partly from the fact that one effect of uniform reinforcement is to increase the neutral axis depth of a section.

The compressive strength of concrete is another parameter related to the shear resistance of concrete, and the relationship is demonstrated in figure 8.7.

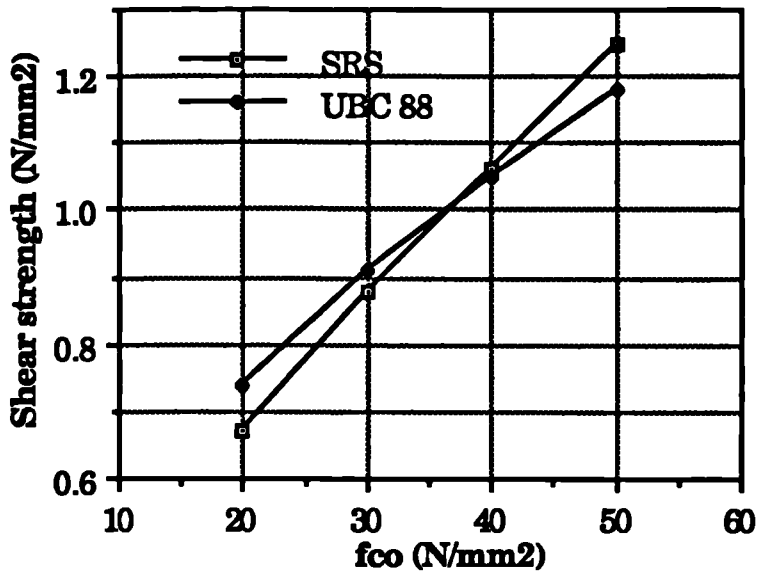


Figure 8.7 Shear strength versus compressive strength

As mentioned in chapter 2, the equation used by UBC (1988) is the same as for ACI 318-83 and is used here for a shear ratio of 2. The normalised value of τ_0 was kept constant for the different strengths of concrete which may not necessarily be true at all values. In figure 8.7, the shear strength is overestimated slightly with respect to the above-mentioned codes of practice for the high values of f_{co}.

The effect of confinement in enhancing the shear strength is not included in any code of practice. As shown in figure 6.8, increasing the confinement does not significantly change the neutral axis position, even though the increase in the concrete compressive strength is very high. If the enhanced compressive strength can be assessed accurately, the SRS method can be easily used to evaluate the corresponding increase in shear resistance.

The steel characteristics also appear to affect the position of the neutral axis as shown in figure 6.13. However, this does not seem to have attracted the attention of researchers in shear behaviour, since the traditional concepts only consider the volumetric ratio of steel and sometimes the yield strength but not other material characteristics.

The variation of the axial load is one of the parameters that implicitly consider the stress conditions within the member. The shear strength as obtained by using the NZ code for the plastic hinge zone, by the ACI 318-83

code and by the SRS method is shown below for the control specimen of the parametric study.

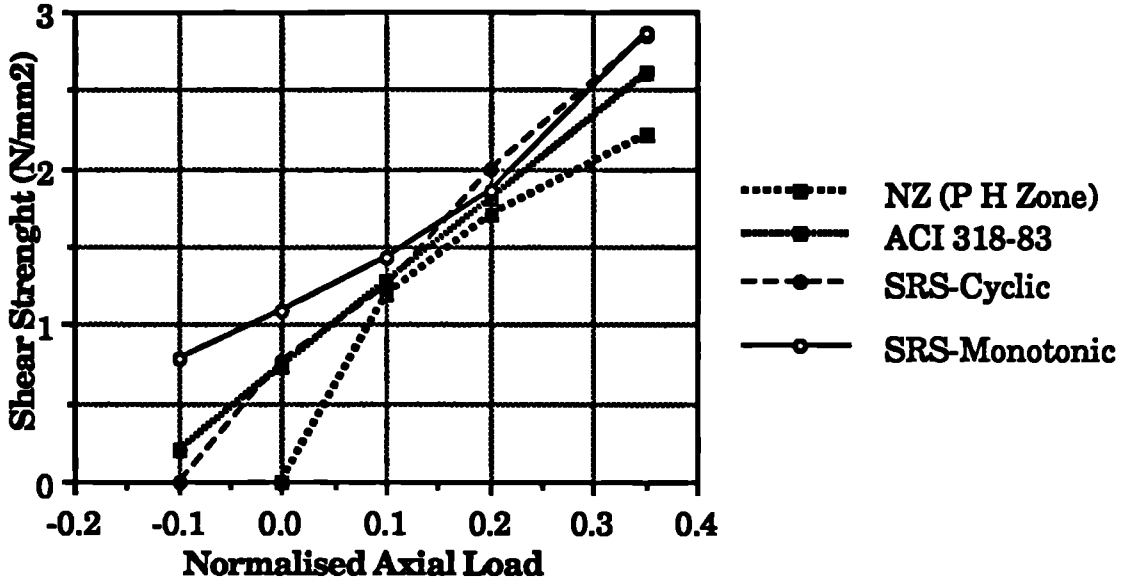


Figure 8.8 Shear strength versus normalised axial load

The closeness between the ACI 318-83 and the SRS method results is again worth commenting on. The ACI approach gives more conservative results for the high axial loads while for the lower values of axial load the results are identical with the SRS cyclic results. However, in the parametric study, fracture of the tensile reinforcement occurred for the cyclic case of negative axial force and hence the value of shear resistance is given as zero.

Appreciably more conservative results are given by the New Zealand code for the shear resistance of the plastic hinge zone. For zero axial load the concrete shear resistance is considered to be zero. This is an attempt to allow for the deterioration of strength that is expected after cycling in the inelastic range. The effect of different cyclic loading regimes on the behaviour of walls without any axial load was investigated in chapter 6. As shown in figure 6.23 a significant reduction in the neutral axis depth occurs for all examined cases. The equivalent reduction in shear strength was never less than 50% of the monotonic strength, and consequently the New Zealand code seems to be over-conservative in its approach.

The excessive strain demands on the flexural reinforcement during cyclic loading with negative axial forces should be of concern to the

designer, but not necessarily in the design for shear.

For design purposes the approach used by NZS 3101 (1982) and EC8 (1988) of treating the plastic hinge zone differently seems to be the best way of concentrating the attention of the designer on the critical areas as well as avoiding over-reinforcing the rest of the structure.

It is, therefore, recommended that the SRS monotonic results be used for the areas in which yielding is not expected. Until further experimental and analytical results are available, in the plastic hinge zone, a 50% reduction of the monotonic shear resistance is proposed.

CHAPTER 9

9 CLOSURE

9.1 General conclusions

A summary of the general conclusions is presented hereafter. Specific conclusions were discussed in the process of the development of the models and presentation of work, but are not included here for the sake of compactness.

- Experimental research into the behaviour of RC walls had identified several aspects in which current design procedures are lacking. The higher ultimate capacity of RC members compared with design estimates was attributed to the unrealistic models used in design. In this respect the draft Eurocode 8 proposed equations for the determination of the enhancement in concrete stress and strain due to confinement and for the first time direct design procedure for specific levels of ductility.

- Notwithstanding the criticism directed towards the truss analogy model, it is still in use for the design for shear. On the other hand, an alternative behavioural model, termed the 'compressive force path', seems to recognise many of the salient parameters, but has not adequately been substantiated nor used to derive robust design expressions.

- A computer program was developed based on section analysis. Cyclic models were implemented for both steel and concrete. The steel model implemented is a modified 'massing' model with stiffness degradation, based on a tri-linear monotonic envelope. The stiffness degradation parameter was calibrated using the experimental results. Modifications were made to the technique including the effect of confinement. The analytical results from the flexural model compared well with the experimental results for a trial case. Significant differences in results were observed in vertical

deformations, for which the dilation of concrete due to the improper closure of cracks during cyclic loading, was considered responsible.

- Significant progress has been achieved in the development of shear models for analysis by the method of sections. A model for shear deformations was developed from first principles which utilises the normal strains and stresses given by the flexural model to estimate the shear stiffness.

- A small scale modelling procedure suitable for RC members under dynamic loading was developed. The procedure was based on the assumption that the member self weight is insignificant compared with the inertia forces to be resisted. The three fundamental quantities modelled were geometry, stiffness and velocity.

- A total of nine isolated RC wall models were tested at scales 1:5 and 1:2.5. One model (scale 1:5) was subjected to earthquake loading on the IC shaking table during a pilot experiment, whilst all the others were subjected to a displacement-controlled severe cyclic loading regime. The link between the two scales was achieved by testing similar models at both scales. Modelling was performed successfully; the only significant difference was observed in the initial stiffness for which a larger deviation from elasticity was shown by the smaller scale. This was attributed to higher shrinkage effects.

- The initial stiffness of all models was much lower than predicted by elasticity. By the first maximum displacement level imposed on the specimens, the secant stiffness was closer to the cracked member stiffness, thus, the use of this stiffness is recommended in the static and dynamic analysis of structures.

- The yield moment was estimated accurately by section analysis, and the effects of confinement were shown not to be important in the calculations at this level. Prior to yield, stiffness deterioration was more dependent on the maximum displacement level and less on the number of cycles at a particular displacement level.

- It was demonstrated analytically that the effect of concrete strength on the section moment capacity is not important for moderately confined walls. However, the use of moment capacity to predict the concrete compressive peak stress was demonstrated to be prone to

gross inaccuracies. Hence, doubts are cast over conclusions arrived by previous researchers at Imperial College regarding the shear capacity based on large concrete overstrength calculated by using the moment capacity.

- The expected moment capacity enhancement under axial loads was shown to be counterbalanced by a drop in ductility. Tensile axial loads demonstrated the opposite effects but imposed a high tensile strain demand on the flexural reinforcement. It was recommended that dimensioning of RC sections is undertaken by considering the maximum expected tensile axial loads

- Decomposition of flexural and shear deformations was shown to be performed accurately only if information on rotations is available throughout the height of the wall. It was demonstrated that by using rotations obtained only from the top, the shear deformations calculated were much higher than in reality.

- Shear reinforcement was activated only after the initiation of cracking. Dilation of concrete through imperfect closure of cracks meant that a permanent tensile strain was maintained even at zero shear load. The strain in this reinforcement increased almost linearly with the applied load. Inadequacy of shear reinforcement led to failure of wall SW5. Inadequacy of the anchorage of the same reinforcement led to shear deterioration of wall SW6 after the ultimate load was achieved. Yielding of this reinforcement in wall SW8 did not affect the deformational behaviour.

- Base wall rotations accounted for less than 2% of the total horizontal displacement at ultimate conditions. Out-of-plane deformations were demonstrated not to have any effect on the in-plane behaviour.

- Vertical dilation of the wall took place even prior to yield. This can only attributed to improper closure of the cracks due to the effect of shear deformations. Following yield, vertical extension took place mostly in the lower quarter of walls where most of the yielding was concentrated.

- Most of the strain energy was dissipated in the main flexural bars at the bottom extremities. Strains of bars further into the section were progressively increasing in tension.

- High levels of strains were also detected at the top of the wall. This is an indication of the partial development of the arch and tie mechanism within the member where less shear is required to be resisted in tension than in compression.

- A simple method for calculating the plastic hinge length was shown to yield good agreement with experimental results. Furthermore, the relationship between displacement and curvature ductility was investigated in the light of the results obtained from the analytical parametric study. Lower levels of displacement ductility were obtained than those predicted by simple method used in the draft EC8 (1988). This was found to be a result of lower calculated curvatures within the plastic hinge zone than assumed in the simplified method. A modified equation for converting displacement to curvature ductility was proposed. The ductility of a member was demonstrated to be enhanced by concentrating the flexural reinforcement at the extremities, by increased confinement and by decreasing the yield strength of the flexural reinforcement.

- A procedure for obtaining the amount confinement required to achieve a certain curvature ductility was outlined. This was based on providing a reliable estimate of the available ductility of the unconfined section in an equation developed which determines the confinement reinforcement for the required enhancement in ductility.

- The contribution of pre-yield cycling and shear deformations to the overall energy dissipation capacity was shown to be rather low. High energy dissipation capability was considered to be a result of plastic flexural deformations and high displacement ductilities.

- Based on the parametric study, an equation for allocating flexural reinforcement was proposed, yielding accurate results for walls with no axial loads. Ways in which the flexural capacity can be estimated in design were also outlined.

- A method for design against shear failure was proposed based on the evaluation of the minimum shear resistance surface (SRS). Comparisons with the experimental data showed that the above mentioned method yielded good results. The contribution of concrete

to shear resistance was evaluated separately for areas in compression and areas in tension.

- The minimum SRS in the compressive area is considered to be in the direction of principle compressive stress. The value of the minimum shear capacity, however, was shown to be dependent on the depth of the neutral axis and the concrete strength only. Parameters influencing the depth of the neutral axis were shown through the parametric study to be the amount and distribution of flexural reinforcement, the concrete strength and confinement, the steel material characteristics, the level of axial load and the effect of cyclic loading.

- In tension, concrete is only capable of resisting shear if appropriate reinforcement is available. The maximum level of shear resistance is dependent on the state of stress and a limit was given as to the maximum level of stress that can be achieved without web failure. By ignoring the effect of aggregate interlock or friction along cracked surfaces, it was shown that the shear resistance in tension is given by the truss analogy.

In summary, the current thesis has contributed towards the understanding of the behaviour of RC walls under repeated loading by identifying the causes of flexural overstrength as obtained from simplified design models, by providing a critical review and new ideas for the new design procedures for ductility and by proposing an original simple design method for shear design in RC members.

9.2 Suggestions for future work

A number of interesting questions still remain unanswered, new topics of research have been opened for investigation and several propositions require validation. Further investigation and development are required in the following:

- Development of a cyclic variable confinement model for concrete that takes into account accurately the effect of confinement with variable axial stress. Derivation of a concrete model that takes into account the contact effects of concrete due to the improper closure of cracks as a result of shear deformations. The further development of the

proposed shear model so as to make it totally independent of empirical relationships.

- The verification of the proposed design method for shear through further experimental studies. The extension of the method for shear in squat walls.

- Production of design charts and/or simple design equations for the estimate of the yield and ultimate capacities of RC members.Derivation of a simple equations for the estimation of the available ductility in unconfined members. The use of an energy balance method to arrive at equations relating the amount of required confinement to achieve a certain level of curvature ductility.

- The experimental study of walls with high percentages of reinforcement in the extremities including composite walls with channel or rectangular perforated hollow sections as boundary elements.

As an extension of the current work with a more global objective in Earthquake Engineering and Reinforced Concrete the following are recommended for future studies:

- Development of verifiable structural unit models for shear and flexure and their full interaction.

- Formulation of fully validated and efficient finite element cyclic models in two and three dimensions.

- The experimental and analytical investigation of the effect of the likely variability in concrete and steel material properties.

- The investigation of repair and strengthening techniques for damaged RC walls and the development of appropriate design and analysis techniques for assessment of the effect of intervention.

REFERENCES

ACI 318-83, " Building Code Requirement for Reinforced Concrete", American Concrete Institute, Detroit,1983, 111 pp.

ACI, "Shear in reinforced concrete", American Concrete Institute, Publication SP-42, Vols 1-2,Detroit,1974

Aktan, A.E. and Bertero, V.V., "RC Structural Walls: Seismic design for shear", Journal of Structural Engineering, ASCE, Vol. 111, No. 8, August 1985, pp 1775-1791

Aoyama, H. and Yoshimura, M., "Tests on RC walls subjected to bi-axial loading", 7th World Conference in Earthquake Engineering, Vol. 7, Istanbul, Turkey, 1980, pp 511-518

ASCE, "Finite element analysis of reinforced concrete",State of the Art report, American Society of Civil Engineers, New York,1982, p.292

Benjamin, J.R. and Williams, H.A., "Behaviour of One-Storey Reinforced Concrete Shear Walls", Journal of Structural Division, ASCE,Vol. 83, ST3, May 1957, pp 1-49

Blume, J.A., Newmark, N.M. and Corning, L.H., "Design of Multistorey Reinforced Concrete Buildings for Earhtquake Motions", Portland Cement Association, Skokie,Illinois,1961

Cardenas, A.E.,Hanson, J.M., Corley, W.G. and Hognestad, E., "Design Provisions for Shear Walls", ACI Journal Proc., 70(3), American Concrete Institute, Detroit, March 1973, pp 221-230

Cardenas, A.E.,Russel, H.G and Corley, W.G., "Strength of low rise structural walls", SP-63, American Concrete Institute, Detroit, 1980, pp 221-241

Clough, R.W., "Effects of Stiffness Degradation on Earthquake Ductility Requirements", Report No. 66-16, Department of Civil Engineering, University of California, Berkley, October 1966

Daniel, J.I., Shiu, K.N. and Corley, W.G., "Openings in Earthquake-Resistant Structural Walls", Journal of Structural Engineering, ASCE, Vol. 112, No. 7, July 1986, pp 1660-1676

Divakar, M.P., Fafitis A. and Shah, S.P., "Constitutive model for shear transfer in cracked concrete", Journal of Structural Engineering, ASCE, Vol. 113, No. 5, May 1987, pp 1046-1062

EC2, "Eurocode No.2 : Common Unified Rules for Concrete Structures", Report EUR 8848 DE, EN, FR, Industrial Processes, Building and Civil Engineering, Commission of the European Communities, 1984

EC8, "Eurocode No.8 : Structures in seismic regions - Design ", Part 1, General and building, Report EUR 12266 EN, Industrial Processes, Building and Civil Engineering, Commission of the European Communities, May 1988

Elnashai, A.S., "Nonlinear analysis of composite tubular joints", PhD Thesis, University of London, 1984

Elnashai, A.S., Pilakoutas, K. and Ambraseys, N.N., "Design of Small Scale Reinforced Concrete Structural Wall Models for Shake-table Testing", Civil Engineering Dynamics Conference, SECED, March Bristol, 1988 a

Elnashai, A.S., Pilakoutas, K., Ambraseys, N.N., "Shake-table testing of small scale structural walls", Procs of 9th World Conference on Earthquake Engineering, Vol. IV, Tokyo-Kyoto, 1988 b, pp541-546

Elwi, A.A., and Murray, D.W., "A 3D hypoelastic concrete constitutive relationship." Journal of Engineering Mechanics, ASCE, Vol. 105, No. 4, pp 623-641

Goodsir, W.J., "The design of coupled frame-wall structures for seismic actions", PhD Thesis, University of Canterbury, Chistchurch, New Zealand,1985

Hays,C.O., "Inelastic Material Models in Earthquake Response", Journal of Structural Engineering, ASCE, Vol. 107, No. 1, January 1981, pp 13-28

Hernandez, O.B. and Zermeno, de L.M.E., "Strength and behaviour of structural wall with shear failure", Proc. 7th World Conference on Earthquake Engineering, Vol. 4, Istanbul,Turkey, September 1980, pp. 121-124

Hiraishi, H., "Evaluation of shear and flexural deformations of flexural type shear walls", 8th World Conference on Earthquake Engineering, San Francisco, 1984, pp 677-685

Hiraishi, H., Nakata, S., Kitagawa, Y.and Kaminosono, T., "Static tests on shear walls and beam-column assemblies and study between shaking table tests and pseudo-dynamic tests", Publication SP-84, American Concrete Institute, Detroit, 1985, pp 11-48

Iliya, R.and Bertero, V.V., "Effects of amount and arrangement of wall-panel reinforcement on hysteretic behaviour of reinforced concrete walls", Report No EERC -80/04, Earthquake Engineering Research Centre, University of California, Berkeley, February 1980

International Association for Earthquake Engineering, "Earthquake resistant regulations", A World List-1988, Tokyo, Japan, July 1988

Kenneally, R.M. and Burns, Jr J.J., "Experimental investigation into the seismic behaviour of nuclear power plant shear wall structures", Nuclear Engineering and Design, 107, Amsterdam, North-Holland, 1988, pp 95-107

Kotsovos, M.D., "A mathematical model of the deformational behaviour of concrete under generalised stress based on fundamental material properties", Materiaux and Construction, RILEM, Vol. 13, No 76, 1980, pp 289-298

Kotsovos, M.D., "Mechanisms of shear failure", Magazine of Concrete Research, Vol. 35, No. 123, 1983 pp 99-106

Kotsovos, M.D. and Newman, J.B., "Fracture mechanics and concrete behaviour", Magazine of Concrete Research, Vol. 33, 1981, pp 103-112

Lefas, I., "Behaviour of Reinforced Concrete Structural Walls", PhD Thesis, University of London, 1988

Lefas, I. and Kotsovos, M.D., "Behaviour of reinforced concrete structural walls: A new interpretation.",Proceedings, Computational Mechanics of Concrete Structures, Advances and applications, IABSE Colloquim, Delft, 1987

Lopes, M.M., "Design of reinforced concrete walls subjected to high cyclic shear",PhD Thesis, University of London, (To be submitted 1991)

Lopes, M.M. and Elnashai, A.S., "Behaviour of reinforced concrete walls subjected to high cyclic shear", Ninth European Conference on Earthquake Engineering, Moscow, 1990, (paper accepted for presentation)

Mander, J.B, Priestley, M.J.N. & Park, R., "Seismic design of bridge piers", Research Report No. 84-2, University of Canterbury, New Zealand, 1984

Mander, J.B, Priestley, M.J.N. & Park, R., "Theoretical Stress-Strain Model for Confined Concrete", Journal of Structural Engineering, ASCE, Vol. 114, No. 8, August 1988a, pp 1804-1826

Mander, J.B, Priestley, M.J.N. & Park R., "Observed Stress-Strain Behaviour of Confined Concrete", Journal of Structural Engineering, ASCE, Vol. 114, No. 8, August 1988b, pp 1827-1849

Menu, J.M., "Interpolation, Fourier analysis and elliptic filtering of strong-motion records", ESEE 87.5, Civil Engineering Department, Imperial College, December 1987.

Menu, J. and Elnashai, A.S., "Earthquake time-history transformation for small-scale dynamic testing", Civil Engineering Dynamics Conference, SECED, March 1988, Bristol

Morgan, B., Hiraishi, H. and Corley, W.G., "Medium scale wall assemblies : Comparison of analysis and results", Publication SP-84, American Concrete Institute, Detroit, 1985, pp 241-269

NZS 3101:1982, Parts 1 &2, "Code of Practice for the Design of Concrete Structures", Standards Association of New Zealand, Wellington, 1982, 283 pp.

NZS 4203:1984, "Code of Practice for General Structural Design and Design Loadings for Buildings", Standards Association of New Zealand, Wellington, 1984, 100 pp.

Noor, F.A., Raveendran, S. and Evans, W., "Production and use of high yield model reinforcement." In Design of concrete structures : The use of model analysis, The informal study group - Model analysis as a design tool, Institution of Structural Engineers, 1985, pp 69-78

Oesterle, R.G., Aristizabal-Ochoa, J.D., Shiu, K.N and Corley, W.G., "Web

crushing of reinforced concrete structural walls", ACI Journal, Vol 81,Detroit Michigan, 1984, pp 231-241

Oesterle, R.G.and Fiorato, A.E., "Seismic design of reinforced concrete walls", 8th World Conference on Earthquake Engineering, San Francisco, 1984, pp 515-522

Oesterle, R.G., Fiorato, A.E., and Corley, W. G., "Design of earthquake resistant structural walls", Proceedings of the Fourth Canadian Conference on Earthquake Engineering, Vancouver, Canada, June 1983, pp.81-91

Park, R. and Paulay, T., "Reinforced Concrete Structures"John Wiley and Sons, New York, 1975, 769 pp.

Paulay, T. and Uzumeri, S.M., "A Critical Review of the Seismic Design Provisions for Ductile Shear Walls of the Canadian Code and Comments", Canadian Journal of Civil Engineering, Vol.2, December 1975, pp. 592-601

Paulay, T. and Williams, R.L., "The analysis and design of and the evaluation of design actions for reinforced concrete ductile shear wall structures", Bulletin of the New Zealand National Society for Earthquake Engineering, Vol. 13 No. 2, June 1980, pp 103-143

Pilakoutas, K., Elnashai A.S. and Ambraseys, N.N., "Experimental observations on the behaviour of reinforced concrete walls under cyclic and earthquake loading", Ninth European Conference on Earthquake Engineering, Moscow, 1990, (paper accepted for presentation)

Popov, E.P. & Peterson, H., "Cyclic Metal Plasticity : Experiments and Theory", Journal of Engineering Mechanics, ASCE, Vol. 104, No.6, December 1978, pp 1371-1888

Probst, E.H. and Combrie, J., (eds), "Civil Engineering Reference Book", Butterworths Scientific Publications, London,1951

Regan, P., "Shear in Reinforced Concrete ; an experimental study", A report to the Construction Industry Research ans Information Association, Imperial College, Department of Civil Engineering, April 1971 a

Regan, P., "Shear in Reinforced Concrete ; an analytical study", A report to the Construction Industry Research ans Information Association, Imperial College, Department of Civil Engineering, 1971 b

Rothe, D. and König G., "Behaviour of reinforced concrete structural wall elements", Procs of 9th World Conference on Earthquake Engineering, Vol. VI, Tokyo-Kyoto, 1988, pp 47-52

Santhanam, T.K., "Model for Mild Steel in Inelastic Frame Analysis", Journal of Structural Engineering, ASCE, Vol. 105, No. 1, January 1979, pp 199-220

Schickert, G., and Winker, H., "Results of tests concerning strength and strain of concrete subjected to multiaxial compressive stresses." Deutscher Ausschuss fur Stahlbeton, Heft 277, Berlin, West Germany, 1979

Sheikh, S.A. and Uzumeri, S.M., "Strength and Ductility of Tied Concrete columns", Journal of Structural Engineering, ASCE, Vol. 106, No. 5, May 1980, pp 1079-1102

Sheikh, S.A. and Uzumeri, S.M., "Analytical Model for Concrete Confinement in Tied Columns", Journal of Structural Engineering, ASCE, Vol. 108, No. 12, December 1982, pp 2703-2722

Tassios, T.P., "Specific rules for concrete structures", In Backround Document for Eurocode 8 - Part 1, Volume 2 - Design Rules, Commission of European Communities, 1989, pp 1-123

Tassios, T.P.and Chronopoulos, M.P., "RC wall cross-section design for a given behaviour factor of the building", Procs of the 9 th World Conference on Earthquake Engineering, Vol. 5, Tokyo-Kyoto, 1988, pp 1125-1130

Tassios, T.P. and Vintzeleou E., "Concrete to Concrete Friction", Journal of Structural Engineering, ASCE, Vol. 113, No. 4, April 1987, pp 832-849

Timoshenko, S.P. and Goodier, J.N., "Theory of Elasticity", McGraw-Hill Book Co., 3rd Edition, Singapore, 1982

Uniform Building Code, International Conference of Building Officials, Whittier, California, 1988

Vallenas, J.M., Bertero, V.V. and Popov, E.P., "Concrete confined by rectangular hoops and subjected to axial loads", Report No EERC-77/13, Earthquake Engineering Research Centre, University of California, Berkeley, August 1977

Vallenas, J.M., Bertero, V.V. and Popov, E.P., "Hysteretic behaviour of reinforced concrete walls", Report No EERC-79/20, Earthquake Engineering Research Centre, University of California, Berkeley, August 1979

Wagner, T.M. and Bertero V.V., "Mechanical behavior of shear wall vertical boundary members: an experimental investigation", Report No EERC-82/18, Earthquake Engineering Research Centre, University of California, Berkeley, October 1982

Wakabayashi, M., "Design of Earthquake Resistant Buildings", McGraw-Hill Inc., USA, 1986

Wallace, B. and Krawinkler, H., "Small scale model tests of structural components and assemblies", Publication SP-84, American Concrete Institute, Detroit, 1985, pp 305-346

Wang, T.T., Bertero, V.V., and Popov, E.P., "Hysteretic behaviour of reinforced concrete framed walls", Report No EERC 75-23, Earthquake Engineering Research Centre, University of California, Berkeley, December 1975

Willam, K.J., and Warnke, E.P., "Constitutive model for the triaxial behaviour of concrete." Proc., International Association for Bridge and Structural Engineering, Vol. 19, 1975, pp.1-30

Yamaguchi, I., Sugano, S., Higashibata, Y. and Nagashima, T.,

"Inelastic, cyclic behaviour of reinforced concrete frame-wall structures subjected to lateral forces", Proc. 7th World Conference on Earthquake Engineering, Vol. 7, Istanbul,Turkey, September 1980, pp. 333-340

Zahn, F.A., Park, R., Priestley, J.N. and Chapman, H.E., "Development of design prcedures for the flexural strength and ductility of reinforced concrete bridge columns", Bulletin of the New Zealand Society for Earthquake Engineering, Vol. 19, No.3, September 1986, pp. 200-212

Zhu, B., Wu, M. and Zhang, K., "A Study of Hysteretic Curve of Reinforced Concrete members under Cyclic Loading", 7th World Conference in Earthquake Engineering, Vol. 6, Istanbul, Turkey, 1980, pp 509-516

APPENDIX A

A Experimental results

A.(2) Load-displacement curves - Scale 1:5 model SW2

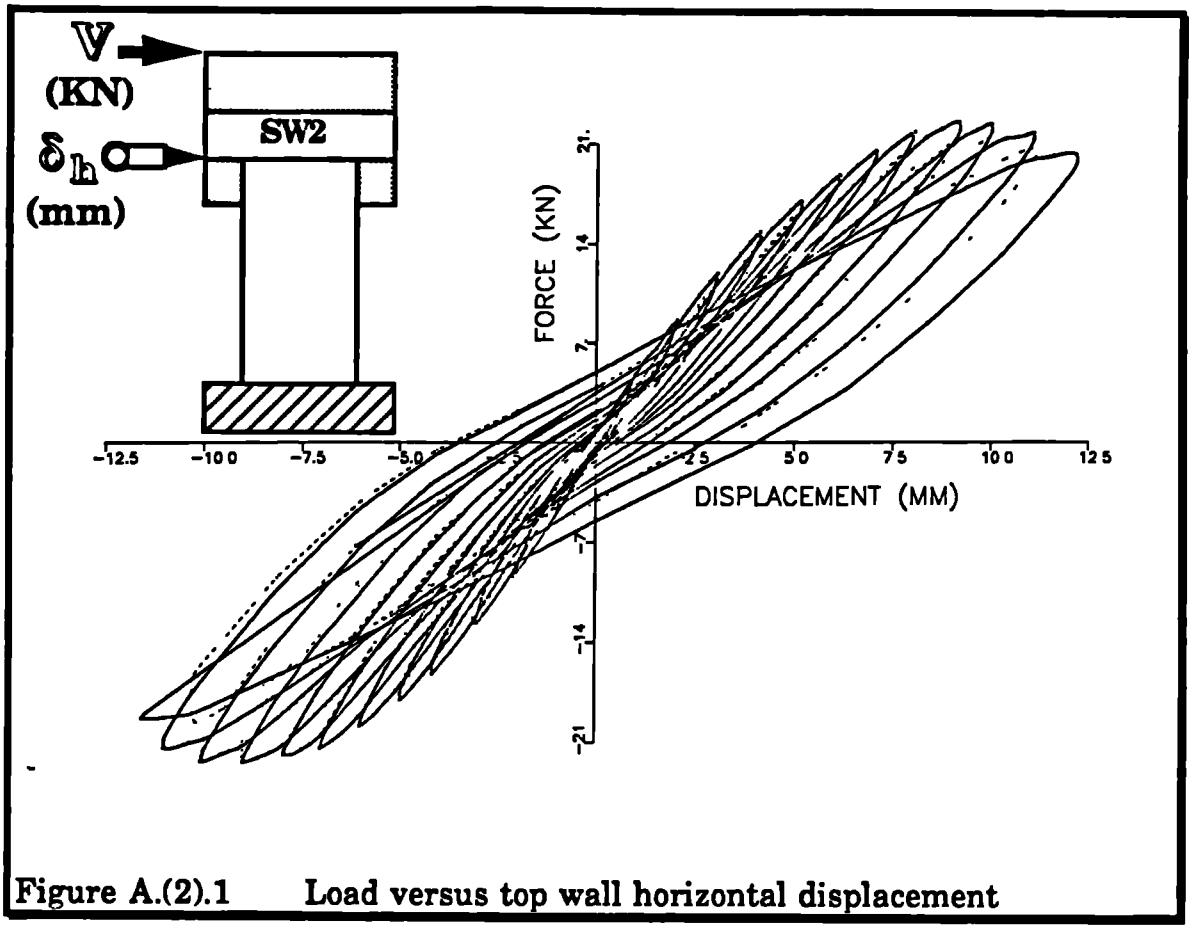


Figure A.(2).1 Load versus top wall horizontal displacement

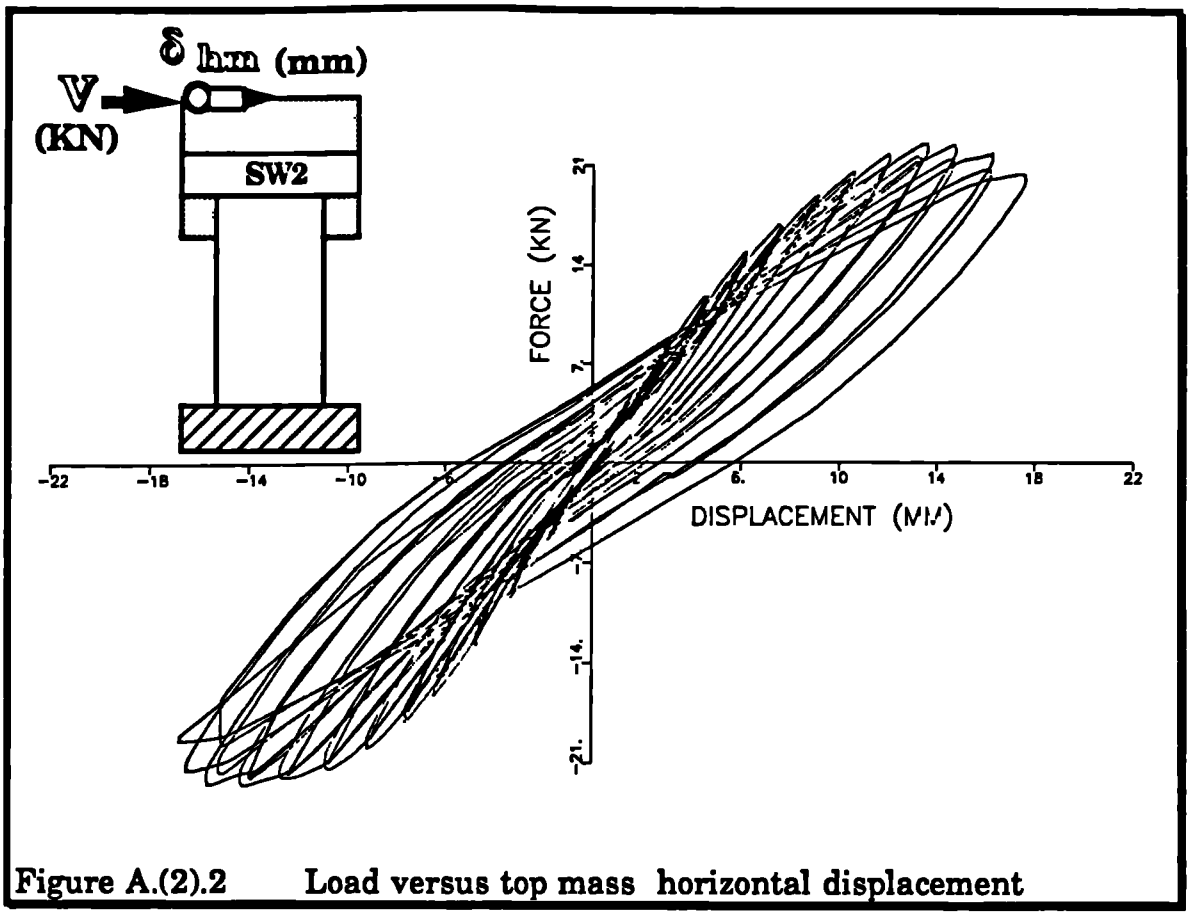


Figure A.(2).2 Load versus top mass horizontal displacement

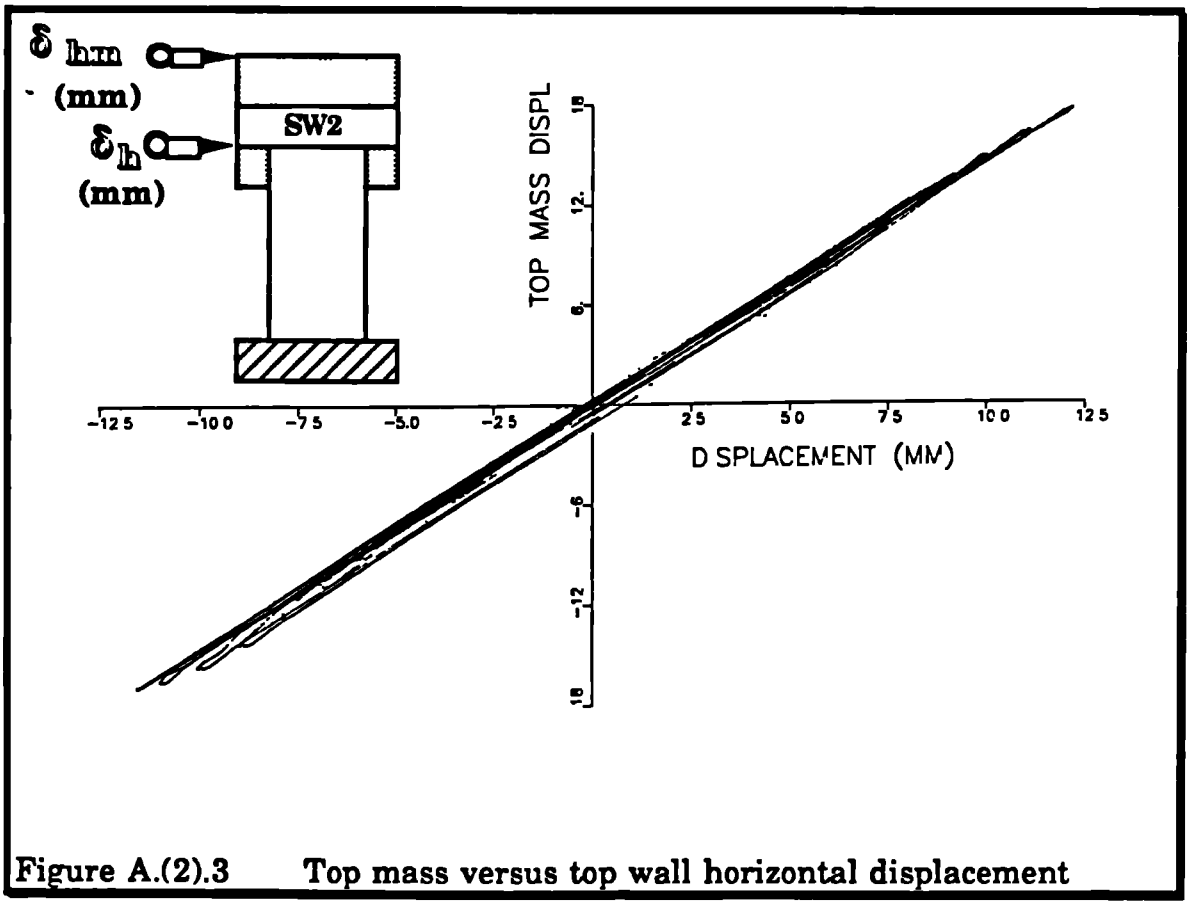


Figure A.(2).3 Top mass versus top wall horizontal displacement

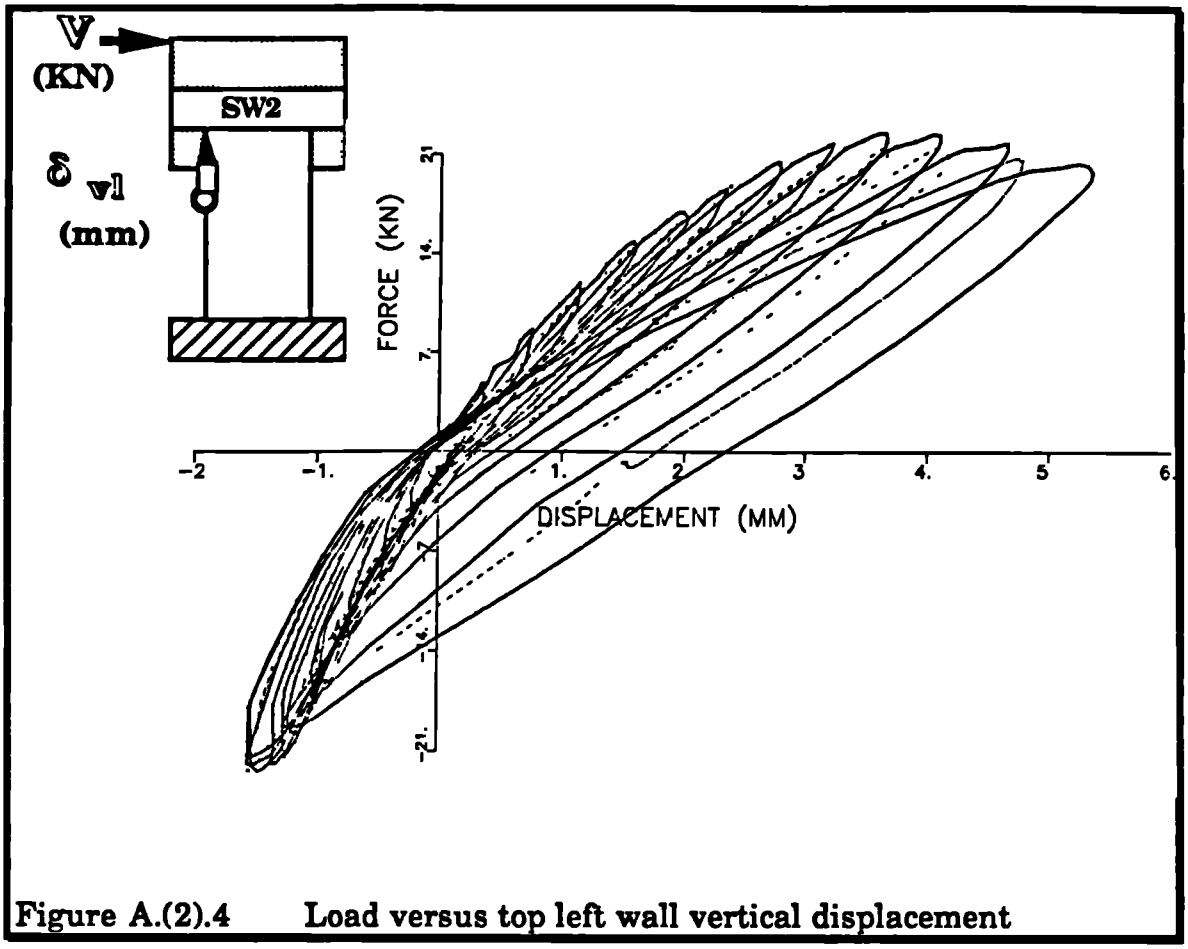


Figure A.(2).4 Load versus top left wall vertical displacement

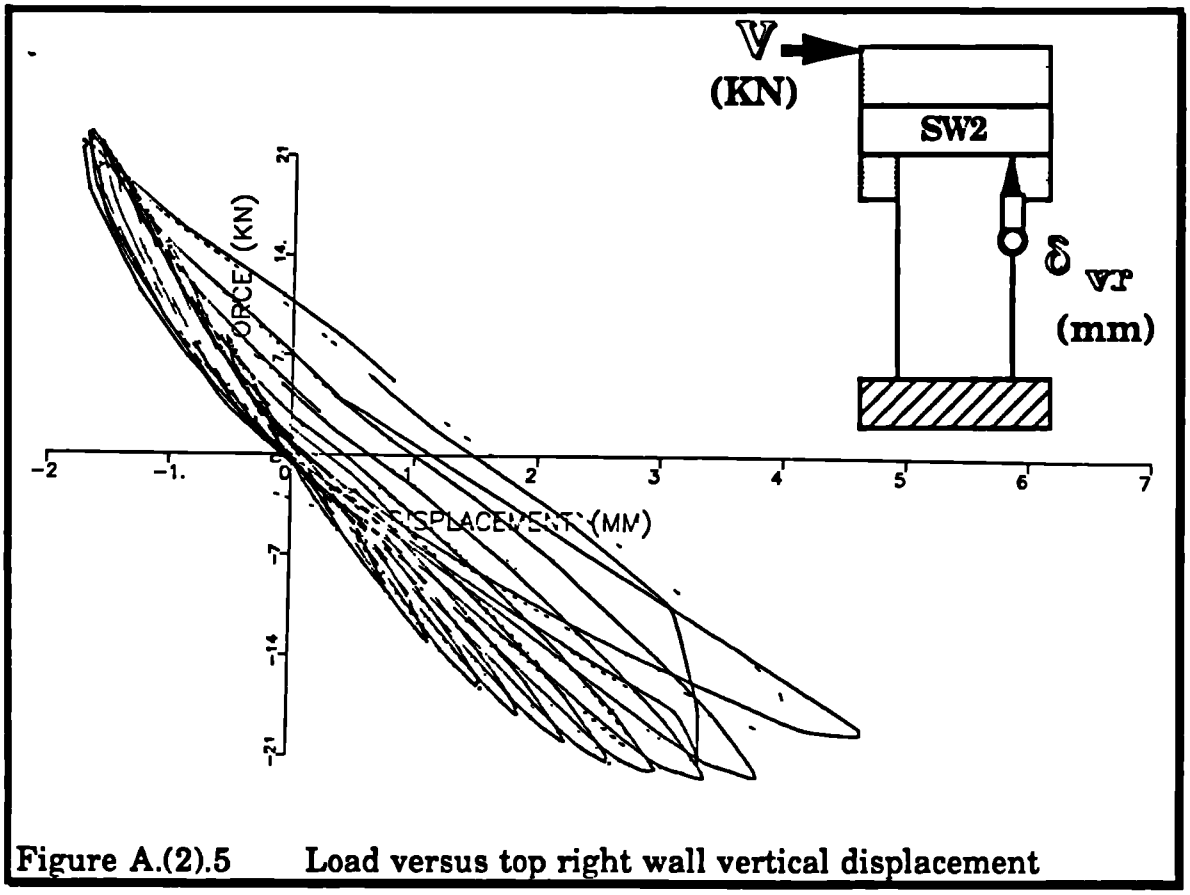


Figure A.(2).5 Load versus top right wall vertical displacement

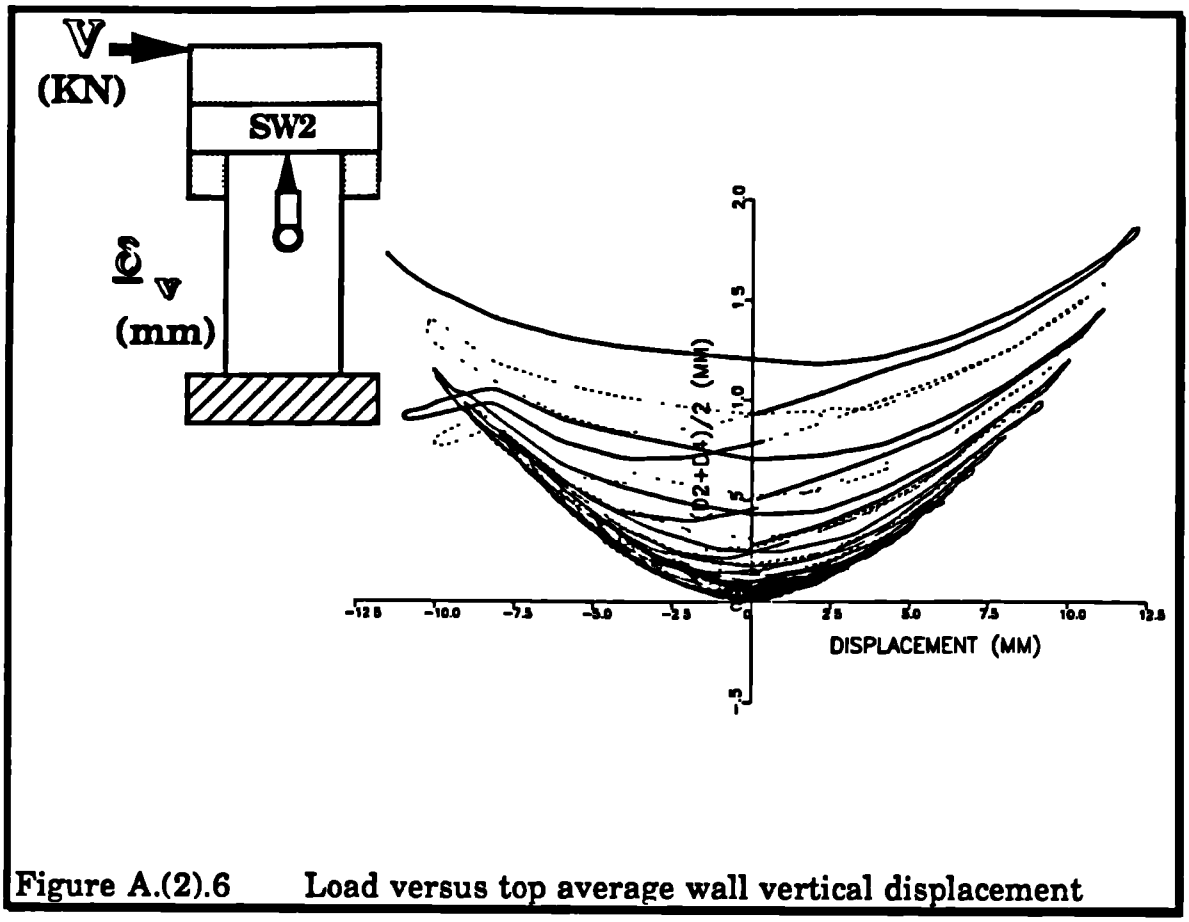


Figure A.(2).6 Load versus top average wall vertical displacement

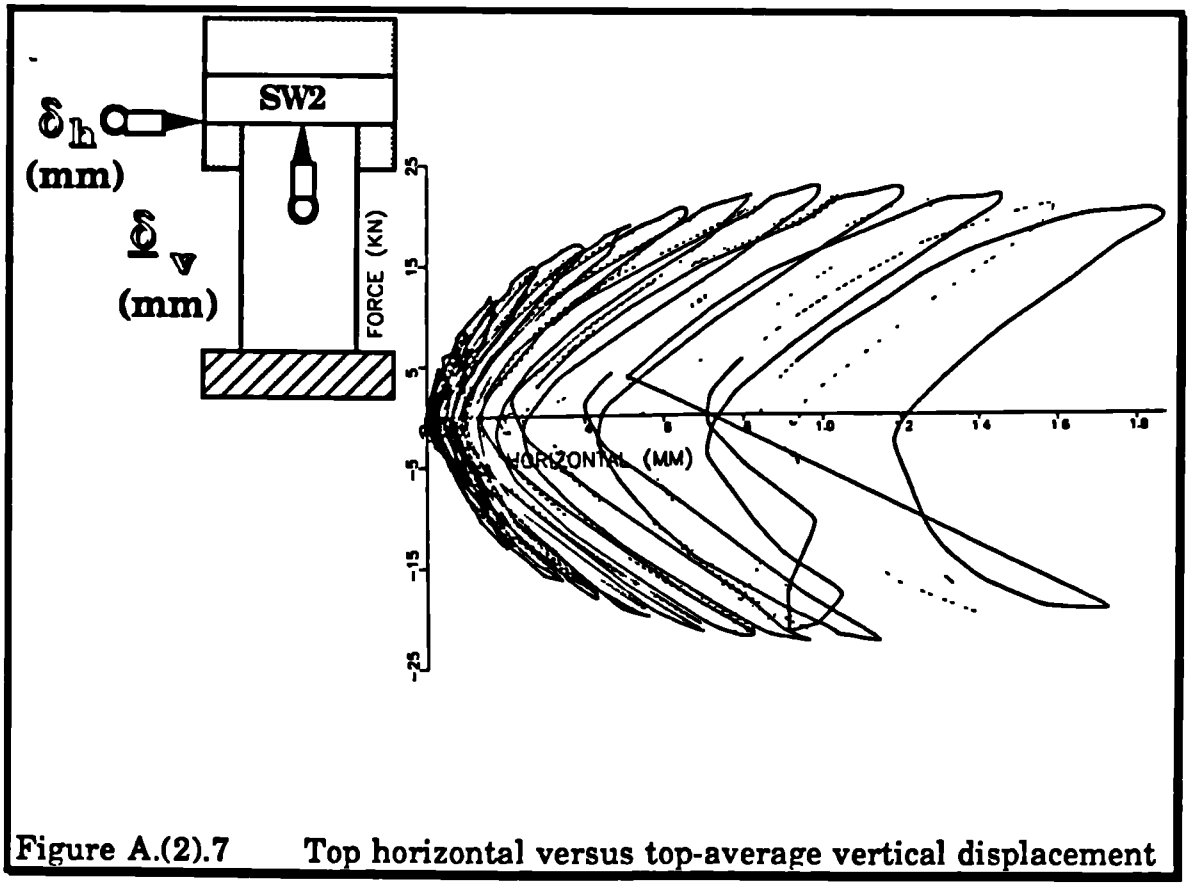


Figure A.(2).7 Top horizontal versus top-average vertical displacement

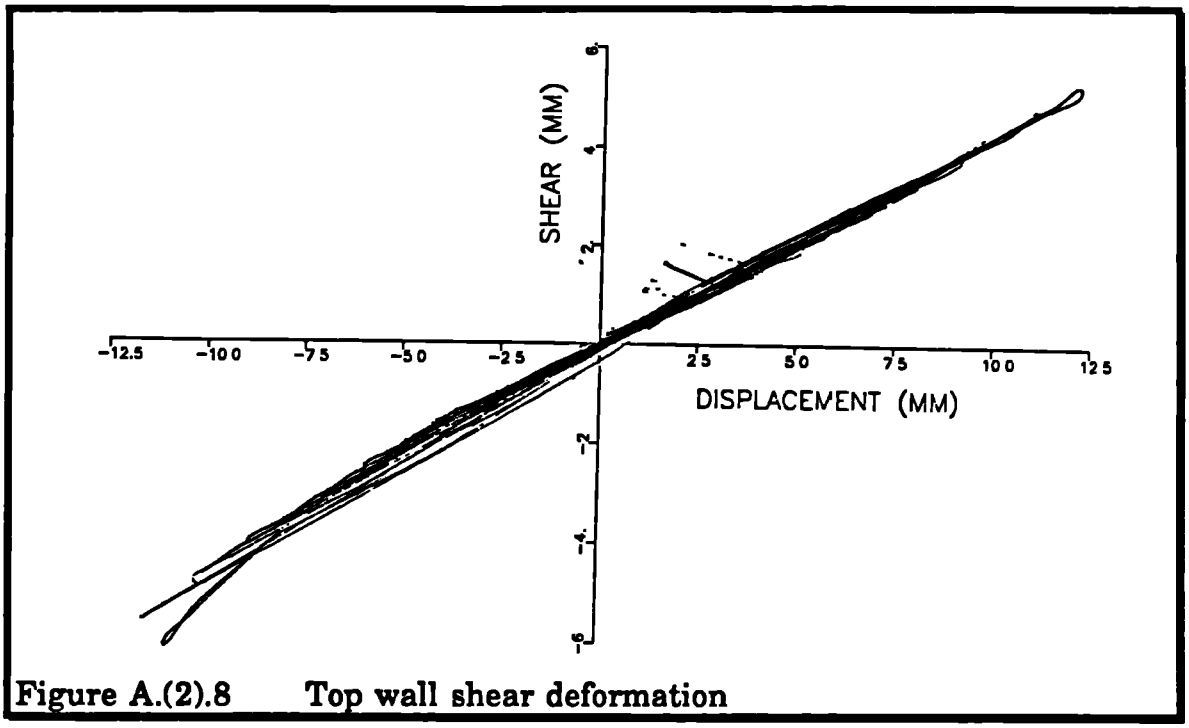


Figure A.(2).8 Top wall shear deformation

A.(2) Strain gauge readings - Scale 1:5 model SW2

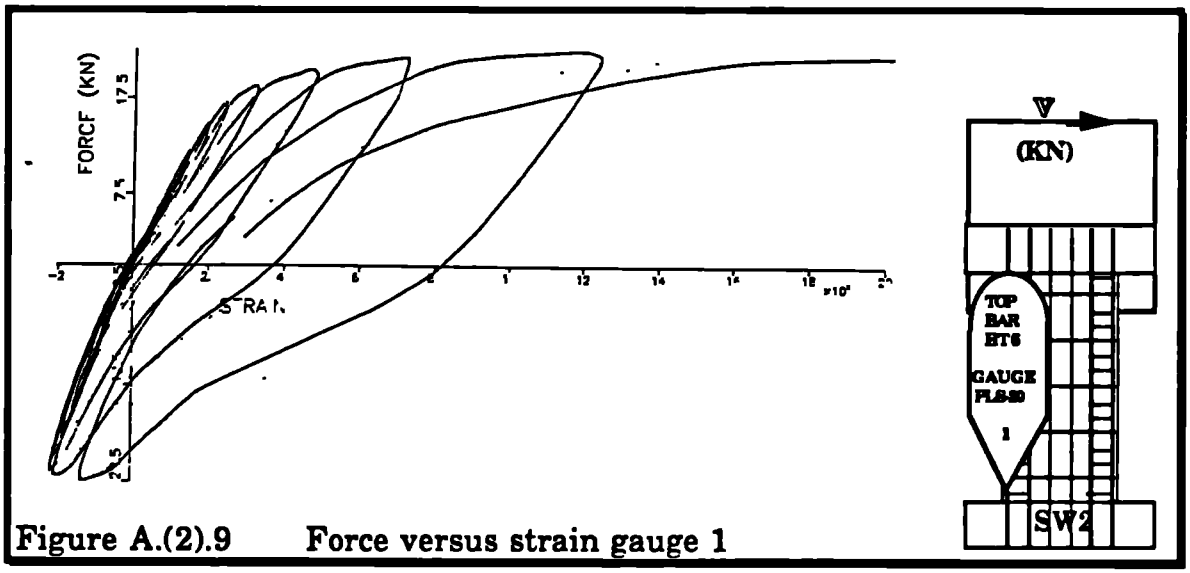


Figure A.(2).9 Force versus strain gauge 1

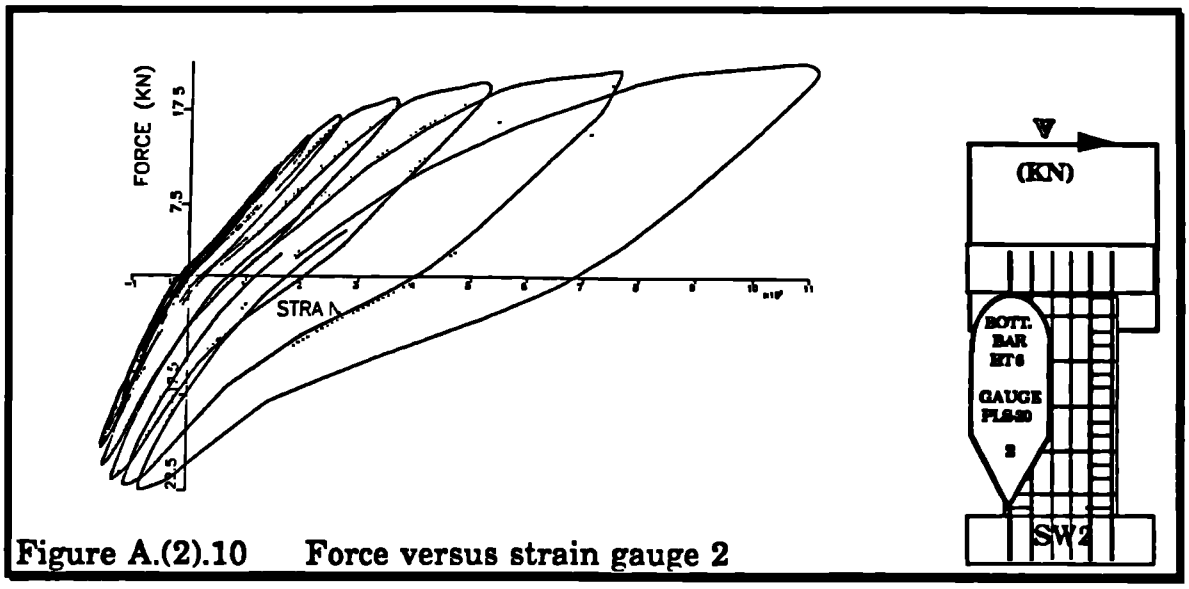


Figure A.(2).10 Force versus strain gauge 2

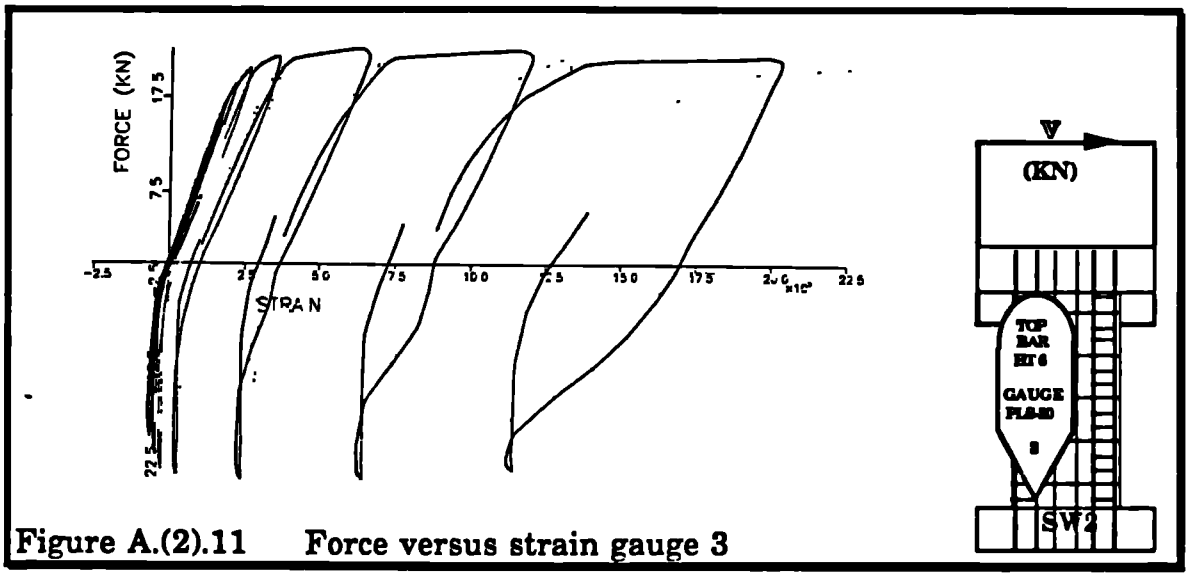


Figure A.(2).11 Force versus strain gauge 3

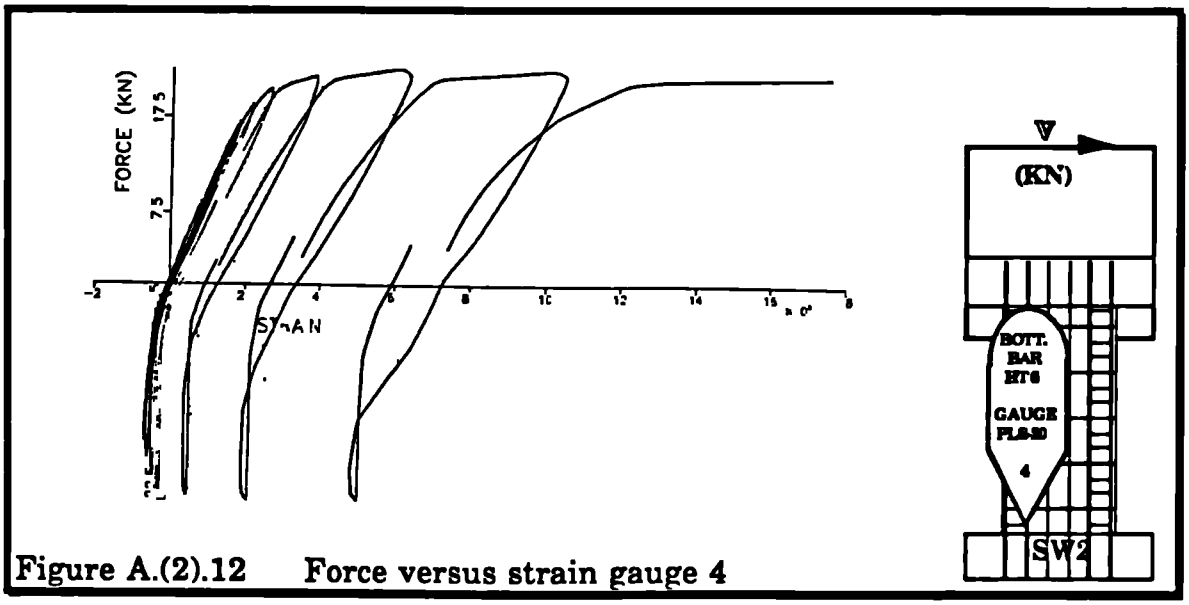


Figure A.(2).12 Force versus strain gauge 4

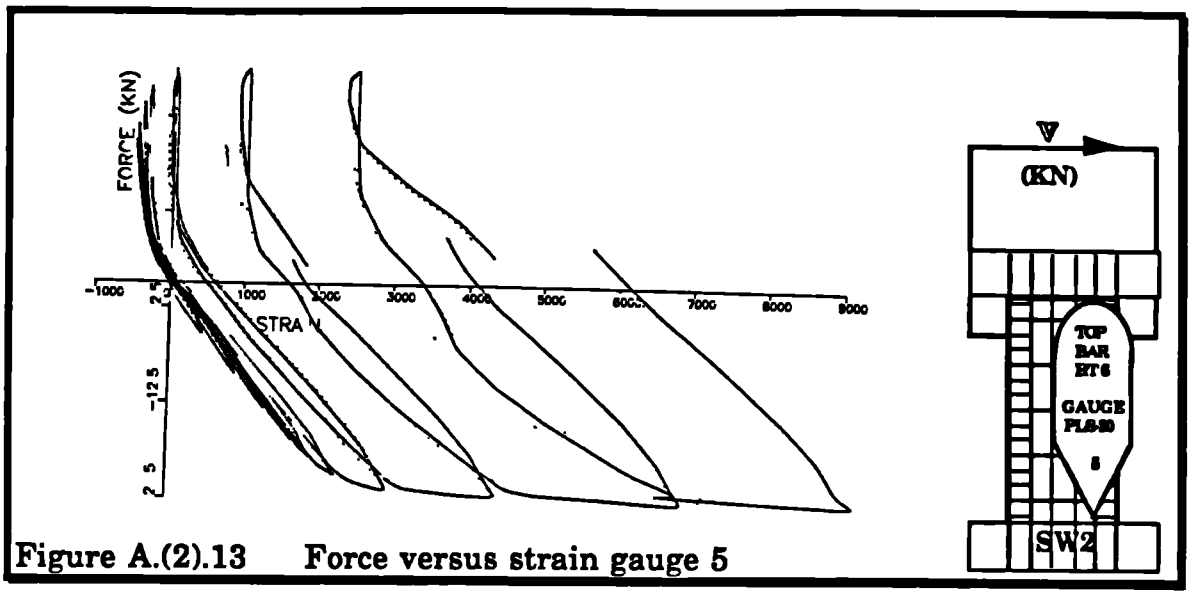


Figure A.(2).13 Force versus strain gauge 5

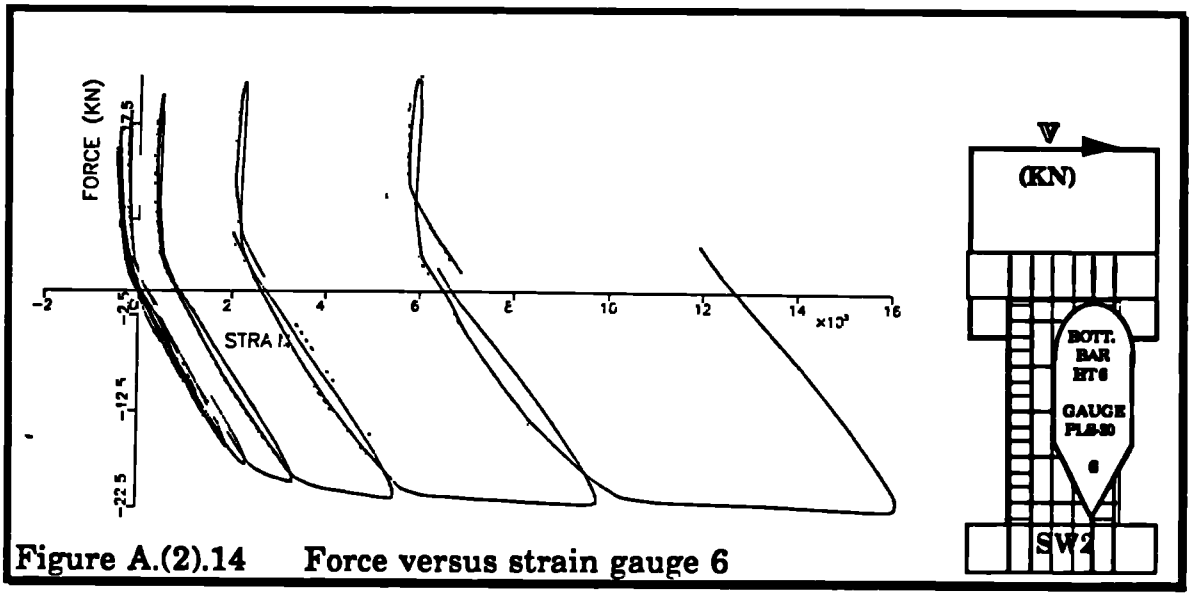


Figure A.(2).14 Force versus strain gauge 6

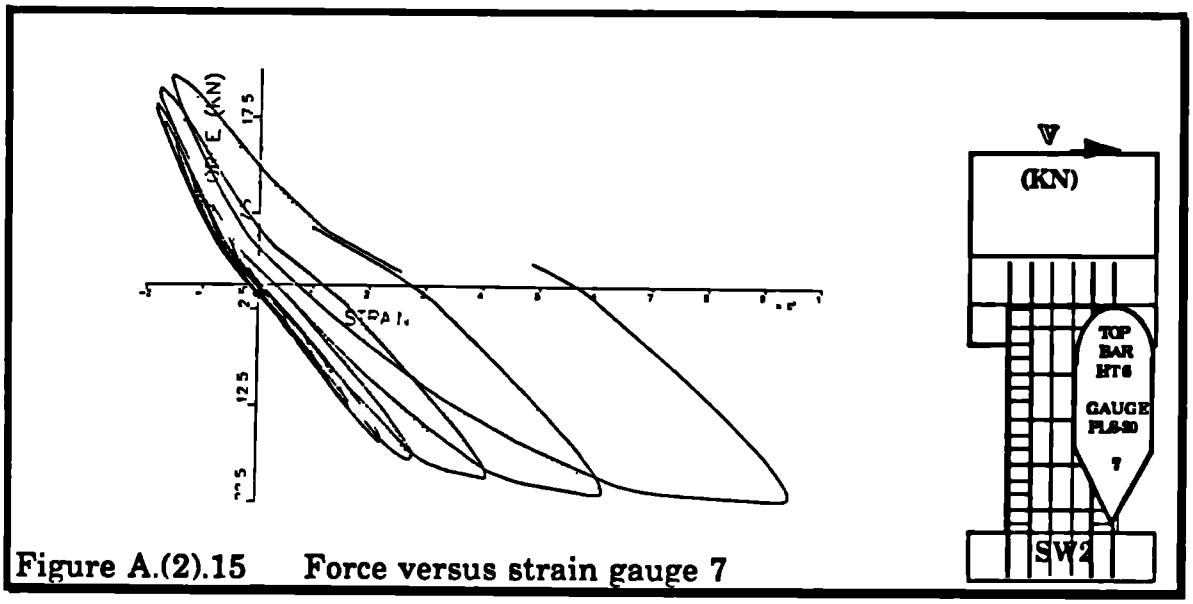


Figure A.(2).15 Force versus strain gauge 7

A.(3) Load-displacement curves - Scale 1:5 model SW3

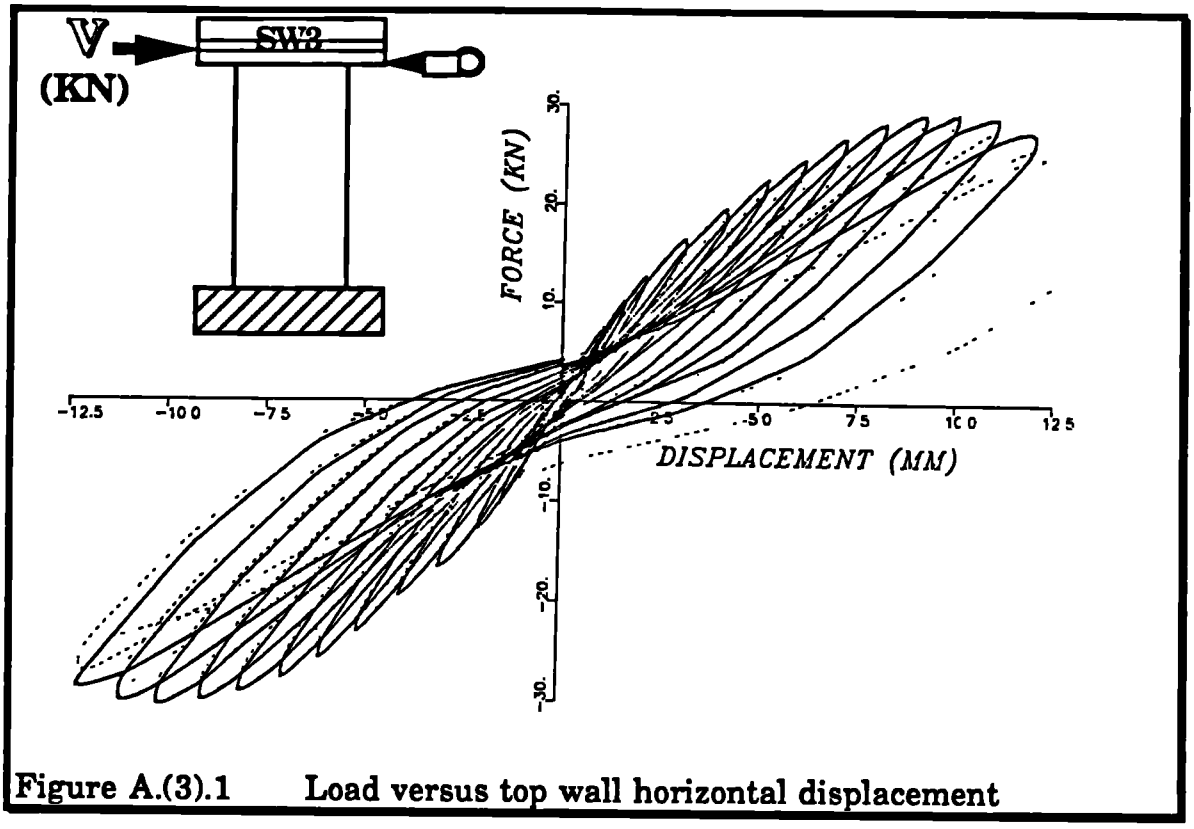


Figure A.(3).1 Load versus top wall horizontal displacement

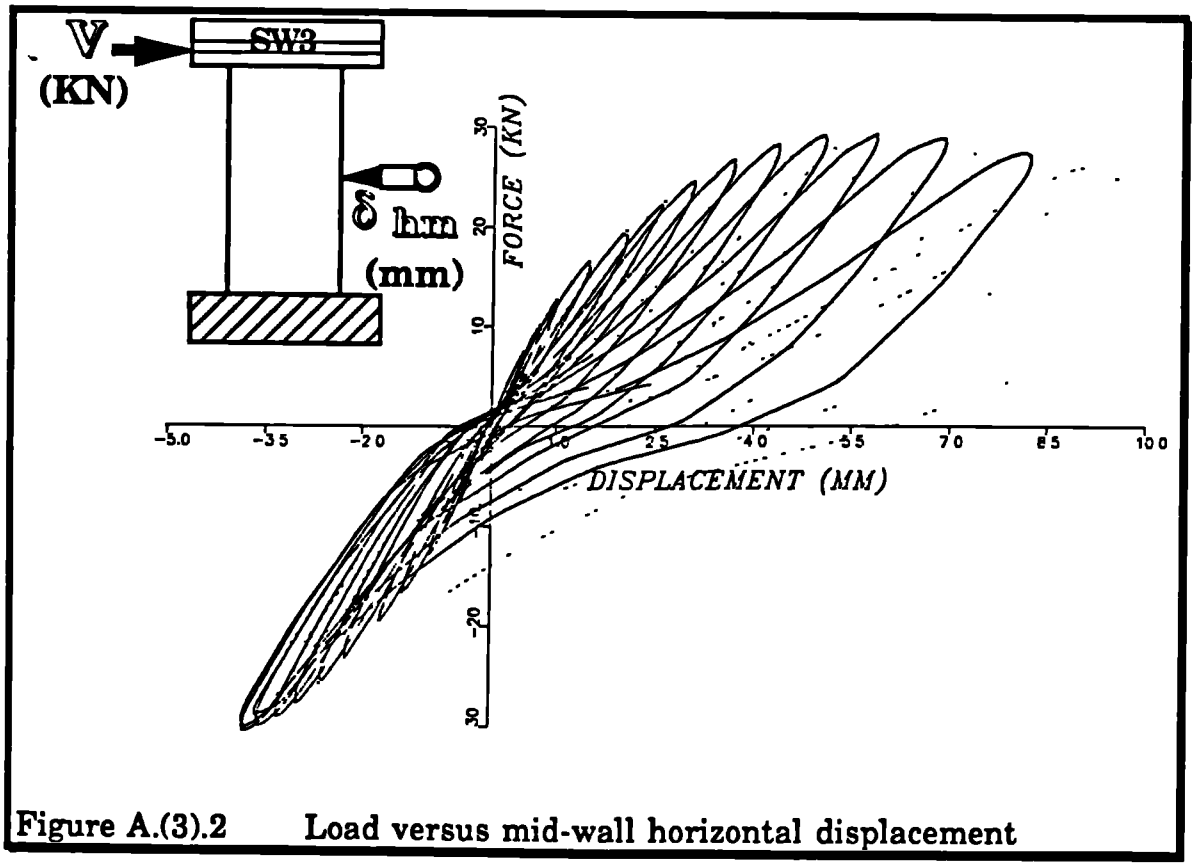


Figure A.(3).2 Load versus mid-wall horizontal displacement

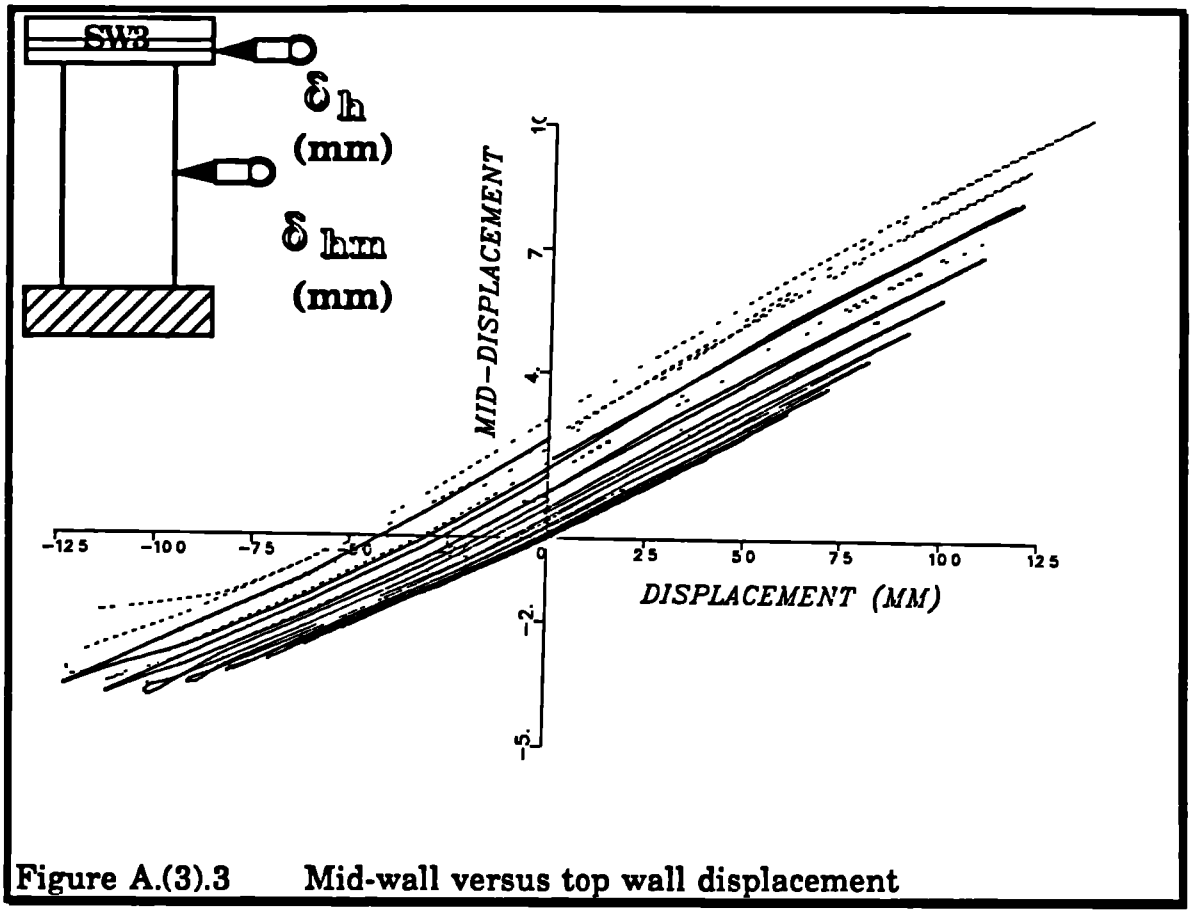


Figure A.(3).3 Mid-wall versus top wall displacement

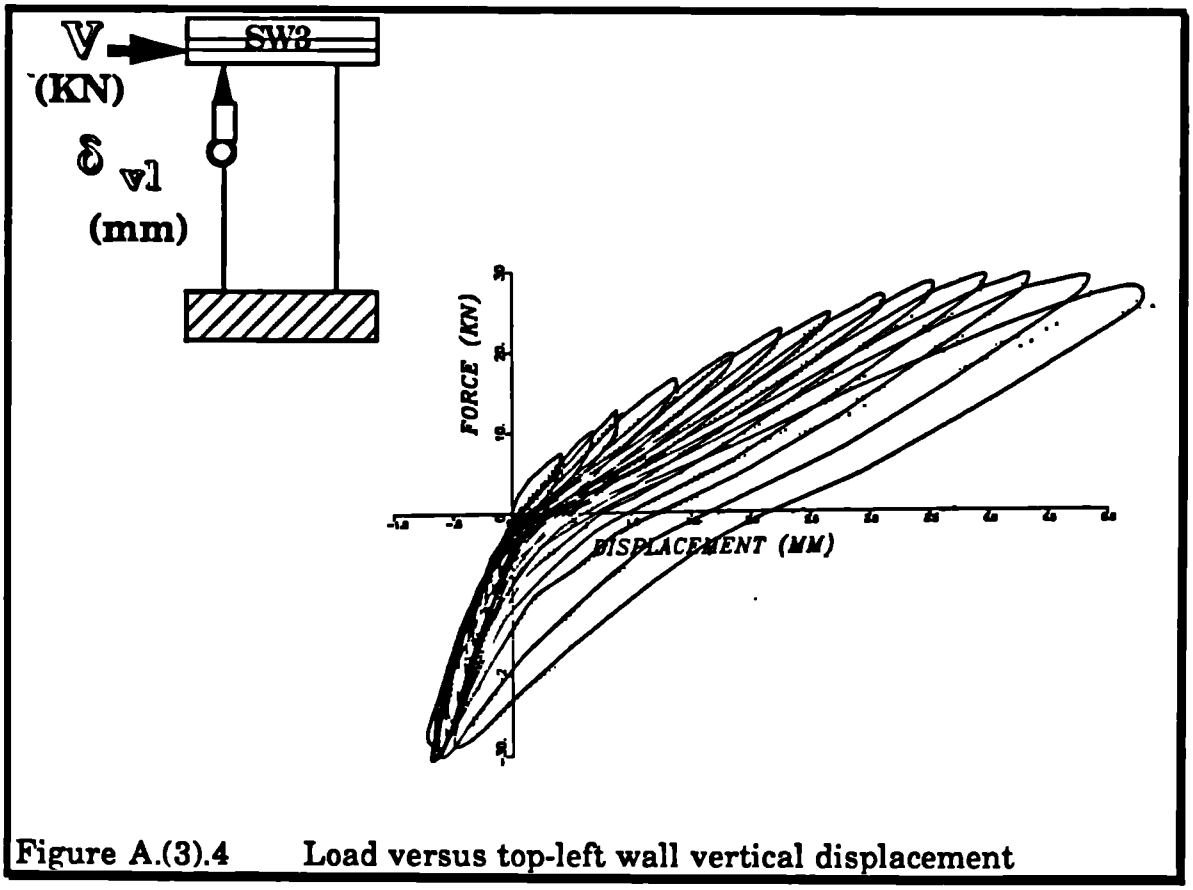


Figure A.(3).4 Load versus top-left wall vertical displacement

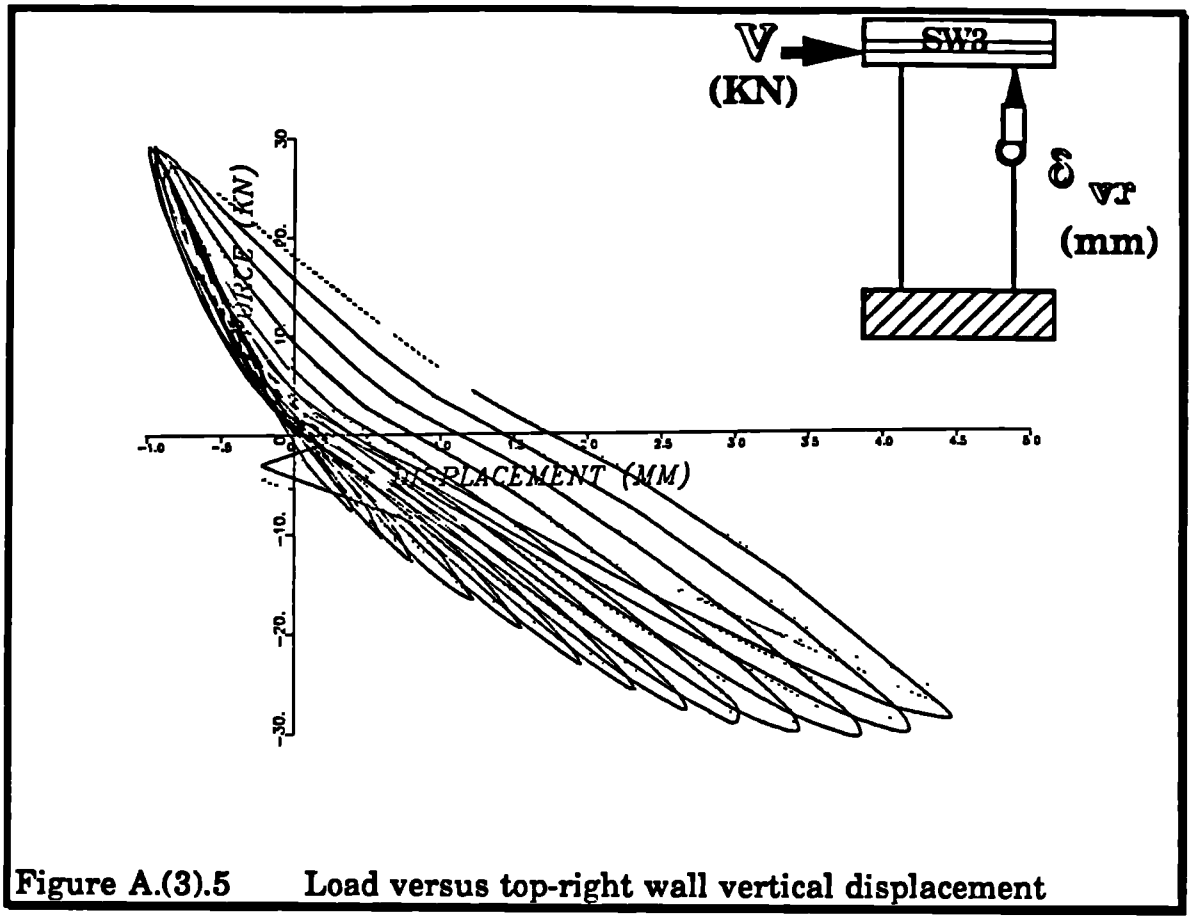


Figure A.(3).5 Load versus top-right wall vertical displacement

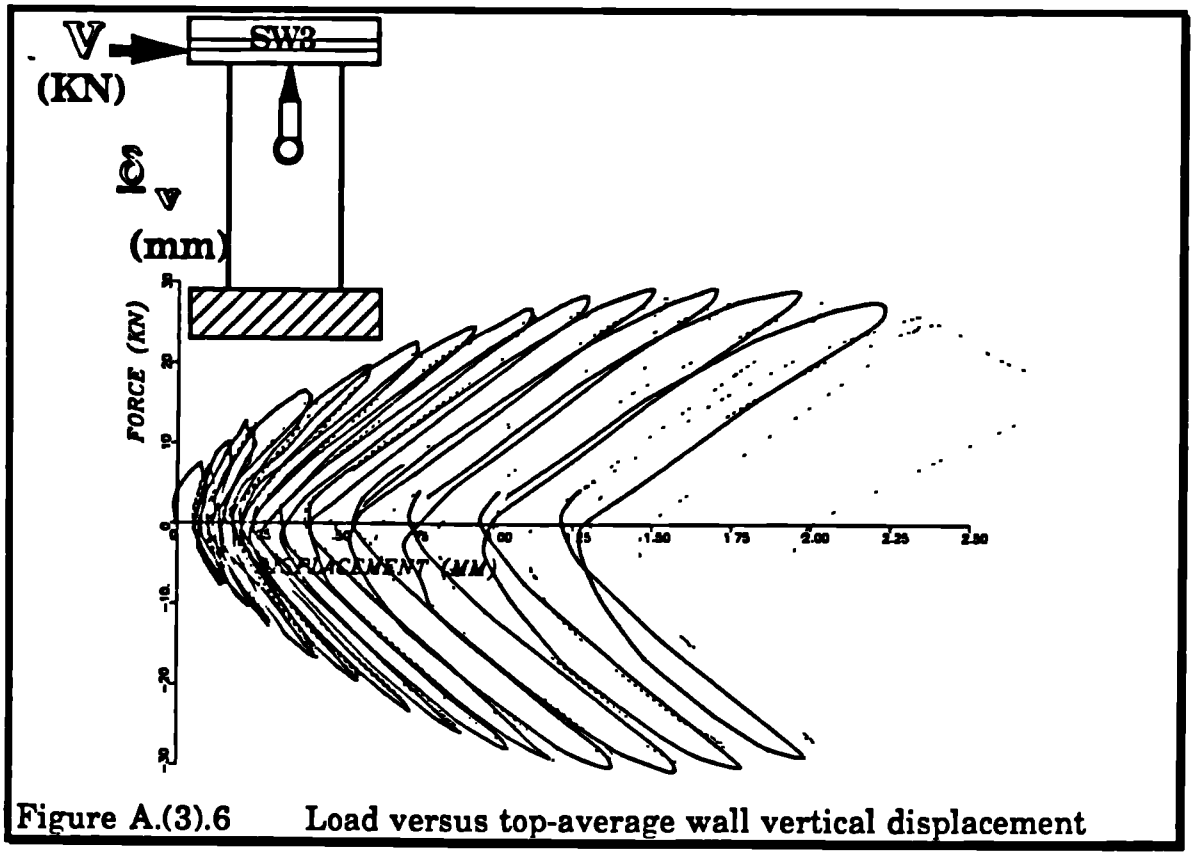


Figure A.(3).6 Load versus top-average wall vertical displacement

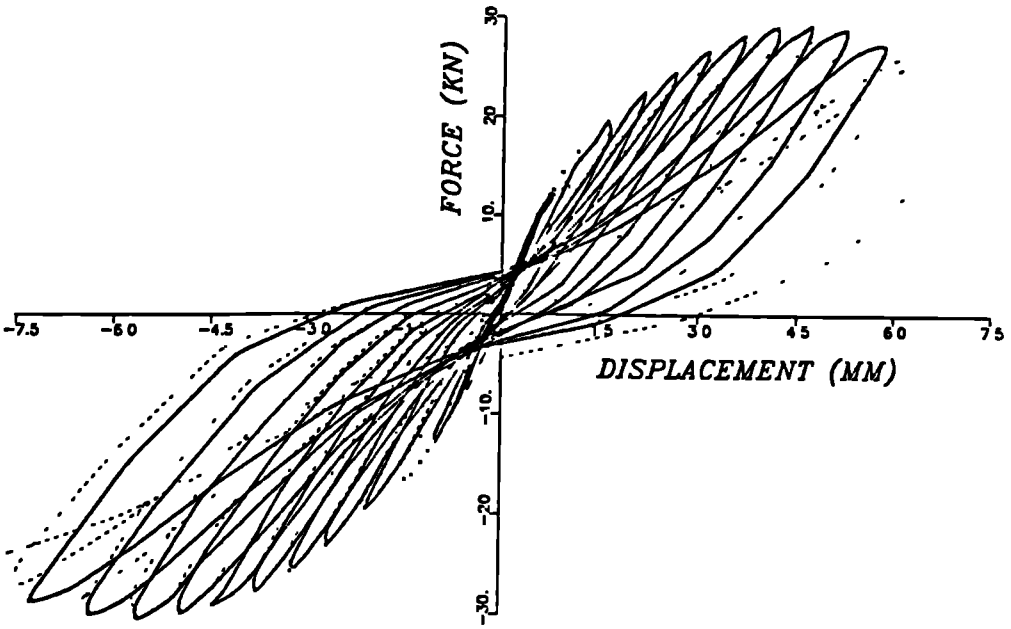


Figure A.(3).7 Top wall shear deformations versus load

A.(3) Load-strain curves - Scale 1:5 model SW3

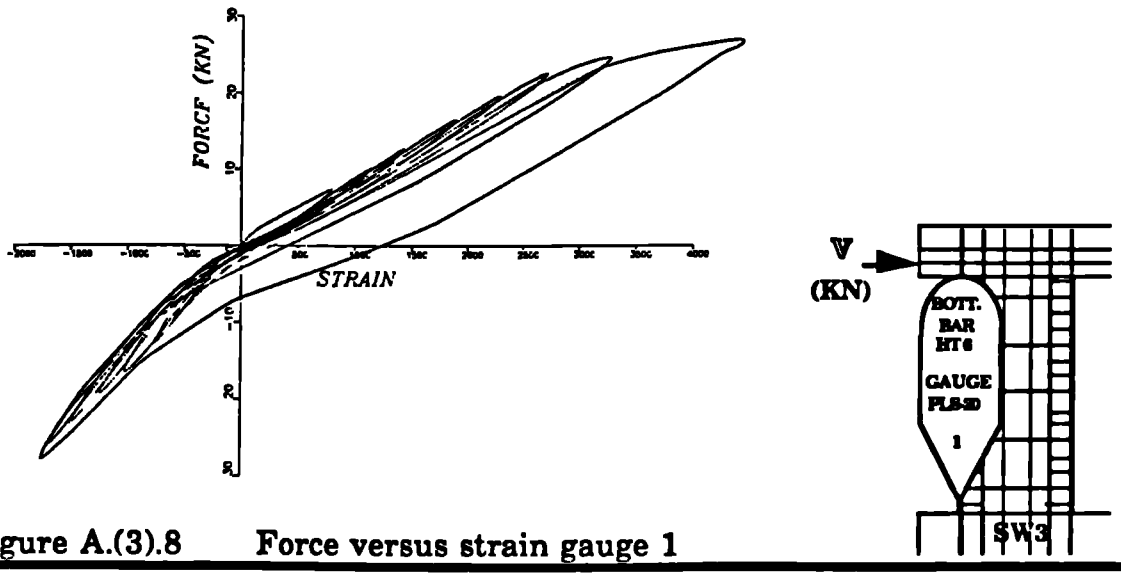


Figure A.(3).8 Force versus strain gauge 1

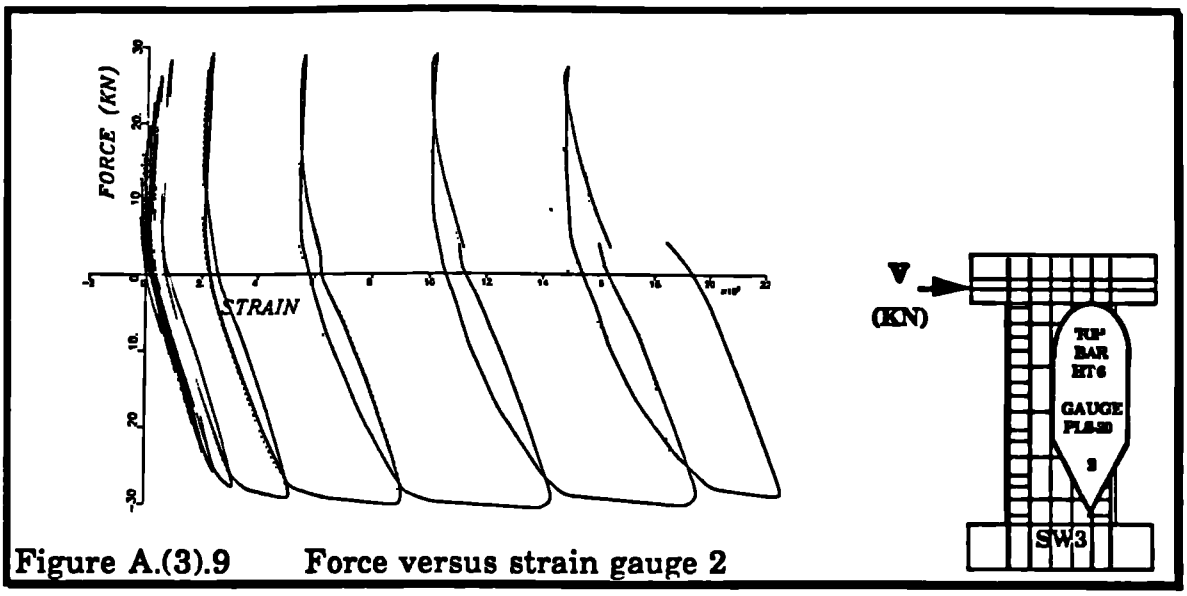


Figure A.(3).9 Force versus strain gauge 2

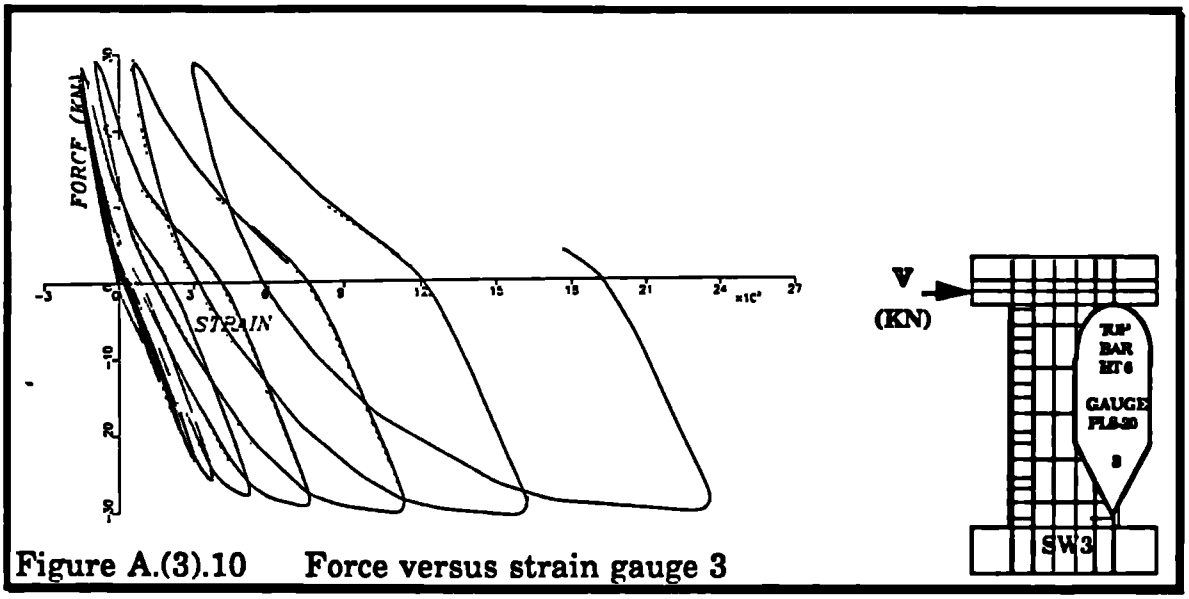


Figure A.(3).10 Force versus strain gauge 3

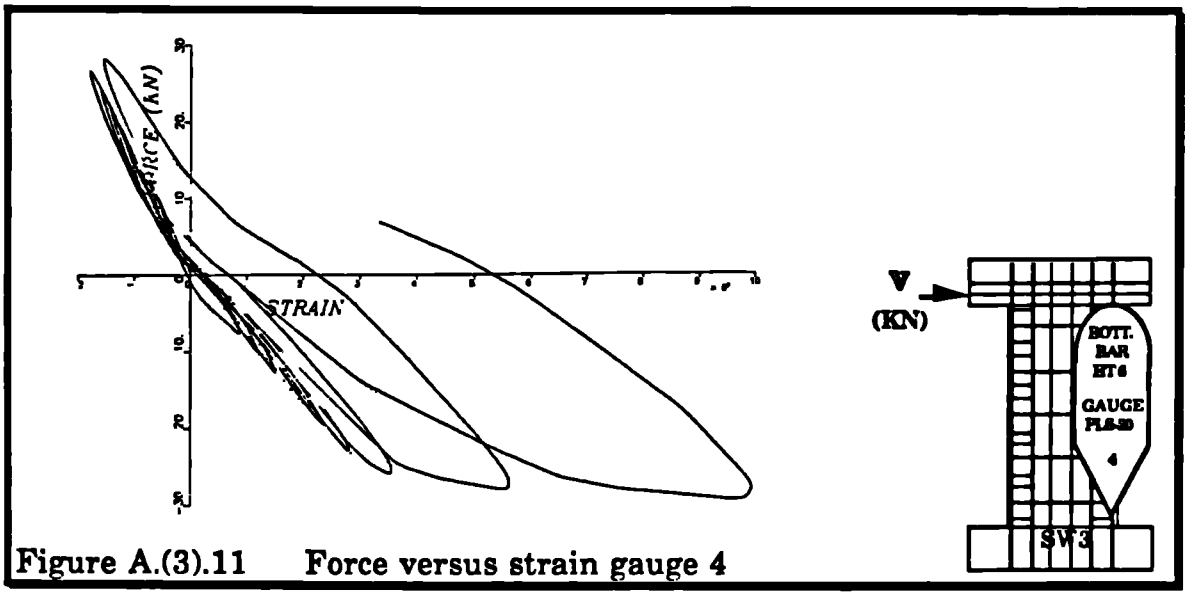


Figure A.(3).11 Force versus strain gauge 4

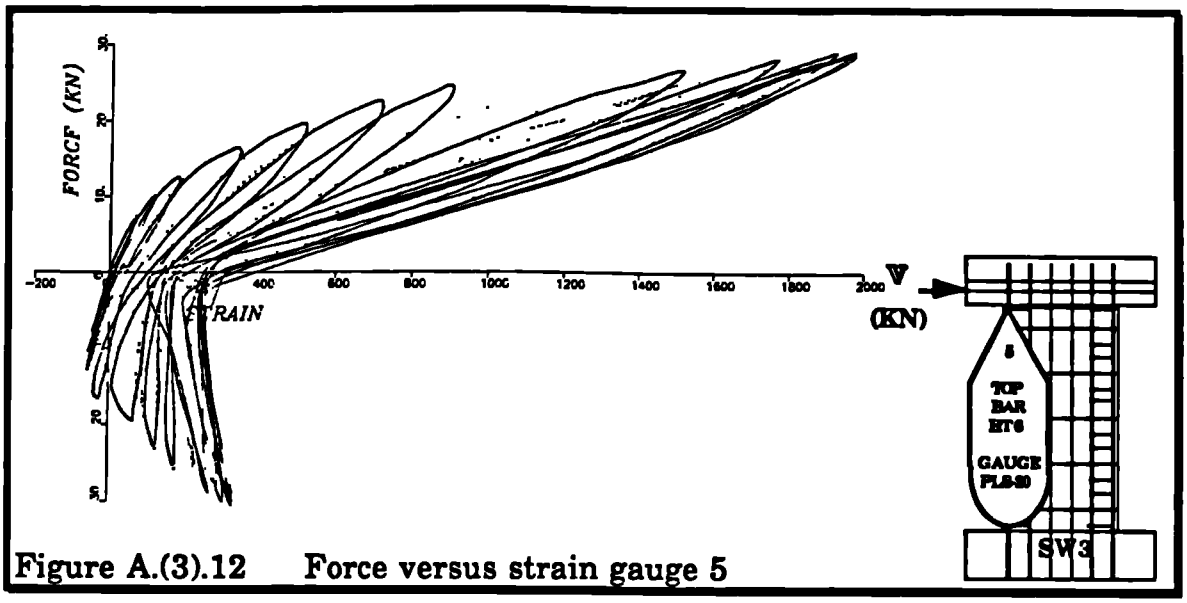


Figure A.(3).12 Force versus strain gauge 5

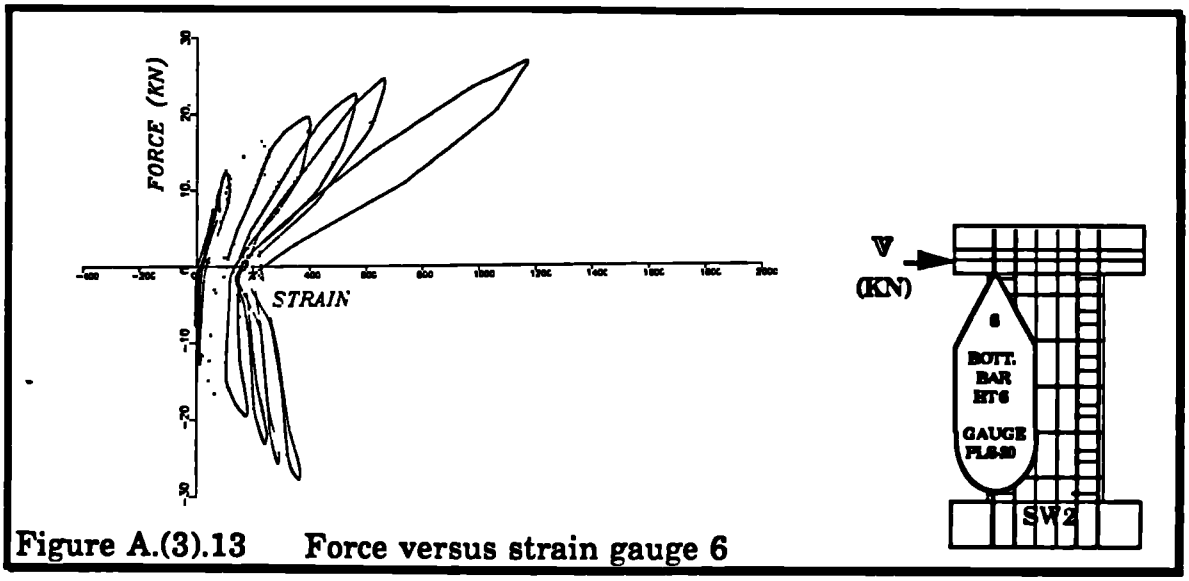


Figure A.(3).13 Force versus strain gauge 6

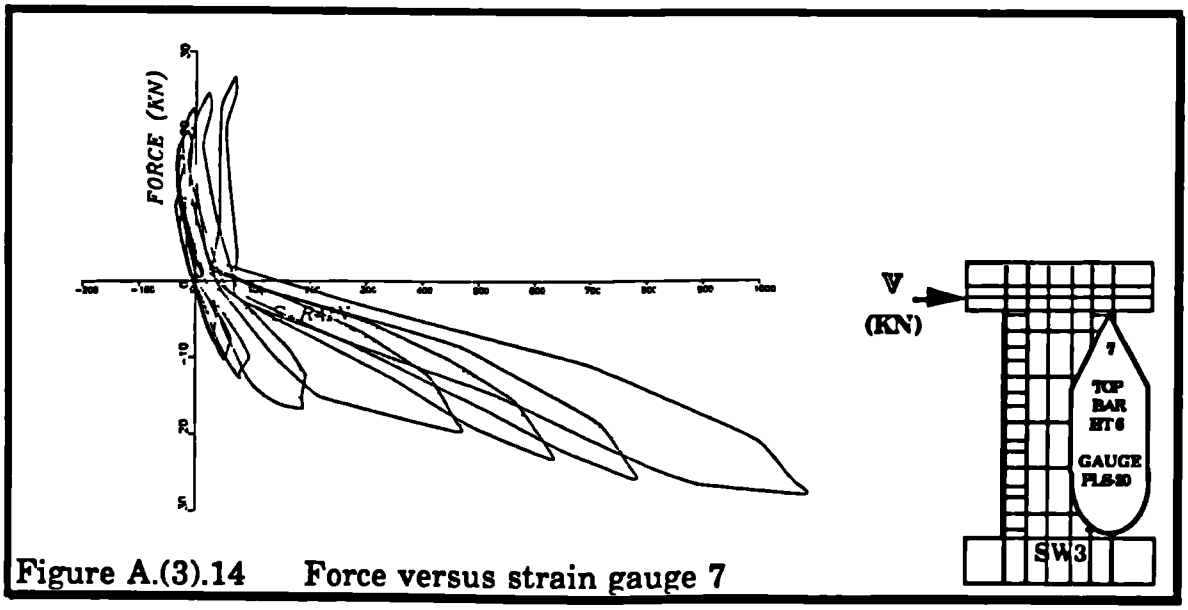


Figure A.(3).14 Force versus strain gauge 7

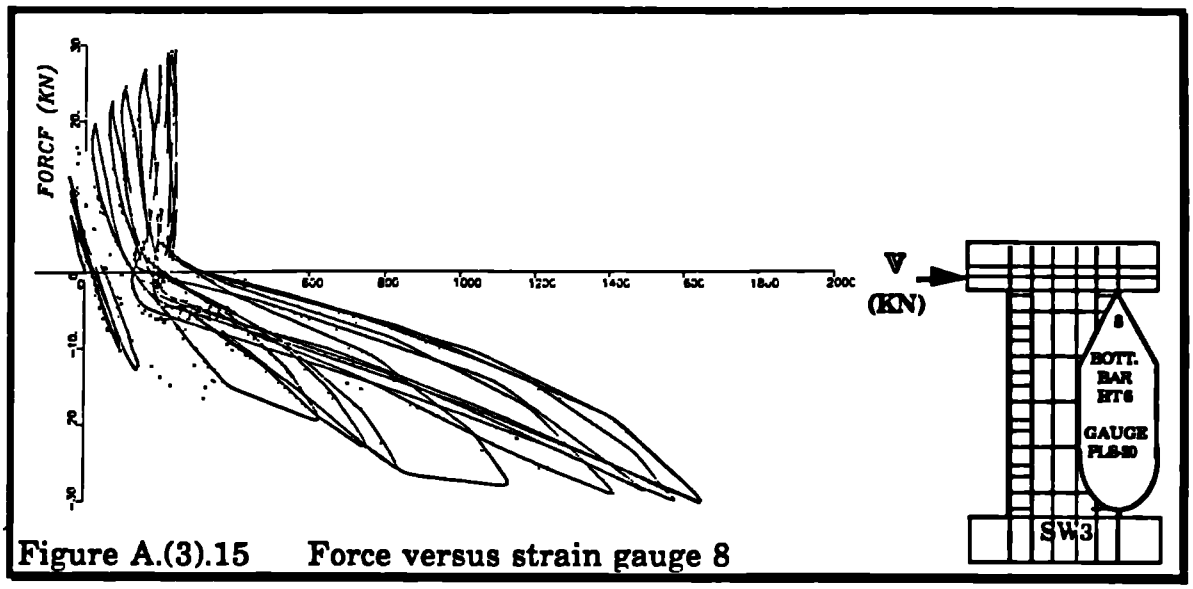


Figure A.(3).15 Force versus strain gauge 8

A.(4) Load-displacement curves - Scale 1:2.5 Model SW4

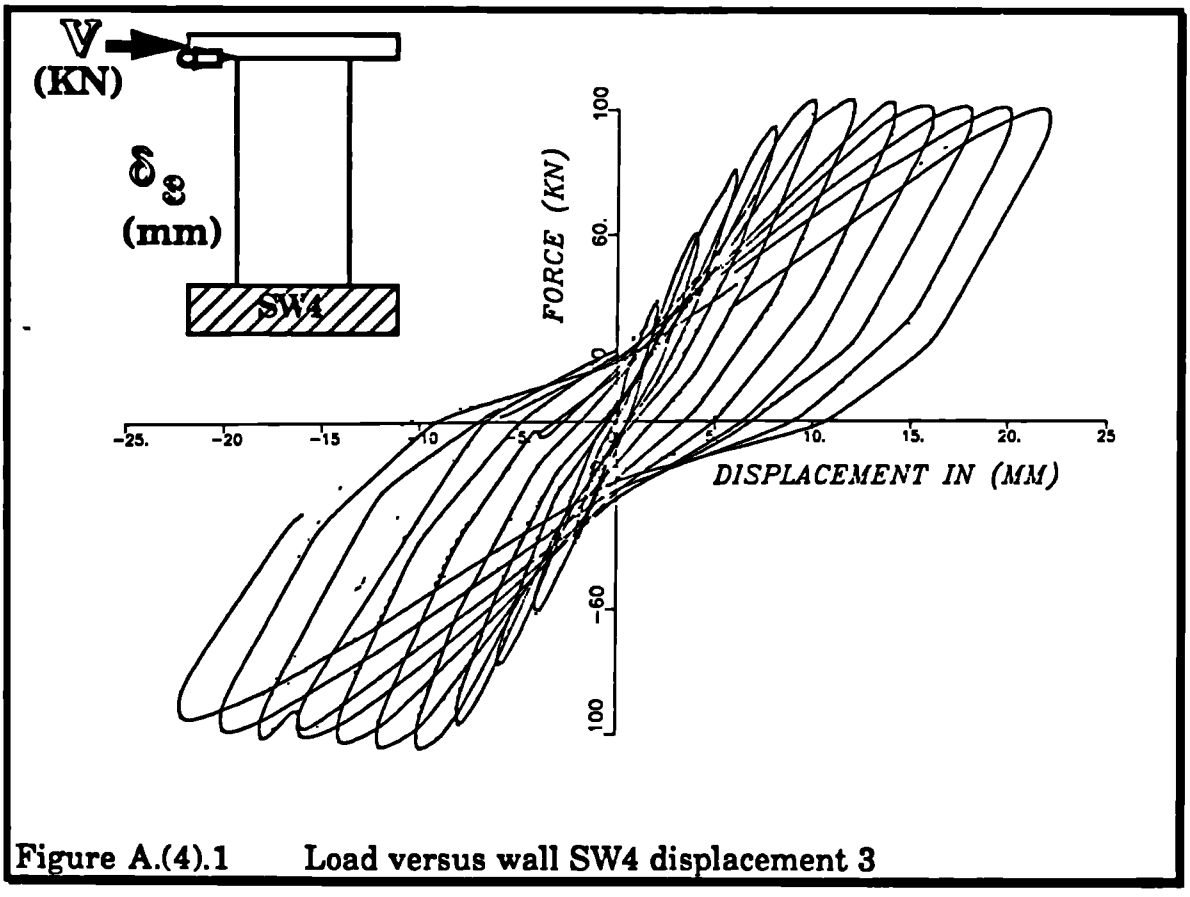


Figure A.(4).1 Load versus wall SW4 displacement 3

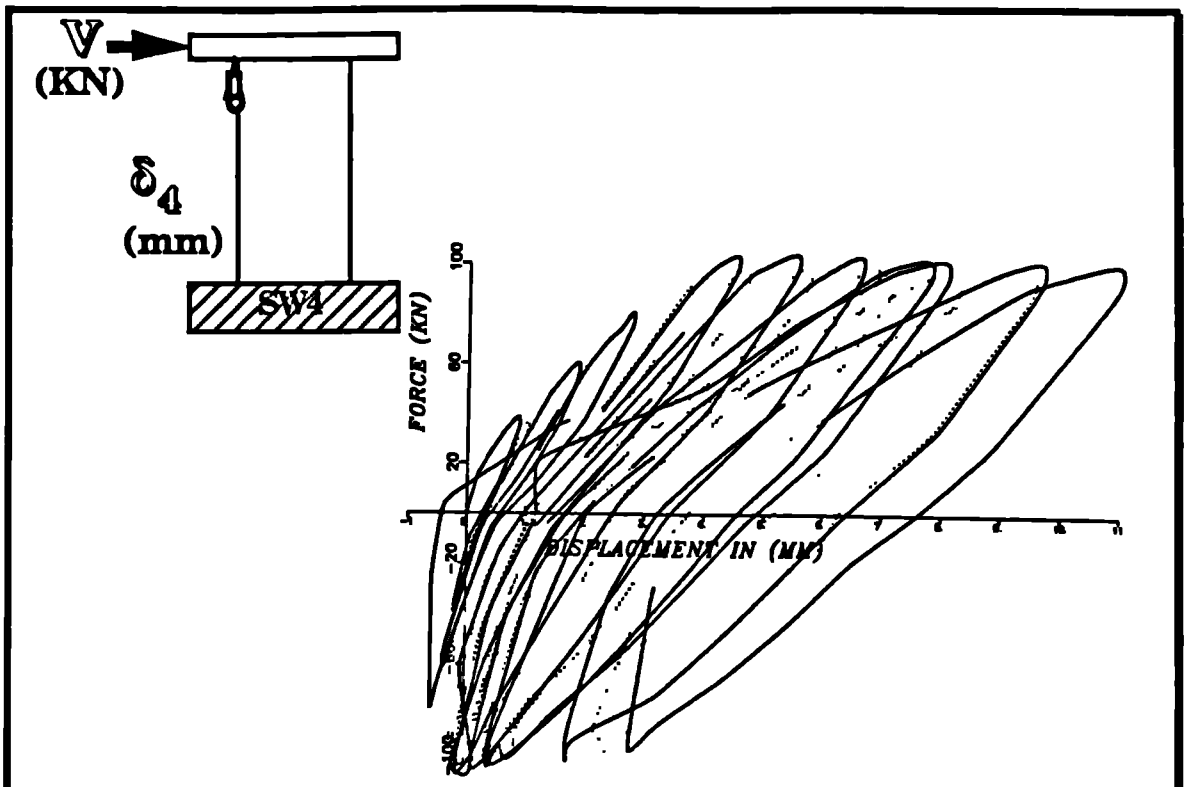


Figure A.(4).2 Load versus wall SW4 displacement 4

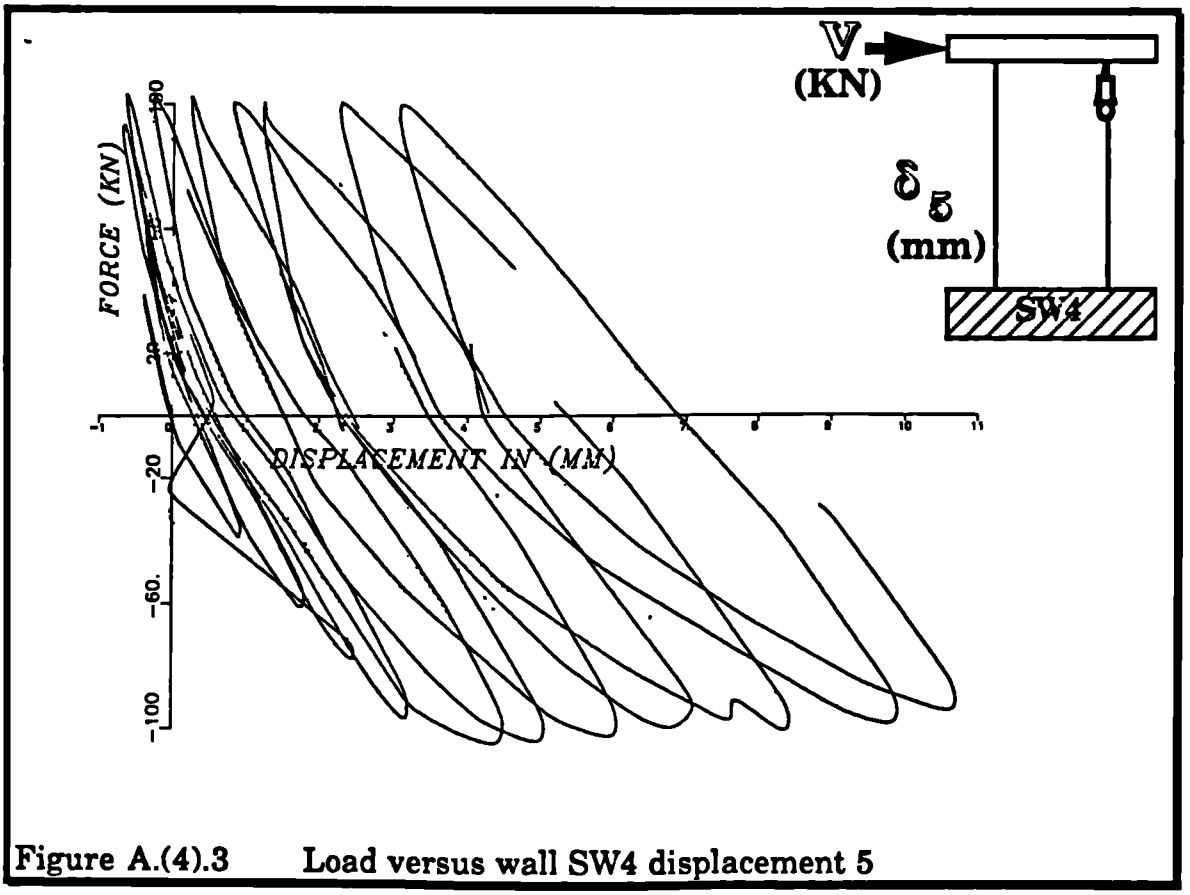


Figure A.(4).3 Load versus wall SW4 displacement 5

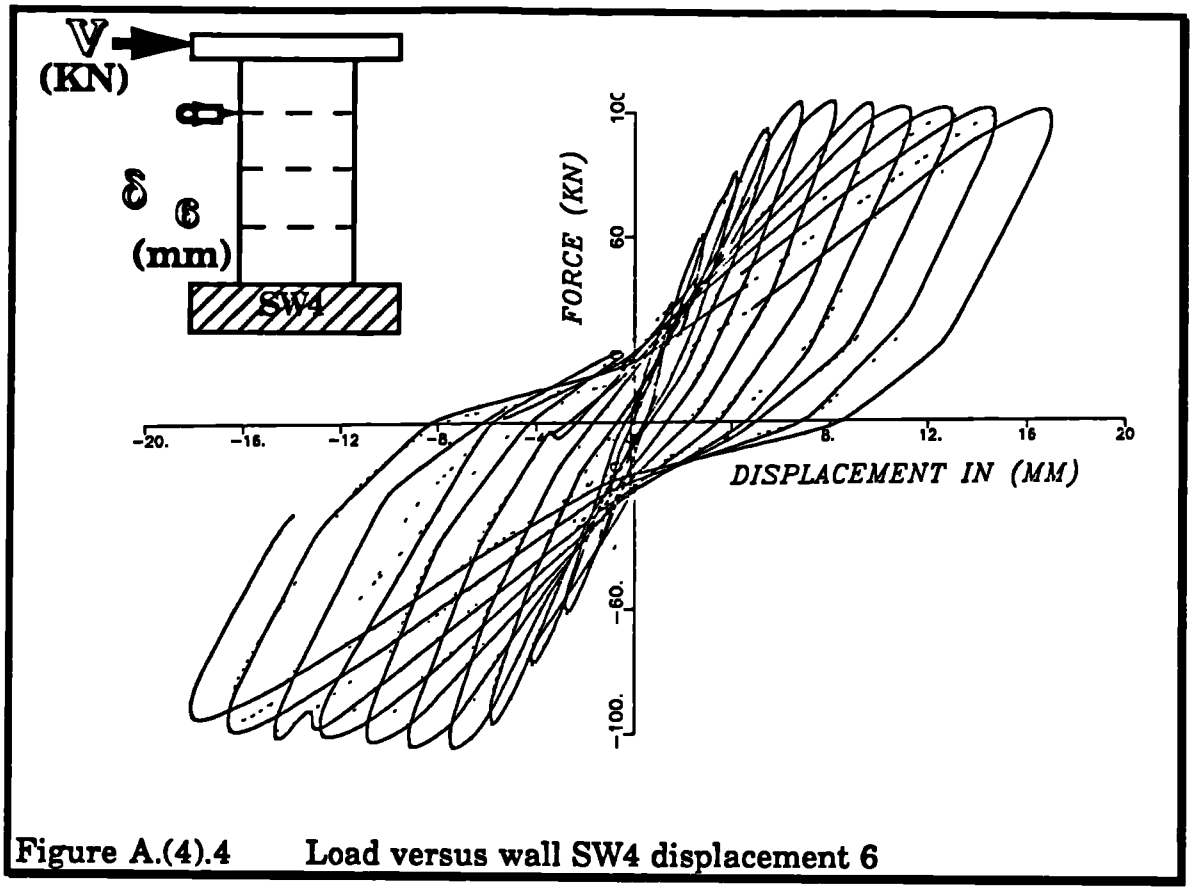


Figure A.(4).4 Load versus wall SW4 displacement 6

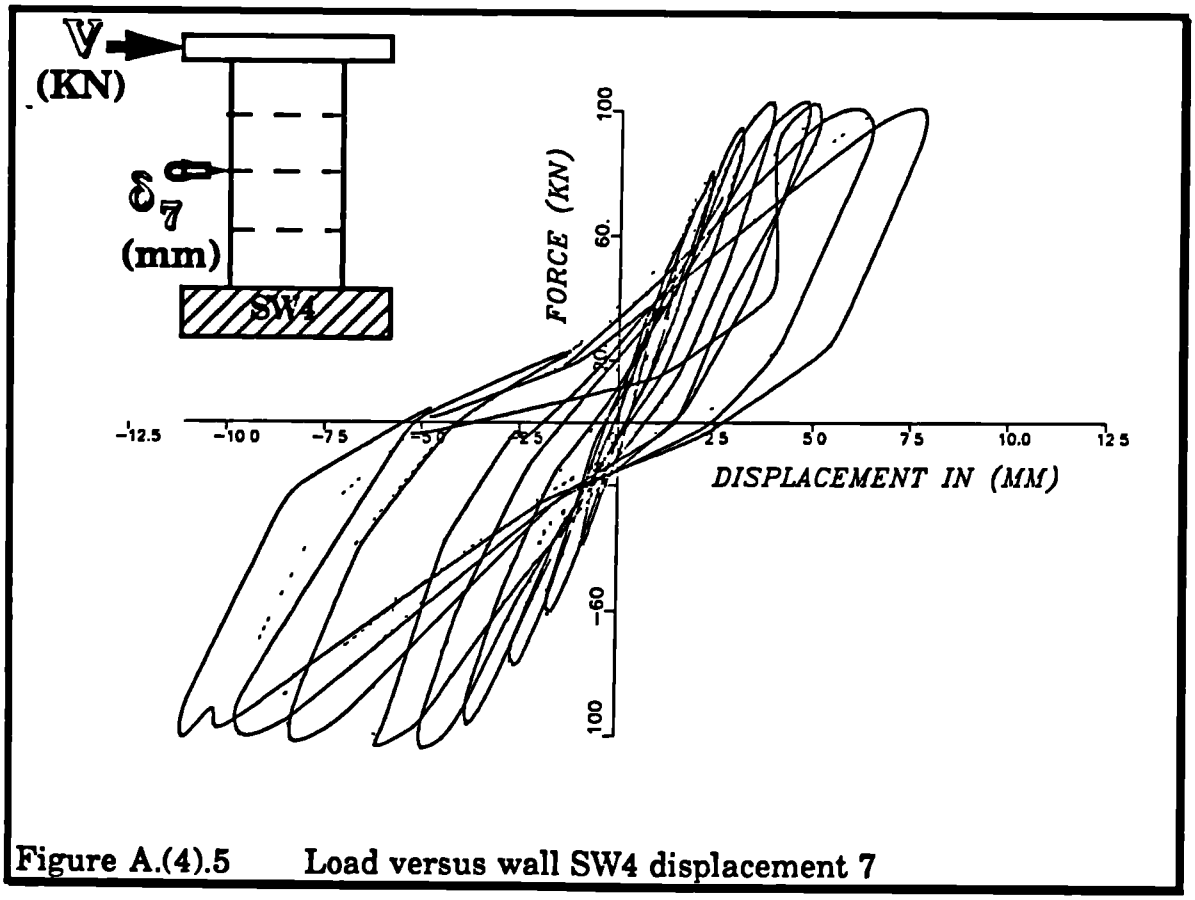


Figure A.(4).5 Load versus wall SW4 displacement 7

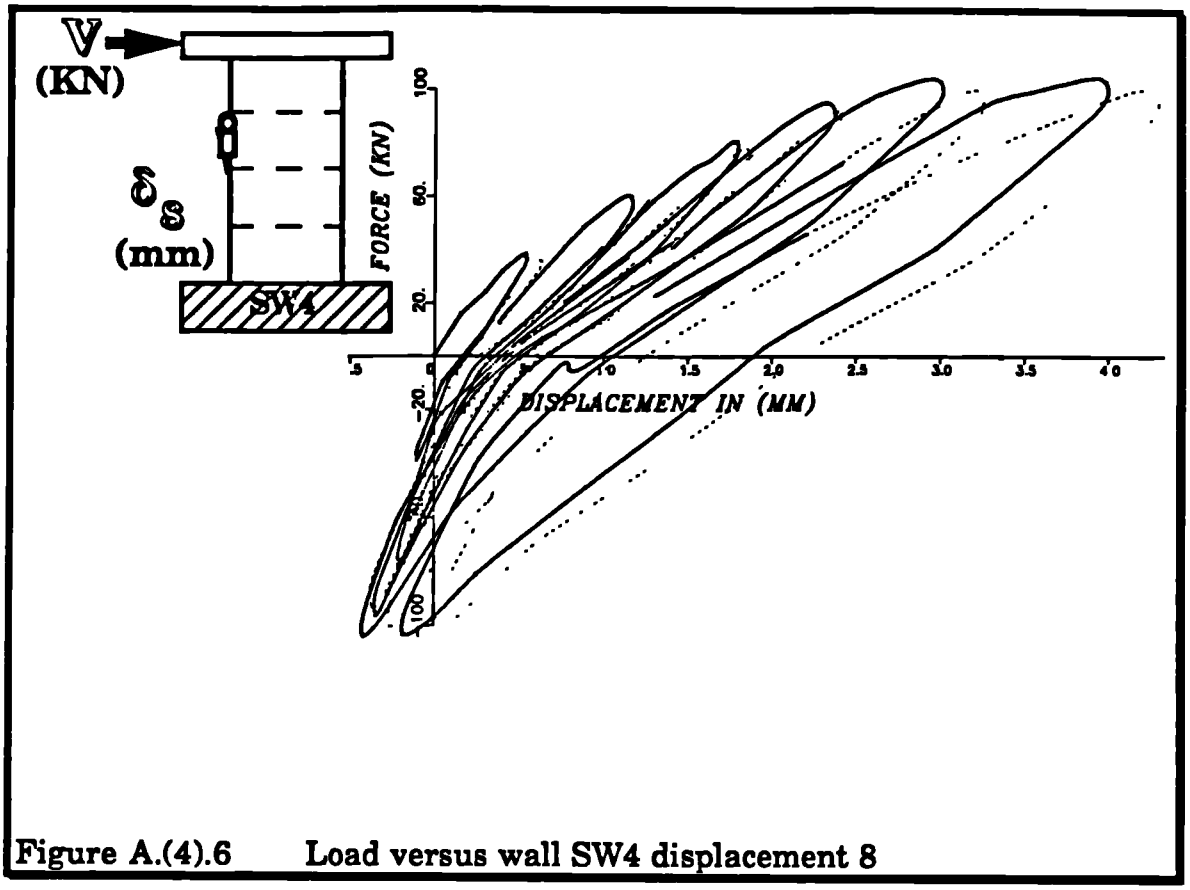


Figure A.(4).6 Load versus wall SW4 displacement 8

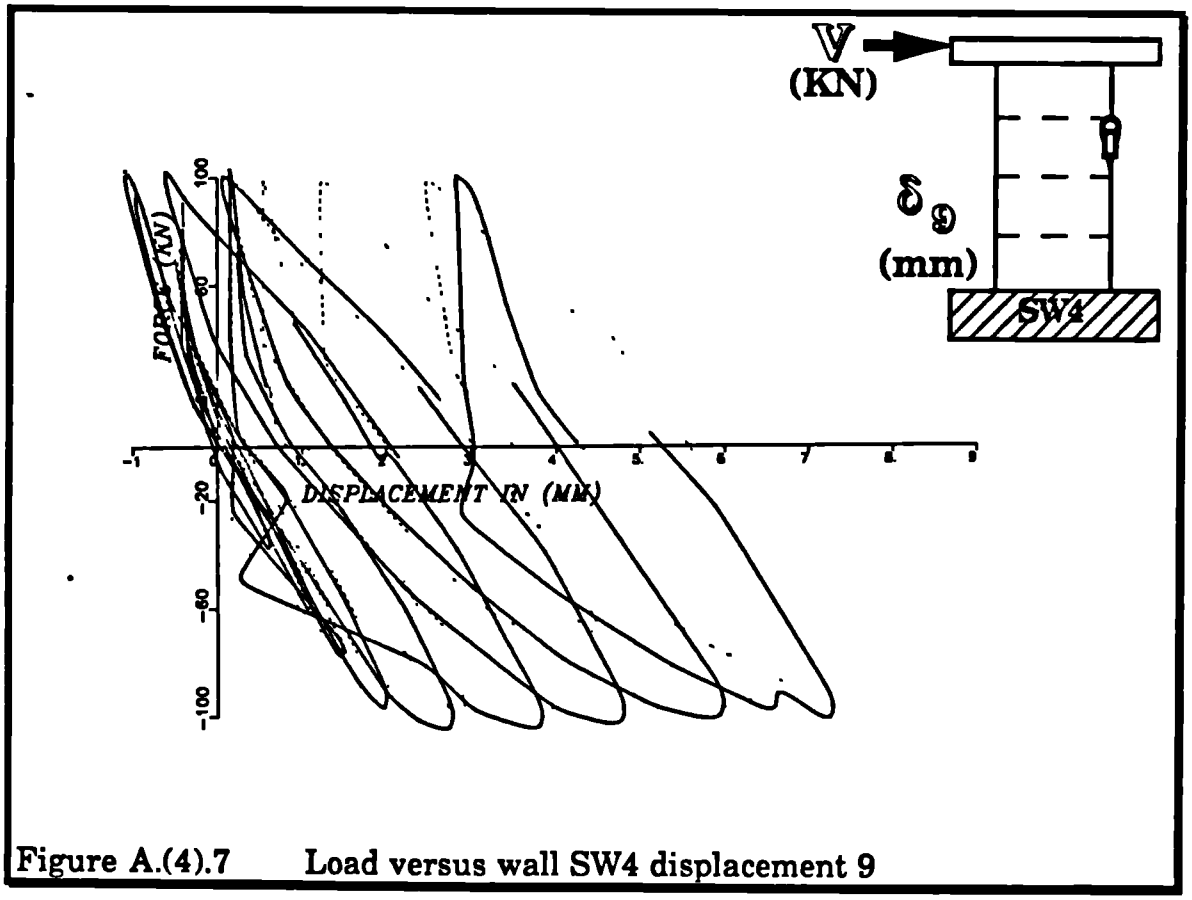


Figure A.(4).7 Load versus wall SW4 displacement 9

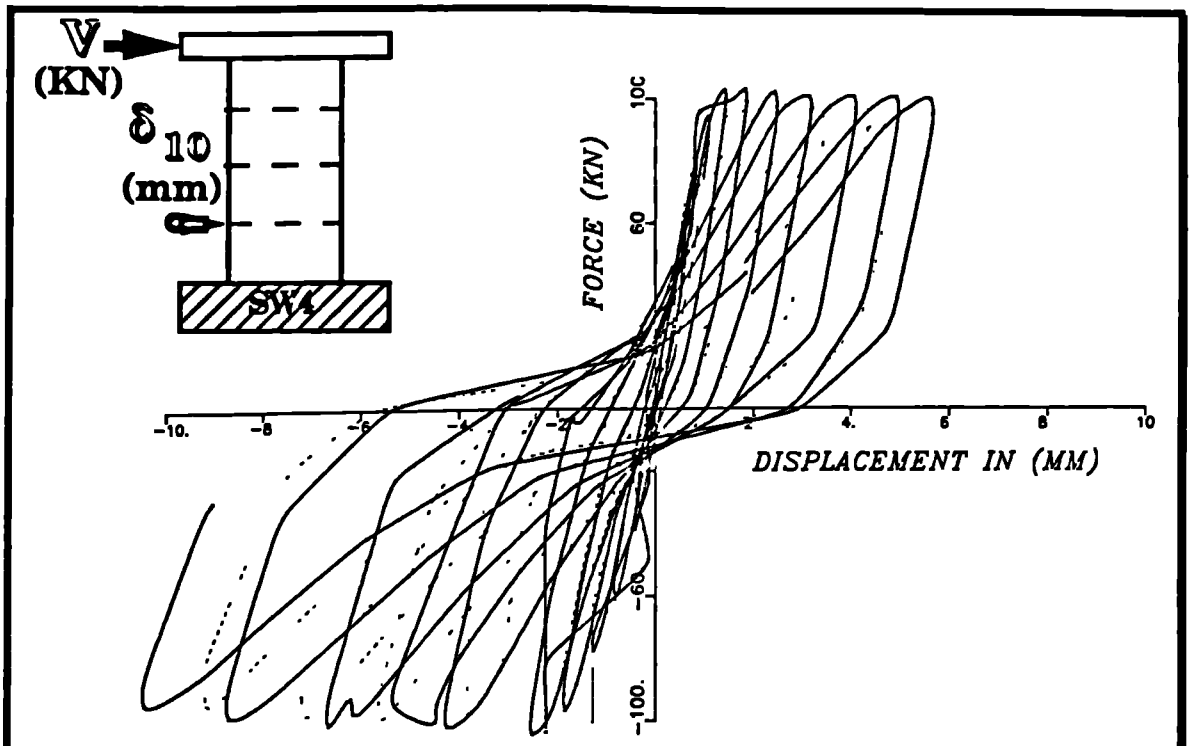


Figure A.(4).8 Load versus wall SW4 displacement 10

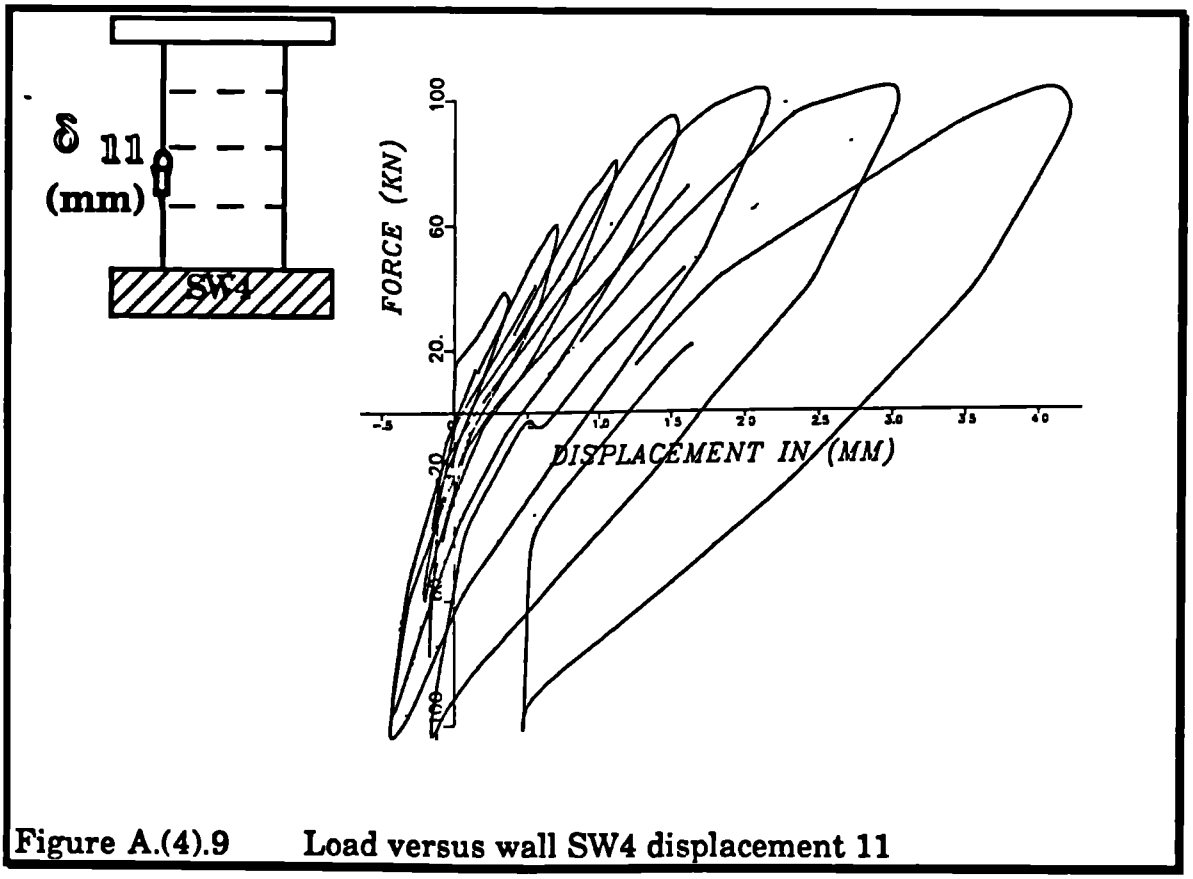


Figure A.(4).9 Load versus wall SW4 displacement 11

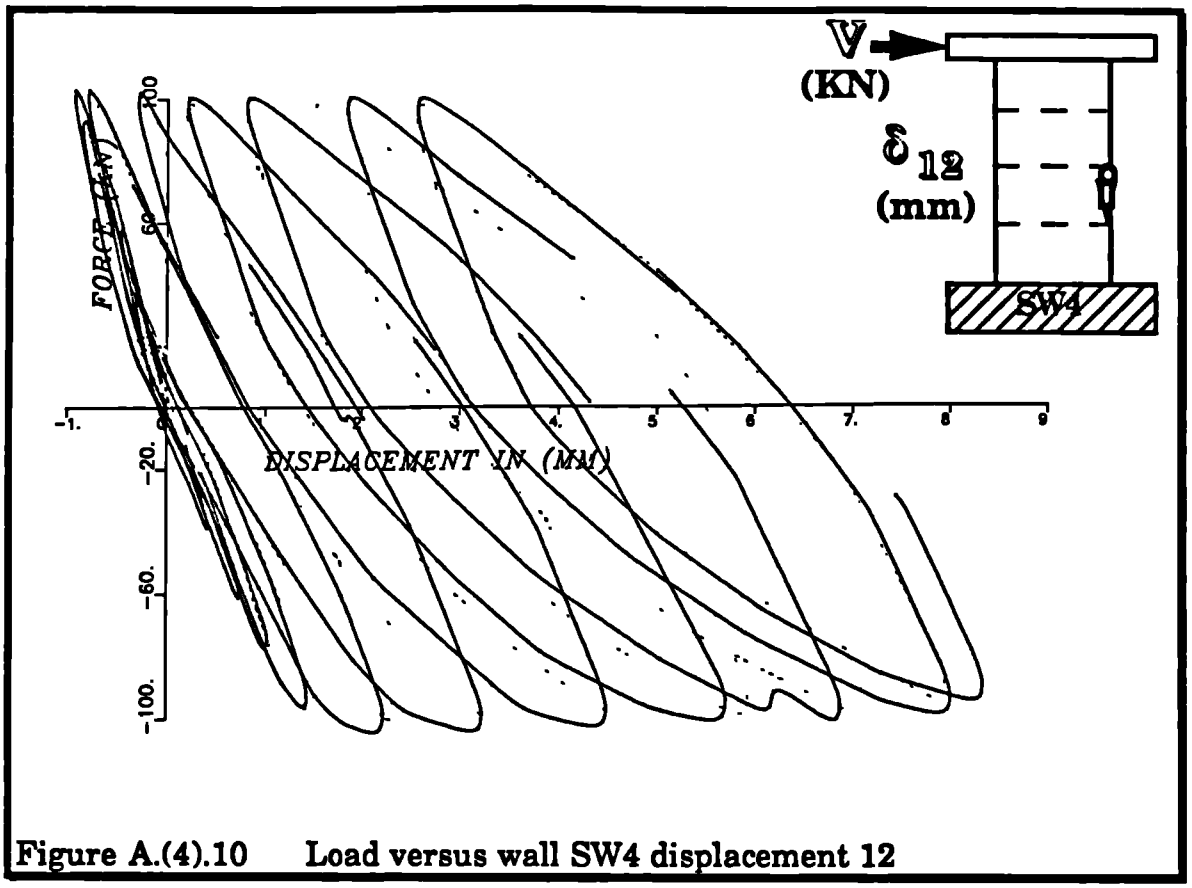


Figure A.(4).10 Load versus wall SW4 displacement 12

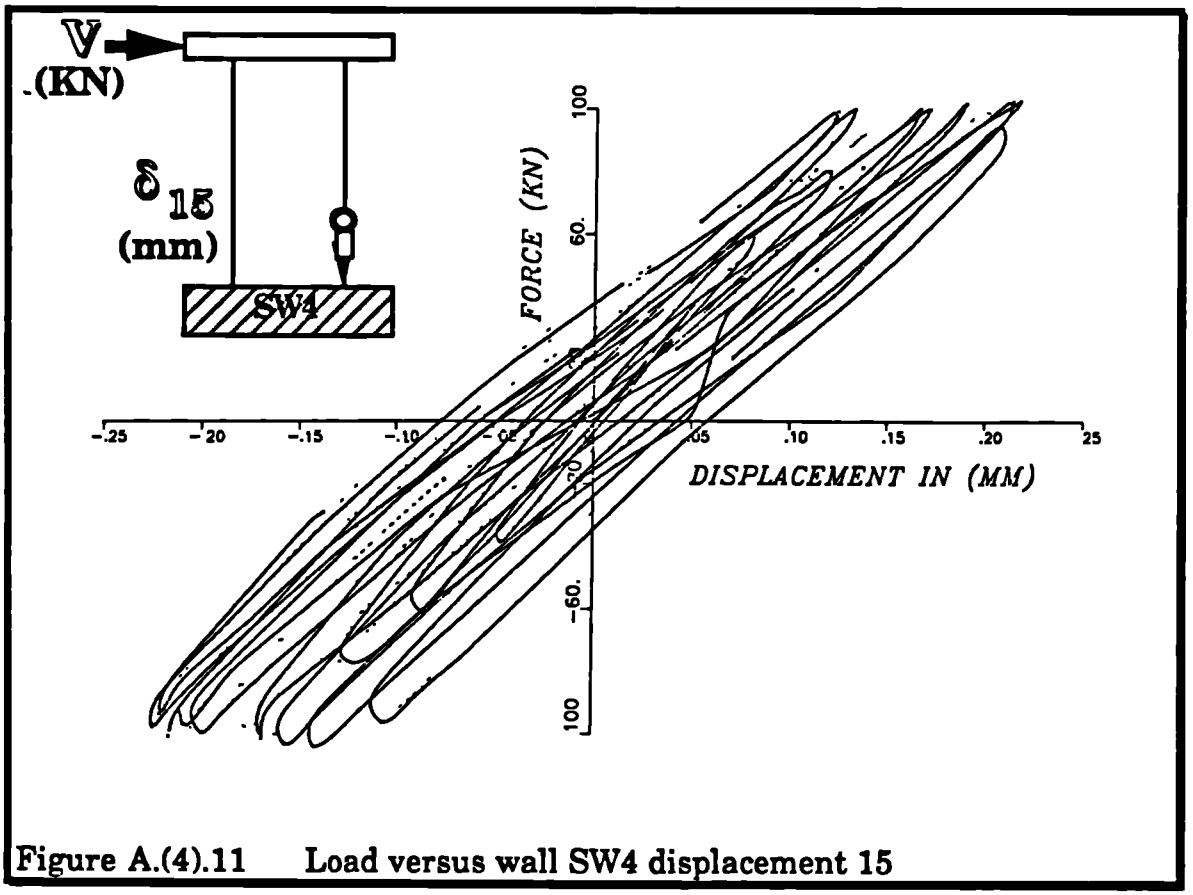


Figure A.(4).11 Load versus wall SW4 displacement 15

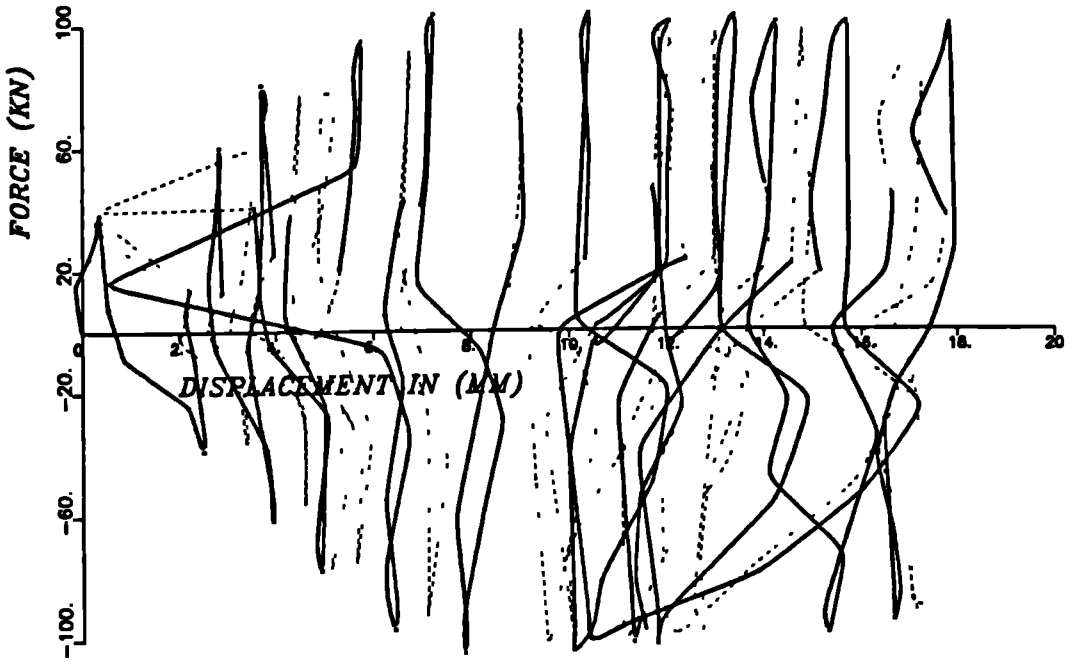


Figure A.(4).12 Load versus wall SW4 displacement 16

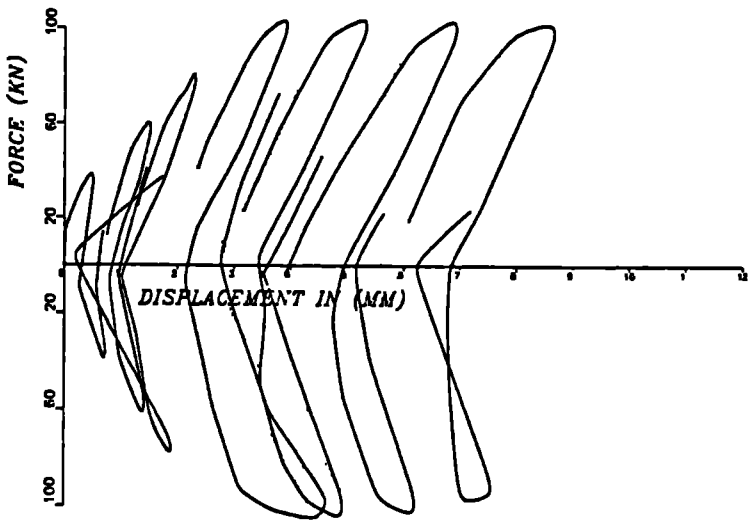


Figure A.(4).13 Load versus wall SW4 top wall average vertical displacement

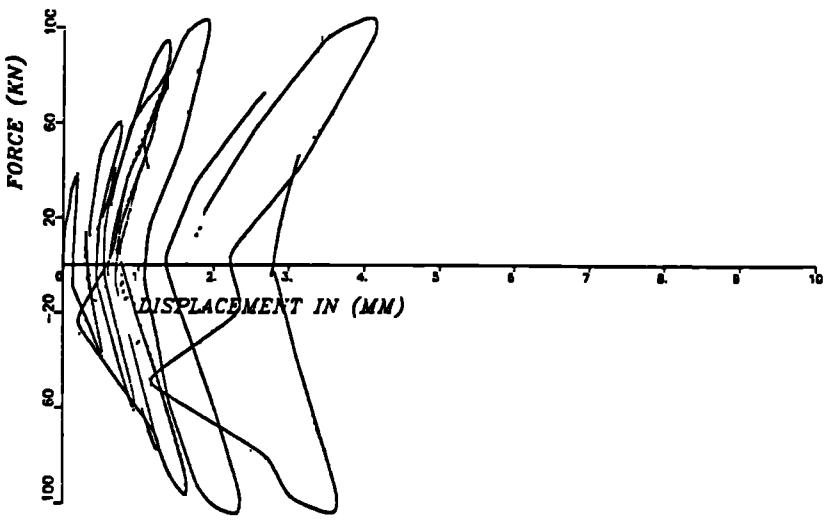


Figure A.(4).14 Load versus wall SW4 mid heigth average vertical displacement

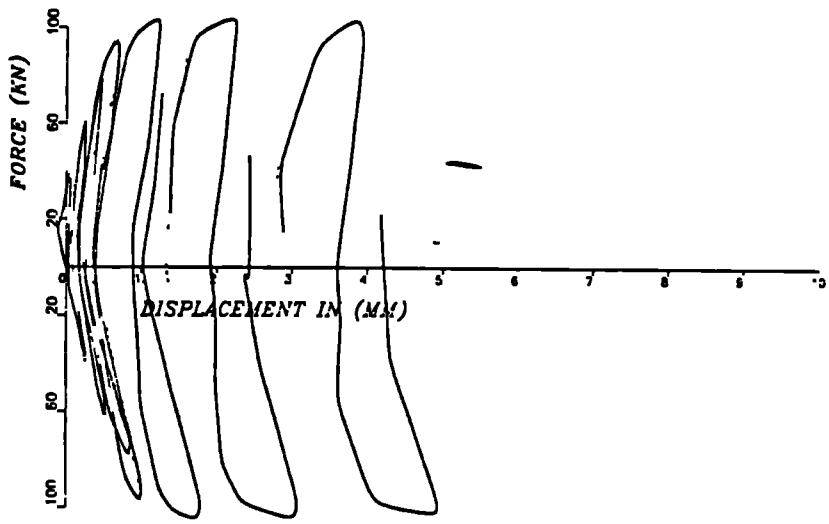
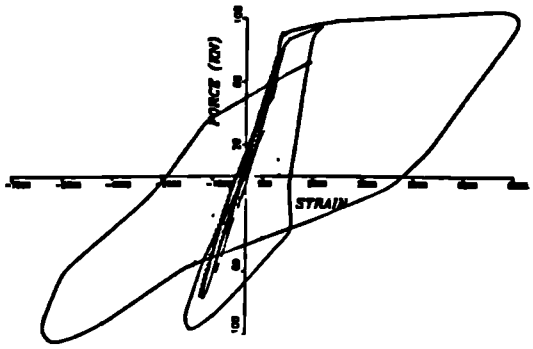


Figure A.(4).15 Load versus wall SW4 quarter heigth average vertical displacement

A.(4) Strain gauge results of wall SW4



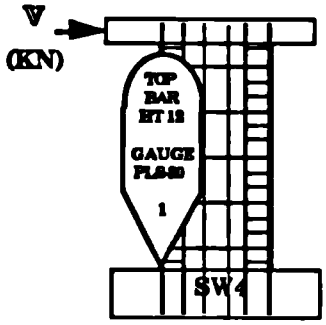
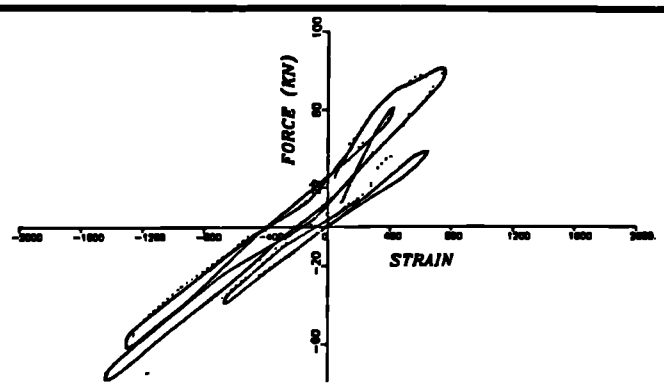


Figure A.(4).16 Load versus strain 1



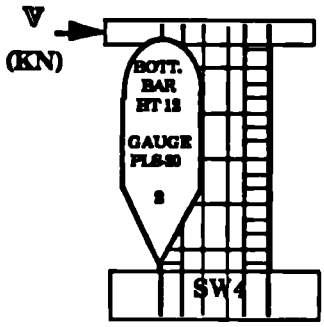
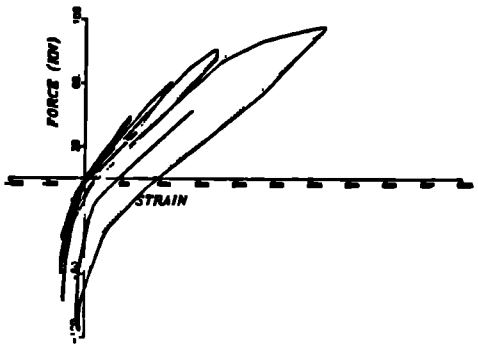


Figure A.(4).17 Load versus strain 2



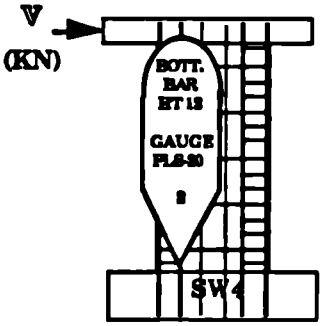
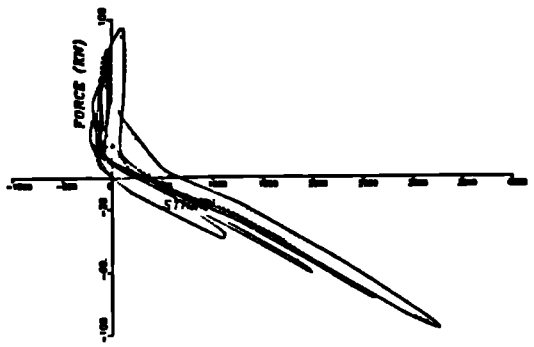


Figure A.(4).18 Load versus strain 3



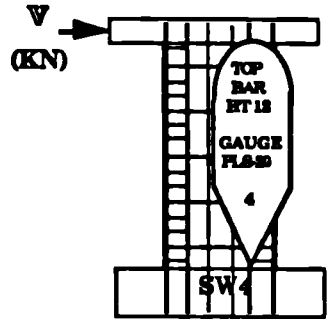
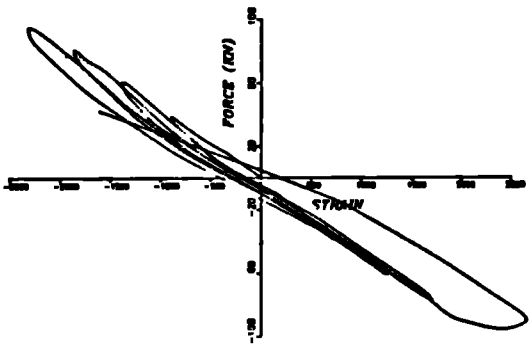


Figure A.(4).19 Load versus strain 4



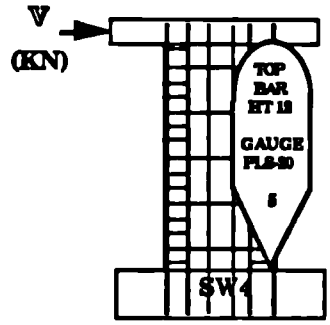
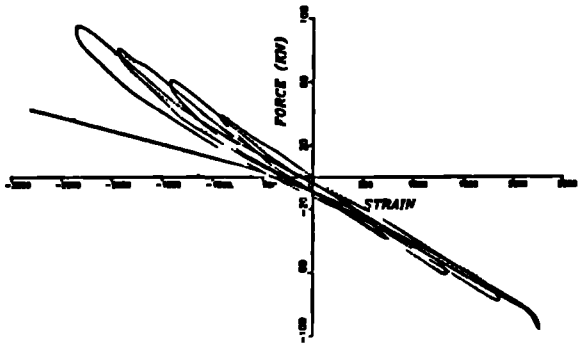


Figure A.(4).20 Load versus strain 5



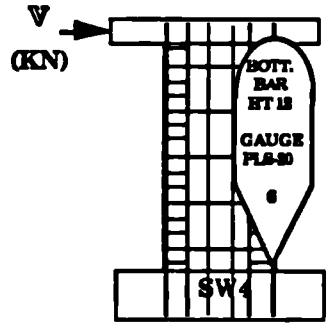
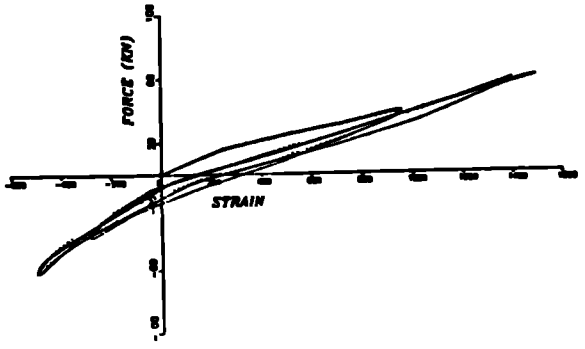


Figure A.(4).21 Load versus strain 6



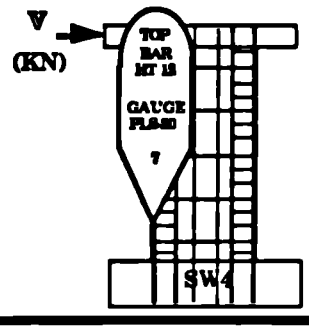
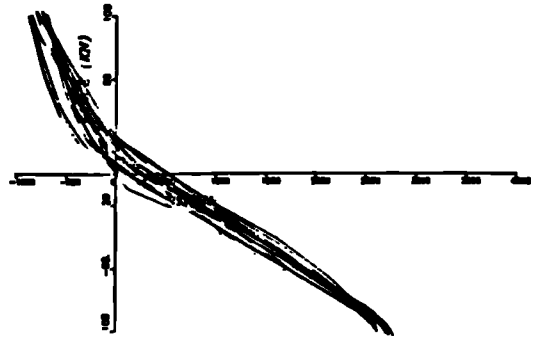


Figure A.(4).22 Load versus strain 7



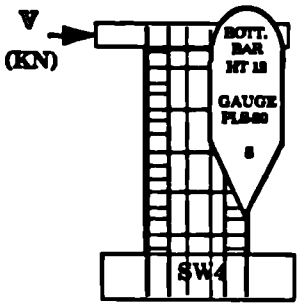
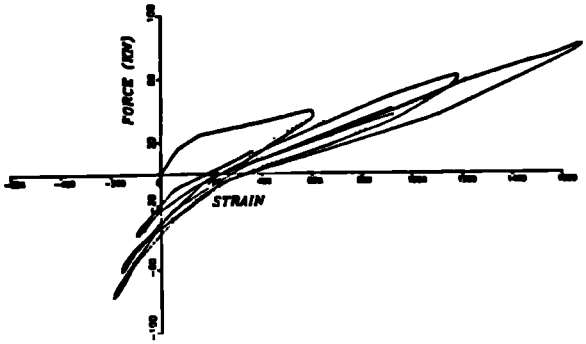


Figure A.(4).23 Load versus strain 8



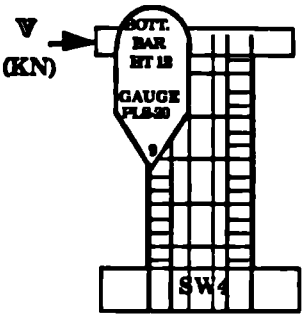
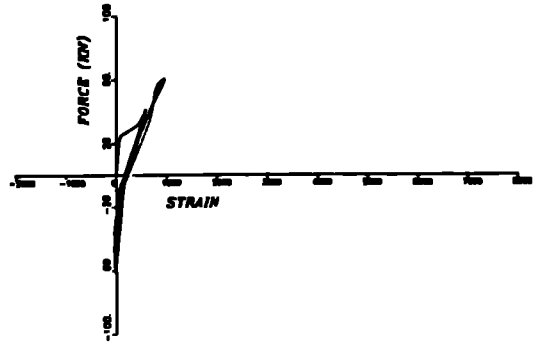


Figure A.(4).24 Load versus strain 9



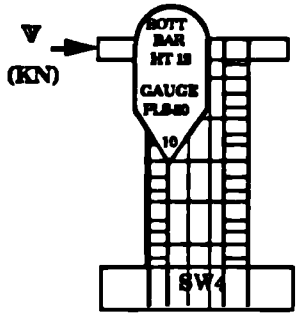
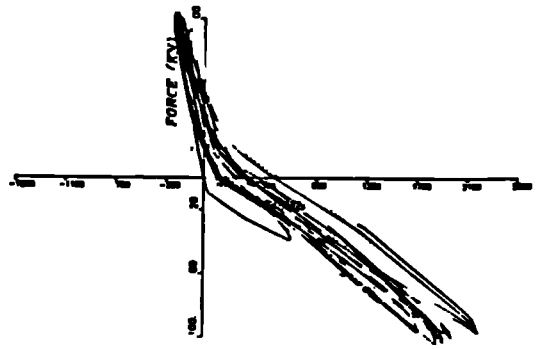


Figure A.(4).25 Load versus strain 10



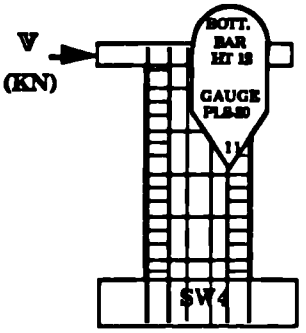


Figure A.(4).26 Load versus strain 11

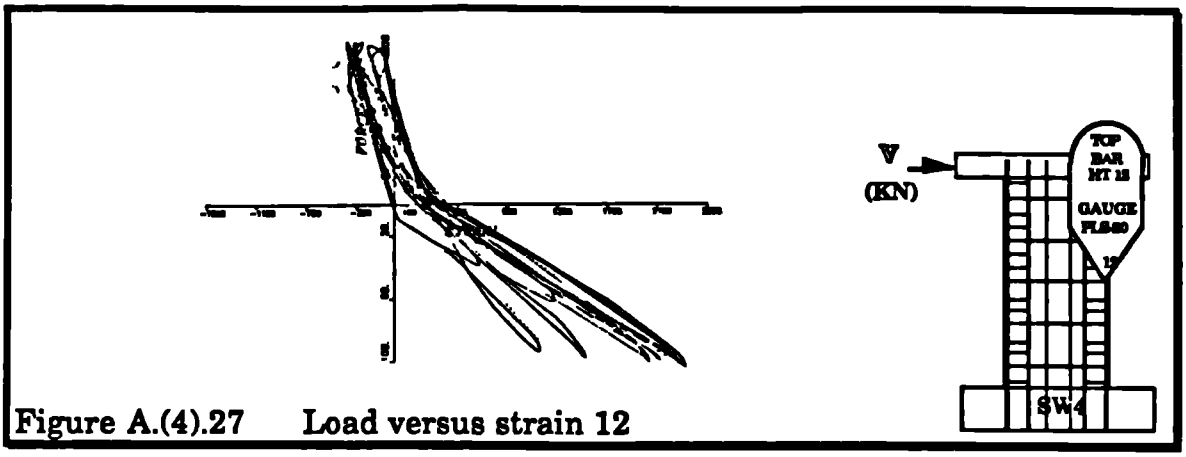


Figure A.(4).27 Load versus strain 12

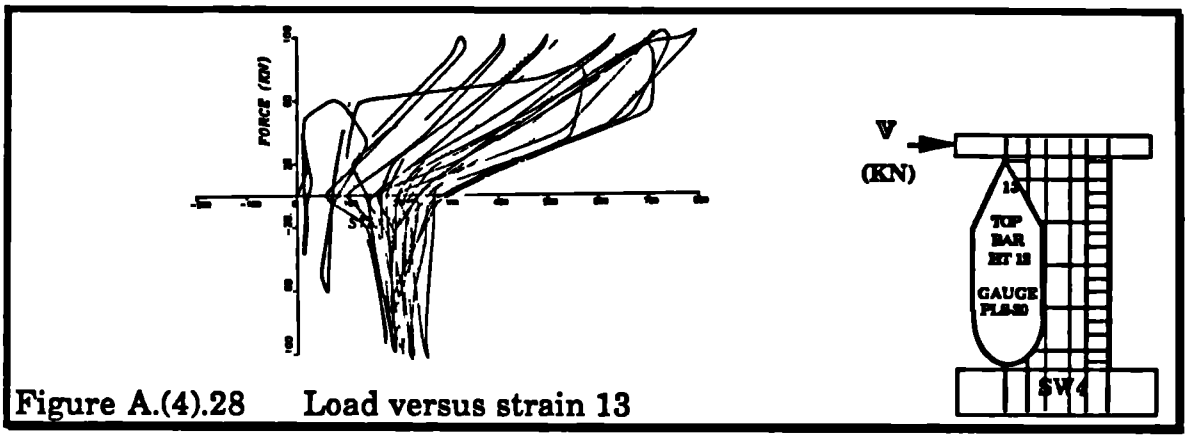


Figure A.(4).28 Load versus strain 13

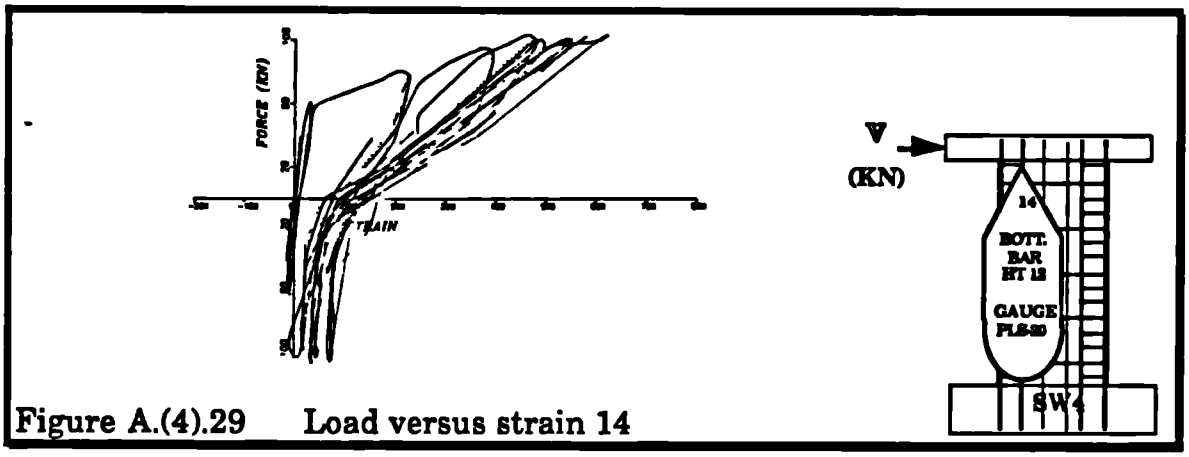


Figure A.(4).29 Load versus strain 14

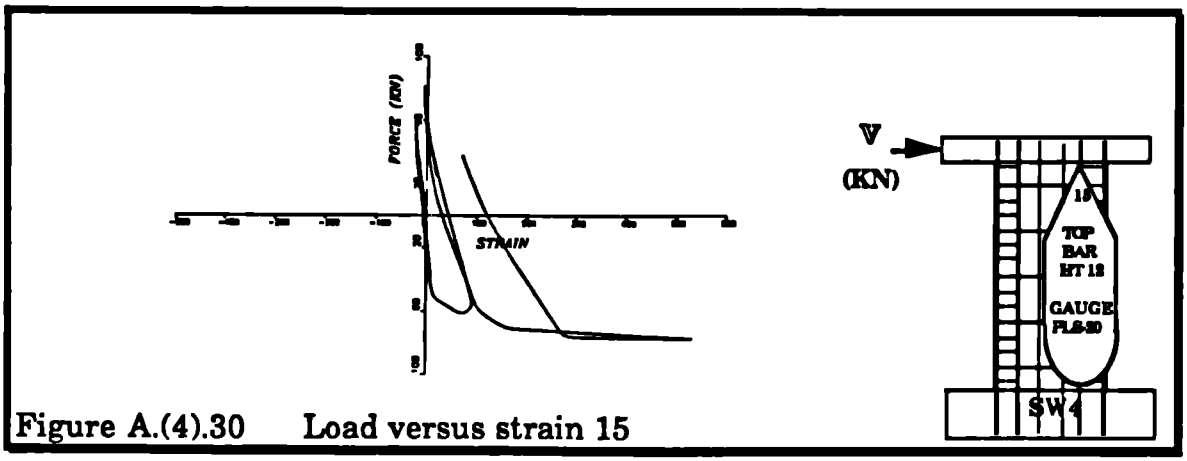
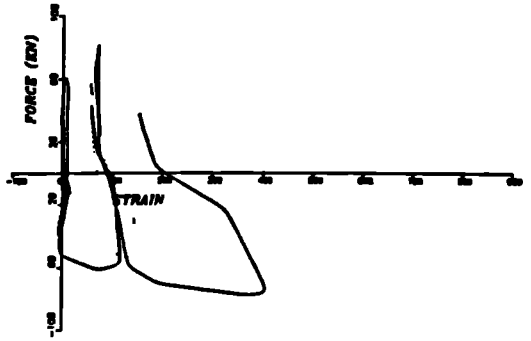


Figure A.(4).30 Load versus strain 15



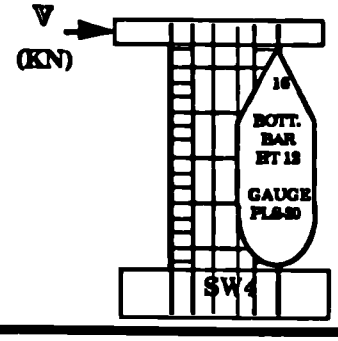
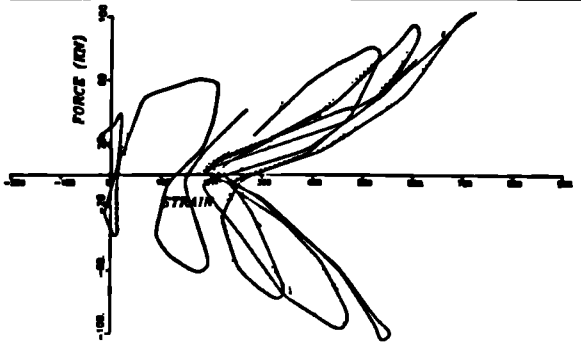


Figure A.(4).31 Load versus strain 16



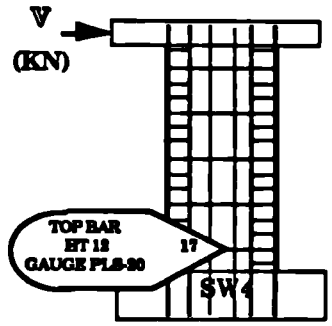
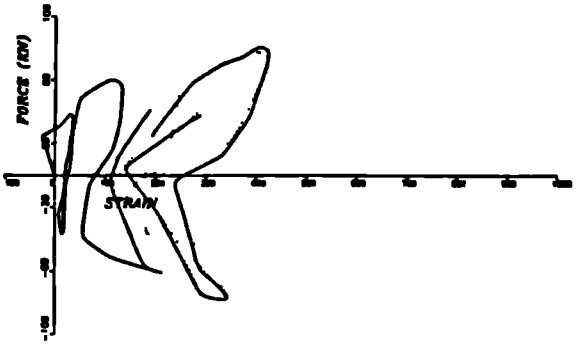


Figure A.(4).32 Load versus link strain 17



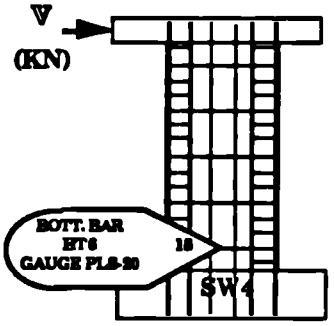
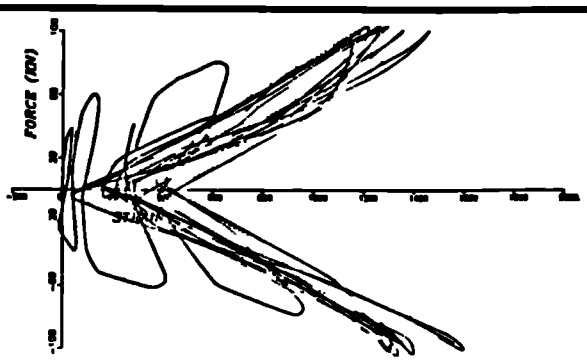


Figure A.(4).33 Load versus link strain 18



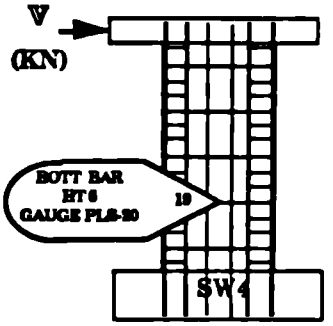


Figure A.(4).34 Load versus link strain 19

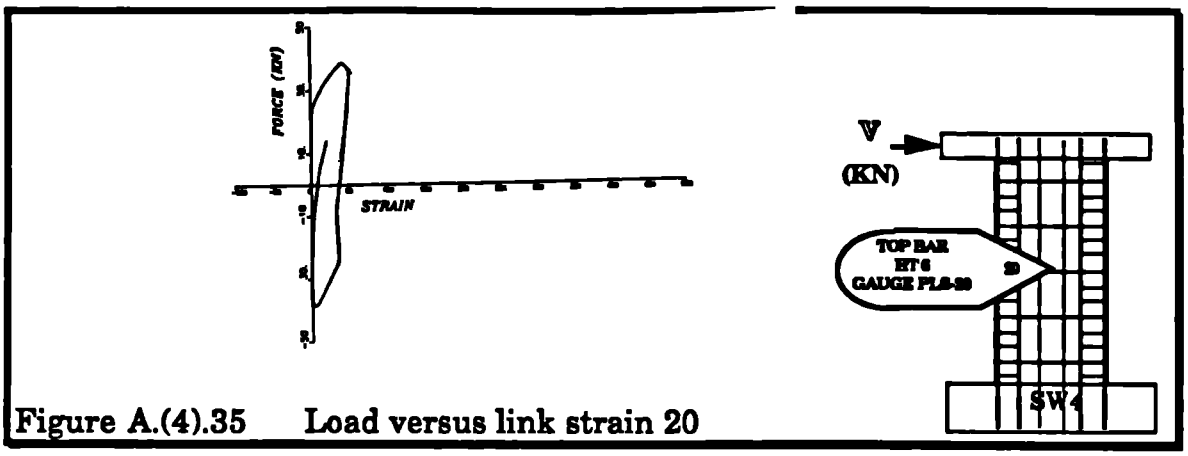


Figure A.(4).35 Load versus link strain 20

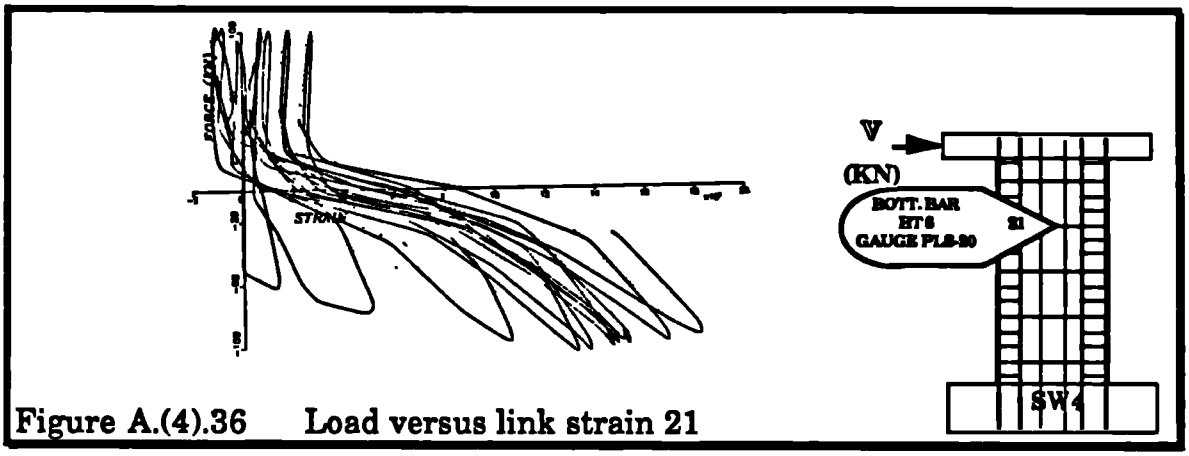


Figure A.(4).36 Load versus link strain 21

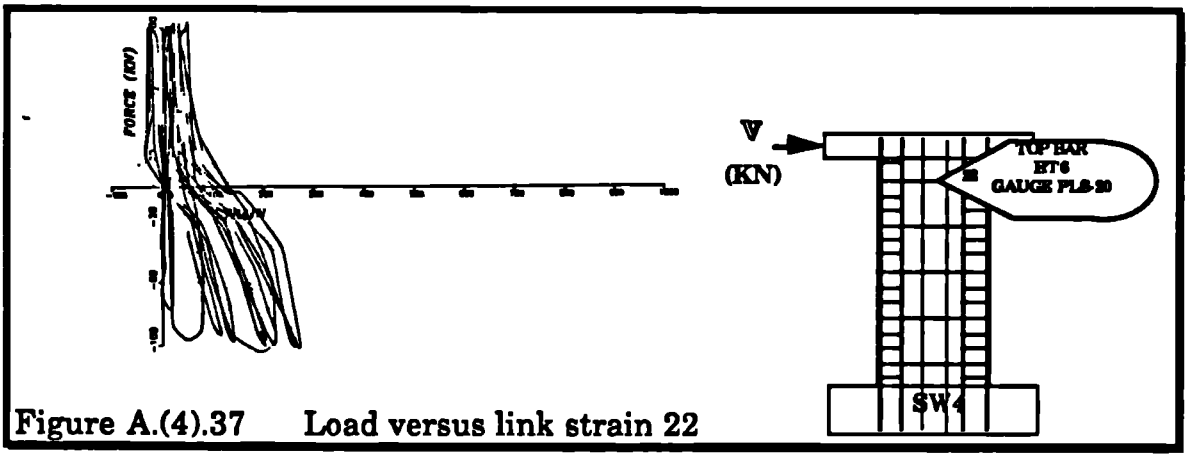


Figure A.(4).37 Load versus link strain 22

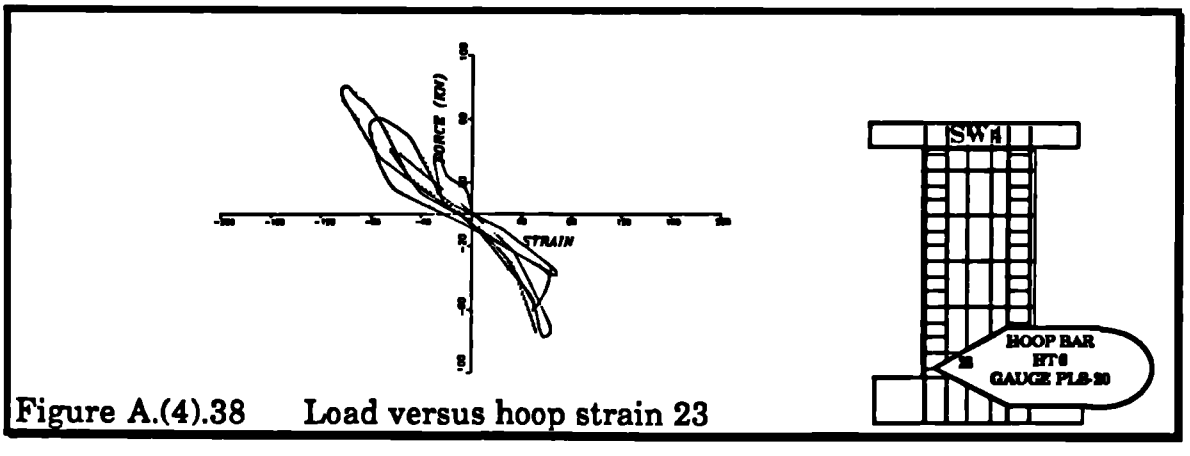


Figure A.(4).38 Load versus hoop strain 23

A.(5) Load-displacement curves - Scale 1:2.5 model SW5

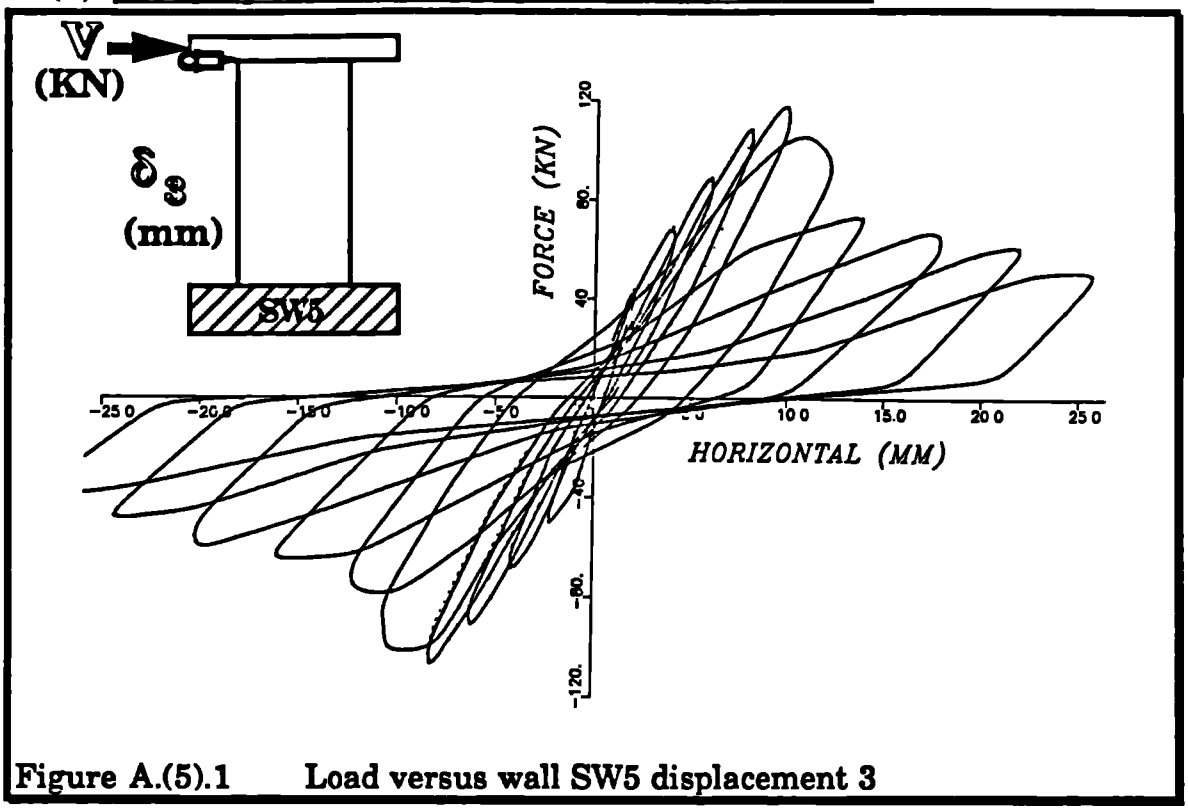


Figure A.(5).1 Load versus wall SW5 displacement 3

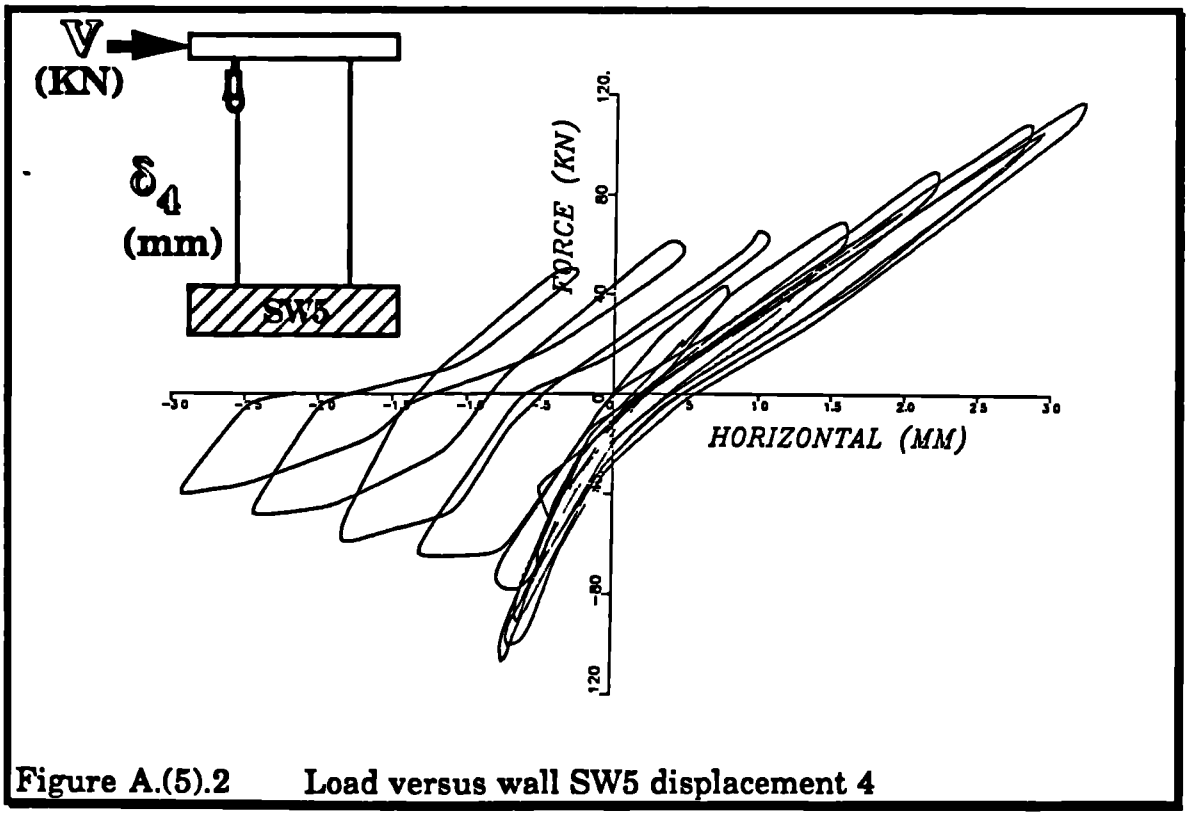


Figure A.(5).2 Load versus wall SW5 displacement 4

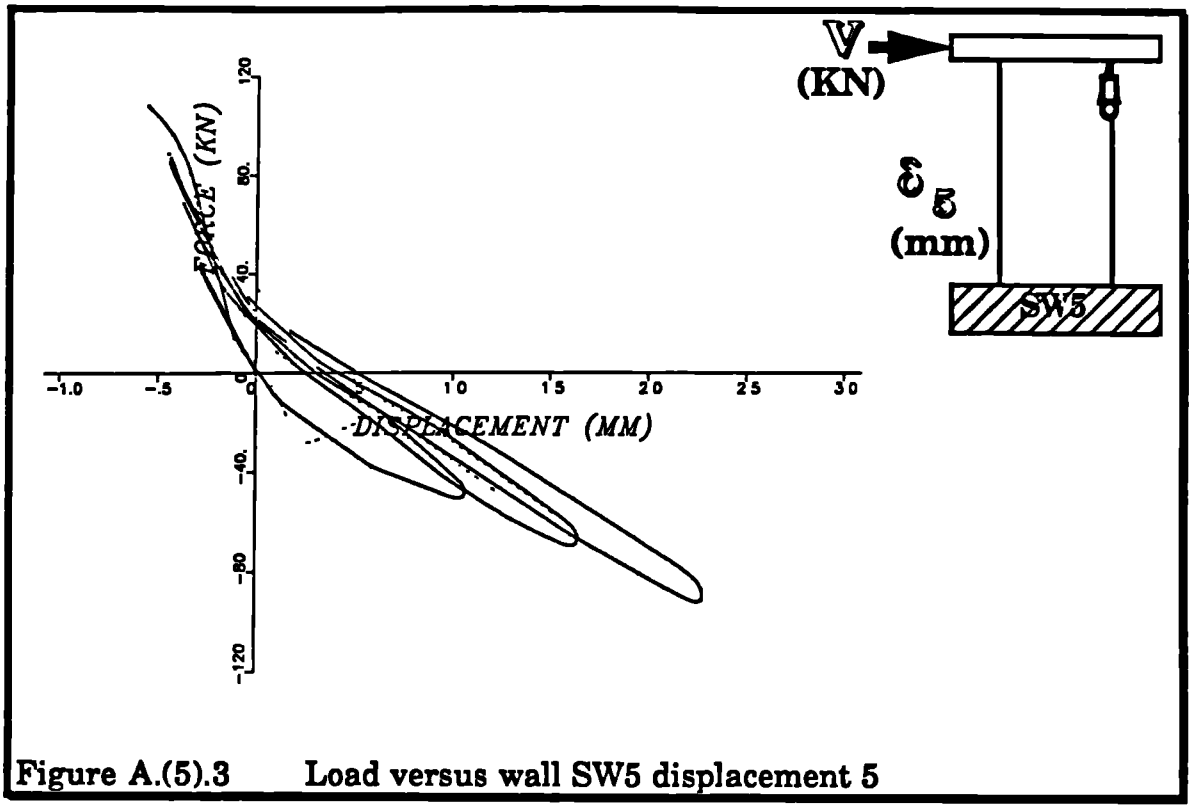


Figure A.(5).3 Load versus wall SW5 displacement 5

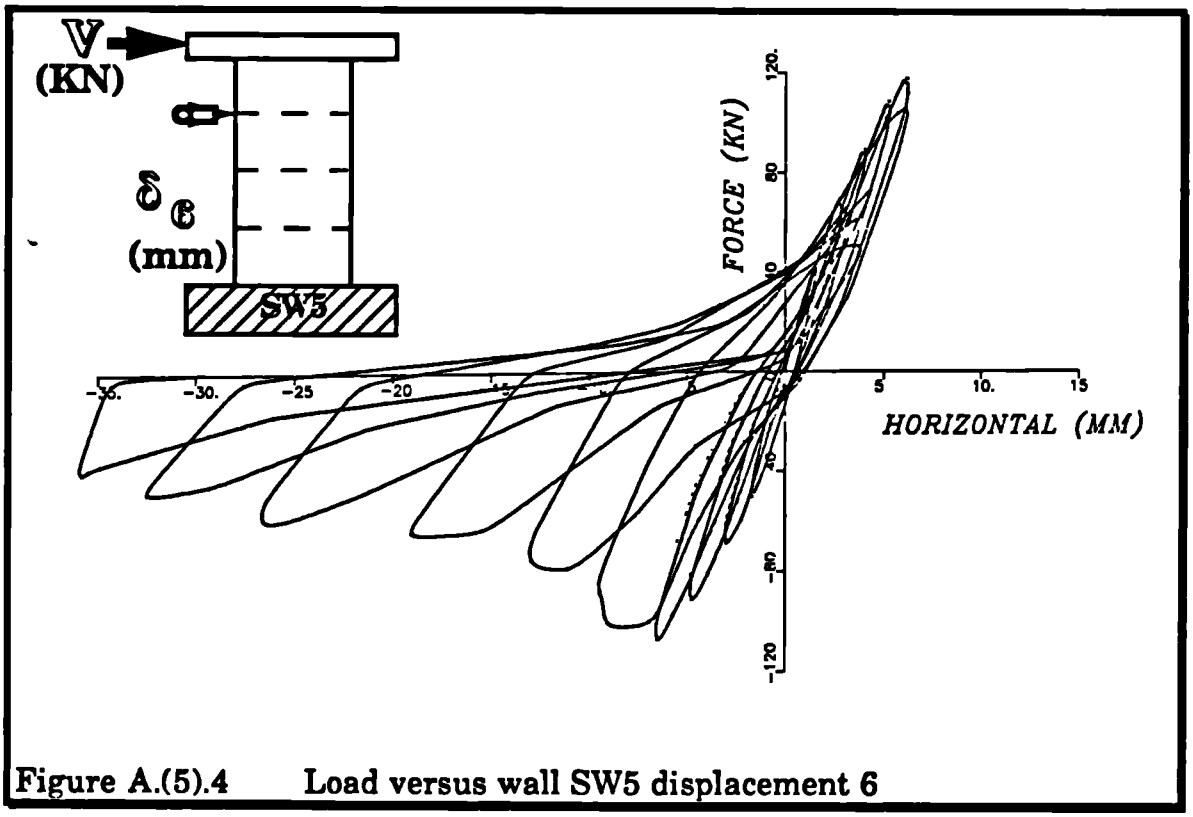


Figure A.(5).4 Load versus wall SW5 displacement 6

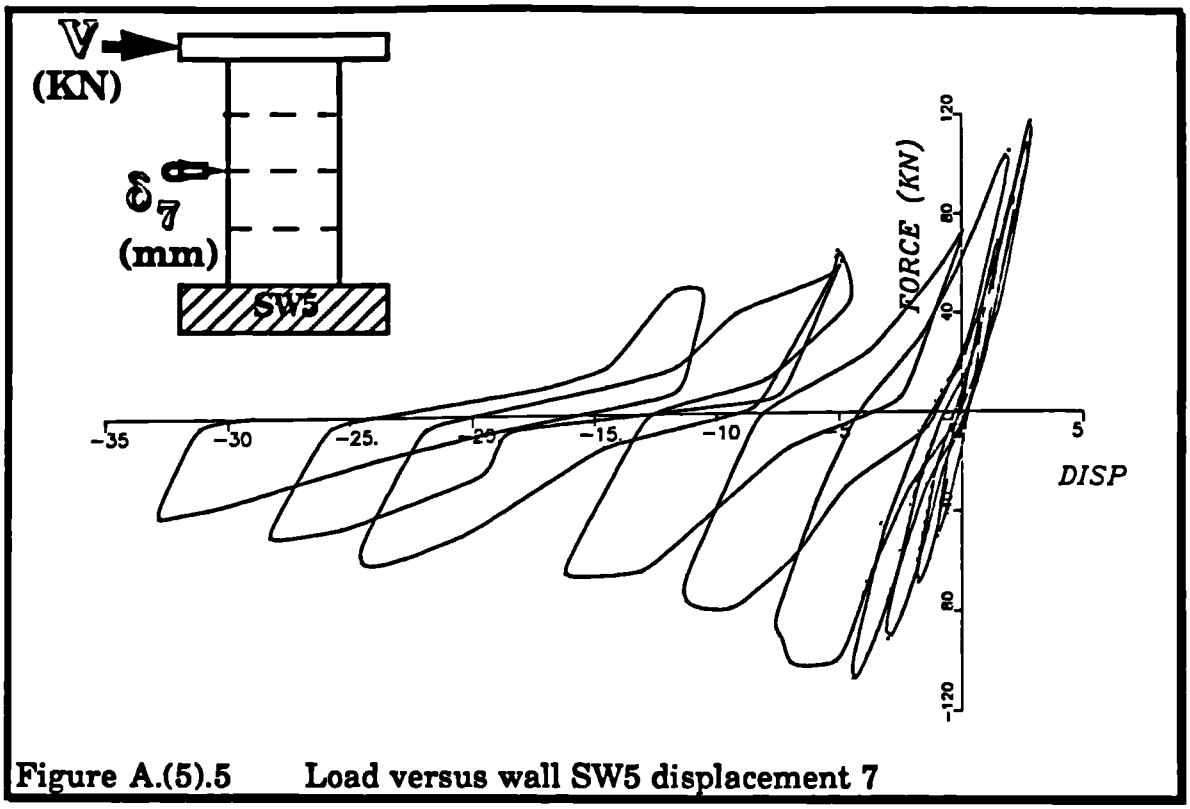


Figure A.(5).5 Load versus wall SW5 displacement 7

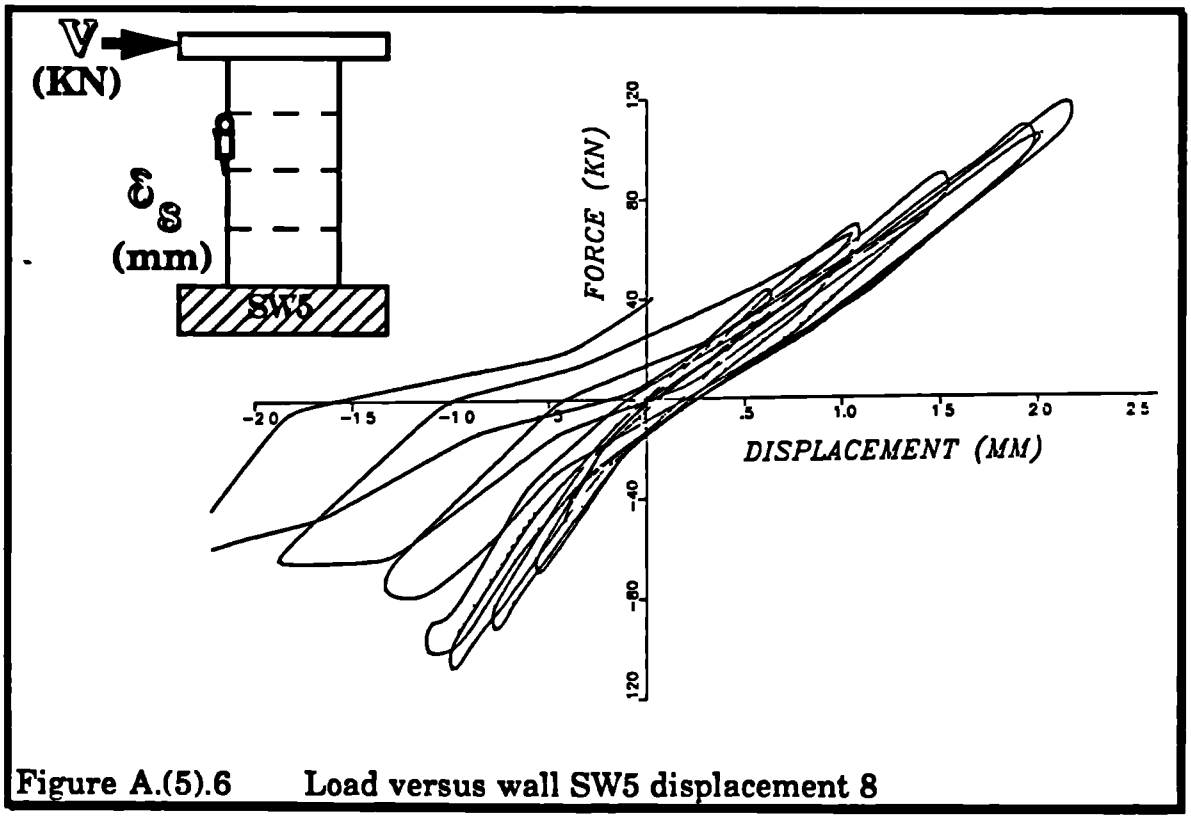


Figure A.(5).6 Load versus wall SW5 displacement 8

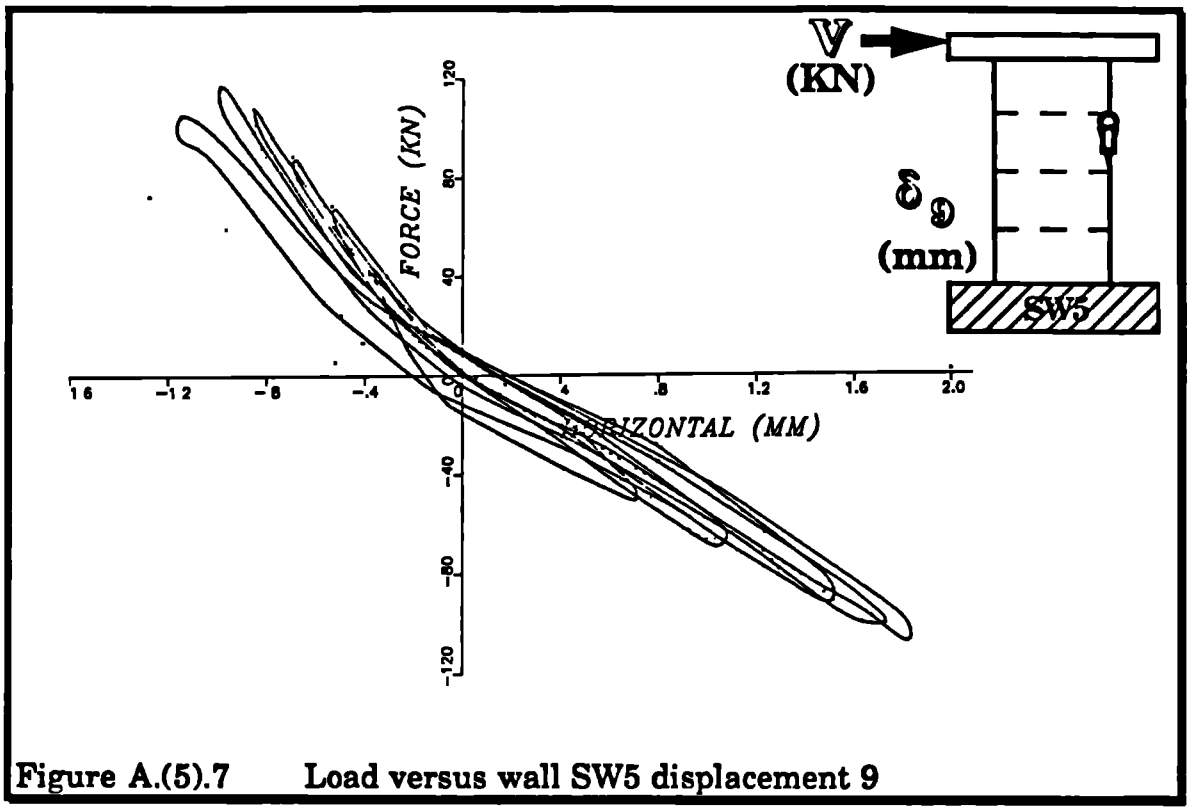


Figure A.(5).7 Load versus wall SW5 displacement 9

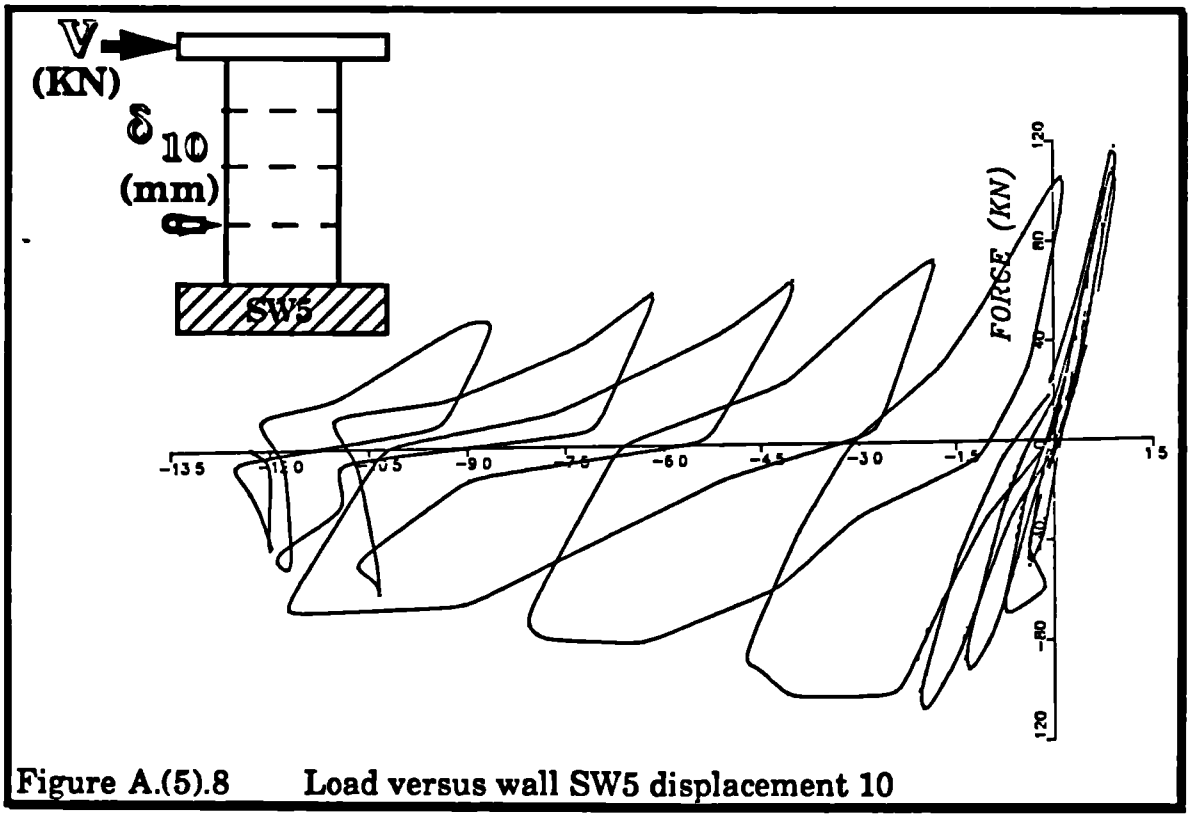


Figure A.(5).8 Load versus wall SW5 displacement 10

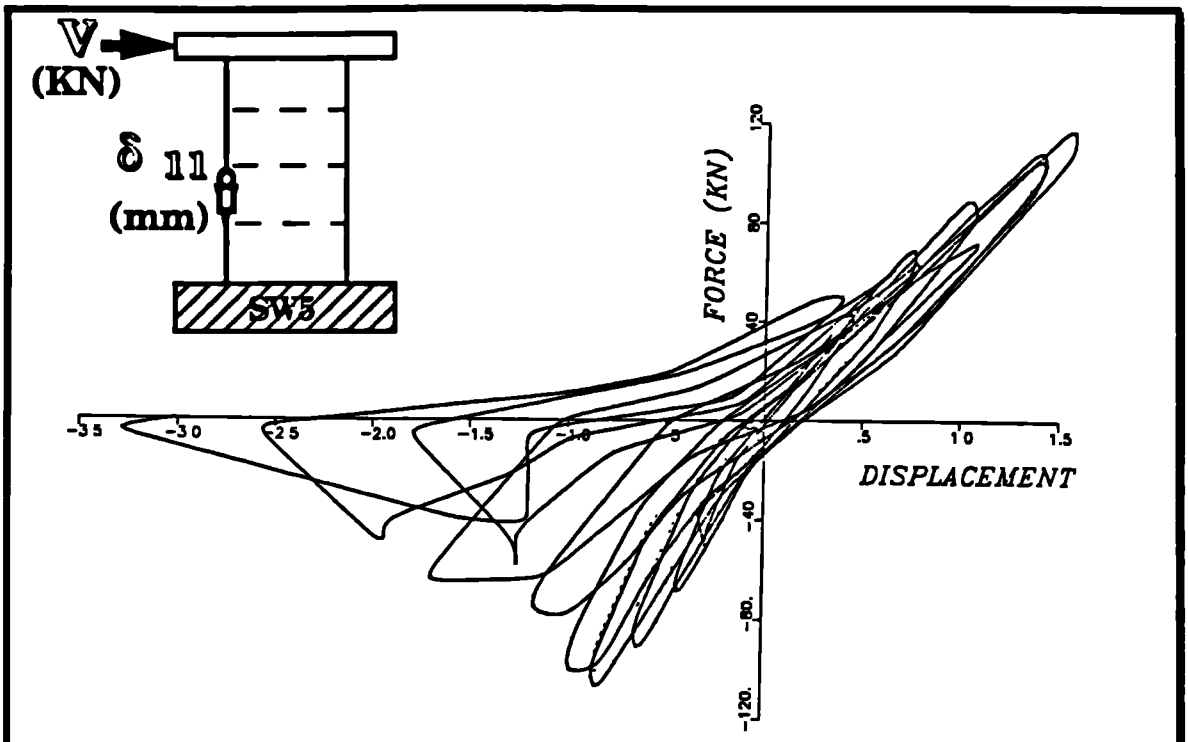


Figure A.(5).9 Load versus wall SW5 displacement 11

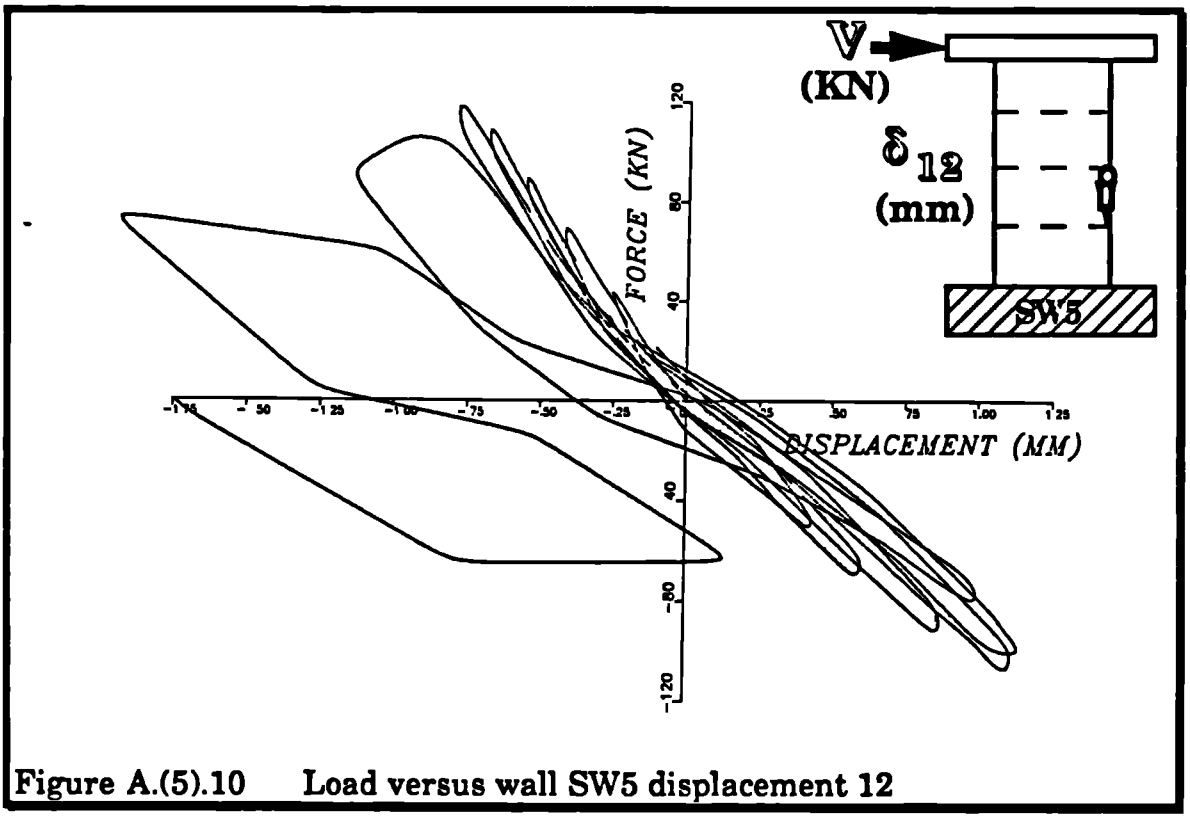


Figure A.(5).10 Load versus wall SW5 displacement 12

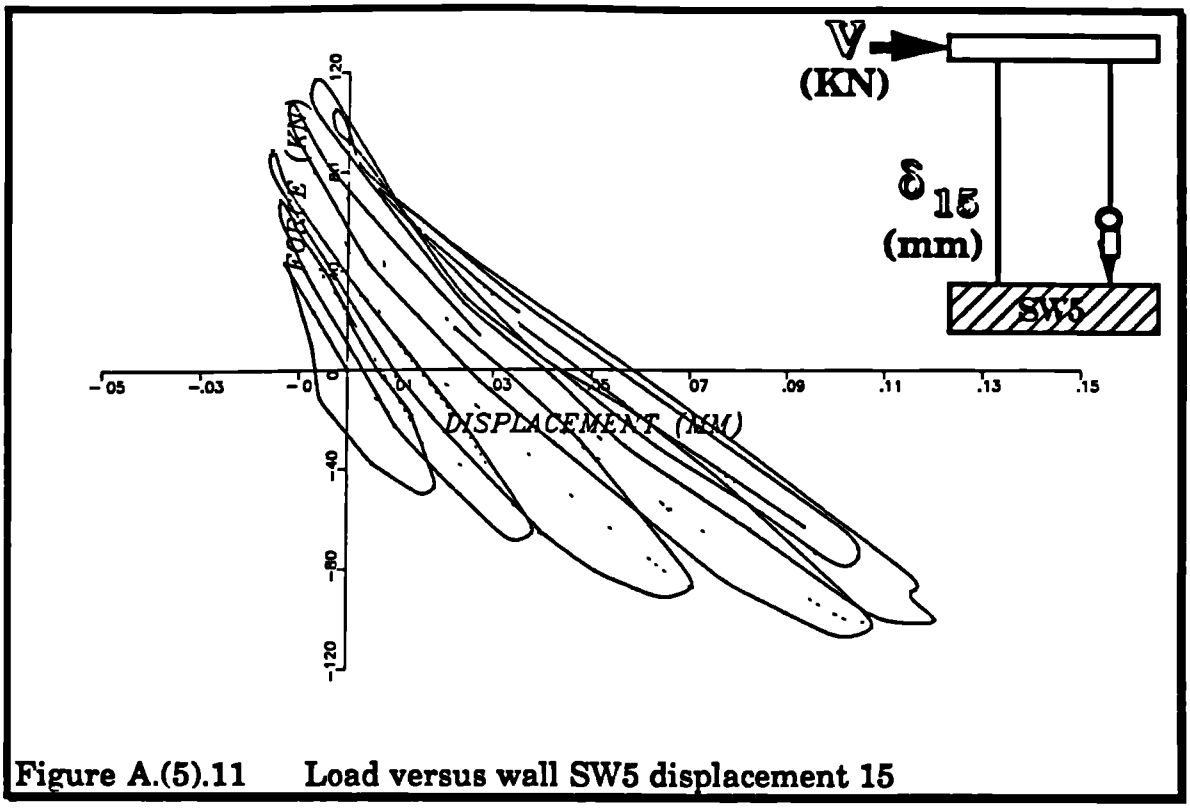


Figure A.(5).11 Load versus wall SW5 displacement 15

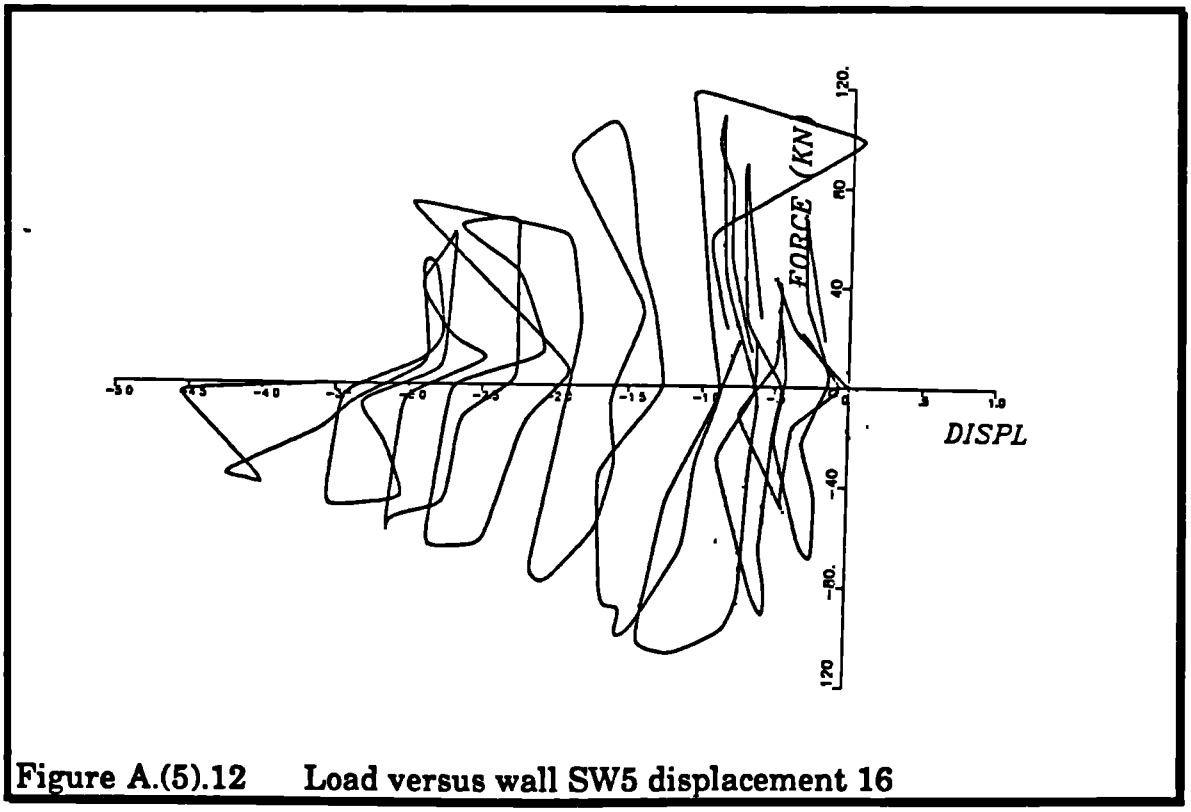


Figure A.(5).12 Load versus wall SW5 displacement 16

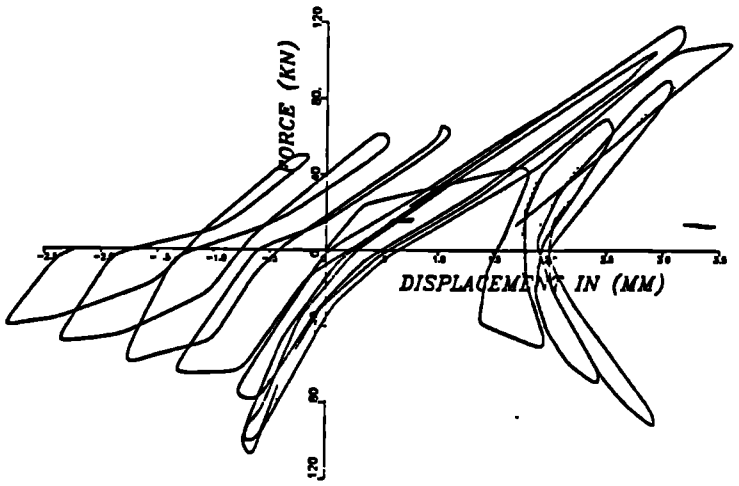


Figure A.(5).13 Load versus wall SW5 top wall average vertical displacement

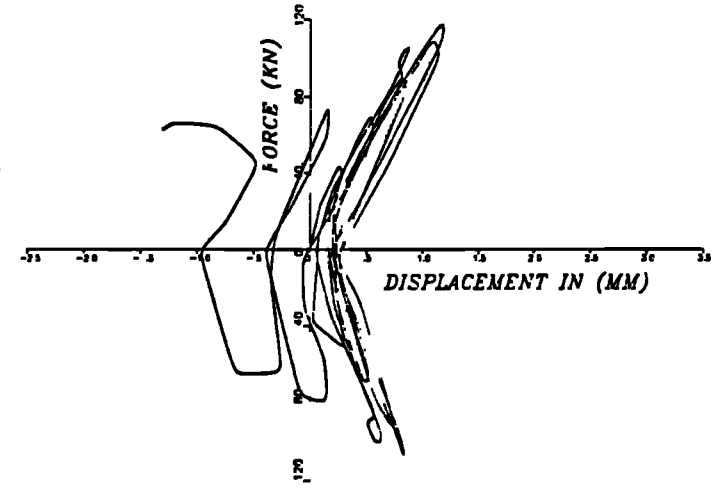


Figure A.(5).14 Load versus wall SW5 mid heigth average vertical displacement

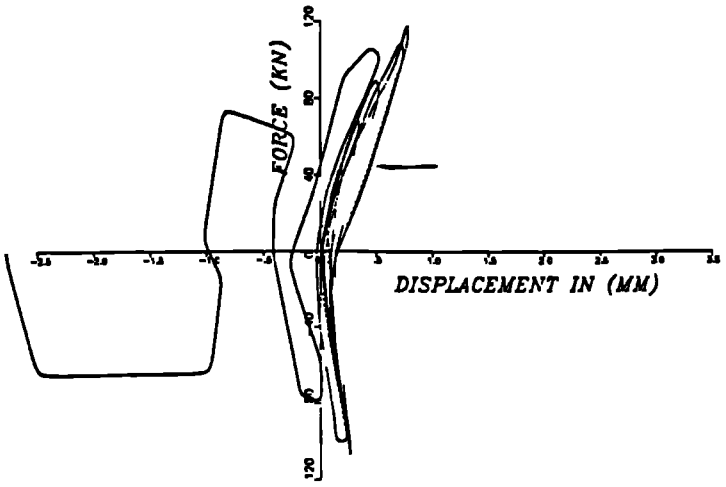
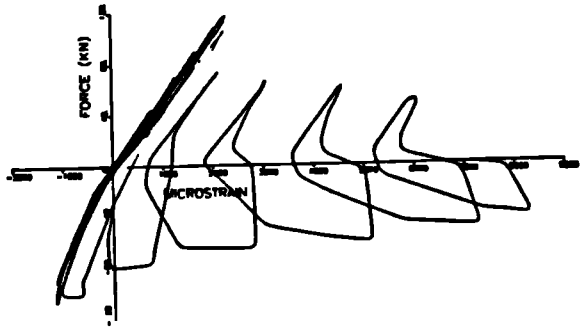


Figure A.(5).15 Load versus wall SW5 quarter heigth average vertical displacement

A.(5) Strain gauge results - Scale 1:2.5 model SW5



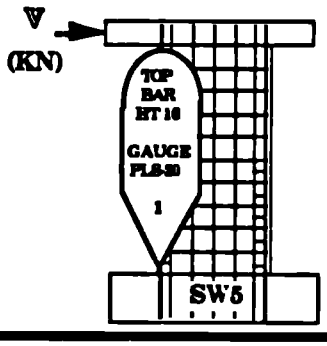


Figure A.(5).16 Load versus strain 1

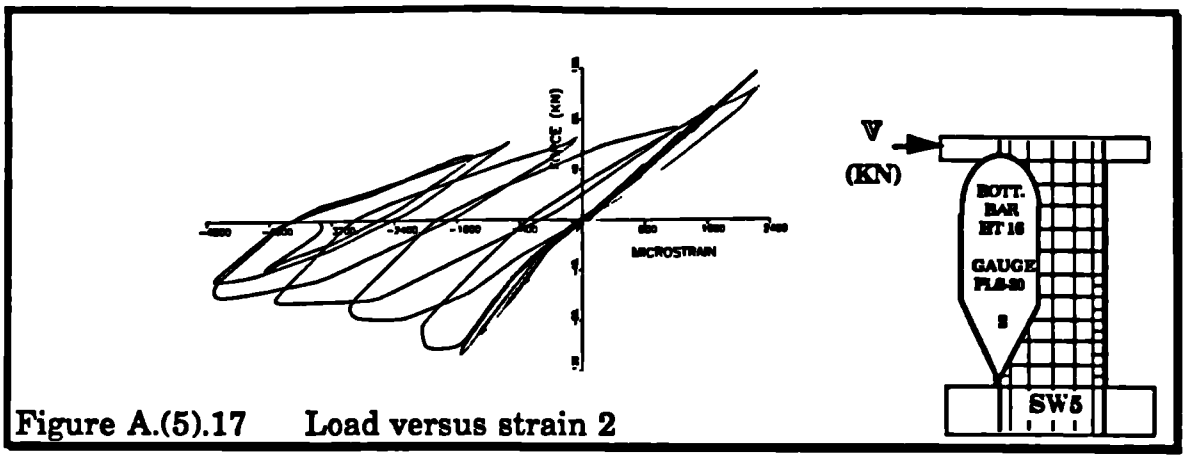


Figure A.(5).17 Load versus strain 2

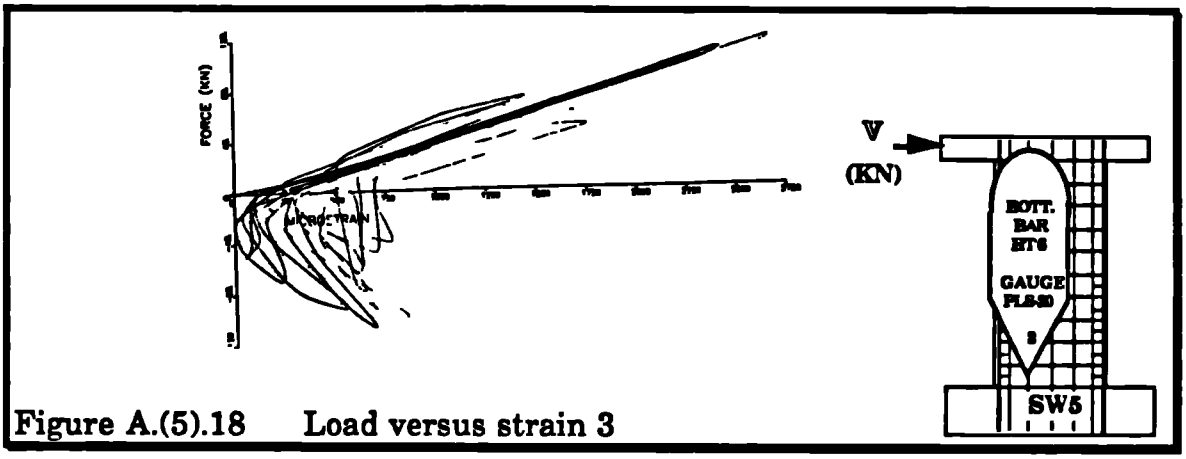


Figure A.(5).18 Load versus strain 3

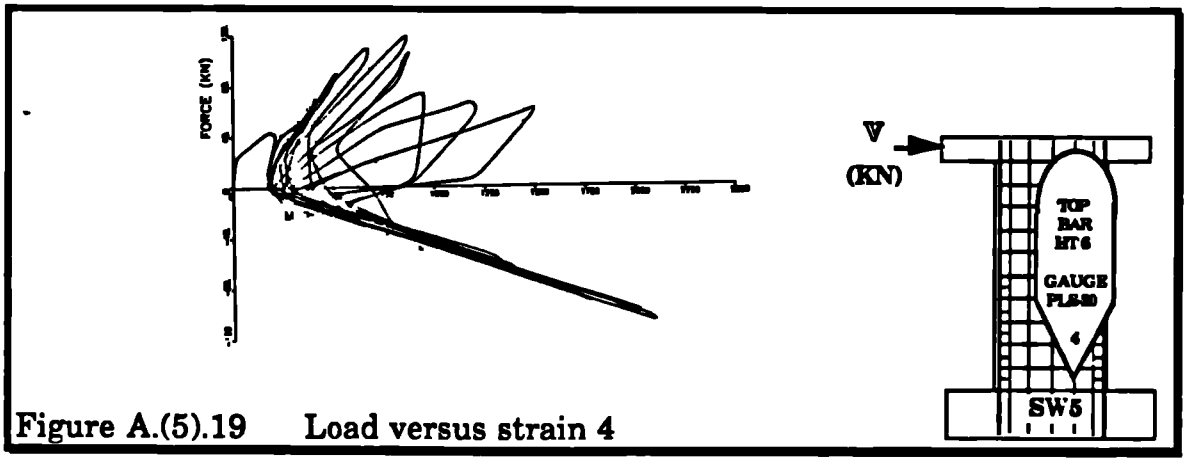


Figure A.(5).19 Load versus strain 4

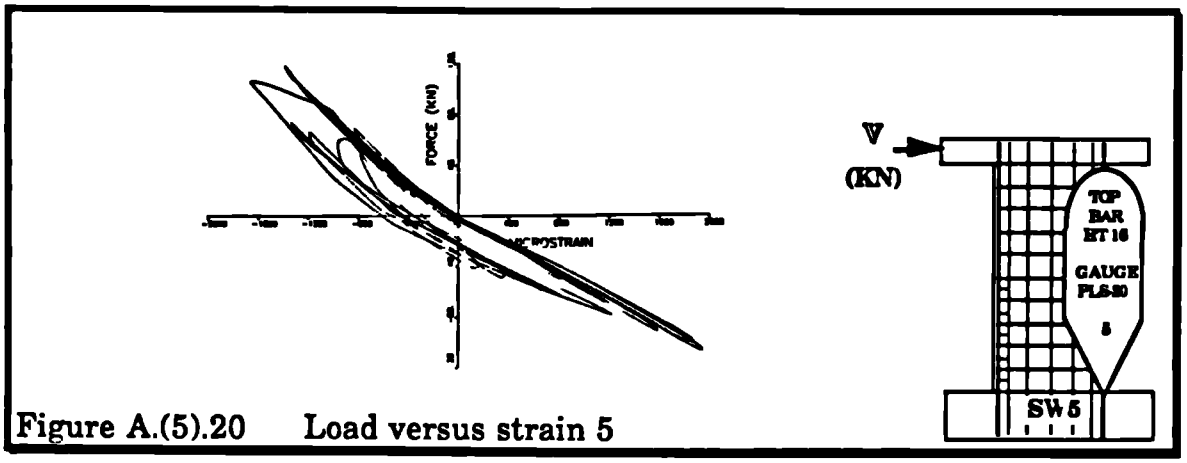


Figure A.(5).20 Load versus strain 5

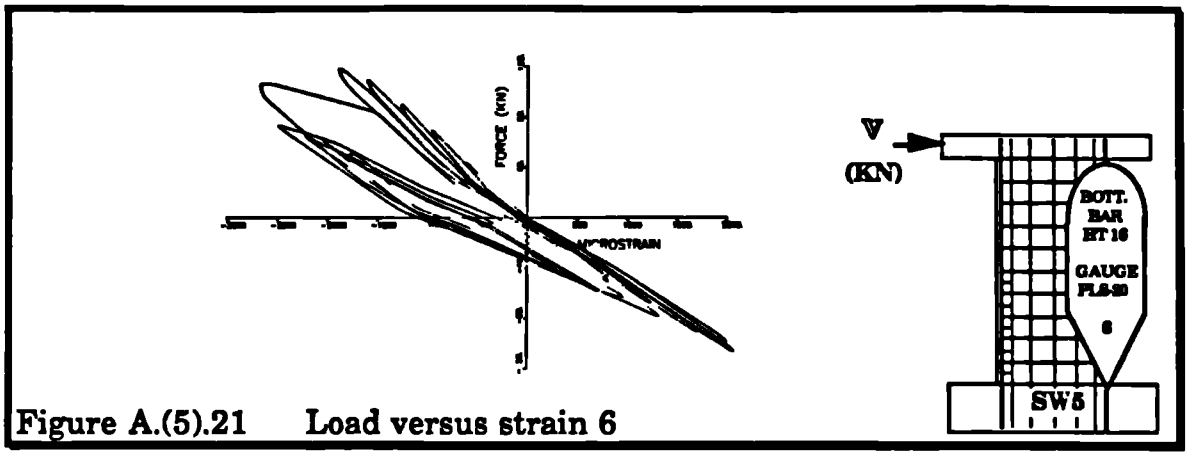


Figure A.(5).21 Load versus strain 6

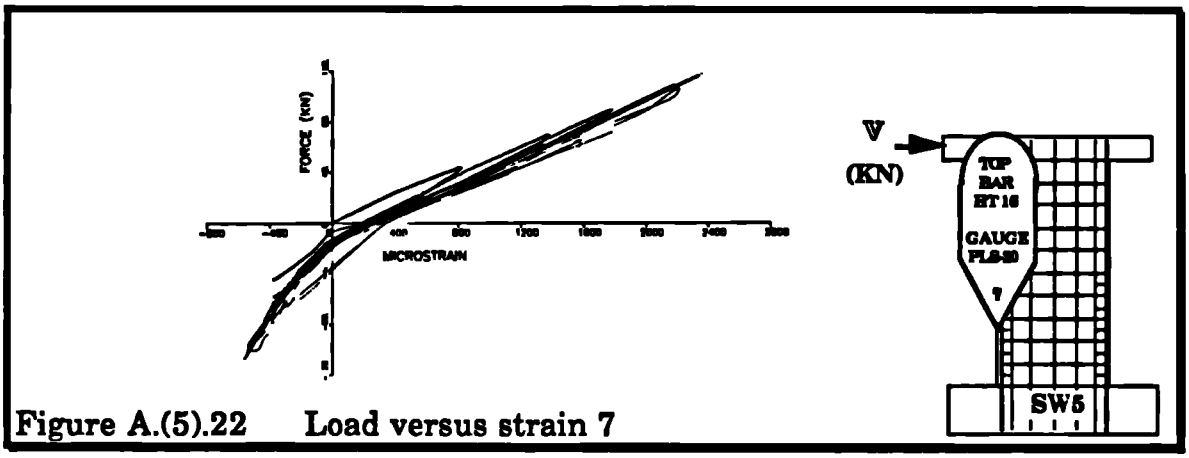


Figure A.(5).22 Load versus strain 7

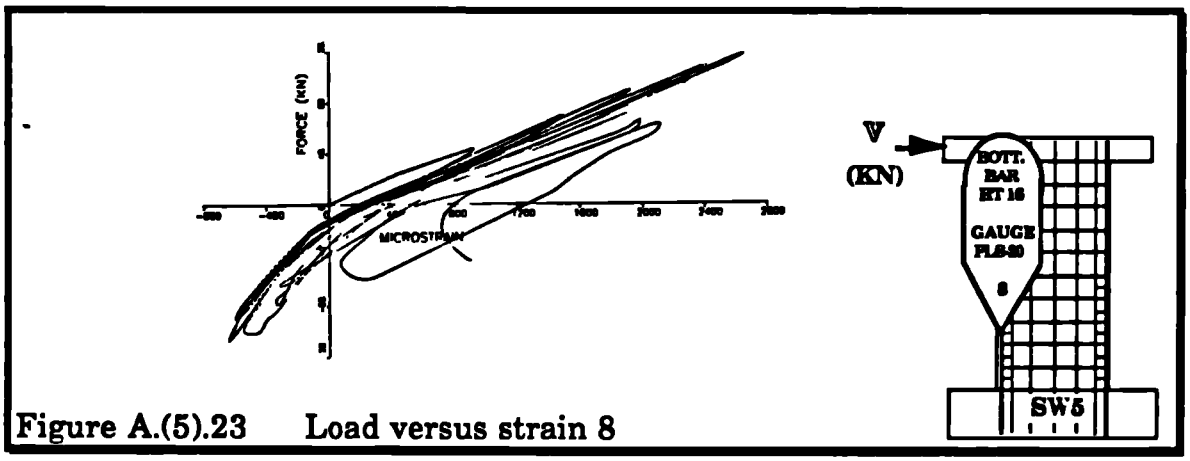


Figure A.(5).23 Load versus strain 8

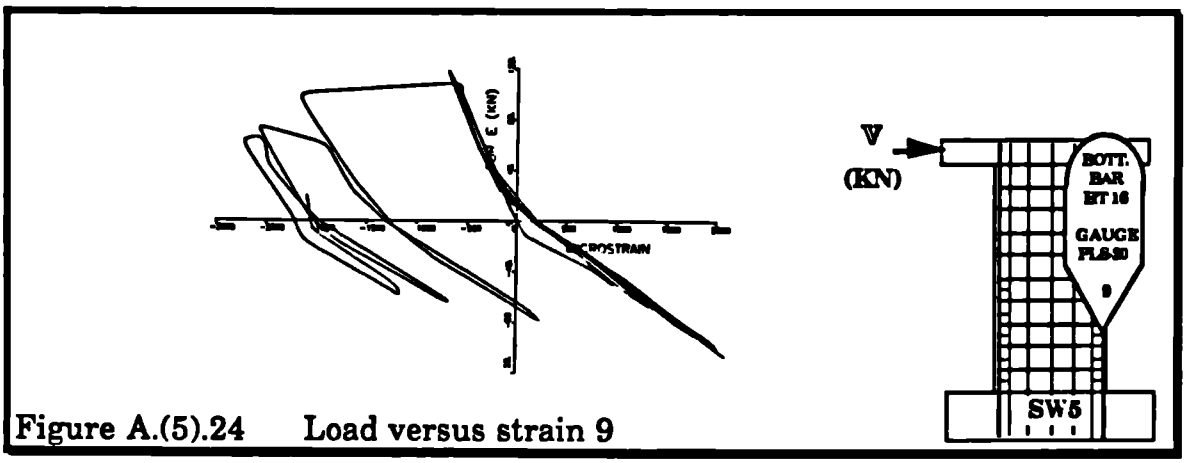
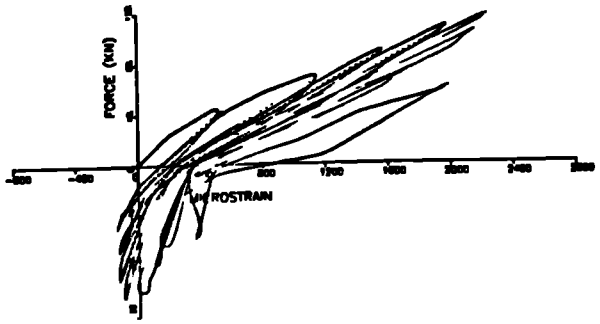


Figure A.(5).24 Load versus strain 9



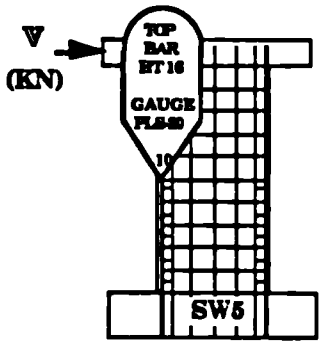
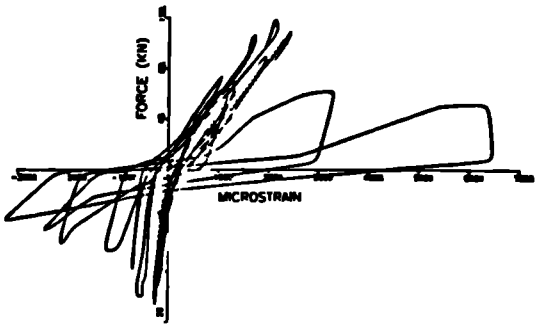


Figure A.(5).25 Load versus strain 10



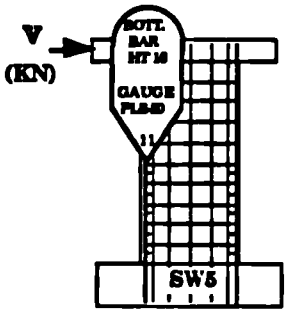
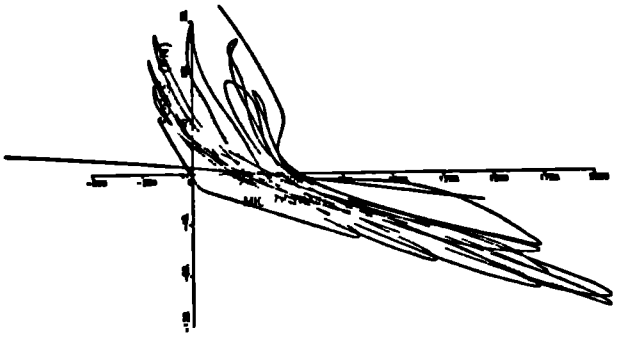


Figure A.(5).26 Load versus strain 11



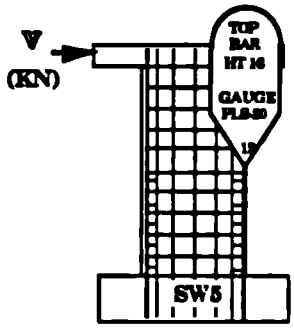
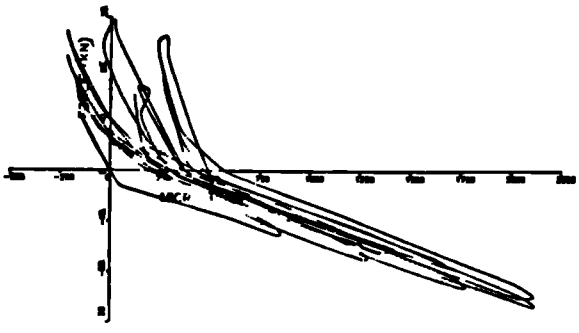


Figure A.(5).27 Load versus strain 12



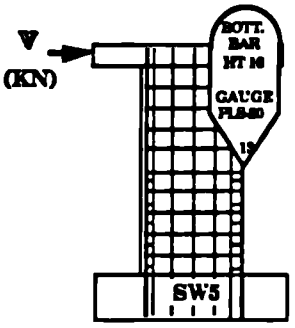


Figure A.(5).28 Load versus strain 13

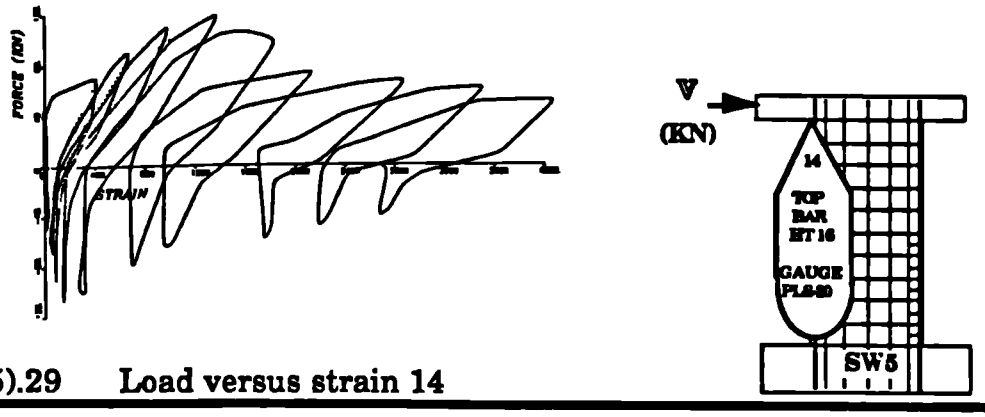


Figure A.(5).29 Load versus strain 14

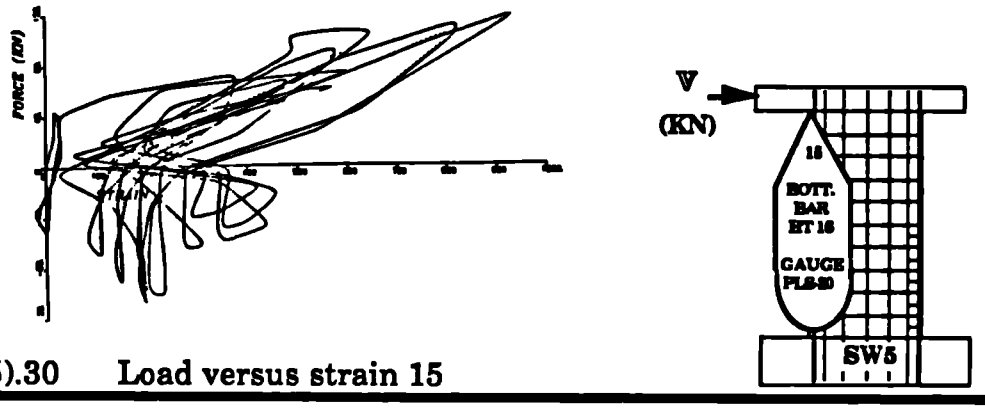


Figure A.(5).30 Load versus strain 15

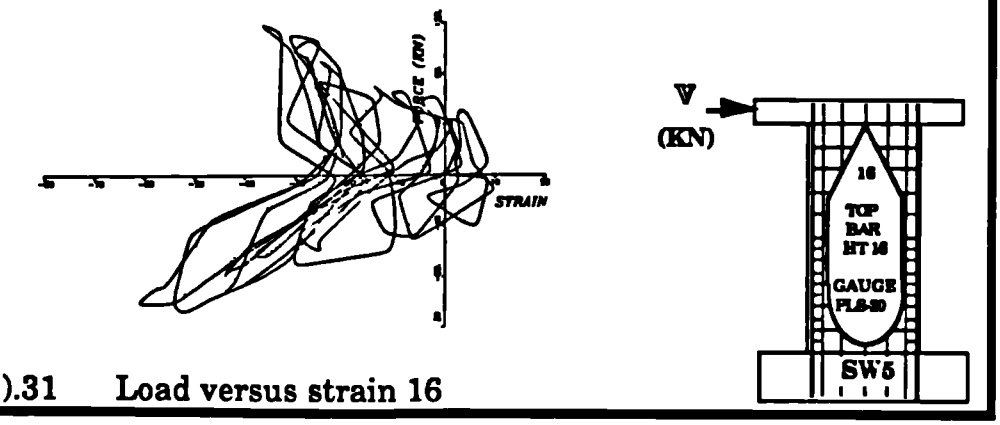


Figure A.(5).31 Load versus strain 16

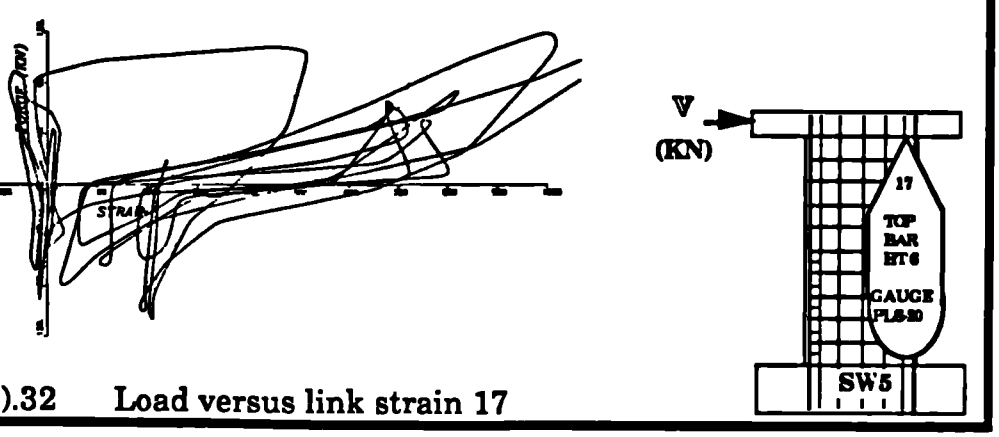


Figure A.(5).32 Load versus link strain 17

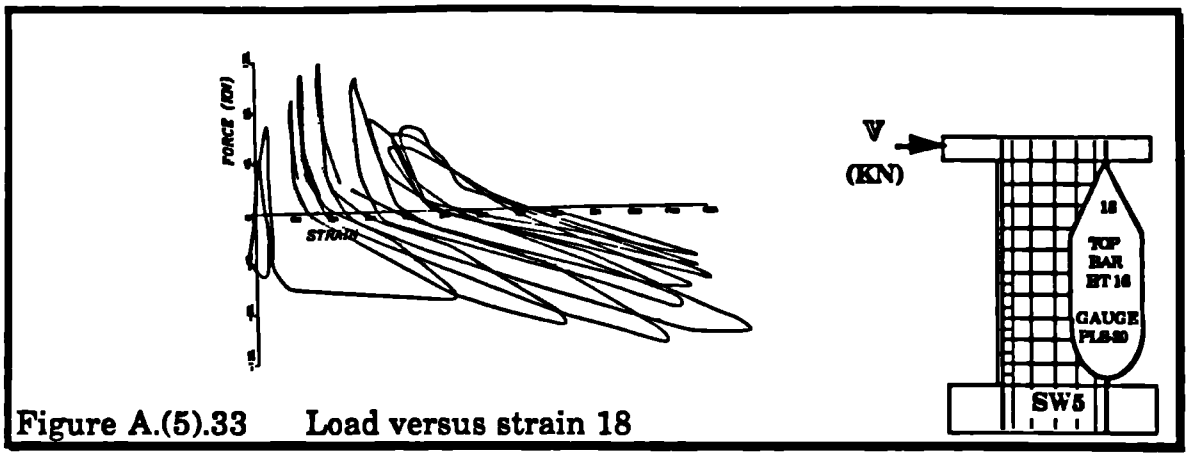


Figure A.(5).33 Load versus strain 18

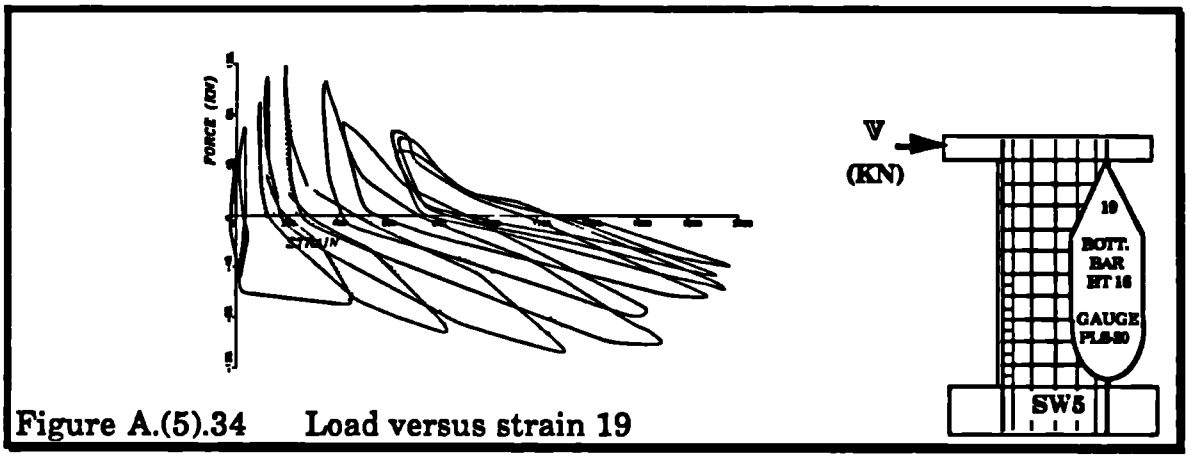


Figure A.(5).34 Load versus strain 19

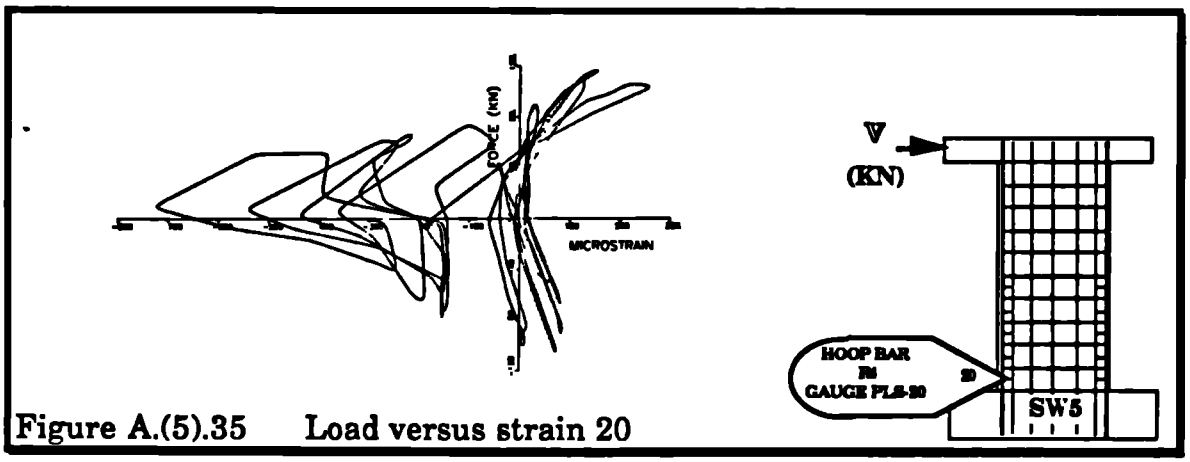


Figure A.(5).35 Load versus strain 20

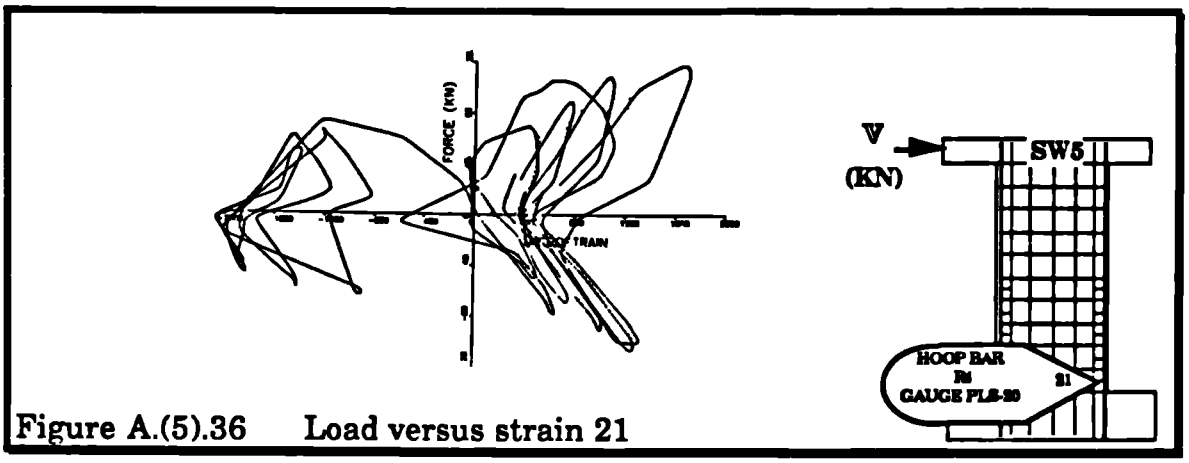


Figure A.(5).36 Load versus strain 21

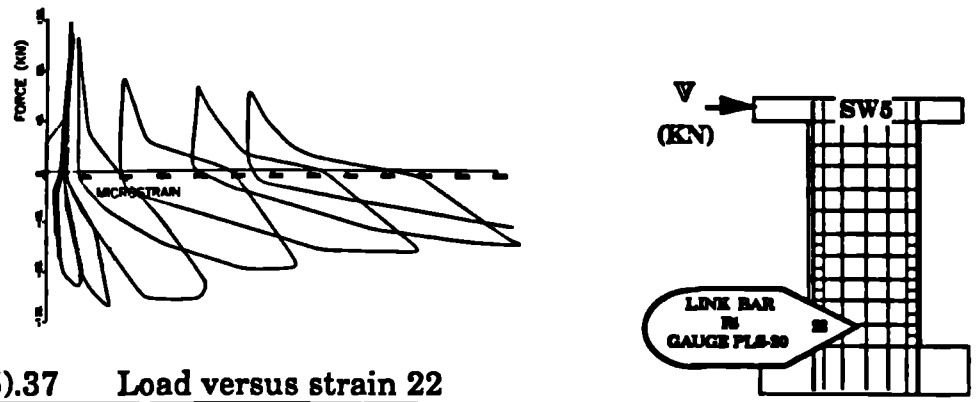


Figure A.(5).37 Load versus strain 22

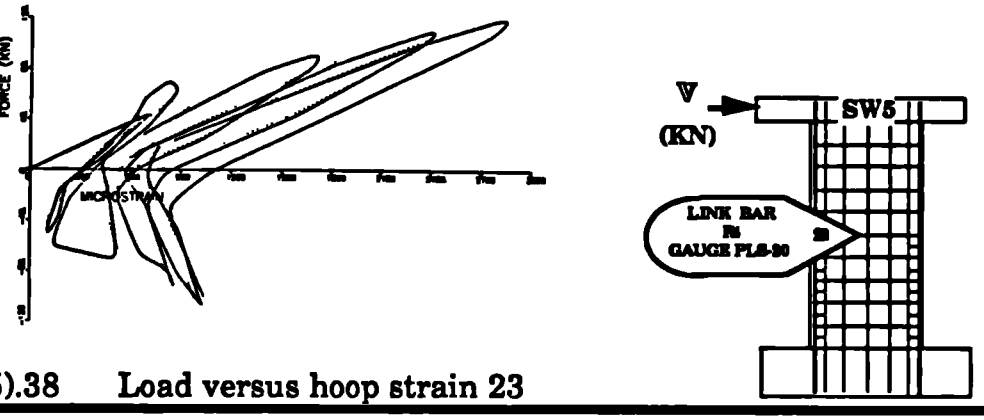


Figure A.(5).38 Load versus hoop strain 23

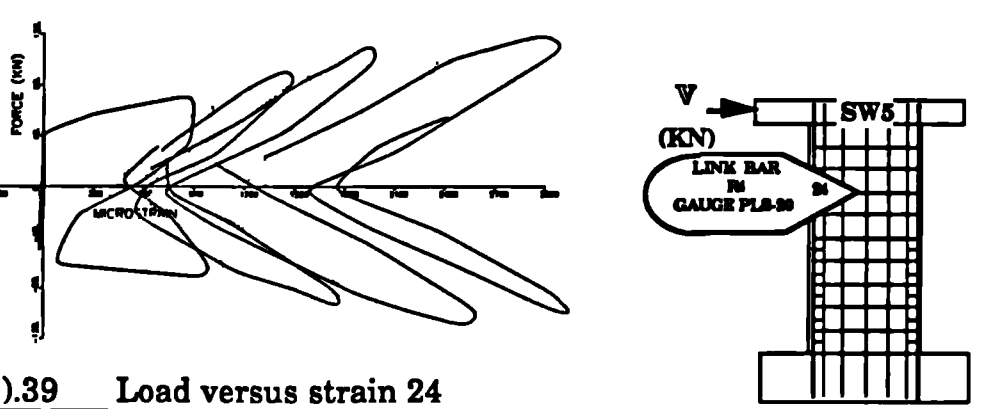
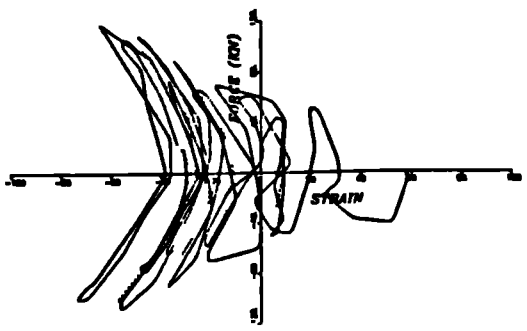


Figure A.(5).39 Load versus strain 24



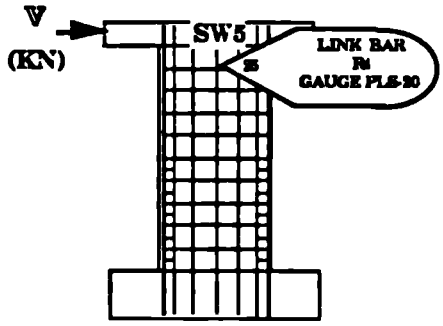


Figure A.(5).40 Load versus hoop strain 25

A.(6) Load-displacement curves - Scale 1:2.5 model SW6

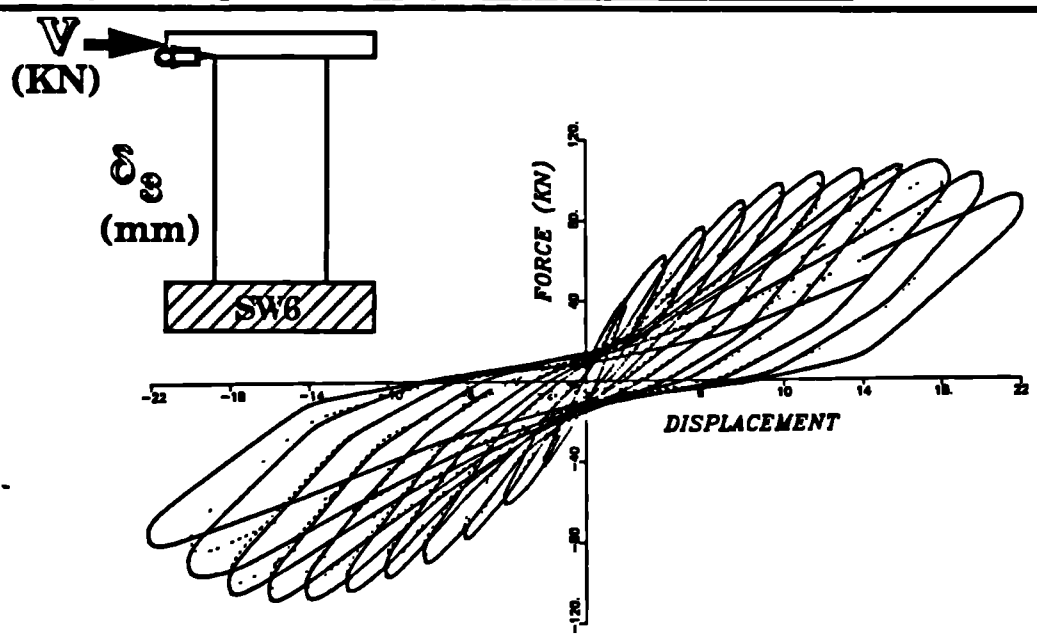


Figure A.(6).1 Load versus wall SW6 displacement 3

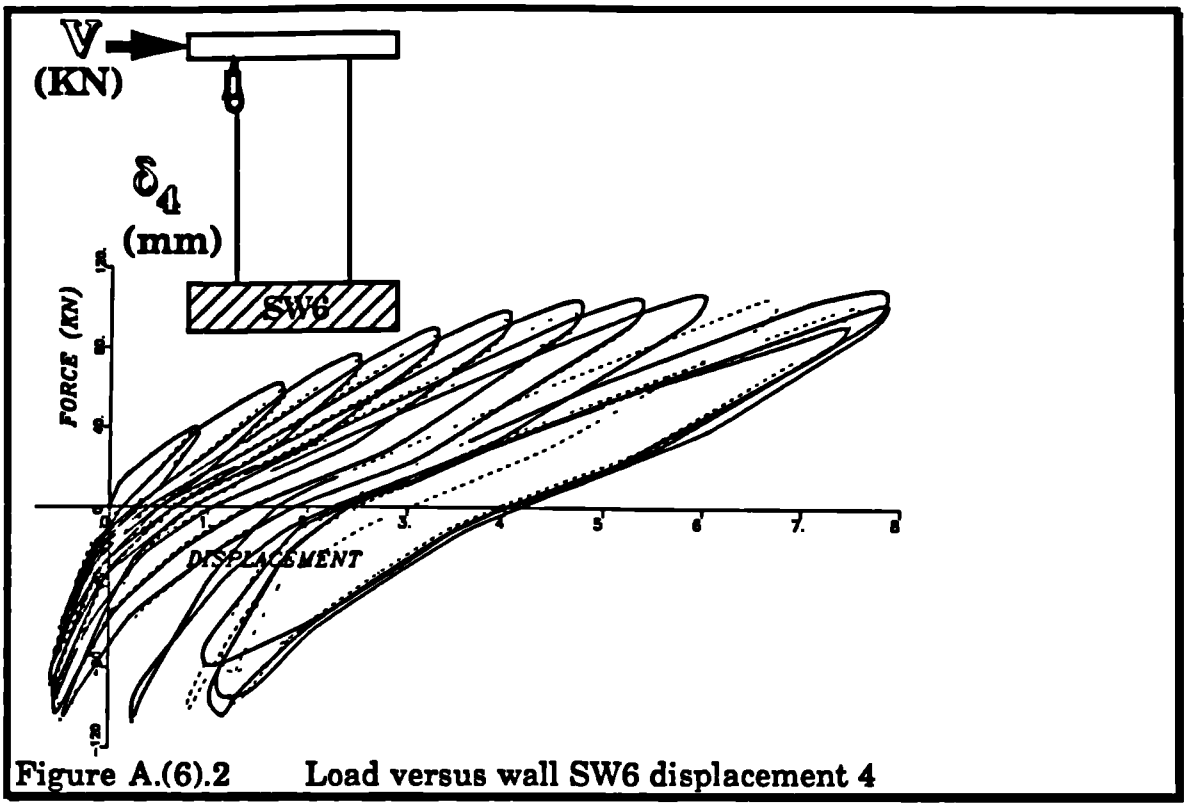


Figure A.(6).2 Load versus wall SW6 displacement 4

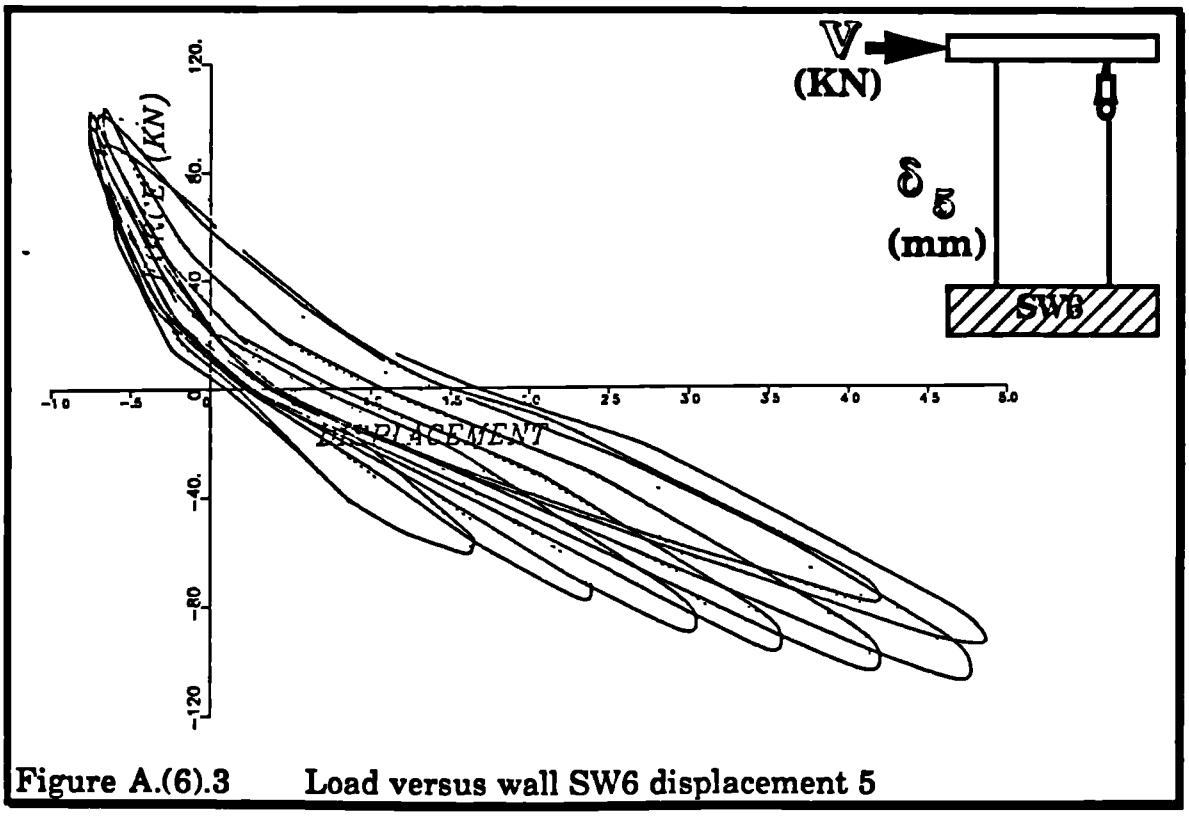


Figure A.(6).3 Load versus wall SW6 displacement 5

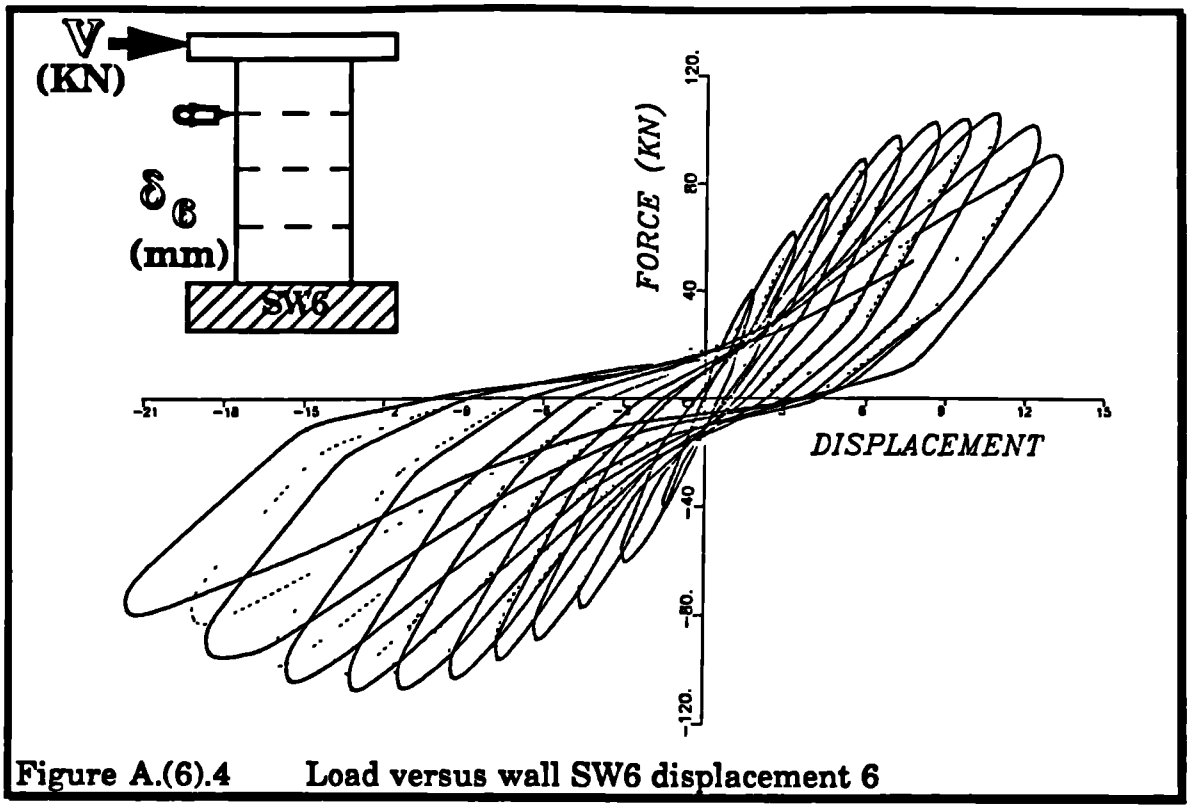


Figure A.(6).4 Load versus wall SW6 displacement 6

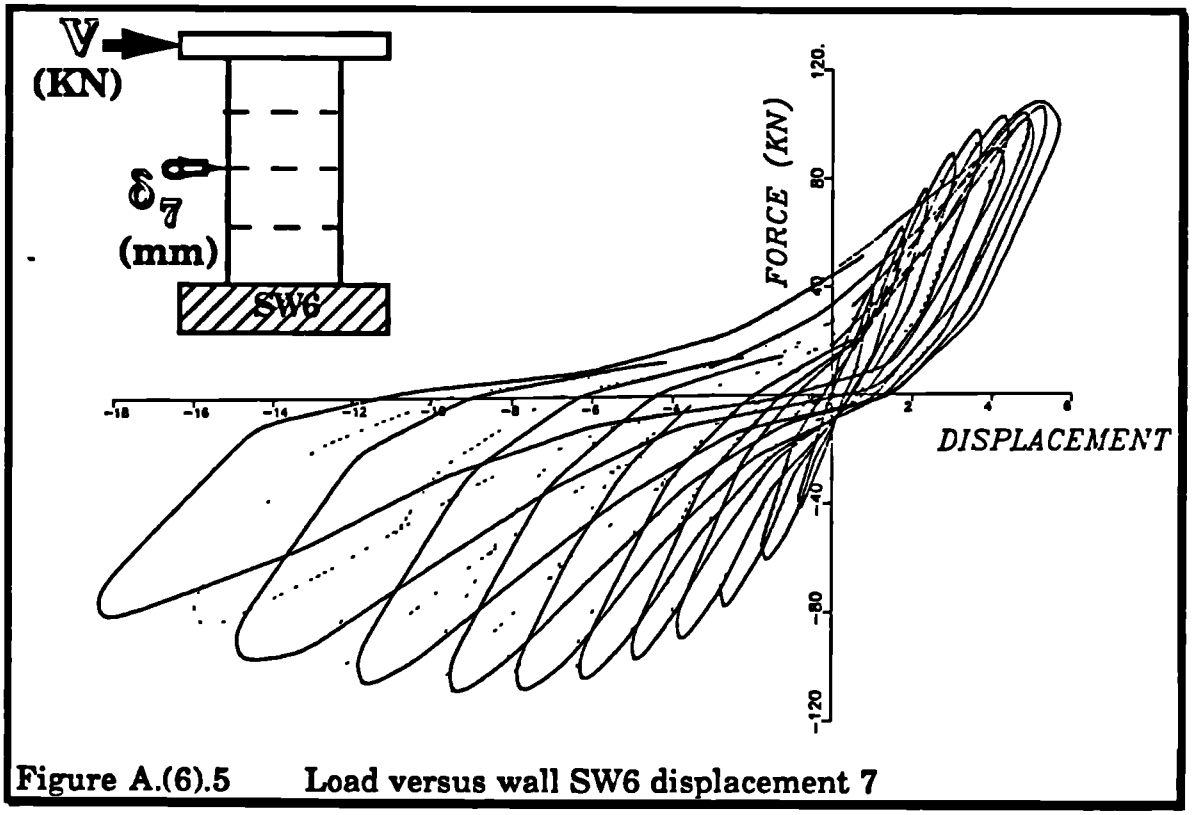


Figure A.(6).5 Load versus wall SW6 displacement 7

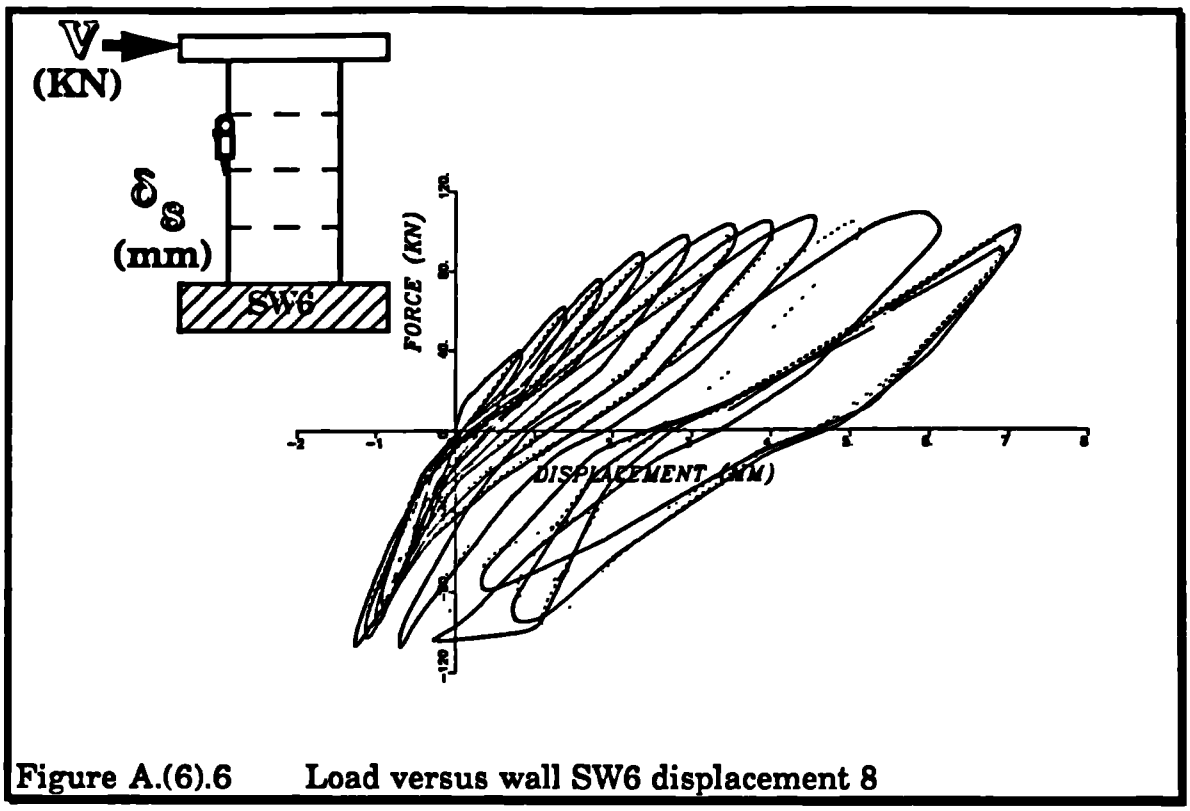


Figure A.(6).6 Load versus wall SW6 displacement 8

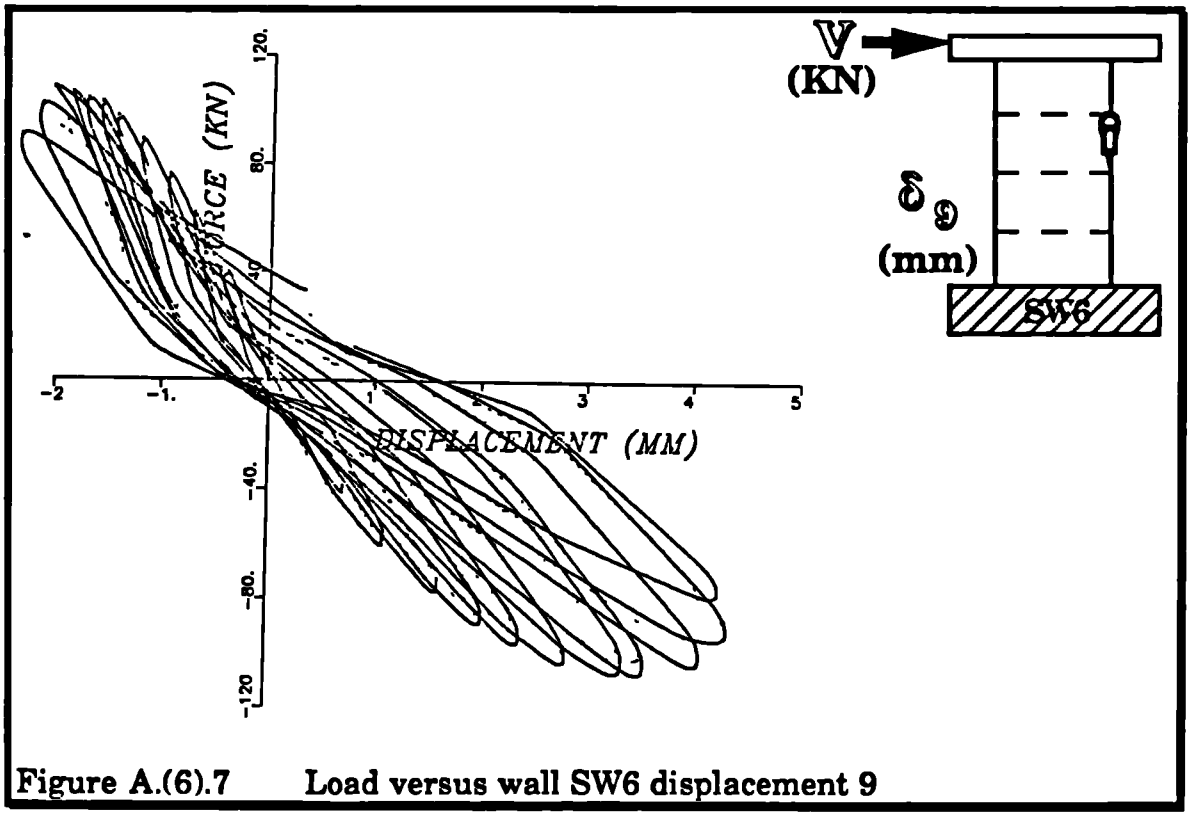


Figure A.(6).7 Load versus wall SW6 displacement 9

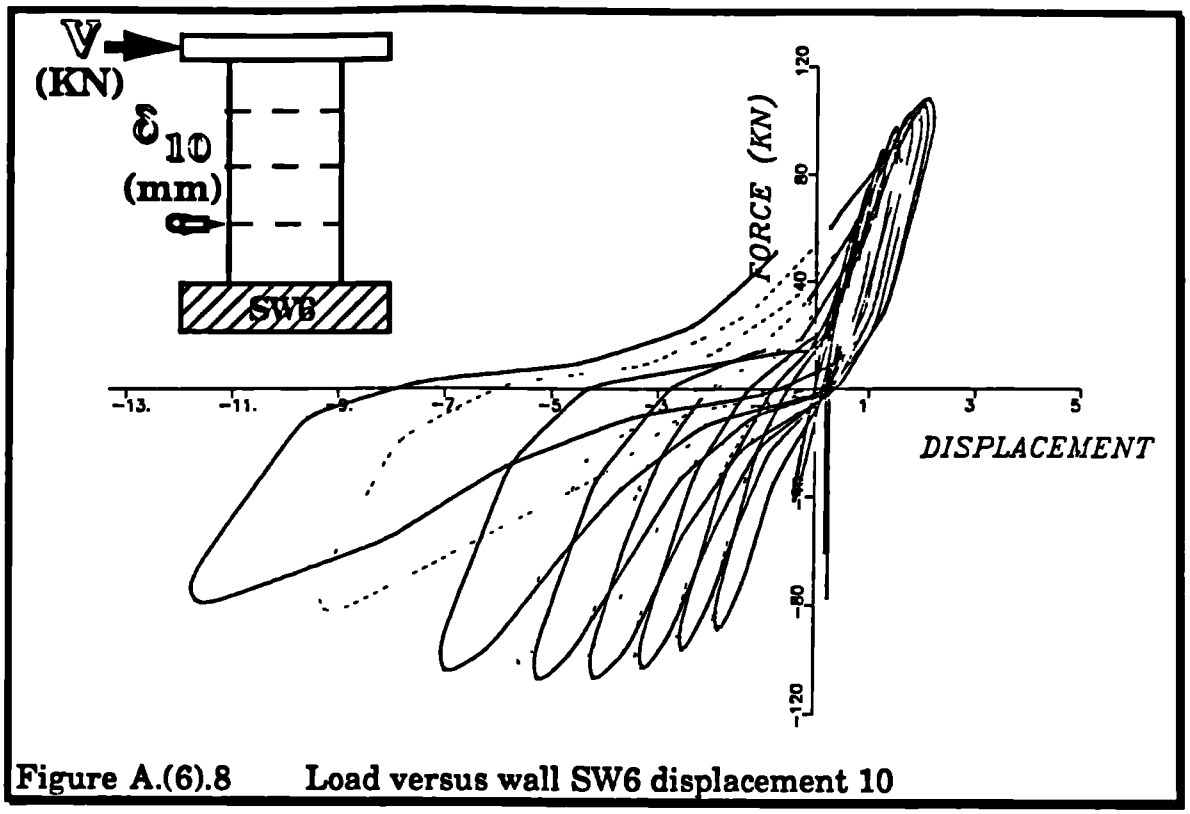


Figure A.(6).8 Load versus wall SW6 displacement 10

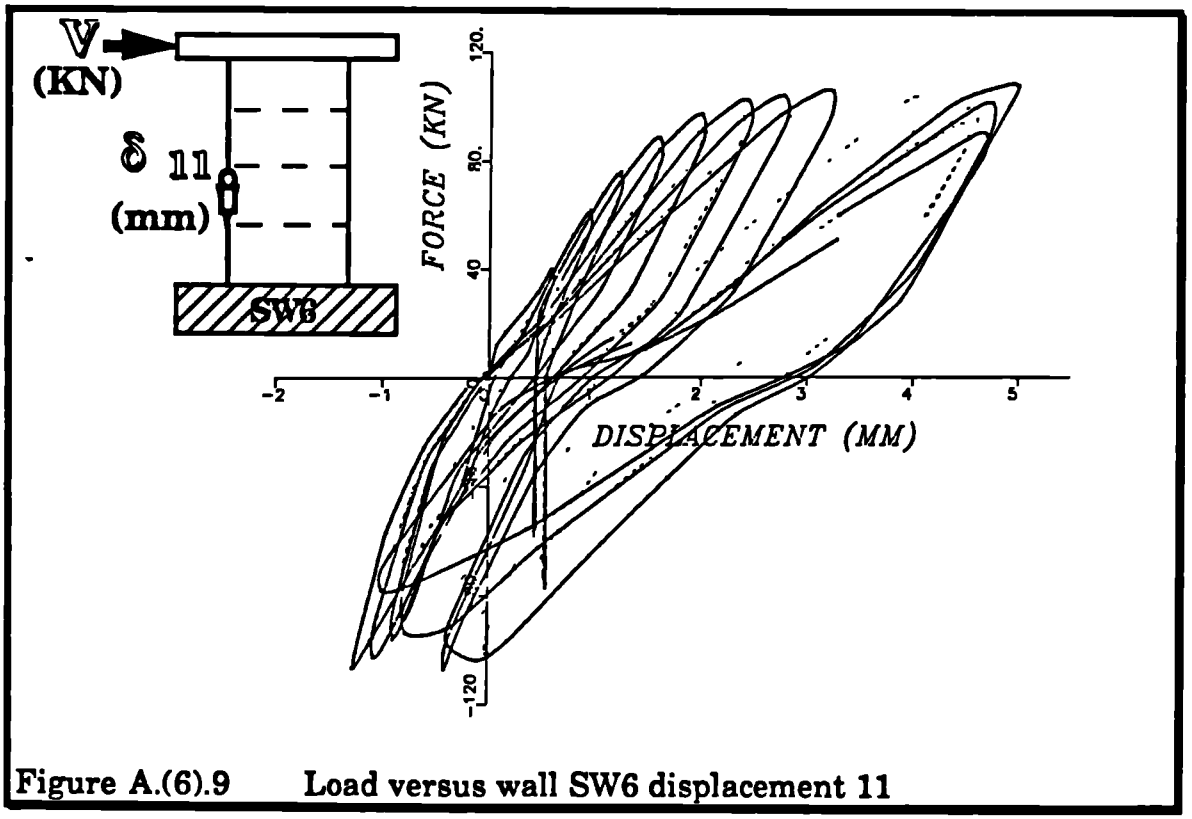


Figure A.(6).9 Load versus wall SW6 displacement 11

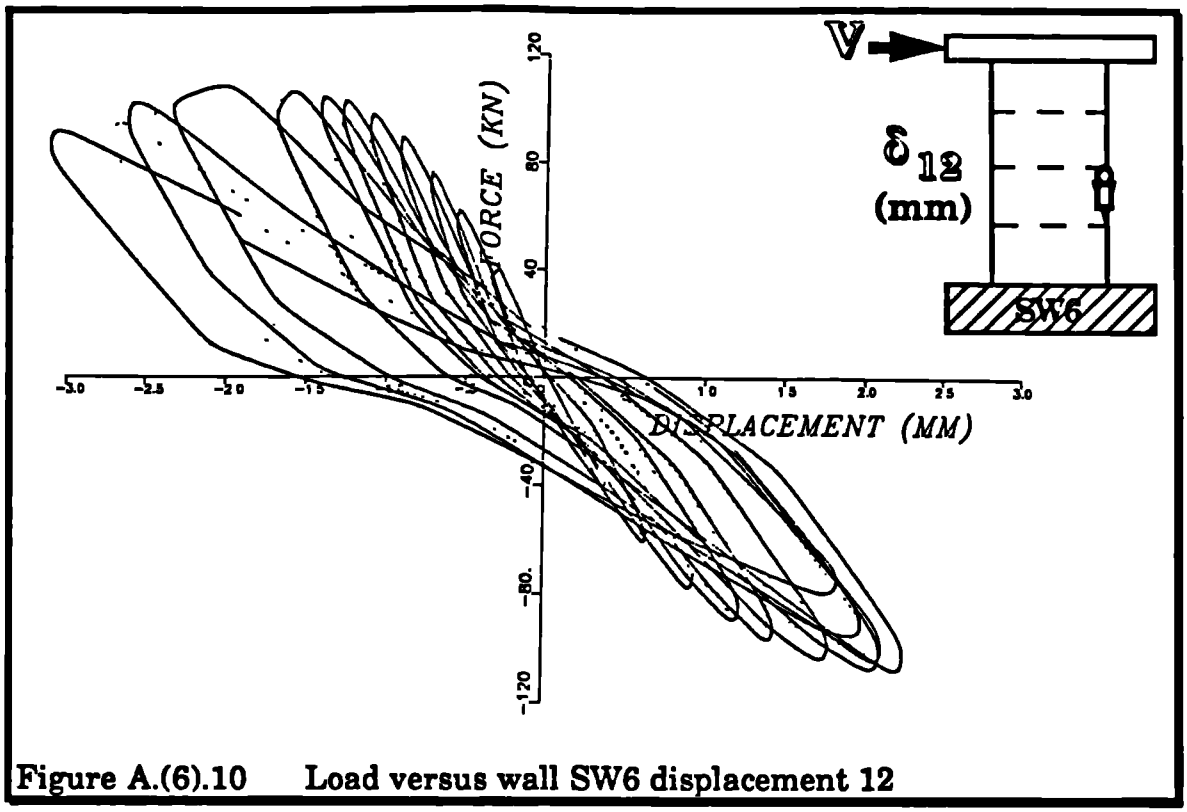


Figure A.(6).10 Load versus wall SW6 displacement 12

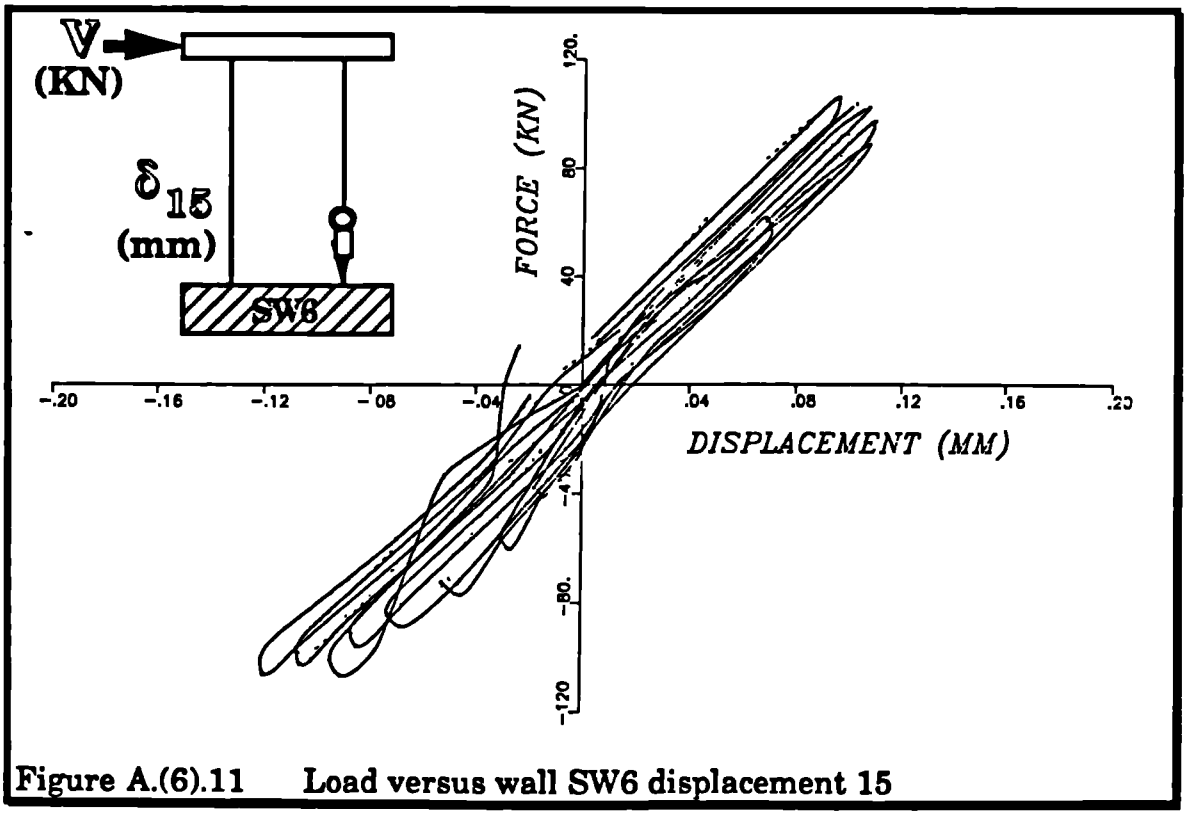


Figure A.(6).11 Load versus wall SW6 displacement 15

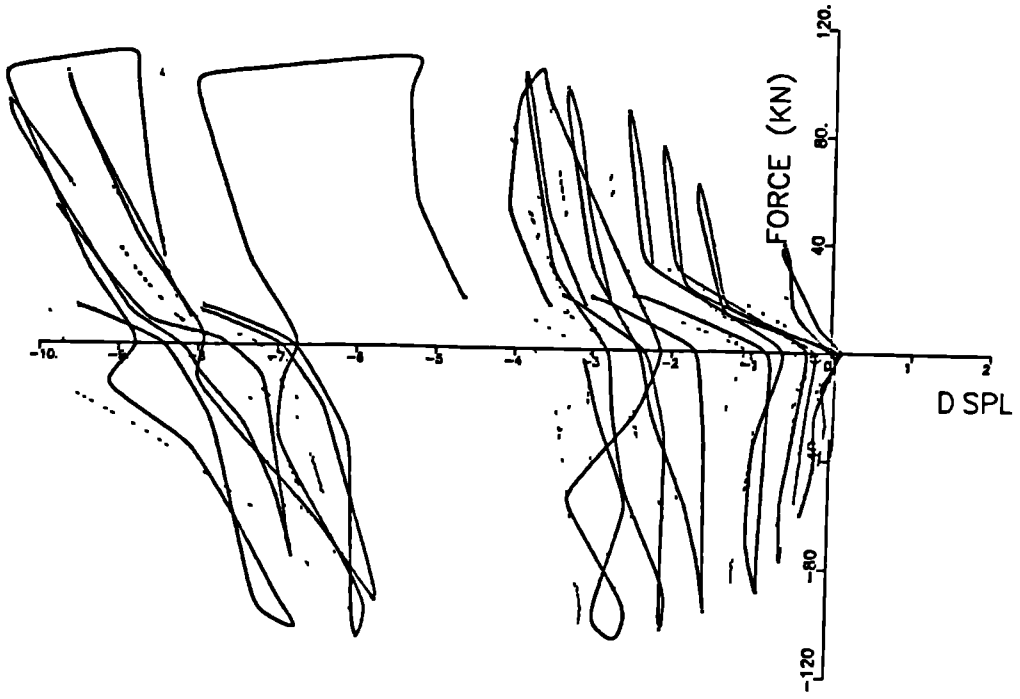


Figure A.(6).12 Load versus wall SW6 displacement 16

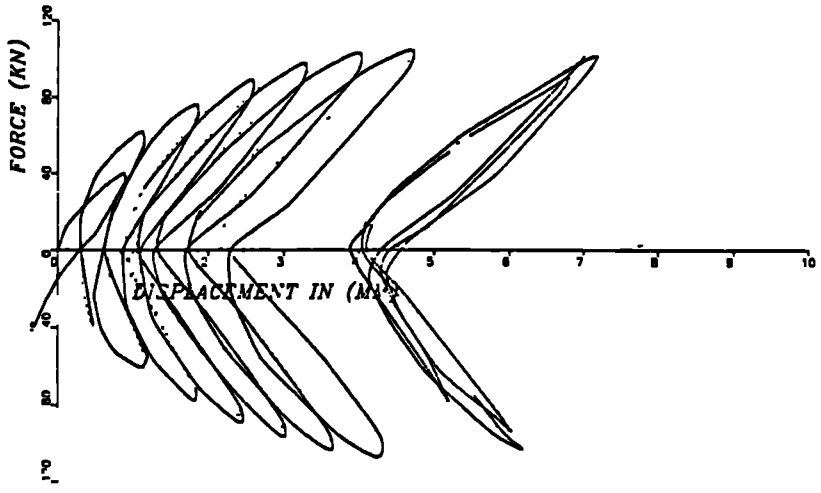


Figure A.(6).13 Load versus wall SW6 top wall average vertical displacement

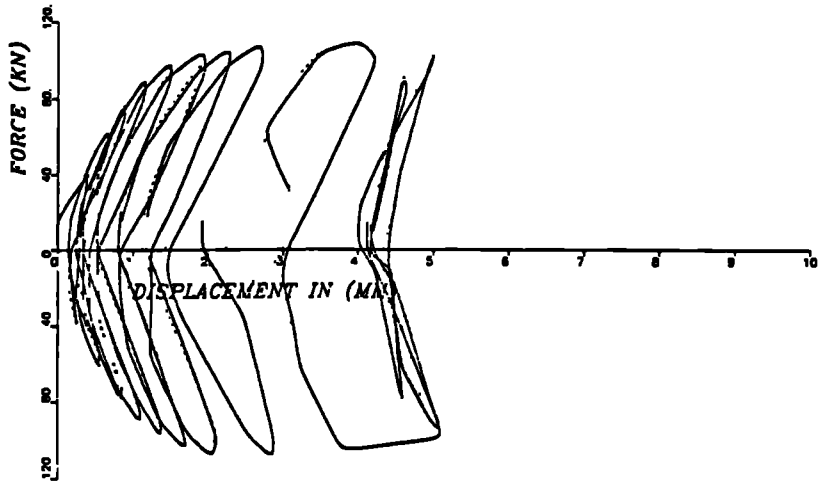


Figure A.(6).14 Load versus wall SW6 mid heigth average vertical displacement

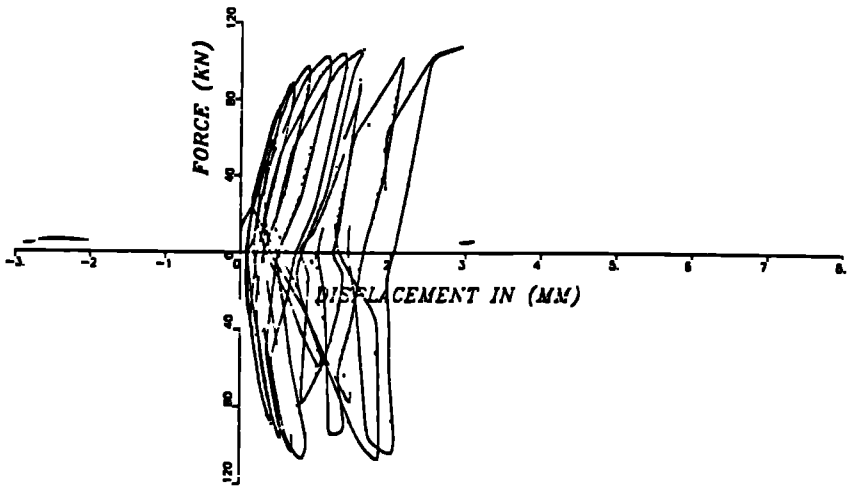
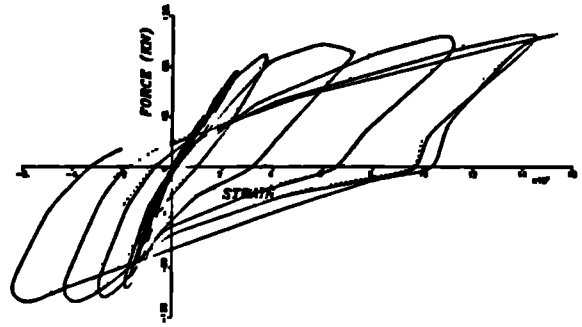


Figure A.(6).15 Load versus wall SW6 quarter heigth average vertical displacement

A.(6) Strain gauge results - Scale 1:2.5 model SW6



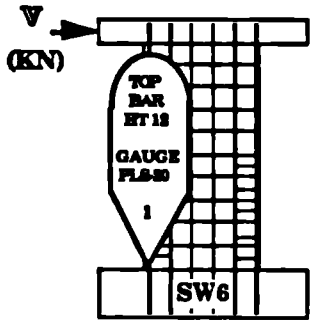
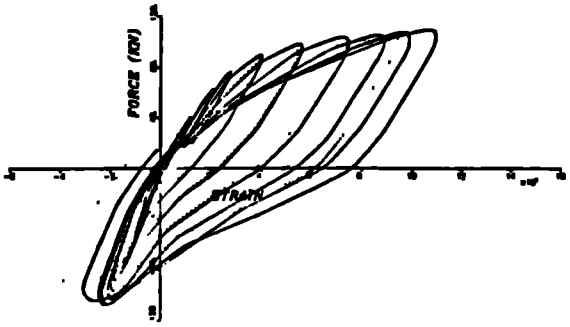


Figure A.(6).16 Load versus strain 1



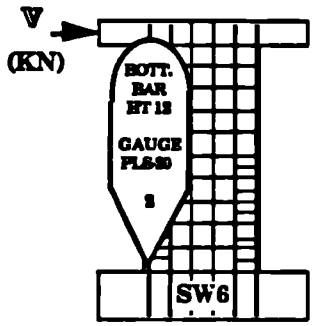
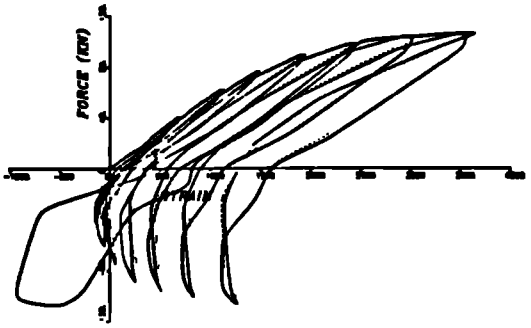


Figure A.(6).17 Load versus strain 2



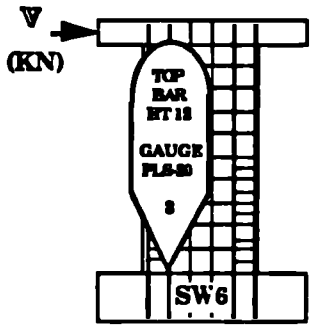
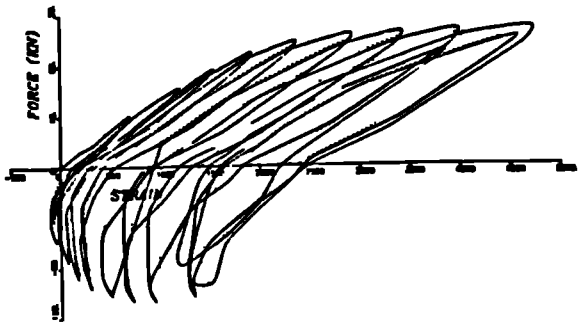


Figure A.(6).18 Load versus strain 3



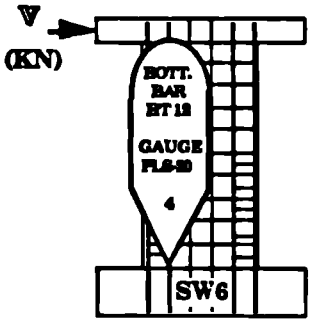
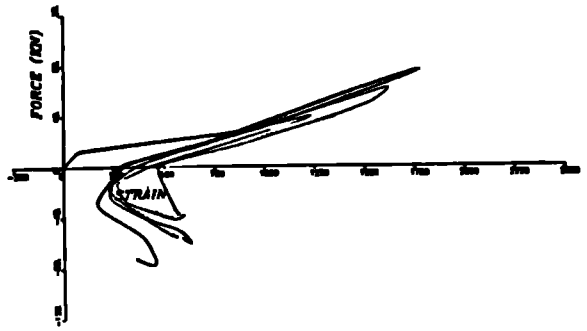


Figure A.(6).19 Load versus strain 4



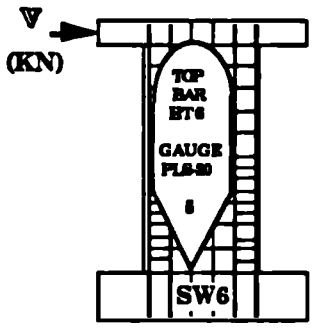
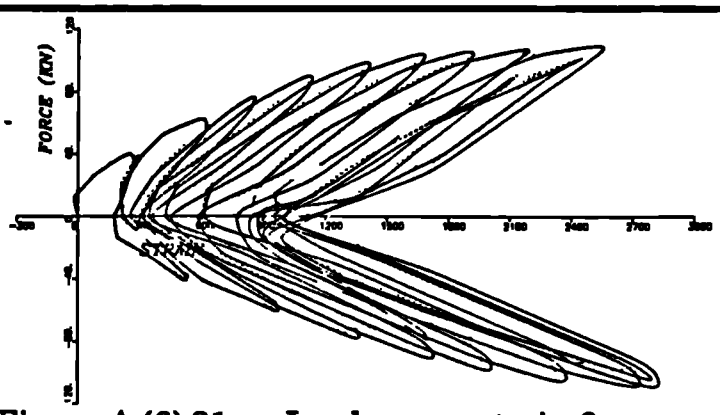


Figure A.(6).20 Load versus strain 5



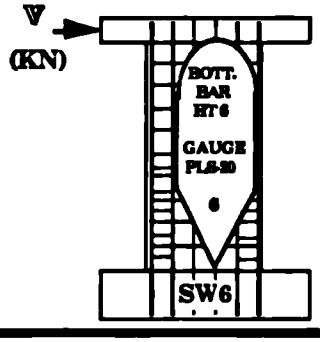
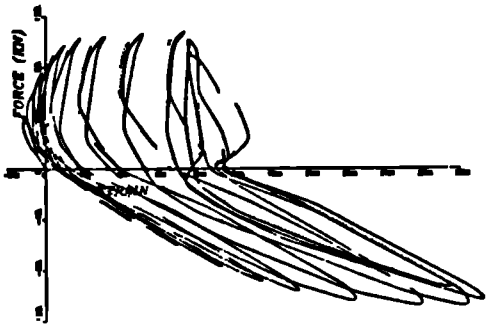


Figure A.(6).21 Load versus strain 6



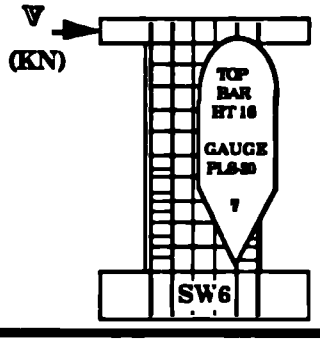
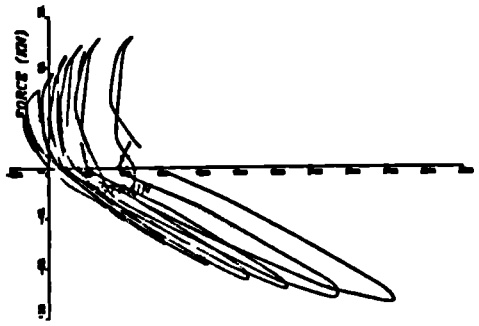


Figure A.(6).22 Load versus strain 7



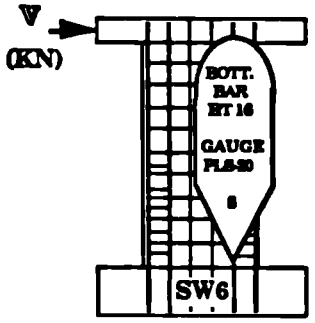
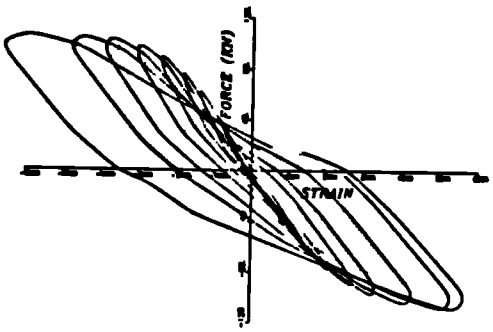


Figure A.(6).23 Load versus strain 8



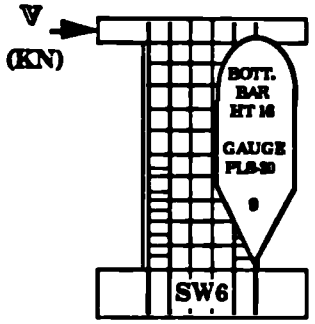
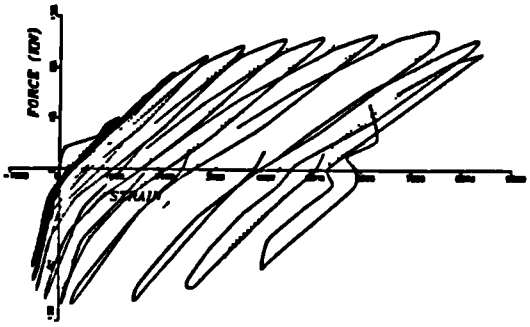


Figure A.(6).24 Load versus strain 9



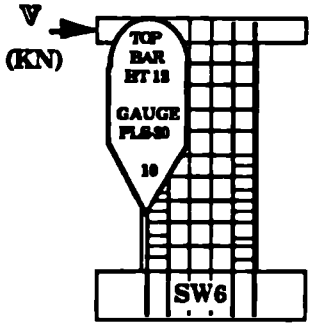
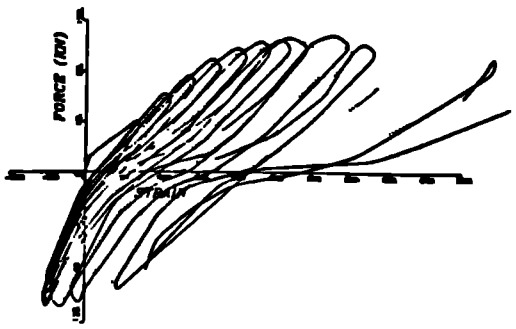


Figure A.(6).25 Load versus strain 10



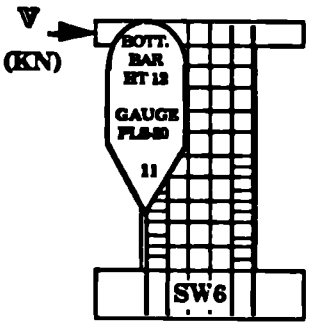
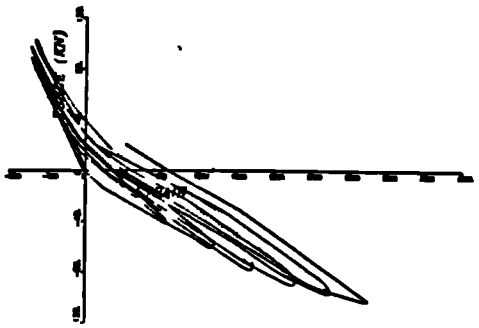


Figure A.(6).26 Load versus strain 11



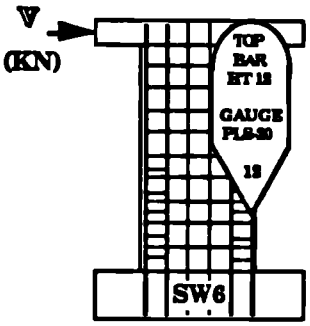
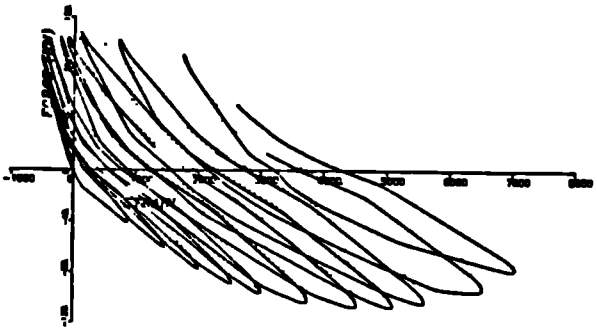


Figure A.(6).27 Load versus strain 12



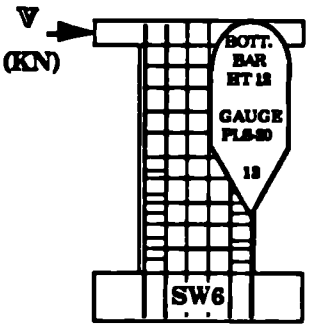
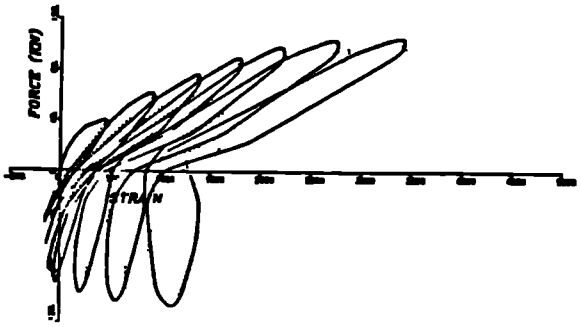


Figure A.(6).28 Load versus strain 13



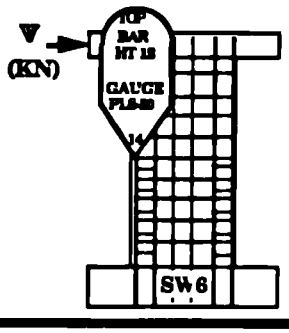


Figure A.(6).29 Load versus strain 14

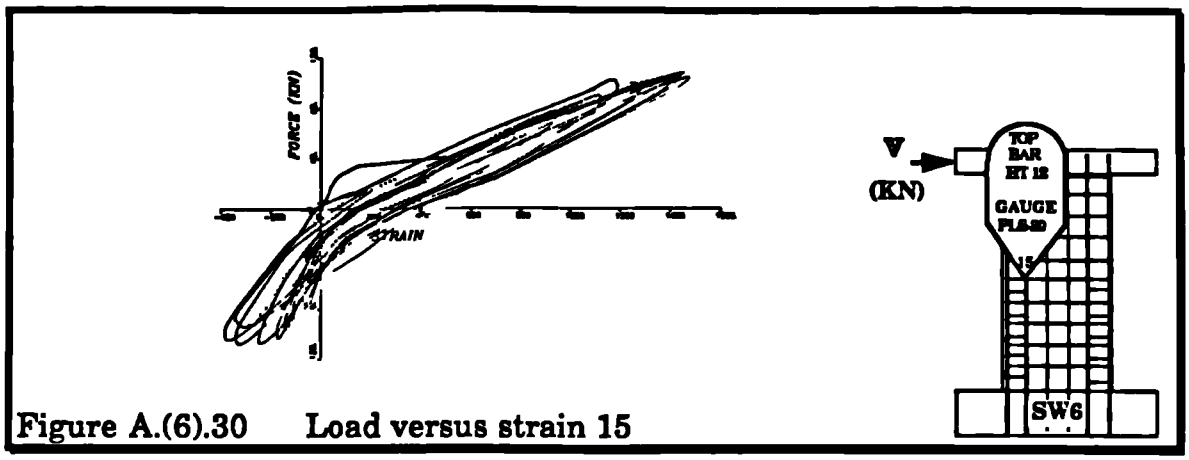


Figure A.(6).30 Load versus strain 15

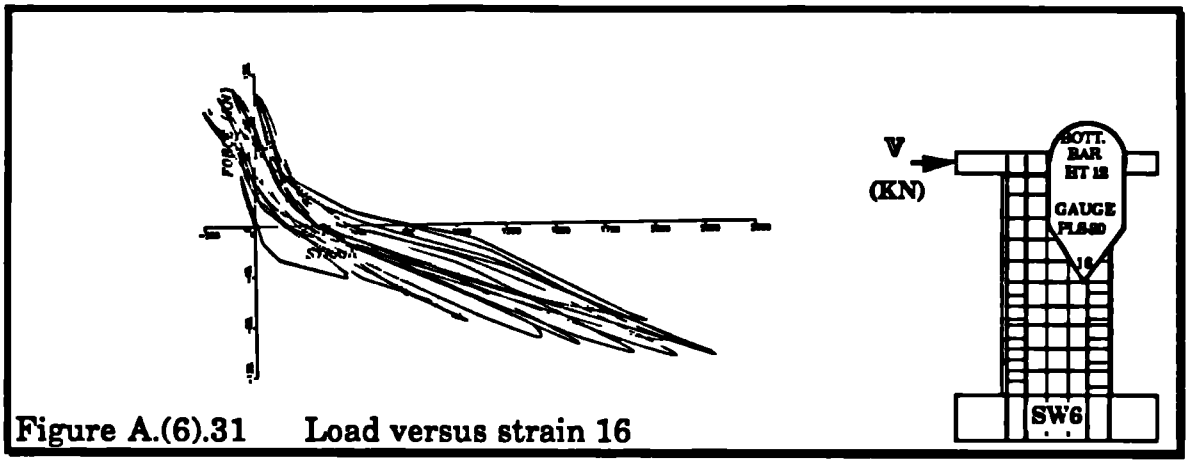


Figure A.(6).31 Load versus strain 16

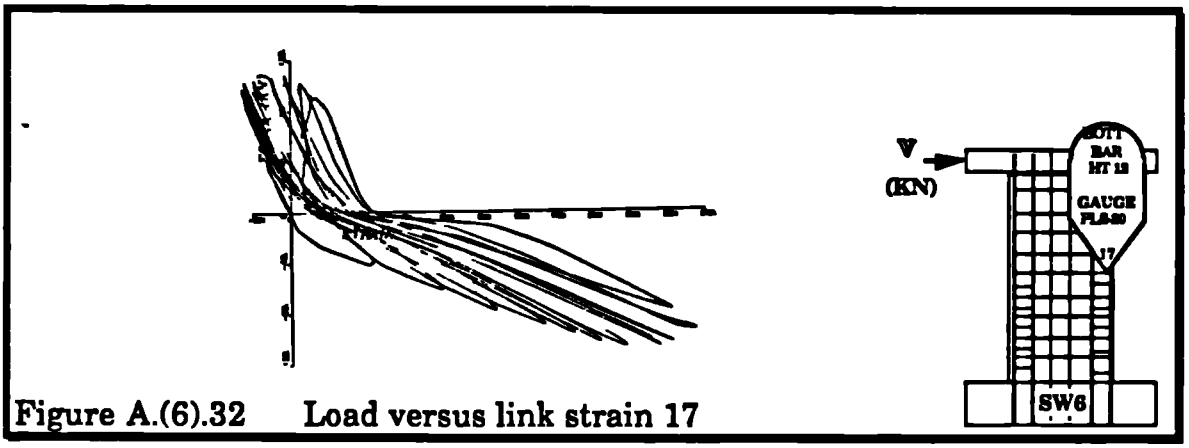


Figure A.(6).32 Load versus link strain 17

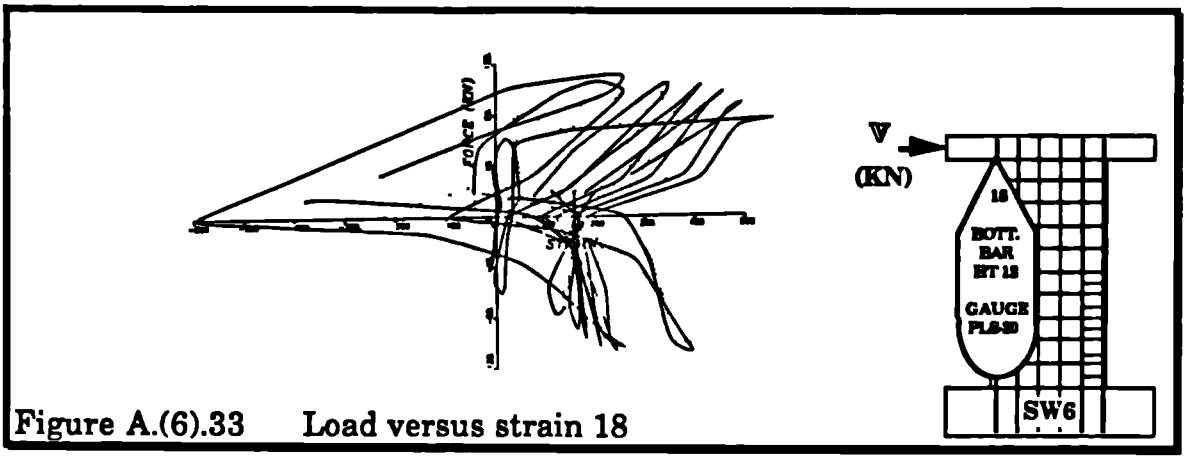
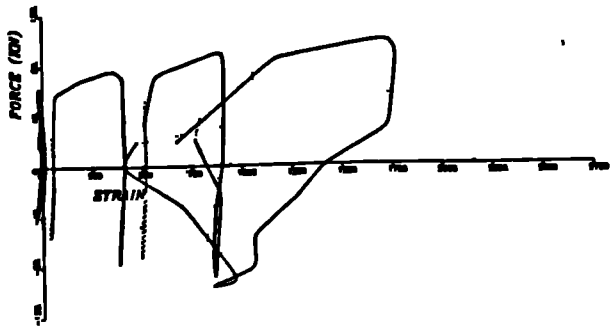


Figure A.(6).33 Load versus strain 18



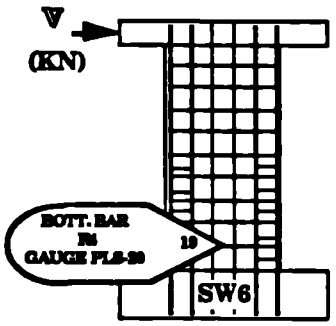
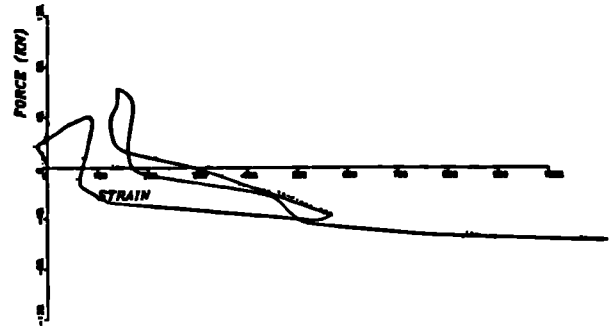


Figure A.(6).34 Load versus strain 19



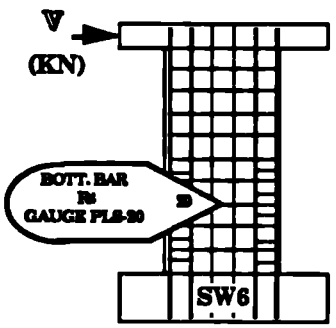
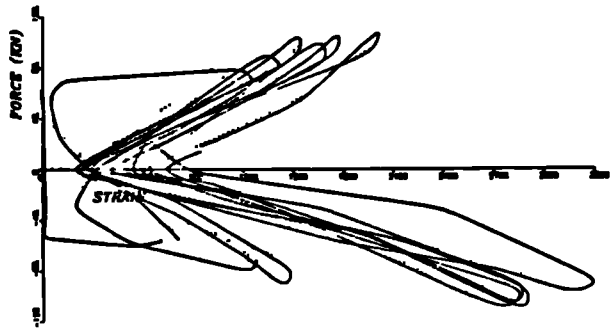


Figure A.(6).35 Load versus strain 20



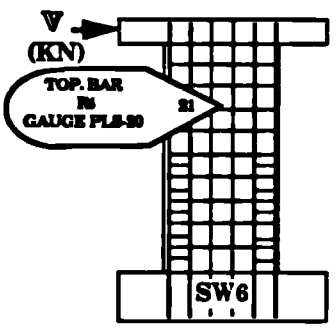
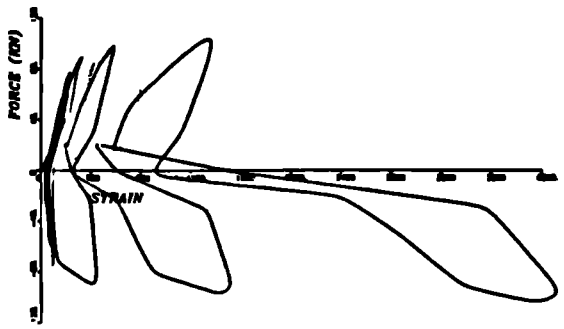


Figure A.(6).36 Load versus strain 21



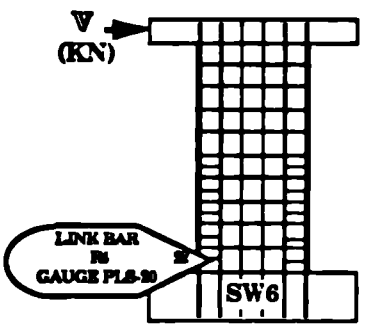


Figure A.(6).37 Load versus strain 22

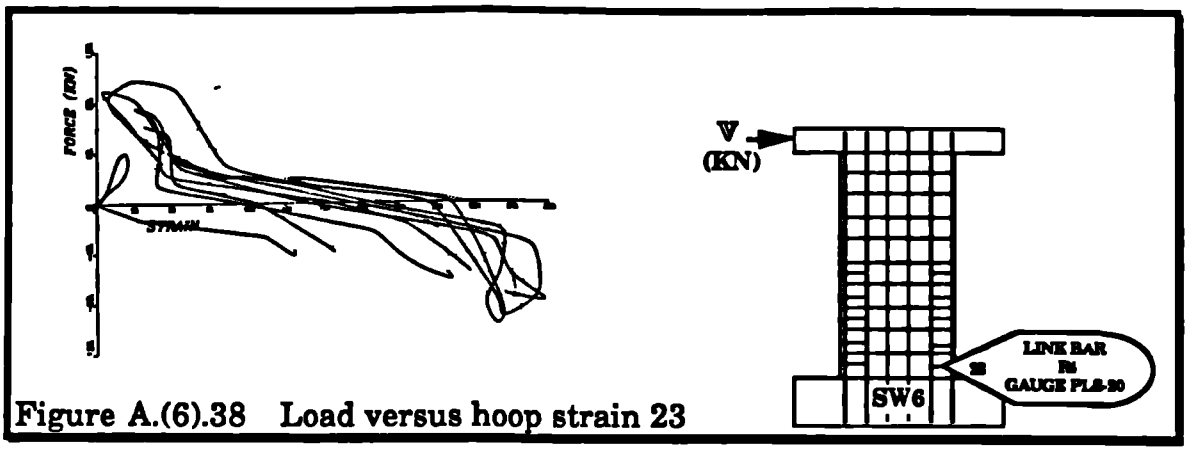


Figure A.(6).38 Load versus hoop strain 23

A.(7) Load-displacement curves - Scale 1:2.5 model SW7

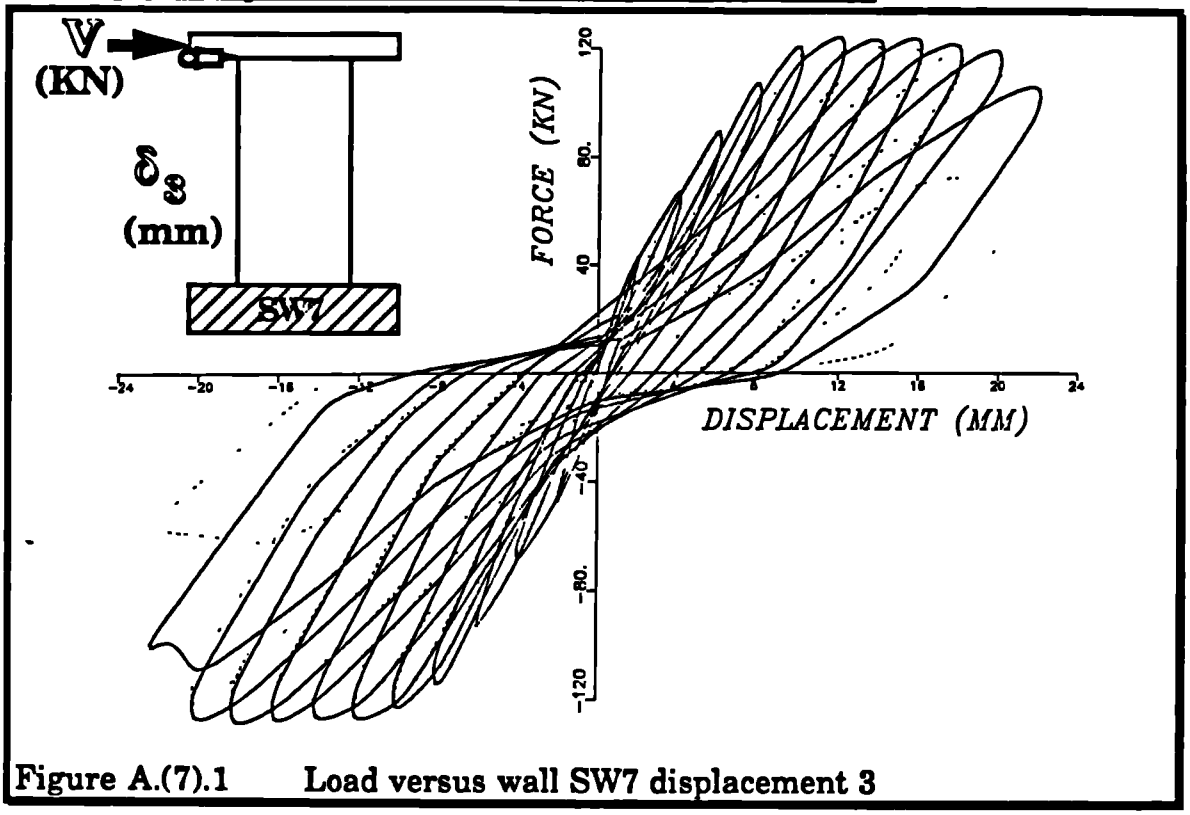


Figure A.(7).1 Load versus wall SW7 displacement 3

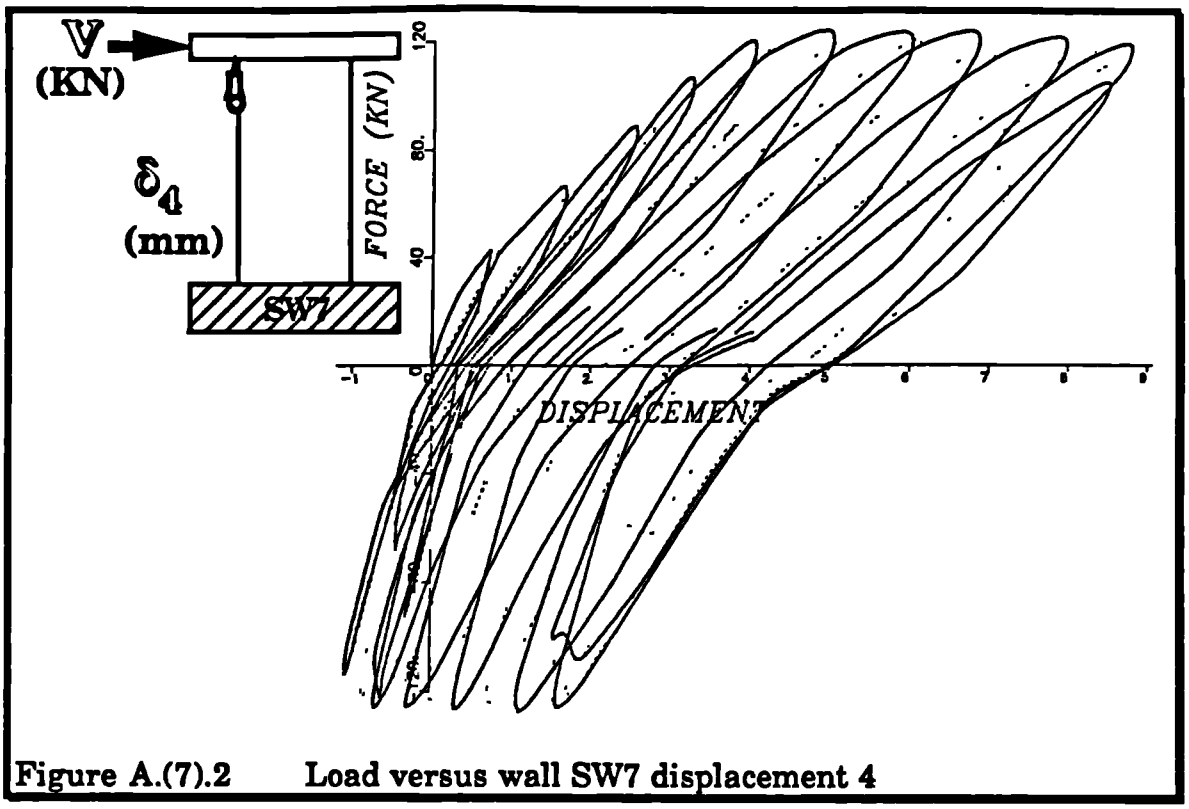


Figure A.(7).2 Load versus wall SW7 displacement 4

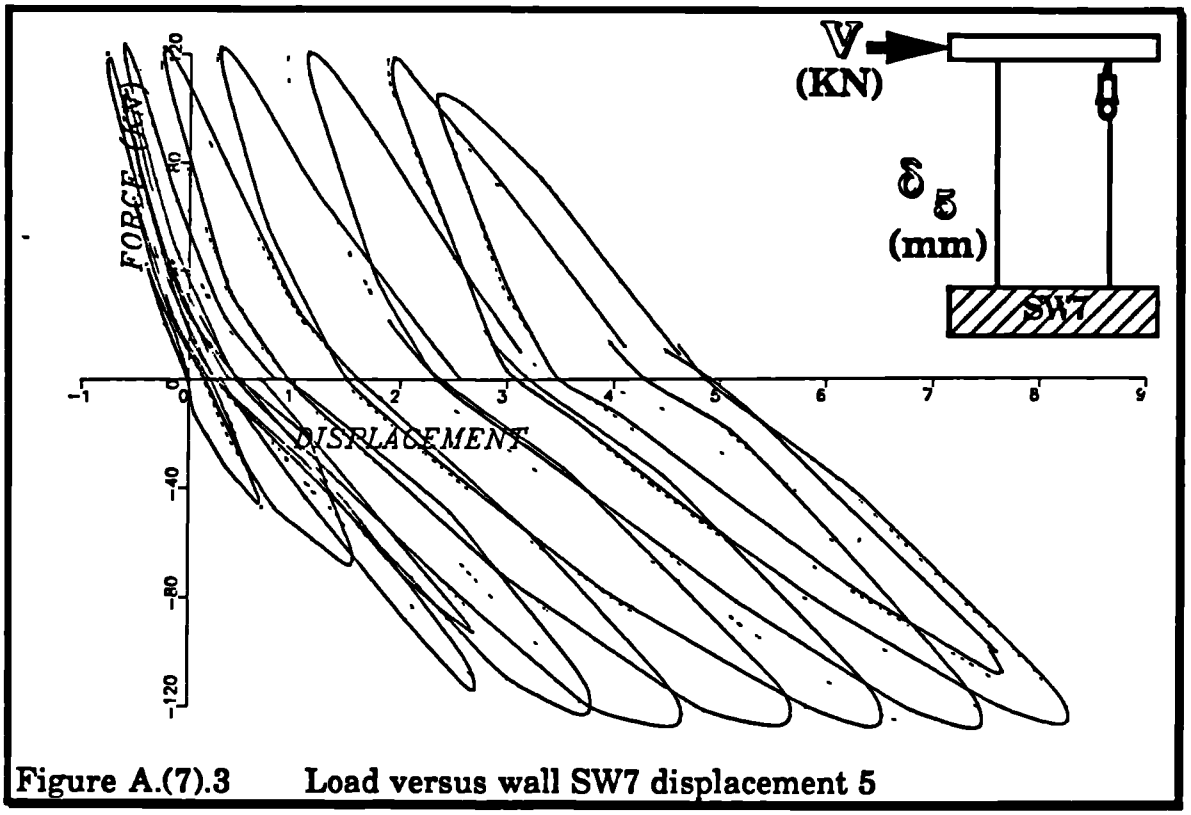


Figure A.(7).3 Load versus wall SW7 displacement 5

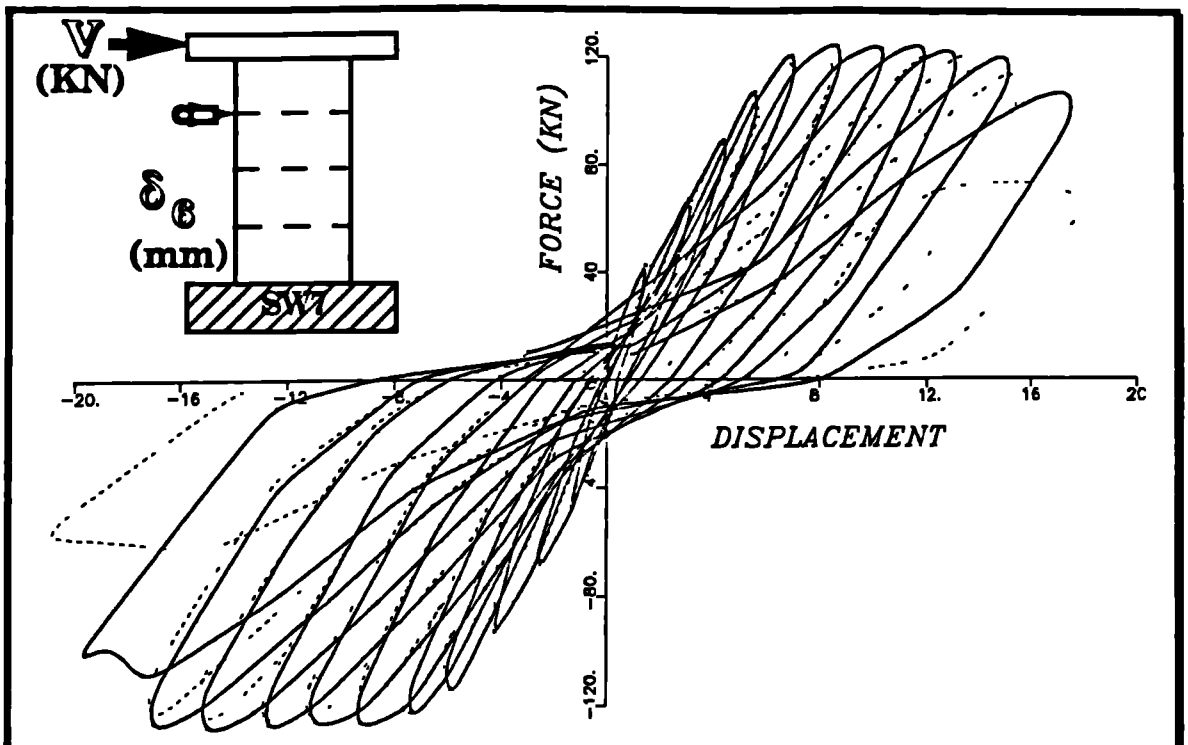


Figure A.(7).4 Load versus wall SW7 displacement 6

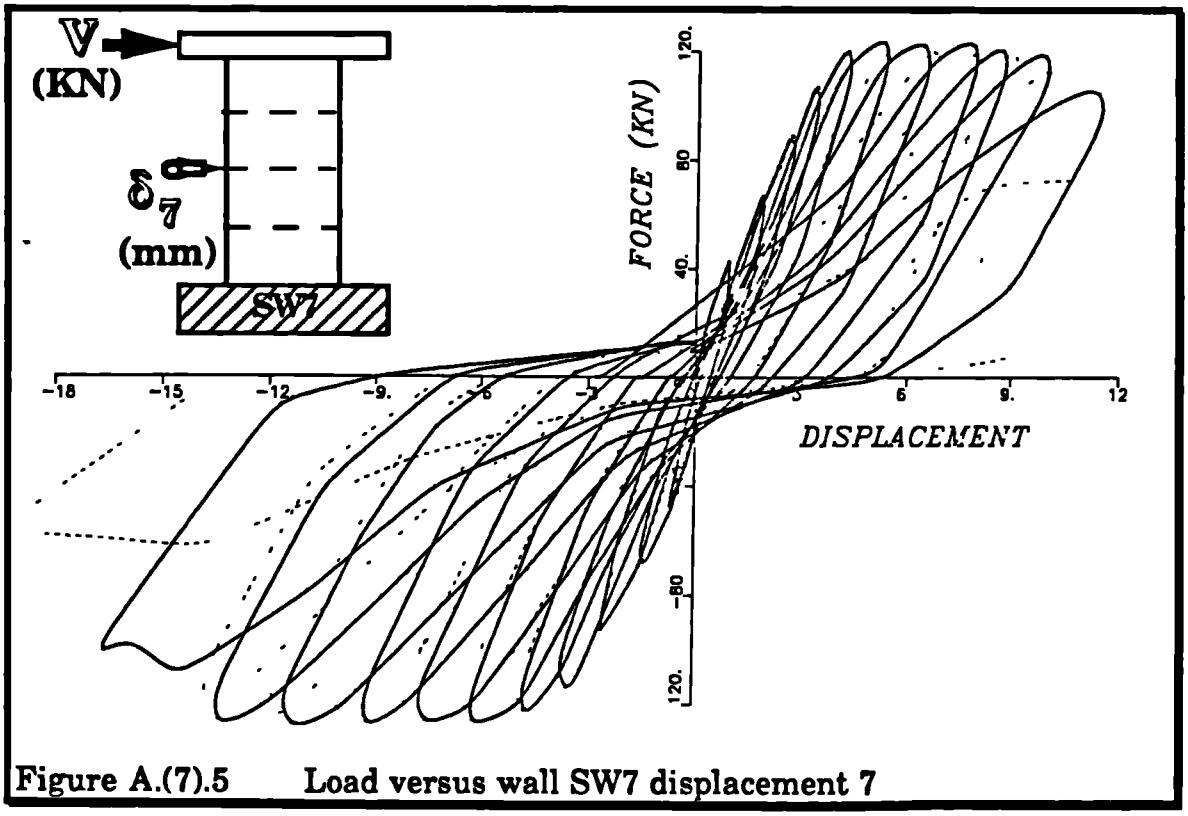


Figure A.(7).5 Load versus wall SW7 displacement 7

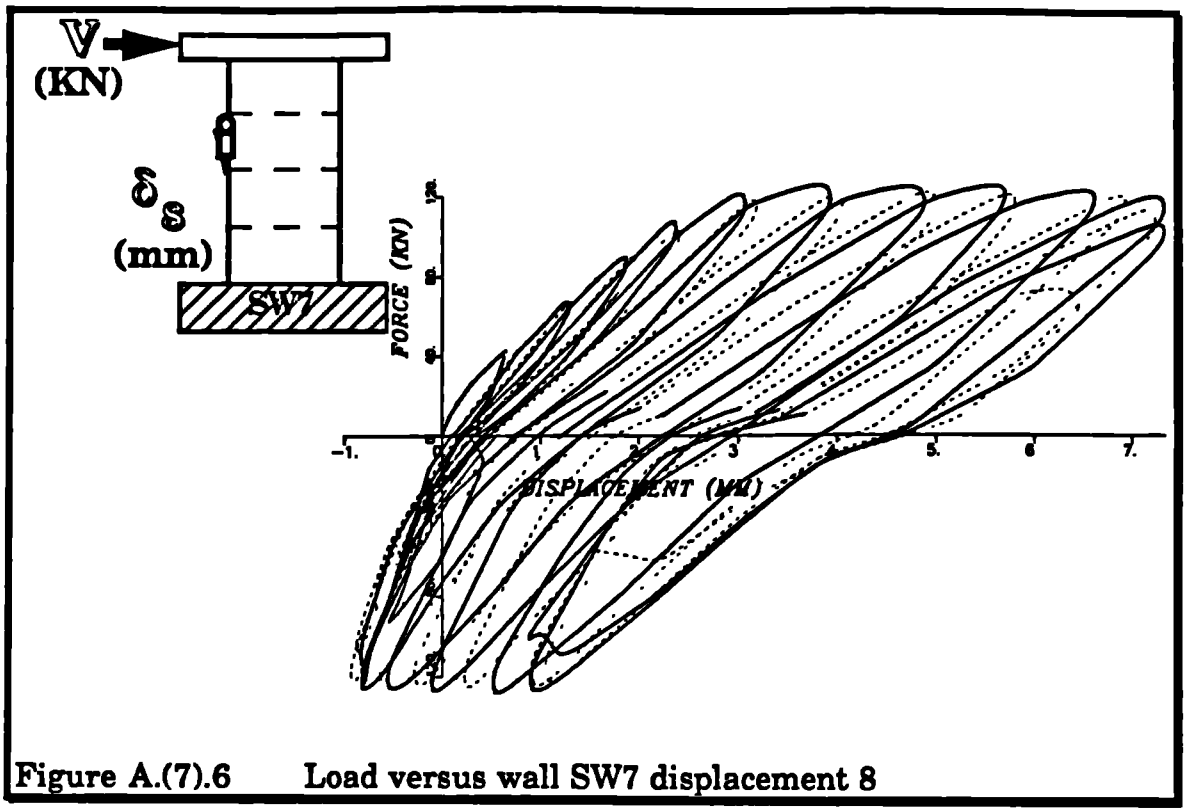


Figure A.(7).6 Load versus wall SW7 displacement 8

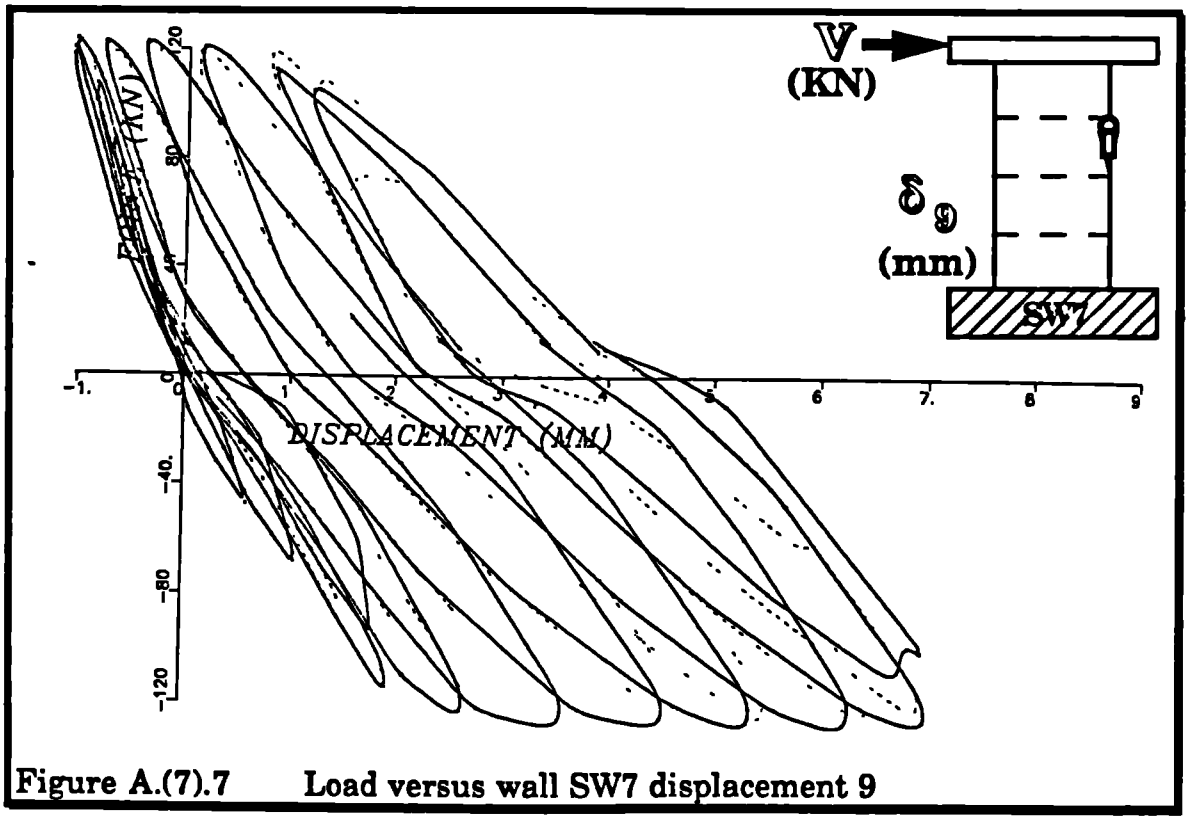


Figure A.(7).7 Load versus wall SW7 displacement 9

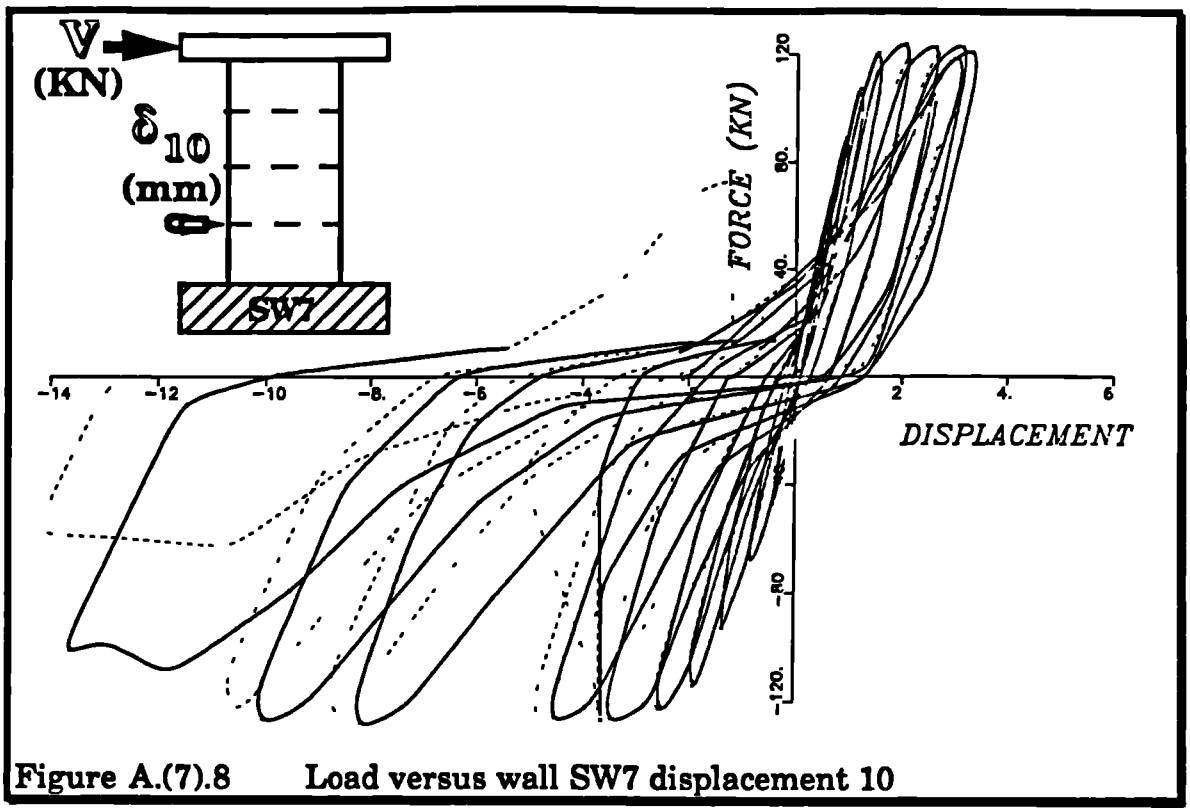


Figure A.(7).8 Load versus wall SW7 displacement 10

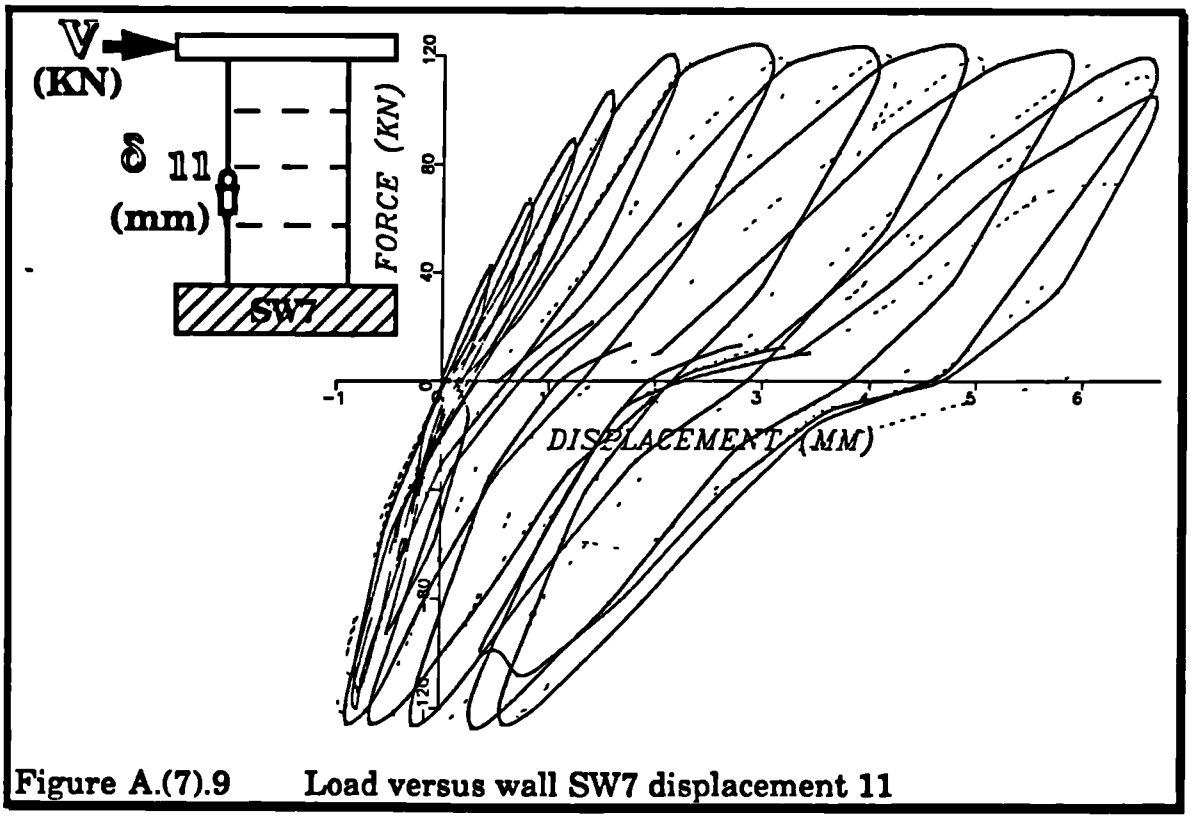


Figure A.(7).9 Load versus wall SW7 displacement 11

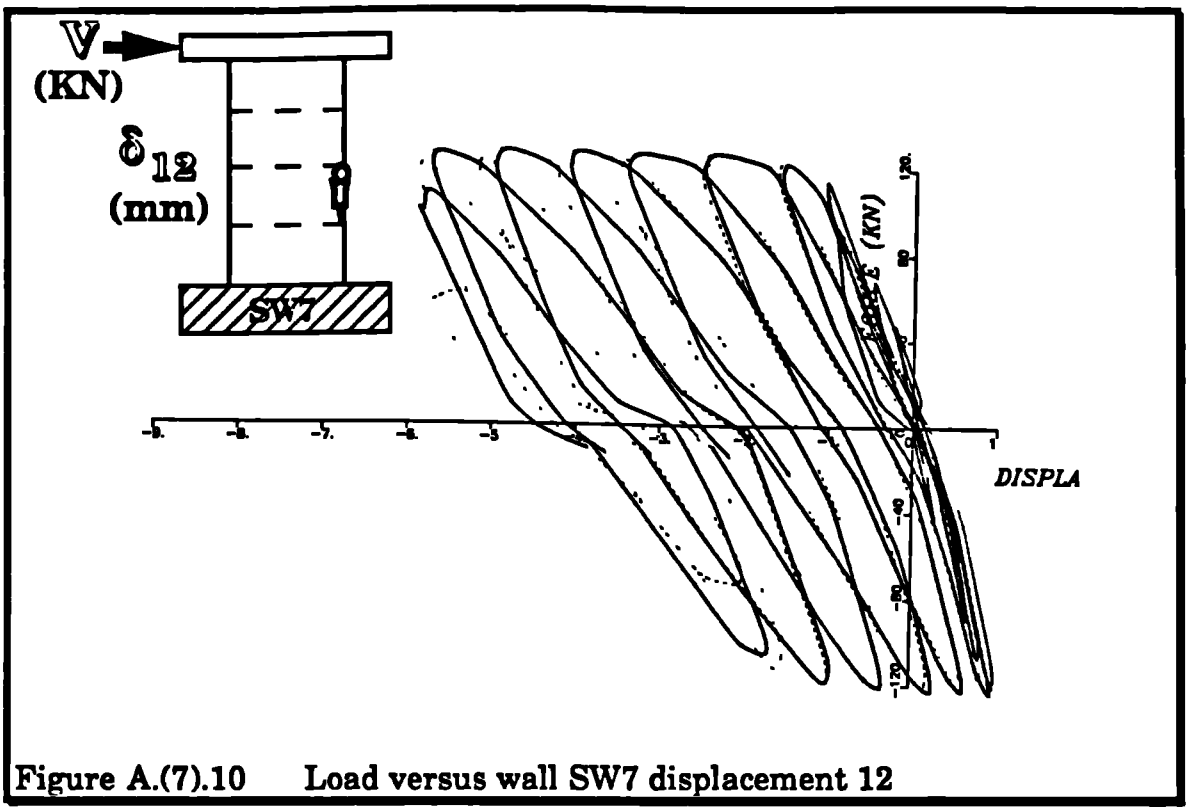


Figure A.(7).10 Load versus wall SW7 displacement 12

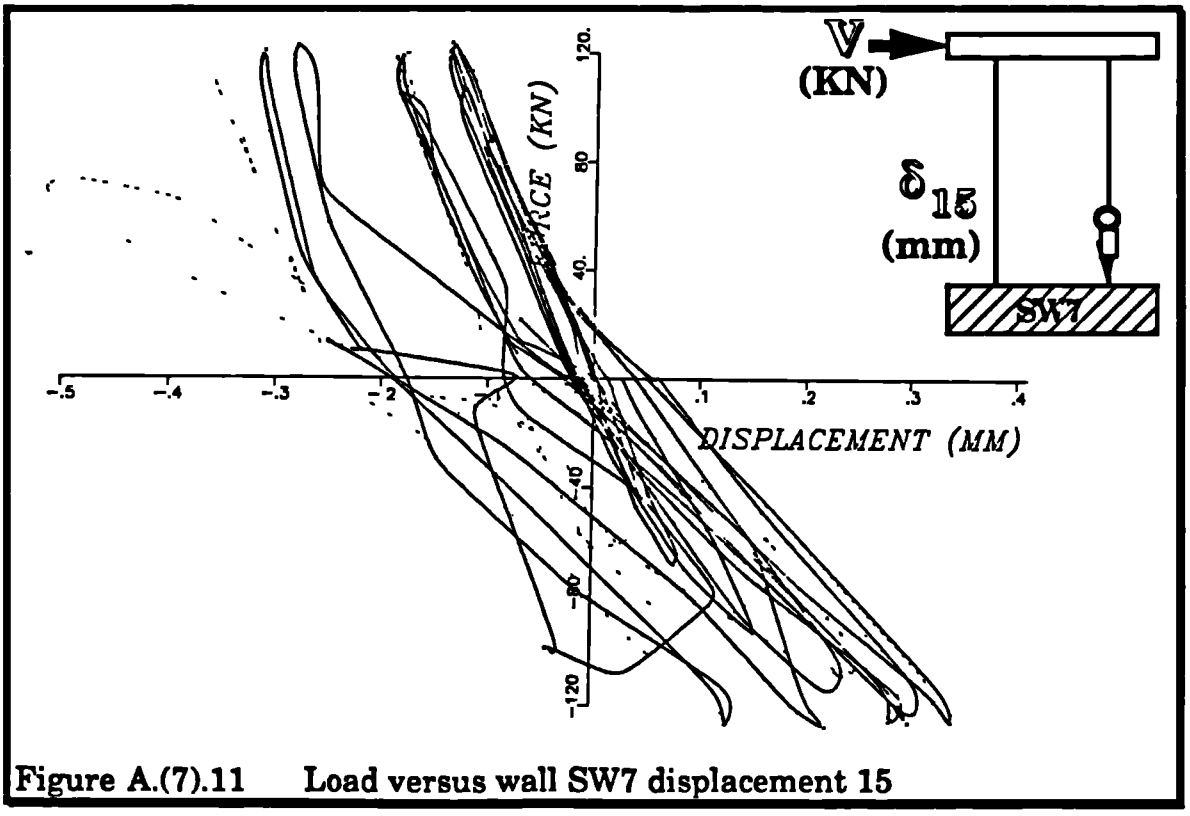


Figure A.(7).11 Load versus wall SW7 displacement 15



Figure A.(7).12 Load versus wall SW7 displacement 16

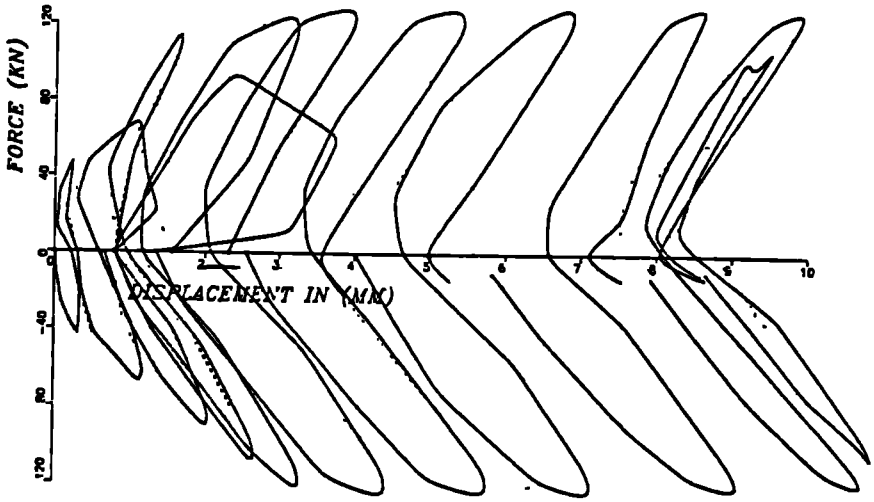


Figure A.(7).13 Load versus wall SW7 top wall average vertical displacement

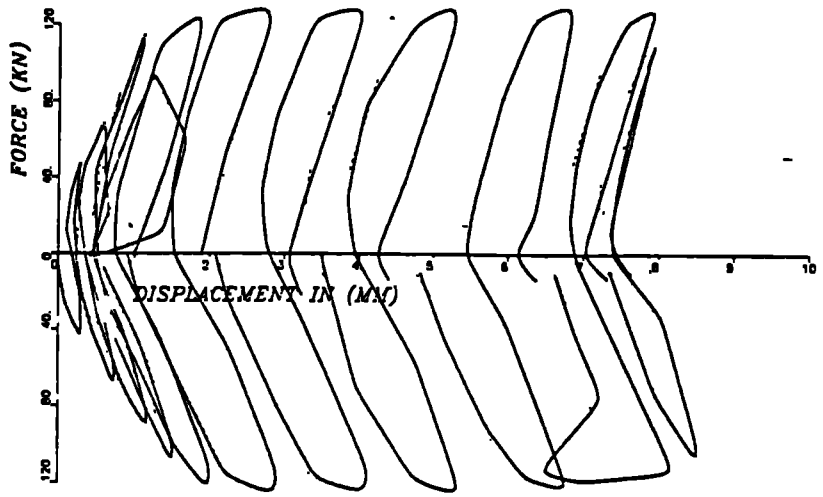


Figure A.(7).14 Load versus wall SW7 mid heigth average vertical displacement

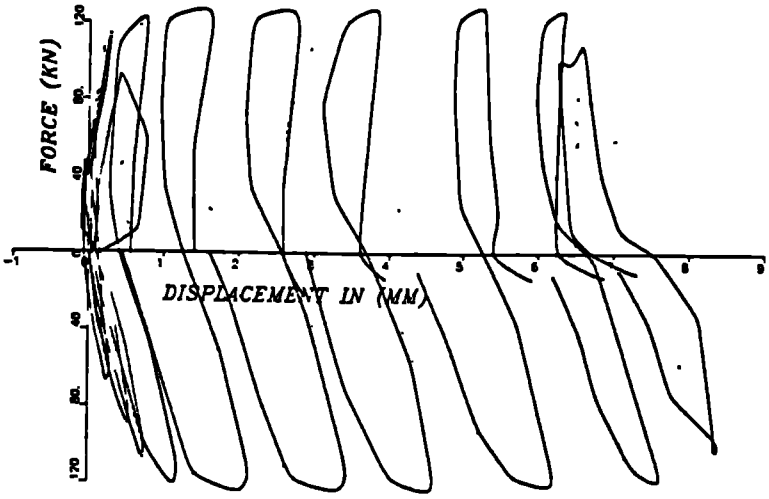
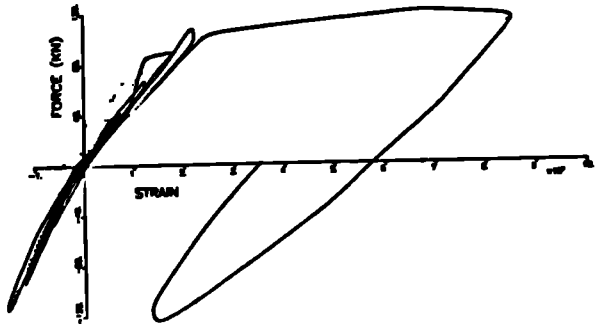


Figure A.(7).15 Load versus wall SW7 quarter heigth average vertical displacement

A.(7) Strain gauge results - Scale 1:2.5 model SW7



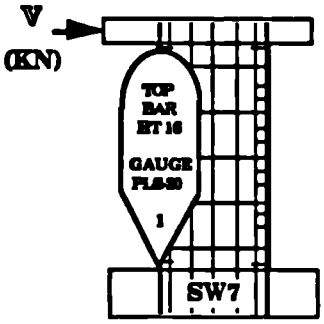
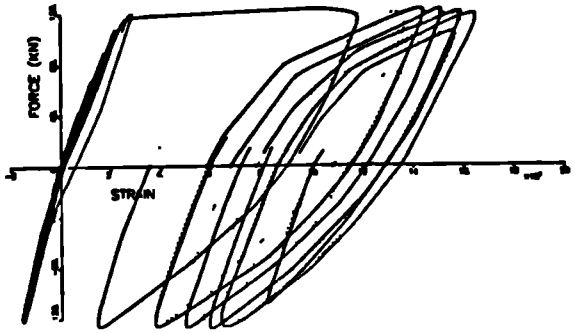


Figure A.(7).16 Load versus strain 1



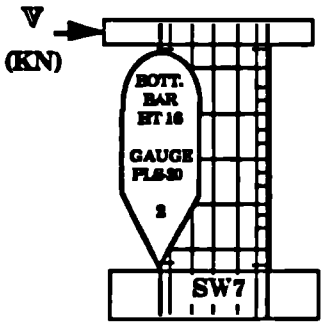
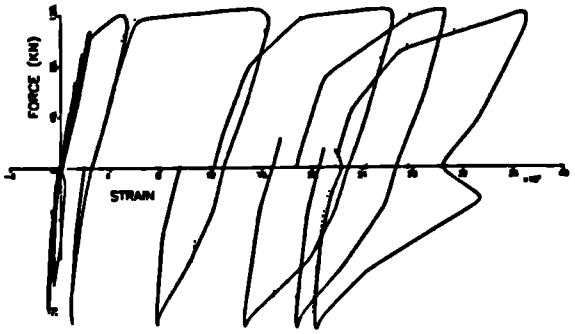


Figure A.(7).17 Load versus strain 2



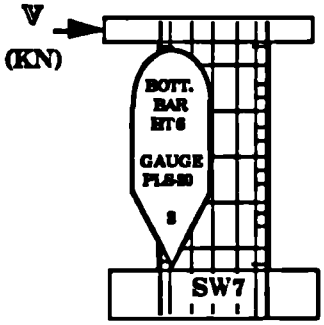
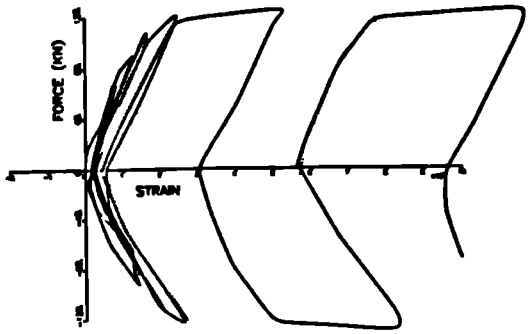


Figure A.(7).18 Load versus strain 3



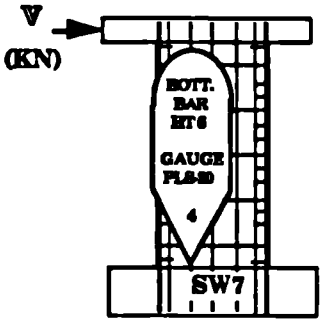
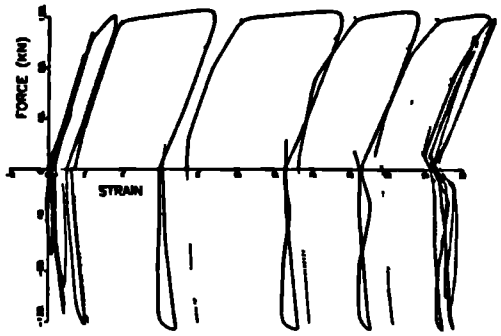


Figure A.(7).19 Load versus strain 4



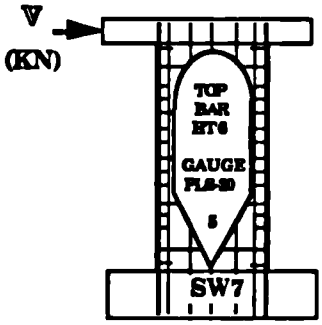
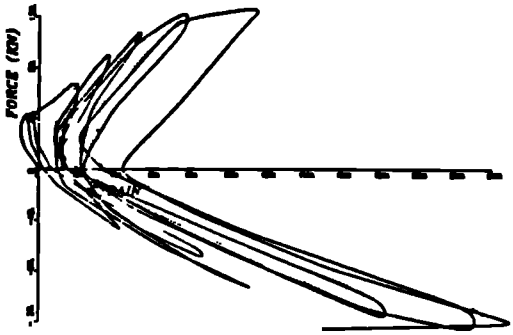


Figure A.(7).20 Load versus strain 5



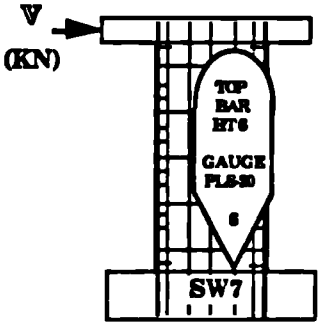
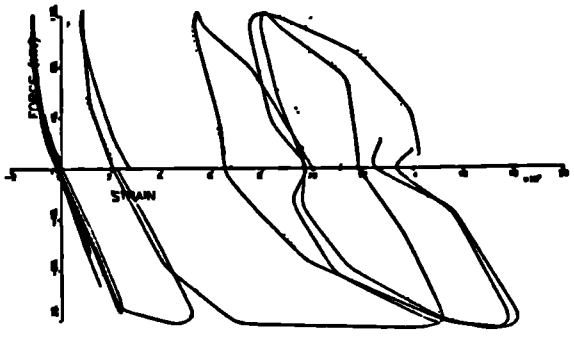


Figure A.(7).21 Load versus strain 6



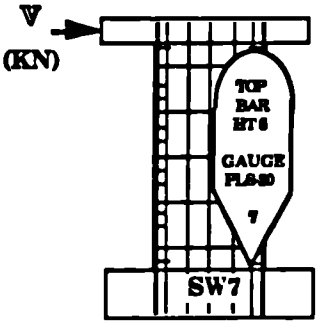


Figure A.(7).22 Load versus strain 7

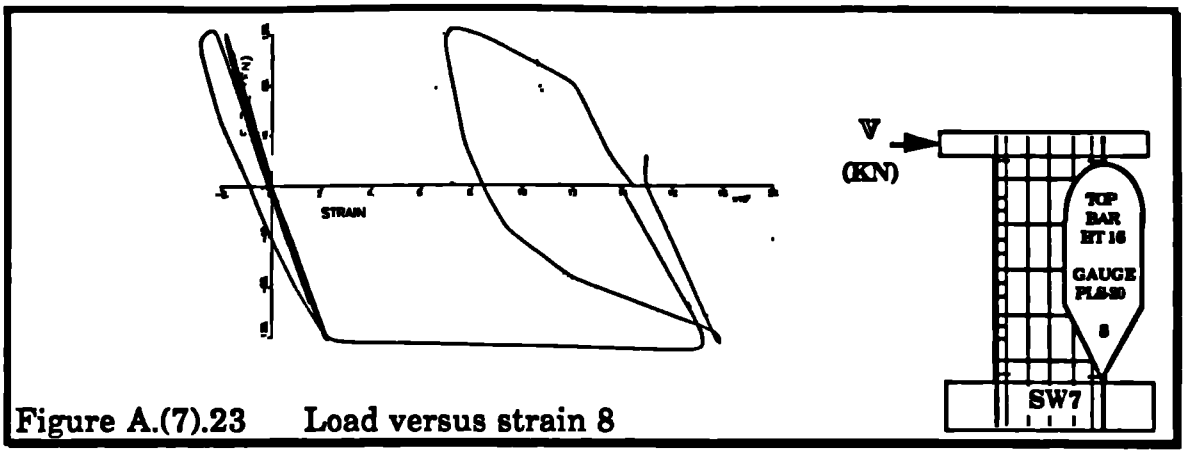


Figure A.(7).23 Load versus strain 8

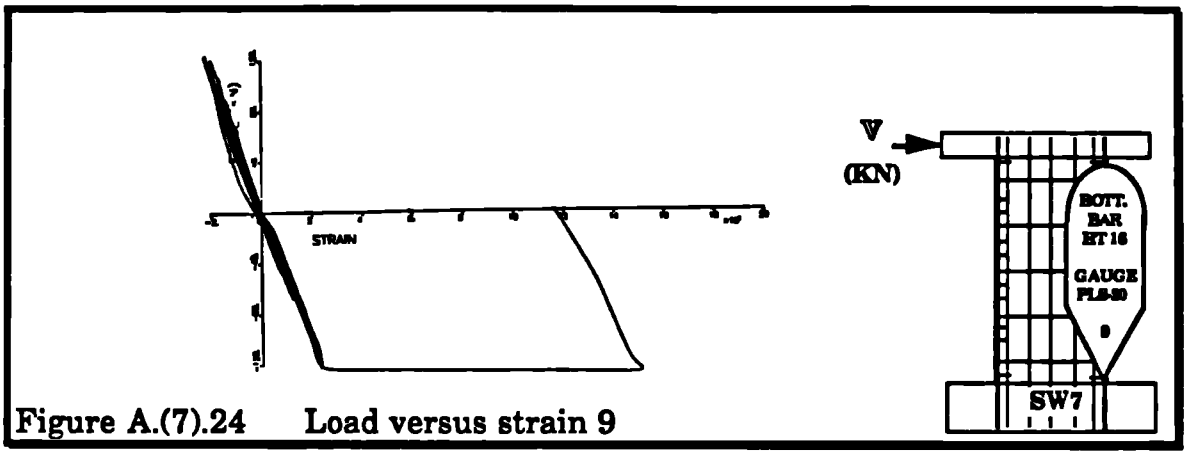


Figure A.(7).24 Load versus strain 9

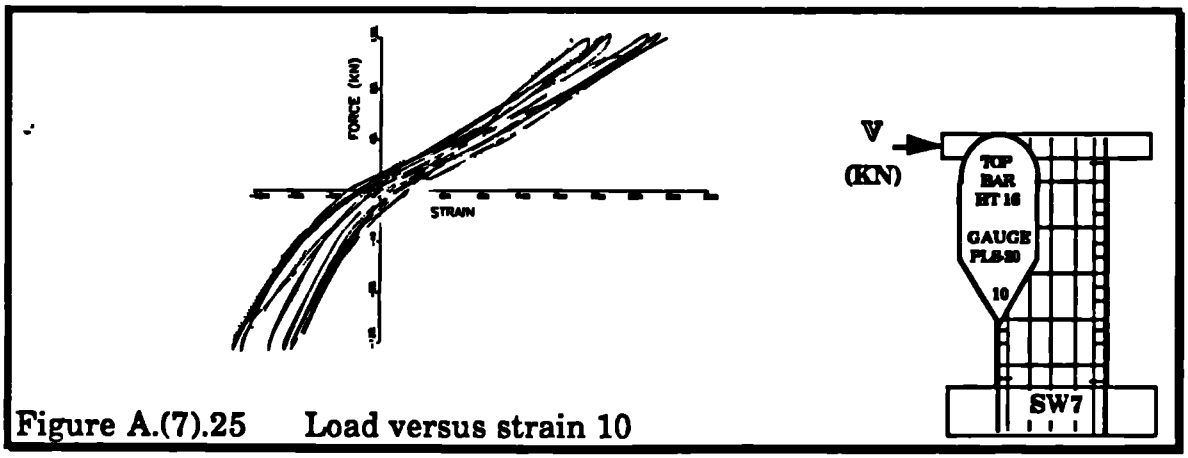


Figure A.(7).25 Load versus strain 10

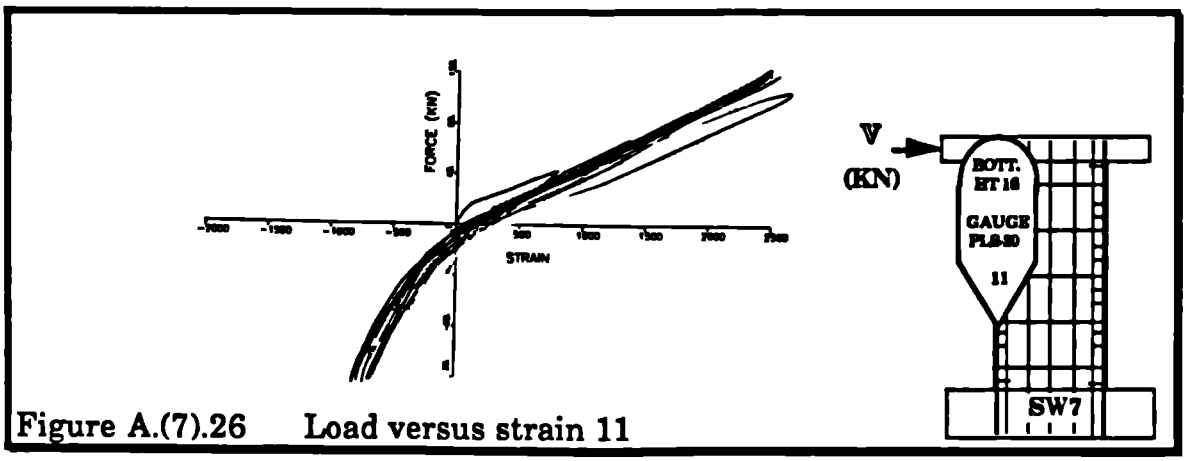


Figure A.(7).26 Load versus strain 11

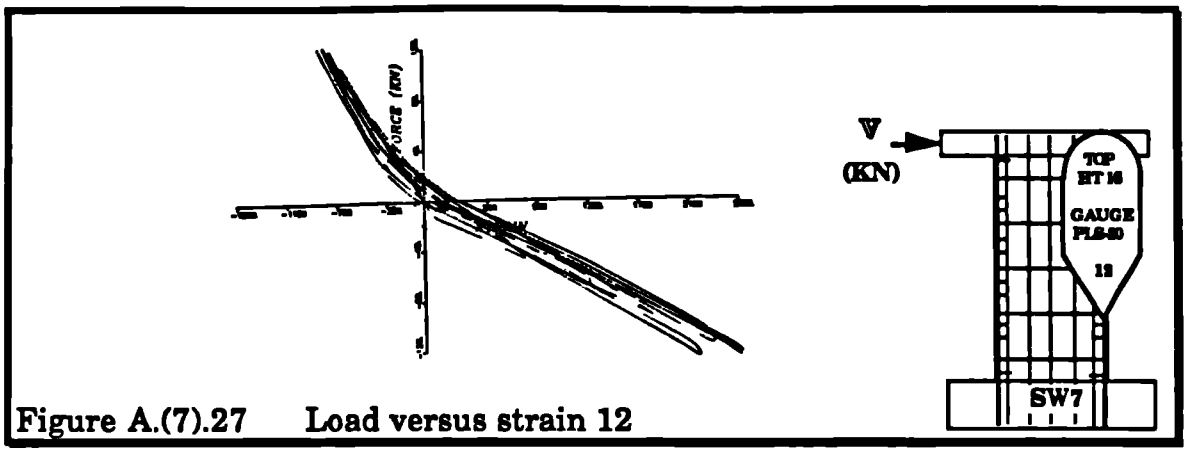


Figure A.(7).27 Load versus strain 12

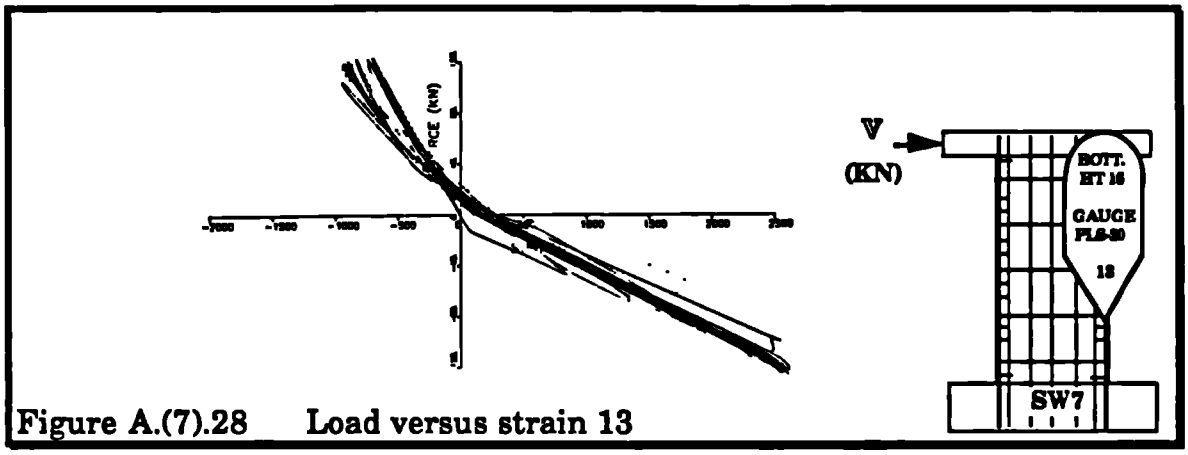


Figure A.(7).28 Load versus strain 13

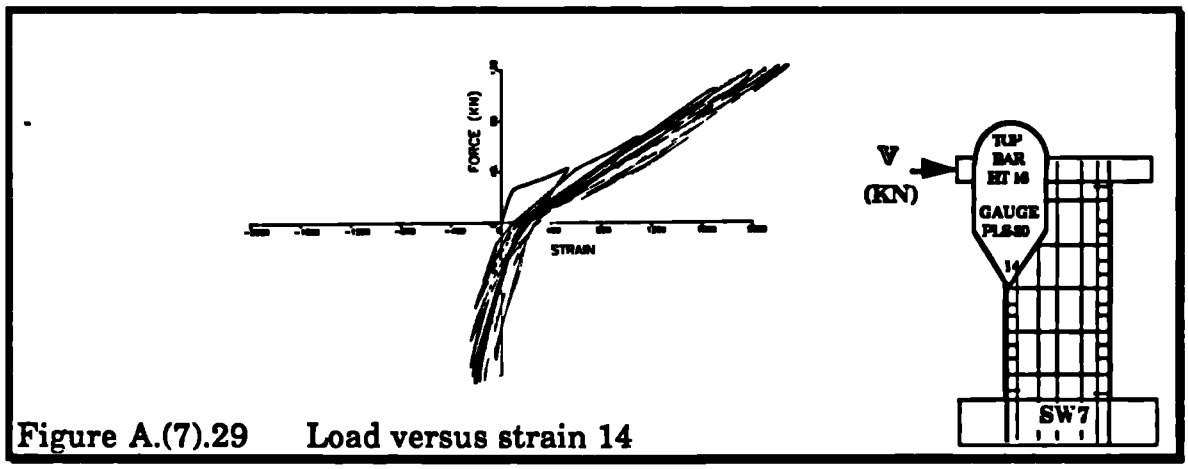


Figure A.(7).29 Load versus strain 14

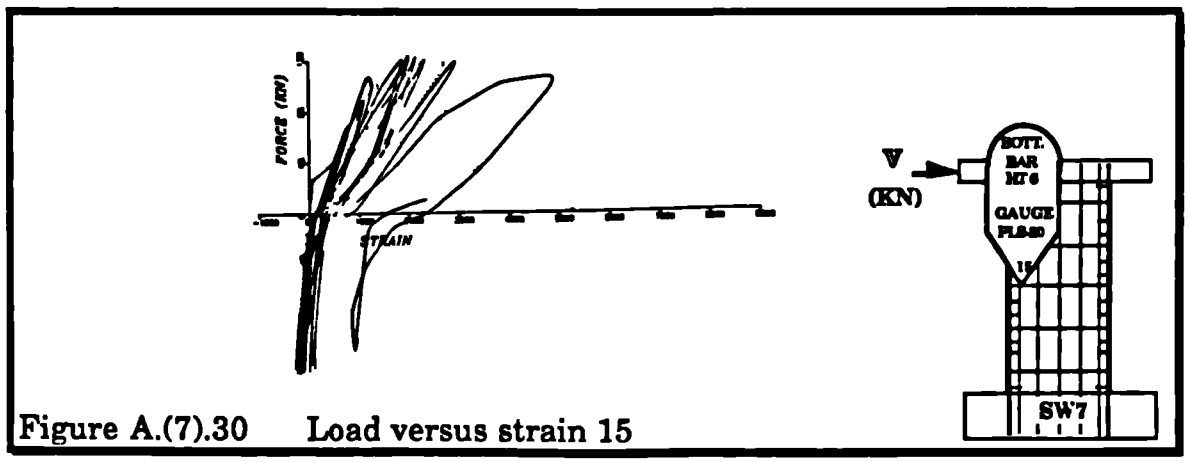


Figure A.(7).30 Load versus strain 15

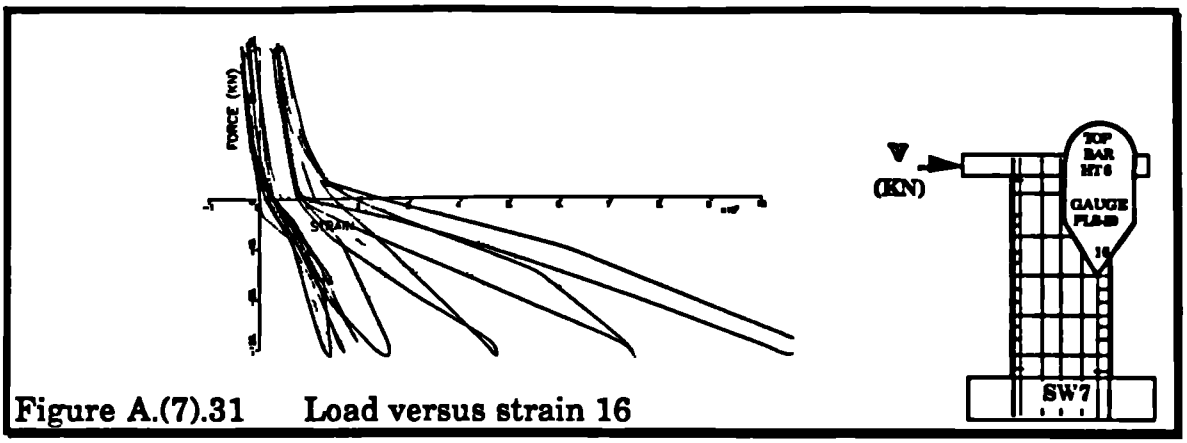


Figure A.(7).31 Load versus strain 16

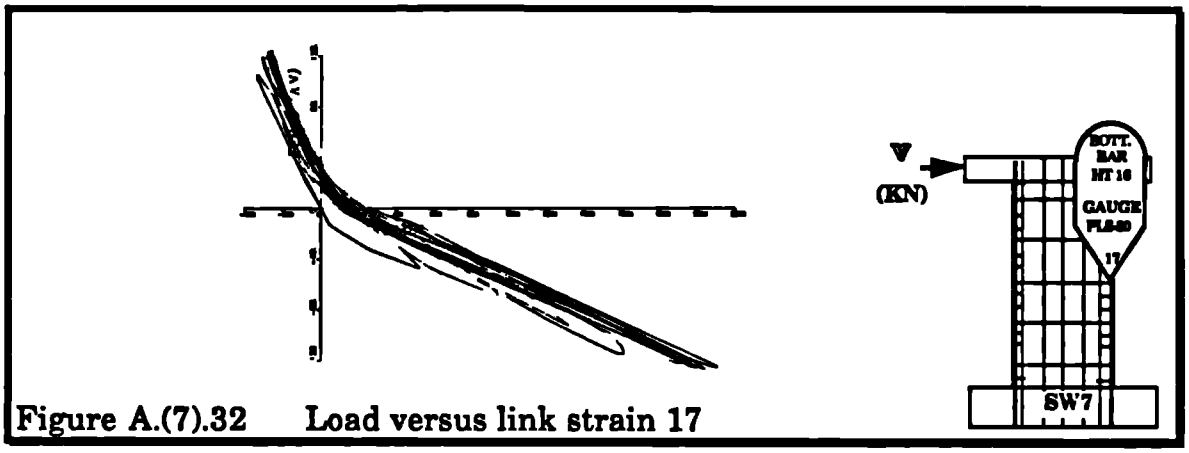


Figure A.(7).32 Load versus link strain 17

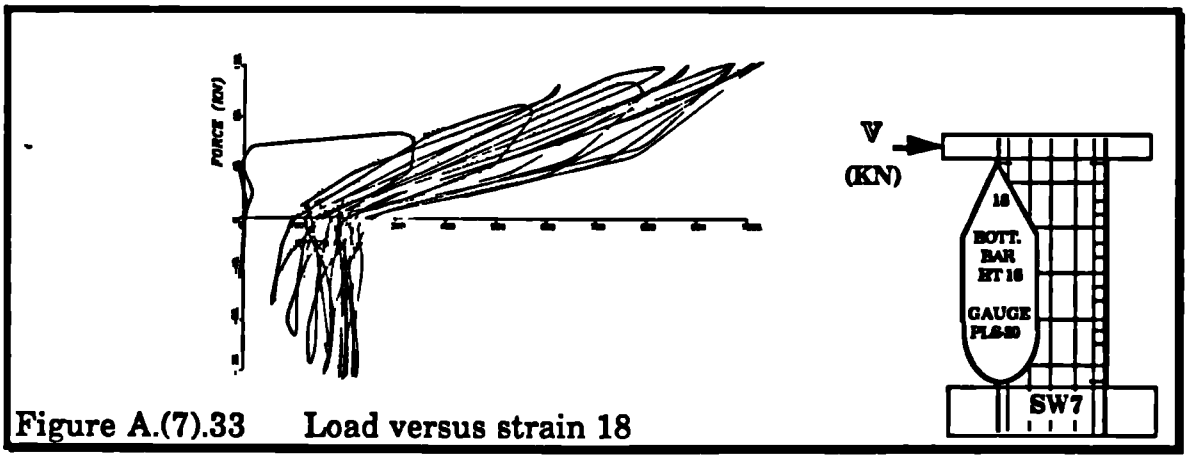


Figure A.(7).33 Load versus strain 18

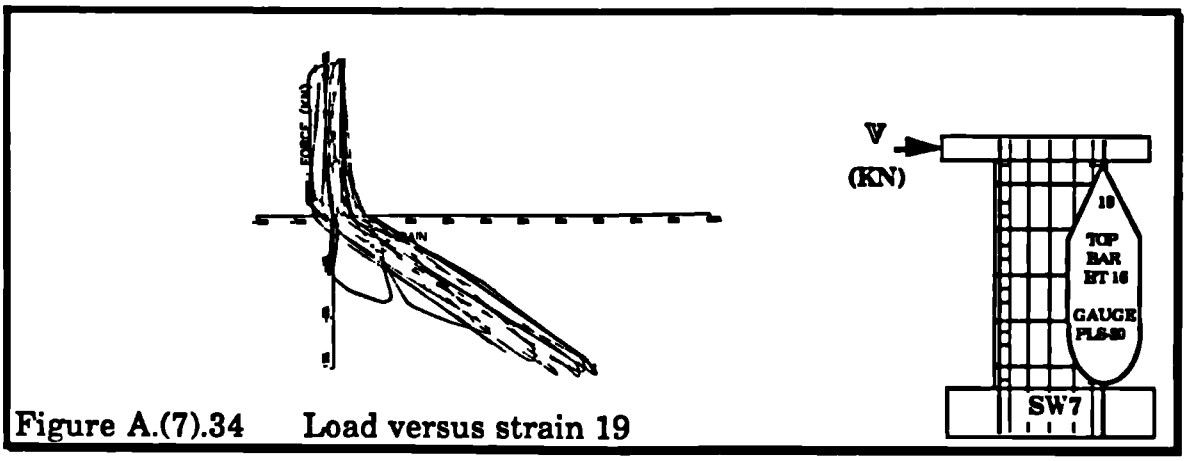


Figure A.(7).34 Load versus strain 19

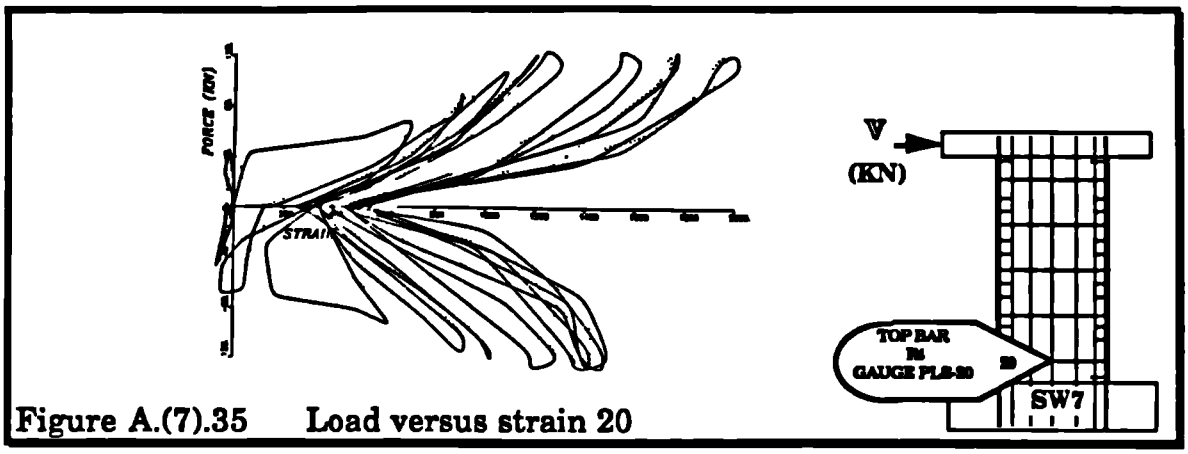


Figure A.(7).35 Load versus strain 20

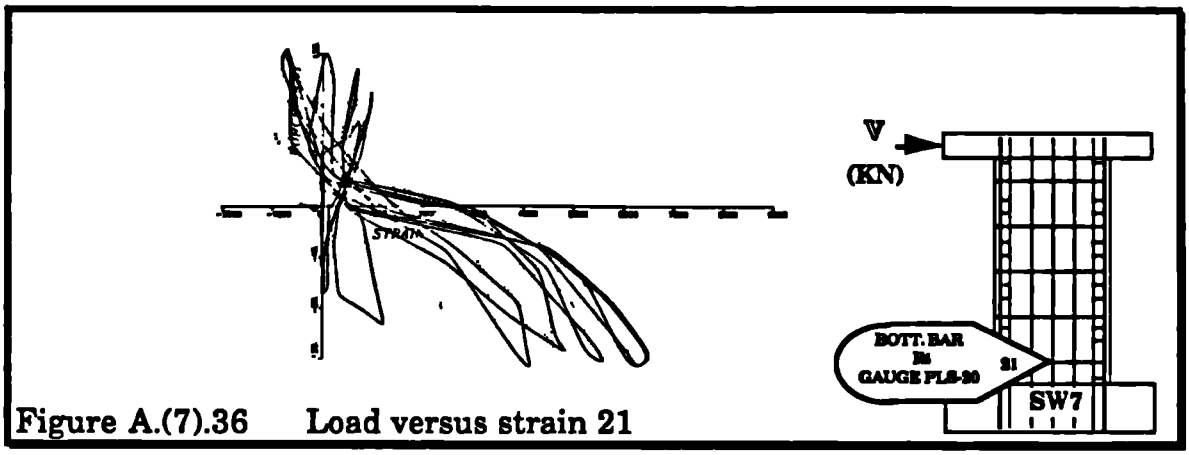


Figure A.(7).36 Load versus strain 21

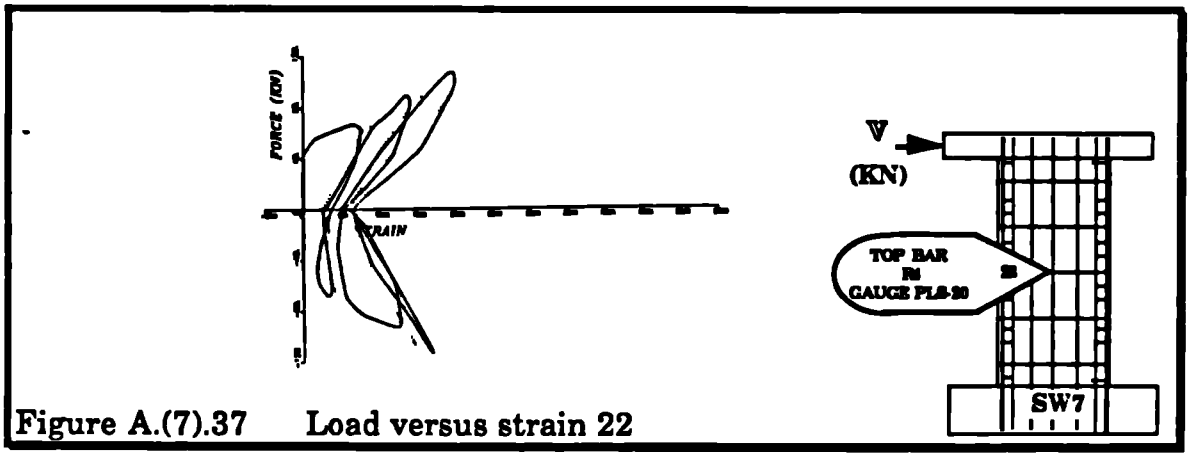


Figure A.(7).37 Load versus strain 22

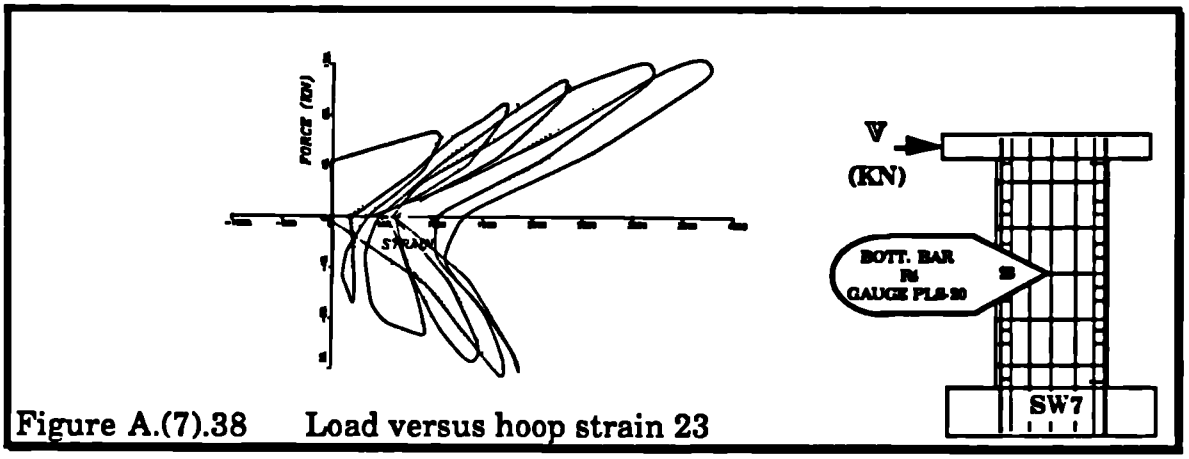


Figure A.(7).38 Load versus hoop strain 23

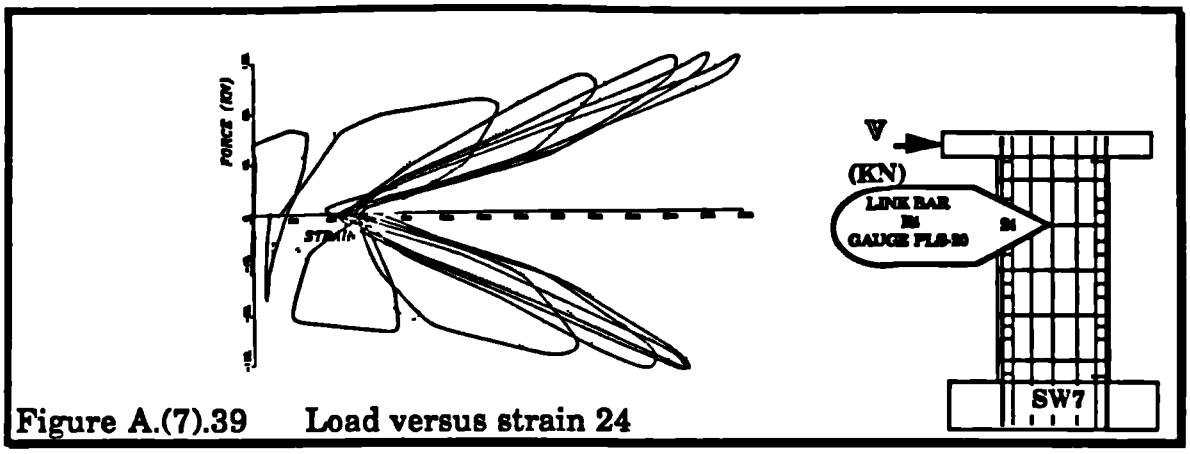


Figure A.(7).39 Load versus strain 24

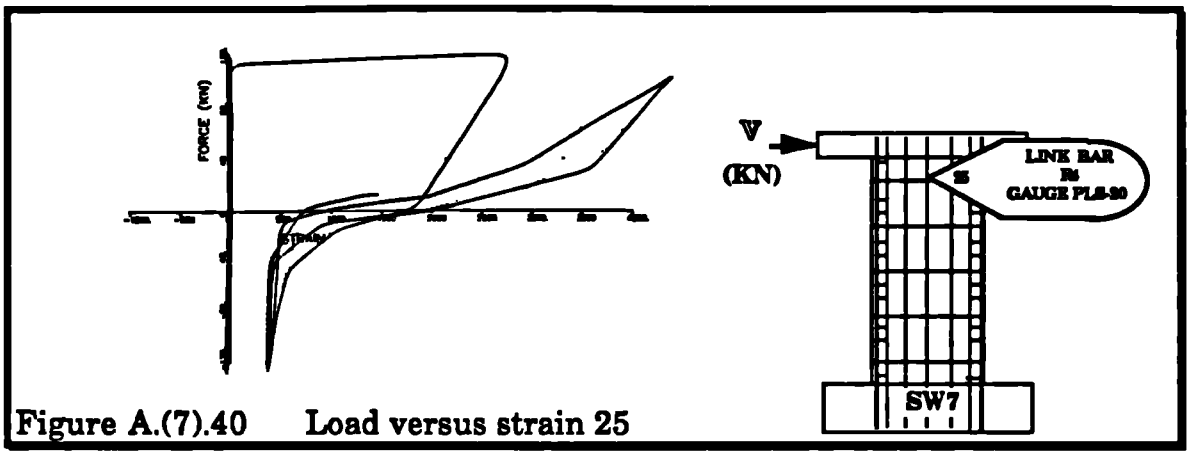


Figure A.(7).40 Load versus strain 25

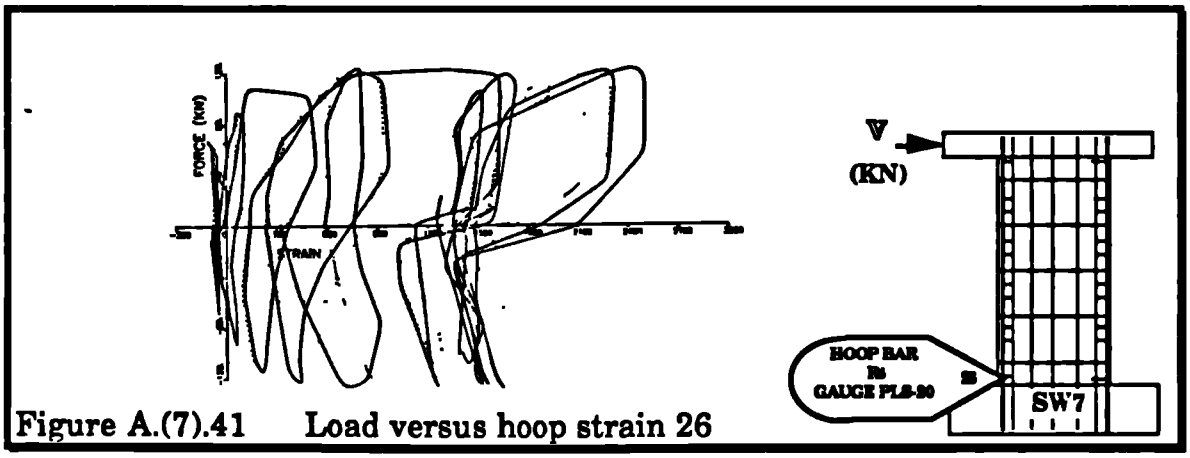


Figure A.(7).41 Load versus hoop strain 26

A.(8) Load-displacement curves - Scale 1:2.5 model SW8

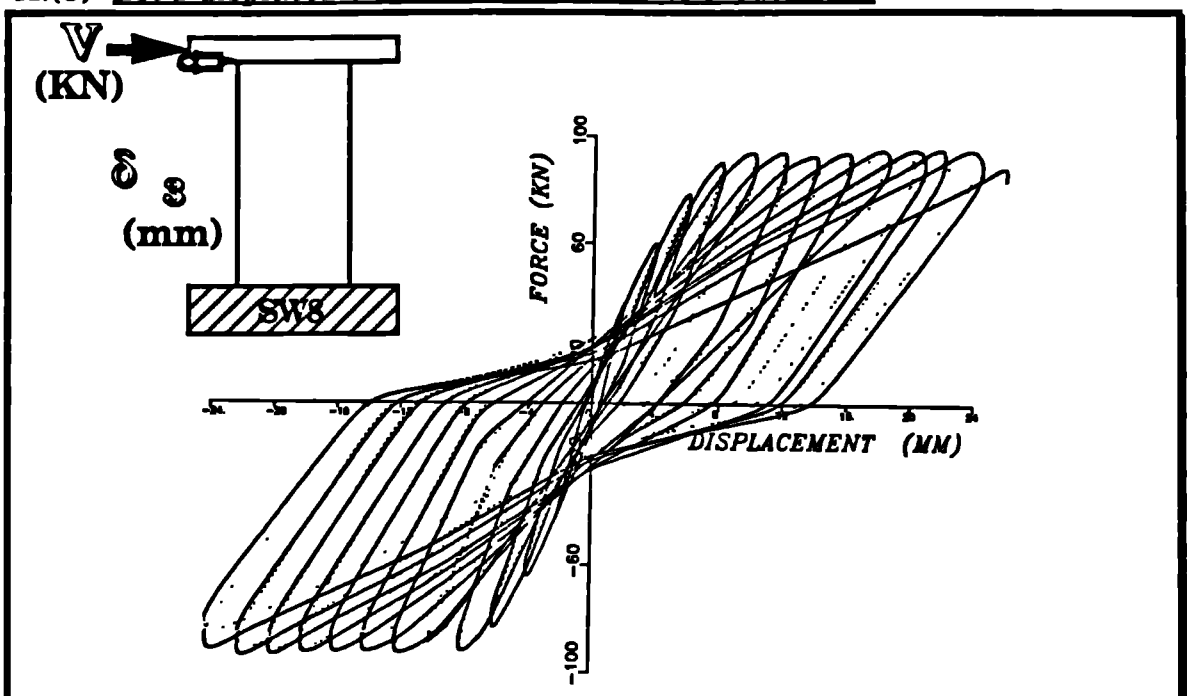


Figure A.(8).1 Load versus wall SW8 displacement 3

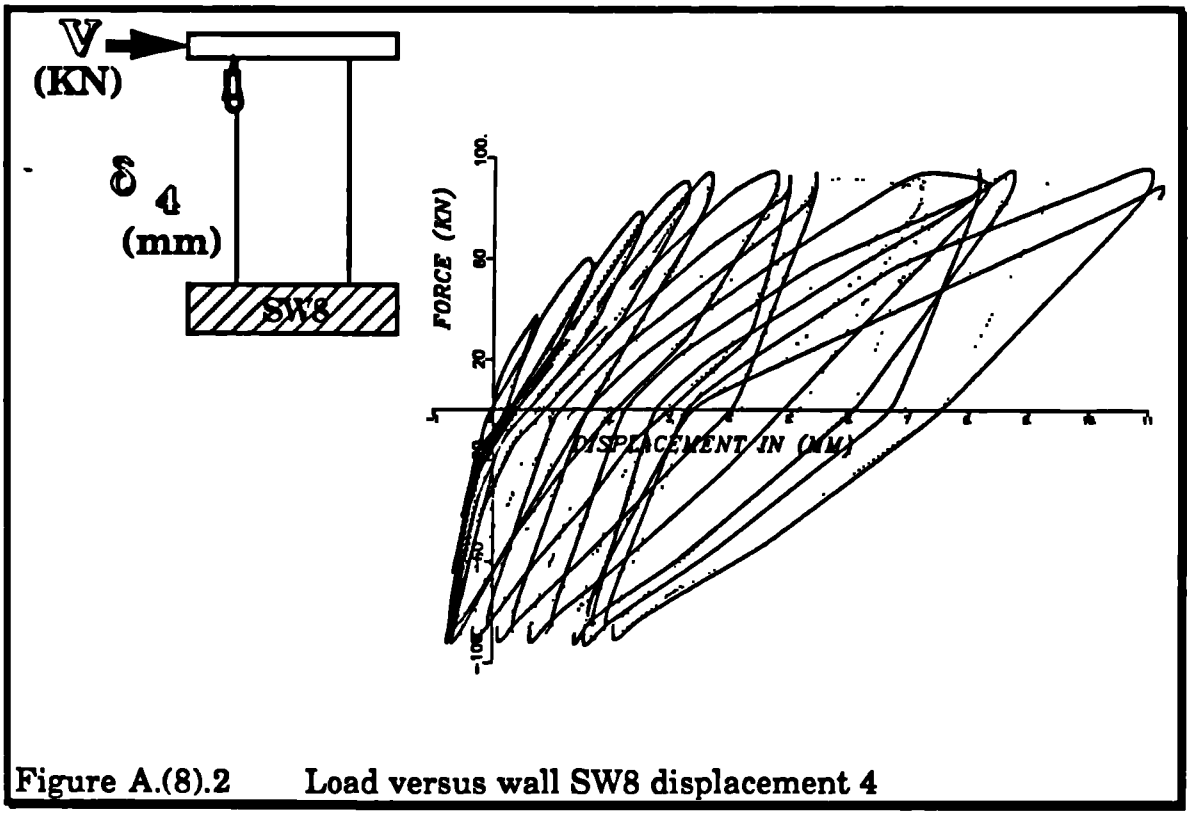


Figure A.(8).2 Load versus wall SW8 displacement 4

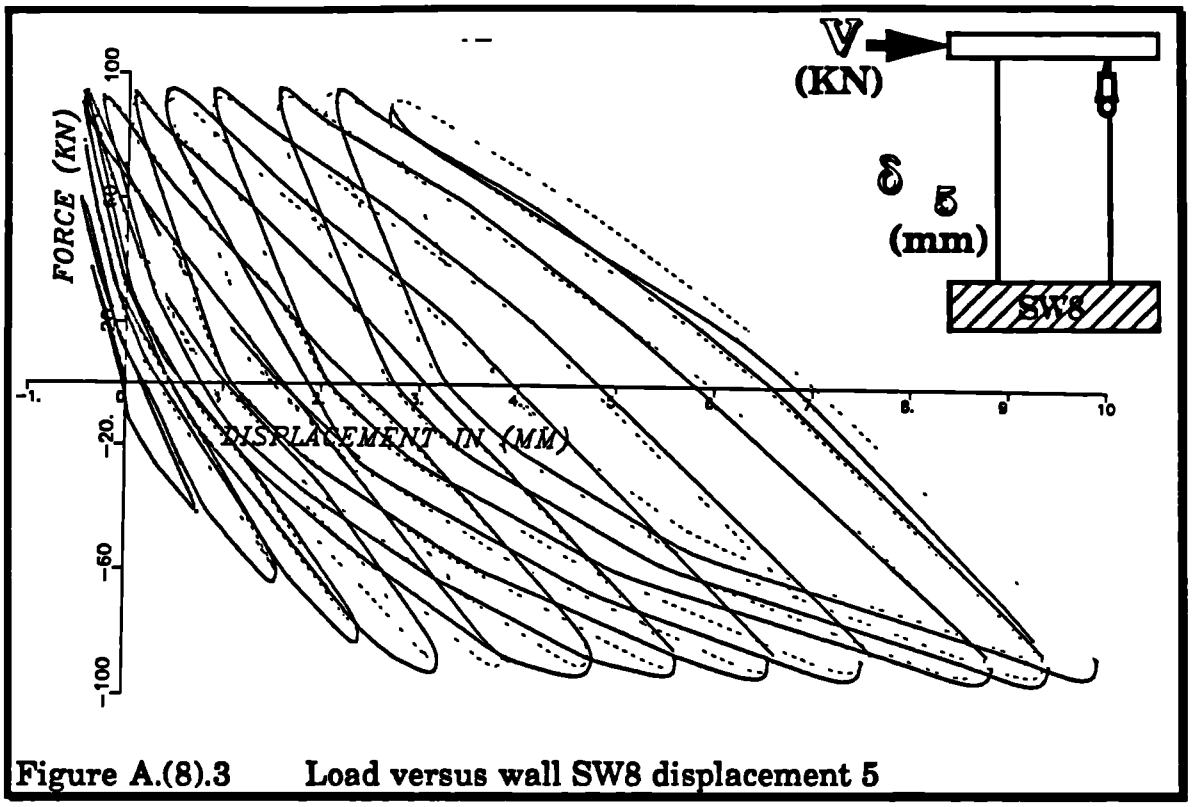


Figure A.(8).3 Load versus wall SW8 displacement 5

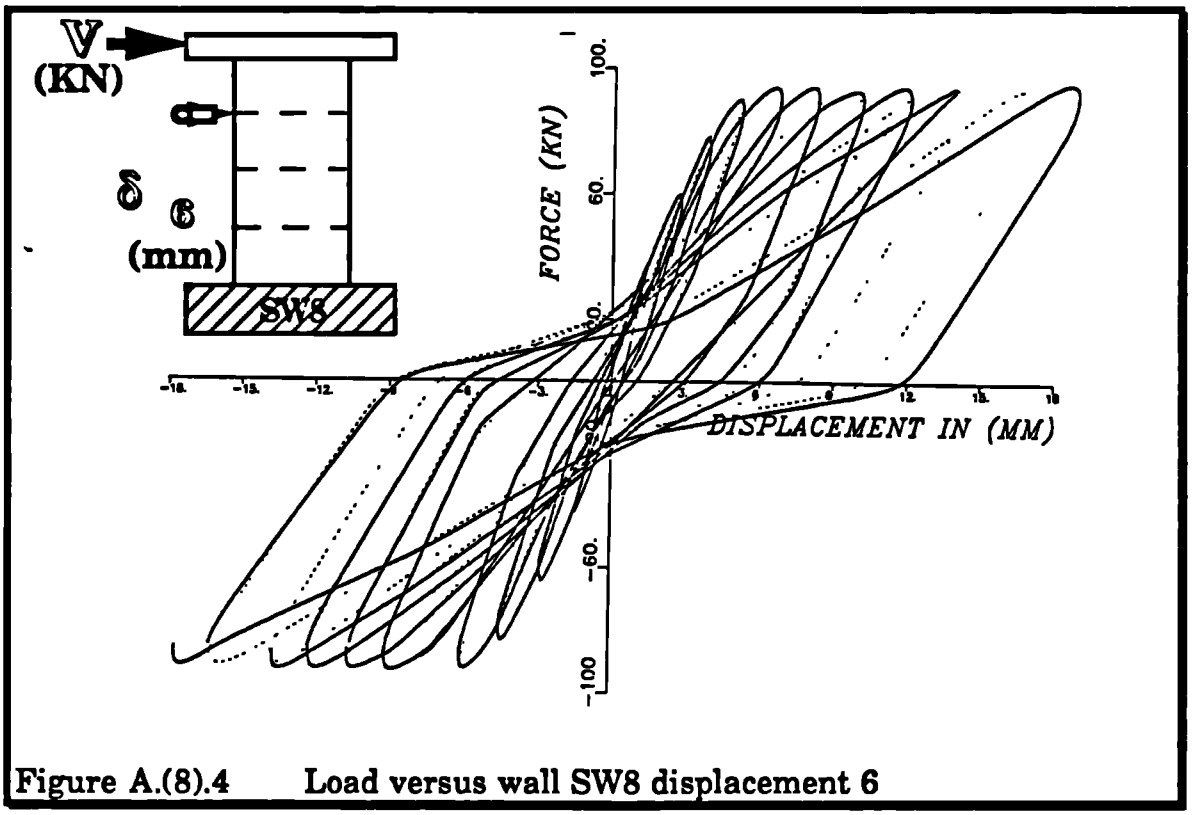


Figure A.(8).4 Load versus wall SW8 displacement 6

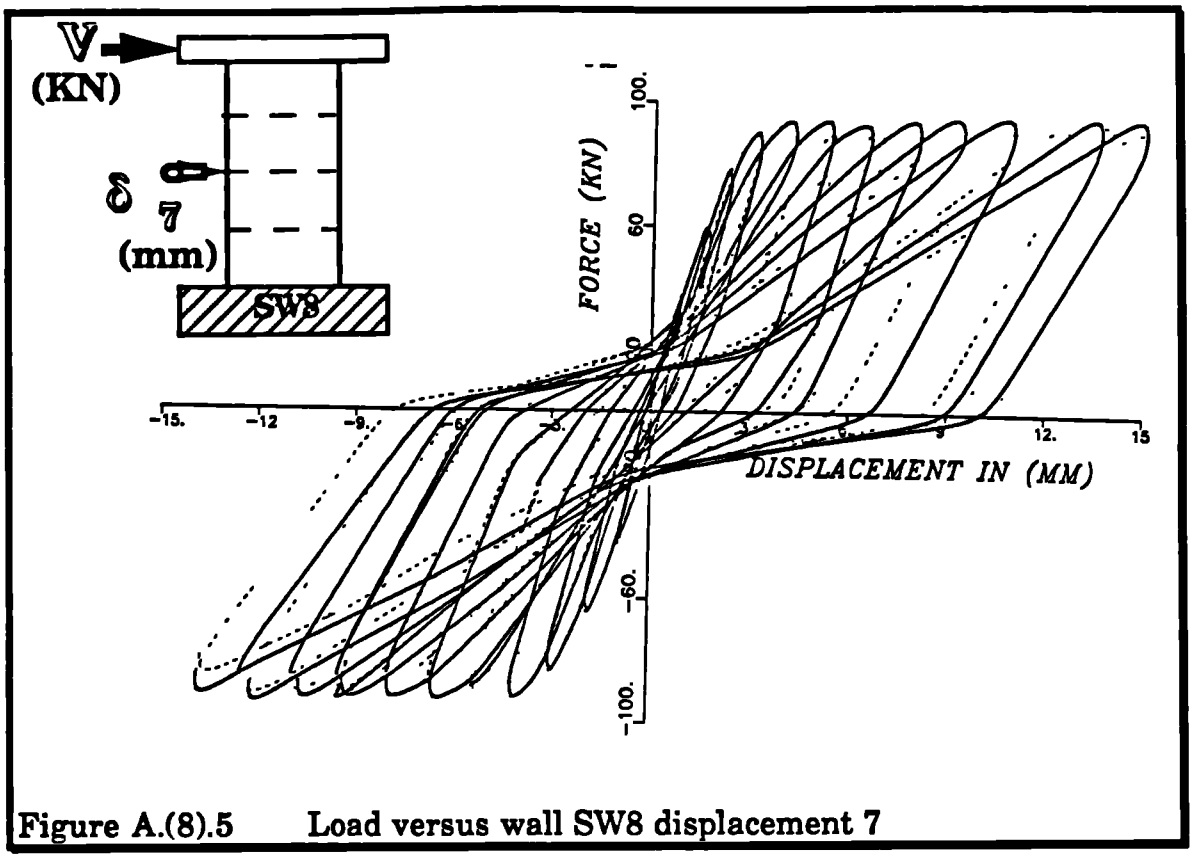


Figure A.(8).5 Load versus wall SW8 displacement 7

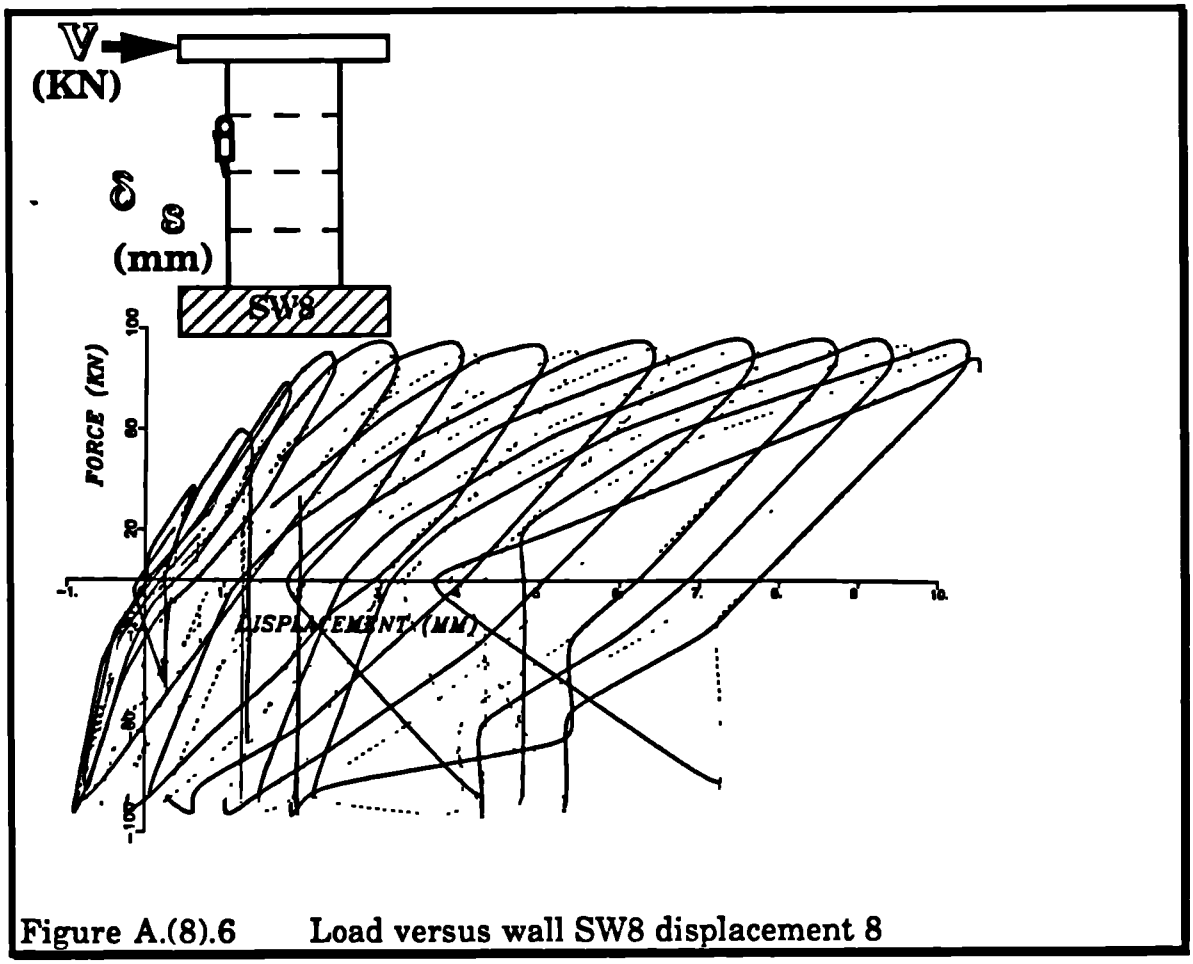


Figure A.(8).6 Load versus wall SW8 displacement 8

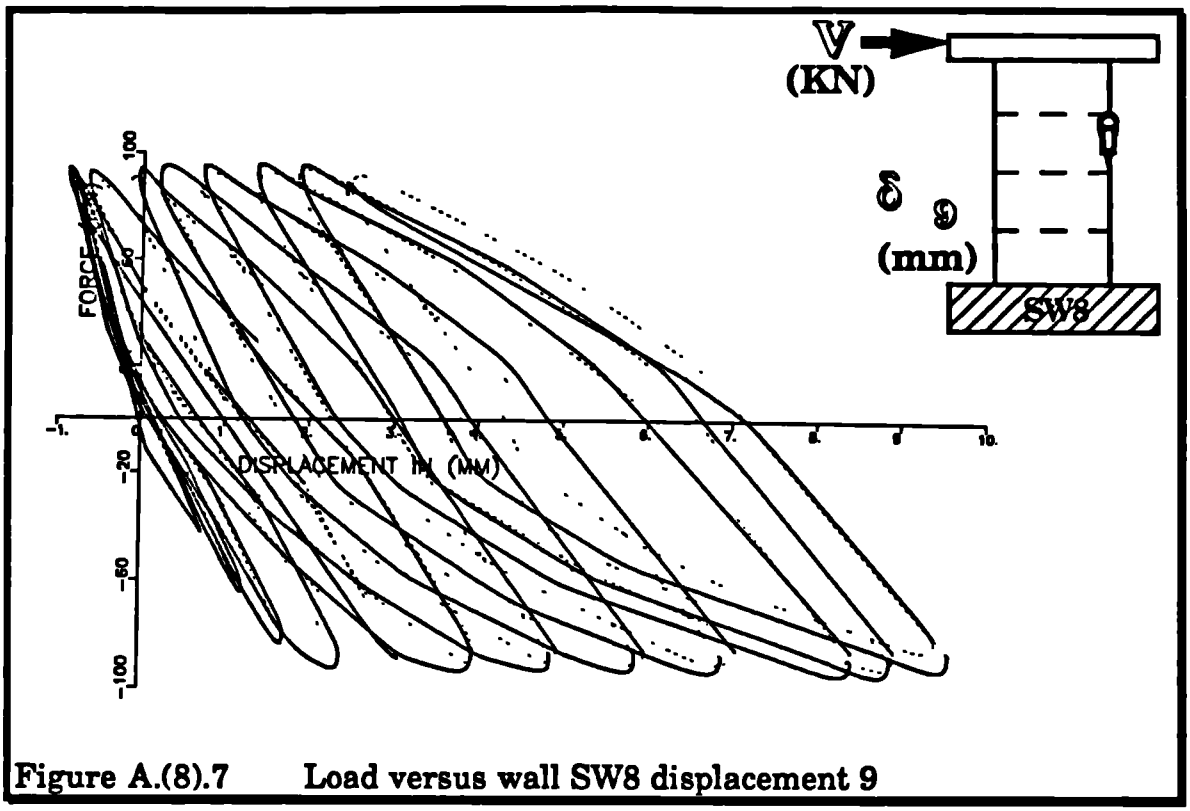


Figure A.(8).7 Load versus wall SW8 displacement 9

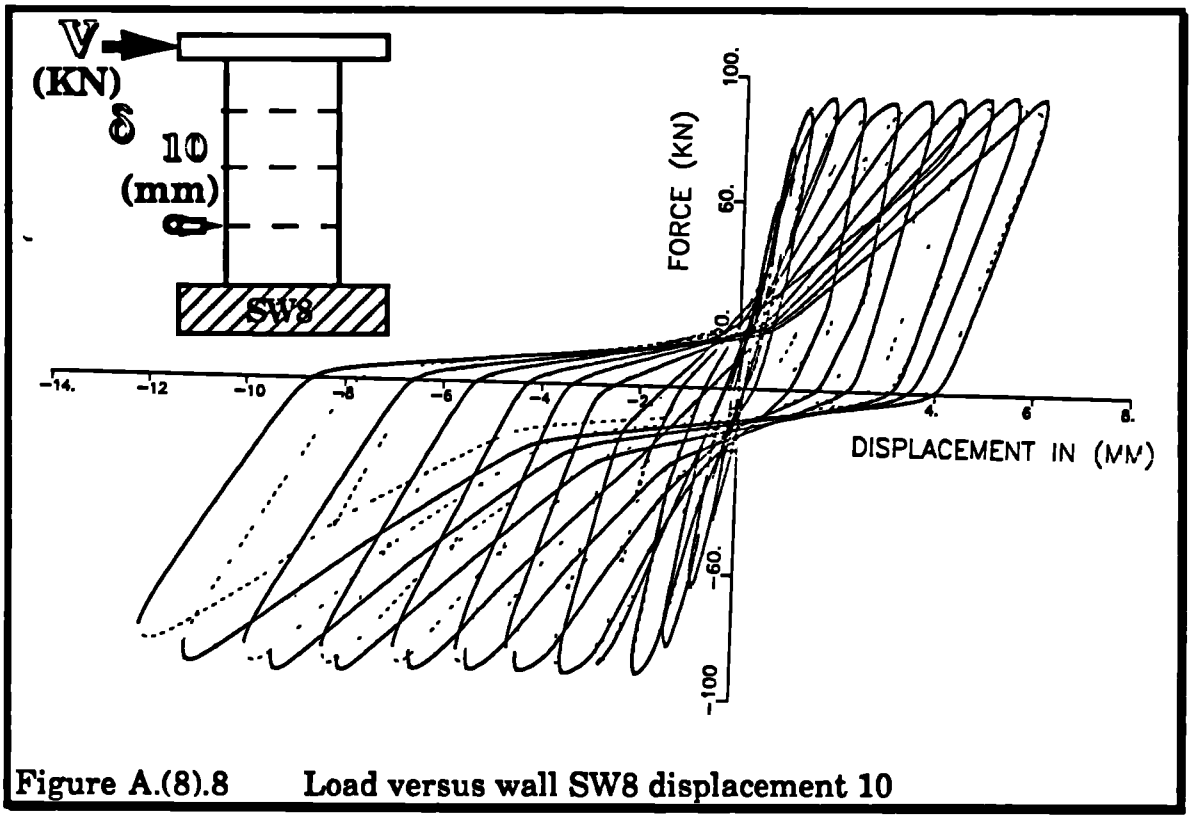


Figure A.(8).8 Load versus wall SW8 displacement 10

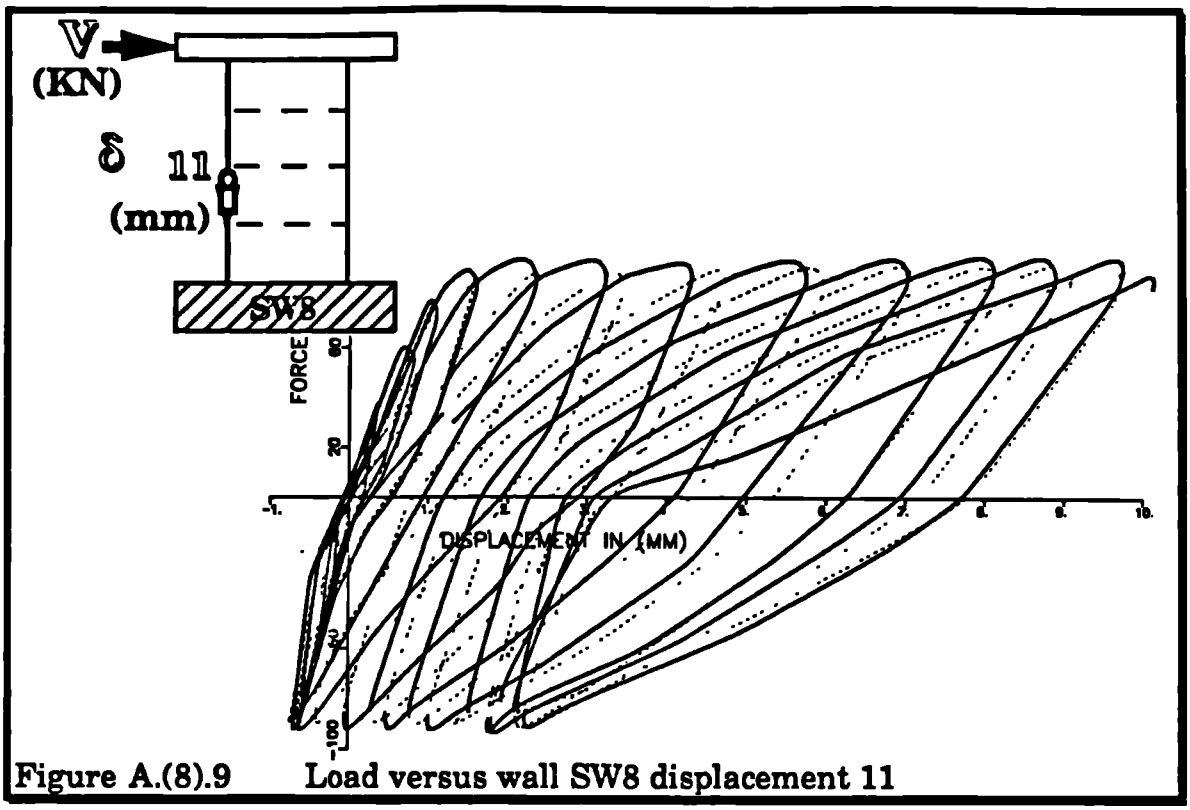


Figure A.(8).9 Load versus wall SW8 displacement 11

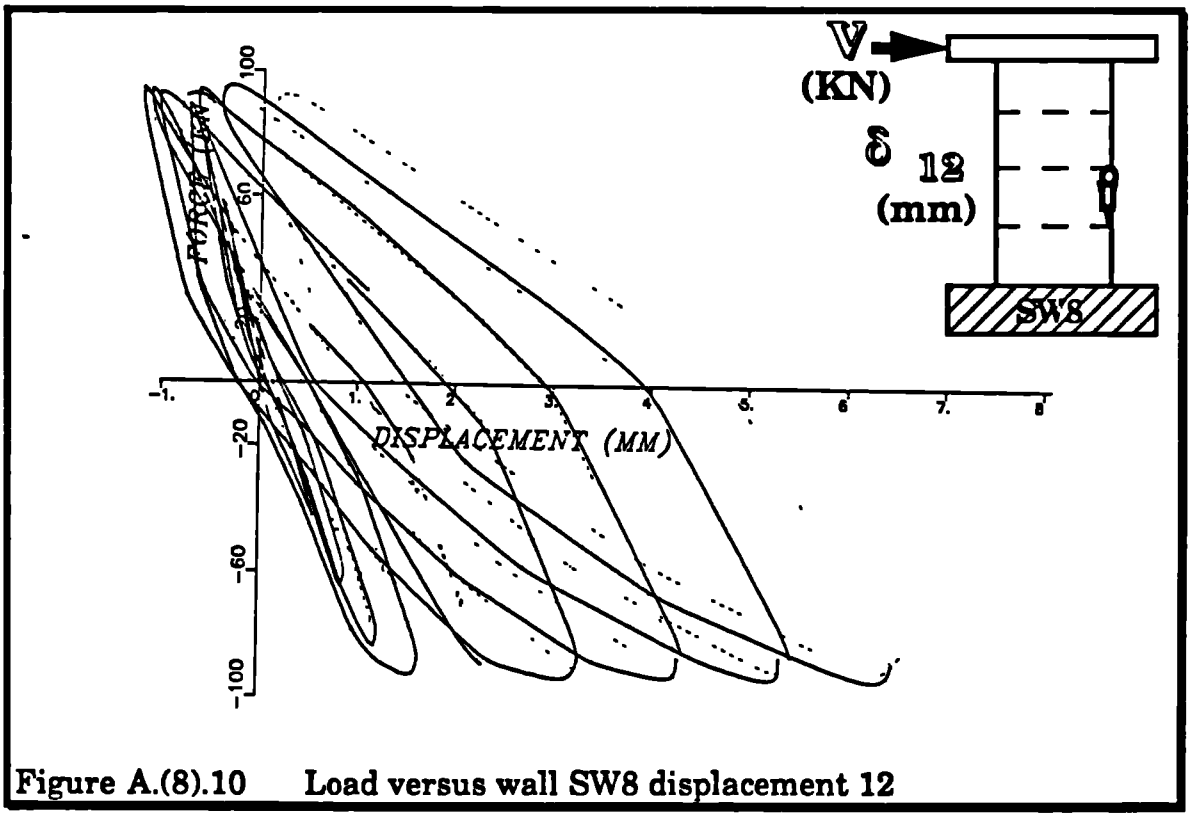


Figure A.(8).10 Load versus wall SW8 displacement 12

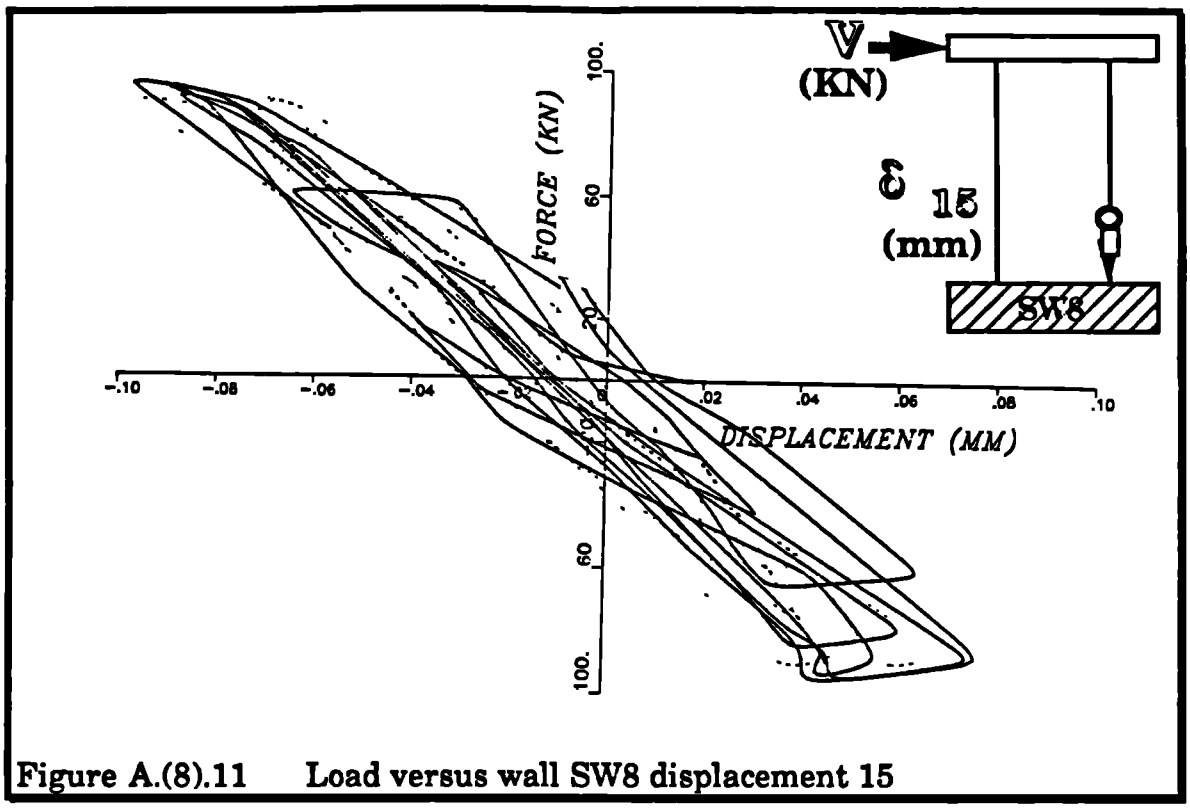


Figure A.(8).11 Load versus wall SW8 displacement 15

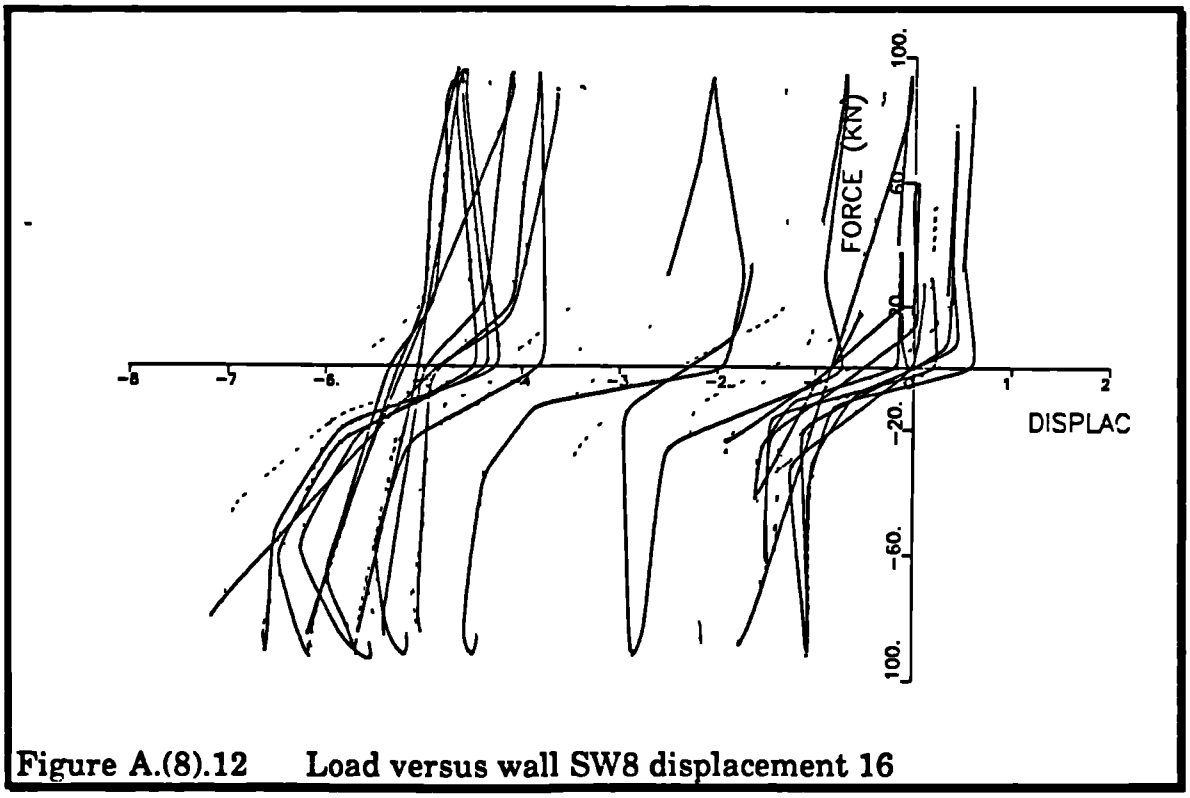


Figure A.(8).12 Load versus wall SW8 displacement 16

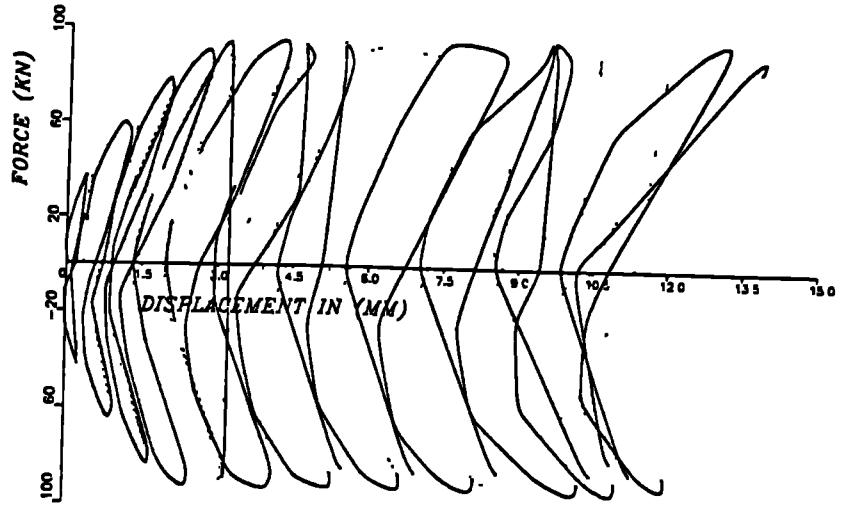


Figure A.(8).13 Load versus wall SW8 top wall average vertical displacement

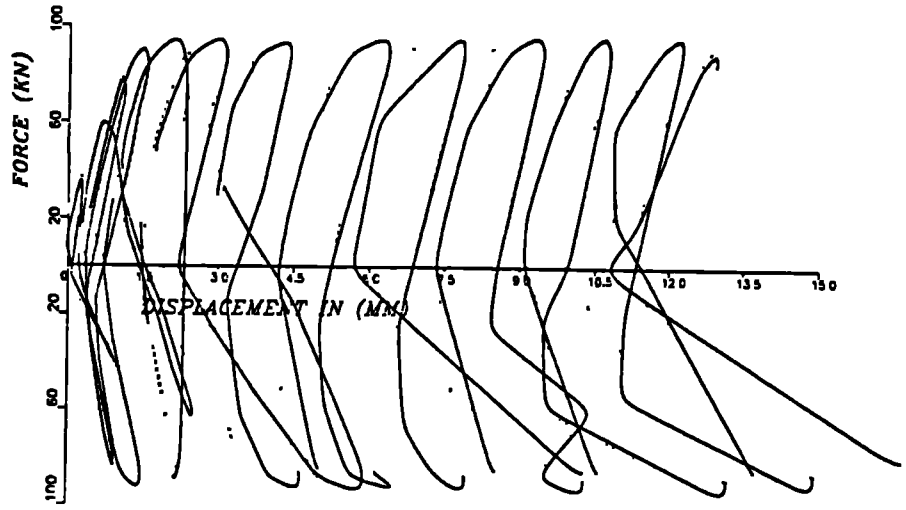


Figure A.(8).14 Load versus wall SW8 mid heigth average vertical displacement

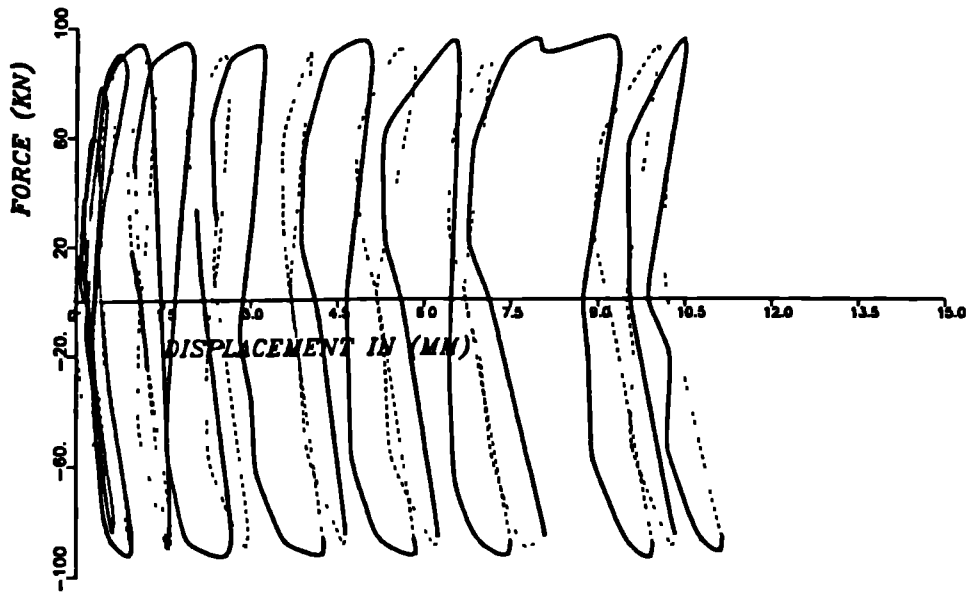


Figure A.(8).15 Load versus wall SW8 quarter heigth average vertical displacement

A.(8) Strain gauge results - Scale 1:2.5 model SW8

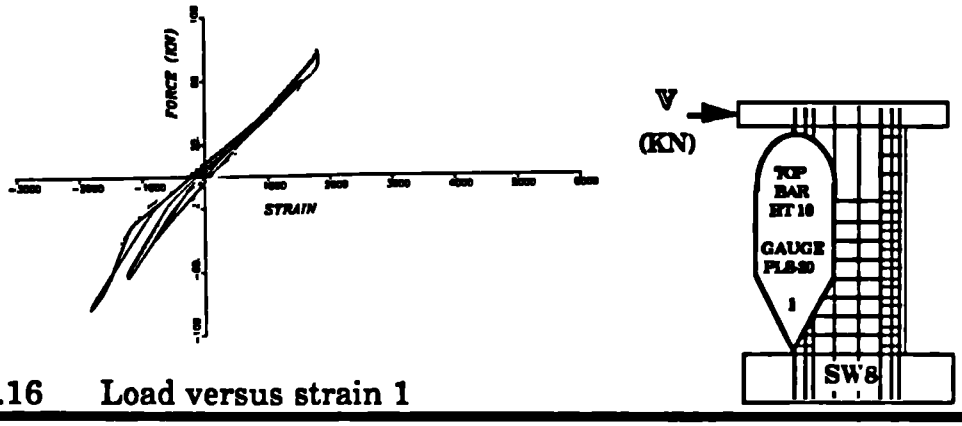


Figure A.(8).16 Load versus strain 1

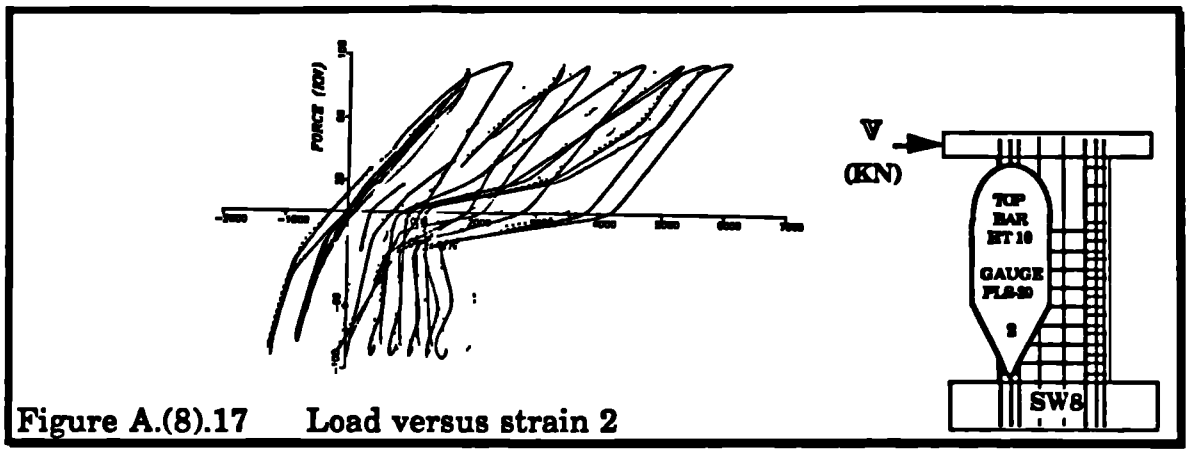


Figure A.(8).17 Load versus strain 2

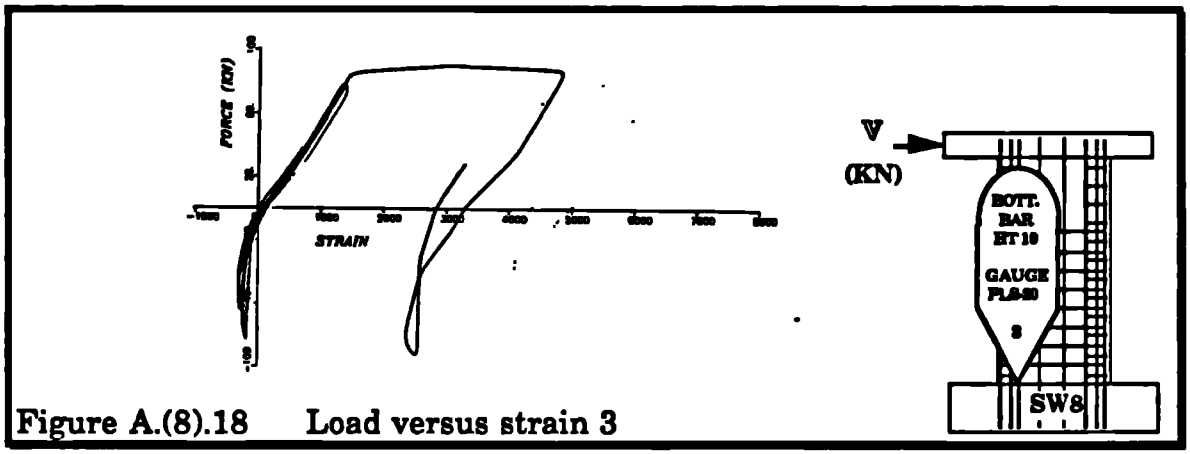


Figure A.(8).18 Load versus strain 3

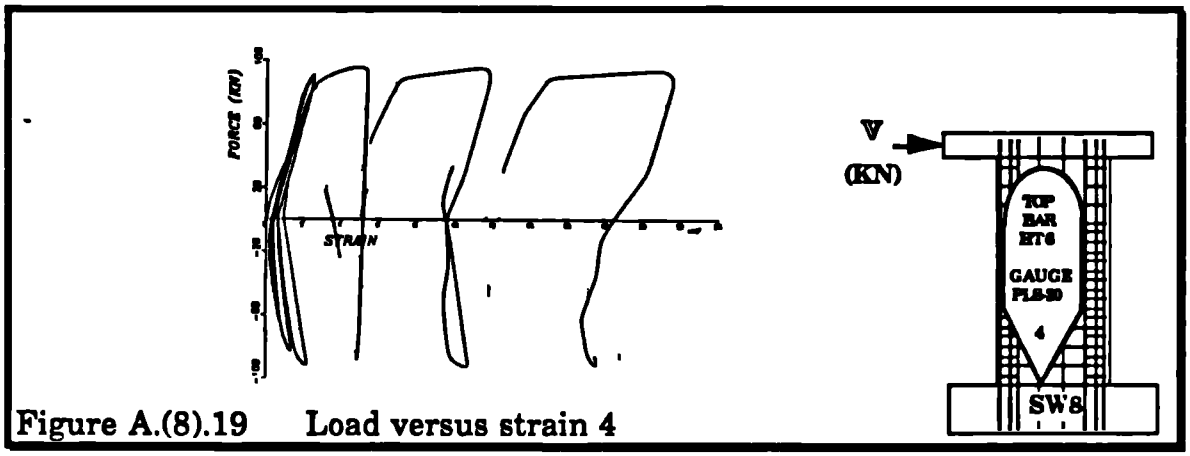


Figure A.(8).19 Load versus strain 4

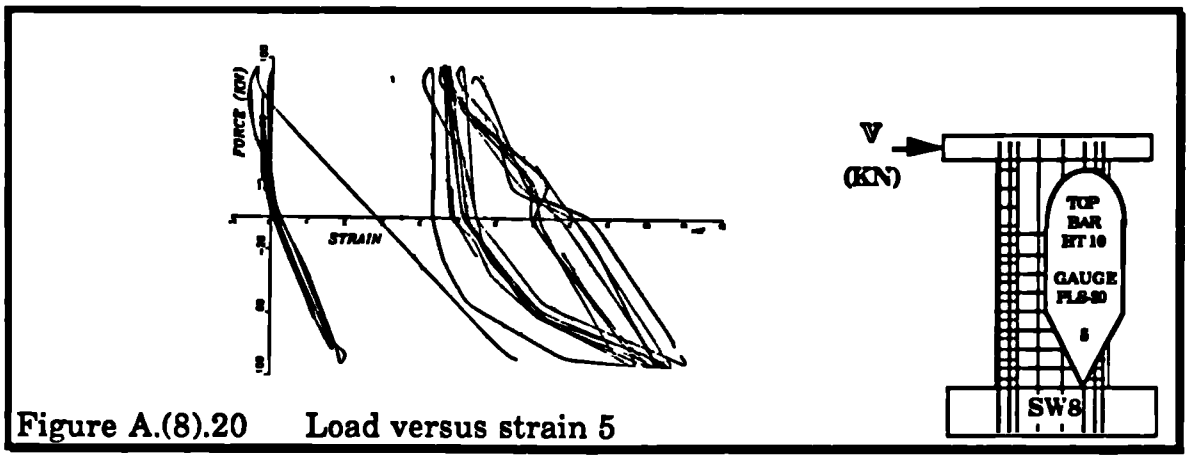


Figure A.(8).20 Load versus strain 5

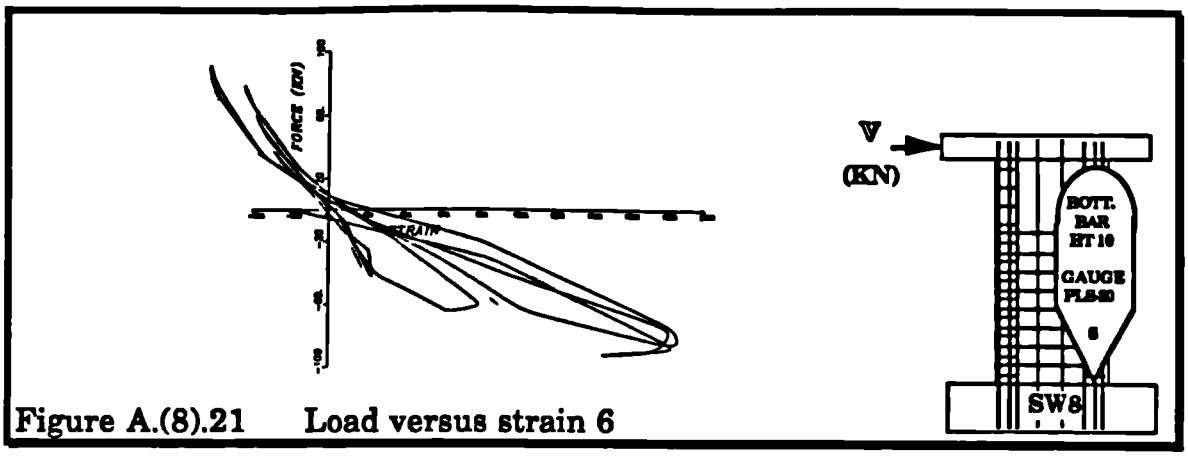


Figure A.(8).21 Load versus strain 6

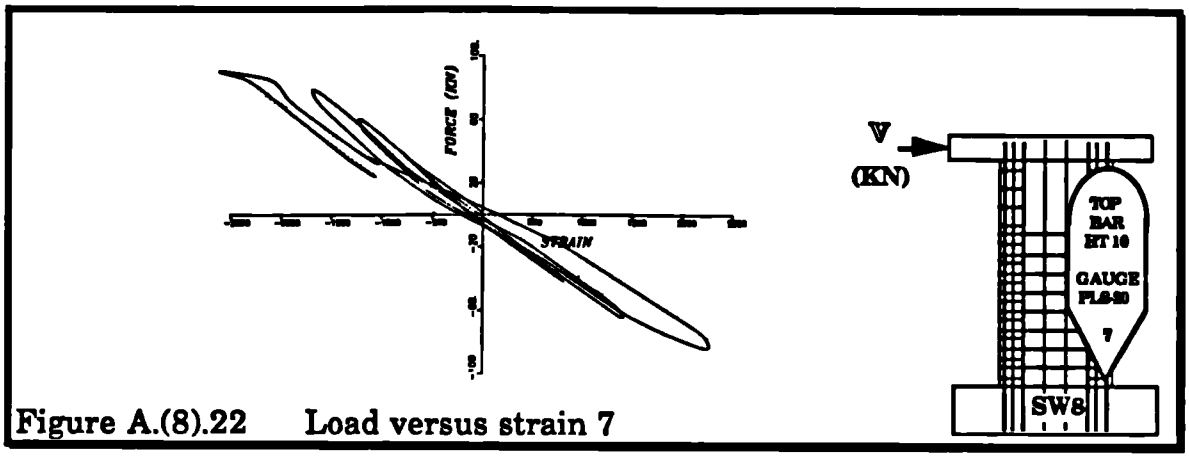


Figure A.(8).22 Load versus strain 7

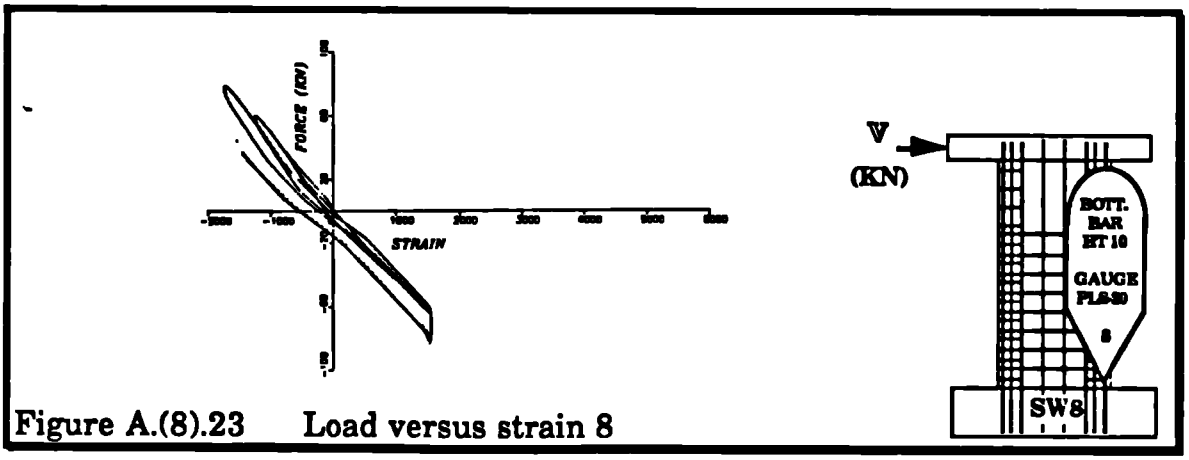


Figure A.(8).23 Load versus strain 8

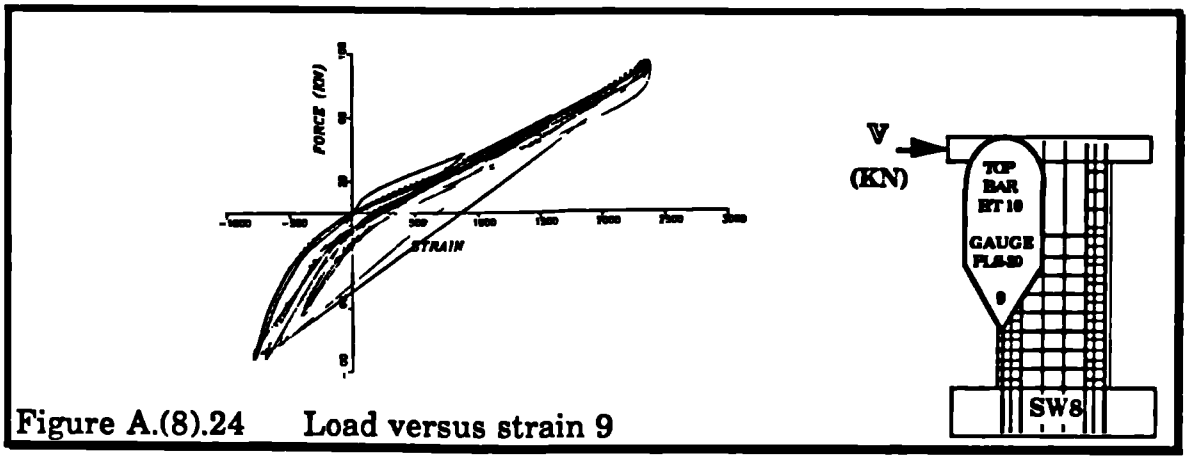
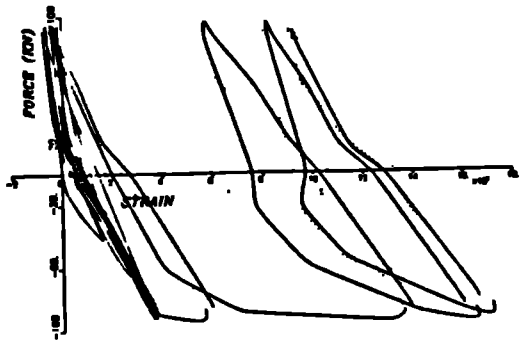


Figure A.(8).24 Load versus strain 9



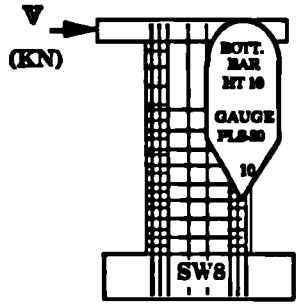
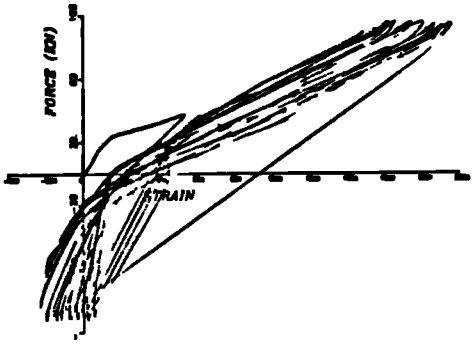


Figure A.(8).25 Load versus strain 10



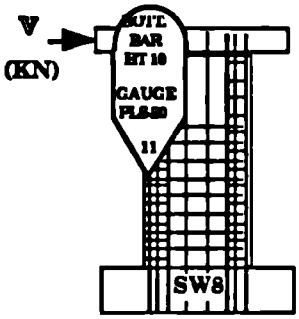
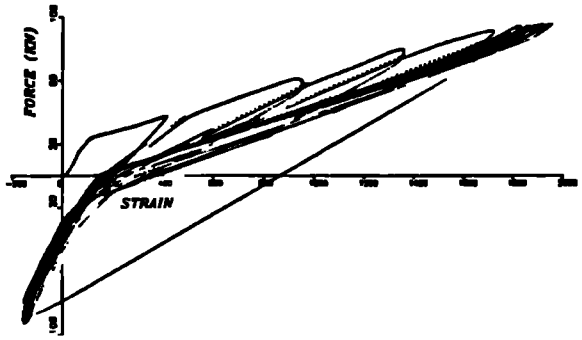


Figure A.(8).26 Load versus strain 11



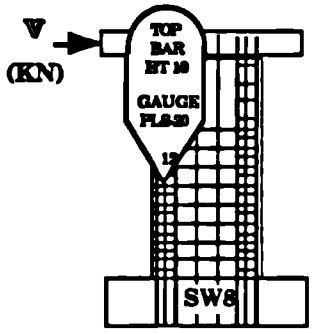
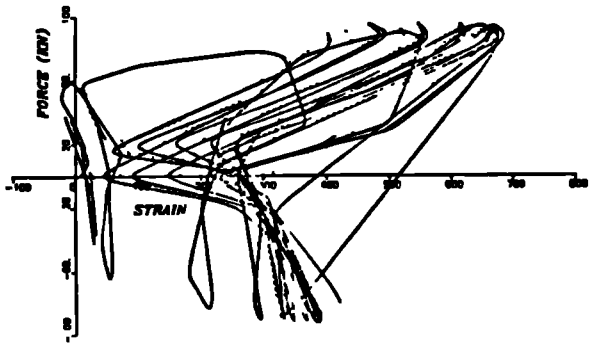


Figure A.(8).27 Load versus strain 12



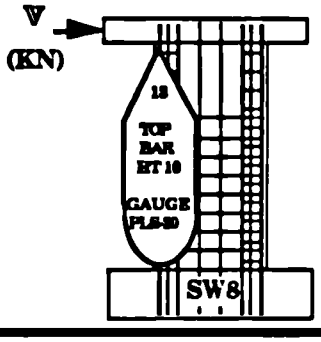
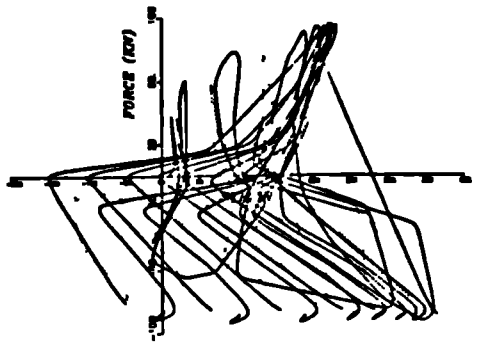


Figure A.(8).28 Load versus strain 13



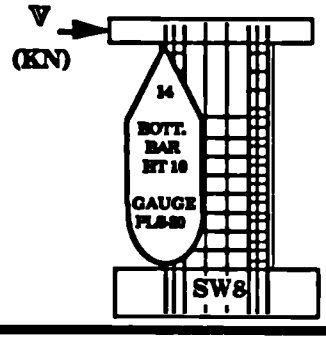
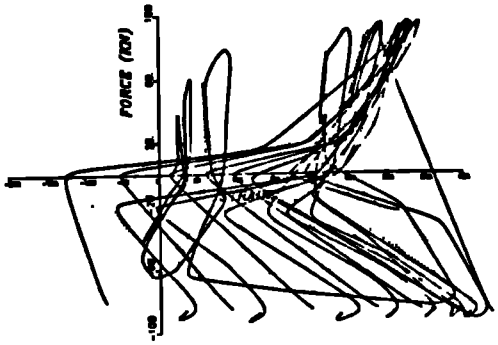


Figure A.(8).29 Load versus strain 14



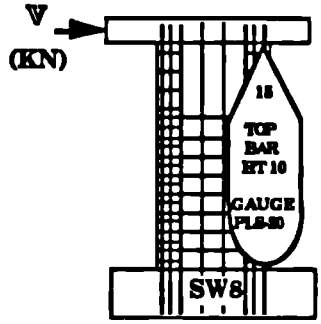
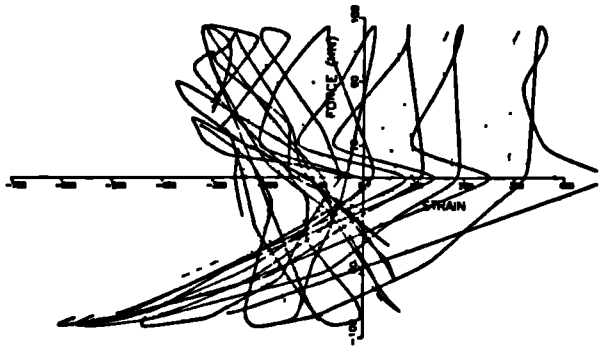


Figure A.(8).30 Load versus strain 15



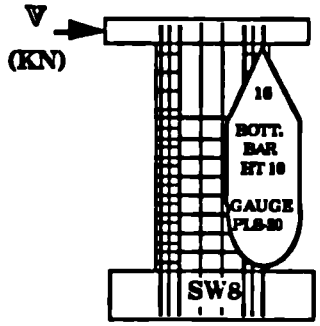
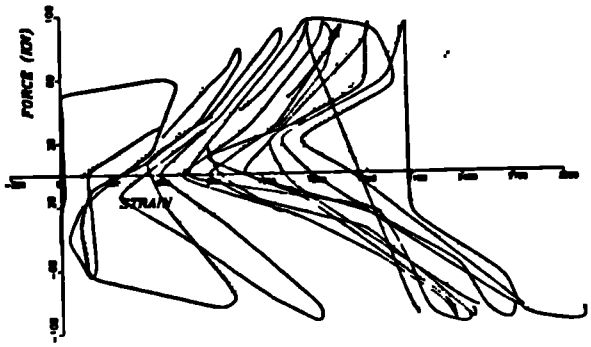


Figure A.(8).31 Load versus strain 16



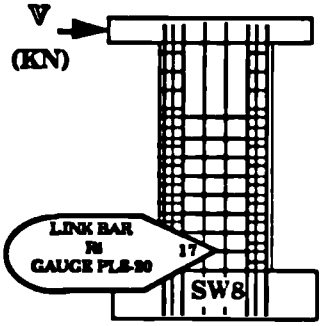


Figure A.(8).32 Load versus link strain 17

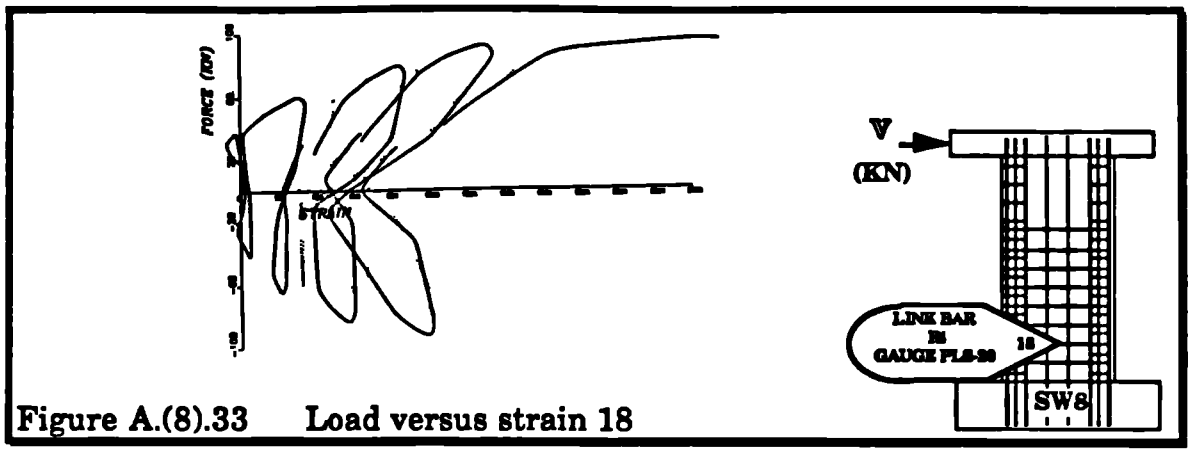


Figure A.(8).33 Load versus strain 18

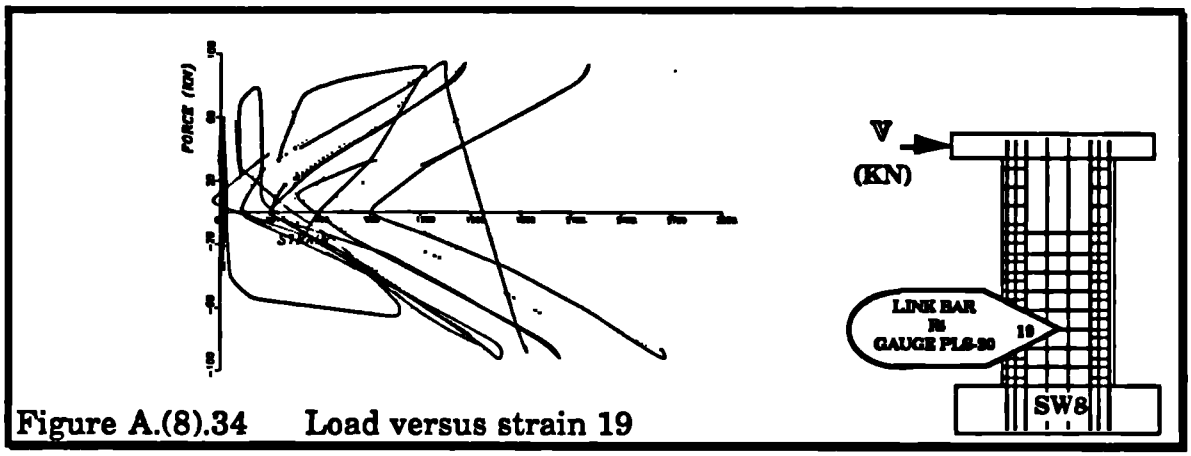


Figure A.(8).34 Load versus strain 19

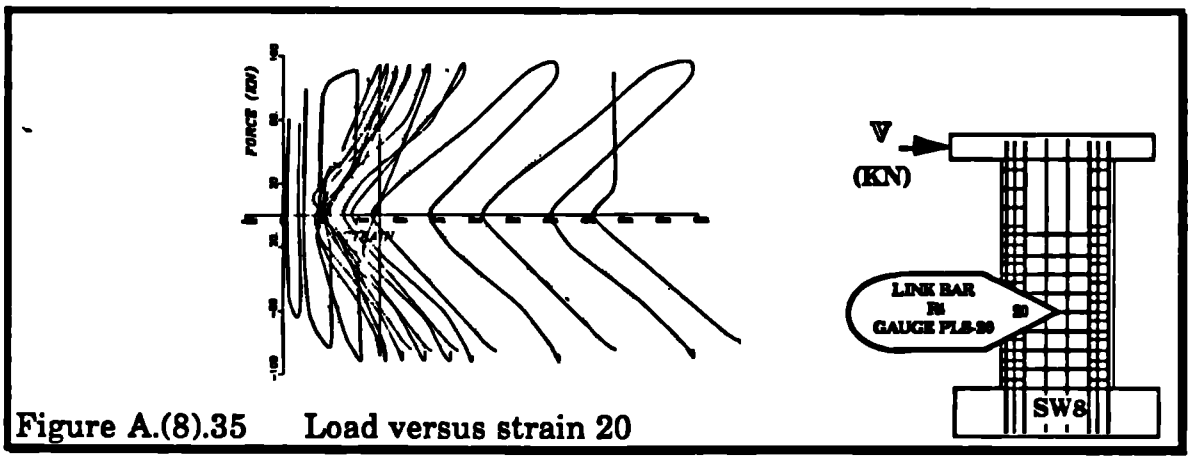


Figure A.(8).35 Load versus strain 20

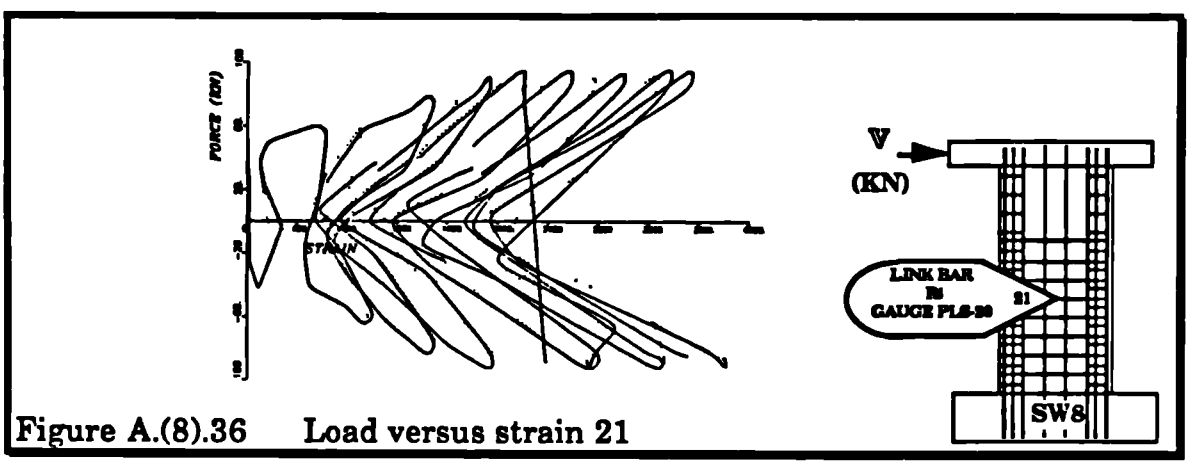


Figure A.(8).36 Load versus strain 21

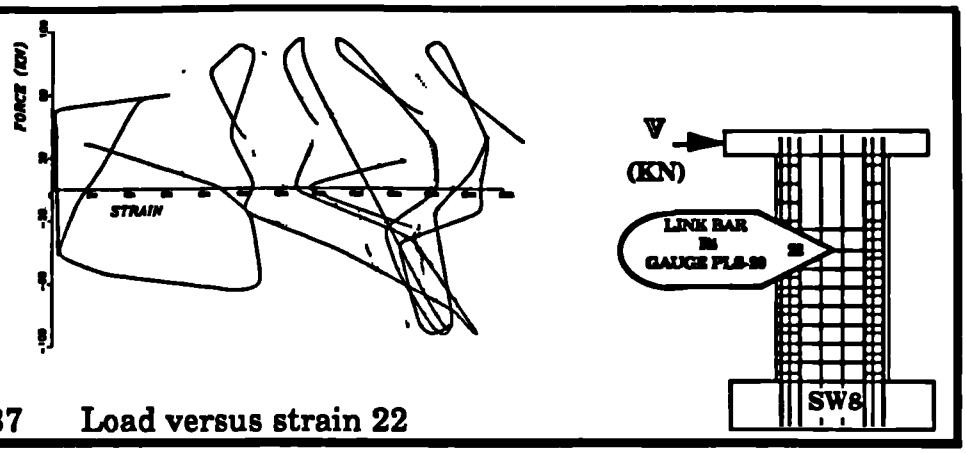


Figure A.(8).37 Load versus strain 22

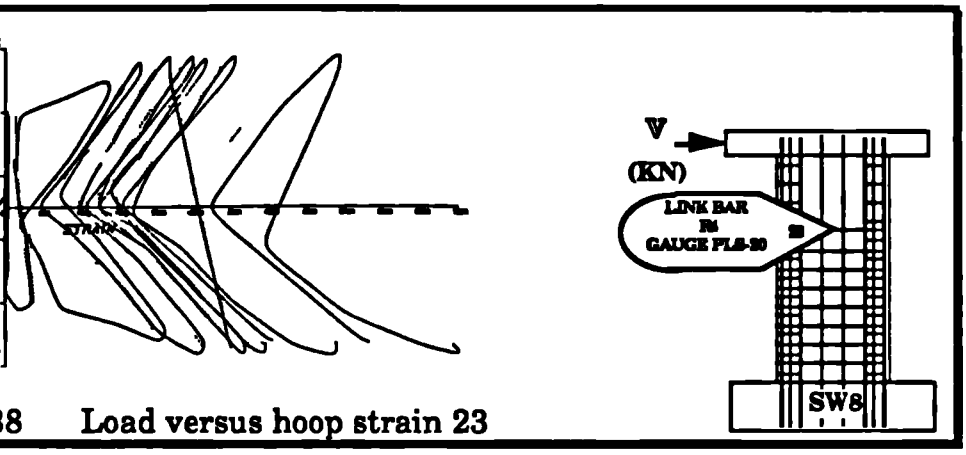


Figure A.(8).38 Load versus hoop strain 23

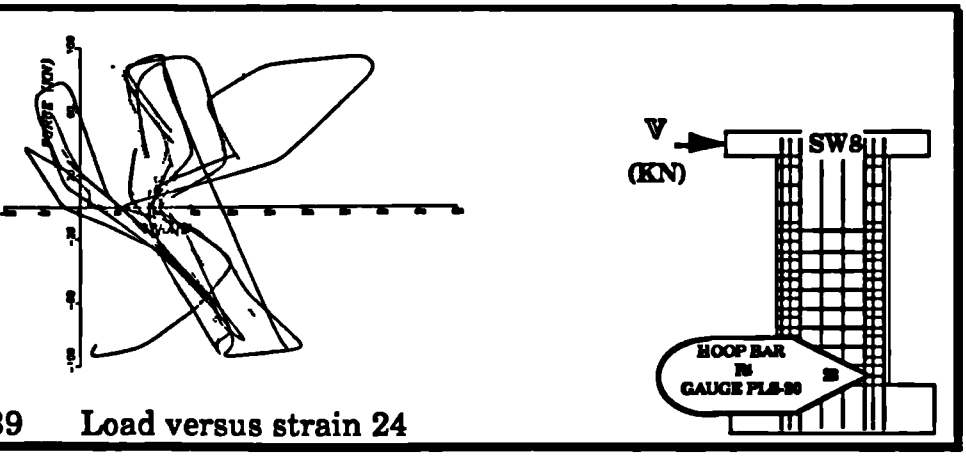


Figure A.(8).39 Load versus strain 24

A.(9) Load-displacement curves - Scale 1:2.5 model SW9

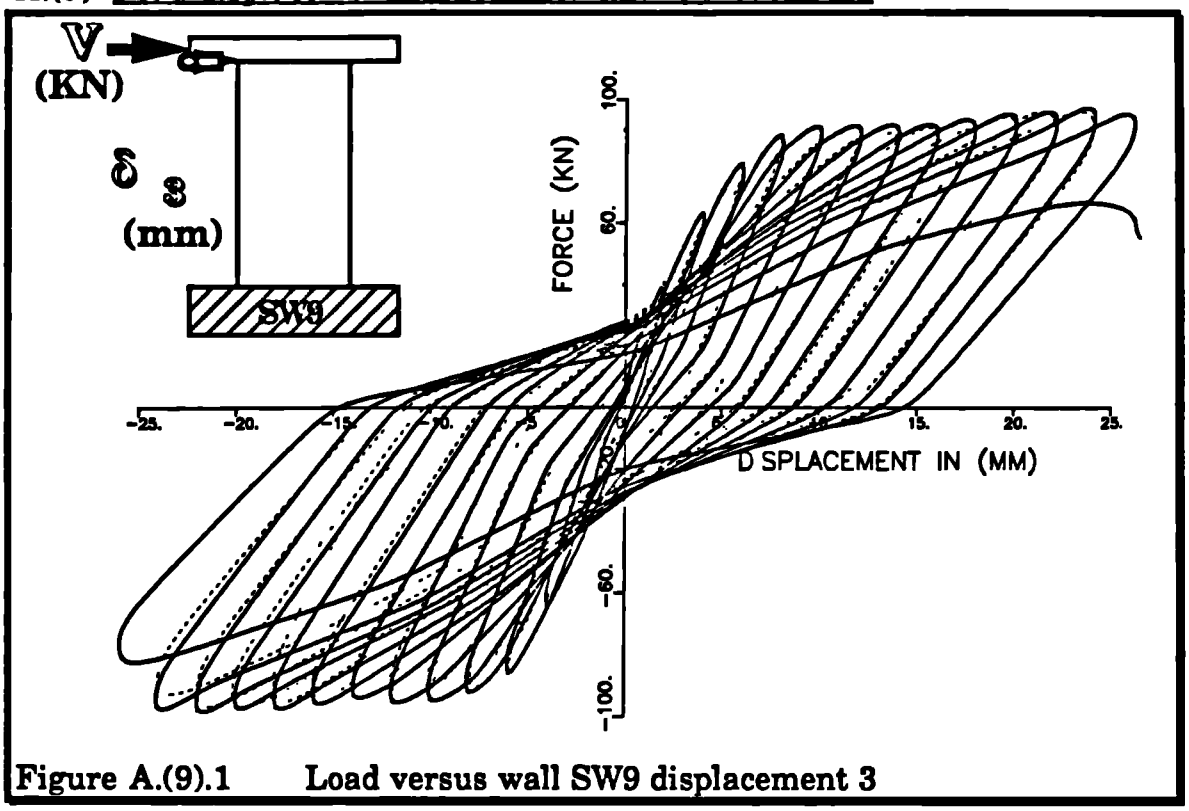


Figure A.(9).1 Load versus wall SW9 displacement 3

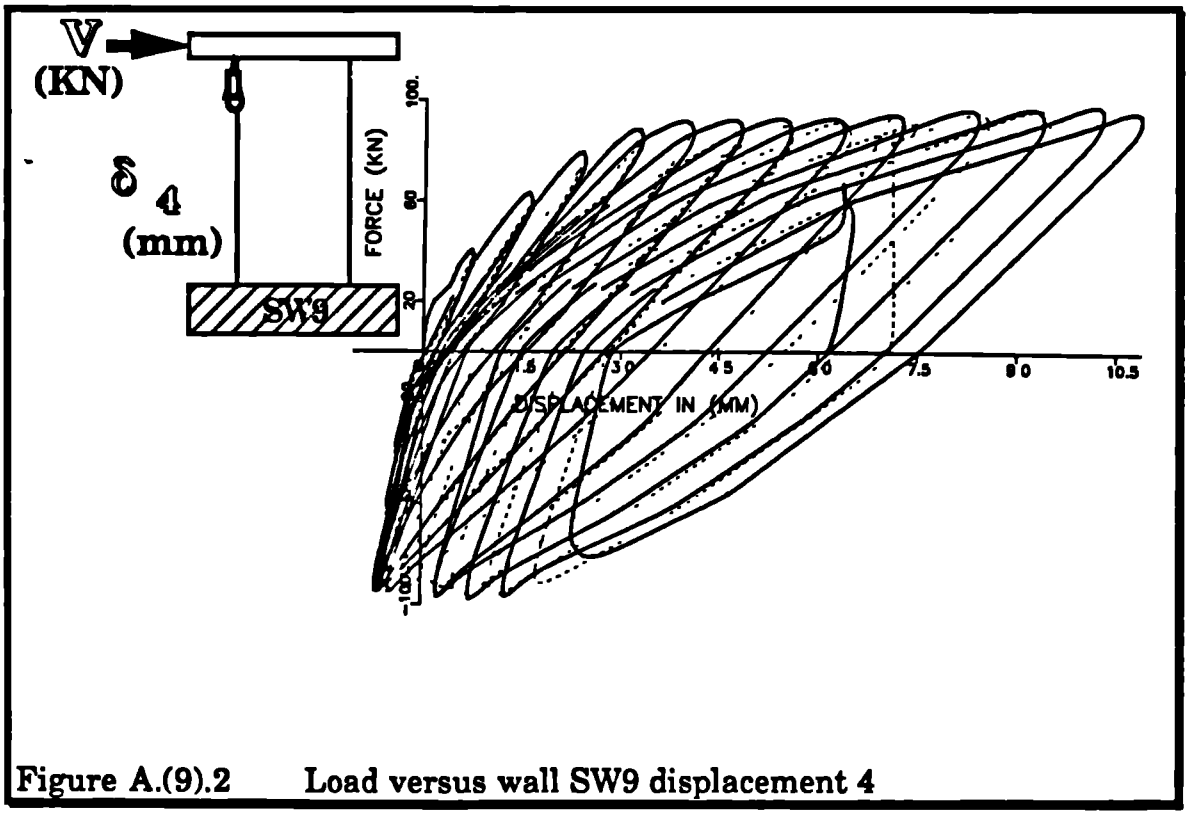


Figure A.(9).2 Load versus wall SW9 displacement 4

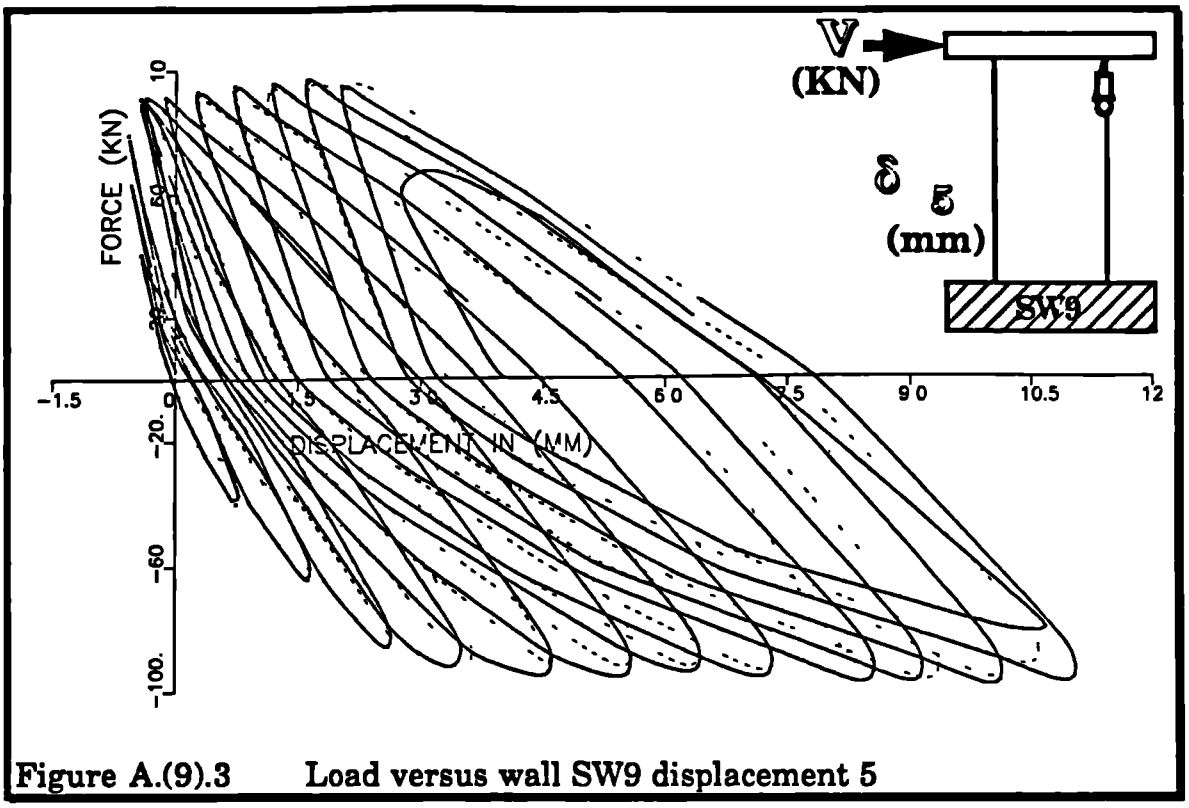


Figure A.(9).3 Load versus wall SW9 displacement 5

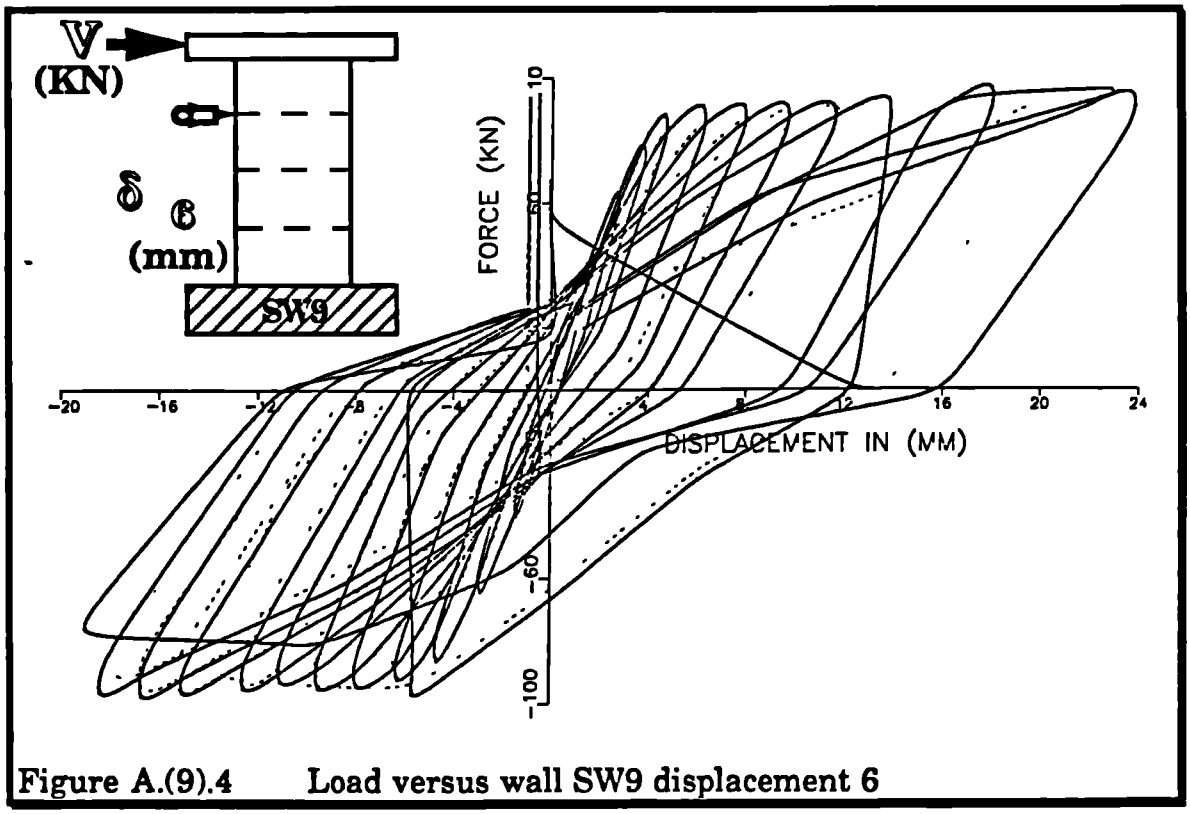


Figure A.(9).4 Load versus wall SW9 displacement 6

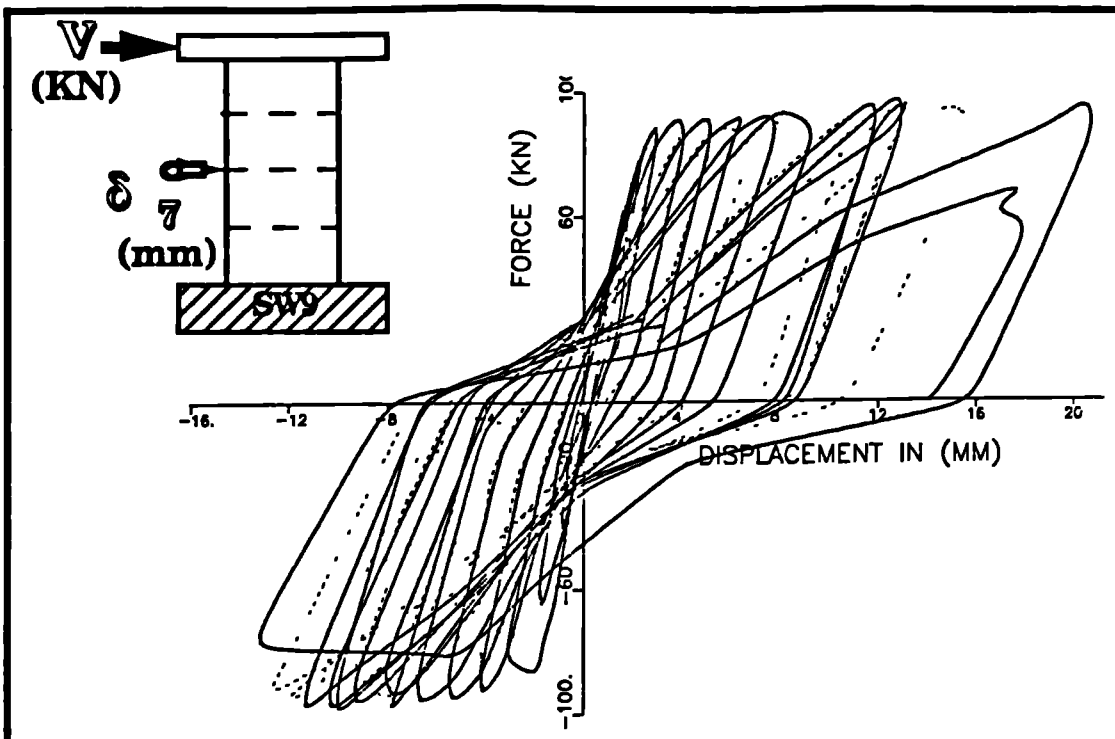


Figure A.(9).5 Load versus wall SW9 displacement 7

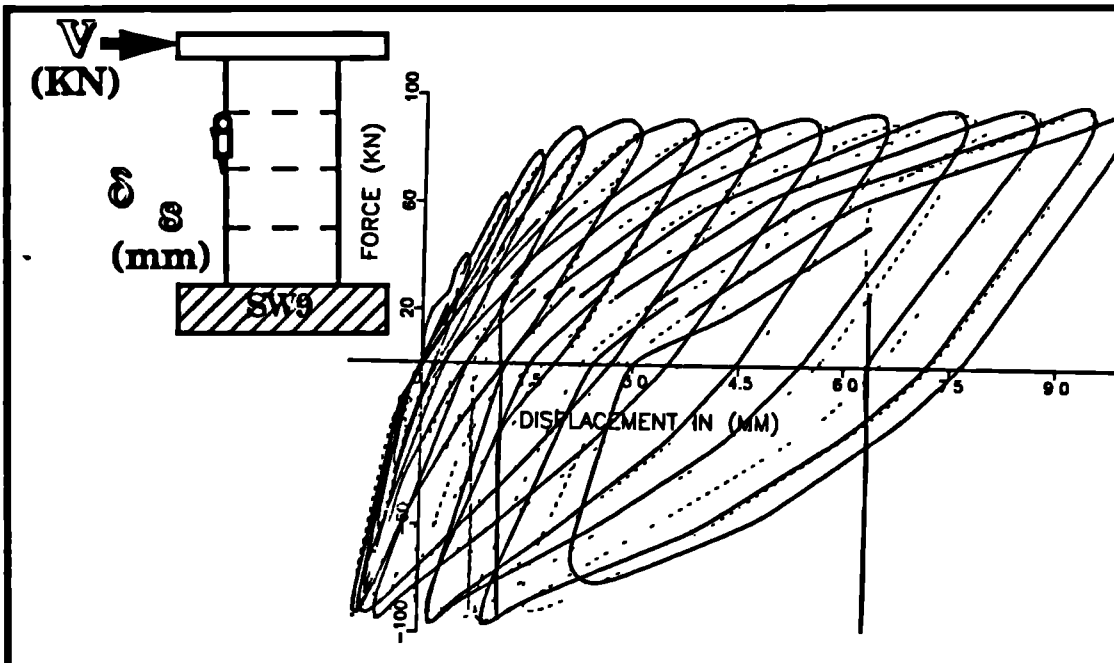


Figure A.(9).6 Load versus wall SW9 displacement 8

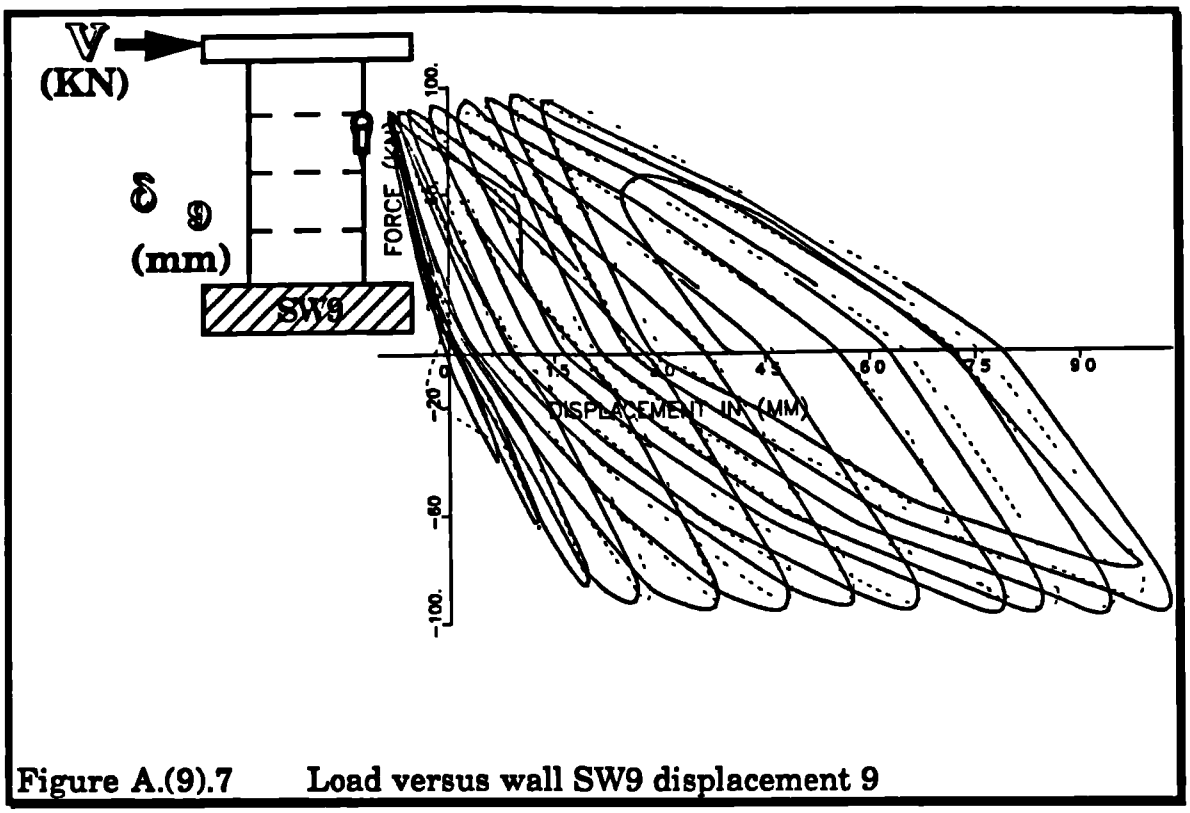


Figure A.(9).7 Load versus wall SW9 displacement 9

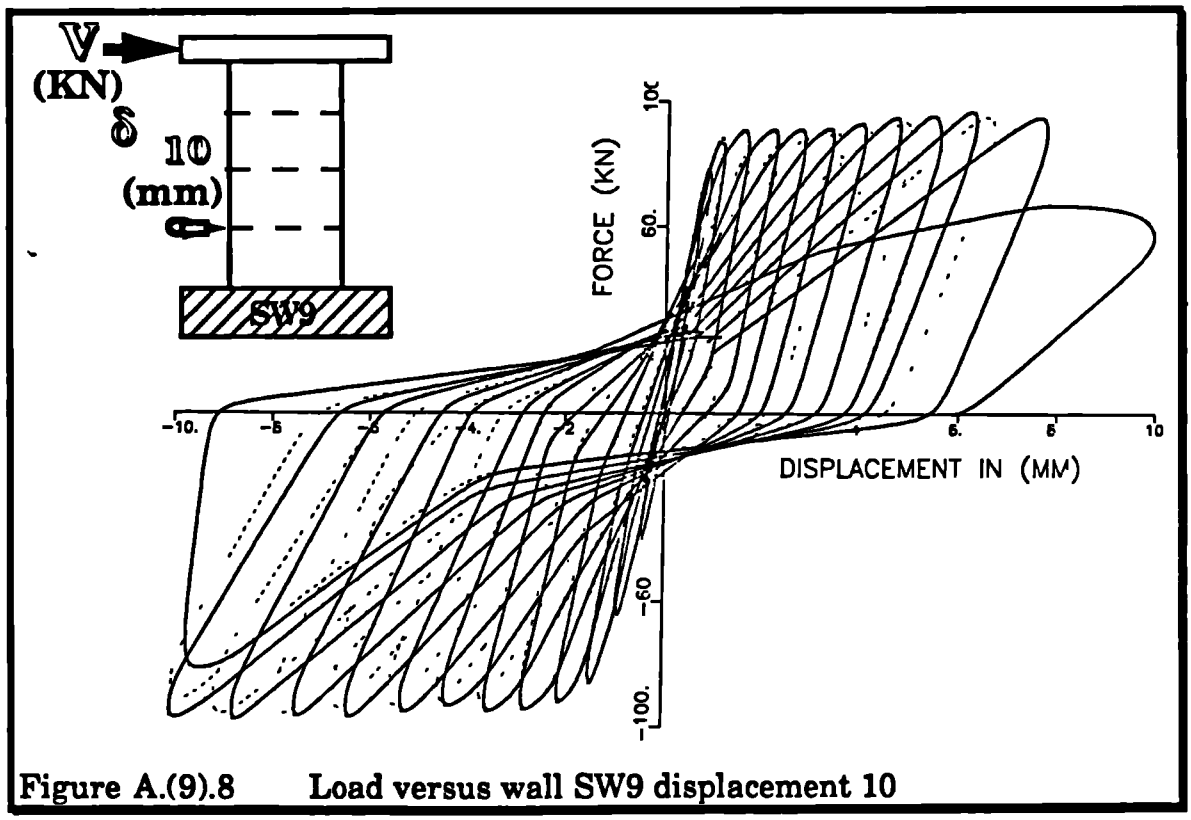


Figure A.(9).8 Load versus wall SW9 displacement 10

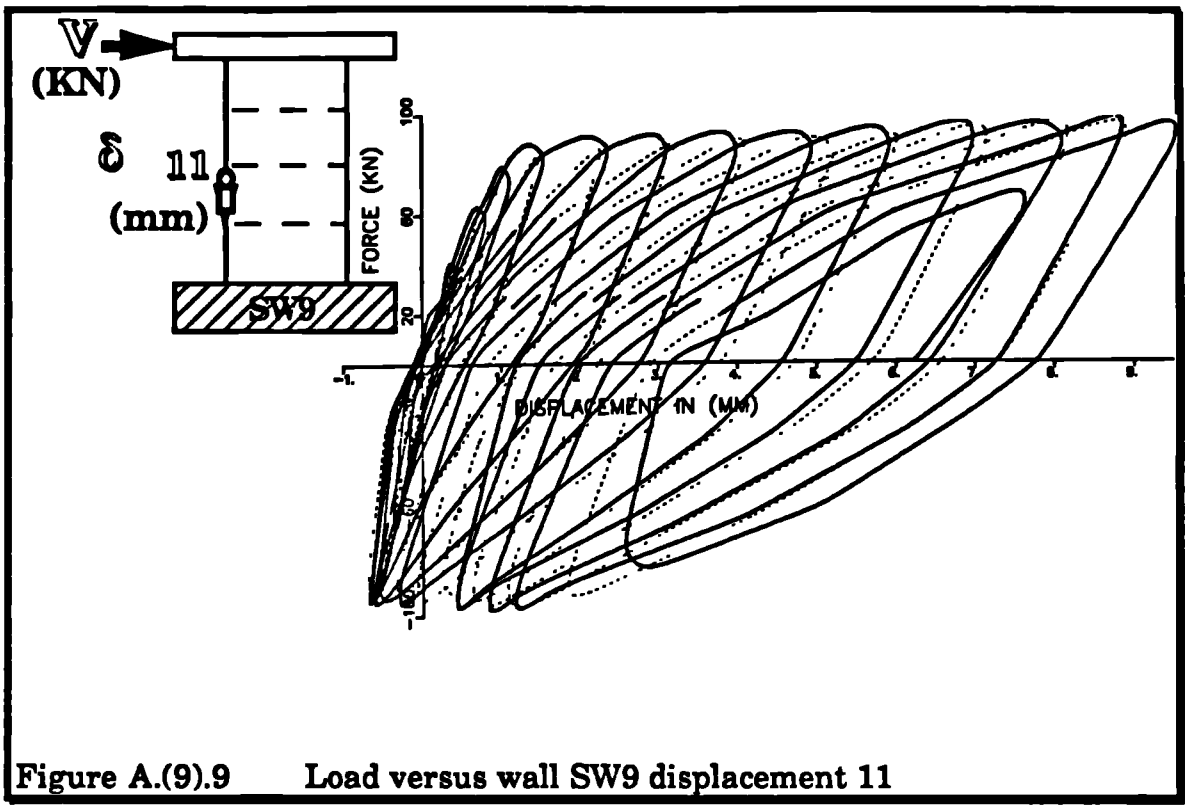


Figure A.(9).9 Load versus wall SW9 displacement 11

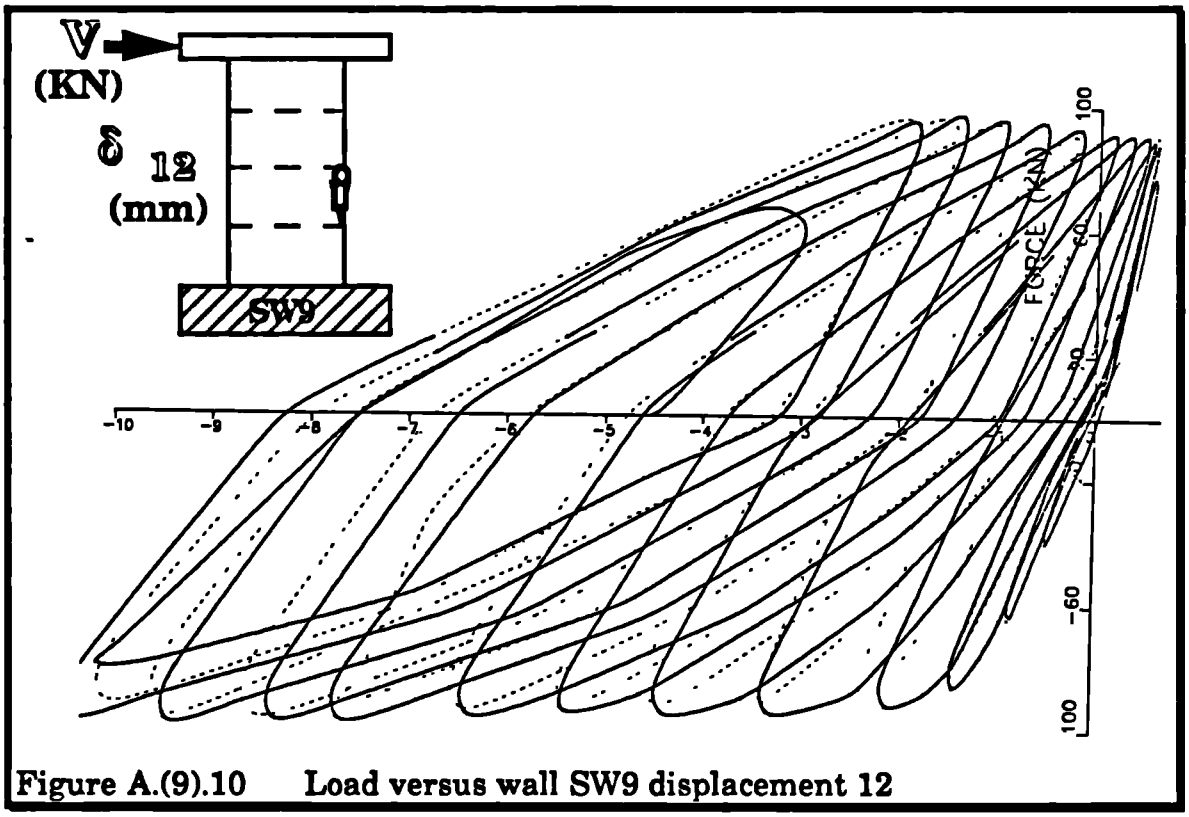


Figure A.(9).10 Load versus wall SW9 displacement 12

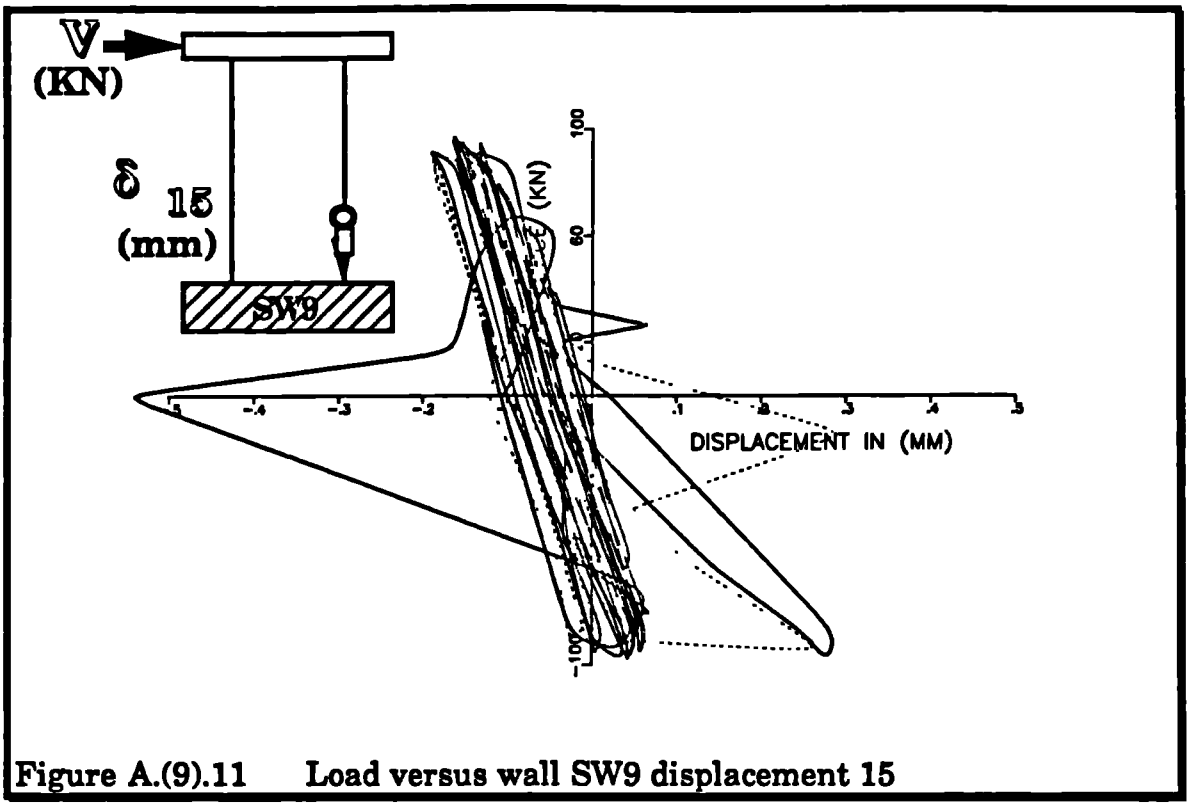


Figure A.(9).11 Load versus wall SW9 displacement 15

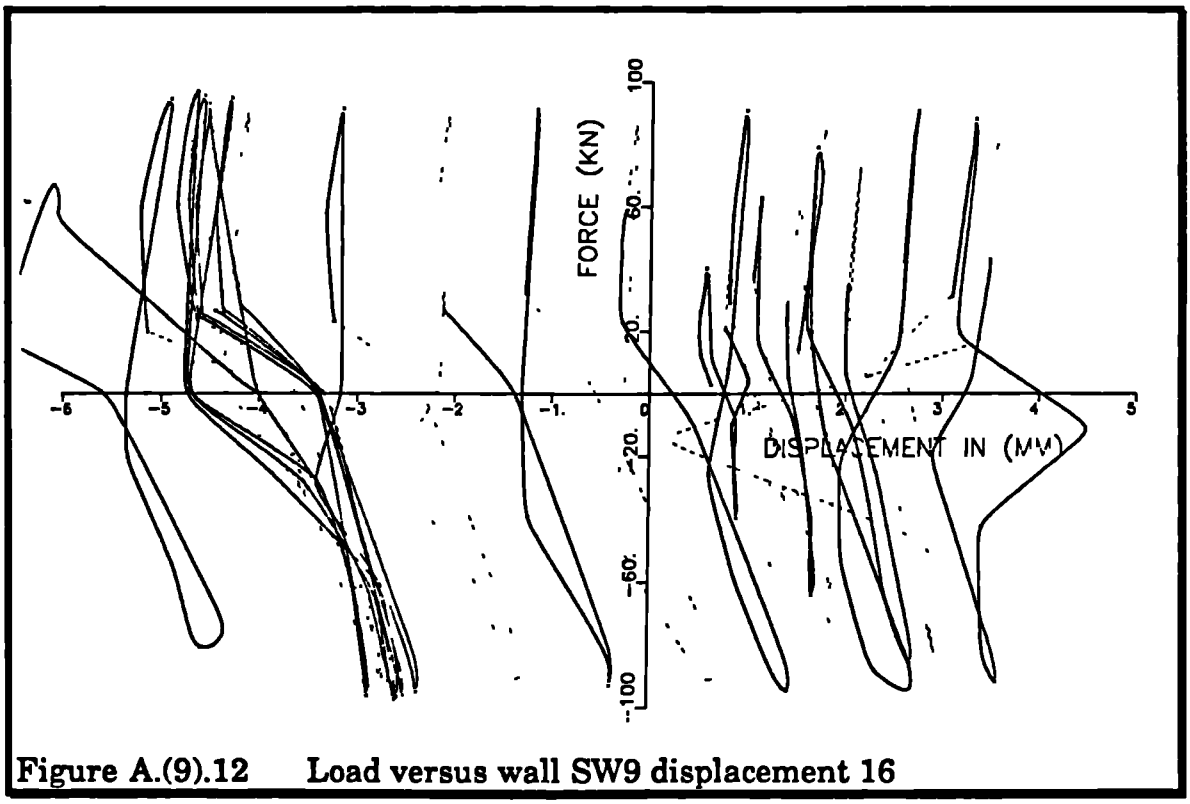


Figure A.(9).12 Load versus wall SW9 displacement 16

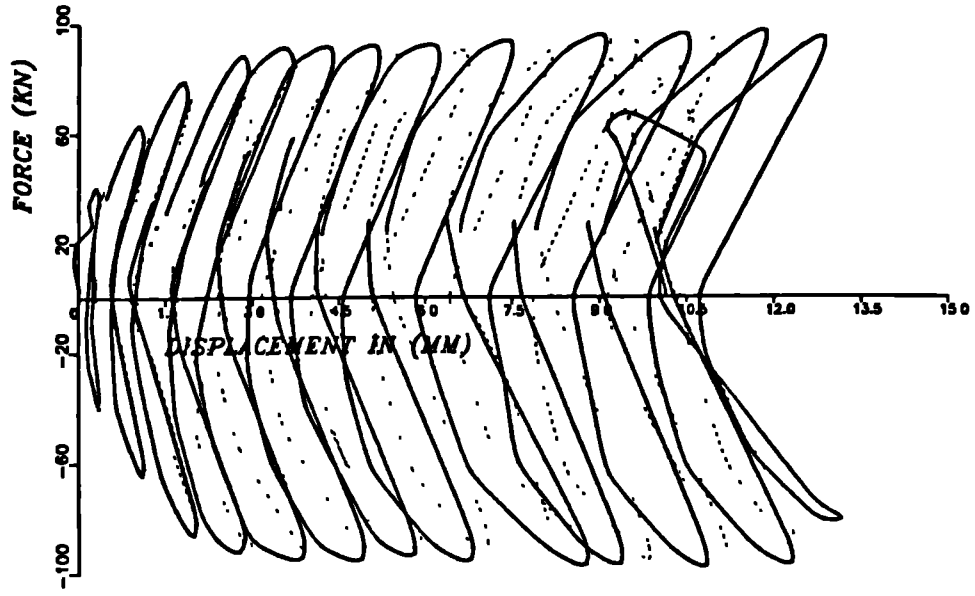


Figure A.(9).13 Load versus wall SW9 top wall average vertical displacement

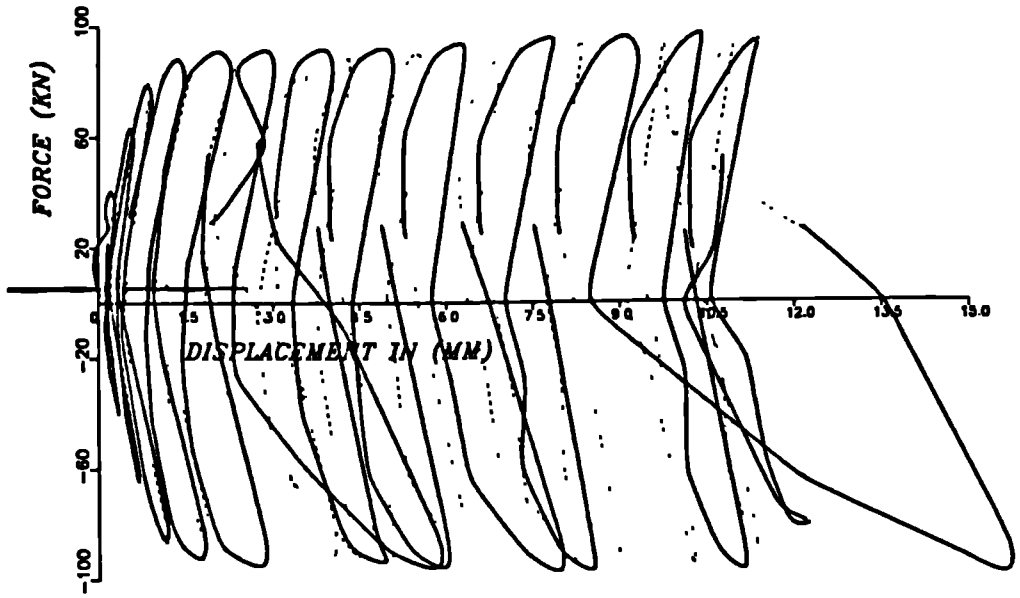


Figure A.(9).14 Load versus wall SW9 mid heigth average vertical displacement

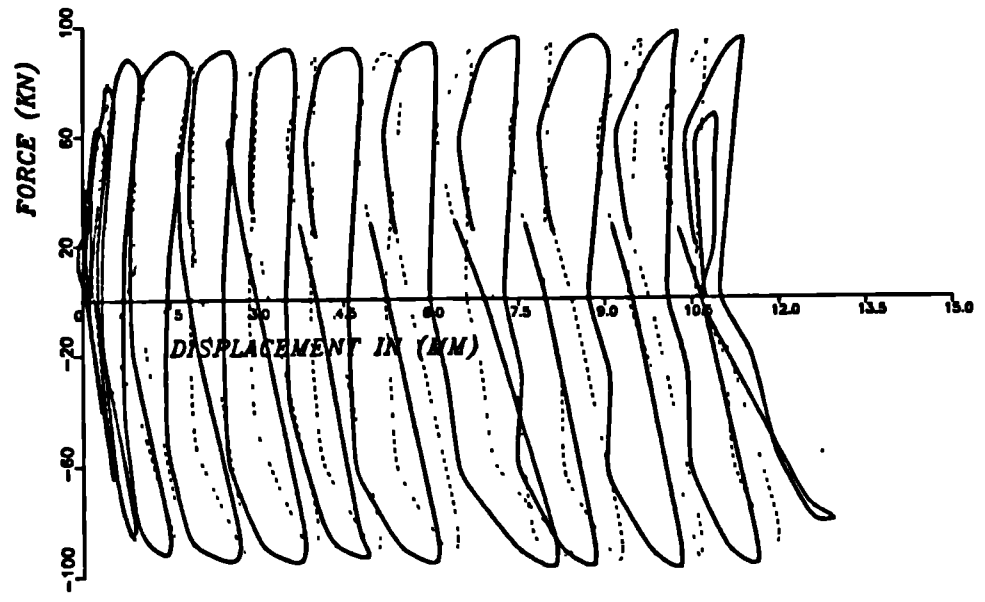


Figure A.(9).15 Load versus wall SW9 quarter heigth average vertical displacement

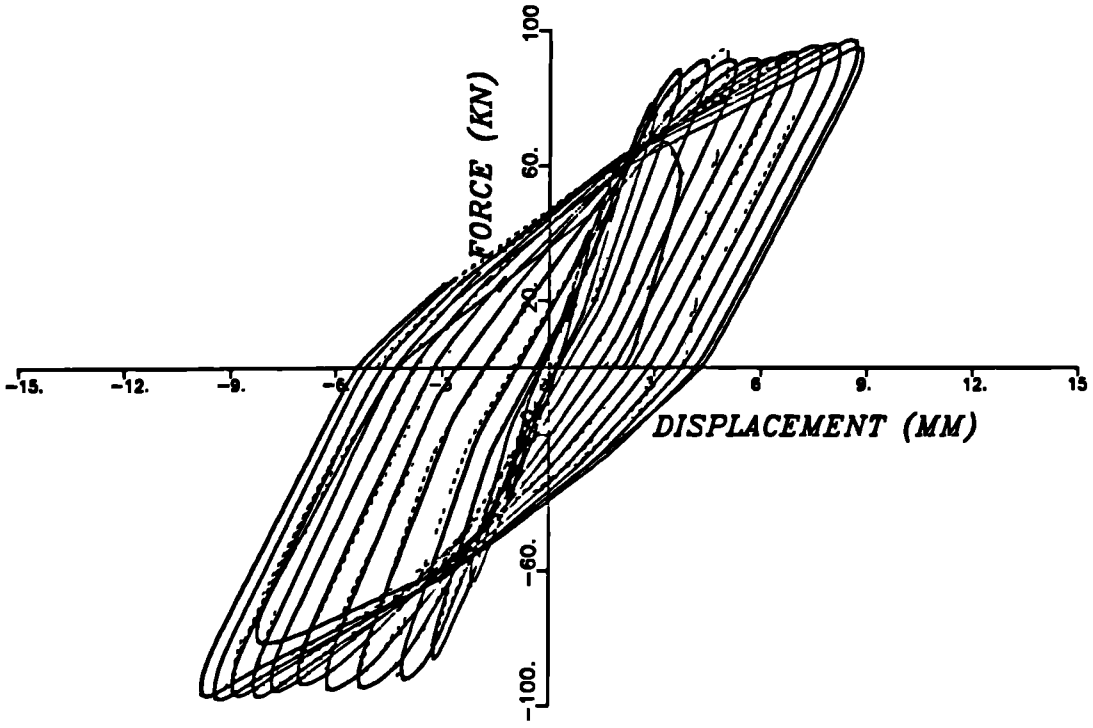


Figure A.(9).16 Force versus flexural component of top horizontal displacement $\delta_{f\varepsilon 1}$ by using method of area $\varepsilon 1$

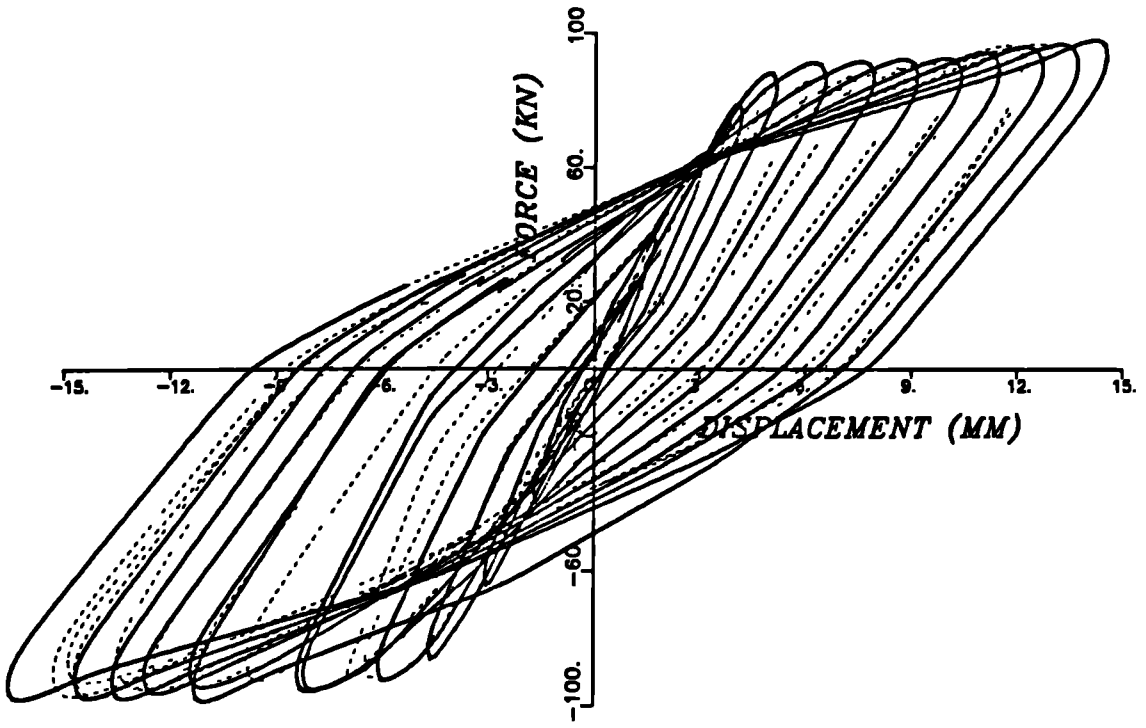


Figure A.(9).17 Force versus flexural component of top horizontal displacement $\delta_{f\varepsilon 2}$ by using method of area ε2

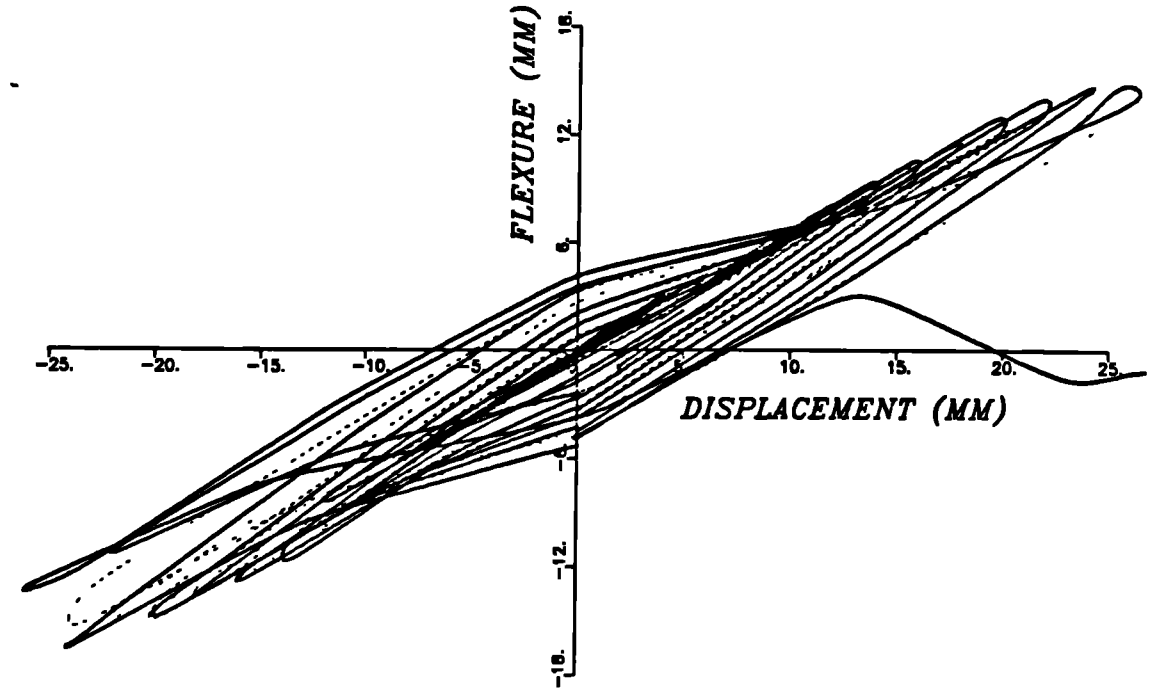


Figure A.(9).18 Top displacement δ_3 versus flexural component of top horizontal displacement $\delta_{f\varepsilon 2}$ by using method of area ε2

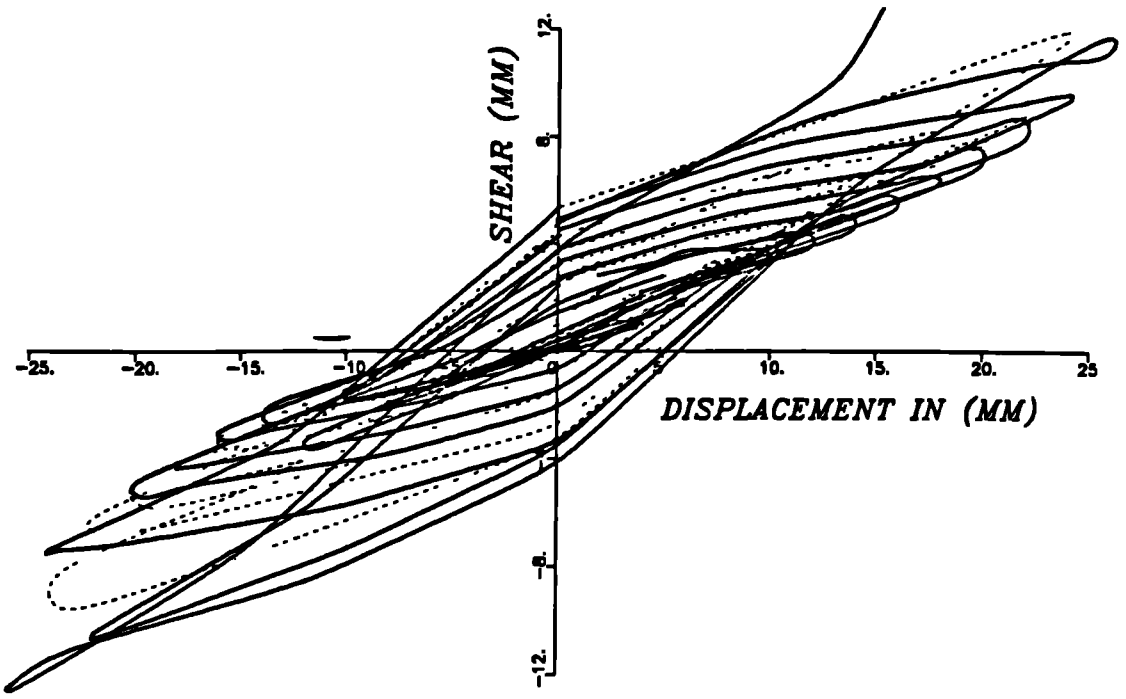


Figure A.(9).19 Top displacement versus shear component of top horizontal displacement by using method of area $\mathfrak{a}2$

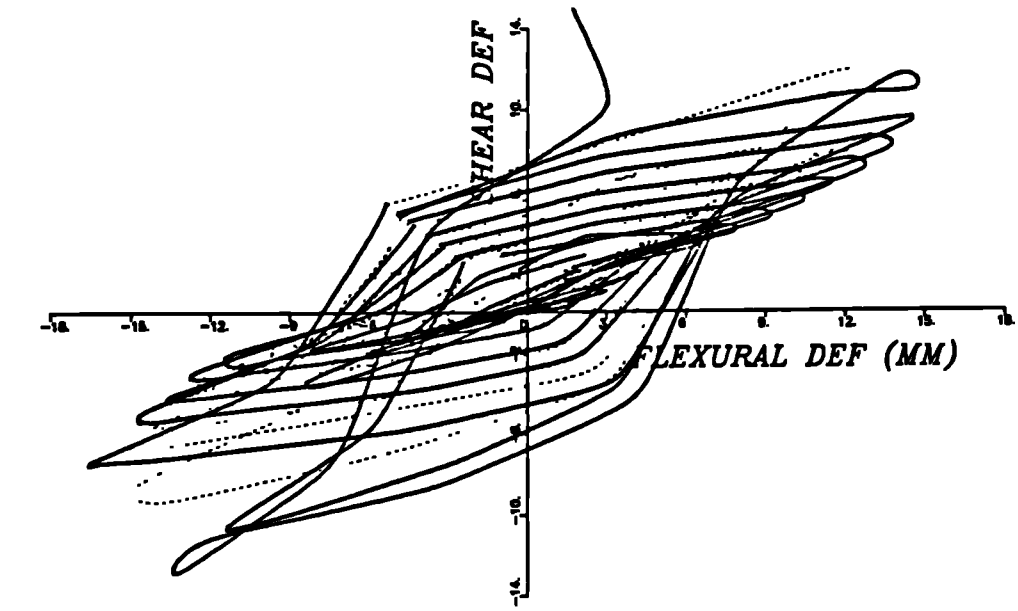


Figure A.(9).20 Flexural displacement $\delta_{f\mathfrak{a}2}$ versus shear component of top horizontal displacement by using method of area $\mathfrak{a}2$

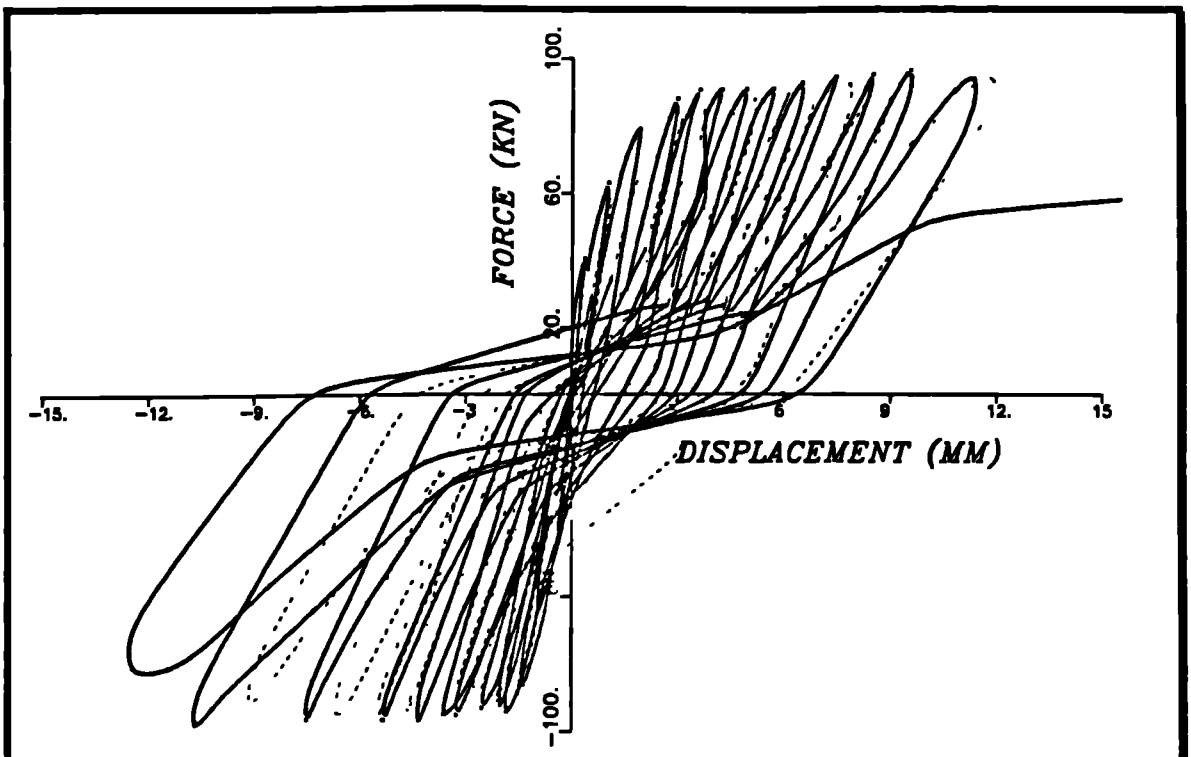
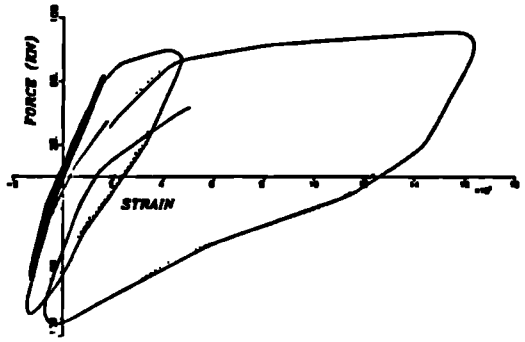


Figure A.(9).21 Force versus shear component of top horizontal displacement by using method of area ε2

A.(9) Strain gauge results



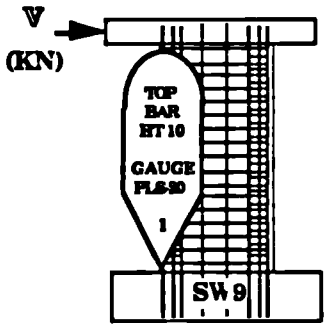
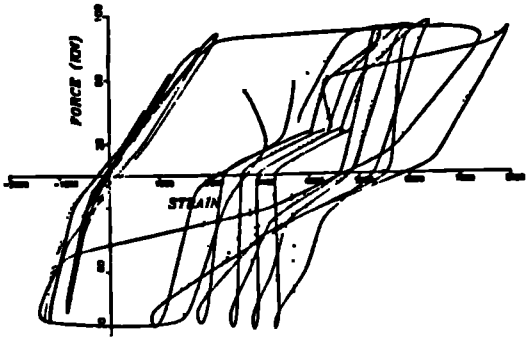


Figure A.(9).22 Load versus strain 1



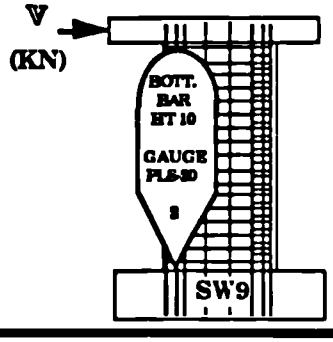


Figure A.(9).23 Load versus strain 2

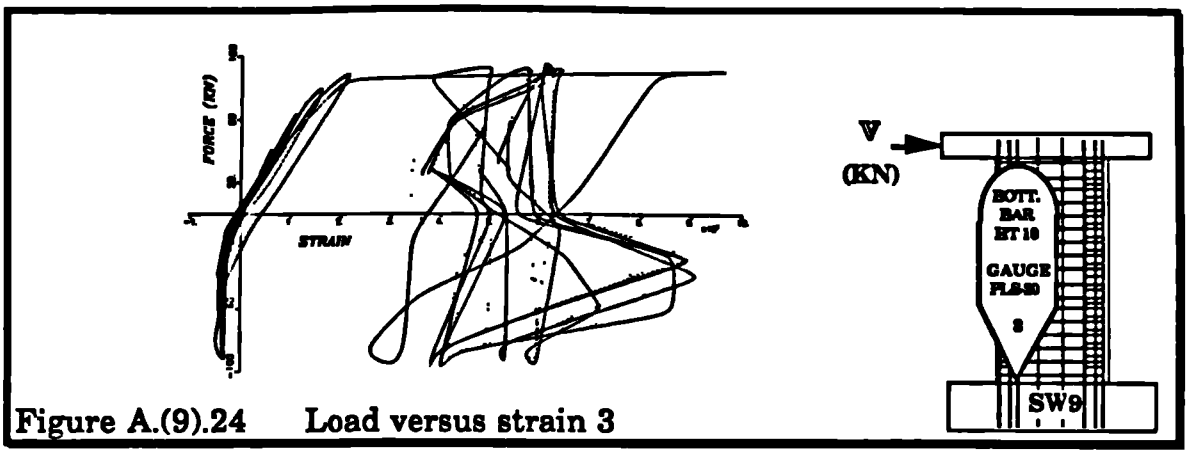


Figure A.(9).24 Load versus strain 3

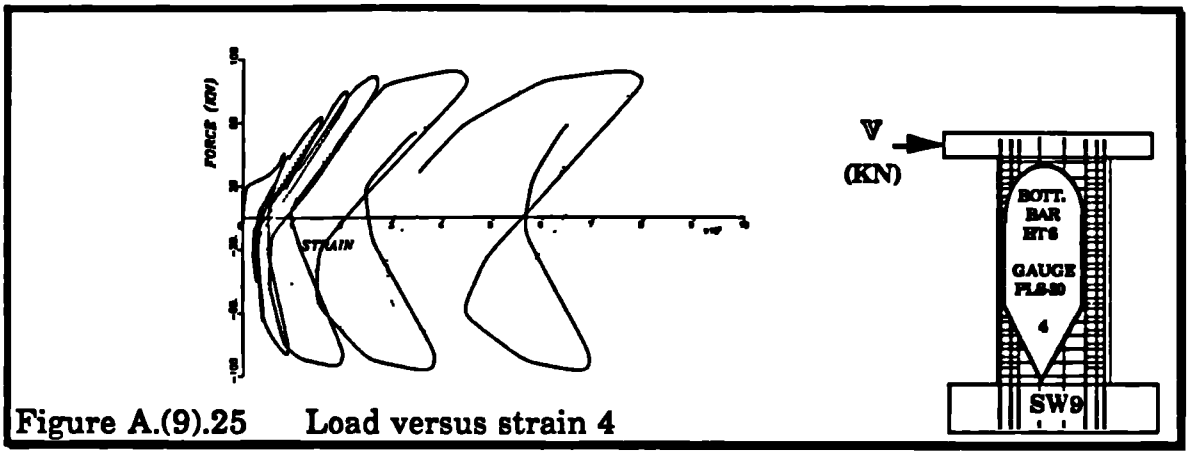


Figure A.(9).25 Load versus strain 4

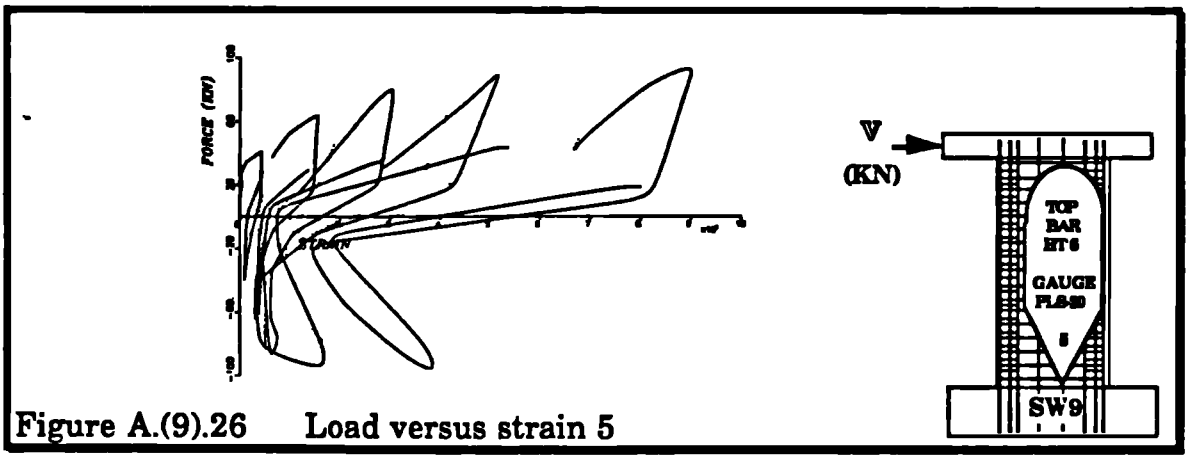


Figure A.(9).26 Load versus strain 5

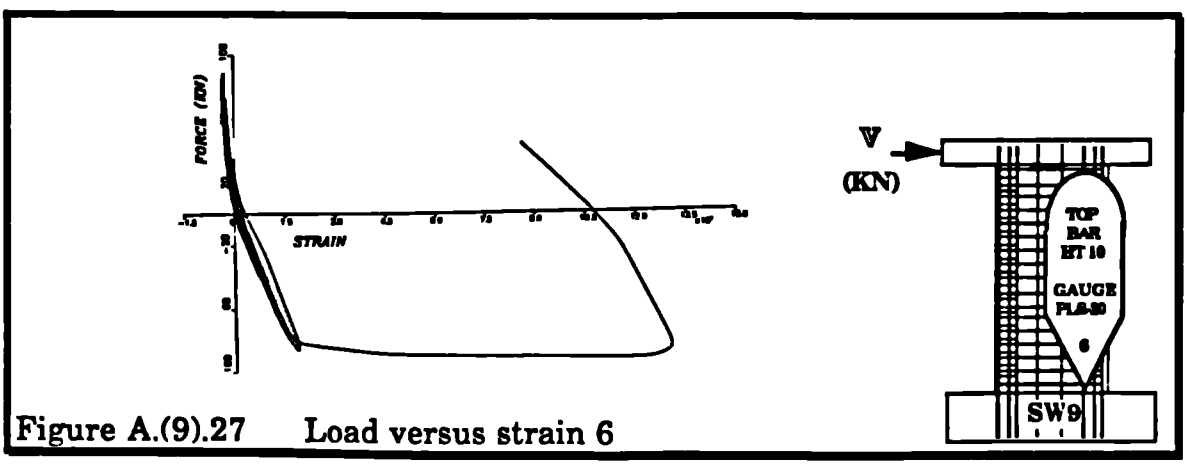
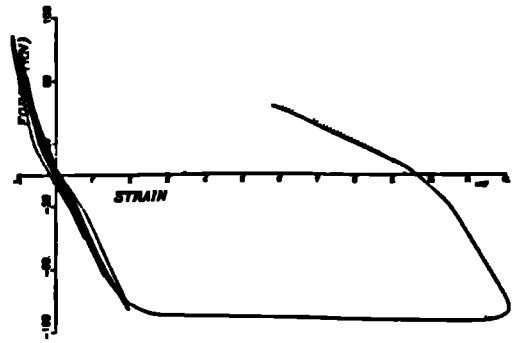


Figure A.(9).27 Load versus strain 6



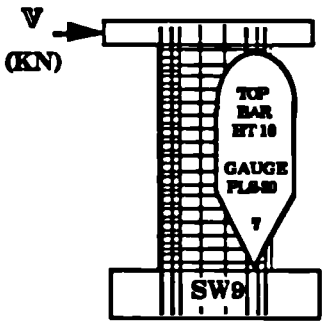
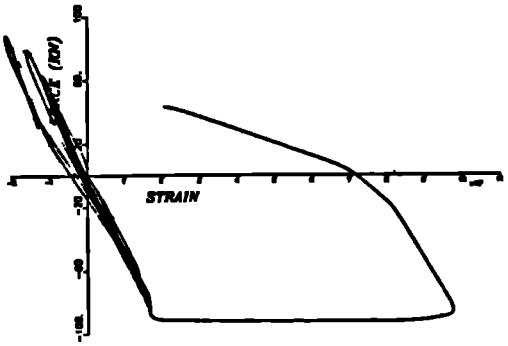


Figure A.(9).28 Load versus strain 7



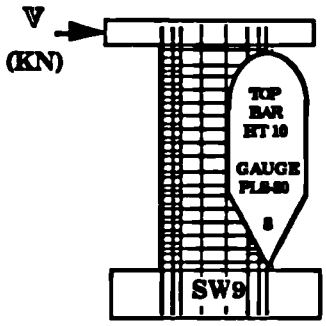
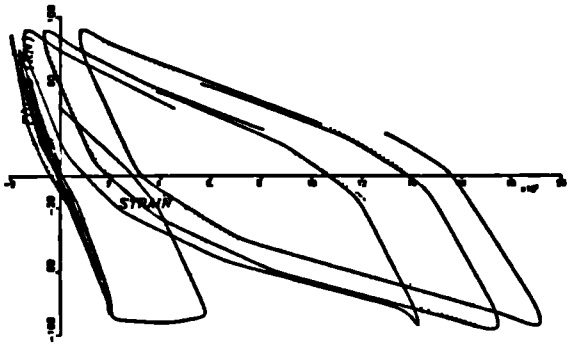


Figure A.(9).29 Load versus strain 8



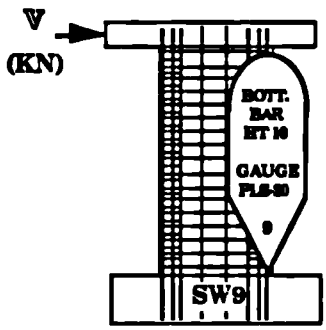
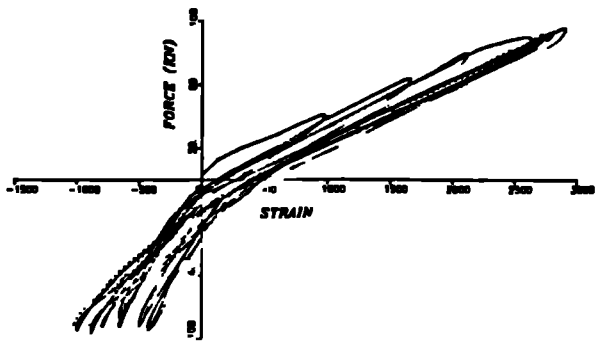


Figure A.(9).30 Load versus strain 9



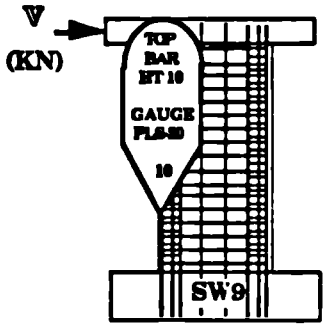
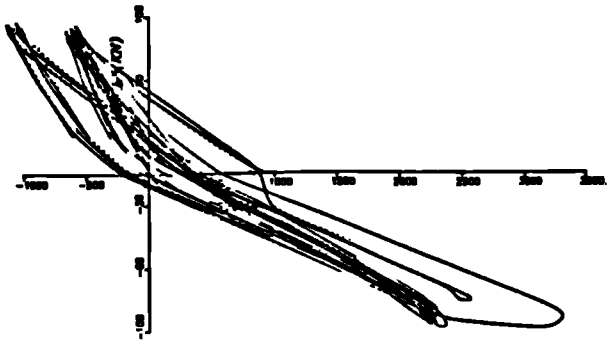


Figure A.(9).31 Load versus strain 10



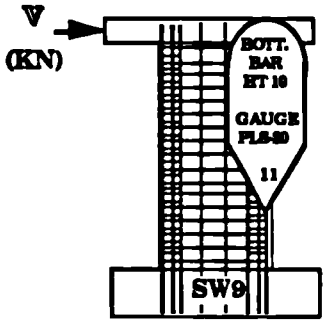
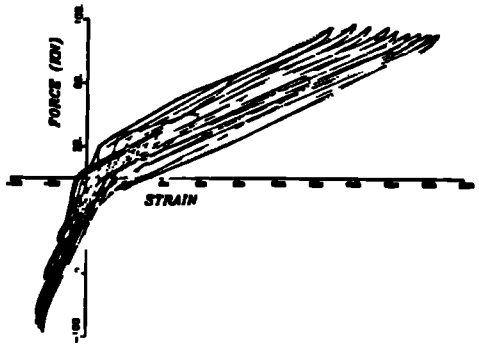


Figure A.(9).32 Load versus strain 11



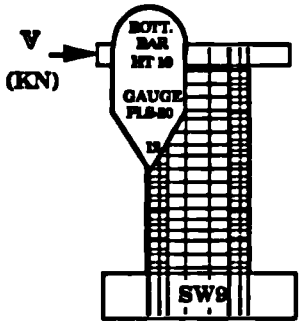
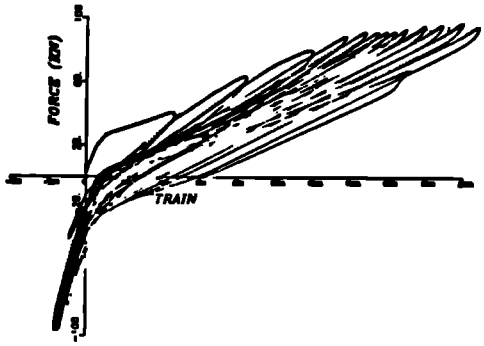


Figure A.(9).33 Load versus strain 12



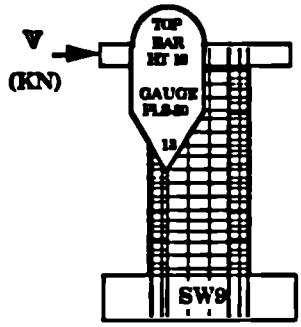
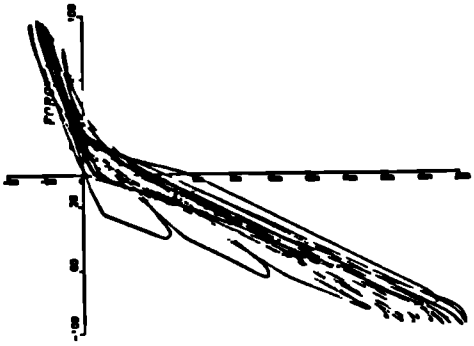


Figure A.(9).34 Load versus strain 13



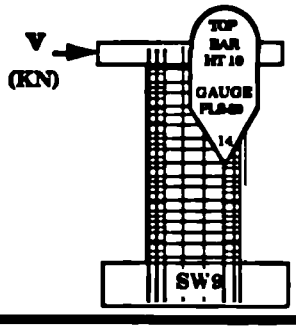
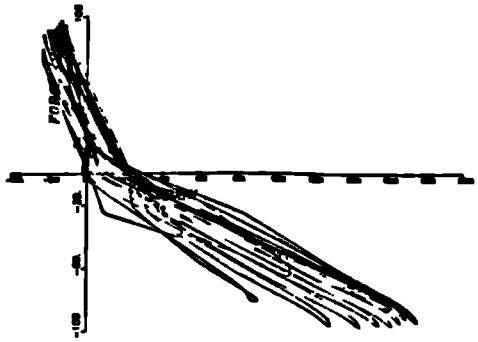


Figure A.(9).35 Load versus strain 14



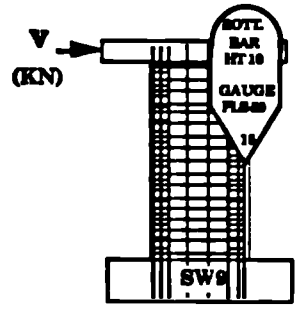
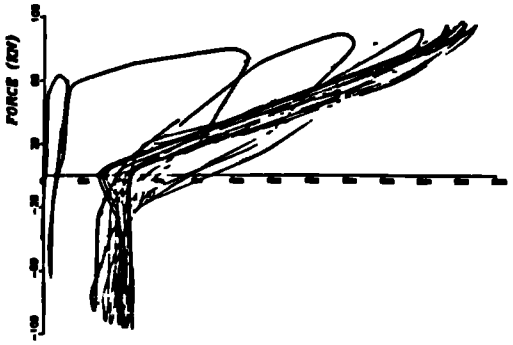


Figure A.(9).36 Load versus strain 15



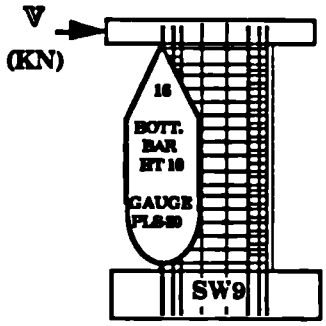
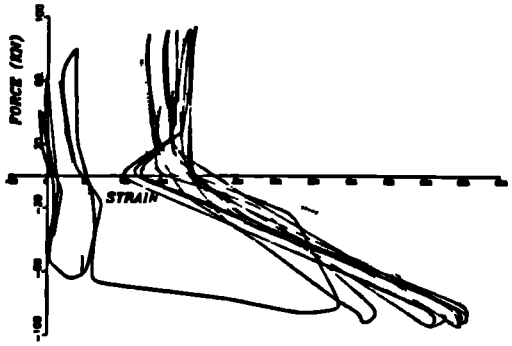


Figure A.(9).37 Load versus strain 16



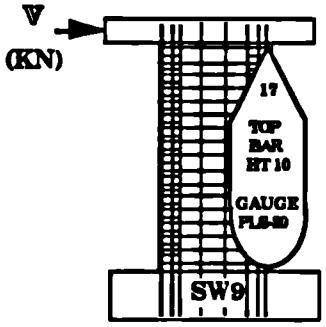
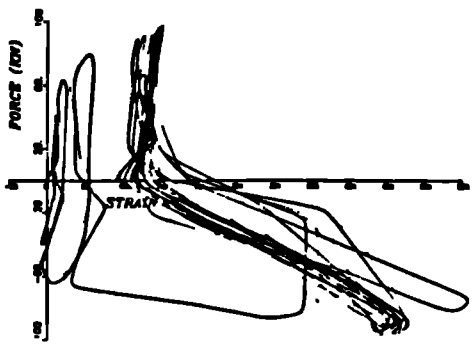


Figure A.(9).38 Load versus link strain 17



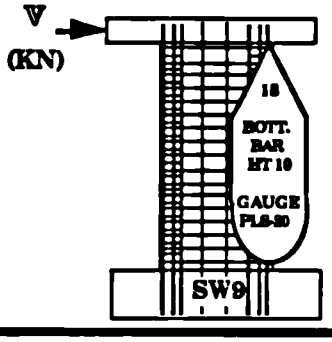


Figure A.(9).39 Load versus strain 18

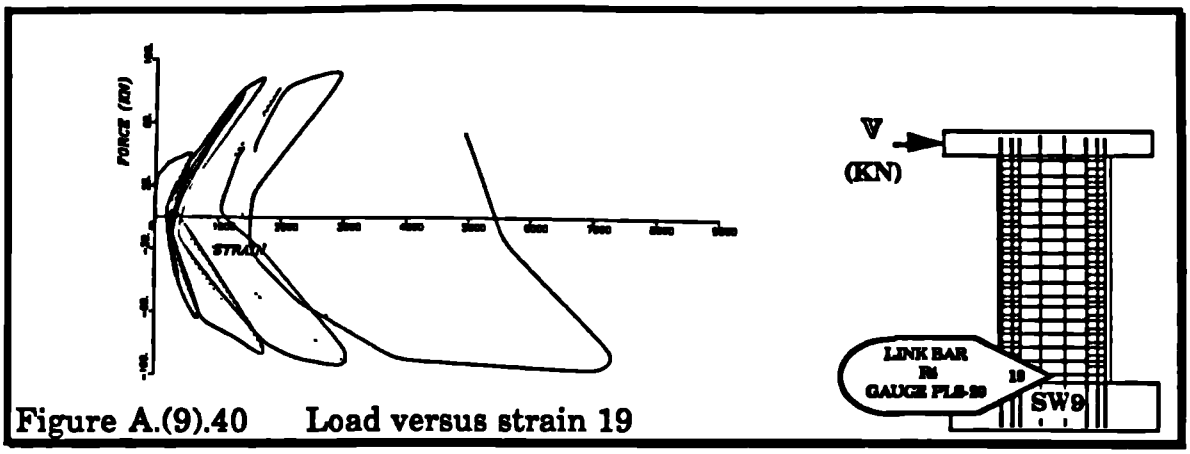


Figure A.(9).40 Load versus strain 19

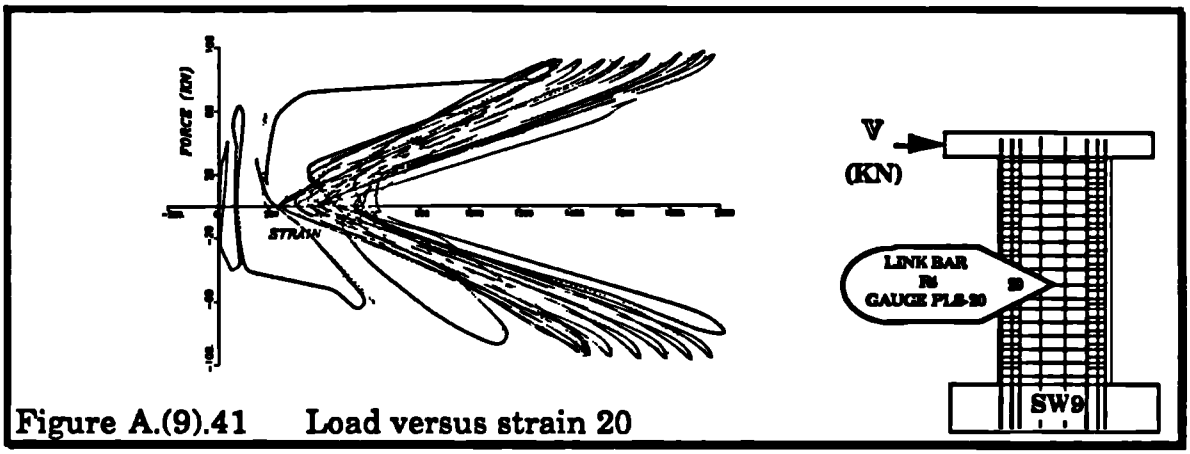


Figure A.(9).41 Load versus strain 20

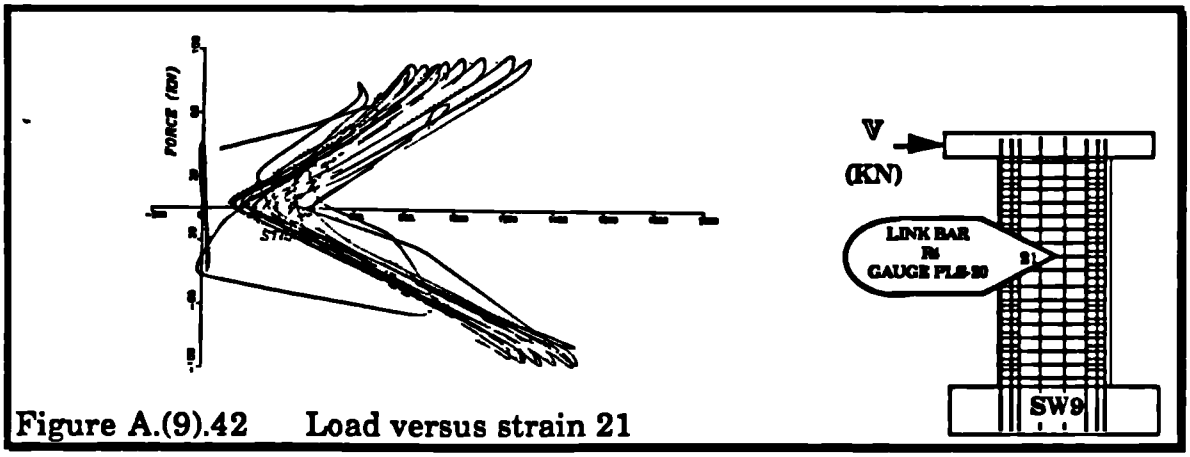


Figure A.(9).42 Load versus strain 21

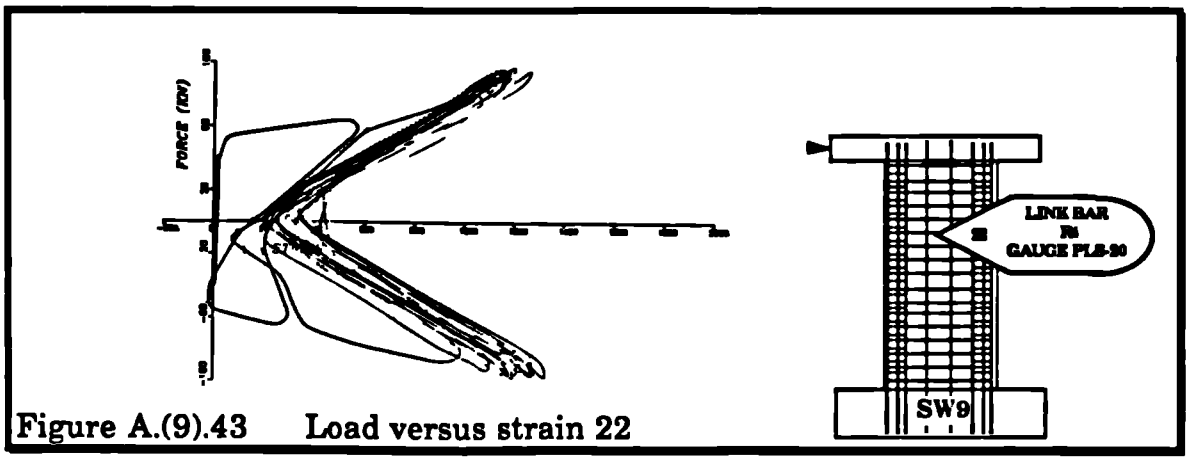
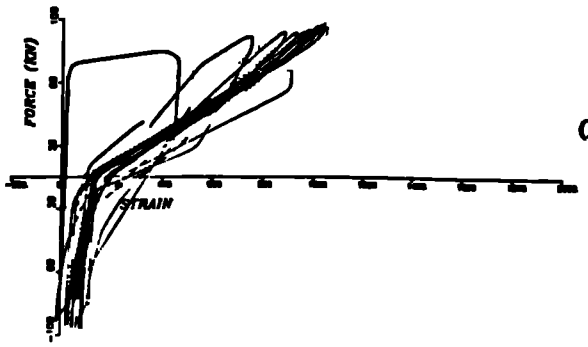


Figure A.(9).43 Load versus strain 22



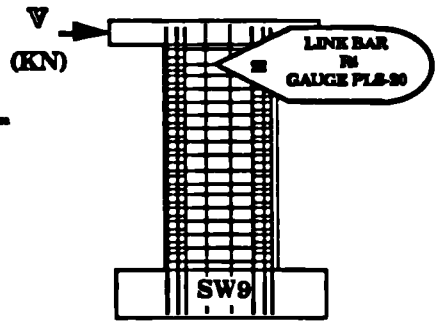


Figure A.(9).44 Load versus strain 23

APPENDIX B

B Reinforced Concrete Analysis Model Results

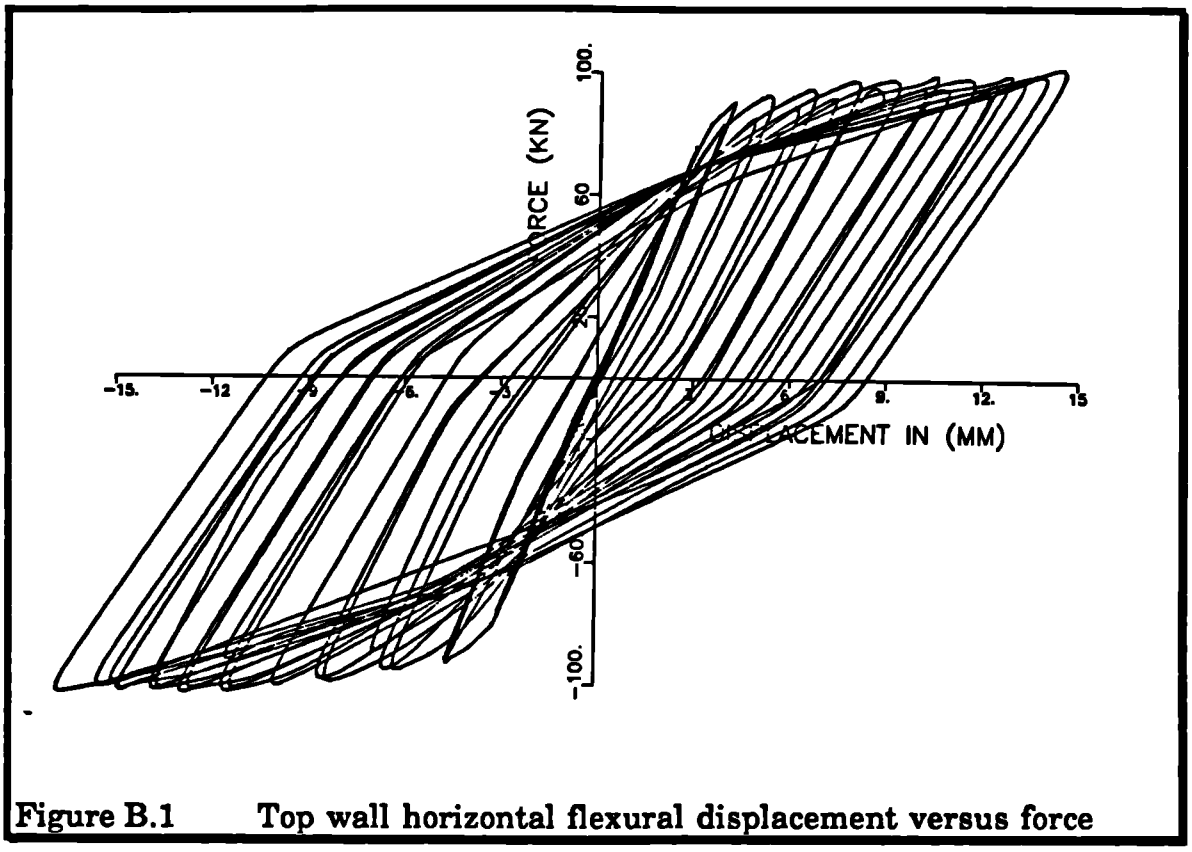


Figure B.1 Top wall horizontal flexural displacement versus force

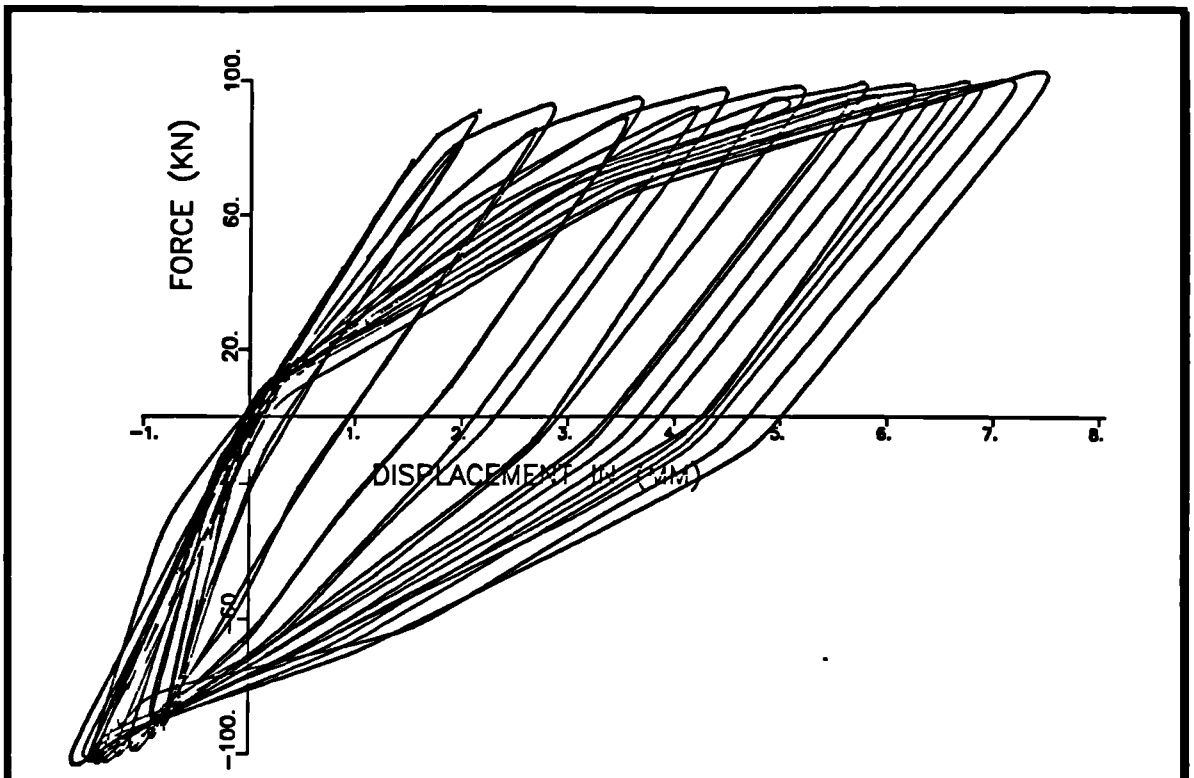


Figure B.2 Top wall vertical displacement versus force

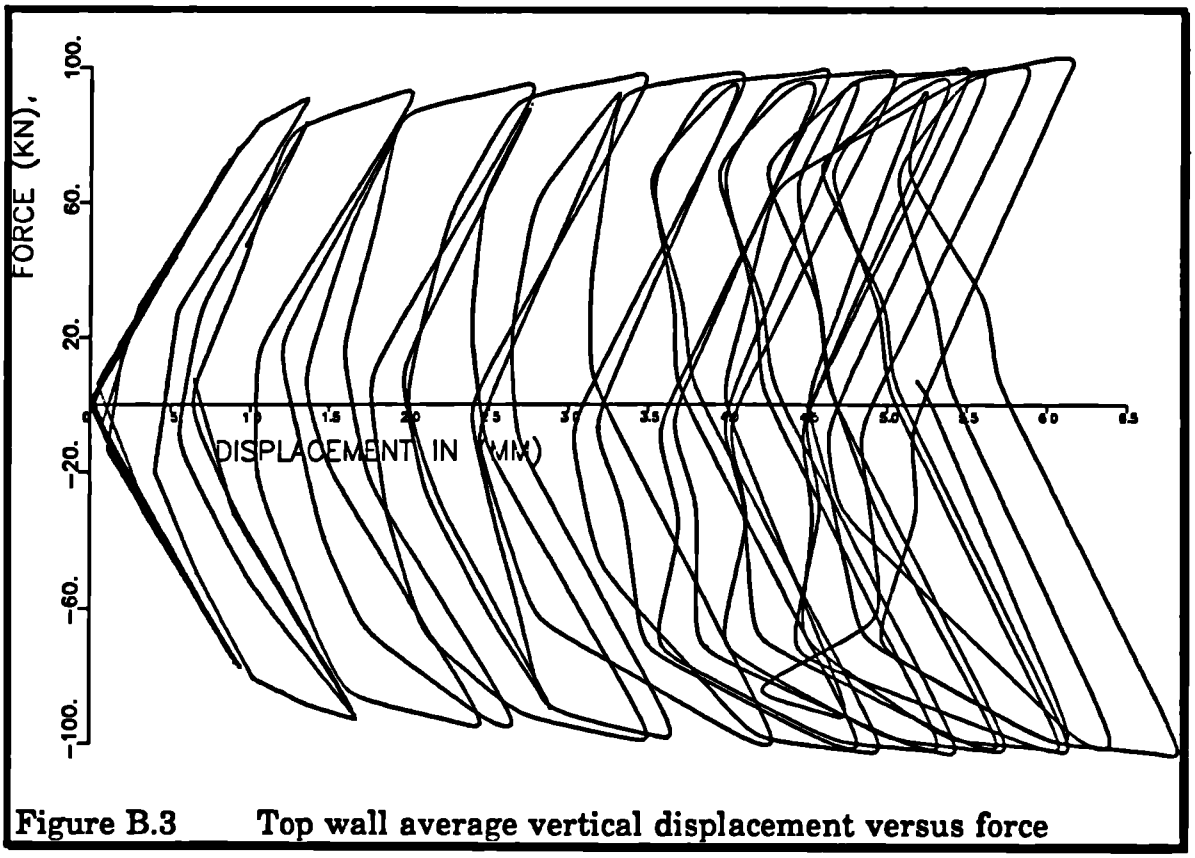


Figure B.3 Top wall average vertical displacement versus force

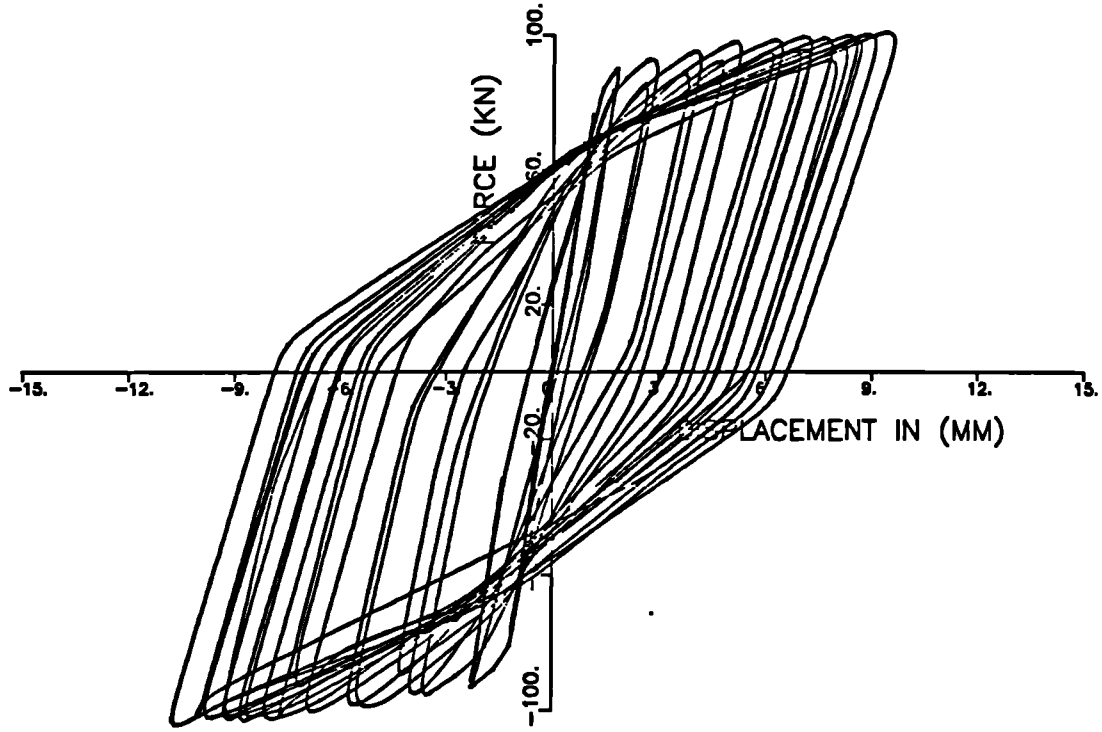


Figure B.4 Quarter height horizontal flexural displacement versus force

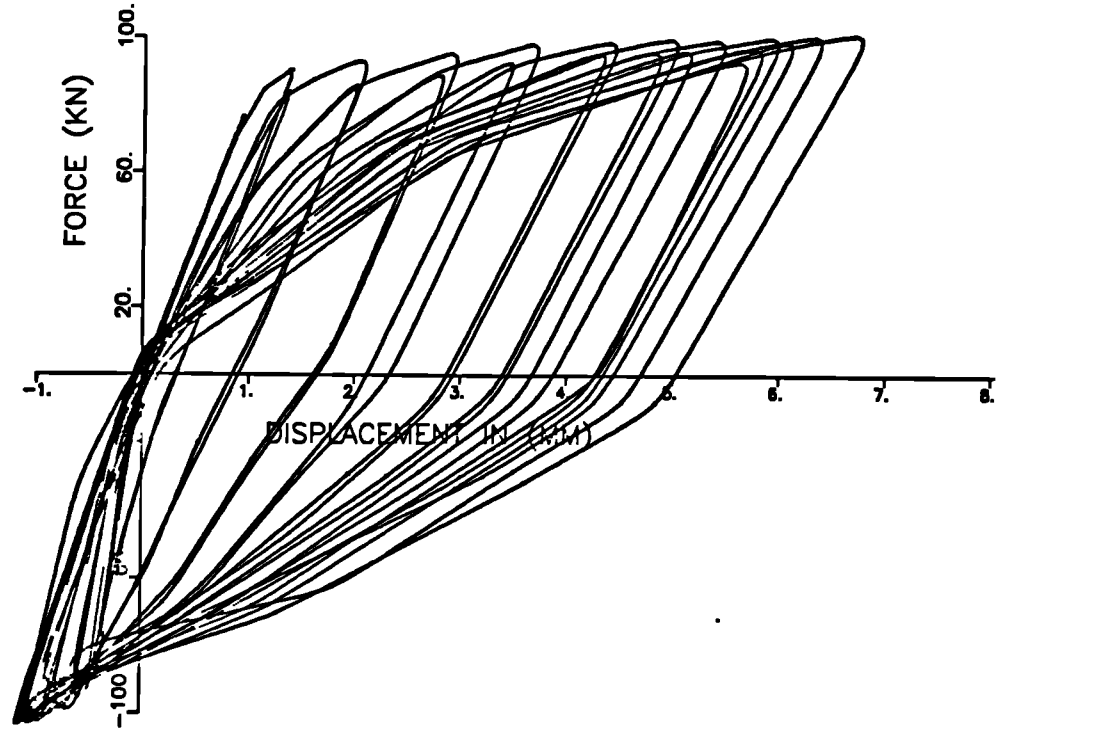


Figure B.5 Quarter height vertical displacement versus force

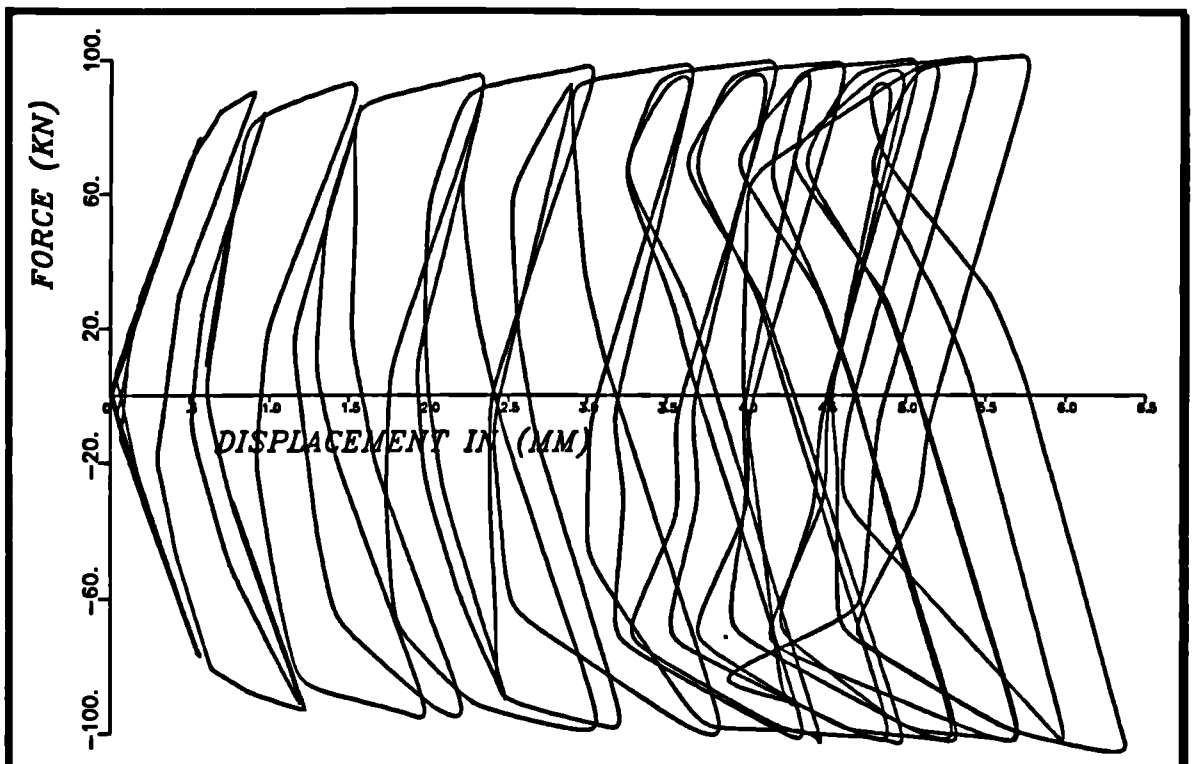


Figure B.6 Quarter height average vertical displacement versus force

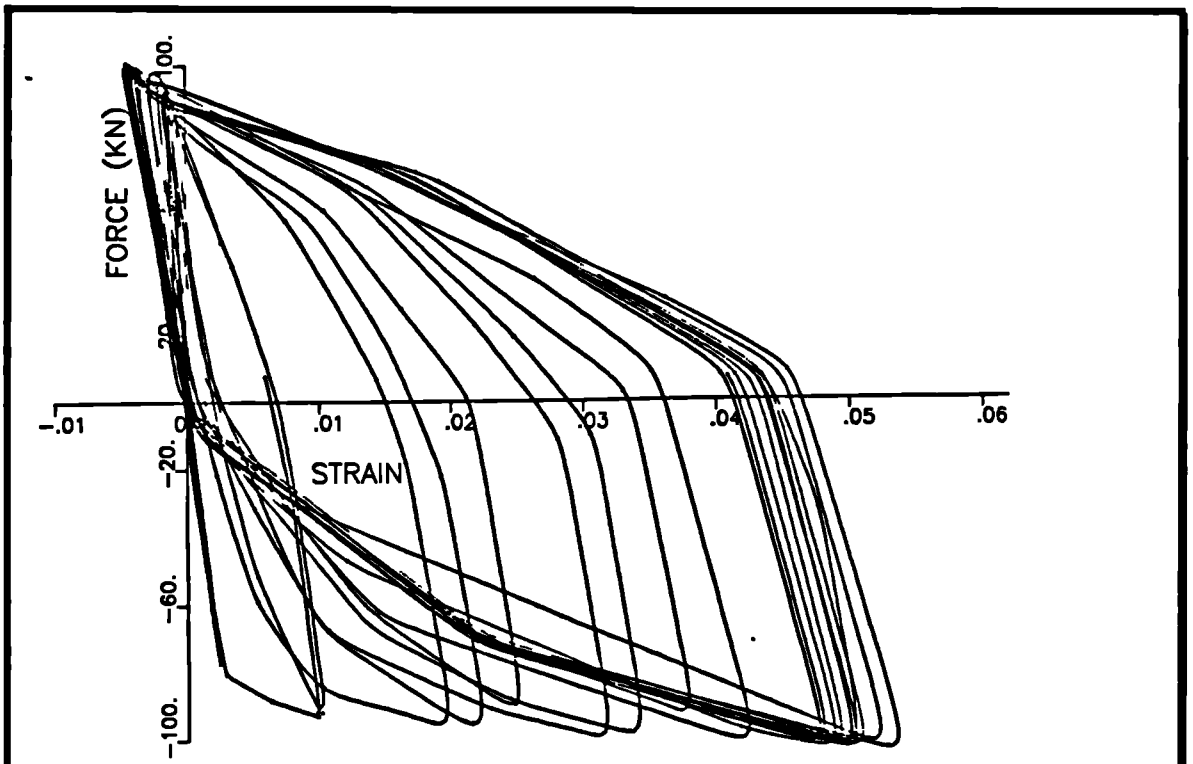


Figure B.7 Bottom strain 1 versus force

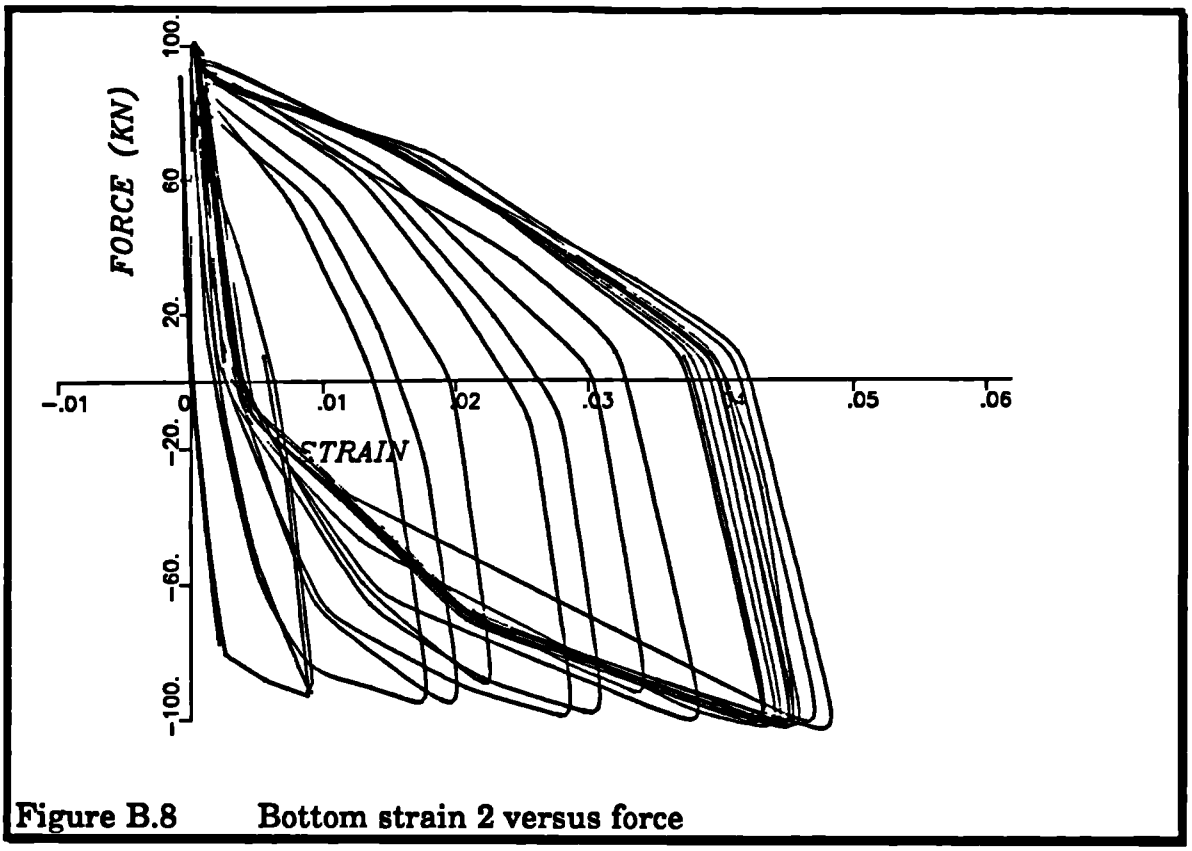


Figure B.8 Bottom strain 2 versus force

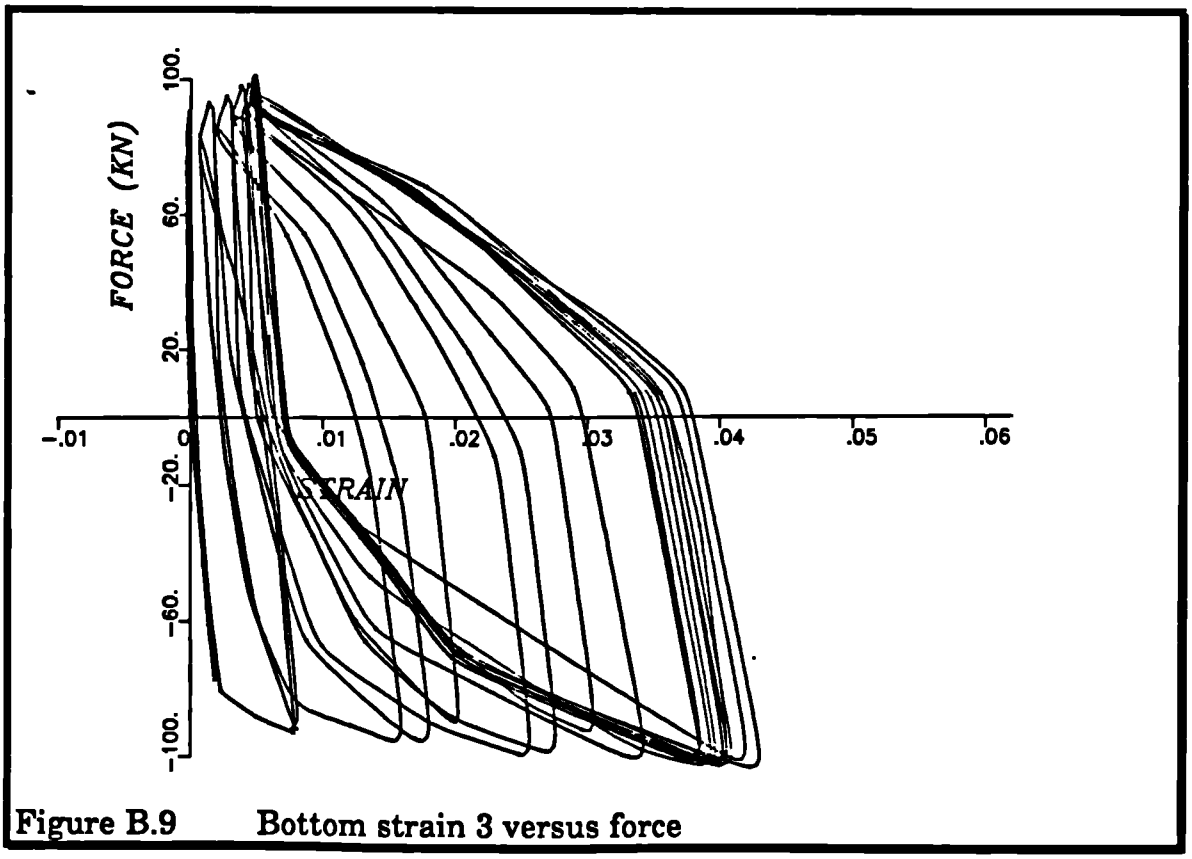


Figure B.9 Bottom strain 3 versus force

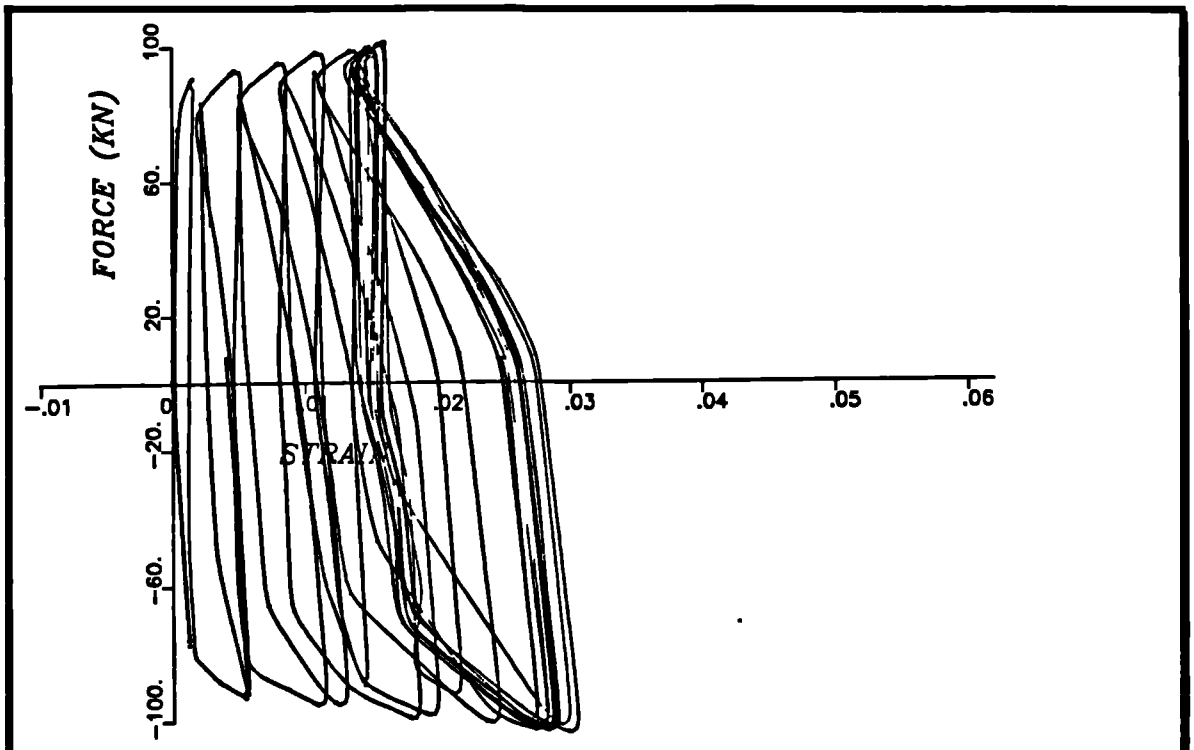


Figure B.10 Bottom strain 4 versus force

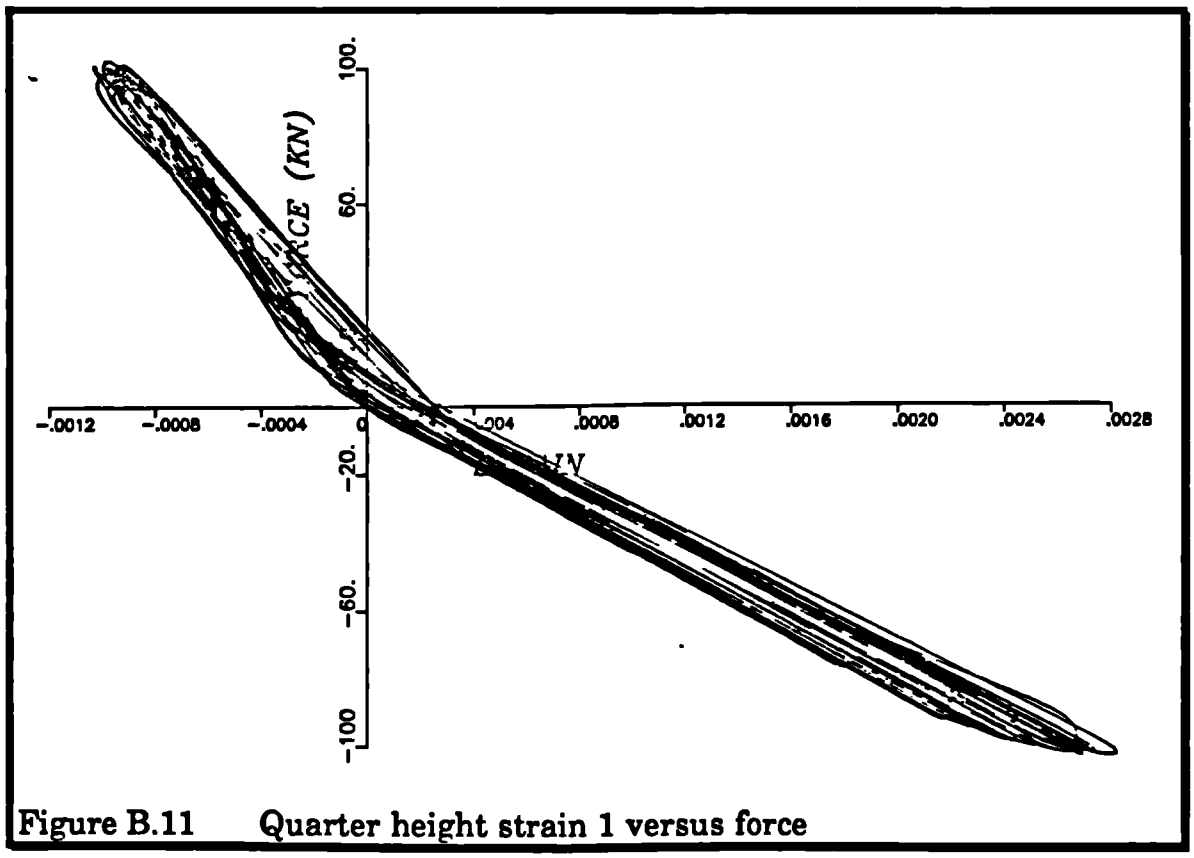


Figure B.11 Quarter height strain 1 versus force

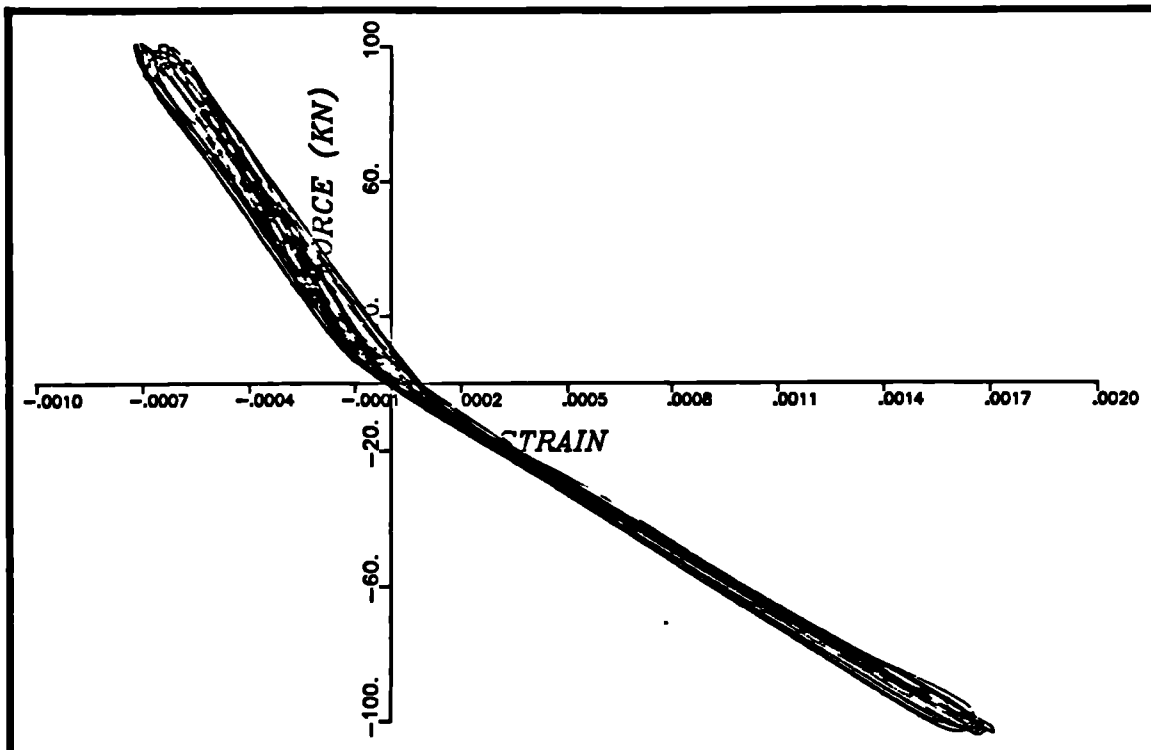


Figure B.12 Top strain 1 versus force

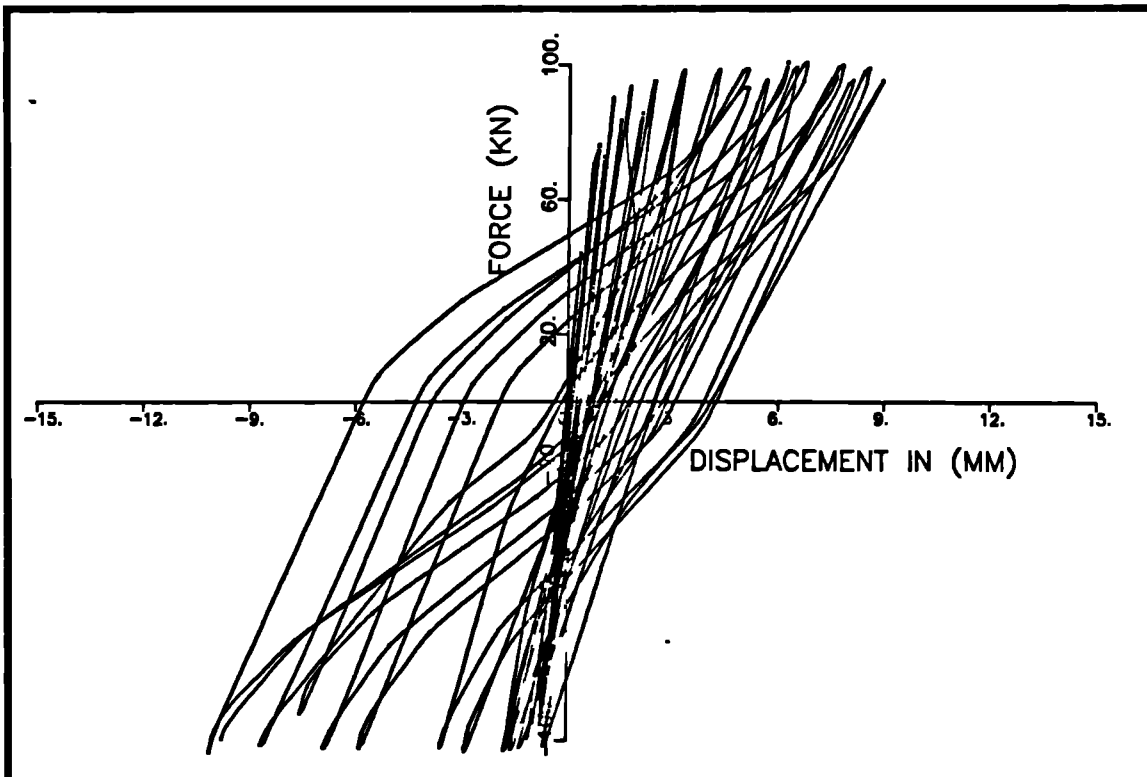


Figure B.13 Force versus shear component of top horizontal displacement

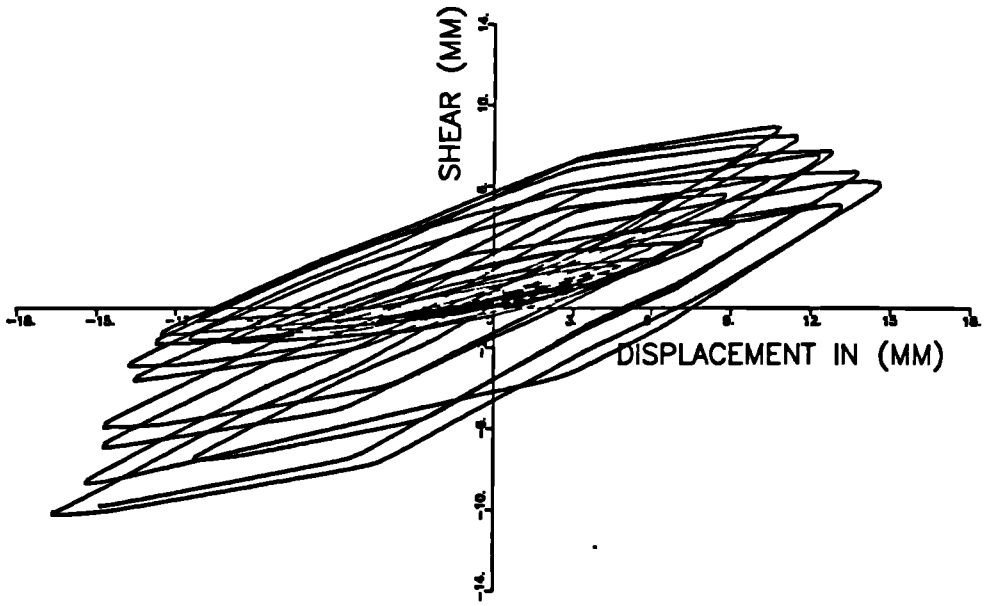


Figure B.14 Flexural displacement versus shear component of top horizontal displacement